East European Journal of Physics. 2. 4–18 (2026)
DOI: 10.26565/2312-4334-2026-2-01 ISSN 2312-4334

EXPLORING BIANCHI TYPE III UNIVERSE WITH QUADRATIC TRACE OF STRESS-ENERGY TENSOR IN $f(R,T)$ THEORY OF GRAVITY

Chandra Rekha Mahanta, **Kankana Pathak***
Department of Mathematics, Gauhati University, Guwahati - 781014 (INDIA)
*Corresponding Author e-mail: kankanapathak@gauhati.ac.in
Received January 22, 2026; revised March 23, 2026; accepted April 6, 2026

In this work, we consider a spatially homogeneous and anisotropic Bianchi type III universe in $f(R,T)$ gravity with the functional form $f(R,T) = f_1(R) + f_2(T)$ with $f_1(R) = \lambda_1 R$ and $f_2(T) = \lambda_2 T + \lambda_3 T^2$, where λ_1, λ_2 and λ_3 are free parameters. We obtain exact solutions of the gravitational field equations by considering a power-law expansion of a directional scale factor. By keeping a check on the current values of the parameters of cosmological significance such as the Hubble parameter H and the deceleration parameter q, the dynamics and physical characteristics of the model are investigated. We also determine the functional form $f(R,T)$ of our model by evaluating the Ricci scalar R and the trace T of the stress-energy tensor. We find that our model remains anisotropic throughout its evolution and the pressure of the cosmic matter remains negative. The equation of state parameter ω is found to lie in the quintessence regime and therefore our model behaves like quintessence model of dark energy.

Keywords: *Bianchi type III space-time; $f(R,T)$ gravity; Deceleration parameter; Hubble parameter*

PACS: 98.80.-k, 98.80.Jk, 95.36.+x
MSC2020 83C10, 83C15

1. INTRODUCTION

Recent advancements in observational astrophysics have significantly improved our understanding of the universe's large-scale dynamics. One of the key discoveries is the observation of high-redshift Type Ia Supernovae (SN Ia) [1, 2], which provide clear evidence that the universe is expanding at an accelerating rate. These supernovae are crucial in cosmological research because their predictable luminosity enables precise distance measurements, shedding light on the evolution of cosmic expansion over time.

Additionally, the study of Cosmic Microwave Background (CMB) radiation [3–5], the remnant heat from the Big Bang, has offered valuable insights into conditions of the early universe. Observations from missions such as the Wilkinson Microwave Anisotropy Probe (WMAP) [6–9] have delivered detailed maps of temperature variations in the Cosmic Microwave Background, which are instrumental in determining key cosmological parameters and understanding the overall geometry of the universe.

Furthermore, Large Scale Structures (LSS) [10] represents the distribution of galaxies and matter on vast scales which has provided critical information about the growth of cosmic structures under the influence of gravity and dark energy. Complementing this, Baryon Acoustic Oscillations (BAO) [11–13] serve as a standard ruler for measuring cosmic distances, offering additional confirmation of accelerating expansion of the universe.

These diverse observational data points collectively support that the expansion rate of our universe is increasing that challenges the traditional framework of Einstein's General Theory of Relativity (GTR). Since in its original form, GTR cannot fully explain this late time cosmic acceleration. It encouraged the creation of alternate ideas, such as modifications to gravity or the introduction of dark energy. The accelerated expansion remains one of the most intriguing mysteries in modern cosmology, prompting both theoretical and observational efforts to figure out its underlying causes.

Consequently, various efforts have been made to explain the observed acceleration, which can be broadly classified into two main categories: the dark energy approach and the modified gravity approach.

In the first approach, one considers Einstein's theory of General Relativity to be the theory of gravity and modifies the right hand side of the Einstein field equations by supplementing the stress-energy tensor T_{ij} an exotic component with large negative pressure. This can be done because of the fact that the same observational data which reveal the late time cosmic acceleration also exhibit that more than 95% of the total content of the universe is in the form of some yet unknown components of energy and matter, dubbed dark energy and dark matter comprising respectively about 68.3% and 26.8% of the total matter-energy allocation of the universe. The existence of such an unusual component with large negative pressure, called dark energy, is to be considered to counteract the gravitational pressure of the baryonic matter which contributes positive pressure that decelerates the expansion rate of the universe. Many dark energy candidates are proposed in the literature, the most favored one being the cosmological constant Λ introduced by Einstein in his field equations. However, the cosmological constant Λ as a candidate of dark energy suffers from some theoretical challenges such as its constant equation of state parameter $\omega = -1$, fine-tuning, cosmic coincidence problems etc. So dynamically evolving

Cite as: C. R. Mahanta, K. Pathak, East Eur. J. Phys. 2, 4 (2026), https://doi.org/10.26565/2312-4334-2026-2-01

scalar field models of dark energy such as quintessence [14], k-essence [15], tachyon [16], phantom [17], Holographic Dark Energy (HDE) [18–20], Chaplygin gas model [21–23] etc. have been proposed in the literature.

In the second approach, modified gravity models are constructed by modifying the gravitational part of the Einstein-Hilbert action. This can be done as the fundamental concept of General Relativity is the curvature of space-time described by the Ricci scalar R. There are a number of modified gravity models available in the literature, the simplest and the most studied one being the $f(R)$ theory of gravity [24] which is constructed by replacing the Ricci scalar R in the standard Einstein-Hilbert action by some general function $f(R)$ of R. Some other modified theories of gravity employed in the study of rapid expansion of the universe are $f(R,T)$ gravity [25], $f(G)$ gravity [26], $f(T)$ gravity [27], $f(Q)$ gravity [28] etc. The $f(R,T)$ theory of gravity, proposed by Harko *et al.* [25], has received a lot of attention from researchers as this theory takes care of the early time rapid expansion, called inflation, as well as the current cosmic acceleration. In this theory, the gravitational Lagrangian is an arbitrary function of R and T, where R is the Ricci scalar and T is the trace of the stress-energy tensor T_{ij} the dependence of which may be induced from exotic imperfect fluids or quantum effects. In their work, Harko *et al.* derived gravitational field equations from a variational, Einstein-Hilbert type, principle and presented field equations for the following three explicit forms of the function $f(R,T)$: $f(R,T) = R+2f(T)$, $f(R,T) = f_1(R) + f_2(T)$ and $f(R,T) = f_1(R) + f_2(R)f_3(T)$ where $f_1(R)$, $f_2(R)$ are arbitrary functions of R and $f(T)$, $f_2(T)$, $f_3(T)$ are arbitrary functions of T.

They have also derived the equations of motion of test particles by considering the stress-energy tensor to be conserved in $f(R,T)$ theory of gravity and investigated the constraints on the magnitude of extra-acceleration on the precession of the perihelion of Mercury with the Newtonian limits. Soon after, a number of authors considered the $f(R,T)$ theory of gravity and studied various aspects of this theory in different contexts. Houndjo [29] developed a cosmological model using $f(R,T)$ gravity and discussed the transition of the universe from a matter-dominated phase to its current phase with accelerating expansion. Sahoo *et al.* [30] studied the anisotropic Bianchi III cosmological model in $f(R,T)$ gravity. Samanta and Bishi [31] explored astrophysical parameters like look-back time, luminosity distance, and jerk parameter of the Bianchi type III model in $f(R,T)$ gravity with wet dark fluid. Arora *et al.* [32] investigated late-time viscous cosmology in $f(R,T)$ gravity. Many other authors have explored different aspects of cosmology within the framework of $f(R,T)$ gravity. Mahanta *et al.* [33, 34] have studied cosmological models in $f(R,T)$ theory of gravity. Most of these studies are conducted in a spatially homogeneous and anisotropic background. This is because, although the current universe appears homogeneous and isotropic on a large scale, recent data from the Cosmic Microwave Background (CMB) and observations of large-scale structures support the idea that the universe was once anisotropic before evolving into its current isotropic state.

In this work, we investigate a spatially homogeneous and anisotropic Bianchi type III cosmological model within the framework of $f(R,T)$ gravity, using the functional form $f(R,T) = f_1(R) + f_2(T)$, where $f_1(R) = \lambda_1 R$ and $f_2(T) = \lambda_2 T + \lambda_3 T^2$. Here, λ_1, λ_2, and λ_3 are free parameters. The paper is organized as follows: In section 2, we present the gravitational field equations for this functional form using the metric formalism, assuming the matter source as a perfect fluid. In section 3, we derive the corresponding field equations for the Bianchi type III metric. In section 4, we obtain exact solutions to these field equations by assuming a power-law expansion in a specific spatial direction. In section 5, we explore the physical characteristics and dynamics of the constructed model by examining the evolution of several cosmologically significant physical parameters. In section 6, we discuss about the functional $f(R,T)$ of our model. Finally, we summarize our results with a brief discussion in section 7.

2. Gravitational field equations for the functional form $f(R,T) = f_1(R) + f_2(T)$

The action for $f(R,T)$ theory of gravity proposed by Harko *et al.* is

$$S = \frac{1}{16\pi}\int f(R,T)\sqrt{-g}\; d^4x + \int L_m\sqrt{-g}\; d^4x \tag{1}$$

where $f(R,T)$ is an arbitrary function of Ricci scalar R and the trace $T = g^{ij}T_{ij}$ of stress-energy tensor, each choice of which would generate a specific set of field equations and L_m is the matter Lagrangian density. The stress-energy tensor of matter is defined by

$$T_{ij} = \frac{-2}{\sqrt{-g}}\frac{\delta(\sqrt{-g}L_m)}{\delta g^{ij}} \tag{2}$$

Assuming L_m to depend only on the metric tensor components g_{ij} and not on its derivatives, T_{ij} is obtained as

$$T_{ij} = g_{ij}L_m - 2\frac{\partial L_m}{\partial g^{ij}} \tag{3}$$

Now taking variation of the action Eq.(1) with respect to the metric tensor components g^{ij}, the field equations of $f(R,T)$ gravity are obtained as

$$f_R(R,T)R_{ij} - \frac{1}{2}f(R,T)g_{ij} + (g_{ij}\Box - \bigtriangledown_i\bigtriangledown_j)f_R(R,T) = 8\pi T_{ij} - f_T(R,T)T_{ij} - f_T(R,T)\Theta_{ij} \tag{4}$$

where, $f_R(R,T) = \frac{\partial f(R,T)}{\partial R}$, $f_T(R,T) = \frac{\partial f(R,T)}{\partial T}$, $\Box = \bigtriangledown_i \bigtriangledown^i$, $\bigtriangledown_i$ being the covariant derivative with respect to the symmetric connection Γ associated to the metric g and

$$\Theta_{ij} = -2T_{ij} + g_{ij}L_m - 2g^{lk}\frac{\partial^2 L_m}{\partial g^{ij}\partial g^{lk}} \tag{5}$$

Considering the functional form

$$f(R,T) = f_1(R) + f_2(T) \tag{6}$$

where $f_1(R)$ and $f_2(T)$ are arbitrary functions of R and T respectively, the gravitational field equations from Eq.(4) are obtained as

$$f_1{}'(R)R_{ij} - \frac{1}{2}f_1(R)g_{ij} + (g_{ij}\Box - \bigtriangledown_i\bigtriangledown_j)f_1{}'(R) = 8\pi T_{ij} - f_2{}'(T)T_{ij} - f_2{}'(T)\Theta_{ij} + \frac{1}{2}f_2(T)g_{ij} \tag{7}$$

where the prime denotes differentiation with respect to the argument. For a perfect fluid described by an energy density ρ and pressure p, the stress-energy tensor T_{ij} is given by

$$T_{ij} = (\rho + p)u_i u_j - pg_{ij} \tag{8}$$

where u^i is the four velocity satisfying the conditions

$$u^i \bigtriangledown_j u_i = 0, \quad u_i u^i = 1 \tag{9}$$

The trace T of T_{ij} is therefore given by

$$T = \rho - 3p \tag{10}$$

Taking the matter Lagrangian to be $L_m = -p$, from Eq. (5), Θ_{ij} is obtained as

$$\Theta_{ij} = -2T_{ij} - pg_{ij} \tag{11}$$

Thus, if the matter source is a perfect fluid then the field equations of $f(R,T)$ gravity for the choice Eq.(6) become

$$f_1{}'(R)R_{ij} - \frac{1}{2}f_1(R)g_{ij} = 8\pi T_{ij} + f_2{}'(T)T_{ij} + \left[f_2{}'(T)p + \frac{1}{2}f_2(T)\right]g_{ij} \tag{12}$$

In particular, for $f_1(R) = \lambda_1 R$ and $f_2(T) = \lambda_2 T + \lambda_3 T^2$, where λ_1, λ_2 and λ_3 are free parameters, the Eq.(12) reduces to

$$R_{ij} - \frac{1}{2}Rg_{ij} = \frac{1}{\lambda_1}\left[(8\pi + \lambda_2 + 2\lambda_3 T)\,T_{ij} + \left(p(\lambda_2 + 2\lambda_3 T) + \frac{1}{2}(\lambda_2 T + \lambda_3 T^2)\right)g_{ij}\right] \tag{13}$$

3. THE METRIC AND FIELD EQUATIONS

We consider the spatially homogeneous and anisotropic Bianchi type III metric in the form

$$ds^2 = dt^2 - A^2dx^2 - B^2e^{-2lx}dy^2 - C^2dz^2 \tag{14}$$

where A, B and C are functions of cosmic time t alone and l is a constant. Using comoving coordinates, the field equations (13) for the metric (14) take the form

$$\frac{\ddot{B}}{B} + \frac{\ddot{C}}{C} + \frac{\dot{B}}{B}\frac{\dot{C}}{C} = \frac{1}{\lambda_1}\left[-\left(8\pi + \frac{3}{2}\lambda_2\right)p + \frac{1}{2}\lambda_2\rho + \frac{9}{2}\lambda_3 p^2 + \frac{1}{2}\lambda_3\rho^2 - 3\lambda_3 p\rho\right] \tag{15}$$

$$\frac{\ddot{C}}{C} + \frac{\ddot{A}}{A} + \frac{\dot{C}}{C}\frac{\dot{A}}{A} = \frac{1}{\lambda_1}\left[-\left(8\pi + \frac{3}{2}\lambda_2\right)p + \frac{1}{2}\lambda_2\rho + \frac{9}{2}\lambda_3 p^2 + \frac{1}{2}\lambda_3\rho^2 - 3\lambda_3 p\rho\right] \tag{16}$$

$$\frac{\ddot{A}}{A} + \frac{\ddot{B}}{B} + \frac{\dot{A}}{A}\frac{\dot{B}}{B} - \frac{l^2}{A^2} = \frac{1}{\lambda_1}\left[-\left(8\pi + \frac{3}{2}\lambda_2\right)p + \frac{1}{2}\lambda_2\rho + \frac{9}{2}\lambda_3 p^2 + \frac{1}{2}\lambda_3\rho^2 - 3\lambda_3 p\rho\right] \tag{17}$$

$$\frac{\dot{A}}{A}\frac{\dot{B}}{B} + \frac{\dot{B}}{B}\frac{\dot{C}}{C} + \frac{\dot{C}}{C}\frac{\dot{A}}{A} - \frac{l^2}{A^2} = \frac{1}{\lambda_1}\left[\left(8\pi + \frac{3}{2}\lambda_2\right)\rho - \frac{1}{2}\lambda_2 p + \frac{5}{2}\lambda_3\rho^2 - \frac{3}{2}\lambda_3 p^2 - 7\lambda_3 p\rho\right] \tag{18}$$

$$\frac{\dot{A}}{A} - \frac{\dot{B}}{B} = 0 \tag{19}$$

where an overhead dot denotes differentiation w.r.t. t. Integrating Eq.(19), we get

$$A = mB \tag{20}$$

where m is a constant of integration.

Hence, the field equations (15)-(18) reduce to

$$\frac{\ddot{A}}{A} + \frac{\ddot{C}}{C} + \frac{\dot{A}}{A}\frac{\dot{C}}{C} = \frac{1}{\lambda_1}\left[-\left(8\pi + \frac{3}{2}\lambda_2\right)p + \frac{1}{2}\lambda_2\rho + \frac{9}{2}\lambda_3 p^2 + \frac{1}{2}\lambda_3\rho^2 - 3\lambda_3 p\rho\right] \tag{21}$$

$$2\frac{\ddot{A}}{A} + \left(\frac{\dot{A}}{A}\right)^2 - \frac{l^2}{A^2} = \frac{1}{\lambda_1}\left[-\left(8\pi + \frac{3}{2}\lambda_2\right)p + \frac{1}{2}\lambda_2\rho + \frac{9}{2}\lambda_3 p^2 + \frac{1}{2}\lambda_3\rho^2 - 3\lambda_3 p\rho\right] \tag{22}$$

$$\left(\frac{\dot{A}}{A}\right)^2 + 2\frac{\dot{C}}{C}\frac{\dot{A}}{A} - \frac{l^2}{A^2} = \frac{1}{\lambda_1}\left[\left(8\pi + \frac{3}{2}\lambda_2\right)\rho - \frac{1}{2}\lambda_2 p + \frac{5}{2}\lambda_3\rho^2 - \frac{3}{2}\lambda_3 p^2 - 7\lambda_3 p\rho\right] \tag{23}$$

4. EXACT SOLUTION OF THE FIELD EQUATIONS

From equations (21) and (22), we have

$$\frac{\ddot{A}}{A} + \left(\frac{\dot{A}}{A}\right)^2 - \frac{\ddot{C}}{C} - \frac{\dot{C}}{C}\frac{\dot{A}}{A} - \frac{l^2}{A^2} = 0 \tag{24}$$

Eq.(24) contains two unknowns A and C. Further, we have three field equations in four unknowns A, C, ρ and p. To derive an exact solution and develop a physically realistic model, we adopt a power-law expansion of the form:

$$C = C_0 t^\beta \tag{25}$$

where β and C_0 are positive constants in accordance with the observational findings of an expanding universe [30, 35, 36]. Using Eq.(25) in Eq.(24) and then solving, we obtain

$$A^2 = \frac{l^2 t^2}{1-\beta^2} + C_0^2 k_1 t^{2\beta} + \frac{2l^2 k_2 t^{1-\beta}}{C_0(1-3\beta)} \tag{26}$$

where k_1 and k_2 are constants of integration. Using Eq.(20), we then obtain

$$B^2 = \frac{1}{m^2}\left(\frac{l^2 t^2}{1-\beta^2} + C_0^2 k_1 t^{2\beta} + \frac{2l^2 k_2 t^{1-\beta}}{C_0(1-3\beta)}\right) \tag{27}$$

In this work, we choose $k_2 = 0$ and $0 < \beta < 1$. Then from equations (26) and (27), we get

$$A^2 = \frac{l^2 t^2}{1-\beta^2} + C_0^2 k_1 t^{2\beta} \tag{28}$$

and

$$B^2 = \frac{1}{m^2}\left(\frac{l^2 t^2}{1-\beta^2} + C_0^2 k_1 t^{2\beta}\right) \tag{29}$$

Therefore, the line element (14) becomes

$$ds^2 = dt^2 - \left(\frac{l^2 t^2}{1-\beta^2} + C_0^2 k_1 t^{2\beta}\right)\left(dx^2 + \frac{e^{-2lx}}{m^2}dy^2\right) - C_0^2 t^{2\beta} dz^2 \tag{30}$$

5. DYNAMICS AND PHYSICAL CHARACTERISTICS OF THE MODEL

In this section, we look forward to study the dynamics and physical characteristics of the constructed model. So, we first obtain the expressions for some important parameters of the model and then investigate their behavior as the universe evolves.

5.1. Physical parameters of the model

For our model, the spatial volume is

$$V = a^3 = ABC = \frac{C_0}{m}\left[\frac{l^2 t^{\beta+2}}{1-\beta^2} + C_0^2 k_1 t^{3\beta}\right] \tag{31}$$

The directional Hubble parameters corresponding to our model are

$$H_1 = \frac{\dot{A}}{A} = \frac{\frac{l^2 t}{1-\beta^2} + C_0^2 k_1 \beta t^{2\beta-1}}{\frac{l^2 t^2}{1-\beta^2} + C_0^2 k_1 t^{2\beta}} \tag{32}$$

$$H_2 = \frac{\dot{B}}{B} = \frac{\frac{l^2 t}{1-\beta^2} + C_0^2 k_1 \beta t^{2\beta-1}}{\frac{l^2 t^2}{1-\beta^2} + C_0^2 k_1 t^{2\beta}} \tag{33}$$

$$H_3 = \frac{\dot{C}}{C} = \frac{\beta}{t} \tag{34}$$

The average Hubble parameter is therefore

$$H = \frac{1}{3}(H_1 + H_2 + H_3) = \frac{1}{3}\left[\frac{\frac{2l^2 t}{1-\beta^2} + 2C_0^2 k_1 \beta t^{2\beta-1}}{\frac{l^2 t^2}{1-\beta^2} + C_0^2 k_1 t^{2\beta}} + \frac{\beta}{t}\right] \tag{35}$$

The deceleration parameter is

$$q = -1 + \frac{d}{dt}\left(\frac{1}{H}\right) = -1 - \frac{3\left[\frac{-(\beta+2)l^4 t^4}{(1-\beta^2)^2} + \frac{2l^2 C_0^2 k_1 (2\beta^2-6\beta+1) t^{2\beta+2}}{1-\beta^2} - 3C_0^4 k_1^2 \beta t^{4\beta}\right]}{\left(\frac{l^2(\beta+2)t^2}{1-\beta^2} + 3C_0^2 k_1 \beta t^{2\beta}\right)^2} \tag{36}$$

The expansion scalar is

$$\theta = 3H = H_1 + H_2 + H_3 = \frac{\frac{2l^2 t}{1-\beta^2} + 2C_0^2 k_1 \beta t^{2\beta-1}}{\frac{l^2 t^2}{1-\beta^2} + C_0^2 k_1 t^{2\beta}} + \frac{\beta}{t} \tag{37}$$

The mean anisotropy parameter is

$$\begin{aligned} A_m &= \frac{1}{3}\Sigma_{i=1}^{3}\left(\frac{H_i - H}{H}\right)^2 \\ &= 2 - \frac{3\left(\frac{\frac{l^2 t}{1-\beta^2} + C_0^2 k_1 \beta t^{2\beta-1}}{\frac{l^2 t^2}{1-\beta^2} + C_0^2 k_1 t^{2\beta}}\right)}{\frac{\frac{2l^2 t}{1-\beta^2} + 2C_0^2 k_1 \beta t^{2\beta-1}}{\frac{l^2 t^2}{1-\beta^2} + C_0^2 k_1 t^{2\beta}} + \frac{\beta}{t}} - \frac{9\left(\frac{\frac{l^2 \beta}{1-\beta^2} + C_0^2 k_1 \beta^2 t^{2\beta-2}}{\frac{l^2 t^2}{1-\beta^2} + C_0^2 k_1 t^{2\beta}}\right)}{\left(\frac{\frac{2l^2 t}{1-\beta^2} + 2C_0^2 k_1 \beta t^{2\beta-1}}{\frac{l^2 t^2}{1-\beta^2} + C_0^2 k_1 t^{2\beta}} + \frac{\beta}{t}\right)^2} \end{aligned} \tag{38}$$

And, the shear scalar is

$$\sigma^2 = \frac{1}{3}\left[\frac{\frac{l^2 t}{1-\beta^2} + C_0^2 k_1 \beta t^{2\beta-1}}{\frac{l^2 t^2}{1-\beta^2} + C_0^2 k_1 t^{2\beta}} - \frac{\beta}{t}\right]^2 \tag{39}$$

5.2. Evolution of the physical parameters

From figure 1, we see that as cosmic time t increases, the volume V grows for different values of the parameter β. This indicates an expanding universe, consistent with observations of cosmic expansion. The increase in volume with time supports the idea of a universe evolving from a smaller, denser state (e.g., near a Big Bang-type singularity) towards a more expansive state. The parameter β likely controls the rate of expansion, possibly linked to anisotropic stresses, matter content, or modified gravity effects in the $f(R,T)$ framework. For larger values of β, the rate of expansion might differ, reflecting the influence of β on the model's dynamics.

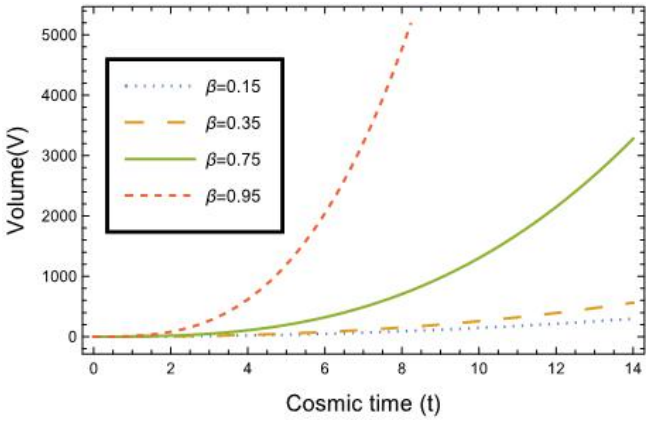

Figure 1. Variation of volume V v/s cosmic time t for different values of β

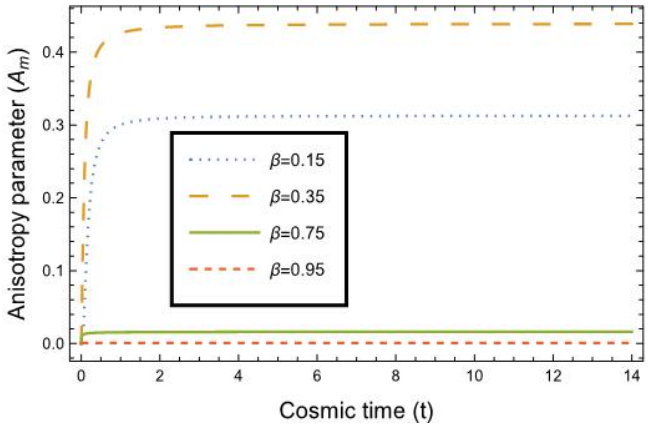

Figure 2. Variation of anisotropy parameter A_m v/s cosmic time t for different values of β

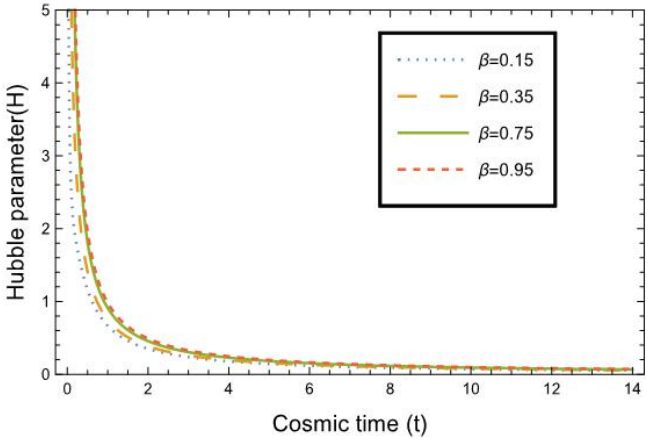

Figure 3. Variation of the average Hubble parameter H v/s cosmic time t for different values of β.

Anisotropy describes the directional variation in the properties of the universe, where the expansion rate differs along various directions. It is quantified by parameters that indicate deviations from isotropy in the metric or the energy-momentum tensor. From figure 2, it is evident that the model retains its anisotropic nature throughout its evolution, implying that the universe does not become perfectly isotropic even at late times. This points to the influence of factors that sustain the directional dependence of the expansion.

In figure 3, we analyze the behavior of the average Hubble parameter (H) as a function of cosmic time t for different values of β viz. $\beta = 0.15$, $\beta = 0.35$, $\beta = 0.75$ and $\beta = 0.95$. The plot reveals that H consistently decreases with increasing cosmic time t, indicating a slowing rate of expansion as the universe evolves. At late times, H asymptotically approaches a constant value, suggesting that the expansion rate stabilizes in the distant future. The variation in β influences the rate at which H decreases, but the overall trend of convergence to a constant value remains the same for all considered

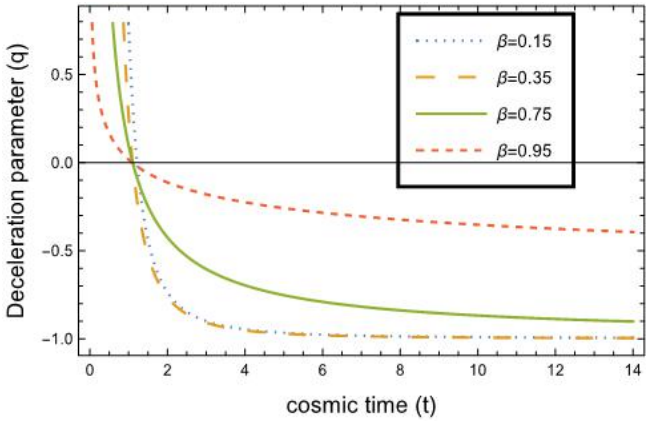

Figure 4. Variation of deceleration parameter q v/s cosmic time t for different values of β

cases. This behavior aligns with the expectation of a universe transitioning toward a steady-state expansion phase.

Figure 4 illustrates the evolution of the deceleration parameter (q) over cosmic time t, highlighting key transitions in the universe's expansion dynamics. The plot clearly shows that the model transitions from an initial decelerating phase ($q > 0$) to the present accelerating phase ($q < 0$), consistent with observational evidence. Furthermore, as cosmic time t progresses toward infinity, the deceleration parameter asymptotically approaches $q \to -1$. This behavior indicates that the universe evolves toward a state of exponential expansion, characteristic of a de Sitter phase dominated by dark energy or a similar cosmological constant-like component.

From the above figures, we find the value $\beta = 0.75$ to be more suitable for our study. So, we stick to this value of β to carry out further studies. Also, we choose $l = 1$, $m = 1$, $C_0 = 1$, $k_1 = 0.1$, $\lambda_1 = -0.1$, $\lambda_2 = 0.2$, $\lambda_3 = 0.3$ for all the plots.

5.3. Jerk parameter

The jerk parameter (j) plays a vital role in cosmology as it provides deeper insights into the dynamics of expansion of the universe. In essence, it provides insights into whether the acceleration itself is speeding up or slowing down over time. The jerk parameter j represents the third derivative of the scale factor $a(t)$ with respect to cosmic time t, normalized in a dimensionless form. It quantifies the rate at which the acceleration of the universe's expansion is changing. The jerk parameter extends the deceleration parameter (q) in a more straightforward way.

A positive jerk indicates that the acceleration is increasing, suggesting a scenario of rapid, ever-accelerating expansion. Conversely, a negative jerk implies that the acceleration is tapering off, hinting at a possible stabilization or deceleration of the expansion in the future. Cosmologists may verify and enhance dark energy and modified gravity models by examining the jerk parameter which helps to uncover whether the current accelerated expansion is driven by a cosmological constant Λ, dynamic dark energy, or other phenomena. This makes it an essential tool for comprehending the universe's past as well as its possible future.

For our model, the jerk parameter $j(t)$ is obtained as

$$
\begin{aligned}
j(t) &= \frac{a^2}{\dot{a}^3}\frac{d^3a}{dt^3} \\
&= 1 + 9\frac{-\frac{(\beta+2)l^4t^2}{(1-\beta^2)^2} + \frac{2C_0^2k_1l^2(2\beta^2-6\beta+1)t^{2\beta}}{(1-\beta^2)} - 3C_0^4k_1^2\beta t^{4\beta-2}}{\left(\frac{(\beta+2)l^2t}{1-\beta^2} + 3C_0^2k_1\beta t^{2\beta-1}\right)^2} \\
&\quad + \frac{9}{\left(\frac{(\beta+2)l^2t}{1-\beta^2} + 3C_0^2k_1\beta t^{2\beta-1}\right)^3 t^3}\left[2t^3\left(\frac{2l^2t}{1-\beta^2} + 2C_0^2k_1\beta t^{2\beta-1}\right)^3\right. \\
&\quad - 3t^3\left(\frac{2l^2}{1-\beta^2} + 2C_0^2k_1\beta(2\beta-1)t^{2\beta-2}\right)\left(\frac{2l^2t}{1-\beta^2} + 2C_0^2k_1\beta t^{2\beta-1}\right)\left(\frac{l^2t^2}{1-\beta^2} + C_0^2k_1t^{2\beta}\right) \\
&\quad \left. + C_0^2k_1\beta(2\beta-1)(2\beta-2)t^{2\beta}\left(\frac{l^2t^2}{1-\beta^2} + C_0^2k_1t^{2\beta}\right)^2 + 2\beta\left(\frac{l^2t^2}{1-\beta^2} + C_0^2k_1t^{2\beta}\right)^3\right]
\end{aligned}
\tag{40}
$$

Figure 5 demonstrates the evolution of the jerk parameter j with respect to cosmic time t. The plot indicates that j decreases as t increases, suggesting a gradual change in the dynamical properties of the universe's expansion. Throughout

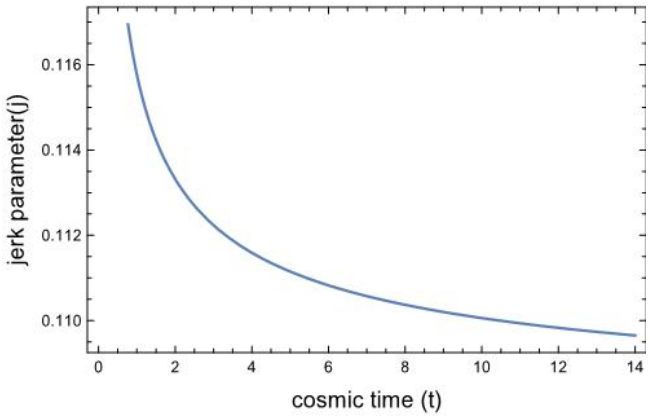

Figure 5. Graph of jerk parameter v/s cosmic time t for $\beta = 0.75$

the evolution, the values of j remain consistently less than 1, which is a key characteristic of cosmological models dominated by quintessence type dark energy.

It is well known that quintessence is a form of dynamic dark energy where the Equation of State parameter ω lies in the range $-1 < \omega < -\frac{1}{3}$, distinguishing it from a cosmological constant ($\omega = -1$). The behavior of the jerk parameter in this model aligns with this description, indicating that the driving force behind the universe's accelerated expansion is not a static cosmological constant but a time varying dark energy component. Thus, the evolution of j in our model provides strong evidence for a quintessence like scenario, where the dynamics of dark energy play a critical role in shaping the universe's expansion history.

5.4. Statefinder diagnostic

The statefinder pair $\{r, s\}$ is defined [37] as

$$r = \frac{1}{aH^3}\frac{d^3a}{dt^3}, \quad s = \frac{r-1}{3(q-\frac{1}{2})} \tag{41}$$

The pair $\{r, s\}$ is a significant geometrical diagnostic tool which can be employed to distinguish different dark energy models such as ΛCDM, Quintessence scalar field model, Holographic dark energy model, Chaplygin gas model etc. ΛCDM model corresponds to the pair $\{1, 0\}$ while the Holographic dark energy model corresponds to $\{1, \frac{2}{3}\}$. The quintessence corresponds to ($r < 1$, $s > 0$) and the Chaplygin gas model corresponds to ($r > 1$, $s < 0$).

For our model, the statefinder pair $\{r, s\}$ is obtained as

$$\begin{aligned}
r &= 1 + 3\frac{\dot{H}}{H^2} + \frac{\ddot{H}}{H^3} \\
&= 1 + 9\frac{-\frac{(\beta+2)l^4t^2}{(1-\beta^2)^2} + \frac{2C_0^2k_1l^2(2\beta^2-6\beta+1)t^{2\beta}}{(1-\beta^2)} - 3C_0^4k_1^2\beta t^{4\beta-2}}{\left(\frac{(\beta+2)l^2t}{1-\beta^2} + 3C_0^2k_1\beta t^{2\beta-1}\right)^2} \\
&\quad + \frac{9}{\left(\frac{(\beta+2)l^2t}{1-\beta^2} + 3C_0^2k_1\beta t^{2\beta-1}\right)^3 t^3}\left[2t^3\left(\frac{2l^2t}{1-\beta^2} + 2C_0^2k_1\beta t^{2\beta-1}\right)^3\right. \\
&\quad - 3t^3\left(\frac{2l^2}{1-\beta^2} + 2C_0^2k_1\beta(2\beta-1)t^{2\beta-2}\right)\left(\frac{2l^2t}{1-\beta^2} + 2C_0^2k_1\beta t^{2\beta-1}\right)\left(\frac{l^2t^2}{1-\beta^2} + C_0^2k_1t^{2\beta}\right) \\
&\quad + C_0^2k_1\beta(2\beta-1)(2\beta-2)t^{2\beta}\left(\frac{l^2t^2}{1-\beta^2} + C_0^2k_1t^{2\beta}\right)^2 \\
&\quad \left. + 2\beta\left(\frac{l^2t^2}{1-\beta^2} + C_0^2k_1t^{2\beta}\right)^3\right]
\end{aligned} \tag{42}$$

$$
\begin{aligned}
s &= \frac{r-1}{3\left(q-\frac{1}{2}\right)} \\
&= \frac{1}{3\left(-\frac{3\left(\frac{-(\beta+2)l^4t^4}{(1-\beta^2)^2}+\frac{2l^2C_0^2k_1(2\beta^2-6\beta+1)t^{2\beta+2}}{1-\beta^2}-3C_0^4k_1^2\beta t^{4\beta}\right)}{\left(\frac{l^2(\beta+2)t^2}{1-\beta^2}+3C_0^2k_1\beta t^{2\beta}\right)^2}-1.5\right)} \\
&\left[9\frac{-\frac{(\beta+2)l^4t^2}{(1-\beta^2)^2}+\frac{2C_0^2k_1l^2(2\beta^2-6\beta+1)t^{2\beta}}{(1-\beta^2)}-3C_0^4k_1^2\beta t^{4\beta-2}}{\left(\frac{(\beta+2)l^2t}{1-\beta^2}+3C_0^2k_1\beta t^{2\beta-1}\right)^2}\right. \\
&\quad +\frac{9}{\left(\frac{(\beta+2)l^2t}{1-\beta^2}+3C_0^2k_1\beta t^{2\beta-1}\right)^3t^3}\left\{2t^3\left(\frac{2l^2t}{1-\beta^2}+2C_0^2k_1\beta t^{2\beta-1}\right)^3\right. \\
&\quad -3t^3\left(\frac{2l^2}{1-\beta^2}+2C_0^2k_1\beta(2\beta-1)t^{2\beta-2}\right)\left(\frac{2l^2t}{1-\beta^2}+2C_0^2k_1\beta t^{2\beta-1}\right)\left(\frac{l^2t^2}{1-\beta^2}+C_0^2k_1t^{2\beta}\right) \\
&\quad \left.\left.+C_0^2k_1\beta(2\beta-1)(2\beta-2)t^{2\beta}\left(\frac{l^2t^2}{1-\beta^2}+C_0^2k_1t^{2\beta}\right)^2+2\beta\left(\frac{l^2t^2}{1-\beta^2}+C_0^2k_1t^{2\beta}\right)^3\right\}\right]
\end{aligned}
\tag{43}
$$

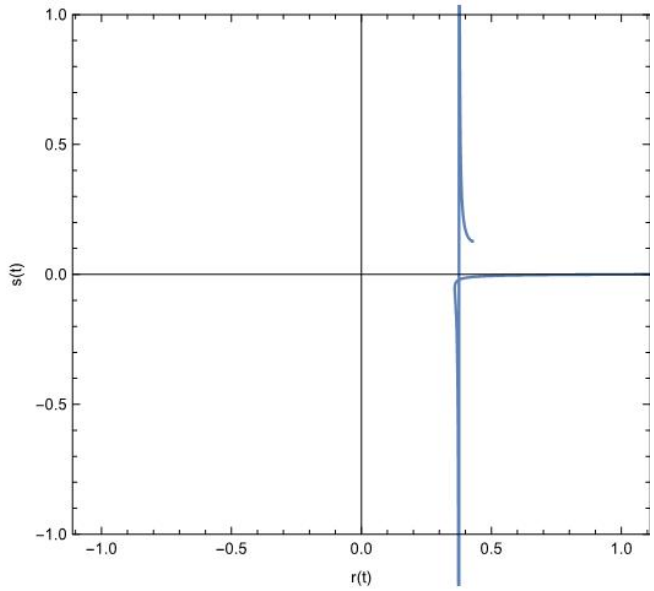

Figure 6. Statefinder pair $r-s$

The model's trajectory in figure 6 suggests that it will continue to exhibit quintessence like behavior in the future, maintaining this specific dynamical profile.

5.5. Evolution of energy density and pressure

In terms of directional Hubble parameters, the field equations (15)-(18) reduce to

$$H_1^2+2H_1H_3-\frac{l^2}{A^2}=\frac{1}{\lambda_1}\left[\left(8\pi+\frac{3}{2}\lambda_2\right)\rho-\frac{1}{2}\lambda_2 p+\frac{5}{2}\lambda_3\rho^2-\frac{3}{2}\lambda_3 p^2-7\lambda_3 p\rho\right] \tag{44}$$

$$\dot{H}_2+H_2^2+\dot{H}_3+H_3^2+H_2H_3=\frac{1}{\lambda_1}\left[-\left(8\pi+\frac{3}{2}\lambda_2\right)p+\frac{1}{2}\lambda_2\rho+\frac{9}{2}\lambda_3 p^2+\frac{1}{2}\lambda_3\rho^2-3\lambda_3 p\rho\right] \tag{45}$$

$$\dot{H}_3+H_3^2+\dot{H}_1+H_1^2+H_3H_1=\frac{1}{\lambda_1}\left[-\left(8\pi+\frac{3}{2}\lambda_2\right)p+\frac{1}{2}\lambda_2\rho+\frac{9}{2}\lambda_3 p^2+\frac{1}{2}\lambda_3\rho^2-3\lambda_3 p\rho\right] \tag{46}$$

$$\dot{H}_1 + H_1^2 + \dot{H}_2 + H_2^2 + H_1H_2 - \frac{l^2}{A^2} = \frac{1}{\lambda_1}\left[-\left(8\pi + \frac{3}{2}\lambda_2\right)p + \frac{1}{2}\lambda_2\rho + \frac{9}{2}\lambda_3 p^2 + \frac{1}{2}\lambda_3\rho^2 - 3\lambda_3 p\rho\right] \tag{47}$$

From equations (44)-(47), we get

$$\begin{aligned} &4\dot{H}_1 + 2\dot{H}_3 + 4H_1^2 + 2H_3^2 \\ &\qquad = \frac{1}{\lambda_1}\left[-\left(8\pi + \frac{3}{2}\lambda_2\right)(3p+\rho) + \frac{1}{2}\lambda_2(p+3\rho) + 15\lambda_3 p^2 - \lambda_3\rho^2 - 2\lambda_3 p\rho\right] \end{aligned} \tag{48}$$

The analysis in the previous sections indicate that our model exhibits characteristics consistent with the quintessence dark energy model. Thus, to investigate the evolution of energy density (ρ) and pressure (p) in our model, over cosmic time t, we adopt the Equation of State parameter $\omega = \frac{p}{\rho}$ within the quintessence regime $-1 < \omega < -\frac{1}{3}$. By analyzing the energy density and pressure in this context, we can further explore the physical implications of the model. Now, considering the equation of state $p = \omega\rho$, from equations (32), (34) and (48), we find

$$\begin{aligned} \rho = \frac{1}{2(5\omega+1)(3\omega-1)\lambda_3}\Bigg[&(8\pi(1+3\omega) + 4\lambda_2\omega) + \Bigg\{(8\pi(1+3\omega) + 4\lambda_2\omega)^2 + \\ &4(5\omega+1)(3\omega-1)\lambda_3\left(\frac{2\lambda_1(\beta^2-\beta)}{t^2} - \frac{4C_0^2k_1\lambda_1 t^{2\beta}}{(\frac{l^2t^2}{1-\beta^2} + C_0^2k_1\beta t^{2\beta})^2(1+\beta)}\left(l^2(2\beta-1) + C_0^2k_1\beta t^{2\beta-2}\right)\right)\Bigg\}^{\frac{1}{2}}\Bigg] \end{aligned} \tag{49}$$

$$\begin{aligned} p = \frac{\omega}{2(5\omega+1)(3\omega-1)\lambda_3}\Bigg[&(8\pi(1+3\omega) + 4\lambda_2\omega) + \Bigg\{(8\pi(1+3\omega) + 4\lambda_2\omega)^2 + \\ &4(5\omega+1)(3\omega-1)\lambda_3\left(\frac{2\lambda_1(\beta^2-\beta)}{t^2} - \frac{4C_0^2k_1\lambda_1 t^{2\beta}}{(\frac{l^2t^2}{1-\beta^2} + C_0^2k_1\beta t^{2\beta})^2(1+\beta)}\left(l^2(2\beta-1) + C_0^2k_1\beta t^{2\beta-2}\right)\right)\Bigg\}^{\frac{1}{2}}\Bigg] \end{aligned} \tag{50}$$

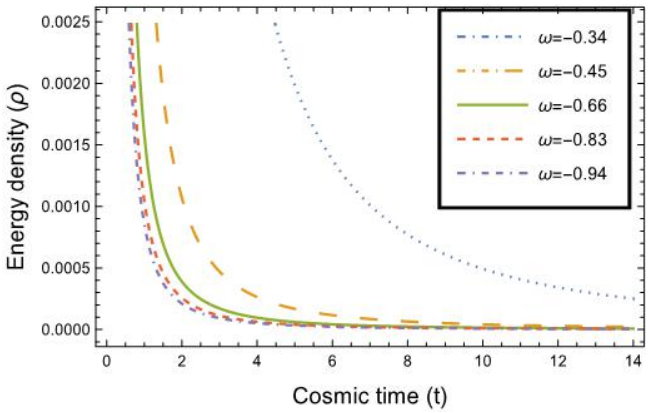

Figure 7. Variation of the energy density ρ v/s cosmic time t

In Figure 7, we present the evolution of the energy density ρ as a function of cosmic time t for different values of the Equation of State parameter viz. $\omega = -0.34, -0.45, -0.66, -0.83, -0.94$ within the quintessence regime. The plot reveals that the energy density starts with significantly large values at the early stages of the universe. As time progresses, ρ decreases steadily, signifying the dilution of energy density due to the universe's expansion.

Figure 8 depicts the evolution of pressure (p) as a function of cosmic time (t). The graph shows that the pressure remains negative throughout the entire evolution, a key characteristic of dark energy. Negative pressure is essential for generating the repulsive gravitational force responsible for the accelerated expansion of the universe. In the early stages of cosmic evolution, the magnitude of the negative pressure is relatively large, corresponding to the dominance of energy components with high density and strong negative pressure, such as quintessence or other dynamic dark energy models. As the universe evolves, the magnitude of p gradually decreases. At late times, the pressure asymptotically approaches

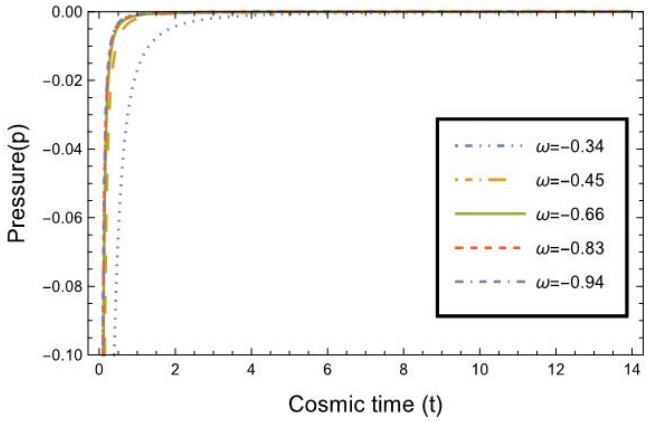

Figure 8. Variation of pressure p v/s cosmic time t with $\omega = -0.34, -0.45, -0.66, -0.83, -0.94$

zero, indicating a transition towards a more stable expansion phase. This behavior is consistent with a dark energy model where the Equation of State parameter (ω) lies in the range $-1 < \omega < -\frac{1}{3}$, as in quintessence. The eventual approach of p to zero suggests that the universe evolves towards a de Sitter like state, characterized by nearly constant energy density and an exponential expansion phase. This result underscores the dynamic nature of the universe's evolution, where negative pressure plays a pivotal role in shaping its expansion history. The gradual reduction in the magnitude of pressure aligns with the transition from a matter dominated phase to an accelerated expansion phase, dominated by dark energy effects.

6. THE FUNCTIONAL $f(R,T)$ OF THE MODEL

From Eq.(10), the trace T of stress-energy tensor T_{ij} is obtained as

$$T = \frac{-1}{2(5\omega+1)\lambda_3}\Bigg[(8\pi(1+3\omega)+4\lambda_2\omega)+ \Bigg\{(8\pi(1+3\omega)+4\lambda_2\omega)^2+4(5\omega+1)(3\omega-1)\lambda_3\left(\frac{2\lambda_1(\beta^2-\beta)}{t^2} - \frac{4C_0^2k_1\lambda_1t^{2\beta}}{(\frac{l^2t^2}{1-\beta^2}+C_0^2k_1\beta t^{2\beta})^2(1+\beta)}\left(l^2(2\beta-1)+C_0^2k_1\beta t^{2\beta-2}\right)\right)\Bigg\}^{\frac{1}{2}}\Bigg] \tag{51}$$

Again, the Ricci scalar R for the metric (14) is obtained as

$$R = -2\left(\frac{\ddot{A}}{A}+\frac{\ddot{B}}{B}+\frac{\ddot{C}}{C}+\frac{\dot{A}}{A}\frac{\dot{B}}{B}+\frac{\dot{B}}{B}\frac{\dot{C}}{C}+\frac{\dot{C}}{C}\frac{\dot{A}}{A}-\frac{l^2}{A^2}\right) \tag{52}$$

For our model, R is obtained as

$$R = \frac{2}{\left(\frac{l^2t^2}{1-\beta^2}+C_0^2k_1t^{2\beta}\right)(1-\beta^2)^2}[l^2(1-\beta^2)^2-l^4(1+\beta+\beta^2)t^2 -2C_0^2k_1(1-\beta^2)(1-2\beta+4\beta^2)t^{2\beta}+3C_0^4k_1^2\beta(1-2\beta)(1-\beta^2)^2t^{4\beta-2}] \tag{53}$$

Therefore, the functional $f(R,T)$ of our model is obtained as

$$
\begin{aligned}
f(R,T) &= f_1(R) + f_2(T) \\
&= \lambda_1 R + \lambda_2 T + \lambda_3 T^2 \\
&= \frac{2\lambda_1}{\left(\frac{l^2t^2}{1-\beta^2} + C_0^2 k_1 t^{2\beta}\right)(1-\beta^2)^2}[l^2(1-\beta^2)^2 - l^4(1+\beta+\beta^2)t^2 \\
&\qquad - 2C_0^2 k_1(1-\beta^2)(1-2\beta+4\beta^2)t^{2\beta} + 3C_0^4 k_1^2 \beta(1-2\beta)(1-\beta^2)^2 t^{4\beta-2}] \\
&\quad - \frac{\lambda_2}{2(5\omega+1)\lambda_3}\Bigg[(8\pi(1+3\omega)+4\lambda_2\omega) + \\
&\Bigg\{(8\pi(1+3\omega)+4\lambda_2\omega)^2 + 4(5\omega+1)(3\omega-1)\lambda_3\Bigg(\frac{2\lambda_1(\beta^2-\beta)}{t^2} \\
&- \frac{4C_0^2 k_1\lambda_1 t^{2\beta}}{(\frac{l^2t^2}{1-\beta^2} + C_0^2 k_1\beta t^{2\beta})^2(1+\beta)}\left(l^2(2\beta-1) + C_0^2 k_1\beta t^{2\beta-2}\right)\Bigg)\Bigg\}^{\frac{1}{2}}\Bigg] \\
&\quad + \frac{1}{4(5\omega+1)^2\lambda_3}\Bigg[(8\pi(1+3\omega)+4\lambda_2\omega) + \\
&\Bigg\{(8\pi(1+3\omega)+4\lambda_2\omega)^2 + 4(5\omega+1)(3\omega-1)\lambda_3\Bigg(\frac{2\lambda_1(\beta^2-\beta)}{t^2} \\
&- \frac{4C_0^2 k_1\lambda_1 t^{2\beta}}{(\frac{l^2t^2}{1-\beta^2} + C_0^2 k_1\beta t^{2\beta})^2(1+\beta)}\left(l^2(2\beta-1) + C_0^2 k_1\beta t^{2\beta-2}\right)\Bigg)\Bigg\}^{\frac{1}{2}}\Bigg]^2
\end{aligned}
\tag{54}
$$

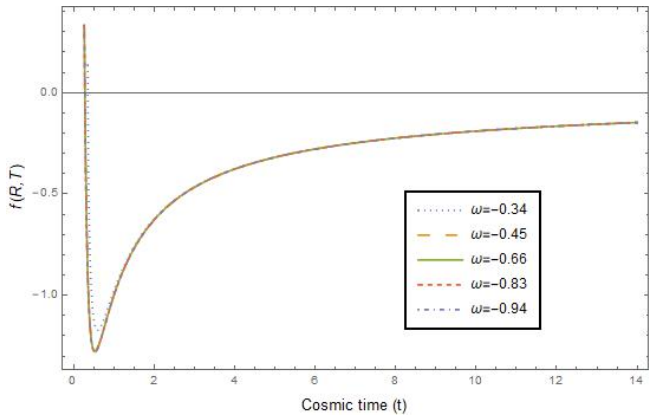

Figure 9. Variation of $f(R,T)$ v/s cosmic time t with $\omega = -0.34, -0.45, -0.66, -0.83, -0.94$

From the graph of $f(R,T)$ versus cosmic time t in figure 9, we see that the functional $f(R,T)$ decreases in the beginning of cosmic evolution but as cosmic time increases, it starts increasing. The graph illustrates the dynamic behavior of the functional $f(R,T)$ throughout the evolution of the universe, revealing a shift in its trend over time.

7. CONCLUSIONS

In this study, we explore a Bianchi type III cosmological model within the framework of $f(R,T)$ gravity, considering the functional form $f(R,T) = f_1(R) + f_2(T)$, where $f_1(R) = \lambda_1 R$, $f_2(T) = \lambda_2 T + \lambda_3 T^2$ and λ_1, λ_2, and λ_3 are free parameters that determine the specific contributions of the Ricci scalar curvature (R) and the trace of the stress-energy tensor (T) to the gravitational dynamics of the model. To solve the gravitational field equations, we assume a power-law expansion, $C = C_0 t^\beta$, where C_0 and β are positive constants. The parameter β is constrained to the range $0 < \beta < 1$, ensuring a physically realistic cosmological model consistent with observed behaviors such as a decelerating phase followed by accelerated expansion.

Exact solutions to the field equations are derived under these assumptions, and the resulting model is analyzed by plotting various parameters of cosmological importance, as functions of cosmic time t. The horizontal axis of the plots is expressed in Gigayears (Gyr), where 1 Gyr corresponds to 10^9 years, to provide a clear representation of the universe's evolution over time.

By varying the parameter β, we examine how the model's qualitative behavior changes with different expansion rates. The plots offer insights into the dynamical properties of the universe, such as its anisotropy, the transition from deceleration to acceleration, and the roles of curvature in driving its evolution. This approach allows us to better understand the implications of $f(R,T)$ gravity and the viability of the chosen functional form in describing the observed universe.

From the variations of cosmologically significant parameters, we observe that volume (V) of the universe increases with cosmic time t which indicates the expansion of the universe. Our model remains anisotropic throughout its evolution. The average Hubble parameter (H) starts at a very high value and decreases over time. The deceleration parameter (q) transits from an early decelerating phase to a late-time accelerating phase, indicating that the universe undergoes accelerated expansion at later times. The jerk parameter (j) decreases with cosmic time t and remains below 1 throughout the universe's evolution, suggesting that our model behaves like a quintessence model of dark energy.

Moreover, the present-day value of the statefinder pair $\{r, s\}$ for our model is found to be in the range $r < 1, s > 0$. For example, with values of the constants $\beta = 0.75$, $k_1 = 0.1$, $C_0 = 1$, $l = 1$, $\lambda_1 = -0.1$, $\lambda_2 = 0.2$, $\lambda_3 = 0.3$, $t = 14$, the present value of the statefinder pair is $\{0.031, 0.126\}$, indicating that the model resembles a quintessence model both in the present and at late times. The statefinder diagnostic provides a deeper insight into the nature of dark energy, with our model's parameters indicating a close resemblance to quintessence, a widely studied candidate for dark energy.

The energy density (ρ) of our model monotonically decreases from a very high initial value to a constant value at late times, while the pressure (p) remains negative throughout its evolution. We also evaluate the Ricci scalar R and the trace T of the stress-energy tensor to determine the functional form $f(R,T)$ of our model. At the early stages of cosmic evolution, the functional $f(R,T)$ exhibits a decreasing pattern. This behavior is primarily driven by the dominance of high curvature (R) and significant contributions from the trace of the stress-energy tensor (T), which characterize the high-energy, dense state of the early universe. During this phase, the rapid expansion and changes in matter-energy densities lead to a reduction in $f(R,T)$. As cosmic time progresses, the functional $f(R,T)$ transitions from a decreasing to an increasing trend. This shift occurs as the influence of matter and radiation diminishes with the universe's expansion. The curvature (R) also evolves due to the decelerating expansion in earlier phases and the subsequent transition to accelerated expansion. The increasing trend of $f(R,T)$ during intermediate times reflects the growing influence of dark energy or the modified gravity terms associated with $f(R,T)$ in shaping the universe's dynamics. This turning point in the behavior of $f(R,T)$ signifies the interplay between the curvature scalar (R) and the trace of the stress-energy tensor (T) as the dominant components of the universe's energy content evolve. The rise in $f(R,T)$ suggests that the modified gravity effects encoded in $f(R,T)$ become increasingly significant as the universe transitions toward its accelerated expansion phase. Overall, the evolution of $f(R,T)$ highlights the adaptability of the $f(R,T)$ framework in capturing the changing dynamics of the universe, from a matter-dominated phase to one governed by dark energy or other modified gravity effects.

In addition to the quantitative analysis, we also discuss the physical implications of our findings in the broader context of cosmological models. The persistent anisotropy in our model suggests that early universe anisotropies can have long-lasting effects, influencing the current and future dynamics of cosmic expansion. The transition of the deceleration parameter from positive to negative values supports the hypothesis that the universe has transitioned from a matter-dominated decelerating phase to a dark energy-dominated accelerating phase.

Acknowledgments

The authors express their profound gratitude to the esteemed referee for his/her valuable comments and suggestions which helped to improve the quality of this paper in the present form.

ORCID

Chandra Rekha Mahanta, https://orcid.org/0000-0002-8019-8824; **Kankana Pathak**, https://orcid.org/0009-0004-0353-809X

REFERENCES

[1] S. Perlmutter, G. Aldering, G. Goldhaber, *et al*. "Measurements of Ω and Λ from 42 high-redshift supernovae," Astrophys. ApJ, **517**, (565) (1999). https://doi.org/10.1086/307221

[2] A. G. Riess, A. V. Filippenko, P. Challis, *et al*. "Observational evidence from supernovae for an accelerating universe and a cosmological constant," The Astronomical Journal, **116** (1009) (1998). https://doi.org/10.1086/300499

[3] R. R. Caldwell, M. Doran, "Cosmic microwave background and supernova constraints on quintessence: Concordance regions and target models," Phys. Rev. D, **69**, 103517 (2004). https://doi.org/10.1103/PhysRevD.69.103517

[4] Zhuo-Yi Huang, B. Wang, E. Abdalla, R.−K, Su, "Holographic explanation of wide-angle power correlation suppression in the Cosmic Microwave Background Radiation," J. Cosmol. Astropart. Phys. **5**, (013) (2006). https://doi.org/10.1088/1475-7516/2006/05/013

[5] K. Land and J. Magueijo, "Examination of Evidence for a preferred Axis in the Cosmic Radiation Anisotropy," Phys. Rev. Lett. **95**, 071301 (2005). https://doi.org/10.1103/PhysRevLett.95.071301

[6] C. L. Bennett, M. Halpern, G. Hinshaw, *et al*. "First-Year Wilkinson Microwave Anisotropy Probe (WMAP)* Observations: Preliminary Maps and Basic Results," Astrophys. J. Suppl. **148**, (1) (2003). https://doi.org/10.1086/377253

[7] C. L. Bennett, D. Larson, J. L. Weiland, *et al*. "Nine-Year Wilkinson Microwave Anisotropy Probe (WMAP) Observations: Final Maps and Results," ApJS, **208**, 20 (2013). https://doi.org/10.1088/0067-0049/208/2/20

[8] D. N. Spergel, L. Verde, H. V. Peiris, *et al*. "First Year Wilkinson Microwave Anisotropy Probe (WMAP) Observations: determination of cosmological parameters," ApJS, **148**, (175) (2003). https://doi.org/10.1086/377226

[9] D. N. Spergel, R. Bean, O. Dor'e, *et al*. "Three-year Wilkinson Microwave Anisotropy Probe (WMAP) observations: implications for cosmology," ApJS, **170**, 377 (2007). https://doi.org/10.1086/513700

[10] M. Tegmark, M. A. Strauss, M. R. Blanton, *et al*. "Cosmological parameters from SDSS and WMAP," Phys. Rev. D, **69**, 103501 (2004). https://doi.org/10.1103/PhysRevD.69.103501

[11] L. Anderson, E. Aubourg, S. Bailey, D. Bizyaev, M. Blanton, A. S. Bolton, *et al*. "The clustering of galaxies in the SDSS-III Baryon Oscillation Spectroscopic Survey: baryon acoustic oscillations in the Data Release 9 spectroscopic galaxy sample," Monthly Notices of the Royal Astronomical Society, **427**(4), 3435-3467 (2012). https://doi.org/10.1093/mnras/stu523

[12] C. Blake, E. A. Kazin, F. Beutler, T. M. Davis, D. Parkinson, S. Brough, *et al*. "The WiggleZ Dark Energy Survey: mapping the distance-redshift relation with baryon acoustic oscillations," Monthly Notices of the Royal Astronomical Society, **418**(3), 1707-1724 (2011). https://doi.org/10.1111/j.1365-2966.2011.19592.x

[13] N. Padmanabhan, X. Xu, D. J. Eisenstein, R. Scalzo, A. J. Cuesta, K. T. Mehta, E. Kazin, "A 2 per cent distance to $z = 0.35$ by reconstructing baryon acoustic oscillations-I. Methods and application to the Sloan Digital Sky Survey," Monthly Notices of the Royal Astronomical Society, **427**(3), 2132-2145 (2012). https://doi.org/10.1111/j.1365-2966.2012.21888.x

[14] T. Barreiro, E. J. Copeland and N. J. Nunes, "Quintessence arising from exponential potentials," Phys. Rev. D. **61**, 127301 (2000). https://doi.org/10.1103/PhysRevD.61.127301

[15] T. Chiba, T. Okabe, M. Yamaguchi, "Kinetically driven quintessence," Phys. Rev. D, **62**, 023511 (2000). https://doi.org/10.1103/PhysRevD.62.023511

[16] T. Padmanabhan, "Accelerated expansion of the universe driven by tachyonic matter,"Phys. Rev. D, **66**, 021301 (2002). https://doi.org/10.1103/PhysRevD.66.021301

[17] R. R. Caldwell, M. Kamionkowski and N. N. Weinberg, "Phantom Energy: Dark Energy with $\omega <$-1 Causes a Cosmic Doomsday," Phys. Rev. Lett. **91**, 071301 (2003). https://doi.org/10.1103/PhysRevLett.91.071301

[18] M. Li, "A model of holographic dark energy,"Phys. Lett. B, **603**, 1 (2004), https://doi.org/10.1016/j.physletb.2004.10.014

[19] C. Tsallis, and L. J. L. Cirto, "Black hole thermodynamical entropy," Eur. Phys. J. C, **73**, 2487 (2013), https://doi.org/10.1140/epjc/s10052-013-2487-6

[20] D. J. Barrow, "The area of a rough black hole," Phys. Lett. B, **808**, 135643 (2020). https://doi.org/10.1016/j.physletb.2020.135643

[21] A. Kamenshchik, U. Moschella, V. Pasquier, "An alternative to quintessence," Phys. Lett. B, **511**, 265-268 (2001). https://doi.org/10.1016/S0370-2693(01)00571-8

[22] M. C. Bento, O. Bertolami, and A. A. Sen, "Generalized Chaplygin gas, accelerated expansion, and dark-energy-matter unification," Phys. Rev. D, **66**, 043507 (2002). https://doi.org/10.1103/PhysRevD.66.043507

[23] H. B. Benaoum, "Modified Chaplygin Gas Cosmology," Advances in High Energy Physics, **2012**, 357802 (2012). https://doi.org/10.1155/2012/357802

[24] S. M. Carroll, V. Duvvuri, M. Trodden, and M. S. Turner, "Is cosmic speed-up due to new gravitational physics?" Phys. Rev. D, **70**, 043528 (2004). https://doi.org/10.1103/PhysRevD.70.043528

[25] T. Harko, F. S. N. Lobo, S. Nojiri and S. D. Odintsov, "$f(R,T)$ gravity," Phys. Rev. D, **84**, 024020 (2011). https://doi.org/10.1103/PhysRevD.84.024020

[26] S. M. Carroll, A. D. Felice, V. Duvvuri, D. A. Easson, M. Trodden, and M. S. Turner, "Cosmology of generalized modified gravity models," Phys. Rev. D, **71**, 063513 (2005). https://doi.org/10.1103/PhysRevD.71.063513

[27] R. Ferraro, and F. Fiorini, "Modified teleparallel gravity: Inflation without an inflaton," Phys. Rev. D, **75**, 084031 (2007). https://doi.org/10.1103/PhysRevD.75.084031

[28] J. B. Jiménez, L. Heisenberg, and T. Koivisto, "Coincident general relativity," Phys. Rev. D, **98**(4), 044048 (2018). https://doi.org/10.1103/PhysRevD.98.044048

[29] M.J.S. Houndjo, "Reconstruction of $f(R,T)$ gravity describing matter dominated and accelerated phases," Int. J. Mod. Phys. D, **21**, 1250003-1250016 (2012). https://doi.org/10.1142/S0218271812500034

[30] P. K. Sahoo, S. K. Sahu, and A. Nath, "Anisotropic Bianchi-III cosmological model in $f(R,T)$ gravity," Eur. Phys. J. Plus, **131**, 18 (2016). https://doi.org/10.1140/epjp/i2016-16018-6

[31] G. C. Samanta, and B. K. Bishi, "Geometry of the Universe Described by Wet Dark Fluid in $f(R,T)$ Theory of Gravity," Iran. J. Sci. Technol. Trans. A Sci. **41**, 223 (2017). https://doi.org/10.1007/s40995-017-0215-z

[32] S. Arora, S. Bhattacharjee, and P. K. Sahoo, "Late-time viscous cosmology in $f(R,T)$ gravity," New Astronomy, **82**, 101452 (2021). https://doi.org/10.1016/j.newast.2020.101452

[33] C. R. Mahanta, S. Deka, and K. Pathak, "Anisotropic Cosmological Model in $f(R,T)$ Theory of Gravity with a Quadratic Function of T," East European Journal of Physics, (3), 43-52 (2023). https://doi.org/10.26565/2312-4334-2023-3-02

[34] C. R. Mahanta, K. Pathak, and D. Das, "FLRW Cosmological Model with Quadratic Functional Form in $f(R,T)$ Theory of Gravity," East European Journal of Physics, (1), 29-43 (2025). https://doi.org/10.26565/2312-4334-2025-1-03

[35] M. K. Verma, M. K. Singh, and S. Ram, "Anisotropic Bulk Viscous Fluid Cosmological Model with Zero-Rest-Mass Scalar Field and Time-Dependent Cosmological Term," Int. J. Theor. Phys. **51**, 1729-1736 (2012). https://doi.org/10.1007/s10773-011-1050-1

[36] D. R. K. Reddy, R. Santikumar, and R. L. Naidu, "Bianchi type-III cosmological model in $f(R,T)$ theory of gravity," Astrophys. Space Sci. **342**, 249-252 (2012). https://doi.org/10.1007/s10509-012-1158-7

[37] V. Sahni, *et al.*, "Statefinder - a new geometrical diagnostic of dark energy," JETP Lett. **77**, 201 (2003). https://doi.org/10.1134/1.1574831

ДОСЛІДЖЕННЯ ВСЕСВІТУ БІАНКІ III ТИПУ З КВАДРАТИЧНИМ СЛІДОМ ТЕНЗОРА ЕНЕРГІЇ-НАПРУЖЕННЯ В $f(R,T)$ ТЕОРІЇ ГРАВІТАЦІЇ

Чандра Рекха Маханта, **Канкана Патхак**

Кафедра математики, Університет Гаухаті, Гувахаті - 781014, Індія

У цій роботі ми розглядаємо просторово однорідний та анізотропний всесвіт Біанкі III типу в гравітації $f(R,T)$ з функціональною формою $f(R,T) = f_1(R) + f_2(T)$ з $f_1(R) = \lambda_1 R$ та $f_2(T) = \lambda_2 T + \lambda_3 T^2$, де λ_1, λ_2 та λ_3 – вільні параметри. Ми отримуємо точні розв'язки рівнянь гравітаційного поля, розглядаючи степеневий розклад коефіцієнта масштабування напрямку. Контролюючи поточні значення параметрів космологічного значення, таких як параметр Хаббла H та параметр уповільнення q, досліджується динаміка та фізичні характеристики моделі. Ми також визначаємо функціональну форму $f(R,T)$ нашої моделі, оцінюючи скаляр Річчі R та слід T тензора енергії-напруження. Ми виявляємо, що наша модель залишається анізотропною протягом усієї своєї еволюції, а тиск космічної матерії залишається негативним. Виявлено, що параметр рівняння стану ω лежить у режимі квінтесенції, і тому наша модель поводиться як модель квінтесенції темної енергії.

Ключові слова: *простір-час типу III Біанкі; $f(R,T)$ гравітація; параметр уповільнення; параметр Хаббла*

East European Journal of Physics. 2. 19–33 (2026)
DOI: 10.26565/2312-4334-2026-2-02 ISSN 2312-4334

CONSTRAINING KANIADAKIS HOLOGRAPHIC DARK ENERGY MODEL IN BIANCHI TYPE–*III* COSMOLOGY

Y. Aditya[1*], **K. Dasunaidu**[1**], **Muralasetti Nookaraju**[2], **P. Silpa**[3], **G. Suryanarayana**[4]
[1]*Department of Mathematics, GMR Institute of Technology (GMRIT) – Deemed to be University, Rajam-532127, India*
[2]*Department of Chemistry, Aditya University, Surampalem-533437, India*
[3]*Department of Chemistry, Sri Vasavi Engineering College, Tadepalligudem-534101, India*
[4]*Department of Mathematics, ANITS, Visakhapatnam-533003, India*
[*]*Corresponding Author e-mail: [*]aditya.y@gmrit.edu.in; [**]dasunaidu.k@gmrit.edu.in*
Received February 6, 2026; revised April 21, 2026; accepted May 6, 2026

In this work, we study the cosmological dynamics of an anisotropic Bianchi type–*III* universe filled with Kaniadakis holographic dark energy and pressureless matter within the framework of Brans–Dicke–Rastall theory of gravity. To obtain exact solutions of the field equations, suitable relations among the metric potentials are assumed, together with a functional relation between the scalar field and the average scale factor. To constrain the model parameters, we perform a Markov Chain Monte Carlo analysis using joint CC+BAO datasets. The reconstructed Hubble parameter shows excellent agreement with observational data within the 1σ and 2σ confidence regions, and the estimated value of the Hubble constant is consistent with recent measurements. We derive several important cosmological parameters, including the Hubble parameter, deceleration parameter, equation of state parameter, scalar field, cosmic time and lookback time. The physical behavior of these parameters is analyzed through graphical representations. The deceleration parameter exhibits a smooth transition from an early decelerated phase to a late–time accelerated phase, with a transition redshift consistent with recent observational bounds. The equation of state parameter remains in the phantom region, indicating a dynamical dark energy behavior capable of driving the current accelerated expansion. Furthermore, the statefinder (r, s) and (r, q) diagnostics reveal that the model closely approaches the ΛCDM behavior at late times, while allowing deviations at earlier epochs. The $Om(z)$ diagnostic further supports the phantom–like nature of dark energy in the present framework. Overall, our results demonstrate that our model in Brans–Dicke–Rastall gravity provides a viable and observationally consistent description of the cosmic expansion history in an anisotropic universe.

Keywords: *Kaniadakis holographic dark energy; Brans–Dicke–Rastall gravity; Bianchi type–III universe; MCMC analysis; Cosmic acceleration*

PACS: 98.80.-k, 04.50.+h, 95.30.Sf

1. INTRODUCTION

Recent technological developments have led to a new era known as precision cosmology, where the large–scale properties of the Universe can be measured with high accuracy [1]. Even with these improvements, most of the Universe is still not fully understood. Observations such as galaxy rotation curves, gravitational lensing, and large–scale surveys confirm the presence of dark matter, which makes up nearly 25% of the total energy content of the Universe [2]. An even bigger mystery is dark energy (DE), which contributes about 70% of the present energy density and is responsible for the accelerated expansion of the Universe. Although strong evidence for DE comes from gravitational waves, baryon acoustic oscillations, and Type Ia supernova observations, its true nature is still unknown [3, 4]. This suggests that new physics beyond the standard model may be needed. One approach is modified gravity, where Einstein's general relativity is extended by adding new terms or scalar fields [5, 6]. A well–known example is the Brans–Dicke theory, where the gravitational constant G is replaced by a changing scalar field ϕ ($G^{-1} = \phi$) [7, 8]. Although this theory can explain cosmic acceleration, its predicted parameters often disagree with observations, so additional dark energy models are usually considered [9, 10, 11].

The cosmological constant was initially regarded as the simplest explanation for dark energy, since it represents vacuum energy and naturally produces accelerated cosmic expansion. Nevertheless, this interpretation faces well–known theoretical difficulties, notably the fine–tuning and coincidence problems. Motivated by these issues, the Holographic Dark Energy (HDE) model emerged as an alternative framework inspired by the holographic principle [12, 13]. The original HDE formulation is based on the Bekenstein–Hawking entropy relation and commonly adopts the Hubble horizon as the infrared (IR) cutoff, providing a quantitative description of dark energy. However, the standard HDE model struggles to fully describe the complete evolutionary history of a flat Friedmann–Robertson–Walker (FRW) Universe. To address these shortcomings, several extensions have been proposed, including the use of alternative IR cutoffs [14] and the introduction of interactions between dark energy and dark matter [15]. More recently, modified HDE models based on entropy–area law deformations have been developed while still employing the Hubble radius as the IR cutoff [16, 17, 18]. Such

Cite as: Y. Aditya, K. Dasunaidu, Muralasetti Nookaraju, P. Silpa, G. Suryanarayana, East Eur. J. Phys. 2, 19 (2026), https://doi.org/10.26565/2312-4334-2026-2-02

generalized models aim to provide a more flexible and observationally compatible explanation of cosmic acceleration. Further progress has been achieved through the introduction of generalized entropy formalisms, including Tsallis [19], Sharma–Mittal [20], and Rényi [21] entropies, to extend the HDE scenario. A significant unifying approach was proposed by Nojiri et al. [22, 23, 24], who introduced a four–parameter generalized entropy encompassing several well–known entropy measures as limiting cases. Among these, the Kaniadakis entropy [25] stands out as a one–parameter deformation of Boltzmann–Gibbs entropy, particularly suitable for strong gravitational regimes [26, 27]. Its incorporation into HDE leads to the Kaniadakis holographic dark energy (KHDE) model [28], which offers enhanced flexibility and potential solutions to long–standing cosmological problems such as fine–tuning and cosmic coincidence.

Rastall's theory of gravity is a non–Lagrangian modification of General Relativity in which the usual conservation of the energy–momentum tensor is relaxed. In Einstein's theory, the divergence of the energy–momentum tensor vanishes due to the divergence–free property of the Einstein tensor. Rastall proposed that in curved space–time the standard conservation law $T^{ij}_{\ ;i} = 0$ may not strictly apply and allowed a non–zero divergence instead [29]. The deviation from standard conservation is controlled by a dimensionless parameter λ, representing a non–minimal coupling between matter and geometry. This idea is physically motivated by cosmological particle creation processes, where classical conservation laws may effectively break down. In this sense, Rastall gravity can be viewed as a classical description that mimics certain quantum effects, since the non–conservation of the energy–momentum tensor is linked to space–time curvature [30, 31]. Similar relaxations of conservation laws have also inspired alternative Lagrangian approaches [32, 33]. The equivalence between Rastall gravity and General Relativity remains debated: some studies treat it as a genuine modification [34], while others argue for mathematical equivalence under specific conditions [35]. Recent works further examine its cosmological and dynamical implications [36, 37].

Rastall Theory: Since the formulation of general relativity, several alternative geometric theories of gravity have been proposed to better understand gravitational phenomena and cosmological evolution (see, for example, Rastall [29]; Brans and Dicke [8]; Moffat [38]; and Bekenstein [39]). A fundamental feature of GR is the conservation of the energy–momentum tensor. One of the earliest attempts to relax this conservation principle appeared in the steady–state cosmological model proposed by Bondi and Gold [40] and Hoyle [41]. Building on this idea, Rastall introduced a non–conservative theory of gravity by modifying the usual conservation law to $T^{ij}{}_{;i} = kR^{;j}$, where T^{ij} is the energy–momentum tensor, R is the Ricci scalar curvature, and k is a coupling constant. This modification implies that particle creation processes in cosmology may lead to an effective violation of classical conservation laws, with the deviation being directly related to the curvature of space–time. In this framework, the geometry and matter fields are non–minimally coupled, leading to a generalized form of Einstein's field equations. Rastall's modified gravitational field equations can be written as $G_{ij} + \lambda g_{ij} R = \kappa T_{ij}$, where λ is the Rastall parameter measuring the departure from standard conservation and κ is the gravitational coupling constant.

$$R_{ij} - \frac{1}{2} g_{ij} R = 8\pi G \left(T_{ij} - \frac{\lambda_{Ras} - 1}{2} g_{ij} T \right) \tag{1}$$

with equation of motion

$$T^{ij}_{\ ;i} = \frac{\lambda_{Ras} - 1}{2} T^{;j} \tag{2}$$

where $T^{ij}_{\ ;i} = \frac{\lambda_{Ras}-1}{16\pi G(2\lambda_{Ras}-3)} R^{;j}$ or $T^{ij}_{\ ;i} = \frac{\lambda_{Ras}-1}{2} T^{;j}$ with $R = 8\pi G(2\lambda_{Ras} - 3)T$, T is the trace of the stress-energy momentum tensor, and λ_{Ras} is Rastall's parameter. One can recover GR field equations by setting $\lambda_{Ras} = 1$.

Brans-Dicke-Rastall Theory: In the BD context, identifying $G = \frac{1}{\phi}$ and $\lambda_{Ras} = \frac{3\lambda-2}{2\lambda-1}$, λ is BDR parameter, in Eq. (2), we obtain the following relation:

$$T^{ij}_{\ ;i} = \frac{(1-\lambda)\phi}{16\pi} R^{;j}. \tag{3}$$

Generalizing Rastall's field equations to the BD case, we obtain:

$$R_{ij} - \frac{\lambda}{2} g_{ij} R = \frac{8\pi}{\phi} T_{ij} + \left(-\frac{1}{2} g_{ij} \phi_{;k} \phi^{;k} + \phi_{;i} \phi_{;j} \right) \frac{w}{\phi^2} + \frac{1}{\phi} \left(-g_{ij} \Box\phi + \phi_{;i;j} \right) \tag{4}$$

in which the dimensionless BD coupling parameter is denoted by w and the BD scalar field is denoted by ϕ. The trace of the Eq. (4) is obtained as

$$R = \frac{1}{1-2\lambda} \left(\frac{8\pi}{\phi} T - \frac{w}{\phi^2} \phi_{;k} \phi^{;k} - 3\frac{\Box\phi}{\phi} \right). \tag{5}$$

Now, using the Eqs. (4) and (5), we obtain the BDR theory field equations as

$$R_{ij} - \frac{1}{2} g_{ij} R = \frac{8\pi}{\phi} \left(T_{ij} - \frac{1-\lambda}{2(1-2\lambda)} g_{ij} T \right) + \left(\frac{\lambda}{2(1-2\lambda)} g_{ij} \phi_{;k} \phi^{;k} + \phi_{;i} \phi_{;j} \right) \frac{w}{\phi^2}$$

$$+\frac{1}{\phi}\left(\frac{1+\lambda}{2(1-2\lambda)}g_{ij}\Box\phi+\phi_{;i;j}\right). \tag{6}$$

The Bianchi identities lead to:

$$\Box\phi=\frac{8\pi\lambda}{3\lambda-2(1-2\lambda)w}T-\frac{w(1-\lambda)}{3\lambda-2(1-2\lambda)w}\frac{\phi^{;k}\phi_{;k}}{\phi}. \tag{7}$$

For $\lambda = 1$, the Brans–Dicke–Rastall (BDR) theory reduces to the standard BD model. BDR is distinctive because it unifies scalar–tensor dynamics with a non–conservative energy–momentum framework inspired by Rastall gravity. Unlike higher–order theories such as $f(R)$ gravity, BDR preserves second–order field equations and involves fewer dynamical degrees of freedom, making it mathematically simpler. The additional parameters λ and ω provide flexibility for fitting cosmological observations and explaining late–time cosmic acceleration. Its non–conservative nature allows effective matter creation or matter–geometry interaction, enabling the model to mimic dark energy effects and slightly modify astrophysical structures compared to GR or BD theory.

The choice of a Bianchi type (BT)-III background allows for the incorporation of spatial anisotropy, which may have been significant in the early universe (Ref. [42]-[52]). While current cosmological observations strongly support isotropy on large scales, considering anisotropic geometries like BT-III offers deeper insights into possible deviations from perfect isotropy and helps to understand how anisotropies might decay or leave imprints on late-time cosmic dynamics. Studies on KHDE are also emerging in various contexts [53, 54, 55, 56]. Ghaffari [57] studied KHDE model in BD theory of gravity and investigated their cosmological consequences. Ali et al. [58] explored the dynamics of isotropic KHDE model in the Chern-Simons modified theory. Murali et al. [59, 60] have investigated anisotropic KHDE models in scalar-tensor theory of gravity. Embedding these two aspects of the universe in the background of BDR theory further enhances its physical relevance. BD gravity introduces a dynamical scalar field, reflecting Mach's principle and varying gravitational coupling, while Rastall's hypothesis modifies the conservation law of the energy–momentum tensor. Their combination (i.e., BDR theory) provides an effective platform to explore non-standard energy exchange between matter, geometry, and DE, which is crucial for explaining cosmic acceleration without relying exclusively on a cosmological constant. The Hubble cutoff provides a simple and large-scale measure of cosmic dynamics. With this motive, the investigation of BT-III KHDE model with Hubble cutoff within the framework of BDR theory provides a promising way to address fundamental questions about the universe's accelerated expansion and the role of extended theories of gravity. We organized the paper as follows: Section-2 consists the field equations of the model and analytical solution of the field equations. Section-3 includes the observational constraints made on these solutions are imposed by cosmic chronometer and BAO Hubble datasets using Markov Chain Monte Carlo analysis. In section-4, we discuss the dynamical behavior of models, and conclusions are given in section-5.

2. KANIADAKIS HOLOGRAPHIC DARK ENERGY MODEL

The BT–III space–time is considered in the following form:

$$ds^2=dt^2-[A(t)]^2dx^2-[B(t)]^2e^{2x}dy^2-[C(t)]^2dz^2. \tag{8}$$

From the non–vanishing components of the Einstein tensor for the BT–III space–time, it is observed that $G_4^1=\frac{\dot{A}}{A}-\frac{\dot{B}}{B}=0$, which, upon integration, yields the relation $A=a_1B$, where a_1 is an integration constant. Without loss of generality, by choosing $a_1=1$, we obtain $A=B$. The total energy–momentum tensor of the source is assumed to be a combination of the matter and dark energy components (in mixed form), $T_i^{j(tot)}=T_i^{j(m)}+T_i^{j(de)}$. We define the matter and DE tensors as diagonal tensors in the comoving frame (i.e., $u^i=(1,0,0,0)$, $u_i=(1,0,0,0)$ and $u^iu_i=1$), namely

$$T_i^{j(m)}=\mathrm{diag}(\rho_m,\,0,\,0,\,0)\,,\qquad \overline{T}_i^{j(de)}=\mathrm{diag}\big(\rho_{de},\,-p_x,\,-p_y,\,-p_z\big)\,, \tag{9}$$

with the anisotropic equation of state

$$p_x=\omega_{de}\rho_{de},\qquad p_y=\omega_{de}\rho_{de},\qquad p_z=(\omega_{de}+\gamma)\rho_{de}, \tag{10}$$

where the EoS parameter ω_{de} and the energy densities of matter are denoted as ρ_m and DE as ρ_{de} in this equation. The deviation parameter, γ, is the deviation along z-direction from the EoS parameter.

The BDR field equations (6) for the metric (8) in a comoving coordinate system can be formally expressed using (9) and (10) as

$$\begin{aligned}\frac{\ddot{A}}{A}+\frac{\ddot{C}}{C}+\frac{\dot{A}\dot{C}}{AC} &= \frac{8\pi}{\phi}\left(\frac{1+\lambda}{2-4\lambda}\omega_{de}\rho_{de}+\frac{1-\lambda}{2-4\lambda}\gamma\rho_{de}+\frac{\lambda-1}{2-4\lambda}(\rho_m+\rho_{de})\right)+w\left(\frac{\dot{\phi}}{\phi}\right)^2\left(\frac{\lambda}{2-4\lambda}\right)\\ &\quad+\left(\frac{2-\lambda}{1-2\lambda}\right)\frac{\dot{A}}{A}\frac{\dot{\phi}}{\phi}+\left(\frac{1+\lambda}{2-4\lambda}\right)\frac{\dot{C}}{C}\frac{\dot{\phi}}{\phi}+\left(\frac{1+\lambda}{2-4\lambda}\right)\frac{\ddot{\phi}}{\phi}\end{aligned} \tag{11}$$

$$2\frac{\ddot{A}}{A}+\left(\frac{\dot{A}}{A}\right)^2-\frac{1}{A^2} = \frac{8\pi}{\phi}\left(\frac{1+\lambda}{2-4\lambda}\omega_{de}\rho_{de}+\frac{3\lambda-1}{2-4\lambda}\gamma\rho_{de}+\frac{\lambda-1}{2-4\lambda}(\rho_m+\rho_{de})\right)+w\left(\frac{\dot{\phi}}{\phi}\right)^2\left(\frac{\lambda}{2-4\lambda}\right) + \left(\frac{1+\lambda}{1-2\lambda}\right)\frac{\dot{A}}{A}\frac{\dot{\phi}}{\phi}+\left(\frac{3-3\lambda}{2-4\lambda}\right)\frac{\dot{C}}{C}\frac{\dot{\phi}}{\phi}+\left(\frac{1+\lambda}{2-4\lambda}\right)\frac{\ddot{\phi}}{\phi} \tag{12}$$

$$2\frac{\dot{A}}{A}\frac{\dot{C}}{C}+\left(\frac{\dot{A}}{A}\right)^2-\frac{1}{A^2} = \frac{8\pi}{\phi}\left(\frac{1-3\lambda}{2-4\lambda}(\rho_m+\rho_{de})+\frac{3-3\lambda}{2-4\lambda}\omega_{de}\rho_{de}+\frac{1-\lambda}{2-4\lambda}\gamma\rho_{de}\right) +w\left(\frac{\dot{\phi}}{\phi}\right)^2\left(\frac{2-3\lambda}{2-4\lambda}\right)+\left(\frac{1+\lambda}{1-2\lambda}\right)\frac{\dot{A}}{A}\frac{\dot{\phi}}{\phi}+\left(\frac{1+\lambda}{2-4\lambda}\right)\frac{\dot{C}}{C}\frac{\dot{\phi}}{\phi} +\left(\frac{3-3\lambda}{2-4\lambda}\right)\frac{\ddot{\phi}}{\phi} \tag{13}$$

$$\ddot{\phi}+\left(\frac{2\dot{A}}{A}+\frac{\dot{C}}{C}\right)\dot{\phi}=\left(\frac{8\pi\lambda(\rho_{de}+\rho_m-3\omega_{de}\rho_{de}-\gamma\rho_{de})}{3\lambda-2(1-2\lambda)w}\right)-\left(\frac{w(1-\lambda)}{3\lambda-2(1-2\lambda)w}\right)\left(\frac{\dot{\phi}^2}{\phi}\right). \tag{14}$$

The field equations given in Eqs. (11)–(14) constitute a system of four independent equations containing six unknown functions, namely the metric potentials A and C, the dark energy density ρ_{de}, its equation of state parameter ω_{de}, the matter density ρ_m, and the skewness parameter γ. To obtain a deterministic solution, two additional physically motivated constraints are required. A commonly adopted assumption is that the expansion scalar $\theta=\frac{2\dot{A}}{A}+\frac{\dot{C}}{C}$ is proportional to the shear scalar $\sigma^2=\frac{1}{3}\left(\frac{\dot{A}}{A}-\frac{\dot{C}}{C}\right)^2$, which leads to a simple relation between the metric potentials of the form $C=A^k$, where $k\neq 1$ is an arbitrary constant. The physical relevance of this proportionality condition has been discussed in detail by Thorne [61]. Observational evidence indicates that the present Hubble expansion of the Universe is nearly isotropic within approximately ±30% [62, 63], and measurements at moderate redshifts further constrain the ratio $\sigma/H\leq 0.3$. The assumption that σ/H remains constant corresponds to a normal congruence, as shown by Collins et al. [64], and is valid for spatially homogeneous space–times. In addition, following common practice in the literature, we assume a power–law relation between the scalar field and the scale factor, $\phi\propto[a(t)]^n$, which has been widely employed in scalar–tensor cosmological studies [65, 66]. Several investigations have examined the dynamical behavior of the scalar field under this assumption [67]-[70]. Motivated by its physical significance and its ability to simplify the system, we adopt the relation $\phi(t)=\phi_0[a(t)]^k$, where ϕ_0 is a constant of proportionality.

Using the above relations in Eqs. (12) and (13), we get

$$\frac{\ddot{A}}{\dot{A}}+\left(\frac{3k+3+kn+2n}{3}\right)\frac{\dot{A}}{A}=\frac{1}{k-1}\left[\frac{8\pi\gamma\rho_{de}}{\phi}-\frac{1}{A^2}\right]\frac{A}{\dot{A}} \tag{15}$$

The relationship between DE's energy density and the skewness or deviation parameter has been the subject of numerous recent investigations. Anisotropic DE models were investigated by Akarsu and Kilinc [71], who took into account a correlation between DE energy density and skewness factors. In a similar vein, Sharif and Zubair [72] examined dynamical anisotropic DE models using the identical relation. We assume the following relationship between $\gamma(t)$ and ρ_{de} in order to completely resolve Eq. (15)

$$\gamma(t)=\frac{\phi}{8\pi\rho_{de}}\left[(k-1)\gamma_0\frac{\dot{A}}{A}+\frac{1}{A^2}\right] \tag{16}$$

in which every given constant is represented by γ_0. Various authors have explored comparable relationships in the literature [73]-[76]. We can find our model's metric potentials by plugging the Eq. (16) into Eq. (15)

$$A = \left(k_1e^{\gamma_0t}+k_2\right)^{\frac{b_2}{k_2}},\quad C=\left(k_1e^{\gamma_0t}+k_2\right)^{\frac{kb_2}{k_2}} \tag{17}$$

where $k_1=\frac{(k+2)(n+3)}{3}\frac{b_1}{\gamma_0}$, $k_2=\frac{(k+2)b_2(n+3)}{3}$, b_1 and b_2 are integrating constants. Now using these metric potentials (17), we can rewrite the space-time as

$$ds^2=dt^2-\left(k_1e^{\gamma_0t}+k_2\right)^{\frac{2b_2}{k_2}}dx^2-\left(k_1e^{\gamma_0t}+k_2\right)^{\frac{2b_2}{k_2}}e^{2x}dy^2-\left(k_1e^{\gamma_0t}+k_2\right)^{\frac{2kb_2}{k_2}}dz^2. \tag{18}$$

Now the scalar field ϕ calculated as

$$\phi=\phi_0\left(k_1e^{\gamma_0t}+k_2\right)^{\frac{n}{n+3}}. \tag{19}$$

The Hubble parameter $H(z)$ can be obtained as

$$H = \frac{1}{3}\left(2\frac{\dot{A}}{A} + \frac{\dot{C}}{C}\right) = \left(\frac{k+2}{3}\right)\left(\frac{b_2}{k_2}\right)\left(\frac{k_1 e^{\gamma_0 t}\gamma_0}{k_1 e^{\gamma_0 t} + k_2}\right) \tag{20}$$

$$= \frac{\gamma_0}{n+3}\left[1 - k_2(1+z)^{n+3}\right]$$

$$= \frac{H_0}{1-k_2}\left(1 - k_2(1+z)^{n+3}\right) \tag{21}$$

where $1 + z = \frac{1}{a(t)}$ and $a(t)$ is average scale factor. Here $\frac{H_0}{1-k_2} = \frac{\gamma_0}{n+3}$. We will constrain following parameters H_0, n and k_2 with observational datasets in section-III. We will evaluate the parameters γ_0 and k from the expression $\gamma_0 = \frac{H_0(n+3)}{1-k_2}$, and $k = \frac{3k_2}{(n+3)b_2} - 2$ for appropriate choice of arbitrary integrating constant b_2 and observationally constrained values of H_0, n and k_2.

KHDE: A generalized single-parameter entropy, known as the Kaniadakis entropy (κ-entropy) [77, 78, 79], is defined as

$$S_\kappa = -\sum_{i=1}^{W} \frac{P_i^{1+\kappa} - P_i^{1-\kappa}}{2\kappa} = \frac{1}{2}\left[\frac{\sum_{i=1}^{W}(P_i^{1-\kappa} - P_i)}{\kappa} + \frac{\sum_{i=1}^{W}(P_i^{1+\kappa} - P_i)}{-\kappa}\right], \tag{22}$$

where P_i denotes the probability of occupation of the i^{th} microstate of a classical system. The parameter κ encodes deviations from extensivity, and in the limit $\kappa \to 0$, the standard Boltzmann–Gibbs entropy is recovered [77, 78]. For an equiprobable distribution $P_i = 1/W$, Eq. (22) yields [77, 78, 79]

$$S_\kappa = \frac{W^\kappa - W^{-\kappa}}{2\kappa} \quad \Longrightarrow \quad S_\kappa = \frac{1}{\kappa}\sinh(\kappa S_{\text{BH}}), \tag{23}$$

where $S_{\text{BH}} \propto \dfrac{\mathcal{A}}{4G} = \dfrac{\pi L^2}{G}$ is the Bekenstein–Hawking entropy and G denotes Newton's constant.

Recently, Nojiri et al. [22, 23, 24] introduced a generalized four-parameter entropy function capable of reproducing several important entropy formalisms—such as Tsallis, Rényi, Barrow, Sharma–Mittal, Kaniadakis, and loop quantum gravity entropies—as special limiting cases. The proposed generalized entropy S_g is given by

$$S_g[\alpha_+, \alpha_-, \beta, \gamma] = \frac{1}{\gamma}\left[\left(1 + \frac{\alpha_+}{\beta}S_{\text{BH}}\right)^{\beta} - \left(1 + \frac{\alpha_-}{\beta}S_{\text{BH}}\right)^{-\beta}\right], \tag{24}$$

where $\alpha_+, \alpha_-, \beta$, and γ are positive parameters. For the particular limit $\beta \to \infty$ and $\alpha_+ = \alpha_- = \gamma/2 = \kappa$, Eq. (24) reduces to

$$S_\kappa = \frac{1}{\kappa}\sinh(\kappa S_{\text{BH}}), \tag{25}$$

which matches the Kaniadakis entropy in Eq. (23). Using the holographic principle, the energy density associated with the Kaniadakis entropy (23) takes the form

$$\rho_{de} \propto \frac{S_\kappa}{L^4} \quad \Longrightarrow \quad \rho_{de} = \frac{3c^2 M_p^2}{\kappa L^4}\sinh\left(\frac{\kappa\pi L^2}{G}\right), \tag{26}$$

where $M_p^2 = 1/(8\pi G)$ is the reduced Planck mass, L is the IR cutoff length scale, c is a model constant, and κ is the Kaniadakis parameter. In the Brans–Dicke (BD) framework, the gravitational coupling is dynamical, with $G = 1/\phi$. Substituting this relation into Eq. (26), the Kaniadakis holographic dark energy (KHDE) density becomes

$$\rho_{de} = \frac{3c^2\phi}{8\pi\kappa L^4}\sinh\left(\kappa\pi L^2\phi\right). \tag{27}$$

In holographic dark energy (HDE) models, the choice of the infrared (IR) cutoff is crucial for determining the cosmic dynamics. Among various possibilities, the Hubble horizon $\mathcal{L} = H^{-1}$ is considered one of the most natural and physically motivated options. The IR cutoff sets the largest length scale that contributes to the dark energy density. Different cutoffs, such as the particle or event horizons, can significantly alter the Universe's evolution. Unlike the event horizon, which depends on the future expansion history, the Hubble horizon is locally defined and free from causality issues. Therefore, adopting the Hubble radius as the IR cutoff provides a local, causal, and observationally consistent description of dark energy. By setting $\mathcal{L} = 1/H$, we obtain

$$\rho_{de} = \frac{3c^2 H^4\phi}{8\pi\kappa}\sinh\left(\frac{\kappa\pi\phi}{H^2}\right) \tag{28}$$

where Hubble parameter H is given by Eq. (20). Using Hubble parameter (20) in Eq. (28), we obtain the energy density of BHDE with Hubble horizon as IR cutoff as

$$\rho_{de} = \frac{3c^2 {k_1}^4 \left(\mathrm{e}^{\gamma_0 t}\right)^4 {\gamma_0}^4 \phi_0 \left(k_1 \mathrm{e}^{\gamma_0 t} + k_2\right)^{\frac{n}{n+3}-4}}{8\,(n+3)^4\,\pi\,\kappa} \sinh\left(\frac{\pi\,\kappa\,\phi_0\,(n+3)^2\left(k_1 \mathrm{e}^{\gamma_0 t} + k_2\right)^{\frac{3n+6}{n+3}}}{{k_1}^2\left(\mathrm{e}^{\gamma_0 t}\right)^2 {\gamma_0}^2}\right). \tag{29}$$

The BT-III universe with KHDE inside the framework of BDR theory of gravity is shown by Eq. (18), the scalar field (19), and the energy density (29). Using Eqs. (11), (12), (17), (19) and (29), we obtain the EoS parameter of our model as

$$\begin{aligned}
\omega_{de} \;=\; & \frac{8}{3}\frac{(n+3)^4\left(k_1 e^{\gamma_0 t}+k_2\right)^4 \pi\kappa}{c^2 k_1^4 e^{4\gamma_0 t}\gamma_0^4\phi_0}\left[\frac{1}{8}\frac{\phi_0(1-3\lambda)}{\pi(2-4\lambda)}\left(k_1 e^{\gamma_0 t}+k_2\right)^{\frac{n}{n+3}}\right. \\
& \times\left\{\frac{b_2^2 k_1^2\gamma_0^2 e^{2\gamma_0 t}+b_2 k_1 k_2^2\gamma_0^2 e^{\gamma_0 t}}{k_2^2(k_1 e^{\gamma_0 t}+k_2)^2}+\frac{k^2 b_2^2 k_1^2\gamma_0^2 e^{2\gamma_0 t}+k b_2 k_1 k_2^2\gamma_0^2 e^{\gamma_0 t}}{k_2^2(k_1 e^{\gamma_0 t}+k_2)^2}\right. \\
& \left.\left.+\frac{k b_2^2 k_1^2\gamma_0^2 e^{2\gamma_0 t}}{k_2^2(k_1 e^{\gamma_0 t}+k_2)^2}\right\}-\frac{1-\lambda}{2-4\lambda}\left(\frac{(k-1)\gamma_0^2 b_2 k_1 e^{\gamma_0 t}}{k_2(k_1 e^{\gamma_0 t}+k_2)}+\left(k_1 e^{\gamma_0 t}+k_2\right)^{-2b_2/k_2}\right)\right. \\
& -\frac{w\lambda n^2 k_1^2\gamma_0^2 e^{2\gamma_0 t}}{(2-4\lambda)(n+3)^2(k_1 e^{\gamma_0 t}+k_2)^2}-\frac{(2-\lambda)b_2 k_1^2\gamma_0^2 e^{2\gamma_0 t} n}{(1-2\lambda)k_2(k_1 e^{\gamma_0 t}+k_2)^2(n+3)} \\
& \left.-\frac{(\lambda+1)k b_2 k_1^2\gamma_0^2 e^{2\gamma_0 t} n}{(2-4\lambda)k_2(k_1 e^{\gamma_0 t}+k_2)^2(n+3)}-\frac{(\lambda+1)\left[n^2 k_1^2\gamma_0^2 e^{2\gamma_0 t}+n(n+3)k_1 k_2\gamma_0^2 e^{\gamma_0 t}\right]}{(2-4\lambda)(n+3)^2(k_1 e^{\gamma_0 t}+k_2)^2}\right] \\
& \times\left[\frac{(\lambda+1)(1-3\lambda)}{(2-4\lambda)^2}-\frac{(\lambda-1)(3-3\lambda)}{(2-4\lambda)^2}\right]^{-1}\left(k_1 e^{\gamma_0 t}+k_2\right)^{-\frac{n}{n+3}} \\
& \times\left[\sinh\left(\frac{\pi\kappa\phi_0(n+3)^2(k_1 e^{\gamma_0 t}+k_2)^2}{k_1^2 e^{2\gamma_0 t}\gamma_0^2}\left(k_1 e^{\gamma_0 t}+k_2\right)^{\frac{n}{n+3}}\right)\right]^{-1}.
\end{aligned} \tag{30}$$

and we find the skewness parameter as

$$\begin{aligned}
\gamma \;=\; & \frac{(n+3)^4\left(k_1\mathrm{e}^{\gamma_0 t}+k_2\right)^4\kappa}{3c^2{k_1}^4\left(\mathrm{e}^{\gamma_0 t}\right)^4{\gamma_0}^4}\left(\frac{(k-1)\,{\gamma_0}^2 b_2 k_1\mathrm{e}^{\gamma_0 t}}{k_2\left(k_1\mathrm{e}^{\gamma_0 t}+k_2\right)}+\left(\left(k_1\mathrm{e}^{\gamma_0 t}+k_2\right)^{\frac{b_2}{k_2}}\right)^{-2}\right) \\
& \times\left(\sinh\left(\frac{\pi\,\kappa\,\phi_0\,(n+3)^2\left(k_1\mathrm{e}^{\gamma_0 t}+k_2\right)^2}{{k_1}^2\left(\mathrm{e}^{\gamma_0 t}\right)^2{\gamma_0}^2}\left(k_1\mathrm{e}^{\gamma_0 t}+k_2\right)^{\frac{n}{n+3}}\right)\right)^{-1}.
\end{aligned} \tag{31}$$

3. OBSERVATIONAL CONSTRAINTS

The Hubble tension refers to the persistent discrepancy between independent determinations of the present-day expansion rate of the Universe, H_0, obtained from early- and late-time observations. Measurements inferred from the cosmic microwave background (CMB), particularly those based on Planck data within the ΛCDM framework, yield a lower value of $H_0 \approx 67$–$68\,\mathrm{km\,s^{-1}\,Mpc^{-1}}$, whereas direct local measurements using the cosmic distance ladder (Cepheids and Type Ia supernovae) favor a higher value of $H_0 \approx 73$–$74\,\mathrm{km\,s^{-1}\,Mpc^{-1}}$ [80, 81, 82, 83]. This discrepancy has now reached a statistical significance of $\sim 5\sigma$ or higher, and in some recent analyses even exceeds 6σ, indicating that it is unlikely to arise from statistical fluctuations alone [84, 85]. Independent observations, including those from the James Webb Space Telescope, continue to support the higher local value, reinforcing the robustness of the tension [86]. At present, no single systematic uncertainty has been identified that can fully account for this disagreement, suggesting that the tension may point toward new physics beyond the standard cosmological model. Proposed resolutions include early-Universe modifications such as early dark energy or additional relativistic species, as well as late-time extensions involving dynamical dark energy, interacting dark sectors, or modified theories of gravity. Consequently, the Hubble tension has emerged as one of the most significant challenges to ΛCDM and provides a powerful probe for testing extensions of the standard cosmological paradigm. The exact solutions of the field equations in Brans–Dicke–Rastall (BDR) gravity with anisotropic dark energy contain three free model parameters, namely (n, H_0, k_2), which explicitly appear in the expression for the Hubble parameter. The primary objective is to constrain these parameters using observational Hubble datasets in order to validate the model in the context of the present Universe. For this purpose, we employed a joint dataset consisting of 57 Hubble parameter measurements obtained from cosmic chronometer (CC) and baryon acoustic oscillation (BAO) observations [87, 88]. The numerical analysis was carried out using the `emcee` Python package, where the parameter space around the local minima was explored through a Gaussian prior centered on the initial estimates with a fixed standard deviation ($\sigma = 1.0$). The chi–square function used for parameter estimation is defined as

$$\chi^2_H(n, H_0, k_2) = \sum_{i=1}^{57} \frac{\left[H_{\mathrm{th}}(z_i; n, H_0, k_2) - H_{\mathrm{obs}}(z_i)\right]^2}{\sigma^2_{H(z_i)}}, \tag{35}$$

where $H_{\rm obs}(z_i)$ denotes the observed Hubble parameter at redshift z_i, $H_{\rm th}(z_i; n, H_0, k_2)$ represents the theoretically predicted value from the model, and $\sigma_{H(z_i)}$ corresponds to the associated observational uncertainty. By minimizing the above chi–square function and performing a Markov Chain Monte Carlo (MCMC) analysis, we obtained the best–fit estimates for the parameters n, H_0, and k_2 using the combined observational datasets.

Datasets	Parameter	Prior	Value
Hubble (CC+BAO Data)	H_0	$(50, 100)$	$67.90^{+0.28}_{-0.89}$
	k_2	$(-1, 0)$	$-0.448^{+0.077}_{-0.068}$
	n	$(-2, -1)$	$-1.215^{+0.079}_{-0.092}$
	b_2	–	-0.26
	k	–	$+0.91^{+0.5265}_{-0.1840}$
	b_1	–	0.3

Table 1. The MCMC estimates.

Fig. 1 presents the marginalized one–dimensional posterior distributions and the two–dimensional confidence contours for the model parameters (k_2, H_0, n) obtained from the joint CC+BAO dataset using the Markov Chain Monte Carlo (MCMC) technique. The MCMC analysis efficiently explores the parameter space and provides robust constraints by minimizing the corresponding χ^2 function. From the one–dimensional posteriors, we obtain the best–fit values $k_2 = -0.448^{+0.077}_{-0.068}$, $H_0 = 67.90^{+0.28}_{-0.89}$, and $n = -1.215^{+0.079}_{-0.092}$ at the 1σ confidence level. The inferred value of the Hubble parameter H_0 is in good agreement with recent observational estimates, indicating the consistency of the present model with late–time cosmic expansion data. The two–dimensional contour plots show well–defined closed regions at 1σ and 2σ confidence levels, implying a strong correlation among the parameters and the statistical stability of the model. Fig. 2 shows the comparison between the reconstructed Hubble parameter $H(z)$ obtained from the best–fit model parameters and the observational CC+BAO data. The solid curve represents the best–fit evolution of $H(z)$, while the shaded regions correspond to the 1σ and 2σ confidence intervals derived from the MCMC analysis. The observational data points are found to lie well within the confidence regions across the entire redshift range, indicating an excellent agreement between the theoretical model and observations. For comparison, the standard ΛCDM prediction is also shown and exhibits a slightly different evolution at intermediate and higher redshifts. The close proximity of the best–fit curve to the ΛCDM model at low redshifts confirms that the present model successfully reproduces the observed late–time cosmic expansion. At higher redshifts, small deviations appear, reflecting the influence of anisotropy and modified gravity effects inherent in the model. Overall, the consistency of the reconstructed $H(z)$ with CC+BAO data demonstrates the robustness and observational viability of the proposed cosmological framework.

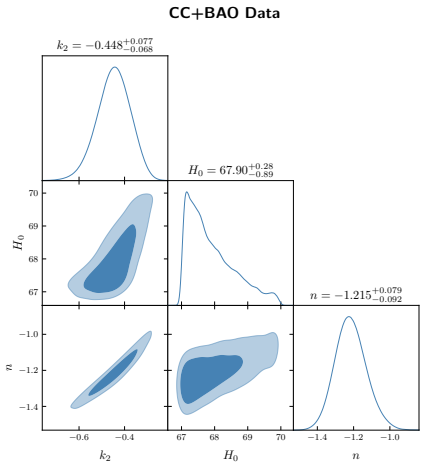

Figure 1. The 2D contour plots of H_0, n, k_2 at $\sigma 1$ and $\sigma 2$ level of confidence in the joint MCMC analysis of CC+BAO datasets.

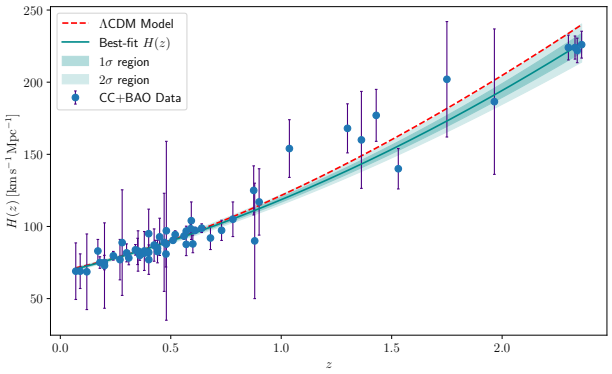

Figure 2. Evolution of Hubble parameter $H(z)$ versus redshift z. The solid line represents our model and dotted-line indicates the ΛCDM model with $\Omega_{m0} = 0.3$ and $\Omega_{\Lambda 0} = 0.7$. The dots are shown the Hubble dataset with error bar.

4. COSMOLOGICAL PARAMETERS

In this section, we examine the expansion dynamics of the Universe within the constructed KHDE model by employing several standard cosmological diagnostics. These include the equation of state (EoS) parameter ω_{de}, the squared

sound speed v_s^2, the deceleration parameter q, and the Om–diagnostic $Om(z)$. Furthermore, we analyze the evolutionary behavior of the model through well–known diagnostic planes such as the ω_{de}–ω'_{de} plane, the statefinder pair (r, s), and the r–q plane. For the graphical and numerical analysis, we adopt the constrained parameter values $H_0 = 67.9$, $k_2 = -0.448$, and $n = -1.215$, obtained from observational datasets. In addition, the derived and auxiliary parameters are chosen as $\gamma_0 = 83.7$, $k = 0.91$, $b_1 = 0.3$, $b_2 = -0.26$, $c = 0.03$, $\lambda = 0.7$, $\phi_0 = 95$, $\omega = 0.6$, and $\kappa = 0.2$. These parameter choices ensure physically consistent behavior of the cosmological quantities and provide a representative visualization of the model's dynamical evolution.

Scalar field

Fig. 3 illustrates the evolution of the scalar field ϕ as a function of redshift z. It is observed that the scalar field exhibits a monotonically increasing behaviour with increasing redshift, indicating that ϕ attains smaller values at late times and grows significantly toward the early universe. This behaviour suggests that the effective gravitational coupling, which is inversely related to the scalar field in Brans–Dicke theory, was stronger in the past and gradually weakens as the universe expands. Such an evolution is physically reasonable and consistent with scalar–tensor cosmological models, where deviations from general relativity are more prominent at early epochs. Moreover, the gradual growth of the scalar field supports a stable cosmic evolution and ensures compatibility with current observational constraints. Hence, the obtained scalar field dynamics reinforces the viability of the present cosmological model.

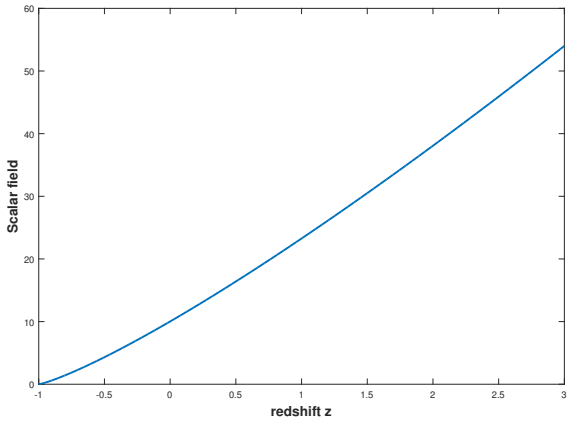

Figure 3. The plot between scalar field $\phi(z)$ and redshift z.

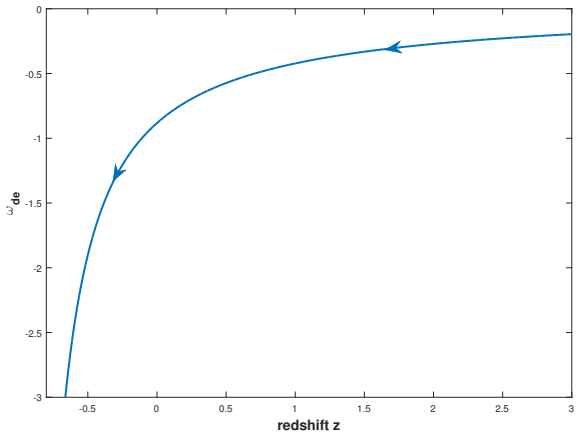

Figure 4. Plot of EoS parameter versus redshift z.

EoS parameter

The equation of state (EoS) parameter $\omega_{de} = p_{de}/\rho_{de}$ plays a fundamental role in understanding the dynamical nature of dark energy and the expansion history of the universe. Different values of ω_{de} correspond to distinct evolutionary phases, ranging from early decelerating epochs to the present accelerated expansion. Fig. 4 illustrates the evolution of the dark energy EoS parameter as a function of redshift z for the present model. From the Fig. 4, it is evident that ω_{de} remains less than -1 over a significant redshift range, indicating a phantom–like behaviour of dark energy. Such a regime is capable of driving strong accelerated expansion and is consistent with recent observational indications that mildly favor phantom or dynamical dark energy over a strict cosmological constant. At higher redshifts, the EoS parameter gradually approaches values closer to $\omega_{de} \to -1$, suggesting that the model effectively mimics a ΛCDM–like behaviour. The continuous transition of the EoS parameter reflects the dynamical nature of dark energy in the model, rather than a constant vacuum energy density. Overall, the evolution of the EoS parameter demonstrates that the proposed model successfully accounts for the present accelerated expansion of the universe while remaining consistent with a smooth cosmic evolution.

Deceleration parameter

The deceleration parameter $q(z)$ plays a crucial role in characterizing the expansion history of the universe, as its sign directly distinguishes between decelerated and accelerated phases of cosmic evolution. Physically, q measures the rate of change of the cosmic expansion relative to the Hubble expansion rate. If $q > 0$, the universe is in a decelerated expansion phase, while $q < 0$ indicates accelerated expansion. The case $q = 0$ corresponds to uniform expansion. The

redshift evolution of $q(z)$ allows us to determine the transition redshift at which the universe shifted from matter-dominated deceleration to dark-energy-driven acceleration. For our models it is defined as

$$q = -\frac{\ddot{a}a}{\dot{a}^2} = -1 - \frac{k_2\,(n+3)}{k_1 e^{\gamma_0 t}}. \tag{32}$$

where $a(t)$ is the scale factor. Fig. 5 depicts the evolution of q as a function of redshift z for the present model constrained by the CC+BAO data. At early times (higher redshifts), the deceleration parameter remains positive ($q > 0$), indicating a decelerating expansion phase dominated by matter and anisotropic effects. This behaviour is consistent with the standard cosmological picture of a matter-dominated universe in the past. As the universe evolves, $q(z)$ decreases monotonically and crosses the phantom divide line $q = 0$ at the transition redshift $z_t \simeq 0.79$, signaling a smooth transition from decelerated to accelerated expansion. Such a transition redshift is well supported by recent observational studies, thereby reinforcing the observational consistency of the model. At the present epoch ($z = 0$), the deceleration parameter attains a negative value $q_0 \approx -0.45$, confirming that the universe is currently undergoing accelerated expansion. Overall, the evolution of the deceleration parameter demonstrates that the model successfully describes a realistic and smooth cosmic expansion history.

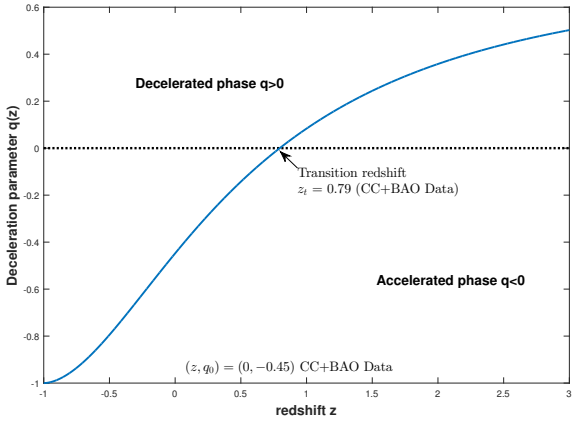

Figure 5. The plot between deceleration parameter q versus redshift z.

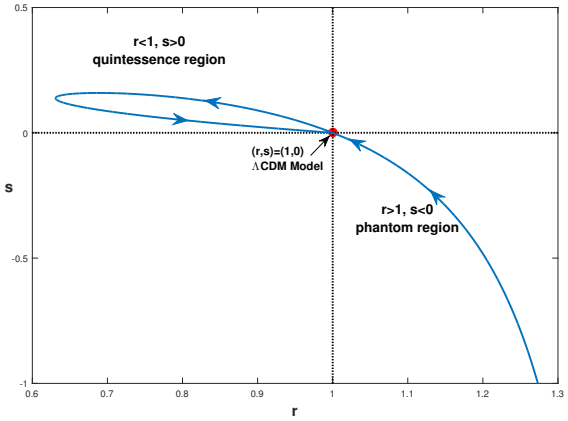

Figure 6. The plot of statefinder parameters.

Satefinders plane

In order to discriminate among various DE models that successfully explain the late–time accelerated expansion of the universe, higher–order geometrical diagnostics are required. Although different DE models can reproduce the same present–day values of the Hubble parameter H and the deceleration parameter q, these quantities alone are insufficient to distinguish between competing scenarios. To overcome this limitation, Sahni et al. [89] introduced the statefinder diagnostic pair (r, s), defined in Eq. (33), which depends on the third derivative of the scale factor and hence captures finer details of cosmic dynamics. Fig. 6 displays the evolution of the present model in the (r, s) plane. The trajectory clearly passes through different DE regimes, thereby offering a clear geometrical interpretation of the cosmic evolution. At early times, the trajectory lies in the region characterized by $r > 1$ and $s < 0$, which corresponds to the phantom–like dark energy regime. This behaviour indicates a strong acceleration phase driven by effective DE with an equation of state less than -1. As the universe evolves, the trajectory approaches the fixed point $(r, s) = (1, 0)$, which represents the standard ΛCDM model. The proximity of the trajectory to this point at late times implies that the present model closely mimics the concordance cosmology and is therefore consistent with current observations. At later epochs, the evolution enters the region $r < 1$ and $s > 0$, which is associated with quintessence–type DE behaviour. This transition signifies a gradual softening of the acceleration mechanism and reflects the dynamical nature of DE in the present framework. Overall, the statefinder analysis demonstrates that the proposed cosmological model is capable of interpolating between different DE regimes while remaining compatible with the ΛCDM limit.

$$r = 1 + \frac{3k_2\,(n+3)}{k_1 e^{\gamma_0 t}} + \frac{{k_2}^2\,(n+3)^2}{{k_1}^2\,(e^{\gamma_0 t})^2} - \frac{k_2\,(n+3)^2}{k_1 e^{\gamma_0 t}}$$

$$s = \left(\frac{3k_2\,(n+3)}{k_1 e^{\gamma_0 t}} + \frac{{k_2}^2\,(n+3)^2}{{k_1}^2\,(e^{\gamma_0 t})^2} - \frac{k_2\,(n+3)^2}{k_1 e^{\gamma_0 t}}\right)\left(-4.5 - \frac{3k_2\,(n+3)}{k_1 e^{\gamma_0 t}}\right)^{-1} \tag{33}$$

$r - q$ plane

The r–q plane provides a useful geometrical diagnostic to study the evolutionary behavior of cosmological models and to distinguish them from standard dark energy scenarios. In this plane, the fixed point $(r, q) = (1, 0.5)$ corresponds to the standard cold dark matter (SCDM) dominated universe, while the point $(r, q) = (1, -1)$ represents the steady state (SS) or de Sitter model, characterized by a constant expansion rate and exponential growth of the scale factor. The evolution of the present model in the r–q plane is shown in Fig. 7. From the Fig. 7, it is evident that the trajectory of the model begins in the vicinity of the SCDM point at early times, indicating that the universe undergoes a decelerated expansion phase dominated by matter. As cosmic time progresses, the trajectory smoothly departs from the SCDM fixed point and moves toward negative values of the deceleration parameter, reflecting the onset of late–time accelerated expansion. This transition signifies the gradual dominance of dark energy–like effects over matter. At late times, the trajectory approaches the steady state point $(r, q) = (1, -1)$, which corresponds to a de Sitter–type expansion. This behavior suggests that the universe evolves toward a phase of exponential expansion driven by an effective cosmological constant. The smooth and continuous nature of the trajectory confirms the absence of abrupt transitions or singular behavior, ensuring the physical stability of the model. Furthermore, the evolutionary path of the model closely resembles the expected behavior of the ΛCDM scenario, which evolves from the SCDM regime toward the steady state limit.

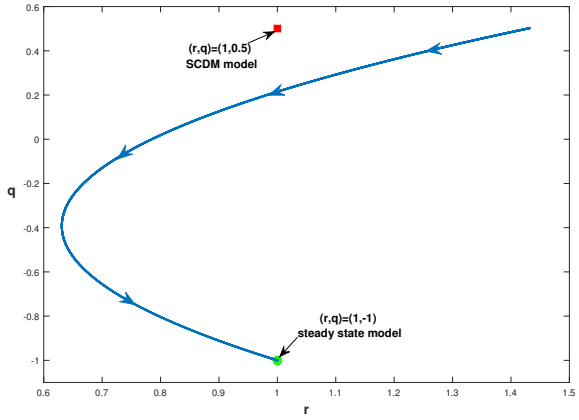

Figure 7. The plot of $Om(z)$ versus z.

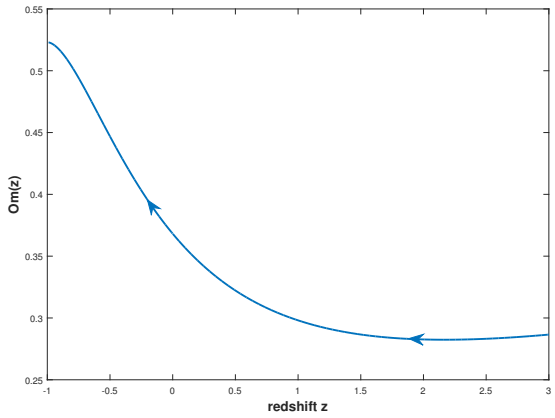

Figure 8. The plot between ω_{de} versus its derivative ω'_{de}.

Om-diagnostic parameter

The $Om(z)$ diagnostic provides an effective and model–independent tool to characterize the nature of dark energy by directly relating the Hubble parameter $H(z)$ to the redshift z. Unlike the equation of state parameter, the $Om(z)$ diagnostic does not require higher–order derivatives of the scale factor, making it particularly robust against observational uncertainties. In the standard ΛCDM cosmology, $Om(z)$ remains constant and positive for all redshifts, reflecting a constant dark energy density associated with a cosmological constant. It is defined as

$$Om(z) = \frac{H^2(z) - H_0^2}{((z+1)^3 - 1)H_0^2} = \frac{\left[\frac{1-k_2(1+z)^{n+3}}{1-k_2}\right]^2 - 1}{(z+1)^3 - 1}. \tag{34}$$

Fig. 8 illustrates the evolution of $Om(z)$ for the present model. It is evident that $Om(z)$ exhibits a clear decreasing trend with increasing redshift over a wide redshift range. Such a monotonic decrease in $Om(z)$ is a characteristic signature of phantom–like dark energy. This behaviour implies that the dark energy density grows with cosmic time, leading to a stronger acceleration at late epochs. The deviation of $Om(z)$ from a constant value further confirms that the present model does not reduce exactly to the ΛCDM scenario but represents a dynamically evolving dark energy framework. At higher redshifts, $Om(z)$ approaches a nearly constant value, indicating that the influence of dark energy becomes subdominant and the cosmic expansion is primarily governed by matter. This feature is consistent with the expected transition from a matter–dominated decelerating phase in the past to a dark energy–dominated accelerated phase at late times. Hence, the $Om(z)$ diagnostic strongly supports the viability of the proposed model as a realistic and physically consistent description of dark energy.

$\omega_{de} - \omega'_{de}$ Plane

The ω_{de}–ω'_{de} phase–space analysis serves as an important diagnostic tool to investigate the dynamical nature of dark energy, where the prime denotes differentiation with respect to $\ln a$. This method, introduced by Caldwell and Linder [90],

enables a clear classification of dark energy models based on their evolutionary behavior. In this framework, dark energy models are broadly categorized into two distinct regions: the thawing region, characterized by $\omega_{de} < 0$ and $\omega'_{de} > 0$, and the freezing region, where $\omega_{de} < 0$ and $\omega'_{de} < 0$. Fig. 9 depicts the evolution of the present model in the ω_{de}–ω'_{de} plane. It is evident that the trajectory lies entirely in the region $\omega_{de} < 0$ with $\omega'_{de} < 0$, which clearly corresponds to the freezing class of dark energy models. This behavior indicates that the dark energy equation of state evolves toward $\omega_{de} = -1$ at late times, gradually slowing down its dynamical evolution and mimicking a cosmological constant–like behavior in the future. The freezing nature of the model suggests that dark energy was more dynamic in the past and becomes increasingly dominant and stable as the universe expands. The ω_{de}–ω'_{de} analysis strongly supports that the present model belongs to the freezing dark energy class and provides a viable dynamical alternative to the standard ΛCDM model while remaining consistent with current observational constraints.

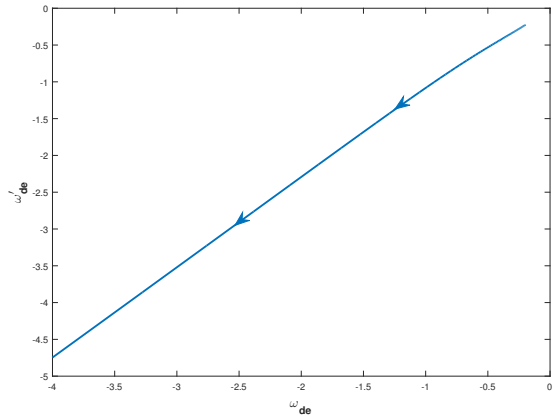

Figure 9. The plot between ω_{de} versus its derivative ω'_{de}.

Age of the model

The cosmic time $t(z)$ and the lookback time $t_0 - t(z)$ are important quantities for understanding the age and evolutionary history of the universe. We estimate the age of our model using:

$$t_0 - t = \int_0^z \frac{dz'}{(1+z')H(z')}. \tag{35}$$

For our model, we have obtained the expression for cosmic age of the universe as

$$t_0 - t = \frac{k_2 - 1}{(n+3)H_0} \ln\left[\frac{1 - k_2(1+z)^{n+3}}{(1-k_2)(1+z)^{n+3}}\right]. \tag{36}$$

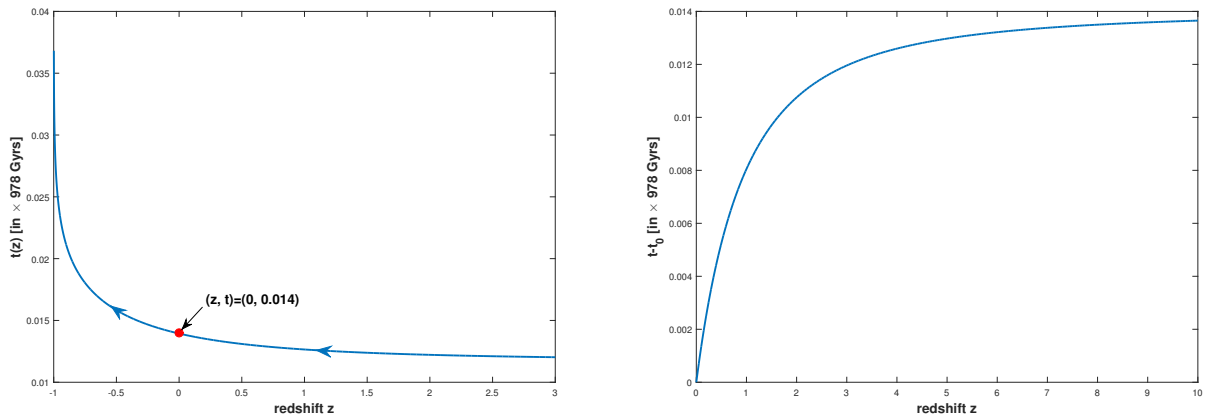

(a) (b)

Figure 10. The plot between cosmic time difference $t_0 - t$ and $t(z)$ versus redshift z.

Fig. 10(a) shows the variation of the cosmic time t as a function of redshift z. At the present epoch ($z = 0$), the cosmic time attains the value $t_0 \simeq 0.014 \times 978$ Gyr = 13.78 Gyr, which represents the current age of the universe in the adopted units. As z increases, $t(z)$ decreases rapidly, reflecting the faster expansion rate in the early universe. Fig. 10(b) illustrates the behaviour of the lookback time $t_0 - t(z)$ as a function of redshift. The lookback time increases monotonically with redshift, indicating that light emitted from higher redshifts has traveled longer durations before reaching the observer. At low redshifts, $t_0 - t(z)$ grows rapidly, while at higher redshifts the curve gradually flattens, showing that most of the cosmic age is accumulated at relatively small redshifts. This behaviour is consistent with an early decelerated expansion followed by a late-time accelerated phase. The smooth and regular evolution of both $t(z)$ and $t_0 - t(z)$ confirms the absence of any sudden transitions or singular behaviour in the cosmic history. Moreover, the consistency between the decreasing cosmic time and increasing lookback time reinforces the physical reliability of the present cosmological model and supports its compatibility with the standard picture of cosmic evolution.

5. CONCLUSIONS

In this work, we have investigated an anisotropic Bianchi type–III cosmological model filled with KHDE and pressureless matter within the framework of BDR theory of gravity. The combination of anisotropic geometry, modified gravity, and generalized holographic dark energy provides a rich and flexible framework to study cosmic evolution. By imposing suitable relations among the metric potentials and assuming a functional dependence between the Brans–Dicke scalar field and the average scale factor, we obtained exact analytical solutions of the field equations. Using these solutions, several key cosmological parameters were derived and analyzed in detail. The evolution of the Hubble parameter shows a smooth and physically reasonable behavior, consistent with observational data. In particular, the reconstructed $H(z)$ profile obtained from the best–fit parameters lies well within the 1σ and 2σ confidence regions of the CC+BAO datasets, demonstrating the robustness of the model against current observations. The model parameters were tightly constrained using a MCMC analysis with CC+BAO datasets. The resulting best–fit values, particularly for the Hubble constant, are in good agreement with recent observational estimates. The well–defined and closed confidence contours in the parameter space confirm the statistical stability and convergence of the MCMC analysis.

The deceleration parameter analysis reveals a clear transition from an early decelerated phase to the present accelerated phase of the universe. The transition redshift obtained in this model is compatible with recent observational constraints, confirming that the model can successfully reproduce the observed cosmic acceleration. This smooth transition further supports the physical viability of the model. The behavior of the equation of state parameter of dark energy plays a crucial role in characterizing the nature of cosmic acceleration. Our analysis shows that the EoS parameter remains in the phantom region throughout the evolution, implying $\omega_{de} < -1$. Such a behavior is capable of driving strong accelerated expansion and is consistent with several recent observational indications favoring dynamical dark energy over a strict cosmological constant. Importantly, the evolution of ω_{de} is smooth and free from divergences, indicating the absence of pathological future singularities within the considered redshift range. To further discriminate the present model from standard dark energy scenarios, we employed several geometrical diagnostics, including the statefinder (r, s) and (r, q) planes, as well as the $Om(z)$ diagnostic. The statefinder analysis shows that the evolutionary trajectory of the model passes through different dark energy regimes and approaches the ΛCDM fixed point at late times, indicating that the model can effectively mimic the concordance cosmology in the recent past while allowing deviations at earlier epochs. Similarly, the r–q plane demonstrates a smooth evolution from the standard cold dark matter dominated era toward a de Sitter–like steady state, reinforcing the consistency of the model with the expected cosmic history. The $Om(z)$ diagnostic exhibits a decreasing trend with redshift, which further confirms the phantom–like nature of dark energy in this framework and rules out a constant ΛCDM behavior. We also analyzed the evolution of the Brans–Dicke scalar field and the cosmic time parameters. The scalar field shows a regular and monotonic behavior, suggesting a time–varying effective gravitational coupling that evolves smoothly with cosmic expansion. The cosmic time and lookback time analyses indicate a consistent and realistic age of the universe, with no abrupt transitions or singular behavior, thereby strengthening the physical reliability of the model.

In conclusion, the present study demonstrates that the KHDE model within the BDR framework provides a viable and observationally consistent description of the cosmic expansion history in an anisotropic universe. The model successfully explains the transition from early deceleration to late–time acceleration, closely mimics ΛCDM behavior at late times, and allows for a dynamical dark energy component with phantom characteristics. These results highlight the potential of generalized holographic dark energy models in modified gravity theories as promising alternatives to the standard cosmological paradigm.

Acknowledgment

We sincerely thank the reviewer for their constructive and insightful comments, which have helped to substantially improve the presentation of this work. The work has been supported financially by National Board for Higher Mathematics, Department of Atomic Energy, Govt. of India under the Research project No.: 02011/8/2023 NBHM(R.P.)/R & D II/3073.

ORCID

Y. Aditya, https://orcid.org/0000-0002-5468-9697; **K. Dasunaidu**, https://orcid.org/0000-0003-3583-2432;
Muralasetti Nookaraju, https://orcid.org/0000-0002-3743-8036;
G. Suryanarayana, https://orcid.org/0000-0002-4866-4020

REFERENCES

[1] J. R. Primack, Nucl. Phys. B Proc. Suppl. **173**, 1 (2007). https://doi.org/10.1016/j.nuclphysbps.2007.08.152
[2] F. Zwicky, Helv. Phys. Acta, **6**, 110 (1933). https://doi.org/10.1007/s10714-008-0707-4
[3] S. Nojiri, and S. D. Odintsov, Phys. Lett. B, 639, 144 (2006). https://doi.org/10.1016/j.physletb.2006.06.065
[4] K. Bamba, *et al*., Astrophys. Space Sci. **342**, 155 (2012). https://doi.org/10.1007/s10509-012-1181-8
[5] E. J. Copeland, *et al*., Int. J. Mod. Phys. D, **15**, 1753 (2006). https://doi.org/10.1142/s021827180600942x
[6] S. Nojiri, and S. D. Odintsov, Phys. Rept. **505**, 59 (2011). https://doi.org/10.1016/j.physrep.2011.04.001
[7] S. Weinberg, *Gravitation and Cosmology*, (Wiley, New York, 1972).
[8] C. Brans, R.H., Dicke, Phys. Rev. **124**, 925 (1961). https://doi.org/10.1103/physrev.124.925
[9] N. Banerjee, and D. Pavon, Phys. Rev. D, **63**, 043504 (2001). https://doi.org/10.1103/physrevd.63.043504
[10] A. Khodam-Mohammadi, *et al*., Int. J. Mod. Phys. D, **23**, 1450081 (2014). https://doi.org/10.1142/S0218271814500813
[11] S. Kazempour, and A. R. Akbarieh, Phys. Rev. D, **105**, 123515 (2022). https://doi.org/10.1103/PhysRevD.105.123515
[12] A. G. Cohen, *et al*., Phys. Rev. Lett. **82**, 4971 (1999). https://doi.org/10.1103/physrevlett.82.4971
[13] P. Horava, and D. Minic, Phys. Rev. Lett. **85**, 1610 (2000). https://doi.org/10.1103/physrevlett.85.1610
[14] S. Wang, *et al*., Phys. Rept. **696**, 1 (2017). https://doi.org/10.1016/j.physrep.2017.06.003
[15] M. Jamil, *et al*., Int. J. Theor. Phys. **51**, 604 (2012). https://doi.org/10.1007/s10773-011-0940-6
[16] M. Tavayef, *et al*., Phys. Lett. B, **781**, 195 (2018). https://doi.org/10.1016/j.physletb.2018.04.001
[17] H. Moradpour, *et al*., Eur. Phys. J. C, **80**, 732 (2020). https://doi.org/10.1140/epjc/s10052-020-8307-x
[18] S. Nojiri, S. D. Odintsov, and V. Faraoni, Phys. Rev. D, **105**, 044042 (2022). https://doi.org/10.1103/physrevd.105.044042
[19] M. Tavayef, *et al*., Phys. Lett. B, **781**, 195 (2018). https://doi.org/10.1016/j.physletb.2018.04.001
[20] A.S. Jahromi, *et al*., Phys. Lett. B, **780**, 21 (2018). https://doi.org/10.1016/j.physletb.2018.02.052
[21] H. Moradpour, *et al*. Eur. Phys. J. C, **78**, 829 (2018). https://doi.org/10.1140/epjc/s10052-018-6309-8
[22] S. Nojiri, *et al*., Phys. Rev. D, **105**, 044042 (2022). https://doi.org/10.1103/PhysRevD.105.044042
[23] S. Nojiri, *et al*., Universe, **10**, 352 (2024). https://doi.org/10.3390/universe10090352
[24] S. Nojiri, *et al*., Phys. Lett. B, **831**, 137189 (2022). https://doi.org/10.1016/j.physletb.2022.137189
[25] G. Kaniadakis, Physica A: Stat. Mech. and its Appl. **296(3-4)**, 405 (2001). https://doi.org/10.1016/s0378-4371(01)00184-4
[26] M. Masi, Phys. Lett. A, **338**, 217 (2005). https://doi.org/10.1016/j.physleta.2005.01.094
[27] E. M. Abreu, *et al*., EPL (Europhysics Letters), **124**, 30003 (2018). https://doi.org/10.1209/0295-5075/124/30003
[28] H. Moradpour, *et al*. Eur. Phys. J. C, **80**, 1 (2020). https://doi.org/10.1140/epjc/s10052-020-8307-x
[29] P. Rastall, Phys. Rev. D, **6**, 3357 (1972). https://doi.org/10.1103/physrevd.6.3357
[30] N. D. Birrell, and P. C. W. Davies, *Quantum fields in curved space*, (Cambridge University Press, Cambridge, 1982).
[31] C. E. M. Batista, *et al*., Phys. Rev. D **85**, 084008 (2012). https://doi.org/10.1103/PhysRevD.85.084008
[32] W. A. G. De Moraes, and A. F. Santos, Gen. Relativ. Grav. **51**, 167 (2019). https://doi.org/10.1007/s10714-019-2652-9
[33] H. Shabani, and A. H. Ziaie, EPL **129**, 20004 (2020). https://doi.org/10.1209/0295-5075/129/20004
[34] F. Darabi, *et al*., Eur. Phys. J. C, **78**, 25 (2018). https://doi.org/10.1140/epjc/s10052-017-5502-5
[35] M. Visser, Phys. Lett. B, **782**, 83 (2018). https://doi.org/10.1016/j.physletb.2018.05.028
[36] A. Singh, G.P. Singh, and A. Pradhan, Int. J. Mod. Phys. A, **37**, 2250104 (2022). https://doi.org/10.1142/S0217751X22501044
[37] A. Singh, and A. Pradhan, Indian J. Phys. **97**, 631 (2023). https://doi.org/10.1007/s12648-022-02406-z
[38] J. W. Moffat, Phys. Lett. B, **355**, 447 (1995). https://doi.org/10.1016/0370-2693(95)00670-g
[39] J. D. Bekenstein, Phys. Rev. D, **70**, 083509 (2004). https://doi.org/10.1103/physrevd.70.083509
[40] H. Bondi, and T. Gold, Mon. Not. R. Astron. Soc. **108**, 252 (1948). https://doi.org/10.1093/mnras/108.3.252
[41] F. Hoyle, Mon. Not. R. Astron. Soc. **108**, 372 (1948). https://doi.org/10.1093/mnras/108.5.372
[42] M.V. Santhi, *et al*., Int. J. Geo. Meth. Mod. Phys. **15**, 1850161 (2018). https://doi.org/10.1142/s021988781850161x
[43] K. D. Raju, *et al*., Astrophys. Space Sci. **365**, 45 (2020). https://doi.org/10.1007/s10509-020-03753-1
[44] K.D. Naidu, *et al*., Mod. Phys. A, **36**, 2150054 (2021). https://doi.org/10.1142/S0217732321500541

[45] Y. Aditya, *et al.*, New Astr. **84**, 101504 (2021). https://doi.org/10.1016/j.newast.2020.101504
[46] M.P.V.V. Bhaskara Rao, *et al.*, Int. J. Mod. Phys. A, **36**, 2150260 (2021). https://doi.org/10.1142/S0217751X21502602
[47] Y. Aditya, *et al.*, Int. J. Mod. Phys. A, **37**, 2250107 (2022). https://doi.org/10.1142/S0217751X2250107X
[48] U.Y.D. Prasanthi, and Y. Aditya, Phys. Dark Univ. **31**, 100782 (2021). https://doi.org/10.1016/j.dark.2021.100782
[49] Y. Aditya, U.Y.D. Prasanthi, Bulg. Astr. Journal, **38**, 52 (2023). https://astro.bas.bg/AIJ/issues/n39/YAditya.pdf
[50] U.Y.D. Prasanthi, and Y. Aditya, Results Phys. **17**, 103101 (2020). https://doi.org/10.1016/j.rinp.2020.103101
[51] Y. Aditya, Bulg. Astr. Journal, **39**, 12 (2023). https://astro.bas.bg/AIJ/issues/n39/YAditya.pdf
[52] Y. Aditya, Bulg. Astr. Journal, **40**, 95 (2024). https://astro.bas.bg/AIJ/issues/n40/YAditya.pdf
[53] U.K. Sharma, *et al.*, IJMPD, **31(03)**, 2250013 (2022). https://doi.org/10.1142/S0218271822500134
[54] J. Sadeghi, et al., Mod. Phys. Lett. A, **38**, 2350076 (2023). https://doi.org/10.1142/S0217732323500761
[55] B.G. Rao, *et al.*, East Eur. J. Phys. (1), 43 (2024). https://doi.org/10.26565/2312-4334-2024-1-03
[56] A.V. Prasanthi, *et al.*, East Eur. J. Phys. (2), 10 (2024). https://doi.org/10.26565/2312-4334-2024-2-01
[57] S. Ghaffari, Mod. Phys. Lett. A, **37**, 2250152 (2022). https://doi.org/10.1142/S0217732322501528
[58] S. Ali, *et al.*, New Astr. **110**, 102226 (2024). https://doi.org/10.1016/j.newast.2024.102226
[59] K. Murali, *et al.*, Mod. Phys. Lett. A, **39**, 2450106 (2024). https://doi.org/10.1142/S0217732324501062
[60] K. Murali, *et al.*, AIP Conf. Proc. **3298**, 040022 (2025). https://doi.org/10.1063/5.0279370
[61] K.S. Thorne, Astrophys. J. **148**, 51 (1967). https://doi.org/10.1086/149127
[62] J. Kristian, and R.K. Sachs, Astrophys. J. **143**, 379 (1966). https://doi.org/10.1086/148522
[63] R. Kantowski, and R.K. Sachs, J. Math. Phys. **7**, 433 (1966). https://doi.org/10.1063/1.1704952
[64] C.B. Collins, *et al.*, Gen. Relativ. Gravit. **12**, 805 (1980). https://doi.org/10.1007/bf00763057
[65] V.B. Johri, and R. Sudharsan, Australian Journal of Physics, **42(2)**, 215 (1989). https://doi.org/10.1071/ph890215
[66] V.B. Johri, and K. Desikan, Gen. Relat. Gravit. **26**, 1217 (1994). https://doi.org/10.1007/bf02106714
[67] M.V. Santhi, *et al.*, Can. J. Phys., **94(6)**, 578 (2016). https://doi.org/10.1139/cjp-2016-0099
[68] Y. Aditya, *et al.*, Astrophys Space Sci. **364**, 190 (2019). https://doi.org/10.1007/s10509-019-3681-2
[69] Y. Aditya, *et al.*, Eur. Phys. J. C, **79**, 1020 (2019). https://doi.org/10.1140/epjc/s10052-019-7534-5
[70] Y. Aditya, and D.R.K. Reddy, Eur. Phys. J. C, **78**, 619 (2018). https://doi.org/10.1140/epjc/s10052-018-6074-8
[71] Ö. Akarsu, and C.B. Kilinc, Gen. Relativ. Gravit. **42**, 119 (2010). https://doi.org/10.1007/s10714-009-0821-y
[72] M. Sharif, and M. Zubair, Astrophys. Space Sci. **330**, 399 (2010). https://doi.org/10.1007/s10509-010-0414-y
[73] K.S. Adhav, Int. J. Astron. Astrophys. **1**, 204 (2011). https://doi.org/10.1007/s10509-011-0773-z
[74] M.V. Santhi, *et al.*, Astrophys. Space Sci. **361**, 142 (2016). https://doi.org/10.1007/s10509-016-2731-2
[75] M.V. Santhi, *et al.*, Can. J. Phys. **95**, 179 (2017). https://doi.org/10.1139/cjp-2016-0628
[76] Y. Aditya, and D.R.K. Reddy, Astrophys Space Sci. **363**, 207 (2018). https://doi.org/10.1007/s10509-018-3429-4
[77] G. Kaniadakis, Physica A: Statistical Mechanics and its Applications, **296**, 405 (2001). https://doi.org/10.1016/s0378-4371(01)00184-4
[78] G. Kaniadakis, Phys. Rev. E, **66**, 5 (2002). https://doi.org/10.1103/physreve.66.056125
[79] H. Moradpour, *et al.*, Eur. Phys. J. C, **80**, 8 (2020). https://doi.org/10.1140/epjc/s10052-020-8307-x
[80] N. Aghanim, *et al.*, A&A, **641**, A6 (2020). https://doi.org/10.1051/0004-6361/201833910
[81] A.G. Riess, *et al.*, Astrophys. J. Lett. **934**, L7 (2022). https://doi.org/10.3847/2041-8213/ac5c5b
[82] V. Poulin, *et al.*, Phys. Rev. D **111**, 083552 (2025). https://doi.org/10.1103/PhysRevD.111.083552
[83] B. Cousins, *et al.*, arXiv:2503.01997 (2026). https://doi.org/10.48550/arXiv.2503.01997
[84] E. Di Valentino, *et al.*, arXiv:2509.25288 (2025). https://doi.org/10.48550/arXiv.2509.25288
[85] I. Pantos, *et al.*, arXiv:2601.00650 (2026). https://doi.org/10.48550/arXiv.2601.00650
[86] A. G. Riess, *et al.*, Astrophys. J. Lett. **962**, L17 (2024). https://doi.org/10.3847/2041-8213/ad1ddd
[87] J. Simon, L. Verde, and R. Jimenez, Phys. Rev. D, **71**, 123001 (2005). https://doi.org/10.1103/PhysRevD.71.123001
[88] G.S. Sharov, and V.O. Vasiliev, Math. Model. Geom. **6**, 1-20 (2018). https://doi.org/10.26456/mmg/2018-611
[89] V. Sahni, *et al.*, JETP Lett. **77**, 201 (2003). https://doi.org/10.1134/1.1574831
[90] R. Caldwell and E. V. Linder, Phys. Rev. Lett. **95**, 141301 (2005). https://doi.org/10.1103/physrevlett.95.141301

ОБМЕЖЕНА ГОЛОГРАФІЧНА МОДЕЛЬ ТЕМНОЇ ЕНЕРГІЇ КАНІАДАКІСА В КОСМОЛОГІЇ БІАНЧІ *III*

Ю. Адитья[1*], **К. Дасунайду**[1**], **Мураласетті Ноокараджу**[2], **П. Сільпа**[3], **Г. Сурьянараяна**[4]

[1]*Кафедра математики, Технологічний інститут GMR (GMRIT) – Вважається університетом, Раджам-532127, Індія*

[2]*Кафедра хімії, Університет Адітья, Сурампалем-533437, Індія*

[3]*Кафедра хімії, Інженерний коледж Шрі Васаві, Тадепаллігудем-534101, Індія*

[4]*Кафедра математики, ANITS, Вішакхапатнам-533003, Індія*

У цій роботі ми вивчаємо космологічну динаміку анізотропного Всесвіту типу Біанкі–*III*, заповненого голографічною темною енергією Каньядакіса та матерією без тиску, в рамках теорії гравітації Бранса–Дікке–Расталла. Для отримання точних розв'язків рівнянь поля припускаються відповідні співвідношення між метричними потенціалами, а також функціональний зв'язок між скалярним полем та середнім масштабним коефіцієнтом. Для обмеження параметрів моделі ми виконуємо аналіз методом Монте-Карло за допомогою ланцюгів Маркова, використовуючи спільні набори даних CC+BAO. Реконструйований параметр Хаббла демонструє чудову відповідність зі спостережними даними в межах довірчих областей 1σ та 2σ, а оцінене значення постійної Хаббла узгоджується з останніми вимірюваннями. Ми виводимо кілька важливих космологічних параметрів, включаючи параметр Хаббла, параметр уповільнення, параметр рівняння стану, скалярне поле, космічний час та час ретроспективного огляду. Фізична поведінка цих параметрів аналізується за допомогою графічних зображень. Параметр уповільнення демонструє плавний перехід від ранньої фази уповільнення до пізньої прискореної фази, з червоним зміщенням переходу, що узгоджується з останніми спостережними межами. Параметр рівняння стану залишається у фантомній області, що вказує на динамічну поведінку темної енергії, здатну керувати поточним прискореним розширенням. Крім того, діагностика за допомогою методів пошуку станів (r, s) та (r, q) показує, що модель близько наближається до поведінки ΛCDM на пізніх етапах, допускаючи водночас відхилення на ранніх епохах. Діагностика $Om(z)$ додатково підтверджує фантомну природу темної енергії в сучасних рамках. Загалом, наші результати демонструють, що наша модель у гравітації Бранса-Дікке-Расталла забезпечує життєздатний та спостережливо узгоджений опис історії розширення космосу в анізотропному Всесвіті.

Ключові слова: *голографічна темна енергія Каньядакіса; гравітація Бранса-Дікке-Расталла; Всесвіт Біанкі III типу; аналіз МСМС; космічне прискорення*

East European Journal of Physics. **2.** 34-44 (2026)
DOI:10.26565/2312-4334-2026-2-03 ISSN 2312-4334

AXIALLY SYMMETRIC COSMOLOGICAL MODEL IN $f(Q,T)$ GRAVITY

M.T. Sarode[1*], V.G. Mete[2#], A.S. Nimkar[3†]
[1]*Shri Shivaji College of Arts, Commerce & Science, Akola (M.S.), India*
[2]*Department of Mathematics, R. D. I. K. & K. D. College, Badnera – Amravati (M.S.), India*
[3]*Shri Dr. R. G. Rathod Arts & Science College, Murtizapur Dist. Akola (M.S.), India*
[*]*Corresponding Author E-mail: mtsarode17@gmail.com ;* [#]*E-mail: vmete5622@gmail.com;* [†]*E-mail: anilnimkar@gmail.com*
Received February 24, 2026; revised April 23, 2026; accepted April 25, 2026

This article is devoted to the study of the dynamical aspects of the domain wall cosmological model in an axially symmetric space-time in $f(Q,T)$ gravity. In this theory of gravity, the action contains an arbitrary function $f(Q,T)$ where Q and T respectively denote the non-metricity and the trace of the energy-momentum tensor. The linear and additive form of $f(Q,T)$ gravity, $f(Q,T)=\mu Q+\nu T$ where μ and ν are non-zero arbitrary constants, is taken into account in this work. A deterministic model of the universe is obtained using the linearly varying deceleration parameter $q=-kt+m-1$ which is linear in time with negative slope. We have assessed all the dynamical and geometrical parameters of the models and examined their physical significance in modern cosmology. We have observed that the deceleration parameter q displays a signature-flipping point where shifting occurs from a decelerating regime to an accelerating regime, signifying cosmic expansion. It is observed that our model is in good agreement with the current scenario of accelerated expansion of the universe.
Keywords: *Domain wall; $f(Q,T)$ gravity; Axially symmetric space-time; Deceleration parameter*
PACS: 04.50.Kd, 98.80.Jk

1. INTRODUCTION

Einstein's general theory of relativity (GTR) is a landmark achievement in modern physics. GTR successfully describes gravitational phenomena, solar-system dynamics and the evolution of the universe through its field equation and cosmological models. Nevertheless, the large-scale structure of the cosmos is best represented by the field equations, implying that GTR does not fully accommodate certain aspects of contemporary cosmology. For instance, it does not incorporate Mach's principle, it does not avoid singularity problems and it fails to explain the current accelerated expansion. Observational and theoretical evidence, especially from type Ia Supernovae data [1-3] suggests that the universe is not only expanding but also accelerating. According to observational evidence, especially from the Wilkinson Microwave Anisotropy Probe (WAMP) [4], energy composition of universe is made up of around 4% ordinary baryonic matter, 23% dark matter and 73% dark energy. To address these findings, two main approaches have emerged to investigate the accelerated universe: 1) developing alternative theories of gravity 2) modifying Einstein's theory of gravitation. Consequently, several modified gravity theories have been proposed by altering the Hilbert-Einstein action, such as $f(G)$ gravity [5], $f(R)$ gravity [6], $f(R,T)$ gravity [7], $f(T)$ gravity [8], $f(G,T)$ gravity [9], $f(R,T,R_{\mu\nu}T^{\mu\nu})$ gravity [10], $f(Q)$ gravity [11] and the recently proposed $f(Q,T)$ gravity [12-15].

Recently Xu et al. [12] proposed $f(Q,T)$ theory of gravity, an extension of symmetric teleparallel gravity where the Lagrangian is an arbitrary function of the non-metricity Q and the trace of energy momentum tensor T. This theory advances general relativity by introducing a coupling between Q and T. The field equations of $f(Q,T)$ can be determined by varying the gravitational action with respect to both the metric and connection. The importance of $f(Q,T)$ gravity is its ability to describe the accelerated expansion of the universe without requiring a cosmological constant, offering a unified framework for investing early-time inflation and late-time cosmic acceleration. It is possible to construct cosmologically viable models in $f(Q,T)$ theory which are consistent with general relativity. Narzary and Dewri [16] have investigated Bianchi type-VI spacetime within $f(Q,T)$ gravity in presence of bulk viscous fluid. They also examined bouncing scenario in $f(Q,T)$ gravity having Bianchi type-VI spacetime [17]. Kaczmarek et al. [18] have investigated an alternative dynamically similar scalar-tensor presentation for the $f(Q,T)$ gravity and discussed its kinetic behaviour for the FLRW cosmology. Venkatesha et al. [19] have introduced wormhole solutions including conformal symmetries and Gaussian noncommutativity within $f(Q,T)$ gravity. Gul et al. [20] studied the bouncing scenarios in a flat FRW spacetime in presence of perfect fluid matter distribution in $f(Q,T)$ gravity. Tayde et al. [21] have investigated wormhole solutions accompanied by dark matter galactic halo profiles in the context of $f(Q,T)$ gravity. Khurana et al. [22] have discussed analysis of FLRW model in $f(Q,T)$ theory produced by the cubic parametrization of the deceleration parameter. Shekh et al. [23] have discussed the dynamics of spatially flat FLRW metric in specific models of $f(Q,T)$ gravity using parametrization of the deceleration parameter. They also studied $f(Q,T)$ model with an emergent scale factor [24]. Kale et al. [25] have studied the observational constraints of two different $f(Q,T)$ models in FLRW framework using specific Hubble parameter in redshift form. Pati et al. [26] have investigated the behaviour of cosmological parameters in an isotropic and homogeneous spacetime within the framework of $f(Q,T)$ gravity. Narawade et al. [27] have investigated

Cite as: M.T. Sarode, V.G. Mete, A.S. Nimkar, East Eur. J. Phys. 2, 34 (2026), https://doi.org/10.26565/2312-4334-2026-2-03

dynamical analysis and observational constraints of $f(Q,T)$ model. Xu et al. [28] studied Weyl type $f(Q,T)$ model and compared it with ΛCDM model.

During the early stages of the evolution of the universe, it is generally assumed that during cosmological phase transition, the symmetry of universe is broken spontaneously and topological stable defects such as cosmic strings and domain walls could form [29]. Domain wall separate regions with distinct vacuum states and possess large surface energy densities. Domain walls are stable due to their topological nature, originating from the configuration of vacuum manifolds during symmetry breaking [30]. Domain walls have garnered considerable interest in cosmology, especially for their involvement in galaxy formation scenario. Zel'dovich et al. [31] investigated domain interfaces, uniformity and the expanding universe. They found that domain walls must vanish early in the universe's evolution. This disappearance enables the transformation of energy density into massive quanta or equilibrium radiation, thereby achieving isotropy and homogeneity. As domain wall naturally breaks isotropy, therefore to study them in anisotropic background, models provide convincing presentation of early universe dynamics. In recent years, lots of work has been done by many researchers on domain walls. Hatkar et al. [32] have studied topological defects in LRS Bianchi type-I space time in $f(T)$ gravity. Junaid et al. [33] have explored the aspects of domain wall in Bianchi type-III universe in $f(R,T)$ theory. Hatkar et al. [34-36] explored various cosmological models with domain wall including FRW, Bianchi type-VI_0 and Bianchi type-I in the context of $f(Q)$, $f(R,T)$ and $f(G)$ theories of gravity. Patil et al. [37] have explored the solution of FRW space-time with bulk viscous domain wall in $f(R,T)$ gravity.

Axially symmetric spacetime plays a crucial role in the large-scale study of the universe particularly when anisotropies and inhomogeneities are not ignored [38]. Kilinc [38] demonstrated axially symmetric cosmological models have significantly contributed to understanding essential features of the universe such as galaxy formation during its early evolutionary stages. Axially symmetric cosmological models both in general relativity and in the alternative theories of gravitation have been extensively studied by Mete et al. [39], Reddy and Naidu [40-41], Adhav et al. [42], Reddy and Rao [43]. Nimkar and Wath [44] investigated an axially symmetric cosmological model with perfect fluid in Lyra geometry. Sahoo et al. [45] explored axially symmetric cosmological model in the framework of $f(R,T)$ gravity.

In this paper, we propose to investigate the axially symmetric space-time given by Bhattacharya and Karade [46] in the presence of domain wall within the framework of $f(Q,T)$ gravity. The paper is structured as follows: Section 1 contains a concise introduction and the motivation behind the current work. $f(Q,T)$ Theory and field equations is given in Section 2. In Section 3, we have derived the metric and field equations. In Section 4, we derived the solution of field equations using the linearly varying deceleration parameter and discussed the physical parameters graphically. Section 5 deals with graphical discussion of Hubble datasets. Conclusion is presented in Section 6.

2. $f(Q,T)$ THEORY AND FIELD EQUATIONS

The field equations of modified $f(Q,T)$ gravity are derived from Hilbert Einstein variational action principle

$$S = \int \left(\frac{1}{16\pi} f(Q,T) + L_m\right)\sqrt{-g}\,d^4x \tag{1}$$

where $f(Q,T)$ is a function of the non-metricity scalar Q and the trace of the matter-energy-momentum tensor T , also L_m is Lagrangian of the matter and $g = \det(g_{\mu\nu})$. The non-metricity scalar Q is defined as

$$Q = -g^{\mu\nu}\left(L^{\alpha}{}_{\beta\mu}L^{\beta}{}_{\nu\alpha} - L^{\alpha}{}_{\beta\alpha}L^{\beta}{}_{\mu\nu}\right) \tag{2}$$

where $L^{\alpha}{}_{\beta\gamma}$ represents the disformation tensor which is given by,

$$L^{\alpha}{}_{\beta\gamma} = -\frac{1}{2}g^{\alpha\delta}\left(\nabla_{\gamma}g_{\beta\delta} + \nabla_{\beta}g_{\delta\gamma} - \nabla_{\delta}g_{\beta\gamma}\right) \tag{3}$$

The non-metricity tensor is defined as

$$Q_{\gamma\mu\nu} = \nabla_{\gamma}g_{\mu\nu} \tag{4}$$

The trace of the non-metricity tensor is derived as follows

$$Q_{\alpha} = g^{\mu\nu}Q_{\alpha\mu\nu}\,, \tilde{Q}_{\alpha} = g^{\mu\nu}Q_{\mu\alpha\nu} \tag{5}$$

The superpotential or the non-metricity conjugate of the model is given by

$$P^{\alpha}{}_{\mu\nu} = -\frac{1}{2}L^{\alpha}{}_{\mu\nu} + \frac{1}{4}\left(Q^{\alpha} - \tilde{Q}^{\alpha}\right)g_{\mu\nu} - \frac{1}{4}\delta^{\alpha}{}_{(\mu}Q_{\nu)} \tag{6}$$

The energy-momentum tensor is defined as

$$T_{\mu\nu} = -\frac{2}{\sqrt{-g}}\frac{\delta(\sqrt{-g}L_m)}{\delta g^{\mu\nu}} \quad \text{and} \quad \theta_{\mu\nu} = g^{\alpha\beta}\frac{\delta T_{\alpha\beta}}{\delta g^{\mu\nu}} \tag{7}$$

The field equation of $f(Q,T)$ gravity is obtained by varying the action (1) with respect to the metric tensor $g_{\mu\nu}$ as

$$-\frac{2}{\sqrt{-g}}\nabla_\alpha\left(f_Q\sqrt{-g}P^\alpha{}_{\mu\nu}\right) - \frac{1}{2}fg_{\mu\nu} + f_T\left(T_{\mu\nu}+\theta_{\mu\nu}\right) - f_Q\left(P_{\mu\alpha\beta}Q_\nu{}^{\alpha\beta} - 2Q^{\alpha\beta}{}_\mu P_{\alpha\beta\nu}\right) = 8\pi T_{\mu\nu} \tag{8}$$

where $f_Q = \frac{\partial f}{\partial Q}$, $f_T = \frac{\partial f}{\partial T}$ and the non-metricity tensors $Q_\nu{}^{\alpha\beta} = -\nabla_\nu g^{\alpha\beta}$, $Q^{\alpha\beta}{}_\mu = g^{\alpha\gamma}g^{\beta\rho}\nabla_\gamma g_{\rho\mu}$

3. THE METRIC AND FIELD EQUATIONS

We have considered the axially symmetric space-time given by Bhattacharya and Karade [46] in the form

$$ds^2 = dt^2 - A^2[d\chi^2 + h^2(\chi)d\phi^2] - B^2dz^2 \tag{9}$$

where the metric potentials A , B are functions of cosmic time t and h is a function of coordinate χ alone.
The energy momentum tensor of domain wall [33] is

$$T_{ij} = \rho\left(g_{ij} + \omega_i\omega_j\right) + p\omega_i\omega_j \tag{10}$$

where ρ is the energy density of the wall, p is the pressure in the direction normal to the plane of the wall and ω_i is a unit space like vector in the same direction with $\omega^i\omega_j = -1$. Here pressure is taken in the direction of x-axis. The quantities ρ and p depends on t only. Additionally, $\rho = \rho_b + \sigma_d$ and $p = p_b - \sigma_d$ where p_b and ρ_b denote the pressure and energy density of barotropic fluid, σ_d stands for the tension of domain wall.
Then, we have

$$T_0^0 = T_2^2 = T_3^3 = \rho \ , \ T_1^1 = -p \ , \ T = \ 3\rho - p \tag{11}$$

θ_j^i is derived as

$$\theta_j^i = \delta_j^i p - 2T_j^i = \text{diag}\,(p-2\rho, 3p, p-2\rho, p-2\rho) \tag{12}$$

For given cosmological model, the non-metricity scalar Q is found to be

$$Q = -2\left(\frac{\dot{A}^2}{A^2} + 2\frac{\dot{A}\dot{B}}{AB}\right) \tag{13}$$

The field equation (8) for the line element (9) with energy momentum tensor (11), also using equation (12) and (13) can be written as

$$\frac{1}{2}f + 2F\left(\frac{\dot{A}^2}{A^2} + 2\frac{\dot{A}\dot{B}}{AB}\right) = 8\pi\left(1+\tilde{G}\right)\rho - 8\pi\tilde{G}p \tag{14}$$

$$\frac{1}{2}f + F\left(\frac{\ddot{A}}{A} + \frac{\ddot{B}}{B} + \frac{\dot{A}^2}{A^2} + 3\frac{\dot{A}\dot{B}}{AB}\right) = 8\pi(1+2\tilde{G})p \tag{15}$$

$$\frac{1}{2}f + F\left(\frac{\ddot{A}}{A} + \frac{\ddot{B}}{B} + \frac{\dot{A}^2}{A^2} + 3\frac{\dot{A}\dot{B}}{AB}\right) = 8\pi\tilde{G}p - 8\pi(1+\tilde{G})\rho \tag{16}$$

$$\frac{1}{2}f + 2F\left(\frac{\ddot{A}}{A} + \frac{\dot{A}^2}{A^2} + \frac{\dot{A}\dot{B}}{AB}\right) = 8\pi\tilde{G}p - 8\pi(1+\tilde{G})\rho \tag{17}$$

where $F = f_Q$, $f_T = 8\pi\tilde{G}$ and an overhead dot refers to derivative with respect to time t.
For the given cosmological model, the physical parameters are defined as follows. The average scale factor a and the spatial volume V are expressed as

$$a = (A^2B)^{\frac{1}{3}} \tag{18}$$

$$V = a^3 = A^2B \tag{19}$$

The generalized mean Hubble's parameter H is expressed as

$$H = \frac{1}{3}(H_1 + H_2 + H_3) \tag{20}$$

where $H_1 = H_2 = \frac{\dot{A}}{A}$, $H_3 = \frac{\dot{B}}{B}$ are the directional Hubble parameters in the direction of χ, ϕ, z respectively.
We define the expansion scalar θ and the shear scalar σ^2 as

$$\theta = 2\frac{\dot{A}}{A} + \frac{\dot{B}}{B} \tag{21}$$

$$\sigma^2 = \frac{1}{2}\left[\sum_{i=1}^{3} {H_i}^2 - \frac{\theta^2}{3}\right] = \frac{1}{3}\left(\frac{\dot{A}}{A} - \frac{\dot{B}}{B}\right)^2 \tag{22}$$

The mean anisotropy parameter Δ is given by

$$\Delta = \frac{1}{3}\sum_{i=1}^{3}\left(\frac{H_i - H}{H}\right)^2 \tag{23}$$

4. SOLUTIONS OF THE FIELD EQUATIONS AND DISCUSSION OF THE PHYSICAL PARAMETERS

There are various forms of the function $f(Q,T)$ which is commonly used in Literature [12]. Here we shall focus on the linear and additive form of $f(Q,T)$ function [28] as $f(Q,T) = \mu Q + \nu T$. Here μ and ν are non-zero arbitrary constants.
Here $F = f_Q = \mu,\ f_T = \nu = 8\pi\tilde{G}$, $\tilde{G} = \frac{\nu}{8\pi}$.

As the system of equations (14) - (17) being highly non-linear, we assume a relation between the metric coefficients by employing the physical assumption that the expansion scalar θ is proportional to shear scalar σ . This assumption was employed by Collins et al. [47] and has recently been used by Junaid et al. [33] and Hatkar et al. [36] to obtain solution of field equations. From this, we derive the following relation.

$$A = B^n \ , \ n > 0 \tag{24}$$

where n is an arbitrary constant such that for $n \neq 1$, the space time is anisotropic nature.

Berman [48] and Berman and Gomide [49] suggested a law of variation of the Hubble parameter in FLRW framework which gives a constant deceleration parameter ($q = m - 1, m \geq 0$ is a constant). After the discovery of the universe's accelerated expansion, researchers have investigated cosmological models that employ Berman's law in the context of dark energy. In Berman's law, deceleration parameter can take values $q \geq -1$ and $-1 \leq q < 0$, corresponding to accelerating expansion. The time-varying deceleration parameter plays a crucial role in the universe's evolution, as it captures the transition in expansion dynamics. We solve the system of highly non-linear equations (14) - (17) with the help of the linearly varying deceleration parameter proposed by Akarsu and Dereli [50] in the form

$$q = -\frac{a\ddot{a}}{\dot{a}^2} = -kt + m - 1 \tag{25}$$

where $k \geq 0$ and $m \geq 0$ are constants. The above deceleration parameter give rise to three different cases as follows:

- $q = -1$ for $k = 0, m = 0$
- $q = m - 1$ for $k = 0, m > 0$
- $q = -kt + m - 1$ for $k > 0, m \geq 0$

For $q > 0$ the universe shows decelerating expansion, for $q = 0$ it shows constant rate of expansion, if $-1 < q < 0$ it represents accelerating expansion (referred as power law expansion), de Sitter expansion for $q = -1$ (called as exponential expansion) & superexponential for $q < -1$. For $k = 0$ i.e. first two cases correspond to Berman's law of constant deceleration parameter. Therefore, only the last case i.e. for $k > 0$ the linearly varying deceleration parameter ($q = -kt + m - 1$) fits well with modern observational data, indicating a time-dependent transition in the universe's expansion. Here we consider case– I: $k = 0$ and $m > 0$ and case– II: $k \neq 0$ and $m \geq 0$ to obtain solution of the field equations.

Case-I: Let $k = 0$ and $m > 0$

After solving equation (25), we obtain mean scale factor as

$$a = (\alpha t + \beta)^{\frac{1}{m}} \tag{26}$$

where α and β are constant of integration.

With the help of (18), (24) and (26), the metric potentials A and B are obtained as

$$A = (\alpha t + \beta)^{\frac{3n}{m(2n+1)}} \tag{27}$$

$$B = (\alpha t + \beta)^{\frac{3}{m(2n+1)}} \tag{28}$$

From equation (27) and (28), it is seen that initially A and B are constants for $t = 0$. When $t \to -\frac{\beta}{\alpha}$, they tend to zero and become infinite for increasing t.
Using equations (27), (28) in (9), we obtain the cosmological model given by Bhattacharya and Karade in $f(Q,T)$ gravity in presence of domain wall in the form:

$$ds^2 = dt^2 - (\alpha t + \beta)^{\frac{6n}{m(2n+1)}}[d\chi^2 + h^2(\chi)d\phi^2] - (\alpha t + \beta)^{\frac{6}{m(2n+1)}} dz^2 \tag{29}$$

From equations (20) – (22) with the use of (27) and (28), the physical parameters such as Hubble parameter H, the expansion scalar θ and the shear scalar σ^2 are obtained as

$$H = \frac{\alpha}{m(\alpha t+\beta)} \tag{30}$$

$$\theta = \frac{3\alpha}{m(\alpha t+\beta)} \tag{31}$$

$$\sigma^2 = \frac{3\alpha^2(n-1)^2}{m^2(2n+1)^2(\alpha t+\beta)^2} \tag{32}$$

We can observe that at the initial time $t = -\frac{\beta}{\alpha}$, all three quantities the Hubble parameter H, the expansion scalar θ and the shear scalar σ^2 are infinite and subsequently decay to zero as $t \to \infty$. This behaviour signifies a very rapid expansion of the universe. The non-zero ratio $\frac{\sigma}{\theta}$ indicates an anisotropic universe, representing the early phase of cosmic evolution.
The spatial volume is

$$V = (\alpha t + \beta)^{\frac{3}{m}} \tag{33}$$

Spatial volume and average scale factor are constant at $t = 0$, indicating that the universe starts evolving with finite volume at initial time and expanded over time.
The mean anisotropy parameter is found to be

$$\Delta = \frac{2(n-1)^2}{(2n+1)^2} \quad , n \neq -\frac{1}{2} \tag{34}$$

The parameter n determines the anisotropic nature of the model such that for $n = 1$ the model becomes isotropic, whereas for $n \neq 1$ the anisotropic character is preserved.
The pressure p is found to be

$$p = \frac{3\mu\alpha^2\xi}{m^2(2n+1)^2(\alpha t+\beta)^2} \tag{35}$$

where $\xi = \frac{\left(8\pi-\frac{\nu}{2}\right)(n+1)(3-2mn-m)+3n[(8\pi+\nu)n+3\nu]}{64\pi^2+16\pi\nu-2\nu^2}$

From Fig. 1, we observed that pressure p is decreasing function of time t .
For this model, energy density ρ is obtained as

$$\rho = \frac{3\mu\alpha^2}{m^2(2n+1)^2(\alpha t+\beta)^2\left(8\pi-\frac{\nu}{2}\right)}\left\{3(n^2+2n)+\frac{\nu\xi}{2}\right\} \tag{36}$$

The relation between pressure and energy density of barotropic fluid is given as

$$p_b = (\gamma - 1)\rho_b \quad \text{where } 1 \leq \gamma \leq 2 \tag{37}$$

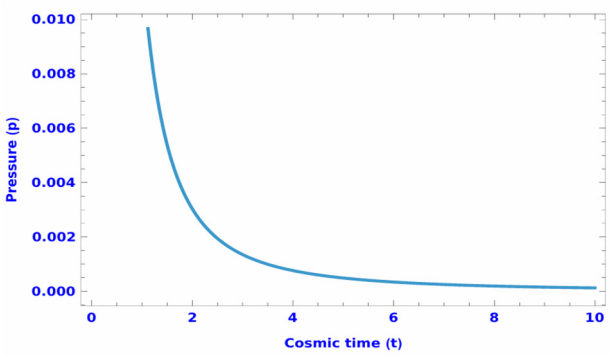

Figure 1. Plot of Pressure vs cosmic time t with $\alpha = 64.15$, $\mu = \nu = \beta = n = 0.1$, $m = 1.12$

The expression for tension of domain wall is found to be

$$\sigma_d = \frac{3\mu\alpha^2}{\gamma m^2(2n+1)^2(at+\beta)^2}\left\{\frac{\gamma-1}{\left(8\pi-\frac{\nu}{2}\right)}\left[3(n^2+2n)+\frac{\nu\xi}{2}\right]-\xi\right\} \tag{38}$$

Figure 2 shows the graphical behaviour of energy density ρ and tension density ρ_d versus cosmic time t. Energy density ρ is a decreasing function of time t, whereas tension of the domain wall is an increasing function of time t. Energy density is large as $t \to 0$ and tends to zero as $t \to \infty$. The tension of the domain wall is negative throughout the universe evolution as shown in Fig. 2. The domain wall acts like invisible matter due to its negative tension. The domain wall exists initially and thereafter vanished which is as per expectation Zel'dovich et al [31].

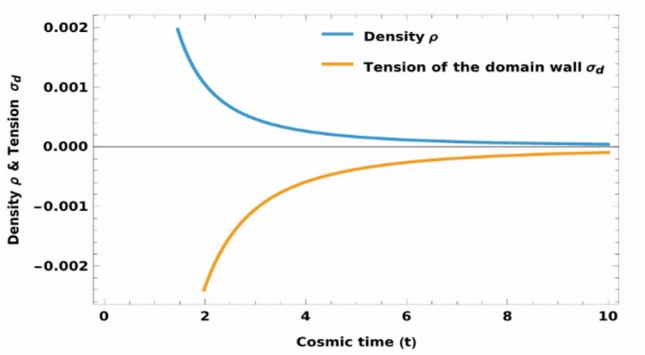

Figure 2. Plot of Density & Tension of the domain wall vs cosmic time t with $\alpha = 64.15$, $\mu = \nu = \beta = n = 0.1$, $m = 1.12$, $\gamma = 1.2$

Case-II: Let $k \neq 0$ and $m \geq 0$

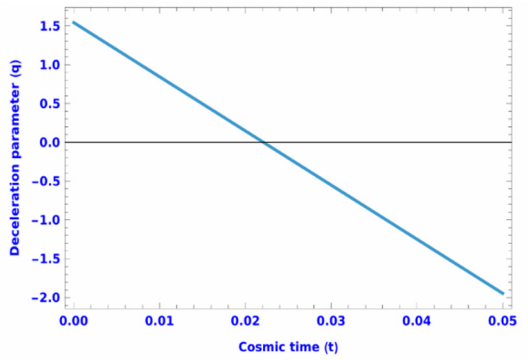

Figure 3. Plot of Deceleration parameter vs cosmic time t with $k = 69.67$, $m = 2.54$

Figure 3 demonstrates that the universe experiences early deceleration and present acceleration. For $q = m - 1 > 0$, the universe begins with decelerating expansion and enters to accelerating phase at $t = \frac{m-1}{k}$.

After solving equation (25), we obtain mean scale factor as

$$a = c_2 exp\left[\frac{2}{\sqrt{m^2-2c_1k}}tanh^{-1}\left(\frac{kt-m}{\sqrt{m^2-2c_1k}}\right)\right] \tag{39}$$

where c_1 and c_2 are constant of integration. For simplifying the expression, we omit the constant c_1 by choosing $c_1 = 0$.

$$a = c_2 exp\left[\frac{2}{m} tanh^{-1}\left(\frac{kt}{m} - 1\right)\right] \tag{40}$$

With the help of (18), (24) and (40), the metric potentials A and B are obtained as

$$A = c_2^{\left(\frac{3n}{2n+1}\right)} exp\left[\frac{6n}{m(2n+1)} tanh^{-1}\left(\frac{kt}{m} - 1\right)\right] \tag{41}$$

$$B = c_2^{\left(\frac{3}{2n+1}\right)} exp\left[\frac{6}{m(2n+1)} tanh^{-1}\left(\frac{kt}{m} - 1\right)\right] \tag{42}$$

From equations (41) and (42), it is noted that both metric potentials A and B are constants for $t = 0$ and diverge as $t \to \infty$. As a result, the obtained model is free from singularity.
Using equations (41), (42) in (9), we obtain the cosmological model given by Bhattacharya and Karade in $f(Q,T)$ gravity in presence of domain wall in the form:

$$ds^2 = dt^2 - \left[c_2^{\left(\frac{3n}{2n+1}\right)} exp\left[\frac{6n}{m(2n+1)} tanh^{-1}\left(\frac{kt}{m} - 1\right)\right]\right]^2 [d\chi^2 + h^2(\chi) d\phi^2] - \left[c_2^{\left(\frac{3}{2n+1}\right)} exp\left[\frac{6}{m(2n+1)} tanh^{-1}\left(\frac{kt}{m} - 1\right)\right]\right]^2 dz^2 \tag{43}$$

From equations (20) – (22) with the use of (41) and (42), the physical parameters such as Hubble parameter H, the expansion scalar θ and the shear scalar σ^2 are obtained as

$$H = \frac{-2}{(kt^2 - 2mt)} \tag{44}$$

$$\theta = \frac{-6}{(kt^2 - 2mt)} \tag{45}$$

$$\sigma^2 = \frac{12(n-1)^2}{(2n+1)^2 (kt^2 - 2mt)^2} \tag{46}$$

The parameters H , θ and σ^2 tends to zero as $t \to \infty$. It is to be noted that for $n = 1$ the model is shear free and its nature will be retained for $n \neq 1$.
The spatial volume given in (19) found to be

$$V = {c_2}^3 exp\left[\frac{6}{m} tanh^{-1}\left(\frac{kt}{m} - 1\right)\right] \tag{47}$$

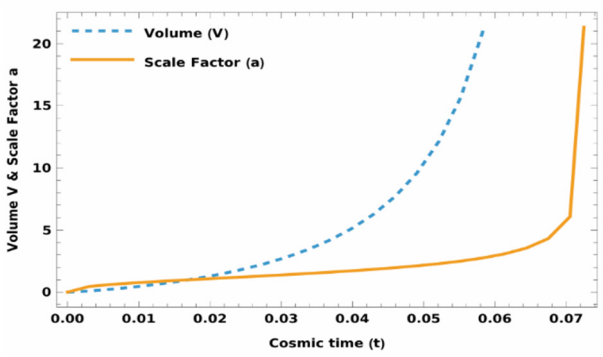

Figure 4. Plot of Volume & Scale factor vs cosmic time t with k = 69.67, m = 2.54, c_2= 1.60

Figure 4 illustrates the graphical evolution of spatial volume and average scale factor. Both these parameters are fixed at $t = 0$, signifying that the universe begins with a finite initial volume at finite time and it expands over time.
The mean anisotropy of the model is

$$\Delta = \frac{2(n-1)^2}{(2n+1)^2} \quad , n \neq -\frac{1}{2} \tag{48}$$

A parameter n decides the anisotropic behaviour of the model in the sense that, if $n = 1$,we get isotropic model and for $n \neq 1$, anisotropic nature will be retained.

The pressure p is found to be

$$p = \frac{6\mu}{(2n+1)^2(32\pi^2+8\pi\nu-\nu^2)(kt^2-2mt)^2}\left\{(n+1)(2n+1)\left(8\pi-\frac{\nu}{2}\right)(kt-m)+k_0\right\} \tag{49}$$

where $k_0 = 3(n+1)\left(8\pi-\frac{\nu}{2}\right)+3n[(8\pi+\nu)n+3\nu]$

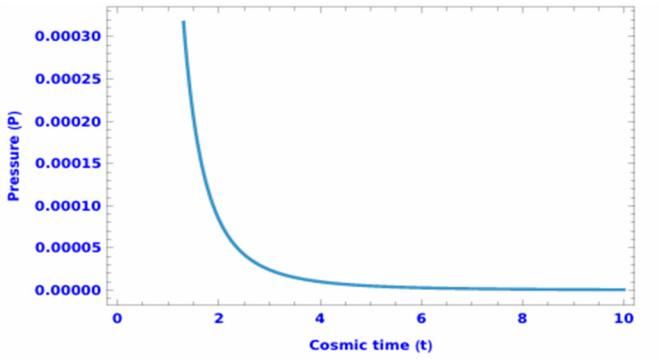

Figure 5. Plot of Pressure vs cosmic time t with k = 69.67, $\mu = \nu = n$ = 0.1, m = 2.54

From Fig. 5, we observed that pressure p is decreasing function of time t .
For this model, energy density ρ is obtained as

$$\rho = \frac{3\mu}{(2n+1)^2\left(8\pi-\frac{\nu}{2}\right)(kt^2-2mt)^2}\left\{12(n^2+2n)+\frac{\nu}{(32\pi^2+8\pi\nu-\nu^2)}\left[(n+1)(2n+1)\left(8\pi-\frac{\nu}{2}\right)(kt-m)+k_0\right]\right\} \tag{50}$$

The expression for tension of domain wall is found to be

$$\sigma_d = \frac{36\mu(\gamma-1)(n^2+2n)}{\gamma(2n+1)^2\left(8\pi-\frac{\nu}{2}\right)(kt^2-2mt)^2}+\frac{3\mu\left[(n+1)(2n+1)\left(8\pi-\frac{\nu}{2}\right)(kt-m)+k_0\right]}{\gamma(2n+1)^2(32\pi^2+8\pi\nu-\nu^2)(kt^2-2mt)^2}\left\{\frac{\gamma(\gamma-1)}{\left(8\pi-\frac{\nu}{2}\right)}-2\right\} \tag{51}$$

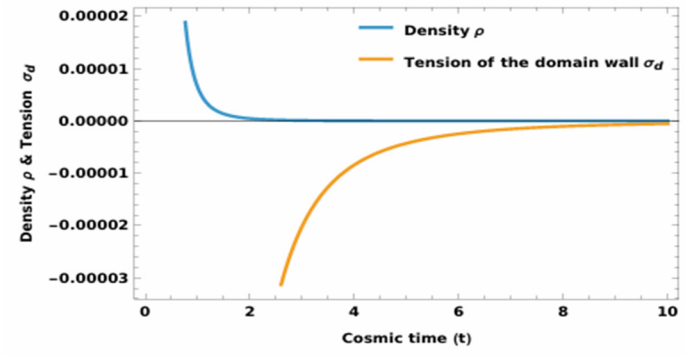

Figure 6. Plot of Density & Tension of the domain wall vs cosmic time t with k = 69.67, $\mu = \nu = n$ = 0.1, m = 2.54, γ = 1.2

Figure 6 illustrates the graphical behaviour of energy density ρ and tension density ρ_d. We observed that energy density ρ is a decreasing function of time t. Density becomes zero as $t \to \infty$. The tension of the domain wall is negative throughout and it gradually increases to zero. The domain wall acts like invisible matter. This shows that the domain wall was present during the early stages of the universe, later on it disappeared.

5. HUBBLE DATASETS

The Hubble parameter is employed in observational cosmology to examine the universe's expansion. The Hubble parameter for case- I and case- II can be expressed in terms of redshift as

$$\text{For case– I}: \quad H = \frac{\alpha}{m(1+z)^{-m}} \tag{52}$$

$$\text{For case– II}: \quad H = \frac{k}{m^2}\left\{1+cosh\left(m\ln\left(\frac{1}{c_2(1+z)}\right)\right)\right\} \tag{53}$$

To estimate $H(z)$ at a given redshift, two widely used techniques are the line-of-sight baryon acoustic oscillation (BAO) method and another is the different age (DA) approach, cited in references [51-69]. In this work, a revised dataset

of 57 points is used which includes 31 points from DA approach and the remaining 26 points measured using BAO and various redshift range $0.07 \leq z \leq 2.42$ [70]. Table 1 shows the 57 points of Hubble parameter values $H(z)$ having errors σ_H along with references from DA (31 points) and BAO and other (26 points) approaches. Additionally, the present Hubble constant $H_0 = 67.8$ km/s/Mpc was adopted for the analysis.

Table 1. Hubble datasets

z	$H(z)$	σ_H	Ref.	z	$H(z)$	σ_H	Ref.
0.070	69	19.6	[51]	1.750	202	40	[52]
0.90	69	12	[52]	1.965	186.5	50.4	[57]
0.120	68.6	26.2	[51]	0.24	79.69	2.99	[58]
0.170	83	8	[52]	0.30	81.7	6.22	[59]
0.1791	75	4	[53]	0.31	78.18	4.74	[60]
0.1993	75	5	[53]	0.34	83.8	3.66	[58]
0.200	72.9	29.6	[54]	0.35	82.7	9.1	[61]
0.270	77	14	[52]	0.36	79.94	3.38	[60]
0.280	88.8	36.6	[54]	0.38	81.5	1.9	[62]
0.3519	83	14	[53]	0.40	82.04	2.03	[60]
0.3802	83	13.5	[55]	0.43	86.45	3.97	[58]
0.400	95	17	[52]	0.44	82.6	7.8	[63]
0.4004	77	10.2	[55]	0.44	84.84	1.83	[60]
0.4247	87.1	11.2	[55]	0.48	87.79	2.03	[60]
0.4497	92.8	12.9	[55]	0.51	90.4	1.9	[62]
0.470	89	34	[56]	0.52	94.35	2.64	[60]
0.4783	80.9	9	[55]	0.56	93.34	2.3	[60]
0.480	97	62	[51]	0.57	87.6	7.8	[64]
0.593	104	13	[53]	0.57	96.8	3.4	[65]
0.6797	92	8	[53]	0.59	98.48	3.18	[60]
0.7812	105	12	[53]	0.60	87.9	6.1	[63]
0.8754	125	17	[53]	0.61	97.3	2.1	[62]
0.880	90	40	[51]	0.64	98.82	2.98	[60]
0.900	117	23	[52]	0.73	97.3	7.0	[63]
1.037	154	20	[53]	2.30	224	8.6	[66]
1.300	168	17	[52]	2.33	224	8	[67]
1.363	160	33.6	[57]	2.34	222	8.5	[68]
1.430	177	18	[52]	2.36	226	9.3	[69]
1.530	140	14	[52]				

Figures 7 and 8 shows the best fit plot of Hubble parameter $H(z)$ as a function of redshift z for case-I , case-II respectively. By comparing the Hubble parameter graph to the Hubble data set , we observed that ΛCDM model fits the best-fit model very closely, matching the data ponits (see Table 1) using the parameters H_0, α, k, m, c_2 . Despite the presence of error bars, the best-fit curve stays within the data's uncertainty range, confirming the reliability of the fit.

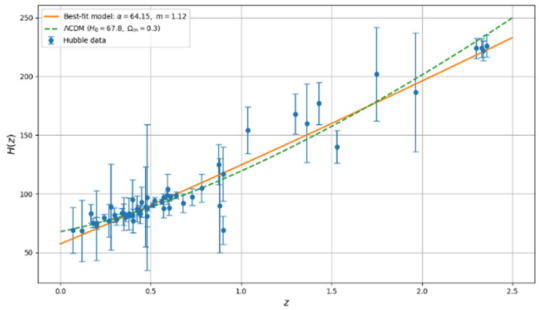

Figure 7. The best fit plot of Hubble parameter *H(z)* vs redshift for case-I

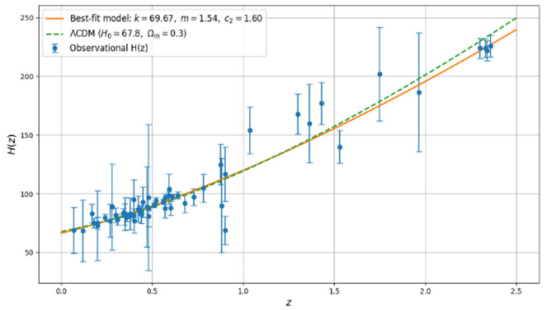

Figure 8. The best fit plot of Hubble parameter *H(z)* vs redshift for case-II

6. CONCLUSION

In this paper, we have investigated the cosmological model given by Bhattacharya and Karade in $f(Q,T)$ gravity in presence of domain wall. We have derived the exact solution of the field equations by considering the linearly varying deceleration parameter in two cases. We have determined some physical parameters to analyze the behaviour of universe. The behaviour of the physical parameters i.e. $\sigma, V, a, \Delta, p, \rho, \sigma_d$ are same in both the cases. The parameters spatial volume and average scale factor are constant at $t = 0$, indicating that the universe starts evolving with finite volume at initial time and expanded over time. The ratio $\frac{\sigma}{\theta} \neq 0$ as $t \to \infty$ and hence the model does not approach isotropy. The mean anisotropy

parameter is uniform throughout expansion of the universe. The deceleration parameter decides whether the universe expansion is accelerating or decelerating. In case–II, Fig. 3 shows that the universe has undergone multiple phases, beginning with an initial deceleration phase and finishing with the present acceleration era. As the cosmic time approaches infinity, both the Hubble parameter and the expansion scalar tend toward zero. This implies the universe's expansion is becoming steady. Pressure and energy density decreases as cosmic time increases. The tension of the domain wall is negative throughout and it gradually increases to zero. Finally, the close match between the plotted curve and the Hubble data confirms the model's accuracy in describing the relationship between redshift and the Hubble parameter, providing further evidence for an expanding universe.

Our findings have shed light on the universe's cosmological evolution, specifically its shift from a decelerating to an accelerating expansion. Our analysis reveals how the cosmological parameters changes over time, highlighting the significance of modified gravity theories in explaining the current rapid expansion. Our results not only confirm the applicability of $f(Q,T)$ gravity in modern cosmological studies but also create opportunities for more in-depth examinations of domain wall and its impact on the universe's evolution.

Acknowledgments

We would like to express sincere gratitude to the anonymous reviewers for their valuable comments and constructive suggestions, which significantly improved the quality and clarity of this manuscript.

ORCID

M.T. Sarode, https://orcid.org/0009-0001-8467-4744; **V.G. Mete,** https://orcid.org/0000-0002-0526-6372

REFERENCES

[1] A. G. Riess, *et al.*, Astron. J. **116**, 1009 (1998). https://doi.org/10.1086/300499
[2] A. G. Riess, *et al.*, Astrophys. J. **560**, 49 (2001). https://doi.org/10.1086/322348
[3] S. Perlmutter, *et al.,* Astrophys. J. **517**, 565 (1999). https://doi.org/10.1086/307221
[4] D. N. Spergel, *et al.,* Astrophys. J. Suppl. Ser. **148**, 175 (2003). https://doi.org/10.1086/377226
[5] S. I. Nojiri, S. D. Odintsov, and P. V. Tretyakov, Phys. Lett. B, **651**, 224 (2007). https://doi.org/10.1016/j.physletb.2007.06.029
[6] H. A. Buchdahl, Mon. Not. R. Astron. Soc. **150**, 1 (1970). https://doi.org/10.1093/mnras/150.1.1
[7] T. Harko, F.S. Lobo, S.I. Nojiri, and S.D. Odintsov, Phys. Rev. D, **84**, 024020 (2011). https://doi.org/10.1103/PhysRevD.84.024020
[8] Y. F. Cai, S. Capozziello, M. De. Laurentis, and E. N. Saridakis, Rep. Prog. Phys. **79**, 106901 (2016). https://doi.org/10.1088/0034-4885/79/10/106901
[9] M. Sharif, and A. Ikram, Eur. Phys. J. C, **76**, 640 (2016). http://doi.org/10.1140/epjc/s10052-016-4502-1
[10] I. Ayuso, J. Beltrán Jiménez, and Á. de la Cruz-Dombriz, Phys. Rev. D, **91**, 104003 (2015). https://doi.org/10.1103/PhysRevD.91.104003
[11] J. M. Nester, and H. J. Yo, arXiv preprint gr-qc/9809049 (1998). https://doi.org/10.48550/arXiv.gr-qc/9809049
[12] Y. Xu, G. Li, T. Harko, and S. D. Liang, Eur. Phys. J. C, **79**, 708 (2019). https://doi.org/10.1140/epjc/s10052-019-7207-4
[13] S. Arora, S. K. J. Pacif, S. Bhattacharjee, and P. K. Sahoo, Phys. Dark Univ. **30**, 100664 (2020). https://doi.org/10.1016/j.dark.2020.100664
[14] S. Arora, J. R. L. Santos, and P. K. Sahoo, Phys. Dark Univ. **31**, 100790 (2021). https://doi.org/10.1016/j.dark.2021.100790
[15] A. Pradhan, and A. Dixit, Int. J. Geom. Methods Mod. Phys. **18**, 2150159 (2020). https://doi.org/10.1142/S0219887821501590
[16] M. Narzary, and M. Dewri, J. Sci. Res. **18**, 53 (2026). https://dx.doi.org/10.3329/jsr.v18i1.81063
[17] M. Narzary, and M. Dewri, Edelweiss Appl. Sci. Technol. **9**, 2623 (2025). https://doi.org/10.55214/25768484.v9i5.7526
[18] A. Z. Kaczmarek, J. L. Rosa, and D. Szczęśniak, Eur. Phys. J. C, **85**, 203 (2025). https://doi.org/10.1140/epjc/s10052-025-13919-2
[19] V. Venkatesha, G. N. Lathakumari, and C. S. Varsha, Indian J. Phys. **99**, 5301 (2025). https://doi.org/10.1007/s12648-025-03727-5
[20] M. Z. Gul, M. Sharif, and S. Shabbir, Eur. Phys. J. C, **84**, 802 (2024). https://doi.org/10.1140/epjc/s10052-024-13162-1
[21] M. Tayde, Z. Hassan, and P. K. Sahoo, Nucl. Phys. B **1000**, 116478 (2024). https://doi.org/10.1016/j.nuclphysb.2024.116478
[22] M. Khurana, H. Chaudhary, S. Mumtaz, S. K. J. Pacif, and G. Mustafa, Phys. Dark Univ. **43**, 101408 (2024). https://doi.org/10.1016/j.dark.2023.101408
[23] S. H. Shekh, A. Caliskan, G. Mustafa, S. K. Maurya, A. Pradhan, and E. Guedekli, Int. J. Geom. Methods Mod. Phys. **21**, 2450054 (2024). https://doi.org/10.1142/S0219887824500543
[24] S. H. Shekh, A. Bouali, A. Pradhan, and A. Beesham, J. High Energy Astrophys. **39**, 53 (2023). https://doi.org/10.1016/j.jheap.2023.06.004
[25] A. P. Kale, Y. S. Solanke, S. H. Shekh, and A. Pradhan, Symmetry **15**, 1835 (2023). https://doi.org/10.3390/sym15101835
[26] L. Pati, B. Mishra, and S. K. Tripathy, Phys. Scr. **96**, 105003 (2021). https://doi.org/10.1088/1402-4896/ac0f92
[27] S. A. Narawade, M. Koussour, and B. Mishra, Nucl. Phys. B **992**, 116233 (2023). https://doi.org/10.1016/j.nuclphysb.2023.116233
[28] Y. Xu, T. Harko, S. Shahidi, and S. D. Liang, Eur. Phys. J. C **80**, 449 (2020). https://doi.org/10.1140/epjc/s10052-020-8023-6
[29] T. W. Kibble, J. Phys. A: Math. Gen. **9**, 1387 (1976). https://doi.org/10.1088/0305-4470/9/8/029
[30] V. G. Mete, S. N. Bayaskar, A. A. Dhanagare, and A. A. Jalamkar, J. Sci. Res. **18**, 107 (2026). http://dx.doi.org/10.3329/jsr.v18i1.82279
[31] Y. B. Zel'dovich, I. Y. Kobzarev, and L. B. Okun, Zh. Eksp. Teor. Fiz. **40**, 3 (1974). https://cds.cern.ch/record/411756
[32] S. P. Hatkar, D. P. Tadas, S. D. Katore, Eur. Phys. J. C **85**, 150 (2025). https://doi.org/10.1140/epjc/s10052-025-13800-2
[33] M. Junaid, N. P. Gaikwad, Punjab Univ. J. Math. **56**, 684 (2024). https://pujm.pu.edu.pk/index.php/pujm/article/view/534

[34] S. P. Hatkar, D. P. Tadas, and S. D. Katore, Int. J. Geom. Methods Mod. Phys. **21**, 2440033 (2024). https://doi.org/10.1142/S0219887824400334
[35] S. P. Hatkar, D. P. Tadas, and S. D. Katore, Astrophys. **67**, 537 (2024). https://doi.org/10.1007/s10511-025-09850-9
[36] S. P. Hatkar, S. P. Saraogi, and S. D. Katore, WJP **1**, 69 (2023). http://doi.org/10.56439/WJP/2023.1108
[37] V. R. Patil, J. L. Pawde, and R. V. Mapari, IJIERT **9**, 92 (2022). https://doi.org/10.17605/OSF.IO/QABKV
[38] C. B. Kilinc, Astrophys. Space Sci. **222**, 171 (1994). http://doi.org/BF00627091
[39] V. G. Mete, A. S. Nimkar, and V. D. Elkar, Int. J. Theor. Phys. **55**, 412 (2016). https://doi.org/10.1007/s10773-015-2675-2
[40] D. R. K. Reddy, R. L. Naidu, Astrophys. Space Sci. **338**, 309 (2012). https://doi.org/10.1007/s10509-011-0872-x
[41] D. R. K. Reddy, R. L. Naidu, Int. J. Theor. Phys. **46**, 2788 (2007). https://doi.org/10.1007/s10773-007-9389-z
[42] K. S. Adhav, A. S. Nimkar, and R. L. Naidu, Astrophys. Space Sci. **312**, 165 (2007). https://doi.org/10.1007/s10509-007-9670-x
[43] D. R. K. Reddy, and M. S. Rao, Astrophys. Space Sci. **305**, 183 (2006). https://doi.org/10.1007/s10509-006-9062-7
[44] A. S. Nimkar, and J. S. Wath, J. Sci. Res. **15**, 685 (2023). http://doi.org/10.3329/jsr.v15i3.64109
[45] P. K. Sahoo, B. Mishra, and G. Chakradhar Reddy, Eur. Phys. J. Plus **129**, 49 (2014). https://doi.org/10.1140/epjp/i2014-14049-7
[46] S. Bhattacharya, and T. M. Karade, Astrophys. Space Sci. **202**, 69 (1993). https://doi.org/10.1007/BF00626917
[47] C. B. Collins, E. N. Glass, and D. A. Wilkinson, Gen. Relativ. Gravit. **12**, 805 (1980). https://doi.org/10.1007/BF00763057
[48] M. S. Berman, Nuovo Cimento B **74**, 182 (1983).
[49] M. S. Berman, and F. de Mello Gomide, Gen. Relativ. Gravit. **20**, 191 (1988). https://doi.org/10.1007/BF00759327
[50] Ö. Akarsu, and T. Dereli, Int. J. Theor. Phys. **51**, 612 (2012). https://doi.org/10.1007/s10773-011-0941-5
[51] D. Stern, R. Jimenez, L. Verde, M. Kamionkowski, and S. A. Stanford, J. Cosmol. Astropart. Phys. **2010**, 008 (2010). http://doi.org/10.1088/1475-7516/2010/02/008
[52] J. Simon, L. Verde, and R. Jimenez, Phys. Rev. D **71**, 123001 (2005). https://doi.org/10.1103/PhysRevD.71.123001
[53] M. Moresco, *et al.,* J. Cosmol. Astropart. Phys. **2012**, 006 (2012). https://doi.org/10.1088/1475-7516/2012/08/006
[54] C. Zhang, H. Zhang, S. Yuan, S. Liu, T. J. Zhang, and Y. C. Sun, Res. Astron. Astrophys. **14**, 1221 (2014). https://doi.org/10.1088/1674-4527/14/10/002
[55] M. Moresco, *et al.,* J. Cosmol. Astropart. Phys. **2016**, 014 (2016). https://doi.org/10.1088/1475-7516/2016/05/014
[56] A. L. Ratsimbazafy, *et al.,* Mon. Not. R. Astron. Soc. **467**, 3239 (2017). https://doi.org/10.1093/mnras/stx301
[57] M. Moresco, Mon. Not. R. Astron. Soc.: Lett. **450**, L16 (2015). https://doi.org/10.1093/mnrasl/slv037
[58] E. Gaztanaga, A. Cabre, and L. Hui, Mon. Not. R. Astron. Soc. **399**, 1663 (2009). https://doi.org/10.1111/j.1365-2966.2009.15405.x
[59] A. Oka, S. Saito, T. Nishimichi, A. Taruya, and K. Yamamoto, Mon. Not. R. Astron. Soc. **439**, 2515 (2014). https://doi.org/10.1093/mnras/stu111
[60] Y. Wang, *et al.,* Mon. Not. R. Astron. Soc. **469**, 3762 (2017). https://doi.org/10.1093/mnras/stx1090
[61] C. H. Chuang, *et al.,* Mon. Not. R. Astron. Soc. **461**, 3781 (2016). https://doi.org/10.1093/mnras/stw1535
[62] S. Alam, *et al.,* Mon. Not. R. Astron. Soc. **470**, 2617 (2017). https://doi.org/10.1093/mnras/stx721
[63] C. Blake, *et al.,* Mon. Not. R. Astron. Soc. **425**, 405 (2012). https://doi.org/10.1111/j.1365-2966.2012.21473.x
[64] C. H. Chuang, *et al.,* Mon. Not. R. Astron. Soc. **433**, 3559 (2013). https://doi.org/10.1093/mnras/stt988
[65] L. Anderson, *et al.,* Mon. Not. R. Astron. Soc. **441**, 24 (2014). https://doi.org/10.1093/mnras/stu523
[66] N. G. Busca, *et al.,* Astron. Astrophys. **552**, A96 (2013). https://doi.org/10.1051/0004-6361/201220724
[67] J. E. Bautista, *et al.,* Astron. Astrophys. **603**, A12 (2017). https://doi.org/10.1051/0004-6361/201730533
[68] T. Delubac, *et al.,* Astron. Astrophys. **552**, A96 (2013). https://doi.org/10.1051/0004-6361/201220724
[69] A. Font-Ribera, *et al.,* J. Cosmol. Astropart. Phys. **2014**, 027 (2014). https://doi.org/10.1088/1475-7516/2014/05/027
[70] G. S. Sharov, and V. O. Vasiliev, arXiv preprint arXiv:1807.07323 (2018). https://doi.org/10.26456/mmg/2018-611

АКСІАЛЬНО-СИМЕТРИЧНА КОСМОЛОГІЧНА МОДЕЛЬ В ГРАВІТАЦІЇ *f(Q,T)*

М.Т. Сароде[1], В.Г. Мете[2], А.С. Німкар[3]
[1]Коледж мистецтв, комерції та науки ім. Шрі Шиваджі, Акола (M.S.), Індія
[2]Кафедра математики, Коледж ім. Р. Д. І. К. та К. Д., Баднера-Амравaті (M.S.), Індія
[3]Коледж мистецтв та наук ім. Шрі доктора Р. Г. Ратода, округ Муртізапур, Акола (M.S.), Індія

Ця стаття присвячена вивченню динамічних аспектів космологічної моделі доменної стінки в осьово-симетричному просторі-часі в гравітації f(Q,T). У цій теорії гравітації дія містить довільну функцію f(Q,T), де Q та T відповідно позначають неметричність та слід тензора енергії-імпульсу. У цій роботі враховується лінійна та адитивна форма гравітації f(Q,T), f(Q,T)=μQ+νT, де μ та ν – ненульові довільні константи. Детерміновану модель Всесвіту отримано з використанням лінійно змінного параметра уповільнення q=-kt+m-1, який є лінійним у часі з негативним нахилом. Ми оцінили всі динамічні та геометричні параметри моделей та дослідили їх фізичне значення в сучасній космології. Ми спостерігали, що параметр уповільнення q демонструє характерну точку перевороту, де відбувається перехід від режиму уповільнення до режиму прискорення, що свідчить про космічне розширення. Помічено, що наша модель добре узгоджується з сучасним сценарієм прискореного розширення Всесвіту.

Ключові слова: *доменна стінка; гравітація f(Q,T); аксіально симетричний простір-час; параметр уповільнення*

East European Journal of Physics. 2. 45-51 (2026)
DOI:10.26565/2312-4334-2026-2-04 ISSN 2312-4334

BIANCHI TYPE–VII COSMOLOGICAL MODEL WITH TSALLIS–BARROW HOLOGRAPHIC DARK ENERGY IN LYRA GEOMETRY

R. Santhi Kumar[1], P. Harikrishan[2], B. Srinivasa Rao[1], V. Gopala Krishna[1], A. Lakshmana Rao[1], S.V. Maruthi Prasad[1], K.P.S. Suryanarayana[1], M. Ramanamurty[1]*, P. Vasu[1], B. Divya[1]

[1]*Aditya Institute of Technology and Management, K. Kotturu, Tekkali, Srikakulam Dist, Andhra Pradesh, India-532203*
[2]*Vigna Institute of Information Technology, Visakhapatnam, India*
**Corresponding Author email: ramanamurtymuddada@gmail.com*
Received March 13, 2026; revised May 14, 2026; accepted May 15, 2026

In this work, we investigate an anisotropic Bianchi type–VII cosmological model in the framework of Lyra geometry filled with perfect fluid matter and Tsallis–Barrow holographic dark energy. The modified Einstein field equations are derived, and exact solutions are obtained by assuming a power-law average scale factor for a decelerating universe. Expressions for various cosmological parameters, such as the Hubble parameter, expansion scalar, shear scalar, matter density, dark energy density, and density parameters, are derived and analyzed. The behaviour of these parameters indicates that the universe is expanding continuously, with the expansion rate decreasing with cosmic time. The anisotropy parameter decreases gradually, indicating that the universe evolves towards isotropy at late times. Energy conditions, stability analysis, and cosmological diagnostics, including the statefinder and Om parameters, are also examined to evaluate the model's physical viability. The results suggest that Tsallis–Barrow entropy corrections in Lyra geometry provide a consistent framework for studying anisotropic cosmological evolution and dark energy dynamics.
Keywords: *Bianchi type–VII cosmology; Lyra geometry; Tsallis–Barrow holographic dark energy; Anisotropic Universe, Modified gravity; Cosmological diagnostics*
PACS: 98.80.-k, 98.80.Jk, 04.20.Jb, 95.36.+x, 04.50.Kd

1. INTRODUCTION

Modern observational cosmology strongly indicates that the universe is currently undergoing accelerated expansion. The first observational evidence for this phenomenon came from high-redshift Type Ia supernova observations, which revealed that distant supernovae appear dimmer than expected in a decelerating universe [1]. Subsequent observations of the cosmic microwave background radiation and baryon acoustic oscillations further confirmed this result [2,3]. These observations suggest that nearly 70% of the universe's total energy density is composed of a mysterious component known as dark energy.

The simplest candidate for dark energy is the cosmological constant introduced by Einstein in the framework of general relativity. Although the cosmological constant model successfully explains many observations, it faces theoretical problems such as the fine-tuning and coincidence problems [4]. These issues have motivated the development of alternative dark energy models, including scalar-field models, modified gravity theories, and holographic dark energy models.

The holographic principle, originally proposed in the context of black hole thermodynamics, provides a theoretical foundation for holographic dark energy models [5]. In this approach, the dark energy density is related to the infrared cutoff of the universe. Recently, entropy-corrected holographic dark energy models have been proposed to incorporate quantum gravitational effects. Among these models, the Tsallis–Barrow holographic dark energy framework has attracted considerable attention because it combines two different entropy modifications arising from non-extensive statistical mechanics and quantum gravitational corrections [6–8].

In addition to modified dark energy models, modified gravitational theories have also been proposed to explain cosmic acceleration. Lyra geometry, introduced as an alternative to Riemannian geometry, modifies Einstein's field equations by introducing a displacement vector field [9-13]. This modification has been used to study various cosmological models.

Furthermore, anisotropic cosmological models such as Bianchi spacetimes provide a more general description of the early universe. Among them, the Bianchi type VII model represents an anisotropic generalization of the Friedmann universe.

Inspired by the above developments, the present study explores a Bianchi type–VII anisotropic cosmological model in the framework of Lyra geometry incorporating Tsallis–Barrow holographic dark energy. The paper is organized as follows. Section 2 introduces the space–time metric and derives the model's field equations. In Section 3, exact solutions of the cosmological model are obtained. Section 4 examines the behaviour of the key physical and cosmological parameters. Section 5 presents various cosmological diagnostic tools used to analyse the model. Section 6 compares the obtained results with standard cosmological models. Section 7 discusses the physical implications of the results, and finally, Section 8 summarizes the main findings and conclusions of the work.

Cite as: R.S. Kumar, P. Harikrishan, B.S. Rao, V.G. Krishna, A.L. Rao, S.V.M. Prasad, K.P.S. Suryanarayana, M. Ramanamurty, P. Vasu, B. Divya, East Eur. J. Phys. 2, 45 (2026), https://doi.org/10.26565/2312-4334-2026-2-04

2. METRIC AND FIELD EQUATIONS

We consider the anisotropic Bianchi type–VII metric given by

$$ds^2 = -dt^2 + A^2(t)dx^2 + B^2(t)e^{2mx}dy^2 + C^2(t)e^{2mx}dz^2. \tag{1}$$

The average scale factor is defined as

$$a = (ABC)^{1/3}. \tag{2}$$

The average spatial volume is

$$V = a^3. \tag{3}$$

The modified Einstein field equations in Lyra geometry are

$$R_{ij} - \frac{1}{2}g_{ij}R + \frac{3}{2}\phi_i\phi_j - \frac{3}{4}g_{ij}\phi_k\phi^k = -T_{ij}. \tag{4}$$

The displacement vector is chosen as

$$\phi_i = (\beta(t),0,0,0). \tag{5}$$

The energy-momentum tensor for a perfect fluid is

$$T_{ij} = (\rho + p)u_iu_j + pg_{ij}. \tag{6}$$

The total density and pressure are

$$\rho = \rho_m + \rho_{TB}, p = p_m + p_{TB}. \tag{7}$$

The energy density of Tsallis–Barrow holographic dark energy is defined as

$$\rho_{TB} = 3c^2H^{2(2-\delta)}. \tag{8}$$

Where c is a model constant, δ is the entropy deformation parameter.

3. SOLUTION OF THE MODEL

To obtain exact solutions, we assume the relation

$$A = B^r, \tag{9}$$

which yields

$$A = a^{\frac{3r}{r+2}}, B = C = a^{\frac{3}{r+2}}. \tag{10}$$

We assume a power-law scale factor

$$a(t) = a_0(t + t_0)^s. \tag{11}$$

The Hubble parameter becomes

$$H = \frac{s}{t+t_0}. \tag{12}$$

$$q = -\frac{a\ddot{a}}{\dot{a}^2} = \frac{1-s}{s}. \tag{13}$$

For $0 < s < 1$, The universe exhibits decelerating expansion.

4. PHYSICAL PROPERTIES OF THE MODEL

The expansion scalar is

$$\theta = 3H = \frac{3s}{t+t_0}. \tag{14}$$

The shear scalar becomes

$$\sigma^2 = \frac{3(r-1)^2s^2}{(r+2)^2(t+t_0)^2}. \tag{15}$$

The anisotropy parameter is

$$\Delta = \frac{2(r-1)^2}{(r+2)^2}. \tag{16}$$

The matter density evolves as

$$\rho_m = \rho_{m0}(t + t_0)^{-3s(1+\omega_m)}. \tag{17}$$

The Matter pressure is
Since $p_m = \omega_m \rho_m$, we obtain

$$p_m = \omega_m \rho_{m0}(t + t_0)^{-3s(1+\omega_m)} \tag{18}$$

The dark energy density becomes

$$\rho_{TB} = 3c^2 \left(\frac{s}{t+t_0}\right)^{2(2-\delta)} \tag{19}$$

Where c= model constant, δ= Tsallis–Barrow entropy parameter.
These expressions indicate that the expansion rate decreases with cosmic time and the universe gradually approaches isotropy.

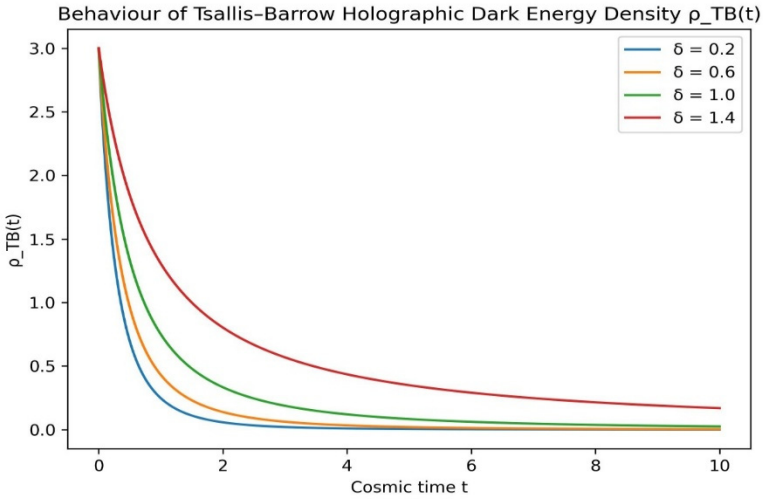

Figure 1. ρ_{TB} vs. Cosmic time t

The graph was plotted using the following parameter values: c =1, s= 1, t_0=0.5, $\delta = 0.2, 0.6, 1.0, 1.4$

We observed from Figure 1, (i) $\rho_{TB}(t)$ decreases with cosmic time t (ii) Larger values of δproduce a slower decay of dark energy density. (iii) For small δ, The density falls rapidly at early times. (iv) At late times, all curves approach zero, indicating dilution of dark energy density during cosmic evolution.

The Tsallis–Barrow equation of state parameter is

$$\omega_{TB} = -1 + \frac{2(2-\delta)}{3s} \tag{20}$$

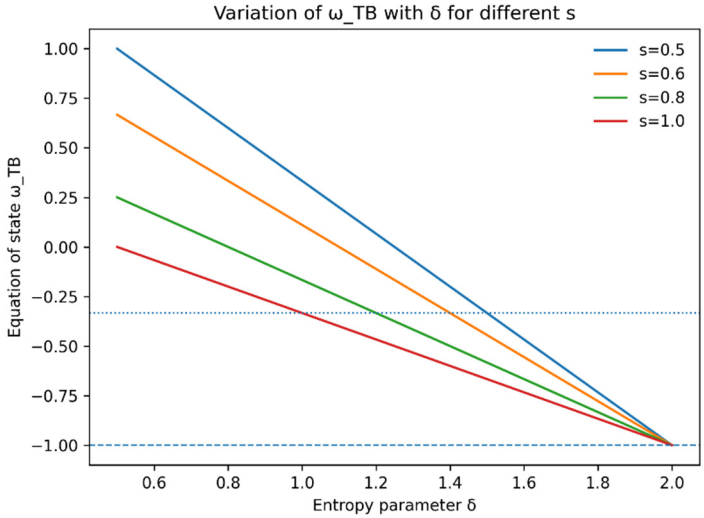

Figure 2. ω_{TB} vs. Cosmic time t

Figure 2 was plotted using: $s = 0.5, 0.6, 0.8, 1.0$ and the entropy parameter range is $0.5 \leq \delta \leq 2.0$ The graph shows that. ω_{TB} decreases linearly with increasing δ. For smaller values of s, The equation of state remains in

the quintessence region for a larger interval. As $\delta \to 2$ The line $\omega_{TB} = -1$ represents the ΛCDM/cosmological constant phase. The dotted lines represent: $\omega = -1/3$(transition to accelerated expansion) and $\omega = -1$(phantom divide/cosmological constant boundary).
From the field equations the Lyra displacement function is

$$\beta^2 = \frac{4}{3}\left[\frac{9(2r+1)s^2}{(r+2)^2(t+t_0)^2} - \frac{3m^2}{A^2} - \rho\right]. \quad (21)$$

If r varies, the curves change in magnitude, and the early-time behaviour is more sensitive to r. If s varies, larger $s$gives higher values of $\beta^2(t)$, especially near the origin. If ρ varies, there is increasing ρ shifts the curve downward. In all cases, the curves generally decrease with cosmic time because of the $\frac{1}{(t+t_0)^2}$term.

Early-Time Behaviour ($t \to 0$), At the beginning of cosmic evolution, the scale factor $a(t)$is very small but non-zero, The spatial volume $V = a^3$is also small, indicating a compact early universe, The Hubble parameter $H = \frac{s}{t+t_0}$ becomes very large. The expansion scalar $\theta = \frac{3s}{t+t_0}$ also takes large values. The shear scalar $\sigma^2 \propto \frac{1}{(t+t_0)^2}$ It is large, showing that anisotropies dominate in the early universe. Matter density is high because the cosmic volume is small. Thus, the early universe is characterized by a high expansion rate, strong anisotropies, and large energy density. Late-Time Behaviour ($t \to \infty$), At late cosmic times, the scale factor becomes very large. The spatial volume increases indefinitely. The Hubble parameter approaches zero $H \to 0$, indicating slow expansion. The expansion scalar decreases steadily, The shear scalar tends to zero. $\sigma^2 \to 0$ showing that the universe becomes nearly isotropic at late times. Matter density decreases significantly due to cosmic expansion. The TBHDE component may dominate the total cosmic energy density depending on the entropy parameter δ. Hence, the model describes a universe evolving from an anisotropic, high-density early phase to a smoother, more isotropic late-time universe.

5. COSMOLOGICAL DIAGNOSTICS

5.1 Energy Conditions

(i) Null Energy Condition

$$\rho + p \geq 0 \quad (22)$$

Using the obtained model,

$$\rho + p = (\rho_m + \rho_{TB}) + (p_m + p_{TB}) \quad (23)$$

$$\rho + p = (1 + \omega_m)\rho_m + (1 + \omega_{TB})\rho_{TB} \quad (24)$$

If this quantity remains positive, the NEC is satisfied.

(ii) Weak Energy Condition

$$\rho \geq 0, \rho + p \geq 0 \quad (25)$$

In the present model

$$\rho = \rho_m + \rho_{TB} \quad (26)$$

Since both densities are positive, the WEC remains satisfied for realistic parameter choices.

(iii) Strong Energy Condition

$$\rho + 3p \geq 0 \quad (27)$$

Substituting the model parameters,

$$\rho + 3p = \rho_m + \rho_{TB} + 3(p_m + p_{TB}). \quad (28)$$

If the TBHDE pressure becomes sufficiently negative, the SEC may be violated. Such a violation is generally associated with cosmic acceleration.

(iv) Dominant Energy Condition

$$\rho \geq | p | \quad (29)$$

which ensures that the energy density dominates over pressure and that energy flow remains causal. In the present model, the DEC depends on the magnitude of dark energy's pressure.

5.2 Stability Analysis

The stability of the cosmological model can be examined using the square of the sound speed.

$$v_s^2 = \frac{dp}{d\rho} \quad (30)$$

A physically stable model requires $0 \leq v_s^2 \leq 1$.
Substituting the model expressions,

$$v_s^2 = \frac{d(p_m+p_{TB})}{d(\rho_m+\rho_{TB})}. \tag{31}$$

Since $p_m = \omega_m \rho_m$, we obtain

$$v_s^2 = \frac{\omega_m d\rho_m + dp_{TB}}{d\rho_m + d\rho_{TB}}. \tag{32}$$

The stability condition depends on the behaviour of the TBHDE pressure and density. If the above inequality holds, the cosmological model remains classically stable.

5.3 State Finder Diagnostic

The state-finder parameters provide a useful tool for distinguishing among different dark energy models. They are defined as

$$r = \frac{\dddot{a}}{aH^3} = \frac{1}{aH^3}\frac{d^3a}{dt^3}. \tag{33}$$

$$s = \frac{r-1}{3(q-\frac{1}{2})}. \tag{34}$$

For the power-law scale factor from eq. (11)

$$a(t) = a_0(t+t_0)^s. \tag{35}$$

The state finder parameters become

$$r = \frac{(s-1)(s-2)}{s^2}. \tag{36}$$

$$s_{sf} = \frac{r-1}{3(q-\frac{1}{2})}. \tag{37}$$

The pair (r, s)helps compare the present model with the standard ΛCDM model, which corresponds to

$$(r, s) = (1,0). \tag{38}$$

Deviation from this point indicates the influence of entropy-corrected holographic dark energy.

5.4 Om Diagnostic

The Om diagnostic is another tool for distinguishing dark energy models in a model-independent manner. It is defined as

$$Om(z) = \frac{H^2(z)-H_0^2}{H_0^2[(1+z)^3-1]} = \frac{(1+z)^{2/s}-1}{(1+z)^3-1}. \tag{39}$$

Where z is redshift, $H_0 = s$ is present Hubble parameter (At $z = 0$),
Using the obtained Hubble parameter $H(t) = \frac{s}{t+t_0}$ and the relation

$$1 + z = \frac{a_0}{a(t)} = \frac{1}{(t+t_0)^s}. \tag{40}$$

The Om diagnostic can be evaluated. If $Om(z)$is constant, this model is the ΛCDM model. If $Om(z)$increases with z then it is phantom behaviour, If $Om(z)$decreases with z then it is quintessence behaviour. Thus, the Om diagnostic helps identify the nature of dark energy in the present cosmological model.

6. COMPARISON WITH STANDARD COSMOLOGICAL MODELS

The ΛCDM model**,** the Standard Holographic Dark Energy (HDE) model, and the present Tsallis–Barrow Holographic Dark Energy (TBHDE) model in Lyra geometry differ mainly in their geometries, gravitational frameworks, and dark energy formulations. The ΛCDM and standard HDE models are constructed within the FRW isotropic spacetime under General Relativity. In contrast, the present model considers a Bianchi type VII anisotropic spacetime in the framework of Lyra modified geometry**.**

In the ΛCDM model, dark energy is represented by the cosmological constant Λ**,** which yields a constant energy density and an exponential expansion of the universe. In contrast, the standard HDE model introduces holographic dark energy**,** in which the energy density depends on an infrared cutoff scale, leading to a time-dependent dark energy density that can explain cosmic acceleration.

Feature	ΛCDM Model	Standard Holographic Dark Energy (HDE)	Present TBHDE–Lyra Model
Geometry	FRW isotropic	FRW isotropic	Bianchi type–VII anisotropic
Gravity	General Relativity	General Relativity	Lyra modified geometry
Dark Energy	Cosmological constant Λ	Holographic dark energy	Tsallis–Barrow holographic dark energy
Scale Factor	Exponential expansion	Depends on the cutoff scale	Power-law expansion
Anisotropy	No anisotropy	No anisotropy	Anisotropic early universe
Dark Energy Behaviour	Constant density	Time-dependent	Entropy-corrected density
Cosmic Evolution	Late-time acceleration	Accelerating universe	Decelerating anisotropic model
Additional Parameters	Λ	c parameter	c, δ entropy parameter
Additional Parameters	Λ	c parameter	c, δ entropy parameter

The present TBHDE–Lyra model extends this idea by incorporating Tsallis–Barrow entropy corrections, which modify the holographic dark energy density through the entropy parameter δ. Unlike the isotropic models, this framework allows an anisotropic early universe, represented by the Bianchi type–VII geometry. The scale factor evolves with a power-law expansion**,** and the dark energy density becomes entropy-corrected and dynamically evolving**.**

Overall, while the ΛCDM and HDE models mainly describe an isotropic accelerating universe, the present TBHDE–Lyra model provides a more general cosmological scenario that includes anisotropy, modified gravity, and entropy-corrected holographic dark energy, characterized by the parameters c $c$and δ.

7. DISCUSSION

The present cosmological model describes an anisotropic Bianchi type–VII universe in the framework of Lyra geometry filled with perfect fluid matter and Tsallis–Barrow holographic dark energy (TBHDE). The model is constructed using a power-law average scale factor, which represents a simple decelerating cosmological evolution.

The obtained solution shows that the scale factor increases monotonically with cosmic time, indicating a continuously expanding universe. The Hubble parameter decreases over time, indicating that the rate of expansion slows as the universe evolves. This behaviour is consistent with a decelerating cosmological phase.

The expansion scalar also decreases over time, indicating that the universe's expansion becomes less rapid at later epochs. The shear scalar, which measures anisotropy in the expansion, decreases proportionally to t^{-2}. This indicates that the universe's anisotropies gradually decrease with cosmic evolution. When the anisotropy parameter $r = 1$, the model reduces to the isotropic Friedmann universe.

The matter density decreases as the universe expands due to the dilution of matter in an increasing volume. In contrast, the Tsallis–Barrow holographic dark energy density evolves according to the entropy deformation parameter δ, which governs the behaviour of dark energy.

The displacement vector $\beta(t)$arising from Lyra geometry contributes additional geometric effects to the cosmic dynamics. This term behaves like a time-dependent cosmological function that affects the model's effective pressure and energy density.

Overall, the obtained cosmological model provides a consistent description of anisotropic cosmic evolution in modified geometry and illustrates how entropy-corrected holographic dark energy can influence the large-scale dynamics of the universe.

8. CONCLUSIONS

In this work, we constructed a Bianchi type–VII cosmological model in Lyra geometry filled with perfect fluid matter and Tsallis–Barrow holographic dark energy. Exact solutions of the modified field equations were obtained using a power-law scale factor. The behaviour of cosmological parameters such as the Hubble parameter, expansion scalar, and shear scalar was analysed. The model shows continuous cosmic expansion with a decreasing rate of expansion. The universe's anisotropies decrease gradually, indicating a transition towards isotropy at late times. Matter density decreases as expected due to cosmic expansion, while the behaviour of dark energy depends on the entropy deformation parameter. The analysis of energy conditions, stability criteria, and cosmological diagnostics confirms the model's physical viability. The results suggest that Tsallis–Barrow holographic dark energy in Lyra geometry provides a useful framework for studying anisotropic cosmological evolution.

ORCID

R. Santhi Kumar, https://orcid.org/0000-0001-5122-3800; **P. Harikrishan,** https://orcid.org/0000-0003-2597-2378;
B. Srinivasa Rao, https://orcid.org/0009-0004-0487-2495; **V. Gopala Krishna,** https://orcid.org/0000-0002-5120-7277;
A. Lakshmana Rao, https://orcid.org/0000-0001-7651-9376; **S.V. Maruthi Prasad,** https://orcid.org/0000-0003-1594-6803;
K.P.S. Suryanarayana, https://orcid.org/0000-0002-8793-3588; **M. Ramanamurty,** https://orcid.org/0009-0009-4086-486X;
P. Vasu, https://orcid.org/0000-0002-7753-7223; **B. Divya**, https://orcid.org/0009-00003-2036-6122

REFERENCES

[1] A.G. Riess, *et al*. "Observational Evidence from Supernovae for an Accelerating Universe and a Cosmological Constant," The Astronomical Journal, **116**(3), 1009–1038 (1998). https://doi.org/0.1086/300499

[2] Planck Collaboration, "Planck 2018 Results. VI. Cosmological Parameters," Astronomy & Astrophysics, **641**, A6 (2020). https://doi.org/10.48550/arXiv.1807.06209
[3] D.J. Eisenstein, *et al*., "Detection of the Baryon Acoustic Peak in the Large-Scale Correlation Function of SDSS Luminous Red Galaxies," The Astrophysical Journal, **633**(2), 560–574 (2005). https://doi.org/10.1086/466512
[4] S. Weinberg, "The Cosmological Constant Problem," Reviews of Modern Physics, **61**(1), 1–23 (1989). https://doi.org/10.1103/RevModPhys.61.1
[5] M. Li, "A Model of Holographic Dark Energy," Physics Letters B, **603**(1–2), 1–5 (2004). https://doi.org/10.1016/j.physletb.2004.10.014
[6] C. Tsallis, "Possible Generalization of Boltzmann–Gibbs Statistics," Journal of Statistical Physics, **52**(1-2), 479–487 (1988). https://doi.org/10.1007/BF01016429
[7] J.D. Barrow, "The Area of a Rough Black Hole," Physics Letters B, **808**, 135643 (2020). https://doi.org/10.1016/j.physletb.2020.135643
[8] E.N. Saridakis, *et al*., "Modified Holographic Dark Energy Models with Tsallis Entropy," Physical Review D, **102**(12), 123525 (2020). https://doi.org/10.1103/PhysRevD.102.123525
[9] G. Lyra, "Über eine Modifikation der Riemannschen Geometrie," Mathematische Zeitschrift, **54**, 52–64 (1951). https://doi.org/10.1007/BF01175135
[10] R. Santhikumar, and B. Satyannarayana, "Accelerating anisotropic cosmological model in f(R, T) theory of gravity," Indian Journal of Physics, **91**(10), 1293–1296 (2017).
[11] M. Krishna, S. Koppala, and R.S. Rajamahanthi, "Accelerating plane-symmetric cosmological model with bulk viscous and cosmic Strings in Lyra's geometry," Indian J. Phys. **98**, 3733–3740 (2024). https://doi.org/10.1007/s12648-024-03100-y
[12] D.R.K. Reddy, and R. Santhi Kumar, "Some anisotropic cosmological models in a modified theory of gravitation," Astrophys. Space Sci. **344**, 253–257 (2013). https://doi.org/10.1007/s10509-012-1304-2
[13] M. Ramanamurty, R. Santhikumar, and K. Sobhanbabu, "Two fluid scenario for dark energy model with LVDP in a scalar–tensor theory of gravitation," Indian J. Phys. **100**, 411–429 (2026). https://doi.org/10.1007/s12648-025-03788-6

КОСМОЛОГІЧНА МОДЕЛЬ Б'ЯНЧІ ТИПУ-VII З ГОЛОГРАФІЧНОЮ ТЕМНОЮ ЕНЕРГІЄЮ ЦАЛЛІСА–БАРРОУ В ГЕОМЕТРІЇ ЛІРИ

Р. Санті Кумар[1], П. Харікрішан[2], Б. Шрініваса Рао[1], В. Гопала Крішна[1], А. Лакшмана Рао[1], С.В. Маруті Прасад[1], К.П.С. Сурьянараяна[1], М. Раманамурті[1], П. Васу[1], Б. Дівья[1]

[1]Інститут технологій та менеджменту Адітья, К. Коттуру, Теккалі, округ Шрікакулам, Андхра-Прадеш, Індія-532203
[2]Інститут інформаційних технологій Вінья, Вішакхапатнам, Індія

У цій роботі ми досліджуємо анізотропну космологічну модель типу Біанкі VII в рамках геометрії Ліри, заповненої ідеальною рідкою матерією та голографічною темною енергією Цалліса-Барроу. Виведено модифіковані рівняння поля Ейнштейна, а точні розв'язки отримано, припускаючи степеневий середній масштабний коефіцієнт для Всесвіту, що сповільнюється. Виведено та проаналізовано вирази для різних космологічних параметрів, таких як параметр Хаббла, скаляр розширення, скаляр зсуву, густина матерії, густина темної енергії та параметри густини. Поведінка цих параметрів вказує на те, що Всесвіт безперервно розширюється, причому швидкість розширення зменшується з космічним часом. Параметр анізотропії поступово зменшується, що вказує на те, що Всесвіт еволюціонує до ізотропії на пізніх етапах. Також досліджуються енергетичні умови, аналіз стабільності та космологічна діагностика, включаючи параметри пошуку стану та Om, для оцінки фізичної життєздатності моделі. Результати показують, що поправки ентропії Цалліса-Барроу в геометрії Ліри забезпечують узгоджену основу для вивчення анізотропної космологічної еволюції та динаміки темної енергії.

Ключові слова: *космологія типу Біанкі VII; геометрія Ліри; голографічна темна енергія Цалліса-Барроу; анізотропний Всесвіт, модифікована гравітація; космологічна діагностика*

East European Journal of Physics. 2. 52–61 (2026)
DOI: 10.26565/2312-4334-2026-2-05 ISSN 2312-4334

MAGNETIZED ANISOTROPIC DARK ENERGY COSMOLOGICAL MODEL IN $f(T)$ GRAVITY WITH A SPECIAL LAW OF THE HUBBLE PARAMETER

K.N. Pawar, **A.S. Khan***, **I.I. Khan**
Department of Mathematics, Shri Shivaji Science College, Nagpur, Maharashtra, India
*Corresponding Author e-mail: alimkhan3101@email.com

Received March 2, 2025; accepted May 16, 2026

In this paper, we investigate a magnetized anisotropic dark energy cosmological model in the framework of $f(T)$ gravity for a locally rotationally symmetric Bianchi type-I spacetime. Choosing $f(T) = 0$ reduces the theory to teleparallel gravity, dynamically equivalent to general relativity, enabling direct comparison with standard cosmology. Exact solutions of the field equations are obtained by assuming a special law of the Hubble parameter with a nonzero constant S, yielding power-law behavior of the directional scale factors. A uniform magnetic field aligned along one spatial direction produces an early-time anisotropy whose energy density decays with cosmic expansion. The energy density, pressure, the equation-of-state parameter, and the energy conditions are analyzed. The pressure remains negative, while the equation-of-state parameter evolves dynamically and approaches the range $-1 \leq \omega < -\frac{1}{3}$ at late times, consistent with SN Ia and CMB constraints. The null and weak energy conditions are violated at late times, whereas the strong energy condition is violated throughout, implying acceleration.

Keywords: *Magnetized dark energy; $f(T)$ gravity; LRS Bianchi type-I model; Anisotropic universe; Cosmic time*

PACS: 04.50.Kd

1. INTRODUCTION

Research on magnetized anisotropic dark energy with constant deceleration parameter in $f(T)$ gravity has emerged as a critical area of inquiry due to its potential to explain the accelerated expansion of the universe while addressing anisotropies observed in cosmic structures. The evolution of modified teleparallel gravity theories,particularly $f(T)$ gravity, has been extensively studied since the early 2010s, offering an alternative to curvature-based modifications such as $f(R)$ gravity by utilizing torsion scalar T as the fundamental geometric quantity [1–3]. Initial models demonstrated the capability of $f(T)$ gravity to reproduce late-time acceleration consistent with observational data [4, 5], while subsequent works incorporated anisotropic cosmologies, such as Bianchi type-I and VI models, to capture large-scale anisotropies hinted by supernova and cosmic microwave background observations [6–8].

The inclusion of magnetic fields alongside anisotropic dark energy components further enriches the modeling of cosmic evolution, reflecting realistic astrophysical conditions [9–11]. These developments underscore the theoretical and observational significance of exploring anisotropic dark energy within $f(T)$frameworks, especially under constraints like constant deceleration parameters that simplify and clarify cosmic dynamics [12].

Despite these advances, the specific problem of characterizing magnetized anisotropic dark energy models with a constant deceleration parameter in the context of $f(T_0)$ gravity remains insufficiently addressed.Although several studies have examined anisotropic models with varying deceleration parameters or without magnetic fields [13, 14], and others have explored magnetized fluids in different gravity theories,a comprehensive treatment combining magnetization, anisotropy, and constant deceleration within $f(T_0)$ gravity is lacking [15, 16].

Studies on modified teleparallel gravity have significantly expanded over the last decade, particularly in the context of anisotropic cosmology and dark energy dynamics.The early foundational work [17–20] explored perturbations, large-scale structure, phantom divide crossing, and the reconstruction of $f(T)$ models capable of describing inflation, ΛCDM behavior, and future singularities. These studies generally did not include magnetic fields but provided key insights into stability, perturbation growth, thermodynamics, and late-time acceleration within torsion-based gravity. Extensions such as $f(T, B)$,$f(T, T_G)$, and $f(T, \mathcal{T})$ [21–23] further broadened the theoretical landscape, addressing unified inflation–acceleration phases, cosmographic constraints, and ghost-free stability features. A large set of works has examined anisotropic dark energy models within f(T) gravity and related theories. [24–26] investigated Bianchi-type cosmologies, incorporating constant or variable deceleration parameters through Hubble parameter variation laws, power-law expansions, or reconstruction schemes. These studies revealed transitions from deceleration to acceleration, isotropization trends, phantom behavior, observational compatibility with SNe Ia, CMB, BAO, and alleviation of tensions such as H0.However, in most cases magnetic fields were either omitted or treated only implicitly through anisotropic pressure components, thus limiting the analysis of realistic anisotropic environments.

Recent observations of cosmic magnetic fields have motivated magnetized anisotropic models, mostly in GR, $f(R)$, or $f(Q, T)$ gravity. Some works such as [27–29] explicitly modeled magnetic fields in Bianchi types I, II, V, VI_0, and

Cite as: K.N. Pawar, A.S. Khan, I.I. Khan, East Eur. J. Phys. 2, 52 (2026), https://doi.org/10.26565/2312-4334-2026-2-05

Kantowski–Sachs universes. These studies demonstrated that magnetic fields significantly influence shear evolution, skewness parameters, isotropization, and the expansion behavior of the universe. Many models exhibited anisotropy persistence, delayed isotropization, or strong early-time magnetic dominance. [30, 31] incorporated magnetic effects indirectly via cosmic string fluids within $f(T)$ or $f(Q)$ gravity, showing that torsion–magnetization interactions modify late-time evolution and observational characteristics. Although these studies highlighted the cosmological importance of magnetic fields, they did not integrate them into the teleparallel framework with a constant deceleration parameter.

Meanwhile, several recent works [32–35] focused on observational constraints, phantom crossings, holographic reconstructions, Kaniadakis entropy, emergent scenarios, and hybrid scale factor dynamics. These contributions further emphasize the viability of modified gravity, but still lack explicit treatment of magnetized anisotropic fluids within $f(T)$ cosmology under CDP assumptions.

Despite significant progress in magnetized anisotropic dark energy models within modified gravity, several important challenges remain unresolved. Most existing studies idealize magnetic fields as uniform or one-directional, neglecting realistic magnetohydrodynamic effects and backreaction on anisotropy, shear evolution, and dark energy dynamics [36,37]. Additionally, the widespread use of constant deceleration parameters oversimplifies cosmic evolution and limits the ability to model realistic transitions between decelerated and accelerated phases, particularly in magnetized anisotropic settings [38]. Observational constraints on such models remain weak, as current datasets primarily focus on isotropic scenarios and insufficiently probe anisotropic and magnetized signatures in CMB, large-scale structure, and polarization data [39].

Moreover, the coupling between magnetic fields and torsion scalar modifications in $f(T)$ gravity, perturbation theory in anisotropic magnetized backgrounds, thermodynamic consistency, and systematic exploration of viable $f(T)$ functional forms remain insufficiently explored. Addressing these issues through numerical simulations, realistic magnetic field modeling, and comprehensive observational analyses is essential for developing physically viable magnetized anisotropic cosmological models.

2. $f(T)$ GRAVITY FORMALISM AND MAGNETIZED DARK ENERGY

Teleparallel gravity provides an equivalent formulation of General Relativity (GR) in which gravitation is described by spacetime torsion rather than curvature. The dynamical variables are the tetrad fields $e^a{}_\mu$, which relate the spacetime metric $g_{\mu\nu}$ to the Minkowski metric η_{ab} through

$$g_{\mu\nu} = \eta_{ab}\, e^a{}_\mu e^b{}_\nu. \tag{1}$$

In teleparallel gravity, the torsion tensor is defined as

$$T^\lambda{}_{\mu\nu} = e_a{}^\lambda \left(\partial_\mu e^a{}_\nu - \partial_\nu e^a{}_\mu\right), \tag{2}$$

and the torsion scalar T is constructed from suitable contractions of the torsion tensor,

$$T = S_\lambda{}^{\mu\nu} T^\lambda{}_{\mu\nu}, \tag{3}$$

where $S_\lambda{}^{\mu\nu}$ denotes the superpotential.

In $f(T)$ gravity, the gravitational action is generalized by replacing the torsion scalar T with an arbitrary function $f(T)$,

$$S = \int [T + f(T) + L_m] e d^4x \tag{4}$$

where $e = \det(e^a{}_\mu) = \sqrt{-g}$ and $\mathcal{L}_m$ represents the matter Lagrangian. Variation of this action with respect to the tetrad fields yields second-order field equations, which constitutes an important advantage of $f(T)$ gravity over curvature-based modifications such as $f(R)$ gravity.

We obtain the following equation of motion by functionally varying the action in equation (3) with regard to the tetrads:

$$S_\mu{}^{\rho\nu}\, \partial_\rho T\, f_{TT} + \left[e^{-1} e^a{}_\mu\, \partial_\rho (e\, e_a{}^\alpha S_\alpha{}^{\rho\nu}) + T^\alpha{}_{\mu\beta}\, S_\alpha{}^{\nu\beta}\right](1 + f_T) + \frac{1}{4}\,\delta^\nu_\mu\,(T + f) = T^\nu_\mu. \tag{5}$$

where $T^\nu{}_\mu$ is the energy–momentum tensor and

$$f_T(T) = \frac{df(T)}{dT}.$$

The field equation (5) is written in terms of tetrads and their partial derivatives and therefore appears formally different from Einstein's field equations. However, by choosing $f(T) = 0$, this is dynamically equivalent to the GR. The energy momentum tensor for magnetized dark energy is given by

$$T^\nu_\mu = \text{diag}\left[-p_x, -p_y, -p_z, \rho\right]. \tag{6}$$

Then, one may parametrize it as follows:

$$T^{\nu}_{\mu} = \text{diag}\left[-p_x + \rho_B,\ -p_y - \rho_B,\ -p_z - \rho_B,\ \rho + \rho_B\right] \tag{7}$$

where ρ is the energy density of the fluid,ρ_B is the energy density of the magnetic field, p_x, p_y, p_z are pressures. Zeldovich et al [40] underlined the importance of magnetic field for a variety of astrophysical phenomena.Magnetic field could have cosmological origin [41].

3. MODEL AND FIELD EQUATIONS

In this work, we consider the spatially homogeneous and anisotropic Bianchi type-I space-time as

$$ds^2 = dt^2 - A^2(t)\,dx^2 - B^2(t)\left(dy^2 + dz^2\right), \tag{8}$$

where the metric potentials A and B are functions of cosmic time t only. The corresponding torsion scalar T is given by

$$T = -2\left(2\frac{\dot{A}\dot{B}}{AB} + \frac{\dot{B}^2}{B^2}\right). \tag{9}$$

Using the equation of motion (4),the stress–energy tensor (6), and the Bianchi type-I space-time (8) , the field equations can be written as

$$(T + f) + 4(1 + f_T)\left(\frac{\ddot{B}}{B} + \frac{\dot{B}^2}{B^2} + \frac{\dot{A}}{A}\frac{\dot{B}}{B}\right) + 4\frac{\dot{B}}{B}\dot{T}f_{TT} = -(p - \rho_B) \tag{10}$$

$$(T + f) + 2(1 + f_T)\left(\frac{\ddot{A}}{A} + \frac{\ddot{B}}{B} + \frac{\dot{B}^2}{B^2} + 3\frac{\dot{A}\dot{B}}{AB}\right) + 2\left(\frac{\dot{A}}{A} + \frac{\dot{B}}{B}\right)\dot{T}f_{TT} = -(p + \rho_B) \tag{11}$$

$$(T + f) + 4(1 + f_T)\left(\frac{\dot{B}^2}{B^2} + 2\frac{\dot{A}\dot{B}}{AB}\right) = \rho + \rho_B \tag{12}$$

The system of equations from equations (10)-(12) may reduce to

$$\left(4\frac{\ddot{B}}{B} + 2\frac{\dot{B}^2}{B^2}\right) = -(p - \rho_B) \tag{13}$$

$$\left(2\frac{\ddot{A}}{A} + 2\frac{\ddot{B}}{B} + 2\frac{\dot{A}\dot{B}}{AB}\right) = -(p + \rho_B) \tag{14}$$

$$\left(2\frac{\dot{B}^2}{B^2} + 4\frac{\dot{A}\dot{B}}{AB}\right) = \rho + \rho_B \tag{15}$$

4. SOLUTION OF THE FIELD EQUATION

The field equations (13)-(15), we get three differential equations containing five unknowns — namely A, B, p, ρ and ρ_B.To determine the values of these unknowns, we use the energy–momentum conservation equation $T^{\nu}_{\mu;\nu} = 0$, which leads to two separate conservation equations corresponding to the anisotropic fluid and the magnetic field [42].

$$\dot{\rho} + (1 + \omega)\rho\left(\frac{\dot{A}}{A} + 2\frac{\dot{B}}{B}\right) = 0 \tag{16}$$

$$\rho_B = \frac{\beta}{B^4} \tag{17}$$

In what follows, we define certain kinematical quantities of the space-time, specifically the mean scale factor and the volume.

$$a^3 = V = AB^2 \tag{18}$$

The directional Hubble parameters along the x-, y-, and z-axes, respectively, for the LRS Bianchi type-I metric are defined as

$$H_x = \frac{\dot{A}}{A}, \quad H_y = \frac{\dot{B}}{B}, \quad H_z = \frac{\dot{B}}{B}. \tag{19}$$

To express volumetric expansion rate of Universe, the mean Hubble parameter is defined as

$$H = \frac{1}{3}(H_x + H_y + H_z) \tag{20}$$

From equations (18)-(20), we obtain

$$H = \frac{1}{3}\frac{\dot{V}}{V} = \frac{\dot{a}}{a} = \frac{1}{3}\left(\frac{\dot{A}}{A} + 2\frac{\dot{B}}{B}\right) \tag{21}$$

For the purpose of solving the field equations, we consider a physical condition according to which the expansion scalar is proportional to the shear scalar, i.e.,

$$A = B^n \tag{22}$$

where n is the proportionality constant. The motivation for considering Eq. (22) which is from the work of [9,43,44]. The line element (6) is fully characterized by the Hubble parameter H. Hence, we assume that the mean Hubble parameter H is related to the average scale factor a through the relation

$$H = k_1 a^{-s} \tag{23}$$

where $k_1 > 0$ and $s \geq 0$ are constants. This particular law of variation of the Hubble parameter leads to a constant value of the deceleration parameter. Such a relation was originally introduced by Bermann [48] in the study of FRW cosmological models. Subsequently, several researchers [45–48] have extensively employed this special law of the Hubble parameter to investigate flat FRW and Bianchi-type cosmological models.

By adopting this special law of variation of the Hubble parameter, we obtain exact solutions of the field equations corresponding to an anisotropic cosmological model exhibiting a negative constant deceleration parameter. The deceleration parameter q is define as,

$$q = -\frac{a\,\ddot{a}}{\dot{a}^2} \tag{24}$$

From eqs (21) and (23), we get

$$\dot{a} = k_1 a^{-s+1}, \tag{25}$$

$$\ddot{a} = -k_1^2(s-1)a^{-2s+1} \tag{26}$$

By using Eqs. (24)–(25), we obtain a constant deceleration parameter for the mean scale factor as

$$q = s - 1, \quad s \neq 0 \tag{27}$$

For $0 < s < 1$, the deceleration parameter satisfies $-1 < q < 0$, indicating accelerated expansion. The case $s = 1$ corresponds to a coasting universe ($q = 0$), while $s > 1$ leads to a decelerating phase ($q > 0$). The special case $s = 0$ yields $q = -1$, representing exponential expansion. Using eq.(25), we get the law of average scale factor as,

$$a = (Dt + c_1)^{\frac{1}{s}}, \quad s \neq 0. \tag{28}$$

where c_1 is the constant of integration. Using Eqs. (20), (21), (22), and (28), the exact expression for the scale function is given by

$$A(t) = l_2\,(Dt + c_1)^{\frac{n}{r}} \tag{29}$$

$$B(t) = l_1\,(Dt + c_1)^{\frac{1}{r}} \tag{30}$$

where

$l_1 = c_1^{-\frac{1}{n+2}}$, $l_2 = l_1^n$ and $r = \frac{n+2}{3}s$

Therefore, model (8) becomes

$$ds^2 = dt^2 - l_2^2\,(Dt + c_1)^{\frac{2n}{r}}\,dx^2 - l_1^2\,(Dt + c_1)^{\frac{2}{r}}\left(dy^2 + dz^2\right) \tag{31}$$

The space–time model (31) describes an LRS Bianchi Type-I anisotropic cosmological model filled with magnetized dark energy, where the magnetic field is aligned along one spatial direction, leading to anisotropic expansion.

For model (31),the expression for kinematical parameters, i.e. the Hubble parameter H, the scalar expansion θ, mean anisotropic parameter A_m and shear scalar σ are given by

$$H = \frac{(2n+1)D}{3r(Dt + c_1)} \tag{32}$$

$$\theta = 3H = \frac{(2n+1)D}{r(Dt + c_1)}, \tag{33}$$

$$A_m = \frac{1}{3}\sum_{i=1}^{3}\left(\frac{H_i - H}{H}\right)^2 = \frac{2(n-1)^2}{(2n+1)^2} \tag{34}$$

$$\sigma^2 = \frac{3}{2}A_m H^2 = \frac{(n-1)^2 D^2}{3r^2(Dt+c_1)^2} \tag{35}$$

The energy density for magnetic field is obtained by substituting eq.(30) in eq.(17)

$$\rho_B = \frac{\beta}{l_1^4 (Dt+c_1)^{\frac{4}{r}}} \tag{36}$$

Figure 1 depicts the variation of the magnetic field energy density ρ_B with cosmic time. It is observed that ρ_B diverges at the initial epoch, indicating a Big Bang type singularity, and decreases monotonically as the universe expands. At late times, the magnetic field contribution becomes negligible, favoring an isotropic dark-energy–dominated universe. Using Eqs. (15), (22), (29), (30) and (36), the energy density of the fluid is obtained as follows:

$$\rho = \frac{2(2n+1)D^2}{r^2 (Dt+c_1)^2} - \frac{\beta}{l_1^4 (Dt+c_1)^{\frac{4}{r}}} \tag{37}$$

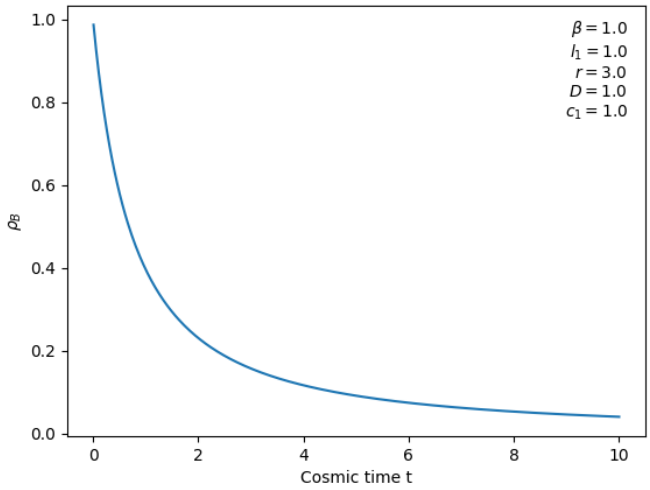

Figure 1. Energy density of the magnetic field versus cosmic time.

Figure 2 illustrates the variation of the fluid energy density ρ with cosmic time. It is observed that ρ diverges at the initial epoch, indicating a Big Bang type singularity. The energy density decreases sharply during the early evolution and attains a minimum before gradually approaching zero at late times. This behavior suggests that magnetic effects dominate the early universe, while the fluid evolves toward a dark-energy–dominated phase at late times. Using Eqs. (14), (22), (29), (30) and (36), the pressure of the fluid is obtained as follows:

$$p = -\left[\frac{\beta}{l_1^4 (Dt+c_1)^{\frac{4}{r}}} + \frac{2D^2(n+1)(n+1-r)}{r^2 (Dt+c_1)^2}\right] \tag{38}$$

Figure 3 illustrates the variation of pressure p with cosmic time t for the magnetized dark energy model. The pressure remains negative throughout the cosmic evolution, diverges at the initial epoch, and asymptotically approaches zero at late times, indicating a transition toward a dark-energy-dominated universe.

$$\omega = -\frac{1}{\rho}\left[\frac{\beta}{l_1^4 (Dt+c_1)^{\frac{4}{r}}} + \frac{2D^2(n+1)(n+1-r)}{r^2 (Dt+c_1)^2}\right] \tag{39}$$

The equation-of-state parameter ω evolves dynamically and attains negative values at late times. For suitable choices of the model parameters, ω lies in the range $-1 \leq \omega < -\frac{1}{3}$, which is consistent with the constraints from SN Ia and CMB observations. Hence, the present model is observationally viable and capable of describing the late-time accelerated expansion of the universe.

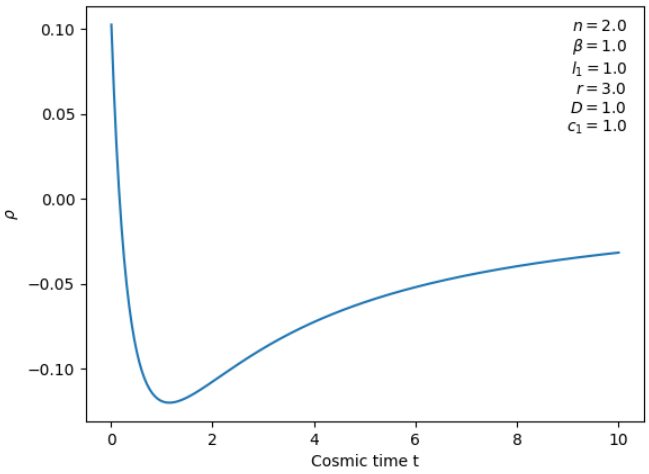

Figure 2. Energy density versus cosmic time.

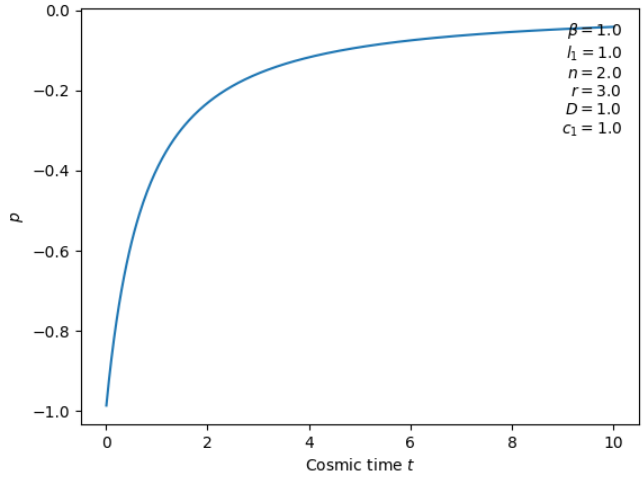

Figure 3. Pressure versus cosmic time.

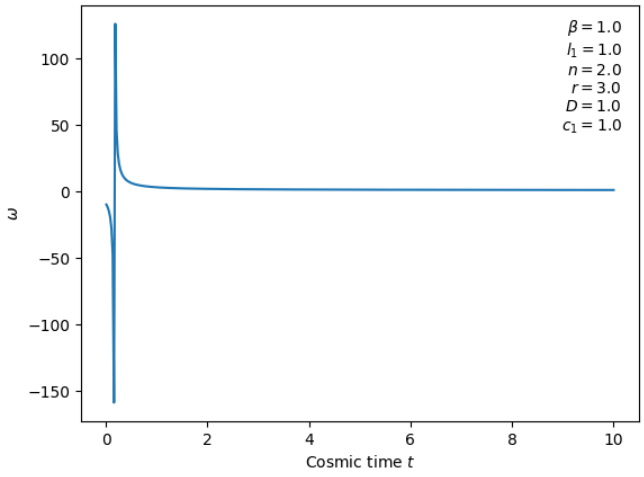

Figure 4. EoS parameter cosmic time.

5. ENERGY CONDITION

The Energy Conditions for the Present Model are given by

Null Energy Condition (NEC) The null energy condition is defined as

$$\rho + p \geq 0. \tag{40}$$

$$\rho + p = \frac{2D^2}{r^2\,(Dt + c_1)^2}\,[(2n+1) - (n+1)(n+1-r)] - \frac{2\beta}{l_1^4\,(Dt + c_1)^{\frac{4}{r}}} \tag{41}$$

For the present model, $\rho + p$ becomes negative at late times, indicating that the NEC is violated in the dark-energy–dominated phase of the universe.

Weak Energy Condition (WEC) The weak energy condition requires

$$\rho \geq 0, \qquad \rho + p \geq 0. \tag{42}$$

Although the energy density ρ remains positive for suitable choices of the model parameters, the violation of $\rho + p$ at late times implies a partial violation of the WEC.

Strong Energy Condition (SEC) The strong energy condition is given by

$$\rho + 3p \geq 0. \tag{43}$$

$$\rho + 3p = \frac{2D^2}{r^2\,(Dt + c_1)^2}\,[(2n+1) - 3(n+1)(n+1-r)] - \frac{4\beta}{l_1^4\,(Dt + c_1)^{\frac{4}{r}}} \tag{44}$$

For the present model, $\rho + 3p$ is found to be negative throughout the cosmic evolution, which signifies a clear violation of the SEC. This violation is a necessary condition for the accelerated expansion of the universe.

Dominant Energy Condition (DEC) The dominant energy condition is expressed as

$$\rho \geq |p|. \tag{45}$$

In the present scenario, the dominance of negative pressure at late times leads to the violation of the DEC, indicating the presence of exotic dark-energy behavior. Figure 5 displays the combined evolution of the energy conditions for the

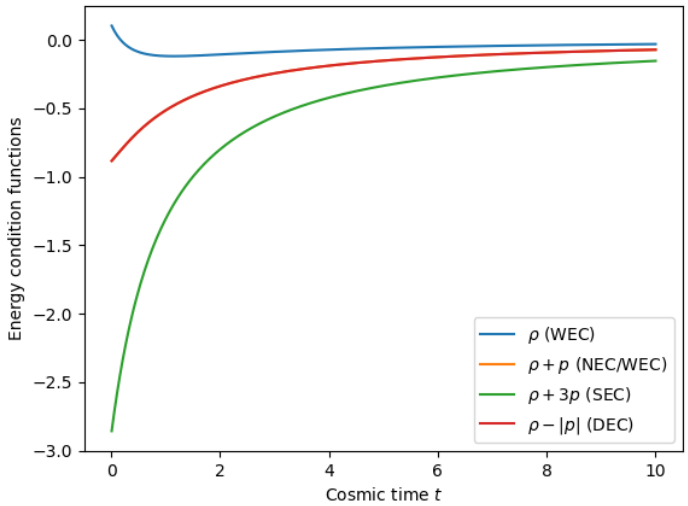

Figure 5. Evolution of the energy conditions with cosmic time t.

present magnetized dark energy model.It is observed that the energy density ρ remains positive, satisfying the weak energy condition at early times. However, the quantity $\rho + p$ becomes negative at late times, indicating the violation of the null and weak energy conditions.Moreover, $\rho + 3p$ remains negative throughout the cosmic evolution, implying a persistent violation of the strong energy condition, which is necessary for late-time accelerated expansion. The violation of $\rho - |p|$ at late times shows that the dominant energy condition is also not satisfied, confirming the presence of exotic dark-energy behavior in the model.

6. CONCLUSIONS

In this work, we have investigated a magnetized anisotropic dark energy cosmological model in the framework of $f(T)$ gravity for an LRS Bianchi type-I space–time. By choosing $f(T) = 0$, the theory reduces to teleparallel gravity, which is dynamically equivalent to general relativity, allowing a consistent comparison with standard cosmological scenarios.

A special law of the Hubble parameter with $S \neq 0$ has been employed to obtain exact solutions of the field equations. The resulting model describes an anisotropic universe with directional scale factors evolving as power-law functions of cosmic time. The presence of a uniform magnetic field aligned along one spatial direction introduces anisotropy at early times, while its contribution decays rapidly as the universe expands.

The physical behavior of the model has been examined through the evolution of the energy density, pressure, equation-of-state parameter, and energy conditions. The pressure remains negative throughout the cosmic evolution, while the energy density is positive for suitable choices of model parameters. The equation-of-state parameter ω evolves dynamically and attains negative values at late times, lying in the range $-1 \leq \omega < -\frac{1}{3}$, which is consistent with the observational constraints from Type Ia supernovae and cosmic microwave background observations.

Furthermore, the null and weak energy conditions are found to be violated at late times, whereas the strong energy condition is violated throughout the cosmic evolution. The violation of the strong energy condition confirms the presence of accelerated expansion in the universe. The dominant energy condition is also violated in the late-time regime, indicating the dominance of dark energy with strong negative pressure.

Overall, the present magnetized anisotropic dark energy model in $f(T)$ gravity with a special law of the Hubble parameter provides a viable description of the late-time accelerated expansion of the universe. The model exhibits a transition from a magnetically dominated anisotropic early universe to an effectively isotropic dark-energy-dominated phase at late times, in agreement with current cosmological observations.

ORCID

K.N. Pawar, https://orcid.org/0000-0002-4388-039X; **A.S. Khan**, https://orcid.org/0000-0002-7092-2735; **I.I. Khan**, https://orcid.org/0009-0002-3698-4200

REFERENCES

[1] M. Sharif, and S. Rani,"F (T) models within bianchi type-i universe," Modern Physics Letters A, **26**(22), 1657–1671 (2011). https://doi.org/10.1142/S0217732311036127.

[2] K. Bamba, R. Myrzakulov, S. Nojiri, S.D. Odintsov, "Reconstruction of f (T) gravity: Rip cosmology, finite-time future singularities, format and thermodynamics," Physical Review D—Particles, Fields, Gravitation, and Cosmology, **85**(10), 104036 (2012). https://doi.org/10.1103/PhysRevD.85.104036

[3] V. Danieli, and A. De Felice, Antonio, "f (T) gravity: Background dependence and propagating degrees of freedom," Physical Review D, **111**(10), 104023 (2025). https://doi.org/10.1103/PhysRevD.111.104023

[4] V.R. Chirde, and S.H. Shekh, "Accelerating universe, dark energy and exponential f (T) gravity," The African Review of Physics, 10, (2015). URL

[5] V. Fayaz, H. Hossienkhani, A. Farmany, M. Amirabadi, and N. Azimi, "Cosmology of f (T) gravity in a holographic dark energy and nonisotropic background," Astrophysics and Space Science, **351**(1), 299–306 (2014). https://doi.org/10.1007/s10509-014-1817-y

[6] G.G.L. Nashed, "Anisotropic models with two fluids in linear and quadratic forms of f (T) gravitational theories," Astrophysics and Space Science, **357**(2), 111 (2015). https://doi.org/10.1007/s10509-015-2339-y

[7] S.D. Katore, and M.M. Sancheti, "Bianchi Type VIo Magnetized Anisotropic Dark Energy Models with Constant Deceleration Parameter," International Journal of Theoretical Physics, **50**(8), 2477–2485 (2011). https://doi.org/10.1007/s10773-011-0736-8

[8] M.F. Shamir, and A. Ali, "Bianchi type-v cosmology with magnetized anisotropic dark energy," Canadian Journal of Physics, **95**(3), 274–282 (2017). https://doi.org/10.1139/cjp-2016-0777

[9] M. Sharif, and M. Zubair, "Dynamics of bianchi i universe with magnetized anisotropic dark energy," Astrophysics and Space Science, **330**(2), 399–405 (2010). https://doi.org/10.1007/s10509-010-0414-y

[10] S.D. Katore, K.S. Adhav, and M.M. Sancheti, "Dynamics of kantowskisachs universe with magnetized anisotropic dark energy," Astrophysics and Space Science, **337**(1), 393–400 (2012). https://doi.org/10.1007/s10509-011-0826-3

[11] B. Mishra, P.P. Ray, S.K. Tripathy, and K. Bamba, "Axially magnetized dark energy cosmological model," Modern Physics Letters A, **34**(27), 1950217, (2019). https://doi.org/10.1142/s0217732319502171

[12] S. Kumar, and C.P. Singh, "Anisotropic dark energy models with constant deceleration parameter," General Relativity and Gravitation, **43**(5), 1427–1442 (2011). https://doi.org/10.1007/s10714-010-1125-y

[13] L.A. Devi, S.S. Singh, and Md.Kh. Alam, "Phase transition of bianchi-type i cosmological model in f (t) gravity," New Astronomy, **107**, 102156 (2024). https://doi.org/10.1016/j.newast.2023.102156

[14] M.E. Rodrigues, I.G. Salako, M.J.S. Houndjo, and J. Tossa, "Locally rotationally symmetric bianchi type-i cosmological model in f (t) gravity: from early to dark energy dominated universe," International Journal of Modern Physics D, **23**(01), 1450004 (2014). https://doi.org/10.1142/S0218271814500047

[15] S. Tarai, F.Md. Esmaeili, B. Mishra, and S.K. Tripathy, "Magnetized cosmological model with variable deceleration parameter," International Journal of Modern Physics D, **29**(13), 2050091 (2020). https://doi.org/10.1142/s0218271820500911

[16] P.P. Ray, B. Mishra, and S.K. Tripathy, "Dynamics of anisotropic dark energy universe embedded in one-directional magnetized fluid," International Journal of Modern Physics D, **28**(07), 1950093 (2019). https://doi.org/10.1142/s0218271819500937

[17] S.-H. Chen, J.B. Dent, S. Dutta, and E.N. Saridakis, "Cosmological perturbations in f (t) gravity. Physical Review," D—Particles, Fields, Gravitation, and Cosmology, **83**(2), 023508 (2011). https://doi.org/10.1103/PhysRevD.83.023508

[18] J.B. Dent, S. Dutta, and E.N. Saridakis, "f (t) gravity mimicking dynamical dark energy. background and perturbation analysis," Journal of Cosmology and Astroparticle Physics, **2011**(01), 009 (2011). https://doi.org/10.1088/1475-7516/2011/01/009

[19] P. Wu, and H. Yu, "f (t) models with phantom divide line crossing," The European Physical Journal C, **71**(2), 1552 (2011). https://doi.org/10.1140/epjc/s10052-011-1552-2

[20] K. Bamba, C.-Q. Geng, C.-C. Lee, and L.-W. Luo, "Equation of state for dark energy in f (t) gravity," Journal of Cosmology and Astroparticle Physics, **2011**(01), 021 (2011). https://doi.org/10.1088/1475-7516/2011/01/021

[21] M. Zubair, L.R. Durrani, and S. Waheed, "Reconciling tsallis holographic dark energy models in modified f (t, b) gravitational framework," The European Physical Journal Plus, **136**(9), 943 (2021). https://doi.org/10.1140/epjp/s13360-021-01905-y

[22] H. Balhara, J.K. Singh, Shaily, and E.N. Saridakis, "Observational constraints and cosmographic analysis of f (t, tg) gravity and cosmology," Symmetry, **16**(10), 1299 (2024). https://doi.org/10.3390/sym16101299

[23] T. Harko, F.S.N. Lobo, G. Otalora, and E.N. Saridakis, "f(t,T) gravity and cosmology," Journal of Cosmology and Astroparticle Physics, **2014**(12), 021 (2014). https://doi.org/10.1088/1475-7516/2014/12/021

[24] S.R. Bhoyar, V.R. Chirde, and S.H. Shekh, "Stability of accelerating universe with linear equation of state in f (t) gravity using hybrid expansion law," Astrophysics, **60**(2), 259–272 (2017). https://doi.org/10.1007/s10511-017-9480-y

[25] Surajit Chattopadhyay, Abdul Jawad, and Shamaila Rani. Holographic polytropic f (t) gravity models. Advances in High Energy Physics, **2015**(1):798902, 2015. URL

[26] L.K. Duchaniya, K. Gandhi, and B. Mishra, "Attractor behavior of f (t) modified gravity and the cosmic acceleration," Physics of the Dark Universe, **44**, 101461 (2024). https://doi.org/10.1016/j.dark.2024.101461

[27] M.S. Borkar, and S.S. Charjan, "Bianchi type i magnetized cosmological model with λ-term in bimetric theory of gravitation," Applications and Applied Mathematics: An International Journal (AAM), **8**(1), 7 (2013).

[28] N.K. Sharma, and J.K. Singh, "Bianchi type-ii string cosmological model with magnetic field in f (r, t) gravity," International Journal of Theoretical Physics, **53**(9), 2912–2922 (2014). https://doi.org/10.1007/s10773-014-2089-6

[29] X. Liu, P. Channuie, and D. Samart, "Cosmological dynamics of magnetic bianchi i in viable f (r) models of gravity," Physics of the dark universe, **17**, 52–62 (2017). https://doi.org/10.1016/j.dark.2017.08.001

[30] S.H. Shekh, and V.R. Chirde, "Accelerating bianchi type dark energy cosmological model with cosmic string in f (t) gravity," Astrophysics and Space Science, **365**(3), 60 (2020). https://doi.org/10.1007/s10509-020-03772-y

[31] D.C. Maurya, and J. Singh, "Modified f (Q)-gravity string cosmological models with observational constraints," Astronomy and Computing, **46**, 100789 (2024). https://doi.org/10.1016/j.ascom.2024.100789

[32] Ö. Akarsu, B. Bulduk, A. De Felice, N. Katrc, and N.M. Uzun, "Unexplored regions in teleparallel f (t) gravity: Signchanging dark energy density," Physical Review D, **112**(8), 083532 (2025). https://doi.org/10.1103/1xd4-k91h

[33] B.G. Rao, D.J. Mohanty, Y. Aditya, and U.Y.D. Prasanthi, "Cosmological evolution of bianchi type-VIo kaniadakis holographic dark energy model," East European Journal of Physics, (1), 43–54 (2024). https://doi.org/10.26565/2312-4334-2024-1-03

[34] Y.S. Solanke, A.P. Kale, D.D. Pawar, and V.J. Dagwal, "Anisotropic dark energy universe in f (q, t) gravity with observational constraints," Canadian Journal of Physics, **102**(2), 85–95 (2023). https://doi.org/10.1139/cjp-2023-0127

[35] S.A. Narawade, M. Koussour, and B. Mishra, "Observational constraints on hybrid scale factor in f (q, t) f(q,t) gravity with anisotropic spacetime," Annalen der Physik, **535**(8), 2300161 (2023). https://doi.org/10.1002/andp.202300161

[36] M. Sharif, and S. Jabbar, "Phase space analysis and anisotropic universe model in f (t) gravity," Communications in Theoretical Physics, 63(2), 168 (2015). https://doi.org/10.1088/0253-6102/63/2/09

[37] S.D. Katore, M.M. Sancheti, and S.P. Hatkar, "Magnetized anisotropic dark energy cosmological models in scale covariant theory of gravitation," International Journal of Modern Physics D, 23(07), 1450065 (2014). https://doi.org/10.1142/s0218271814500655

[38] J.D. Dent, S. Dutta, and E.N. Saridakis, "f (t) gravity mimicking dynamical dark energy. background and perturbation analysis," **2011**, 1475-7516 (2011). https://doi.org/10.1088/1475-7516/2011/01/009

[39] M. Koussour, A. Altaibayeva, S. Bekov, F. Holmurodov, S. Muminov, and J. Rayimbaev, "Exploring cosmological evolution and constraints in f (t) teleparallel gravity," Physics of the Dark Universe, **46**, 101664 (2024). https://doi.org/10.1016/j.dark.2024.101664

[40] Ia.B. Zeldovich, A.A. Ruzmaikin, and D.D. Sokolov, "Magnetic fields in astrophysics," (The Fluid Mechanics of Astrophysics and Geophysics, New York, 1983), Vol.3.

[41] V.U.M. Rao, and D. Neelima, "Field of a charged particle in bimetric theory of gravitation,' The African Review of Physics, 8, (2013).

[42] E.J. King, and P. Coles, "Dynamics of a magnetized bianchi i universe with vacuum energy," Classical and Quantum Gravity, **24**(8), 2061 (2007). https://doi.org/10.1088/0264-9381/24/8/008

[43] A.K. Yadav, and L. Yadav, "Bianchi type iii anisotropic dark energy models with constant deceleration parameter," International Journal of Theoretical Physics, **50**(1), 218–227 (2011). https://doi.org/10.1007/s10773-010-0510-3

[44] A.Y. Shaikh, and S.D. Katore, "Magnetized anisotropic dark energy models with constant deceleration parameter," Pramana, **87**(6), 88 (2016). https://doi.org/10.1007/s12043-016-1272-0

[45] B. Saha, and A.K. Yadav, "Dark energy model with variable q and ω in lrs bianchi-ii space-time," Astrophysics and Space Science, **341**(2), 651–656 (2012). https://doi.org/10.1007/s10509-012-1070-1

[46] C.P. Singh, and S. Kumar, "Bianchi type-ii cosmological models with constant deceleration parameter," International Journal of Modern Physics D, **15**(03), 419–438 (2006). https://doi.org/10.1142/s0218271806007754

[47] D.R.K. Reddy, M.V.S. Rao, and G.K. Rao, "A cosmological model with negative constant deceleration parameter in a scalar-tensor theory," Astrophysics and Space Science, **306**(3), 171–174 (2006). https://doi.org/10.1007/s10509-006-9210-0

[48] K.S. Adhav, A.S. Nimkar, M.R. Ugale, and M.V. Dawande, "Bianchi type-iii cosmological model with negative constant deceleration parameter in brans dicke theory of gravitation," International Journal of Theoretical Physics, **47**(3), 634–639 (2008). https://doi.org/10.1007/s10773-007-9487-y

КОСМОЛОГІЧНА МОДЕЛЬ НАМАГНІЧЕНОЇ АНІЗОТРОПНОЇ ТЕМНОЇ ЕНЕРГІЇ В $f(T)$ ГРАВІТАЦІЇ ЗІ СПЕЦІАЛЬНИМ ЗАКОНОМ ПАРАМЕТРА ХАББЛА

К.Н. Павар, **А.С. Хан**, **І.І. Хан**

Кафедра математики, Науковий коледж Шрі Шиваджі, Нагпур, Махараштра, Індія

У цій статті ми досліджуємо космологічну модель намагніченої анізотропної темної енергії в рамках $f(T)$ гравітації для локально обертально-симетричного простору-часу типу Біанкі I. Вибір $f(T) = 0$ зводить теорію до телепаралельної гравітації, динамічно еквівалентної загальній теорії відносності, що дозволяє пряме порівняння зі стандартною космологією. Точні розв'язки рівнянь поля отримуються, припускаючи спеціальний закон параметра Хаббла з ненульовою константою S, що призводить до степеневої поведінки напрямлених масштабних коефіцієнтів. Однорідне магнітне поле, орієнтоване вздовж одного просторового напрямку, створює анізотропію на ранніх етапах часу, густина енергії якої зменшується з розширенням космосу. Аналізуються густина енергії, тиск, параметр рівняння стану та енергетичні умови. Тиск залишається негативним, тоді як параметр рівняння стану динамічно розвивається та наближається до діапазону $-1 \leq \omega < -\frac{1}{3}$ на пізніх етапах часу, що узгоджується з обмеженнями SN Ia та реліктового випромінювання. Умови нульової та слабкої енергії порушуються на пізніх етапах часу, тоді як умова сильної енергії порушується протягом усього часу, що передбачає прискорення.

Ключові слова: *намагнічена темна енергія; $f(T)$ гравітація; LRS модель Біанкі типу I; анізотропний Всесвіт; космічний час*

East European Journal of Physics. 2. 62–78 (2026)
DOI: 10.26565/2312-4334-2026-2-06 ISSN 2312-4334

A PEN-PICTURE OF THE MODIFIED (2+1)-DIMENSIONAL KdV-CALOGERO BOGOYAVLENSKII-SCHIFF EQUATION IN SHALLOW WATER WAVES: LIE SYMMETRY ANALYSIS AND CONSERVATION LAWS

Sivenathi O. Mbusi[1], **Abdullahi R. Adem**[2], **Ben Muatjetjeja**[1,3], **Mohammed E. M. Alngar**[4], **Husham M. Ahmed**[5], **Anjan Biswas**[6,7,8,9]

[1]*School of Mathematical and Statistical Sciences, North-West University, Private Bag X1290, Potchefstroom, 2520, South Africa*
[2]*Department of Mathematical Sciences, University of South Africa, P.O. Box 392, Unisa, 0003, South Africa*
[3]*Department of Mathematics, Faculty of Science, University of Botswana, Private Bag 22, Gaborone, Botswana*
[4]*Mathematics Education Program, Faculty of Education and Arts, Sohar University, 311, Sohar, Oman*
[5]*College of Engineering University of Technology, Bahrain, Kingdom of Bahrain*
[6]*Department of Mathematics and Physics, Grambling State University, Grambling, LA 71245-2715, USA*
[7]*Department of Mathematics, Faculty of Science, Karadeniz Technical University, Trabzon-61080, Turkiye*
[8]*Department of Physics and Electronics, Khazar University, Baku, AZ-1096, Azerbaijan*
[9]*Department of Mathematics and Applied Mathematics, Sefako Makgatho Health Sciences University, Medunsa-0204, Pretoria, South Africa*
[*]*Corresponding Author e-mail: biswas.anjan@gmail.com*

Received January 27, 2026; revised April 25, 2026; accepted April 28, 2026

This work investigates the KdV-Calogero Bogoyavlenkskii-Schiff equation in modified (2+1) dimensions. The Lie symmetries are created using Lie group analysis, and the similarity solutions are then found using the symmetries. Using the multiple exp-function approach, numerous wave solutions are obtained. Furthermore, we use the multiplier approach to express the conserved currents, which is essential for comprehending the nature of non-linear equations, particularly in engineering and physics.

Keywords: *KdV-Calogero Bogoyavlenkskii-Schiff Equation; Conserved currents; Lie group analysis; Multiple exp-function method*

PACS: 47.35Fg; 47.10.ab

1. INTRODUCTION

In domains such as oceanography, superfluids, hydrodynamics, plasma physics, optical systems, and other relevant nonlinear science [1–8] topics, nonlinear evolution equations (NLEEs) exhibit a variety of fascinating nonlinear dynamic phenomena. The physical insights offered by the solutions to NLEEs can help us better understand the underlying phenomena and possibly pave the way for novel applications. Therefore, it is essential to look for precise answers to these equations. But finding precise answers for NLEEs is frequently difficult, and their answers can only be simplified in rare circumstances. Numerous techniques have been used to address NLEEs [9–25].

The illustrious Korteweg-de Vries (KdV) equation

$$\omega_\tau + 6\omega\omega_\chi + \omega_{\chi\chi\chi} = 0 \tag{1.1}$$

is an example of a nonlinear evolution equation (NLEE) [26–44]. It describes the dynamics of solitary waves. It was first developed to characterize long-wavelength, small-amplitude waves in shallow water. Its multiple-soliton solutions, unlimited number of conservation laws, and numerous other physical characteristics make it an important equation in the study of integrable systems.

We study one such NLEE namely a modified (2+1)-dimensional KdV-Calogero Bogoyavlenkskii-Schiff (KdV-CBS) equation [45, 46]:

$$4\omega_\tau - h_1\left(4\omega\omega_\mu + 2\omega_\chi\partial_\chi^{-1}\omega_\mu + \omega_{\chi\chi\mu}\right) - h_2\left(6\omega\omega_\chi + \omega_{\chi\chi\chi}\right) = 0, \tag{1.2}$$

where h_1 and h_2 are arbitrary constant. It should be noted that when $h_1 \neq 0$, $h_2 = 0$, equation (1.2) becomes to Calogero Bogoyavlenkskii-Schiff equation [47].

$$4\omega_\tau - h_1\left(4\omega\omega_\mu + 2\omega_\chi\partial_\chi^{-1}\omega_\mu + \omega_{\chi\chi\mu}\right) = 0. \tag{1.3}$$

Cite as: S.O. Mbusi, A.R. Adem, B. Muatjetjeja, M.E.M. Alngar, H.M. Ahmed, A. Biswas, East Eur. J. Phys. 2, 62 (2026), https://doi.org/10.26565/2312-4334-2026-2-06

Furthermore, when $h_1 = 0$ and $h_2 \neq 0$, equation (1.2) is reduced to the well known KdV equation

$$4\omega_\tau - h_2\left(6\omega\omega_\chi + \omega_{\chi\chi\chi}\right) = 0. \tag{1.4}$$

The transformation $\omega = \nu_\chi$, casts(1.2) into

$$4\nu_{\tau\chi} - h_1\left(4\nu_\chi\nu_{\chi\mu} + 2\nu_\mu\nu_{\chi\chi} + \nu_{\chi\chi\chi\mu}\right) - h_2\left(6\nu_\chi\nu_{\chi\chi} + \nu_{\chi\chi\chi\chi}\right) = 0. \tag{1.5}$$

There are five sections in this study. The calculation of exact solutions and similarity reductions using Lie point symmetry analysis is shown in Section 2. In Section 3, we use the multiple exp-function method, an extension of Hirota's perturbation technique, to investigate a number of physically relevant waves with novel general wave frequencies and phase shifts. The multiplier approach is used to discuss the conservation laws in Section 4. Lastly, the closing remarks are given in Section 5.

2. LIE SYMMETRIES AND REDUCTION (1.5)

The Norwegian mathematician Sophus Lie (1842–1899) created the Lie symmetry method, a potent mathematical instrument for evaluating and resolving differential equations. This approach focuses on detecting differential equation symmetries, which can be utilized to simplify the solution-seeking process by lowering the number of independent variables. Closed-form solutions are frequently the outcome of this. Numerous disciplines, including physics, fluid dynamics, electromagnetic, and engineering, heavily rely on the Lie symmetry technique [48–51].

We now compute the symmetry group of the transformed (2+1)-dimensional KdV-Calogero Bogoyavlenkskii-Schiff equation (1.5). The vector field of the form

$$\mathbf{\Gamma} = \xi^1(\tau,\chi,\mu,\nu)\frac{\partial}{\partial\tau} + \xi^2(\tau,\chi,\mu,\nu)\frac{\partial}{\partial\chi} + \xi^3(\tau,\chi,\mu,\nu)\frac{\partial}{\partial\mu} + \eta(\tau,\chi,\mu,\nu)\frac{\partial}{\partial\nu}.$$

would generate all the desired Lie point symmetries of (1.5). It should be noted that this would be initiated by applying the fourth prolongation $\mathrm{pr}^{(4)}\mathbf{\Gamma}$ to (1.5). This algorithmic procedure yields an overdetermined system of linear partial differential equations of the following form:

$$\begin{aligned}
&\xi^3_\chi = 0,\ \xi^1_\chi = 0,\ \xi^1_\mu = 0,\ \xi^2_\nu = 0,\ \xi^3_\nu = 0,\ \xi^1_\nu = 0,\\
&\eta_{\tau\chi} = 0,\ \eta_{\chi\chi} = 0,\ \xi^2_{\chi\chi} = 0,\ \eta_{\chi\nu} = 0,\ \eta_{\nu\nu} = 0,\\
&\eta_\nu + \xi^2_\chi = 0,\ h_1\eta_\chi - \xi^3_\tau = 0,\ 3\xi^2_{\chi\mu} - \eta_{\nu\mu} = 0,\\
&\xi^2_{\chi\mu} - \eta_{\nu\mu} = 0, h_1\eta_\mu + 3h_2\eta_\chi + 2\xi^2_\tau = 0,\\
&h_1\eta_{\chi\mu} - \eta_{\tau\nu} - \xi^2_{\tau\chi} = 0,\ h_1\xi^2_\mu - h_2\xi^3_\mu + h_2\xi^2_\chi = 0,\\
&\xi^1_\tau - \xi^3_\mu + \eta_\nu - \xi^2_\chi = 0,\ h_1\xi^2_\mu - h_2\xi^3_\mu + h_2\eta_\nu + 2h_2\xi^2_\chi = 0.
\end{aligned}$$

Hence the above system yields the following Lie point symmetries:

$$\mathbf{\Gamma_1} = -2h_1\tau\frac{\partial}{\partial\tau} + (h_2\mu - h_1\chi)\frac{\partial}{\partial\chi} + h_1\nu\frac{\partial}{\partial\nu},\ \text{dilation \& space \& time} - \text{dependent shift}$$

$$\mathbf{\Gamma_2} = h_1\tau\frac{\partial}{\partial\tau} + h_2\mu\frac{\partial}{\partial\chi} + h_1\mu\frac{\partial}{\partial\mu},\ \text{space \& time} - \text{dependent shift}$$

$$\mathbf{\Gamma_3} = -2h_1^2\tau^2\frac{\partial}{\partial\tau} - \left(h_1^2\tau\chi + h_1h_2\tau\mu\right)\frac{\partial}{\partial\chi} - 2h_1^2\tau\mu\frac{\partial}{\partial\mu} + \left(h_1^2\nu\tau + 2h_1\chi\mu - 2h_2\mu^2\right)\frac{\partial}{\partial\nu},$$
$$\text{dilation \& space \& time} - \text{dependent shift}$$

$$\mathbf{\Gamma_4} = \frac{h_2}{(h_1+h_2)}\frac{\partial}{\partial\chi} + \frac{h_1}{(h_1+h_2)}\frac{\partial}{\partial\mu},\ \text{space translation}$$

$$\mathbf{\Gamma_5} = h_1h_2\tau\frac{\partial}{\partial\chi} + h_1^2\tau\frac{\partial}{\partial\mu} + (h_2\mu - h_1\chi)\frac{\partial}{\partial\nu},\ \text{rotational \& space} - \text{dependent shift}$$

$$\mathbf{\Gamma_6} = \frac{\partial}{\partial\tau},\ \text{time translation}$$

$$\mathbf{\Gamma_{F(\tau)}} = h_1F(\tau)\frac{\partial}{\partial\chi} + 2F'(\tau)\mu\frac{\partial}{\partial\nu},\ \text{space \& time} - \text{dependent shift}$$

$$\mathbf{\Gamma_{G(\tau)}} = G(\tau)\frac{\partial}{\partial\nu}.\ \text{space \& time} - \text{dependent shift}$$

2.1. Symmetry reduction and invariant solutions of (1.5)

Our goal is to use the symmetries we discovered above to achieve symmetry reduction of (1.5). The related Lagrange equations must be solved in order to achieve symmetry reduction.

$$\frac{d\tau}{\xi^1(\tau,\chi,\mu,\nu)} = \frac{d\chi}{\xi^2(\tau,\chi,\mu,\nu)} = \frac{d\mu}{\xi^3(\tau,\chi,\mu,\nu)} = \frac{d\nu}{\eta(\tau,\chi,\mu,\nu)}.$$

We examine the three cases listed below.

Case 1. First, we look at infinitesimal generator $\mathbf{\Gamma_1}$

$$\frac{d\tau}{-2h_1\tau} = \frac{d\chi}{(h_2\mu - h_1\chi)} = \frac{d\mu}{0} = \frac{d\nu}{h_1\nu}$$

which gives rise to the group invariant

$$\Psi = \mu,\ \gamma = \frac{\tau}{(h_1\chi - h_2\mu)^2},\ \Theta = -\nu\,(h_1\chi - h_2\mu)\,.$$

Equation (1.5) reduces to the nonlinear partial differential equation when Ψ and γ are taken into consideration as the new independent variables and Θ as the new dependent variable.

$$\begin{aligned}&4\gamma^3h_1^3\Theta_{\gamma\gamma\gamma\Psi} + 8\gamma^2h_1^2\Theta_\gamma\Theta_{\gamma\Psi} + 24\gamma^2h_1^3\Theta_{\gamma\gamma\Psi} + 4\gamma^2h_1^2\Theta_\Psi\Theta_{\gamma\gamma} + 4\gamma h_1^2\Theta\Theta_{\gamma\Psi} + 27\gamma h_1^3\Theta_{\gamma\Psi} + 14\gamma h_1^2\Theta_\gamma\Theta_\Psi\\ &+4h_1^2\Theta\Theta_\Psi + 3h_1^3\Theta_\Psi - 4\gamma\Theta_{\gamma\gamma} - 6\Theta_\gamma = 0.\end{aligned} \tag{2.6}$$

We now further reduce (2.6) by using its symmetries, it can be seen that the corresponding vector of (2.6) is as follows:

$$\begin{aligned}S_1 &= \Psi\frac{\partial}{\partial\Psi} + \gamma\frac{\partial}{\partial\gamma},\\ S_2 &= 2h_1^2\gamma^{\frac{3}{2}}\frac{\partial}{\partial r} + \left(-\sqrt{\gamma}\Theta h_1^2 - \frac{\Psi}{\sqrt{\gamma}}\right)\frac{\partial}{\partial\Theta},\\ S_3 &= \frac{\partial}{\partial\Psi},\\ S_4 &= \frac{1}{\sqrt{\gamma}}\frac{\partial}{\partial\Theta}.\end{aligned}$$

Taking symmetry $S_3 + S_4$, yields the following invariants:

$$\kappa = \gamma,\ \Phi = \frac{\Theta\sqrt{\gamma} - \Psi}{\sqrt{\gamma}},$$

and making use of them, we obtain a second order ordinary differential equation

$$2\kappa^2h_1^2\Phi''(\kappa) + 5\kappa h_1^2\Phi'(\kappa) - 2\Phi''(\kappa) + h_1^2\Phi(\kappa) - 3\sqrt{\kappa}\Phi'(\kappa) = 0,$$

which gives the general solution of the form

$$\Phi(\kappa) = \frac{\sqrt{\kappa}C_1 + C_2}{\sqrt{\kappa}\left(h_1^2\sqrt{\kappa} - 1\right)}, \tag{2.7}$$

where the arbitrary integration constants C_1 and C_2 are used. The invariant solution of (1.5), when rewritten in our original variables, looks like this:

$$\begin{aligned}\nu\,(\tau,\chi,\mu) \quad = \quad & -\frac{1}{h_1\,\chi - h_2\,\mu}\left(\sqrt{\frac{\tau}{(h_1\,\chi - h_2\,\mu)^2}}{h_1}^2\mu + C_1\sqrt{\frac{t}{(h_1\,\chi - h_2\,\mu)^2}} + C_2 - \mu\right)\\ & \left(\frac{1}{\sqrt{\frac{\tau}{(h_1\,\chi - h_2\,\mu)^2}}}\left({h_1}^2\sqrt{\frac{\tau}{(h_1\,\chi - h_2\,\mu)^2}} - 1\right)\right)^{-1}.\end{aligned} \tag{2.8}$$

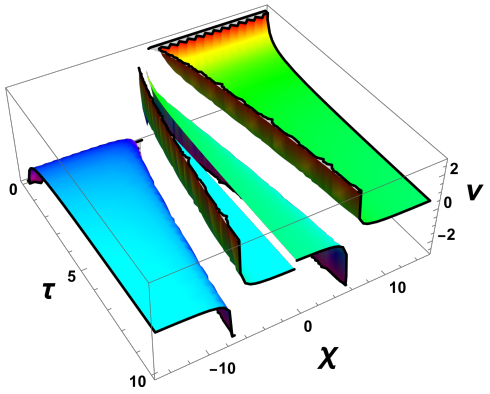

Figure 1. A 3D wave solution (2.8)

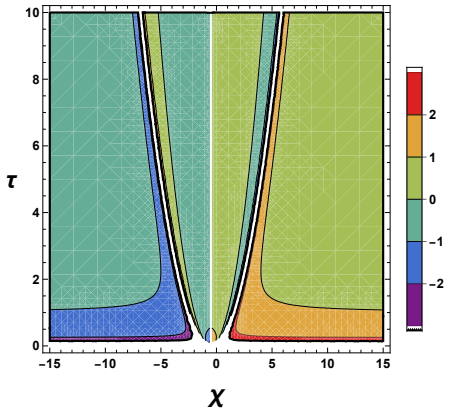

Figure 2. A density plot of solution (2.8)

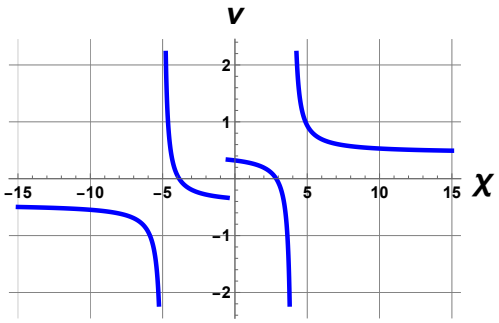

Figure 3. A 2D plot of (2.8)

Case 2. We consider infinitesimal generator $\mathbf{\Gamma_2}$

$$\frac{d\tau}{h_1\tau} = \frac{d\chi}{h_2\mu} = \frac{d\mu}{h_1\mu} = \frac{d\nu}{0}$$

we obtained the group invariant

$$\Psi = \frac{h_1\chi - h_2\mu}{h_2}, \quad \gamma = \frac{\tau}{h_2\tau}, \quad \Theta = \nu.$$

Equation (1.5) changes to Θ as the new dependent variable and Ψ and γ as new independent variables.

$$4\gamma h_1^2 h_2 \Theta_\Psi \Theta_{\Psi\gamma} + 2\gamma h_2 h_1^2 \Theta_\gamma \Theta_{\Psi\Psi} - \gamma h_1^3 \Theta_{\gamma\Psi\Psi\Psi} - 4h_2 \Theta_{\gamma\Psi} = 0. \tag{2.9}$$

After employing its symmetries to reduce (2.9), we can observe that the equivalent vector of (2.9) is as follows:

$$\begin{aligned}
\mathbf{S_1} &= \frac{\partial}{\partial \Theta}, \\
\mathbf{S_2} &= h_1^2 \gamma^2 \frac{\partial}{\partial \gamma} - \Psi \frac{\partial}{\partial \Psi}, \\
\mathbf{S_3} &= \frac{\partial}{\partial \Psi}, \\
\mathbf{S_4} &= \Psi \frac{\partial}{\partial f} + 2\gamma \frac{\partial}{\partial \gamma} - \Theta \frac{\partial}{\partial \Theta}.
\end{aligned}$$

Taking symmetry $\mathbf{S_2}$, yields the following invariants:

$$\kappa = \Psi, \ \Phi = \frac{\Theta \gamma h_1^2 - \Psi}{h_1^2 \gamma},$$

and making use of them, we obtain a second order ordinary differential equation

$$\kappa \Phi''(\kappa) + 2\Phi'(\kappa) = 0,$$

which yields the general solution of the form

$$\Phi(\kappa) = C_1 + \frac{1}{\kappa} C_2, \tag{2.10}$$

where C_1 and C_2 are arbitrary constant of integration. Reverting back to our original variables, the invariant solution of (1.5) takes the form

$$v(\tau, \chi, \mu) = \frac{C_1 {h_1}^3 \tau \chi - C_1 {h_1}^2 h_2 \tau \mu - C_2 {h_1}^2 h_2 \tau - {h_1}^2 \chi^2 \mu + 2 h_1 h_2 \chi \mu^2 - {h_2}^2 \mu^3}{(h_1 \chi - h_2 \mu) {h_1}^2 \tau}. \tag{2.11}$$

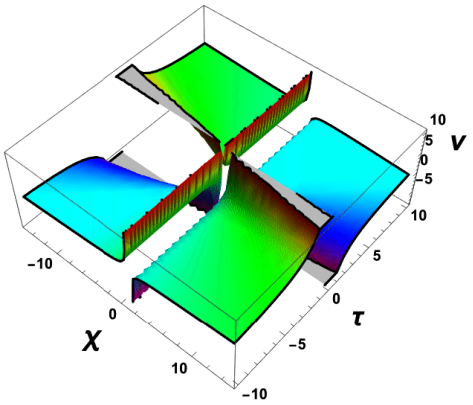

Figure 4. The profile structure of solution (2.11)

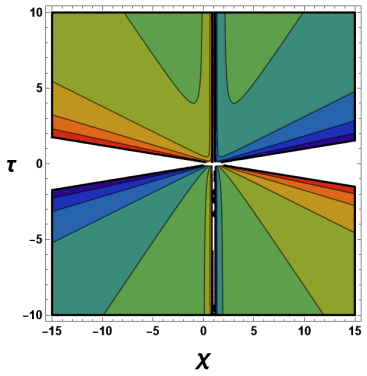

Figure 5. A density plot of (2.11)

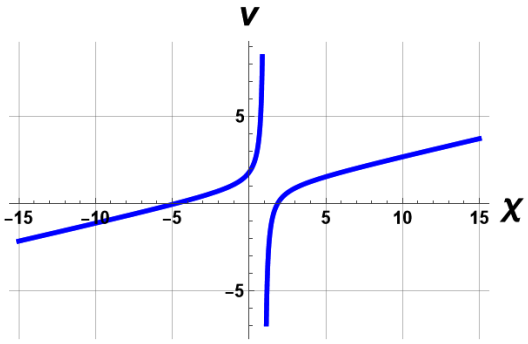

Figure 6. A 2D side view of (2.11)

Case 3. The symmetry $\mathbf{\Gamma_5}$ leads to

$$v(\tau,\chi,\mu)=\frac{1}{\tau^{3/2}{h_1}^2}\left(g(\tau)\tau^{3/2}{h_1}^2-\sqrt{\tau}h_1\,\chi\mu+\sqrt{\tau}h_2\,\mu^2+z\left(\frac{h_1\,\chi-h_2\,\mu}{h_1\,\sqrt{\tau}}\right){h_1}^2\tau\right) \tag{2.12}$$

with invariants

$$\Psi=\tau,\ \ \gamma=\frac{h_1\chi-h_2\mu}{h_1},\ \ \Theta=\frac{h_1^2\tau v+h_1\chi\mu-h_2\mu^2}{h_1^2\tau},$$

and $\Theta(\gamma,\Psi)$ satisfies the nonlinear partial differential equation

$$2\Psi\Theta_{\Psi\gamma}+\gamma\Theta_{\gamma\gamma}+2\Theta=0. \tag{2.13}$$

The integration of (2.13) leads to

$$\Theta(\Psi,\gamma)=g(\Psi)+\frac{z\left(\frac{\gamma}{\sqrt{\tau}}\right)}{\sqrt{\Psi}}, \tag{2.14}$$

where g and z are arbitrary functions of f and $\gamma/\sqrt{\tau}$ respectively. Finally, (2.14) accomplishes the group invariant solution (2.12).

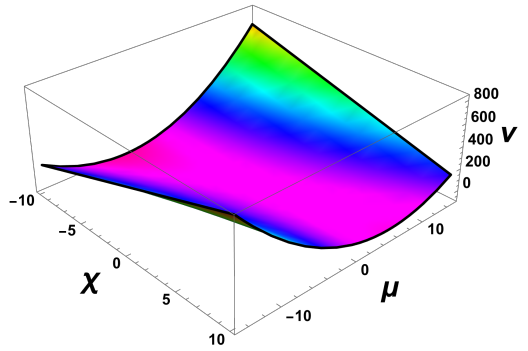

Figure 7. A 3D of solution (2.12)

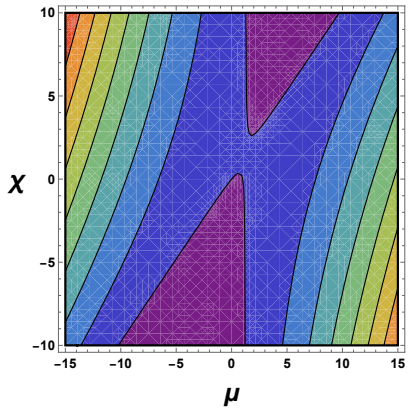

Figure 8. A density plot of solution (2.12)

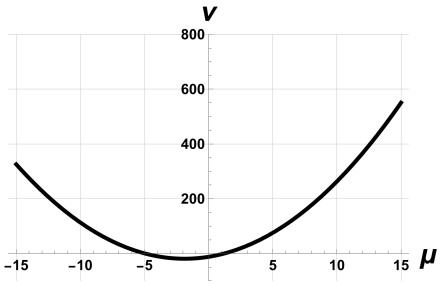

Figure 9. A 2D side view of (2.12)

The limiting behavior of problems that are distant from their beginning or boundary conditions is often captured by group invariant solutions.

3. MULTIPLE EXP-FUNCTION METHOD

The multiple exp-function technique operates independently in constructing bilinear forms. It begins with the notion that polynomials of exponential functions can be used to define multi-soliton solutions. In essence, Hirota's perturbation approach is expanded upon by the multiple exp-function algorithm. Furthermore, general wave frequencies and phase shifts are included in the resultant solutions. The following is a summary of the multiple exp-function method's main steps. [52–56]:

Step 1. Let us consider the following (1 + 1)-dimensional NLEE:

$$P(\chi, \tau, \nu_\chi, \nu_\tau, \cdots) = 0. \tag{3.15}$$

Step 2. Suppose the solution of above NLEE can be expressed as

$$\nu(\tau, \chi) = \frac{p(\eta_1, \eta_2, \cdots, \eta_n)}{q(\eta_1, \eta_2, \cdots, \eta_n)}, \quad p = \sum_{r,s=1}^{n} \sum_{i,j=0}^{M} p_{rs,ij} \eta_r^i \eta_s^j,$$

$$q = \sum_{r,s=1}^{n} \sum_{i,j=0}^{N} q_{rs,ij} \eta_r^i \eta_s^j, \tag{3.16}$$

in which $p_{rs,ij}$ and $q_{rs,ij}$ are unknowns to be determined and

$$\eta_i = c_i e^{\xi_i}, \quad \xi_i = k_i \chi - \rho_i \tau, \quad 1 \leqslant i \leqslant n. \tag{3.17}$$

Step 3. Substituting (3.16) and its derivatives into (3.15) yields the following transformed equation

$$Q(\chi, \tau, \eta_1, \eta_2, \cdots, \eta_n) = 0. \tag{3.18}$$

Step 4. The multiple wave solution of (3.15) can be obtained by solving an algebraic system whose numerator is set to zero for the function $Q(\chi, \tau, \eta_1, \eta_2, \cdots, \eta_n)$,

$$\nu(\tau, \chi) = \frac{p(c_1 e^{k_1 \chi - \rho_1 \tau}, \cdots, c_n e^{k_n \chi - \rho_n \tau})}{q(c_1 e^{k_1 \chi - \rho_1 \tau}, \cdots, c_n e^{k_n \chi - \rho_n t})}. \tag{3.19}$$

3.1. Application of the multiple exp-function algorithm in (1.5)

The multiple exp-function approach will be used in this subsection to get the one- and two-wave solutions of (1.5).

3.1.1. One-wave solution of (1.5) We start with one-wave function

$$v(\chi,\tau,\mu)=\frac{p}{q},\quad p=A_1e^{k_1\chi+l_1\mu-\rho_1\tau},\quad q=1+e^{k_1\chi+l_1\mu-\rho_1\tau} \tag{3.20}$$

where A_1 is a constant. By applying the multiple exp-function algorithm, we obtain with the aid of Maple:

$$A_1=2k_1,\quad \rho_1=-\frac{1}{4}k_1^2\left(h_1l_1+h_2k_1\right). \tag{3.21}$$

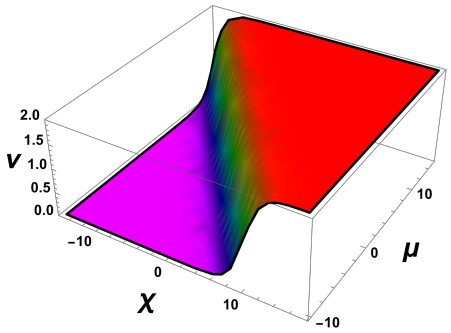

Figure 10. A 3D plot of solution (3.20).

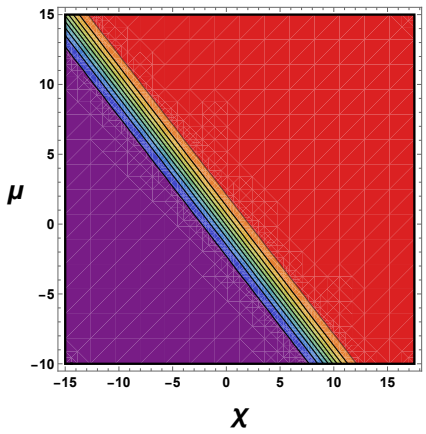

Figure 11. A density plot of solution (3.20)

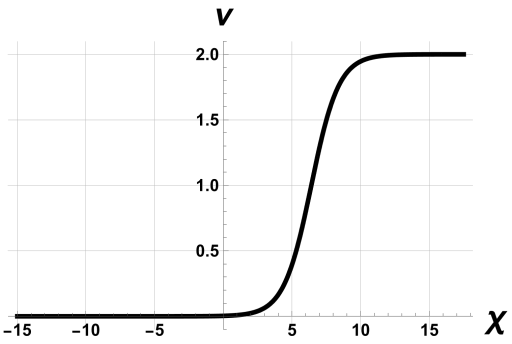

Figure 12. A 2D side view of solution (3.20).

3.1.2. Two-wave solution of (1.5) Based on the assertion made in Step 2, we examine two-wave solutions and suppose that equation (1.5) has the rational function of two-wave solutions, which is represented as follows:

$$v(\chi,\tau,\mu)=\frac{p}{q}, \tag{3.22}$$

with p and q being defined by

$$\begin{aligned} p &= 2\,k_1 e^{k_1\chi+l_1\mu-\rho_1\tau}+2\,k_2 e^{k_2\chi+l_2\mu-\rho_2\tau} \\ &\quad +2\,A_{12}\,(k_1+k_2)\,e^{k_1\chi+l_1\mu-\rho_1\tau}e^{k_2\chi+l_2\mu-\rho_2\tau}, \qquad (3.23)\\ q &= 1+e^{k_1\chi+l_1\mu-\rho_1\tau}+e^{k_2\chi+l_2\mu-\rho_2\tau}+A_{12}e^{k_1\chi+l_1\mu-\rho_1\tau}e^{k_2\chi+l_2\mu-\rho_2\tau}, \qquad (3.24)\end{aligned}$$

where

$$\lambda_i=k_i\chi+l_i\mu-\rho_i\tau,\quad i=1,2 \tag{3.25}$$

and A_{12} is a constant. Applying the multiple exp-function algorithm, with the aid of Maple leads to

$$A_{12}=\frac{k_1^2-2k_1k_2+k_2^2}{(k_1+k_2)^2},\quad \rho_1=-\frac{1}{4}k_1^2\,(h_1l_1+h_2k_1)\,,\quad \rho_2=-\frac{1}{4}k_2^2\,(h_1l_2+h_2k_2)\,. \tag{3.26}$$

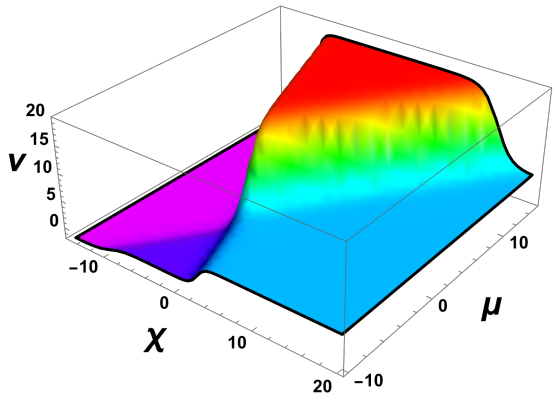

Figure 13. A 3 dimensional simulation of solution (3.22).

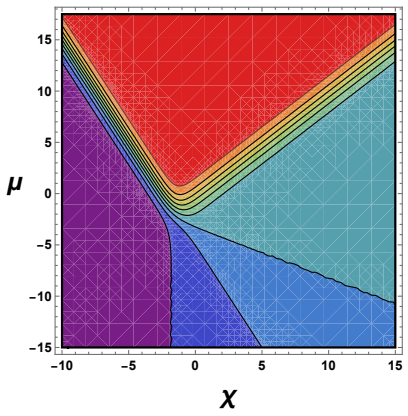

Figure 14. A density plot of solution (3.22).

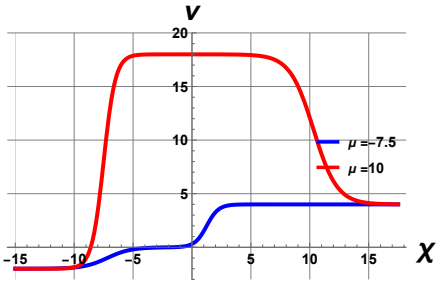

Figure 15. A 2D side view of solution (3.22).

4. ANALYSIS AND DISCUSSION OF THE RESULTS

The first solution in Fig.1, Fig.2 and Fig.3 portrays a multi-singular wave structure, with spatial variables restricted to the intervals of $-15 \leq \chi \leq 15$ and $0 \leq \tau \leq 10$, with $h_2 = 1$, $\mu = -1$, $h_1 = 1$, $C_1 = 1$, $C_2 = 0$. Conversely, the second illustration in Fig.4, Fig.5 and Fig.5, presents a singular wave structure , with spatial variables restricted to $-15 \leq \chi \leq 15$ and $-10 \leq \tau \leq 10$, with $h_2 = 1$, $\tau = 1$, $h_1 = 1$, $C_2 = 1$ and $C_1 = 1$. Singular periodic waves are employed in the study of wave dynamics across different optical systems and fibers. Additionally, they are relevant in the examination of chaotic phenomena, providing essential insights into the behavior of these systems, as they facilitate the interactions of particles in the fields of physics and chemistry. In Fig.7, Fig.8 and Fig.9 , the graphical representation shows a concave-up structure which is analyzed within the spatial variables constrained to the range of $-10 \leq \tau \leq 10$ and $-15 \leq \chi \leq 15$ $h_2 = 1$, $\tau = 1$, $h_1 = 1$, $g(\tau) = 0$, $z\left(\frac{h_1\chi - h_2\mu}{h_1\sqrt{\tau}}\right) = \text{sech}^2(\chi - \mu)$. Furthermore, Fig.10, Fig.11 and Fig.12, engenders a one-wave solution portraying a kink profile defined within the intervals of $-15 \leq \chi \leq 20$ and $-10 \leq \mu \leq 15$ and the rest of the elements equated to unity. Finally, Fig.13, Fig.14 and Fig.15, presents a two-wave kink profile structure with spatial variables restricted to the intervals of$-15 \leq \chi \leq 15$ and $-15 \leq \chi \leq 20$, with the parameter with $h_1 = 5$, $h_2 = 2.5$, $k_1 = 2$ and $t = 0.5$ and the rest set one. Kink solitary waves have been extensively utilized in optics and various fields of nonlinear science. They serve as logic units or polarization switches connecting two separate points. Additionally, they are applied in the analysis and comprehension of the propagation of extremely short light pulses within a cubic-quintic nonlinear medium.

5. CONSERVATION LAWS

Key physical quantities like mass, energy, momentum, electric charge, and other constants of motion can be understood through the framework provided by conservation laws [56]. Because they define conserved quantities and shed light on the characteristics and behavior of partial differential equation solutions, conservation laws are essential to the study of differential equations. They play a crucial role in establishing whether solutions to nonlinear partial differential equations exist, are unique, and are stable. Conservation laws also aid in the evaluation of linearization, integrability, and the validity of numerical techniques for resolving these equations.

Our goal in this section is to use the multiplier approach to construct the conservation laws of (1.5). We start by reviewing some fundamental findings that will be applied later in this section. Examine a system of partial differential equations of pth order with n independent variables $\chi = (\chi^1, \chi^2, \ldots, \chi^n)$ and m dependent variables $\nu = (\nu^1, \nu^2, \ldots, \nu^m)$, i.e.,

$$H_\alpha(\chi, \nu, \nu_{(1)}, ..., \nu_{(p)}) = 0, \quad \alpha = 1, ...m, \tag{5.27}$$

where $\nu_{(1)}, \nu_{(2)}, \ldots, \nu_{(\zeta)}$ denote the collections of all first, second, ..., ζth-order partial derivatives, that is, $\nu_i^\alpha = D_i(\nu^\alpha), \nu_{ij}^\alpha = D_j D_i(\nu^\alpha), \ldots$ respectively, with the *total derivative operator* with respect to χ^i is given by

$$D_i = \frac{\partial}{\partial \chi^i} + \nu_i^\alpha \frac{\partial}{\partial \nu^\alpha} + \nu_{ij}^\alpha \frac{\partial}{\partial \nu_j^\alpha} + \ldots, \quad i = 1, \ldots, n, \tag{5.28}$$

where the summation convention is used whenever appropriate.

The *Euler-Lagrange operator*, for each α, is given by

$$\frac{\delta}{\delta \nu^\alpha} = \frac{\partial}{\partial \nu^\alpha} + \sum_{s \geq 1} (-1)^s D_{i_1} \ldots D_{i_s} \frac{\partial}{\partial \nu_{i_1 i_2 \ldots i_s}^\alpha}, \quad \alpha = 1, \ldots, m. \tag{5.29}$$

The n-tuple vector $T = (T^1, T^2, \ldots, T^n)$, $T^j \in \mathcal{A}$, $j = 1, \ldots, n$, is a *conserved vector* of (5.27) if T^i satisfies

$$D_i T^i|_{(5.27)} = 0. \tag{5.30}$$

The equation (5.30) defines a *local conservation law* of system (5.27).

A multiplier $\Lambda_\alpha(\chi, \nu, \nu_{(1)}, \ldots)$ has the property that

$$\Lambda_\alpha H_\alpha = D_i T^i \tag{5.31}$$

holds identically. Here we will consider multiplier of the third order, i.e.,
$\Lambda_\alpha = \Lambda_\alpha(\tau, \chi, \mu, \nu, \nu_\tau, \nu_\chi, \nu_\mu, \nu_{\tau\chi}, \nu_{\tau\mu}, \nu_{\chi\mu}, \nu_{\tau\tau}, \nu_{\chi\chi}, \nu_{\mu\mu}, \nu_{\tau\tau\tau}, \nu_{\tau\tau\chi}, \nu_{\tau\chi\chi}, \nu_{\tau\tau\mu}, \nu_{\tau\mu\mu}, \nu_{\chi\chi\chi}, \nu_{\chi\chi\mu}$,
$\nu_{\chi\mu\mu}, \nu_{\mu\mu\mu})$. The right hand side of (5.31) is a divergence expression. The determining equation for the multiplier Λ_α is

$$\frac{\delta(\Lambda_\alpha H_\alpha)}{\delta \nu^\alpha} = 0. \tag{5.32}$$

5.1. Conservation Laws of (1.5)

The (2+1) dimensional KdV-Calogero-Bogoyavlenkskii-Schiff equation (1.5) has a multiplier of the form

$$\begin{aligned}
\Lambda &= \left(\frac{1}{2}h_1\tau\nu + h_1\tau\mu\nu_\mu + h_1\tau^2\nu_\tau + \frac{1}{2}h_2\tau\mu\nu_\chi + \frac{1}{2}h_1\tau\chi\nu_\chi - \frac{h_2\mu^2}{h_1} + \chi\mu\right)C_1 + \nu_\mu C_4 \\
&+ \left(h_1\tau\nu_\mu - \frac{3h_2\mu}{h_1} + \chi\right)C_2 + \left(\frac{h_2\mu\nu_\chi}{h_1} + 4\tau\nu_\tau + \nu + \chi\nu_\chi + 2\mu\nu_\mu\right)C_3 + \nu_\tau C_5 \\
&+ \frac{4\mu^2 f''(\tau)}{h_1^2} + \frac{4\mu f'(\tau)\nu_\chi}{h_1} + f(\tau)\nu_{\chi\chi\chi} + 3f(\tau){\nu_\chi}^2 + \frac{2\mu r'(\tau)}{h_1} + r(\tau)\nu_\chi + g(\tau),
\end{aligned} \tag{5.33}$$

where C_1, C_2, C_3, C_4 and C_5 are arbitrary constant and $f(\tau), r(\tau)$ and $g(\tau)$ are arbitrary functions of τ. Corresponding to the above multiplier we have the following conserved vectors of (1.2):

$$\begin{aligned}
T_1^\tau &= \frac{1}{3h_1}\Big(-16\tau\nu\nu_\chi\nu_{\chi\mu}h_1^2 - 8\tau\nu\nu_\mu\nu_{\chi\chi}h_1^2 - 6\tau\nu\nu_{\chi\chi\chi\mu}h_1^2 + 3\chi{\nu_\chi}^2h_1 - 3\nu\nu_\chi h_1 + 6\mu\nu_\mu\nu_\chi h_1 \\
&-3\chi\nu\nu_{\chi\chi}h_1 - 24\tau h_2\nu\nu_\chi\nu_{\chi\chi}h_1 - 6\tau h_2\nu\nu_{\chi\chi\chi\chi}h_1 + 12\tau\nu_\chi\nu_\tau h_1 + 12\tau\nu\nu_{\tau\chi}h_1 + 3\mu h_2{\nu_\chi}^2 \\
&-6\mu\nu\nu_{\chi\mu}h_1 - 3\mu h_2\nu\nu_{\chi\chi}\Big), \\
T_1^\chi &= \frac{1}{24h_1}\Big(-48\mu h_2^2{\nu_\chi}^3 - 48\chi h_1h_2{\nu_\chi}^3 + 64h_1h_2\nu{\nu_\chi}^2 - 32\chi h_1^2\nu_\mu{\nu_\chi}^2 - 128\mu h_1h_2\nu_\mu{\nu_\chi}^2 \\
&-64\mu h_1^2{\nu_\mu}^2\nu_\chi + 48h_1^2\nu\nu_\mu\nu_\chi + 32\mu h_1^2\nu\nu_{\mu\mu}\nu_\chi - 12h_1^2\nu_{\chi\mu}\nu_\chi - 16\chi h_1^2\nu\nu_{\chi\mu}\nu_\chi + 80\mu h_1h_2\nu\nu_{\chi\mu}\nu_\chi \\
&-15h_1h_2\nu_{\chi\chi}\nu_\chi - 15\chi h_1^2\nu_{\chi\chi\mu}\nu_\chi - 39\mu h_1h_2\nu_{\chi\chi\mu}\nu_\chi - 24\mu h_2^2\nu_{\chi\chi\chi}\nu_\chi - 24\chi h_1h_2\nu_{\chi\chi\chi}\nu_\chi \\
&-128\tau h_1^2\nu_\mu\nu_\tau\nu_\chi + 64\tau h_1^2\nu\nu_{\tau\mu}\nu_\chi + 192\tau h_1h_2\nu\nu_{\tau\chi}\nu_\chi - 24\tau h_1^2\nu_{\tau\chi\mu}\nu_\chi - 48\tau h_1h_2\nu_{\tau\chi\chi}\nu_\chi \\
&+96\tau h_1{\nu_\tau}^2 + 32\mu h_1^2\nu\nu_\mu\nu_{\chi\mu} + 6\mu h_1^2\nu_{\mu\mu}\nu_{\chi\chi} + 9\chi h_1^2\nu_{\chi\mu}\nu_{\chi\chi} + 33\mu h_1h_2\nu_{\chi\mu}\nu_{\chi\chi} + 36h_1^2\nu\nu_{\chi\chi\mu} \\
&+18\mu h_1^2\nu\nu_{\chi\chi\mu\mu} + 45h_1h_2\nu\nu_{\chi\chi\chi} - 3\chi h_1^2\nu_\mu\nu_{\chi\chi\chi} - 27\mu h_1h_2\nu_\mu\nu_{\chi\chi\chi} - 3\chi h_1^2\nu\nu_{\chi\chi\chi\mu} \\
&+48\mu h_1\nu_\mu\nu_\tau - 36\tau h_1^2\nu_{\chi\chi\mu}\nu_\tau - 48\tau h_1h_2\nu_{\chi\chi\chi}\nu_\tau - 48\mu h_1\nu\nu_{\tau\mu} + 12\tau h_1^2\nu_{\chi\chi}\nu_{\tau\mu} + 24\chi h_1\nu\nu_{\tau\chi} \\
&+64\tau h_1^2\nu\nu_\mu\nu_{\tau\chi} + 24\tau h_1^2\nu_{\chi\mu}\nu_{\tau\chi} + 48\tau h_1h_2\nu_{\chi\chi}\nu_{\tau\chi} - 12\tau h_1^2\nu_\mu\nu_{\tau\chi\chi} + 36\tau h_1^2\nu\nu_{\tau\chi\chi\mu} \\
&-24\mu h_1^2\nu_\mu\nu_{\chi\chi\mu} - 12\mu h_1^2\nu_{\chi\mu\mu}\nu_\chi + 24\mu h_2\nu_\tau\nu_\chi + 12\mu h_2^2{\nu_{\chi\chi}}^2 - 96h_1\nu\nu_\tau - 96\tau h_1\nu\nu_{\tau\tau} \\
&-192\tau h_1h_2\nu_\tau{\nu_\chi}^2 + 12\chi h_1h_2{\nu_{\chi\chi}}^2 + 48\tau h_1h_2\nu\nu_{\tau\chi\chi\chi} + 24\chi h_1\nu_\tau\nu_\chi + 12\mu h_1^2{\nu_{\chi\mu}}^2 \\
&+24\mu h_2\nu\nu_{\tau\chi} + 21\mu h_1h_2\nu\nu_{\chi\chi\chi\mu}\Big), \\
T_1^\mu &= \frac{1}{24}\Big(-16\chi h_1{\nu_\chi}^3 - 16\mu h_2{\nu_\chi}^3 + 16h_1\nu{\nu_\chi}^2 - 32\mu h_1\nu_\mu{\nu_\chi}^2 - 64\tau h_1\nu_\tau{\nu_\chi}^2 - 32\mu h_1\nu\nu_{\chi\mu}\nu_\chi \\
&+16\chi h_1\nu\nu_{\chi\chi}\nu_\chi - 80\mu h_2\nu\nu_{\chi\chi}\nu_\chi - 6\mu h_1\nu_{\chi\chi\mu}\nu_\chi - 6\chi h_1\nu_{\chi\chi\chi}\nu_\chi - 6\mu h_2\nu_{\chi\chi\chi}\nu_{,\chi} + 64\tau h_1\nu\nu_{\tau\chi}\nu_\chi \\
&-12\tau h_1\nu_{\tau\chi\chi}\nu_\chi + 3\chi h_1{\nu_{\chi\chi}}^2 + 3\mu h_2{\nu_{\chi\chi}}^2 - 32\mu h_1\nu\nu_\mu\nu_{\chi\chi} + 6\mu h_1\nu_{\chi\mu}\nu_{\chi\chi} + 9h_1\nu\nu_{\chi\chi\chi} \\
&-18\mu h_1\nu\nu_{\chi\chi\chi\mu} + 3\chi h_1\nu\nu_{\chi\chi\chi\chi} - 21\mu h_2\nu\nu_{\chi\chi\chi\chi} - 12\tau h_1\nu_{\chi\chi\chi}\nu_\tau + 96\mu\nu\nu_{\tau\chi} - 6\mu h_1\nu_\mu\nu_{\chi\chi\chi} \\
&+12\tau h_1\nu_{\chi\chi}\nu_{\tau\chi} + 12\tau h_1\nu\nu_{\tau\chi\chi\chi} - 3h_1\nu_{\chi\chi}\nu_\chi\Big);
\end{aligned}$$

$$T_2^\tau = \frac{\tau\nu_\mu\nu_\chi h_1^2 - \tau\nu\nu_{\chi\mu}h_1^2 - 2\nu h_1 + 2\chi\nu_\chi h_1 - 6\mu h_2\nu_\chi}{h_1},$$

$$
\begin{aligned}
T_2^{\chi} &= \frac{1}{24h_1}\Big(6\tau\nu_{\chi\mu}{}^2h_1^3-32\tau\nu_\mu{}^2\nu_\chi h_1^3+16\tau\nu\nu_{\mu\mu}\nu_\chi h_1^3+16\tau\nu\nu_\mu\nu_{\chi\mu}h_1^3-6\tau\nu_\chi\nu_{\chi\mu\mu}h_1^3\\
&\quad+3\tau\nu_{\mu\mu}\nu_{\chi\chi}h_1^3-12\tau\nu_\mu\nu_{\chi\chi\mu}h_1^3+9\tau\nu\nu_{\chi\chi\mu\mu}h_1^3-48\tau h_2\nu_\mu\nu_\chi{}^2h_1^2-48\chi\nu_\mu\nu_\chi h_1^2\\
&\quad+48\tau h_2\nu\nu_\chi\nu_{\chi\mu}h_1^2+12\nu_{\chi\mu}h_1^2+12\tau h_2\nu_{\chi\mu}\nu_{\chi\chi}h_1^2-18\chi\nu_{\chi\chi\mu}h_1^2-12\tau h_2\nu_\chi\nu_{\chi\chi\mu}h_1^2\\
&\quad+12\tau h_2\nu\nu_{\chi\chi\chi\mu}h_1^2+24\tau\nu_\mu\nu_\tau h_1^2-24\tau\nu\nu_{\tau\mu}h_1^2-72\chi h_2\nu_\chi{}^2h_1+144\mu h_2\nu_\mu\nu_\chi h_1+6h_2\nu_{\chi\chi}h_1\\
&\quad+54\mu h_2\nu_{\chi\chi\mu}h_1-24\chi h_2\nu_{\chi\chi\chi}h_1+48\chi\nu_\tau h_1+216\mu h_2^2\nu_\chi{}^2+72\mu h_2^2\nu_{\chi\chi\chi}-144\mu h_2\nu_\tau\\
&\quad-12\tau h_2\nu_\mu\nu_{\chi\chi\chi}h_1^2\Big),\\
T_2^{\mu} &= \frac{1}{24}\Big(-16\tau\nu_\mu\nu_\chi{}^2h_1^2-16\tau\nu\nu_\chi\nu_{\chi\mu}h_1^2-16\tau\nu\nu_\mu\nu_{\chi\chi}h_1^2+3\tau\nu_{\chi\mu}\nu_{\chi\chi}h_1^2-3\tau\nu_\chi\nu_{\chi\chi\mu}h_1^2\\
&\quad-3\tau\nu_\mu\nu_{\chi\chi\chi}h_1^2-9\tau\nu\nu_{\chi\chi\chi\mu}h_1^2-24\chi\nu_\chi{}^2h_1+24\nu\nu_\chi h_1-48\tau h_2\nu\nu_\chi\nu_{\chi\chi}h_1+6\nu_{\chi\chi}h_1\\
&\quad-6\chi\nu_{\chi\chi\chi}h_1-12\tau h_2\nu\nu_{\chi\chi\chi\chi}h_1+48\tau\nu\nu_{\tau\chi}h_1+72\mu h_2\nu_\chi{}^2+18\mu h_2\nu_{\chi\chi\chi}\Big);
\end{aligned}
$$

$$
\begin{aligned}
T_3^{\tau} &= \frac{1}{6h_1}\Big(-8\tau^2\nu\nu_\chi\nu_{\chi\mu}h_1^3-4\tau^2\nu\nu_\mu\nu_{\chi\chi}h_1^3-3\tau^2\nu\nu_{\chi\chi\chi\mu}h_1^3+3\tau\chi\nu_\chi{}^2h_1^2-3\tau\nu\nu_\chi h_1^2+6\tau\mu\nu_\mu\nu_\chi h_1^2\\
&\quad-6\tau\mu\nu\nu_{\chi\mu}h_1^2-3\tau\chi\nu\nu_{\chi\chi}h_1^2-12\tau^2h_2\nu\nu_\chi\nu_{\chi\chi}h_1^2-3\tau^2h_2\nu\nu_{\chi\chi\chi\chi}h_1^2+6\tau^2\nu_\chi\nu_\tau h_1^2+6\tau^2\nu\nu_{\tau\chi}h_1^2\\
&\quad+3\tau\mu h_2\nu_\chi{}^2h_1-12\mu\nu h_1+12\chi\mu\nu_\chi h_1-3\tau\mu h_2\nu\nu_{\chi\chi}h_1-12\mu^2h_2\nu_\chi\Big),\\
T_3^{\chi} &= \frac{1}{48h_1}\Big(-32\tau\chi\nu_\mu\nu_\chi{}^2h_1^3+12\tau\mu\nu_{\chi\mu}{}^2h_1^3-64\tau\mu\nu_\mu{}^2\nu_\chi h_1^3+48\tau\nu\nu_\mu\nu_\chi h_1^3+32\tau\mu\nu\nu_{\mu\mu}\nu_\chi h_1^3\\
&\quad+32\tau\mu\nu\nu_\mu\nu_{\chi\mu}h_1^3-12\tau\nu_\chi\nu_{\chi\mu}h_1^3-16\tau\chi\nu\nu_\chi\nu_{\chi\mu}h_1^3-12\tau\mu\nu_\chi\nu_{\chi\mu\mu}h_1^3+6\tau\mu\nu_{\mu\mu}\nu_{\chi\chi}h_1^3\\
&\quad+36\tau\nu\nu_{\chi\chi\mu}h_1^3-24\tau\mu\nu_\mu\nu_{\chi\chi\mu}h_1^3-15\tau\chi\nu_\chi\nu_{\chi\chi\mu}h_1^3+18\tau\mu\nu\nu_{\chi\chi\mu\mu}h_1^3-3\tau\chi\nu_\mu\nu_{\chi\chi\chi}h_1^3\\
&\quad-64\tau^2\nu_\mu\nu_\chi\nu_\tau h_1^3-18\tau^2\nu_{\chi\chi\mu}\nu_\tau h_1^3+32\tau^2\nu\nu_\chi\nu_{\tau\mu}h_1^3+6\tau^2\nu_{\chi\chi}\nu_{\tau\mu}h_1^3+32\tau^2\nu\nu_\mu\nu_{\tau\chi}h_1^3\\
&\quad-12\tau^2\nu_\chi\nu_{\tau\chi\mu}h_1^3-6\tau^2\nu_\mu\nu_{\tau\chi\chi}h_1^3+18\tau^2\nu\nu_{\tau\chi\chi\mu}h_1^3-48\tau\chi h_2\nu_\chi{}^3h_1^2-24\nu^2h_1^2+64\tau h_2\nu\nu_\chi{}^2h_1^2\\
&\quad-128\tau\mu h_2\nu_\mu\nu_\chi{}^2h_1^2+12\tau\chi h_2\nu_{\chi\chi}{}^2h_1^2+48\tau^2\nu_\tau{}^2h_1^2+24\chi\nu\nu_\chi h_1^2-96\chi\mu\nu_\mu\nu_\chi h_1^2-24\nu_\chi h_1^2\\
&\quad+80\tau\mu h_2\nu\nu_\chi\nu_{\chi\mu}h_1^2+12\chi\nu_{\chi\chi}h_1^2-15\tau h_2\nu_\chi\nu_{\chi\chi}h_1^2+33\tau\mu h_2\nu_{\chi\mu}\nu_{\chi\chi}h_1^2-36\chi\mu\nu_{\chi\chi\mu}h_1^2\\
&\quad+45\tau h_2\nu\nu_{\chi\chi\chi}h_1^2-27\tau\mu h_2\nu_\mu\nu_{\chi\chi\chi}h_1^2-24\tau\chi h_2\nu_\chi\nu_{\chi\chi\chi}h_1^2+21\tau\mu h_2\nu\nu_{\chi\chi\chi\mu}h_1^2-96\tau^2h_2\nu_\chi{}^2\nu_\tau h_1^2\\
&\quad-96\tau\nu\nu_\tau h_1^2+48\tau\mu\nu_\mu\nu_\tau h_1^2+24\tau\chi\nu_\chi\nu_\tau h_1^2-24\tau^2h_2\nu_{\chi\chi\chi}\nu_\tau h_1^2-48\tau\mu\nu\nu_{\tau\mu}h_1^2+24\tau\chi\nu\nu_{\tau\chi}h_1^2\\
&\quad+24\tau^2h_2\nu_{\chi\chi}\nu_{\tau\chi}h_1^2-24\tau^2h_2\nu_\chi\nu_{\tau\chi\chi}h_1^2+24\tau^2h_2\nu\nu_{\tau\chi\chi\chi}h_1^2-48\tau^2\nu\nu_{\tau\tau}h_1^2-48\tau\mu h_2^2\nu_\chi{}^3h_1\\
&\quad+12\tau\mu h_2^2\nu_{\chi\chi}{}^2h_1+24\mu h_2\nu\nu_\chi h_1+96\mu^2h_2\nu_\mu\nu_\chi h_1+24\mu h_2\nu_{\chi\chi}h_1+36\mu^2h_2\nu_{\chi\chi\mu}h_1\\
&\quad-24\tau\mu h_2^2\nu_\chi\nu_{\chi\chi\chi}h_1+96\chi\mu\nu_\tau h_1+24\tau\mu h_2\nu_\chi\nu_\tau h_1+24\tau\mu h_2\nu\nu_{\tau\chi}h_1+144\mu^2h_2^2\nu_\chi{}^2\\
&\quad-96\mu^2h_2\nu_\tau-48\chi\mu h_2\nu_{\chi\chi\chi}h_1+96\tau^2h_2\nu\nu_\chi\nu_{\tau\chi}h_1^2-144\chi\mu h_2\nu_\chi{}^2h_1+48\mu^2h_2^2\nu_{\chi\chi\chi}\\
&\quad+9\tau\chi\nu_{\chi\mu}\nu_{\chi\chi}h_1^3-3\tau\chi\nu\nu_{\chi\chi\chi\mu}h_1^3+12\tau^2\nu_{\chi\mu}\nu_{\tau\chi}h_1^3+24\mu\nu_{\chi\mu}h_1^2-39\tau\mu h_2\nu_\chi\nu_{\chi\chi\mu}h_1^2\Big),\\
T_3^{\mu} &= \frac{1}{48}\Big(-16\tau\chi h_1^2\nu_\chi{}^3-16\tau\mu h_1h_2\nu_\chi{}^3-48\chi\mu h_1\nu_\chi{}^2+48\mu^2h_2\nu_\chi{}^2+16\tau h_1^2\nu\nu_\chi{}^2\\
&\quad+48\mu h_1\nu\nu_\chi-32\tau\mu h_1^2\nu\nu_{\chi\mu}\nu_\chi-3\tau h_1^2\nu_{\chi\chi}\nu_\chi+16\tau\chi h_1^2\nu\nu_{\chi\chi}\nu_\chi-80\tau\mu h_1h_2\nu\nu_{\chi\chi}\nu_\chi\\
&\quad-6\tau\chi h_1^2\nu_{\chi\chi\chi}\nu_\chi-6\tau\mu h_1h_2\nu_{\chi\chi\chi}\nu_\chi+32\tau^2h_1^2\nu\nu_{\tau\chi}\nu_\chi-6\tau^2h_1^2\nu_{\tau\chi\chi}\nu_\chi+3\tau\chi h_1^2\nu_{\chi\chi}{}^2\\
&\quad-32\tau\mu h_1^2\nu\nu_\mu\nu_{\chi\chi}+6\tau\mu h_1^2\nu_{\chi\mu}\nu_{\chi\chi}-12\chi\mu h_1\nu_{\chi\chi\chi}+12\mu^2h_2\nu_{\chi\chi\chi}+9\tau h_1^2\nu\nu_{\chi\chi\chi}\\
&\quad+3\tau\chi h_1^2\nu\nu_{\chi\chi\chi\chi}-21\tau\mu h_1h_2\nu\nu_{\chi\chi\chi\chi}-6\tau^2h_1^2\nu_{\chi\chi\chi}\nu_\tau+96\tau\mu h_1\nu\nu_{\tau\chi}+6\tau^2h_1^2\nu_{\chi\chi}\nu_{\tau\chi}\\
&\quad-32\tau^2h_1^2\nu_\tau\nu_\chi{}^2+12\mu h_1\nu_{\chi\chi}-18\tau\mu h_1^2\nu\nu_{\chi\chi\chi\mu}+6\tau^2h_1^2\nu\nu_{\tau\chi\chi\chi}-6\tau\mu h_1^2\nu_{\chi\chi\mu}\nu_\chi\\
&\quad+3\tau\mu h_1h_2\nu_{\chi\chi}{}^2-6\tau\mu h_1^2\nu_\mu\nu_{\chi\chi\chi}-32\tau\mu h_1^2\nu_\mu\nu_\chi{}^2\Big);
\end{aligned}
$$

$$
T_4^{\tau} = \nu_\chi\nu_\mu-\nu_{\chi\mu}\nu,
$$

$$
\begin{aligned}
T_4^{\chi} &= \frac{1}{24}\Big(16h_1\nu_\mu\nu_{\chi\mu}\nu + 16h_1\nu_\chi\nu_{\mu\mu}\nu + 48h_2\nu_\chi\nu_{\chi\mu}\nu + 9h_1\nu_{\chi\chi\mu\mu}\nu + 12h_2\nu_{\chi\chi\chi\mu}\nu - 24\nu_{\tau\mu}\nu \\
&\quad -32h_1\nu_\chi{\nu_\mu}^2 - 48h_2{\nu_\chi}^2\nu_\mu - 12h_1\nu_\mu\nu_{\chi\chi\mu} - 12h_2\nu_{\chi\chi\chi}\nu_\mu + 6h_1{\nu_{\chi\mu}}^2 - 6h_1\nu_\chi\nu_{\chi\mu\mu} \\
&\quad +3h_1\nu_{\chi\chi}\nu_{\mu\mu} + 12h_2\nu_{\chi\chi}\nu_{\chi\mu} - 12h_2\nu_\chi\nu_{\chi\chi\mu} + 24\nu_\tau\nu_\mu\Big), \\
T_4^{\mu} &= \frac{1}{24}\Big(-16h_1\nu_\chi\nu_{\chi\mu}\nu - 48h_2\nu_{\chi\chi}\nu_\chi\nu - 16h_1\nu_{\chi\chi}\nu_\mu\nu - 9h_1\nu_{\chi\chi\chi\mu}\nu - 12h_2\nu_{\chi\chi\chi\chi}\nu \\
&\quad +48\nu_{\tau\chi}\nu - 16h_1{\nu_\chi}^2\nu_\mu - 3h_1\nu_\chi\nu_{\chi\chi\mu} + 3h_1\nu_{\chi\chi}\nu_{\chi\mu} - 3h_1\nu_{\chi\chi\chi}\nu_\mu\Big);
\end{aligned}
$$

$$
\begin{aligned}
T_5^{\tau} &= \frac{1}{6}\Big(-8h_1\nu_\chi\nu_{\chi\mu}\nu - 4h_1\nu_{\chi\chi}\nu_\mu\nu - 12h_2\nu_\chi\nu_{\chi\chi}\nu - 3h_1\nu_{\chi\chi\chi\mu}\nu - 3h_2\nu_{\chi\chi\chi\chi}\nu + 6\nu_{\tau\chi}\nu + 6\nu_\tau\nu_\chi\Big), \\
T_5^{\chi} &= \frac{1}{24}\Big(16h_1\nu_\chi\nu_{\tau\mu}\nu + 48h_2\nu_\chi\nu_{\tau\chi}\nu + 16h_1\nu_\mu\nu_{\tau\chi}\nu + 9h_1\nu\nu_{\tau\chi\chi\mu} + 12h_2\nu_{,\,\tau\chi\chi\chi}\nu - 24\nu_{\tau\tau}\nu \\
&\quad -6h_1\nu_\chi\nu_{\tau\chi\mu} - 9h_1\nu_\tau\nu_{\chi\chi\mu} + 3h_1\nu_{\chi\chi}\nu_{\tau\mu} + 6h_1\nu_{\tau\chi}\nu_{\chi\mu} - 3h_1\nu_\mu\nu_{\tau\chi\chi} - 48h_2\nu_\tau{\nu_\chi}^2 \\
&\quad -12h_2\nu_\tau\nu_{\chi\chi\chi} + 12h_2\nu_{\chi\chi}\nu_{\tau\chi} + 24{\nu_\tau}^2 - 32h_1\nu_\tau\nu_\chi\nu_\mu - 12h_2\nu_{\,\chi}\nu_{\tau\chi\chi}\Big), \\
T_5^{\mu} &= \frac{1}{24}\Big(16h_1\nu_\chi\nu_{\tau\chi}\nu + 3h_1\nu_{\tau\chi\chi\chi}\nu - 16h_1\nu_\tau{\nu_\chi}^2 - 3h_1\nu_\chi\nu_{\tau\chi\chi} - 3h_1\nu_\tau\nu_{,\,\chi\chi\chi} + 3h_1\nu_{\chi\chi}\nu_{\tau\chi}\Big);
\end{aligned}
$$

$$
\begin{aligned}
T_6^{\tau} &= \frac{1}{h_1^2}\Big(2f(\tau)h_1^2{\nu_{,\,\chi}}^3 + 4\mu h_1 f'(\tau){\nu_\chi}^2 + 8\mu^2 f''(\tau)\nu_\chi - 4f(\tau)h_1^2\nu\nu_{\chi\chi}\nu_\chi + f(\tau)h_1^2\nu_{\chi\chi\chi}\nu_\chi \\
&\quad -f(\tau)h_1^2\nu\nu_{\chi\chi\chi\chi} - 4\mu h_1\nu f'(\tau)\nu_{\chi\chi}\Big), \\
T_6^{\chi} &= \frac{1}{24h_1^2}\Big(-108f(\tau)h_1^2h_2{\nu_\chi}^4 - 192\mu h_1h_2f'(\tau){\nu_\chi}^3 - 72f(\tau)h_1^3\nu_\mu{\nu_\chi}^3 + 16h_1^2\nu f'(\tau){\nu_\chi}^2 \\
&\quad -128\mu h_1^2f'(\tau)\nu_\mu{\nu_\chi}^2 - 72f(\tau)h_1^3\nu\nu_{\chi\mu}{\nu_\chi}^2 - 10f(\tau)h_1^3\nu_{\chi\chi\mu}{\nu_\chi}^2 - 72f(\tau)h_1^2h_2\nu_{\chi\chi\chi}{\nu_\chi}^2 \\
&\quad -192\mu^2h_1f''(\tau)\nu_\mu\nu_\chi - 64\mu h_1^2\nu f'(\tau)\nu_{\chi\mu}\nu_\chi - 12h_1^2f'(\tau)\nu_{\chi\chi}\nu_\chi + 28f(\tau)h_1^3\nu_{\chi\mu}\nu_{\chi\chi}\nu_\chi \\
&\quad -28f(\tau)h_1^3\nu_\mu\nu_{\chi\chi\chi}\nu_\chi - 28f(\tau)h_1^3\nu\nu_{\chi\chi\chi\mu}\nu_\chi + 6f(\tau)h_1^3\nu_{\chi\chi\chi\chi\mu}\nu_\chi + 96\mu h_1f'(\tau)\nu_\tau\nu_\chi \\
&\quad -48f(\tau)h_1^2\nu_{\tau\chi\chi}\nu_\chi + 48\mu h_1h_2f'(\tau){\nu_{\chi\chi}}^2 - 28f(\tau)h_1^3\nu_\mu{\nu_{\chi\chi}}^2 - 12f(\tau)h_1^2h_2{\nu_{\chi\chi\chi}}^2 \\
&\quad +36\mu h_1^2f'(\tau)\nu_{\chi\mu}\nu_{\chi\chi} - 72\mu^2h_1f''(\tau)\nu_{\chi\chi\mu} - 8f(\tau)h_1^3\nu\nu_{\chi\chi}\nu_{\chi\chi\mu} + 12h_1^2\nu f'(\tau)\nu_{\chi\chi\chi} \\
&\quad -28f(\tau)h_1^3\nu\nu_{\chi\mu}\nu_{\chi\chi\chi} - 9f(\tau)h_1^3\nu_{\chi\chi\mu}\nu_{\chi\chi\chi} - 12\mu h_1^2\nu f'(\tau)\nu_{\chi\chi\chi\mu} - 9f(\tau)h_1^3\nu_{\chi\chi}\nu_{\chi\chi\chi\mu} \\
&\quad -3f(\tau)h_1^3\nu_\mu\nu_{\chi\chi\chi\chi\chi} - 3f(\tau)h_1^3\nu\nu_{\chi\chi\chi\chi\chi\mu} + 192\mu^2f''(\tau)\nu_\tau + 24f(\tau)h_1^2\nu_{\chi\chi\chi}\nu_\tau \\
&\quad +24f(\tau)h_1^2\nu\nu_{\tau\chi\chi\chi} - 96\mu h_1h_2f'(\tau)\nu_{\chi\chi\chi}\nu_\chi + 96\mu h_1\nu f''(\tau)\nu_\chi + 48f(\tau)h_1^2\nu_{\chi\chi}\nu_{\tau\chi} \\
&\quad +48\mu h_1f''(\tau)\nu_{\chi\chi} - 288\mu^2h_2f''(\tau){\nu_\chi}^2 + 48f(\tau)h_1^2\nu_\tau{\nu_\chi}^2 - 60\mu h_1^2f'(\tau)\nu_{\chi\chi\mu}\nu_\chi \\
&\quad -12\mu h_1^2f'(\tau)\nu_\mu\nu_{\chi\chi\chi} + 96\mu h_1\nu f'(\tau)\nu_{\tau\chi} + 96f(\tau)h_1^2\nu\nu_{\tau\chi}\nu_\chi - 192\mu^2\nu f'''(\tau) \\
&\quad -96\mu^2h_2f''(\tau)\nu_{\,\chi\chi\chi} + 6f(\tau)h_1^3\nu_{\chi\mu}\nu_{\chi\chi\chi\chi}\Big), \\
T_6^{\mu} &= \frac{1}{24h_1}\Big(-36f(\tau)h_1^2{\nu_\chi}^4 - 64\mu h_1f'(\tau){\nu_\chi}^3 - 96\mu^2f''(\tau){\nu_\chi}^2 + 72f(\tau)h_1^2\nu\nu_{\chi\chi}{\nu_\chi}^2 \\
&\quad -34f(\tau)h_1^2\nu_{\chi\chi\chi}{\nu_\chi}^2 - 24\mu h_1f'(\tau)\nu_{\chi\chi\chi}\nu_\chi + 28f(\tau)h_1^2\nu\nu_{\chi\chi\chi\chi}\nu_\chi - 3f(\tau)h_1^2\nu_{\chi\chi\chi\chi\chi}\nu_{,\,\chi} \\
&\quad +12\mu h_1f'(\tau){\nu_{\chi\chi}}^2 - 3f(\tau)h_1^2{\nu_{\chi\chi\chi}}^2 + 64\mu h_1\nu f'(\tau)\nu_{\chi\chi}\nu_\chi + 3f(\tau)h_1^2\nu\nu_{\chi\chi\chi\chi\chi\chi} \\
&\quad -24\mu^2f''(\tau)\nu_{\chi\chi\chi} + 36f(\tau)h_1^2\nu\nu_{\chi\chi}\nu_{\chi\chi\chi} + 12\mu h_1\nu f'(\tau)\nu_{\chi\chi\chi\chi} + 3f(\tau)h_1^2\nu_{\chi\chi}\nu_{\chi\chi\chi\chi}\Big);
\end{aligned}
$$

$$
T_7^{\tau} = \frac{-h_1r(\tau)\nu_{\chi\chi}\nu + h_1r(\tau){\nu_\chi}^2 + 4\mu r'(\tau)\nu_\chi}{h_1},
$$

$$
\begin{aligned}
T_7^{\chi} &= \frac{1}{24h_1}\Big(24h_1r'(\tau)v_{\chi}v - 16h_1^2r(\tau)v_{\chi}v_{\chi\mu}v - 3h_1^2r(\tau)v_{\chi\chi\chi\mu}v + 24h_1r(\tau)v_{\tau\chi}v - 96\mu r''(\tau)v \\
&\quad -96h_1\mu r'(\tau)v_{\chi}v_{\mu} - 36h_1\mu r'(\tau)v_{\chi\chi\mu} - 48h_2\mu r'(\tau)v_{\chi\chi\chi} + 12h_1r'(tau)v_{\chi\chi} - 32h_1^2r(\tau){v_{\chi}}^2v_{\mu} \\
&\quad -48h_1h_2r(\tau){v_{\chi}}^3 - 24h_1h_2r(\tau)v_{\chi\chi\chi}v_{\chi} + 24h_1r(\tau)v_{\tau}v_{\chi} + 12h_1h_2r(\tau){v_{\chi\chi}}^2 + 96\mu r'(\tau)v_{\tau} \\
&\quad +9h_1^2r(\tau)v_{\chi\chi}v_{\chi\mu} - 144h_2\mu r'(\tau){v_{\chi}}^2 - 15h_1^2r(\tau)v_{\chi}v_{\chi\chi\mu} - 3h_1^2r(\tau)v_{\chi\chi\chi}v_{\mu}\Big),
\end{aligned}
$$

$$
\begin{aligned}
T_7^{\mu} &= \frac{1}{24}\Big(16h_1r(\tau)v_{\chi\chi}v_{\chi}v + 3h_1r(\tau)v_{\chi\chi\chi\chi}v - 16h_1r(\tau){v_{\chi}}^3 - 6h_1r(\tau)v_{\chi\chi\chi}v_{\chi} + 3h_1r(\tau){v_{\chi\chi}}^2 \\
&\quad -48\mu r'(\tau){v_{\chi}}^2 - 12\mu r'(\tau)v_{\chi\chi\chi}\Big);
\end{aligned}
$$

$$
\begin{aligned}
T_8^{\tau} &= 2g(\tau)v_{\chi}, \\
T_8^{\chi} &= \frac{1}{4}\left(-8g'(\tau)v - 8h_1g(\tau)v_{\chi}v_{\mu} - 3h_1g(\tau)v_{\chi\chi\mu} - 12h_2g(\tau){v_{\chi}}^2 - 4h_2g(\tau)v_{\chi\chi\chi} + 8g(\tau)v_{\tau}\right), \\
T_8^{\mu} &= \frac{1}{4}\left(-4h_1g(\tau){v_{\chi}}^2 - h_1g(\tau)v_{\chi\chi\chi}\right);
\end{aligned}
$$

Physical principles such as the conservation of energy, mass, and momentum are mathematically formulated as conservation laws. These laws are fundamental for the analysis and simplification of partial differential equations. The laws of conservation of momentum, energy, and angular momentum are originally derived from classical mechanics. However, these conservation laws hold true and are preserved in both relativistic mechanics and quantum mechanics. As a result, they transcend classical mechanics and stand as some of the most fundamental and universally valid principles in physics. Conservation laws have been extensively employed in investigating the existence, uniqueness, and stability of solutions to nonlinear partial differential equations, as well as in the development of numerical methods for these equations. It is important to recognize that an infinite number of conservation laws can be derived, given that the multiplier involves an arbitrary function.

6. CONCLUDING REMARKS

Eight symmetries were found when we calculated the Lie point symmetries of the modified (2+1)-dimensional KdV-Calogero Bogoyavlenkskii-Schiff equation. We performed group invariant solutions and symmetry reductions. After that, we obtained one-wave and two-wave solutions using the multiple exp-function approach. Lastly, we used the multiplier approach to derive the conserved currents. In the future, the modified (2+1)-dimensional KdV-Calogero Bogoyavlenkskii-Schiff equation can be solved more precisely using conserved currents.

ORCID

Sivenathi O. Mbusi, https://orcid.org/0000-0002-7656-625X; **Abdullahi R. Adem**, https://orcid.org/0000-0002-3319-9971; **Ben Muatjetjeja**, https://orcid.org/0000-0002-1586-7307; **Mohammed E. M. Alngar**, https://orcid.org/0000-0002-5436-7268; **Husham M. Ahmed**, https://orcid.org/0000-0001-7610-7160; **Anjan Biswas**, https://orcid.org/0000-0002-8131-6044

REFERENCES

[1] H. Aljarrah, M. Alaroud, A. Ishak, M. Darus, S. Al-Omari, and M. Khandaqji, "Laplace fractional residual power series scheme for Caputo time-Schrodinger fractional equations," Progress in Fractional Differentiation and Applications, **11**, 177–198 (2025). https://doi.org/10.18576/pfda/110113

[2] A. Burqan, M. Khandaqji, Z. Al-Zhour, A. El-Ajou, and T. Alrahamneh. "Analytical approximate solutions of Caputo fractional KdV-Burgers equations using Laplace residual power series technique," Journal of Applied Mathematics, **2024**, 7835548 (2024). https://doi.org/10.1155/2024/7835548

[3] A.S. Heilat, "A comparison between Euler's method and 4-th order Runge– Kutta method for numerical solutions of neutrosophic and dual differential problems," Neutrosophic Sets and Systems, 81, 1 (2025).

[4] O. Alsayyed, A. Hioual, G. M. Gharib, M. Abualhomos, H. Al-Tarawneh, H. Al-Tarawneh, M. S. Alsauodi, *et al.*, "On stability of a fractional discrete reactiondiffusion epidemic model," Fractal and Fractional, **7**, 729 (2023). https://doi.org/10.3390/fractalfract7100729

[5] I. Al-Shbeil, A. A. Abubaker, S. A. Khalil, M. Alammari, M. Soueycatt, and A. Al-Husban, "A numerical study of neutrosophic finite difference method and some applications," International Journal of Neutrosophic Science, **27**, 36–42 (2026). https://doi.org/10.54216/IJNS.270104

[6] A.H. Arnous, A. Biswas, A.H. Kara, Y. Yldrm, L. Moraru, S. Moldovanu, P.L. Georgescu, and A.A. Alghamdi, "Dispersive optical solitons and conservation laws of Radhakrishnan-Kundu-Lakshmanan equation with dual-power law nonlinearity," Heliyon, **9**, 3 (2023). https://doi.org/10.1016/j.heliyon.2023.e14036

[7] E.M.E. Zayed, M.E.M. Alngar, R.M.A. Shohib, A. Biswas, Y. Yldrm, L. Moraru, S. Moldovanu, and P.L. Georgescu, "Dispersive optical solitons with differential group delay having multiplicative white noise by it calculus," Electronics (Switzerland), **12**, 3 (2023). https://doi.org/10.3390/electronics12030634

[8] G. Ma, J. Zhao, Q. Zhou, A. Biswas, and W. Liu, "Soliton interaction control through dispersion and nonlinear effects for the fifth-order nonlinear schrdinger equation," Nonlinear Dynamics, **106**(3), 2479–2484 (2021). https://doi.org/10.1007/s11071-021-06915-0

[9] Y. L. Ma, A. M. Wazwaz, and B. Q. Li, "A new (3+1)-dimensional Kadomtsev-Petviashvili equation and its integrability, multiple-solitons, breathers and lump waves," Mathematics and Computers in Simulation, **187**, 505–519 (2021). https://doi.org/10.1016/j.matcom.2021.03.012

[10] A. M. Wazwaz, and S. A. Khuri, "Two (3+1)-dimensional Schrödinger equations with cubic-quintic-septic nonlinearities: Bright and dark optical solitons," Optik, **235**, 666 (2021). https://doi.org/10.1016/j.ijleo.2021.166646

[11] V. Kumar, and A. M. Wazwaz, "Lie symmetry analysis for complex soliton solutions of coupled complex short pulse equation," Mathematical Methods in the Applied Sciences, **44**(7), 5238-5250 (2021). https://doi.org/10.1002/mma.7105

[12] G. Wang, and A. M. Wazwaz, "Perturbation, symmetry analysis, B¨acklund and reciprocal transformation for the extended Boussinesq equation in fluid mechanics," Communications in Theoretical Physics, **73**, 045003 (2021). https://doi.org/10.1088/1572-9494/abe03a

[13] S. Malik, H. Almusawa, S. Kumar, A. M. Wazwaz, and M. S. Osman, "A (2+1)-dimensional Kadomtsev-Petviashvili equation with competing dispersion effect: Painleve analysis, dynamical behavior and invariant solutions," Results in Physics, **23**, 104043 (2021). https://doi.org/10.1016/j.rinp.2021.104043

[14] S. A. Khuri, and A. M. Wazwaz, "Soliton solutions through optical fibers for quadratic-cubic nonlinear medium: A complex ansätze approach," Optik, **229**, 166646 (2021). https://doi.org/10.1016/j.ijleo.2021.166268

[15] A. Ghorbani, and A. M. Wazwaz, "A multiple variational iteration method for nonlinear two–point boundary value problems with nonlinear conditions. International Journal of Computational Methods, **18**(1), 2050028 (2022). https://doi.org/10.1142/s0219876220500280

[16] J. G. Liu, and A. M. Wazwaz, "Breather wave and lump–type solutions of new (3 + 1)-dimensional Boiti-Leon-Manna-Pempinelli equation in incompressible fluid," Mathematical Methods in the Applied Sciences, **44**, 2200–2208 (2021). https://doi.org/10.1002/mma.6931

[17] A. M. Wazwaz, "A new (3+1)-dimensional Painleve-integrable Sakovich equation: multiple soliton solutions," International Journal of Numerical Methods for Heat and Fluid Flow, **31**(9), 3030–3035 (2021). https://doi.org/10.1108/hff-11-2020-0687

[18] A. M. Wazwaz, "Bright and dark optical solitons for (3+1)-dimensional Schrödinger equation with cubic-quintic-septic nonlinearities," Optik, **225**, 165752 (2021). https://doi.org/10.1016/j.ijleo.2020.165752

[19] A. M. Wazwaz, "On integrability of an extended Bogoyavlenskii–Kadomtsev–Petviashvili equation: Multiple soliton solutions," International Journal of Numerical Modelling: Electronic Networks, Devices and Fields, **34**, (2021). https://doi.org/10.1002/jnm.2817

[20] A. M. Wazwaz, "A variety of multiple-soliton solutions for the integrable (4+1)-dimensional Fokas equation," Waves in Random and Complex Media, **31**, 46–56 (2021), https://doi.org/10.1080/17455030.2018.1560515

[21] L. Kaur, and A. M. Wazwaz, "Einstein's vacuum field equation: Painleve analysis and Lie symmetries," Waves in Random and Complex Media, **31**, 199–206 (2021). https://doi.org/10.1080/17455030.2019.1574410

[22] Y. L. Ma, A. M. Wazwaz, and B. Q. Li, "New extended Kadomtsev-Petviashvili equation: multiple soliton solutions, breather, lump and interaction solutions," Nonlinear Dynamics, 104, 1–14 (2021). https://doi.org/10.1007/s11071-021-06357-8

[23] A. S. Rashed, S. M. Mabrouk, and A. M. Wazwaz, "Unsteady three–dimensional laminar flow over a submerged plate in electrically conducting fluid with applied magnetic field," Waves in Random and Complex Media, **33**, 1–20 (2021). https://doi.org/10.1080/17455030.2021.1883147

[24] R. Saleh, S. M. Mabrouk, and A. M. Wazwaz, "Lie symmetry analysis of a stochastic gene evolution in double-chain deoxyribonucleic acid system," Waves in Random and Complex Media, **32**, 1–15 (2021). https://doi.org/10.1080/17455030.2020.1871109

[25] S. Noeiaghdam, D. Sidorov, A. M. Wazwaz, N. Sidorov, and V. Sizikov, "The numerical validation of the adomian decomposition method for solving volterra integral equation with discontinuous kernels using the CESTAC method," Mathematics, **9**, 1–15 (2021). https://doi.org/10.3390/math9030260

[26] W. X. Ma, X. Yong, and X. Lü, "Soliton solutions to the B-type Kadomtsev-Petviashvili equation under general dispersion relations," Wave Motion, **103**, 102719 (2021). https://doi.org/10.1016/j.wavemoti.2021.102719

[27] S. J. Chen, X. Lü, and X. F. Tang, "Novel evolutionary behaviors of the mixed solutions to a generalized Burgers equation with variable coefficients," Communications in Nonlinear Science and Numerical Simulation, **95**, 105628 (2021). https://doi.org/10.1016/j.cnsns.2020.105628

[28] X. Lü, Y. F. Hua, S. J. Chen, and X. F. Tang, "Integrability characteristics of a novel (2+1)-dimensional nonlinear model: Painleve analysis, soliton solutions, Bäcklund transformation, Lax pair and infinitely many conservation laws," Communications in Nonlinear Science and Numerical Simulation," **95**, 105612 (2021). https://doi.org/10.1016/j.cnsns.2020.105612

[29] X. J. He, X. Lü, and M. G. Li, "Bäcklund transformation, Pfaffian, Wronskian and Grammian solutions to the (3+1)-dimensional generalized Kadomtsev-Petviashvili equation. Analysis and Mathematical Physics, **11**, 4 (2021). https://doi.org/10.1007/s13324-020-00414-y

[30] C. C. Zhou, X. Lü, and H. T. Xu, "Symbolic computation study on exact solutions to a generalized (3+1)-dimensional Kadomtsev-Petviashvili-type equation," Modern Physics Letters B, **35**, 2150116 (2021). https://doi.org/10.1142/s0217984921501165

[31] W. T. Huang, C. C. Zhou, X. Lü, and J. P. Wang, "Dispersive optical solitons for the Schrödinger-Hirota equation in optical fibers," Modern Physics Letters B, **35**, 2150060 (2021). https://doi.org/10.1142/s0217984921500603

[32] X. Lü and S. J. Chen, "Interaction solutions to nonlinear partial differential equations via Hirota bilinear forms: one–lump–multi–stripe and one-lump-multi-soliton types," Nonlinear Dynamics, **103**, 947–977 (2021). https://doi.org/10.1007/s11071-020-06068-6

[33] Y. H. Yin, S. J. Chen, and X. Lü, "Localized characteristics of lump and interaction solutions to two extended Jimbo-Miwa equations," Chinese Physics B, 29, 120502 (2020). https://doi.org/10.1088/1674-1056/aba9c4

[34] F. Liu, C. C. Zhou, X. Lü, and H. Xu, "Dynamic behaviors of optical solitons for Fokas-Lenells equation in optical fiber," Optik, **224**, 165237 (2020). https://doi.org/10.1016/j.ijleo.2020.165237

[35] J. W. Xia, Y. W. Zhao, and X. Lü, "Predictability, fast calculation and simulation for the interaction solutions to the cylindrical Kadomtsev-Petviashvili equation," Communications in Nonlinear Science and Numerical Simulation, **90**, 105260 (2020). https://doi.org/10.1016/j.cnsns.2020.105260

[36] A. M. Wazwaz, "A study on KdV and Gardner equations with time-dependent coefficients and forcing terms," Appl. Math. Comput. **217**, 2277-2281 (2010). https://doi.org/10.1016/j.amc.2010.06.038

[37] X. Lü and M. Peng, "Systematic construction of infinitely many conservation laws for certain nonlinear evolution equations in mathematical physics," Commun. Nonlinear Sci. Numer. Simul. **18**, 2304-2312 (2013). https://doi.org/10.1016/j.cnsns.2012.11.006

[38] D. J. Korteweg and G. de Vries, "On the change of form of long waves advancing in a rectangular canal, and on a new type of long stationary waves," Phil. Mag. **39**, 422-443 (1895). https://doi.org/10.1080/14786449508620739

[39] B. B. Kadomtsev and V. I. Petviashvili, "On the stability of solitary waves in weakly dispersive media," Sov. Phys. Dokl. 15, 539-541 (1970).

[40] G. Q. Xu, "Painleve analysis, lump-kink solutions and localized excitation solutions for the (3+1)-dimensional Boiti-Leon-Manna-Pempinelli equation," Appl. Math. Lett. **97**, 81-87 (2019). https://doi.org/10.1016/j.aml.2019.05.025

[41] J. G. Liu, Y. Tian, and J. G. Hu, "Painleve analysis, lump–kink solutions and localized excitation solutions for the (3+1)-dimensional Boiti-Leon-Manna-Pempinelli equation," Appl. Math. Lett. **79**, 162-168 (2018). https://doi.org/10.1016/j.aml.2017.12.011

[42] J. G. Liu, J. Q. Du, Z. F. Zeng, and B. Nie, "New three-wave solutions for the (3+1)-dimensional Boiti-Leon-Manna-Pempinelli equation," Nonlinear Dyn. **88**, 655-661 (2017). https://doi.org/10.1007/s11071-016-3267-2

[43] W. Q. Peng, S. F. Tian, and T. T. Zhang, "Breather waves and rational solutions in the (3+1)-dimensional Boiti-Leon-Manna-Pempinelli equation," Comput. Math. Appl. 77, 715-723 (2019). https://doi.org/10.1016/j.camwa.2018.10.008

[44] Q. Zhou and Q. Zhu, "Optical solitons in medium with parabolic law nonlinearity and higher order dispersion," Waves Random Complex Media, 25, 52-59 (2014). https://doi.org/10.1080/17455030.2014.956847

[45] Y. Li, and T. Chaolu, "Exact solutions for (2+1)-dimensional KdV-Calogero-Bogoyavlenkskii-Schiff equation via symbolic computation," Journal of Applied Mathematics and Physics, **8**, 197-209 (2020). https://doi.org/10.4236/jamp.2020.82015

[46] Y. Wang, and Y. Chen, "Binary Bell polynomial manipulations on the integrability of a generalized (2+1)-dimensional Korteweg-de Vries equation," Journal of Mathematical Analysis and Applications, **400**, 624-634 (2013). https://doi.org/10.1016/j.jmaa.2012.11.028

[47] K. Toda, and S. J. Yu, "The investigation into the Schwarz-Korteweg-de Vries equation and the Schwarz Derivative in (2 + 1)-dimensional," Journal of Mathematical Physics, **41**, 4747-4751 (2000). https://doi.org/10.1063/1.533374

[48] P. J. Olver, *Applications of Lie groups to differential equations*, (Springer-Verlag, New York, NY, USA, 1986).

[49] M. Alquran, I. Jaradat, and A. Yusuf, "Heart-cusp and bell-shaped-cusp optical solitons for an extended two-mode version of the complex Hirota model: application in optics," Optical and Quantum Electronics, **53**, 26 (2021). https://doi.org/10.1007/s11082-020-02674-1

[50] A. Yusuf, T. A. Sulaiman, E. M. Khalil, M. Bayram, and H. Ahmad, "Construction of multi-wave complexiton solutions of the Kadomtsev-Petviashvili equation via two efficient analyzing techniques," Results in Physics, **21**, 103775 (2021). https://doi.org/10.1016/j.rinp.2020.103775

[51] M. Alquran, F. Yousef, F. Alquran, T. A. Sulaiman, and A. Yusuf, "Dual-wave solutions for the quadratic-cubic conformable-Caputo time-fractional Klein-Fock-Gordon equation," Mathematics and Computers in Simulation, **185**, 62-76 (2021). https://doi.org/10.1016/j.matcom.2020.12.014

[52] W. X. Ma, T. Huang, and Y. Zhang, "A multiple exp-function method for nonlinear differential equations and its application," Physica Scripta, **82**, 065003 (2010). https://doi.org/10.1088/0031-8949/82/06/065003

[53] W. X. Ma, and Z. Zhu, "Solving the (3+1)-dimensional generalized KP and BKP equations by the multiple exp-function algorithm," Journal of Applied Mathematics and Computation, **218**, 11871-11879 (2012). https://doi.org/10.1016/j.amc.2012.05.049

[54] M. C. Sebogodi, B. Muatjetjeja, and A. R. Adem, "Traveling wave solutions and conservation laws of a generalized Chaffee-Infante equation in (1+3) dimensions," Universe, **9**, 224 (2023). https://doi.org/10.3390/universe9050224

[55] T. J. Podile, S. O. Mbusi, A. R. Adem, and B. Muatjetjeja, "Multiple exp-function solutions, group invariant solutions and conservation laws of a generalized (2+1)-dimensional Hirota-Satsuma-Ito equation," Malaysian Journal of Mathematical Sciences, **16**, 793-811 (2022). https://doi.org/10.47836/mjms.16.4.11

[56] S. O. Mbusi, A. R. Adem, and B. Muatjetjeja, "Lie symmetry analysis, multiple exp-function method and conservation laws for the (2+1)-dimensional Boussinesq equation," Optical and Quantum Electronics, 56, 670 (2024). https://doi.org/10.1007/s11082-024-06339-1

ОПИС МОДИФІКОВАНОГО (2+1)-ВИМІРНОГО РІВНЯННЯ KdV-КАЛОДЖЕРО БОГОЯВЛЕНСЬКОГО-ШИФФА У ХВИЛЯХ НА МІЛКОВОДДІ: АНАЛІЗ СИМЕТРІЇ ЛІ ТА ЗАКОНИ ЗБЕРЕЖЕННЯ

Сівенаті О. Мбусі[1], **Абдуллахі Р. Адем**[2], **Бен Муатджетжеджа**[1,3], **Мохаммед Е. М. Алнгар**[4], **Хушам М. Ахмед**[5], **Анджан Бісвас**[6,7,8,9]

[1]*Школа математичних та статистичних наук, Північно-Західний університет, Private Bag X1290, Потчефструм, 2520, Південна Африка*

[2]*Кафедра математичних наук, Університет Південної Африки, P.O. Скринька 392, Уніса, 0003, Південна Африка*

[3]*Кафедра математики, факультет природничих наук, Університет Ботсвани, Private Bag 22, Габороне, Ботсвана*

[4]*Програма математичної освіти, факультет освіти та мистецтв, Університет Сохар, 311, Сохар, Оман*

[5]*Інженерний коледж Технологічного університету, Бахрейн, Королівство Бахрейн*

[6]*Кафедра математики та фізики, Державний університет Грамблінга, Грамблінг, Луїзіана 71245-2715, США*

[7]*Кафедра математики, факультет природничих наук, Технічний університет Караденіз, Трабзон-61080, Туреччина*

[8]*Кафедра фізики та електроніки, Університет Хазар, Баку, Аризона-1096, Азербайджан*

[9]*Кафедра математики та прикладної математики, Сефако Макгатхо Університет медичних наук, Медунса-0204, Преторія, Південна Африка*

У цій роботі досліджується рівняння KdV-Калоджеро Богоявленського-Шиффа у модифікованих вимірах (2+1). Симетрії Лі створюються за допомогою аналізу групи Лі, а потім за допомогою цих симетрій знаходяться розв'язки подібності. Використовуючи метод множинних експоненційних функцій, отримано численні хвильові розв'язки. Крім того, ми використовуємо метод множників для вираження збережених струмів, що є важливим для розуміння природи нелінійних рівнянь, зокрема в інженерії та фізиці.

Ключові слова: *рівняння KdV-Калоджеро Богоявленського-Шиффа; збережені струми; аналіз методом групи Лі; метод множинних експоненційних функцій*

East European Journal of Physics. **2.** 79-87 (2026)
DOI:10.26565/2312-4334-2026-2-07 ISSN 2312-4334

EFFECTS OF NON-THERMAL ELECTRONS AND NON-EXTENSIVE POSITRONS ON SOLITARY WAVES IN A MULTI-COMPONENT DUSTY PLASMA

Satyendra Nath Barman[1], Kingkar Talukdar[2]*
[1]*B. Borooah College, Guwahati 781007, Assam, India*
[2]*Department of Mathematics, Gauhati University, Guwahati 781014, Assam, India*
**Corresponding Author email kingkartalukdar5@gmail.com*
Received March 2, 2026; Revised April 15, 2026; Accepted May 13, 2026

In this study, we have investigated the existence and characteristics of solitons in an unmagnetized dusty plasma composed of cold ions, negatively charged dust grains, positively charged dust grains, non-thermal electrons, and non-extensive positrons. The properties of solitons are usually studied through the Reductive Perturbation method and the Sagdeev Potential method. We have derived the energy integral equation using the Sagdeev Potential method. We have also discussed the variation of the Sagdeev potential for different values of the parameters involved in our plasma model. The non-extensive parameter (q), the non-thermal parameter (β), charge density ratio of positively charged dust (δ_+), charge density ratio of negatively charged dust (δ_-), positron to ion density ratio (δ_p), electron to ion density ratio (δ_e), electron to positron temperature ratio (σ_p) and the Mach number (M) found to influence the amplitude of solitons. Our study reveals that non-thermality of electrons and non-extensivity of positrons significantly modify the soliton features. The results from our study can be useful for investigating plasma in space environments such as cometary tails and interstellar clouds.
Keywords: *Non-thermal; Solitary waves; Sagdeev potential; Energy integral; Dusty plasma*
PACS: 95.30.Qd, 05.45.Yv, 52.35.Fp, 05.10.−a, 52.35.Mw

1. INTRODUCTION

Unmagnetized plasma is vital in studying astrophysical phenomena, such as solar winds, cometary tails, interstellar clouds and also in industrial applications like plasma processing, etching, and coating. Several studies have been conducted on unmagnetized plasma in recent years [1-17]. The presence of dust grains in unmagnetized plasma transforms it from a simple ionized gas into a complex plasma. In unmagnetized state, the physics is driven entirely by the local electric environment and the inertia of the dust, rather than being forced along magnetic field lines. Dust grains in plasma are essential for understanding astrophysical phenomena, including the formation of celestial bodies in protoplanetary disks, the structure of planetary rings (e.g., Saturn's rings), and also the behaviour in comet tails. Dust particles in plasma transform standard electron-ion plasma into a complex system that acts as a model for atomic structures, creating plasma crystals. Presence of dust grains can affect the soliton amplitude and Mach number for both compressive and rarefactive solitons [18].In some plasma model presence of positively charged dust grains results in existence of compressive solitons; however, the presence of negatively charged dust grains results in compressive solitons only up to a certain concentration of dust, and above the critical concentration of negative charge, the dusty plasma supports rarefactive solitons[19]. The effect of variable dust charge, dust temperature and trapped electrons on small-amplitude dust acoustic waves is investigated in [20].The presence of dust charge of immobile dust plays crucial role to form compressive and rarefactive solitons in plasma where the massive dust particles are in the stationary background of the plasma, and the lighter ions and relativistic electrons get appreciable initial drifts which makes great change in the growth of solitons[21]. The Dust-Ion-Acoustic (DIA) solitary waves are highly sensitive to the ion streaming speed and their amplitude decreases with an increase of the ion streaming speed [22]. In the presence of low dust charges and lower ion streaming, compressive and rarefactive solitons of either concave or convex characters reflect. The higher streaming of mobile dusts causes the amplitudes of rarefactive solitons characteristically change from higher to lower, showing convex character [23]. Dust grain density enhances the amplitude of solitary waves but weakens their reflection. In which, the amplitudes of both the incident and reflected solitons remain higher for fluctuating charge on the dust grains in comparison with the case of fixed charge [24]. In plasma physics, researchers often assume particles to follow a Maxwellian distribution; however, real-world plasmas often contain nonthermal electrons. These nonthermal electrons are high-energy particles that exist in the tail of the distribution. In unmagnetized plasmas, there is no external magnetic field to constrain particle motion, which indicates that non-thermal electrons are critical in unmagnetized plasma as they dominate the transport of energy and the stability of the system. The non-thermal electrons in unmagnetized plasma significantly alters the formation, behaviour, and structural characteristics of nonlinear waves and electrostatic structures, often departing from standard Maxwellian behaviour to model realistic space and laboratory scenarios. Large amplitude solitary structures significantly depend on various plasma parameters such as ion drift velocity, non-thermal parameter, electron to positron temperature ratio, positron density, and Mach number [25]. The presence of non-thermal electrons significantly modifies the parametric region where electron acoustic solitons can exist [26]. In some plasma model, increase of nonthermal parameter decreases the peak amplitude of solitons [27]. The solitary excitations also strongly depend on the mass and density ratios of the

Cite as: S.N. Barman, K. Talukdar, East Eur. J. Phys. 2, 79 (2026), https://doi.org/10.26565/2312-4334-2026-2-07

positive and negative ions as well as the nonthermal electron parameter [28]. When the non-thermality of hot electrons rises, the speed of electron beam decreases, the density ratio of the beam to the cold electron increases, and the existence domain for electron acoustics solitons gets bigger [29]. The presence of non-thermal electrons also significantly affects the existence of super solitons [30]. Increase in the non-thermal electron effects based on a Cairns (kappa) distribution has the effect of reducing (increasing) the width of the stopband [31]. Non-extensive positrons in unmagnetized plasma are important as they more accurately model particle distributions in systems characterized by long-range correlations and non-equilibrium states, where standard Maxwellian distributions fail. These non-extensive distributions, often described by the q-nonextensive or Tsallis statistics, significantly modify the fundamental characteristics of nonlinear waves. These non-extensive distributions also provide efficient modelling for observed particle populations in scenarios such as solar winds, planetary rings, cometary tails, and galactic clusters. Different values of the non-extensive parameter q show significant effect on chaotic motions of ion acoustic waves [32]. Ion-acoustic solitary wave can also depend on non-extensive parameter, electron to positron temperature ratio, ion to electron temperature ratio and streaming velocity. Fast ion-acoustic modes solely can produce the coexistence of small amplitude rarefactive solitons [33]. Particle non-extensivity can affect the properties of nonplanar ion-acoustic rarefactive and compressive solitons [34]. The non-extensive parameter, positron-to-electron density ratio, ion-to-electron temperature ratio, electron-to-positron temperature ratio and relativistic factor can significantly influence the phase shifts of solitary waves [35]. While solitons have been studied in various plasma configurations, their characteristics in a system featuring both positively and negatively charged dust grains, cold ions alongside non-extensive positrons and nonthermal electrons remain underexplored.

In this paper, we have represented the introduction in Section 1. The fluid equations (that govern our plasma model) and the standard energy integral equation is represented in section 2. Effects of several parameters on the characteristics of solitons are discussed in Section 3. Finally, we have concluded our research in Section 4.

2. EQUATIONS GOVERNING DYNAMICS OF PLASMA

We consider an unmagnetized plasma model composed of cold ions, positively charged dust grains, negatively charged dust grains, non-thermal electrons and non-extensive positrons. The equations governing dynamics of plasma are as follows:

For cold ions

$$\frac{\partial n_i}{\partial t} + \frac{\partial}{\partial x}(n_i u_i) = 0, \tag{1}$$

$$\frac{\partial u_i}{\partial t} + u_i \frac{\partial u_i}{\partial x} = -\frac{\partial \phi}{\partial x}. \tag{2}$$

For positively charged dust grains,

$$\frac{\partial n_{d+}}{\partial t} + \frac{\partial}{\partial x}(n_{d+} u_{d+}) = 0, \tag{3}$$

$$\frac{\partial u_{d+}}{\partial t} + u_{d+} \frac{\partial u_{d+}}{\partial x} = -\mu_{d+} \frac{\partial \phi}{\partial x}. \tag{4}$$

For negatively charged dust grains,

$$\frac{\partial n_{d-}}{\partial t} + \frac{\partial}{\partial x}(n_{d-} u_{d-}) = 0, \tag{5}$$

$$\frac{\partial u_{d-}}{\partial t} + u_{d-} \frac{\partial u_{d-}}{\partial x} = \mu_{d-} \frac{\partial \phi}{\partial x}. \tag{6}$$

Here, $\mu_{d+} = \frac{Z_{d+} m_i}{m_{d+}}$ and $\mu_{d-} = \frac{Z_{d-} m_i}{m_{d-}}$, where Z_{d+} and Z_{d-} are positive and negative dust charge number respectively, and m_i, m_{d+} and m_{d-} are the mass of ion, mass of positively charged dust grain and mass of negatively charged dust grain respectively.

Following the procedure in [36], the non-thermal electron's number density is obtained over velocity space with dimensionless potential ϕ as,

$$n_e = (1 - \beta\phi + \beta\phi^2) e^{\phi}. \tag{7}$$

Here, $\beta = \frac{4\alpha}{1+3\alpha}$ represents the non-thermality, where α determines the non-thermal electrons in the non- thermal plasma model. The parameter α determines the population of dynamic nonthermal electrons in the nonthermal plasma model.

In many space and laboratory plasmas, the distribution of particles does not follow the usual Boltzmann–Gibbs statistics which is an efficient tool for investigating the system when the memories and microscopic interactions are short ranged. The generalization of Boltzmann–Gibbs–Shannan (BGS) entropy for statistical equilibrium with long-range interactions, long-time memories, and dissipation is noted by Renyi [38] and Tsallis [39]. For two independent systems α and β the rule of composition can be written as $S_q(\alpha + \beta) = S_q(\alpha) + S_q(\beta) + (1 - q)S_q(\alpha) + S_q(\beta), q \neq 1$ where the parameters show the grade of correlation of the system under consideration.

The non-extensive distribution function for positrons can be obtained as,

$$f_p(q) = C_q\left[1-(q-1)\left(\frac{m_p u^2}{k_B T_p}+\frac{Q_p\phi}{k_B T_p}\right)\right]^{\frac{1}{q-1}}.$$

Where:

$C_q = \frac{n_{p_0}\Gamma\left(\frac{1}{1-q}\right)}{\Gamma\left(\frac{1}{1-q}-\frac{1}{2}\right)}\sqrt{\frac{m_p(1-q)}{2\pi T_p}}$, $-1 < q < 1$, and, $C_q = n_{p_0}\left(\frac{1+q}{2}\right)\frac{\Gamma\left(\frac{1}{1-q}+\frac{1}{2}\right)}{\Gamma\left(\frac{1}{1-q}\right)}\sqrt{\frac{m_p(1-q)}{2\pi T_p}}$, $q > 1$.

Where, C_q is the normalization constant and Γ represents gamma function. The normalized positron number density can be given by [40],

$$n_p = (1-(q-1)\sigma_p\phi)^{\frac{q+1}{2(q-1)}}. \tag{8}$$

Equation (8) can be written as

$$n_p = 1-\sigma_p\frac{(q+1)}{2}\phi. \tag{9}$$

Where, $\sigma_p = \frac{T_e}{T_p}$ is the electron to positron temperature ratio and q represents the non-extensive strength. Extensivity, sub extensivity and super extensivity are represented by q =1, q >1 and q < 1 respectively.
The normalized Poisson equation can be written as,

$$\frac{\partial^2\phi}{\partial x^2} = \delta_e n_e - \delta_p n_p + \delta_- n_{d-} - \delta_+ n_{d+} - n_i. \tag{10}$$

The Charge neutrality condition is, $\delta_e + \delta_- = 1 + \delta_+ + \delta_p$

Here, $\delta_e = \frac{n_{e_0}}{n_{i_0}}$, $\delta_p = \frac{n_{p_0}}{n_{i_0}}$ are the equilibrium electron-to-ion density ratio and the equilibrium positron-to-ion density ratio respectively. Also, $\delta_+ = \frac{Z_{d+}n_{d+0}}{n_{i_0}}$ and $\delta_- = \frac{Z_{d-}n_{d-0}}{n_{i_0}}$ are the equilibrium charge density ratio of positively charged dust and negatively charged dust respectively. The number density of ions, positively charged dust grains, negatively charged dust grains, non-thermal electrons and non-extensive positrons are represented by n_i, n_{d+}, n_{d-} n_e and n_p respectively. The number densities are normalized by the equilibrium density of ion n_{i_0}.

The fluid velocity of ion, positively charged dust grains and negatively charged dust grains are represented by u_i, u_{d+} and u_{d-} respectively, which are normalized by the ion acoustic speed $c_i = \sqrt{\frac{k_B T_e}{m_i}}$ and the electrostatic potential ϕ is normalized by $\frac{k_B T_e}{e}$, where, T_e, k_B, m_i and e represents electron temperature, Boltzmann's constant, ion mass and electronic charge respectively. The time and space variables are normalized by the inverse of the ion plasma frequency ${\omega_{pi}}^{-1} = \sqrt{\frac{m_i}{4\pi e^2 n_{i_0}}}$ and Debye length $\lambda_D = \sqrt{\frac{k_B T_e}{4\pi e^2 n_{i_0}}}$ respectively.

We consider a variable $\xi = x - Mt$ (where, M represents the Mach number), that influences all the dependent variables in the nonlinear equations to employ the Sagdeev potential (pseudopotential) method.

Applying the boundary conditions $\xi \to \pm\infty$, $n_i \to 1$, $n_{d+} \to 1$, $n_{d-} \to 1$, $u_i \to 0$, $u_{d+} \to 0$, $u_{d-} \to 0$, $\phi \to 0$, we obtain the overall solution for n_i, n_{d+} and n_{d-}as,

$$n_i = \left(1-\frac{2\phi}{M^2}\right)^{-\frac{1}{2}}, \tag{11}$$

$$n_{d+} = \left(1-\frac{2\mu_{d+}\phi}{M^2}\right)^{-\frac{1}{2}}, \tag{12}$$

$$n_{d-} = \left(1+\frac{2\mu_{d-}\phi}{M^2}\right)^{-\frac{1}{2}}. \tag{13}$$

Applying the fundamental densities from the equations (7), (9), (11), (12) and (13) into the equation (10) and then multiplying $\frac{d\phi}{d\xi}$, we get the standard energy integral equation as,

$$\frac{1}{2}\left(\frac{d\phi}{d\xi}\right)^2 + V(\phi) = 0. \tag{14}$$

Here, $V(\phi)$ represents the Sagdeev Potential in the energy integral equation (14). The $V(\phi)$ is given by,

$$V(\phi) = -M^2\left[\sqrt{1-\frac{2\phi}{M^2}}-1\right] - \frac{\delta_+ M^2}{\mu_{d+}}\left[\sqrt{1-\frac{2\mu_{d+}\phi}{M^2}}-1\right] - \frac{\delta_- M^2}{\mu_{d-}}\left[\sqrt{1+\frac{2\mu_{d-}\phi}{M^2}}-1\right] -$$
$$\delta_e\left((1+3\beta-3\beta\phi+\beta\phi^2)e^{\phi}-(1+3\beta)\right) + \delta_p\left(\phi-\frac{q+1}{4}\sigma_p\phi^2\right) \tag{15}$$

For a localized solution of equation (14) to exist, certain requirements must be satisfied [37]. It is clear that, for $\phi = 0$, the fixed point at the origin is unstable since $V(\phi) = 0$, $\frac{dV(\phi)}{d\phi} = 0$ and $\frac{d^2V(\phi)}{d\phi^2} < 0$. All the requirements are found to be met. Again, $V(\phi) < 0$ must be satisfied between $\phi = 0$ and $\phi = \phi_m$, where ϕ_m represents the maximum (or minimum) value of ϕ for which $V(\phi_m) = 0$.

The condition, $\frac{d^2V(\phi)}{d\phi^2} < 0$ at $\phi = 0$ gives the lower limit of Mach number (M_{min}) as,

$$M_{min} = \sqrt{\frac{1 + \delta_+\mu_{d+} + \delta_-\mu_{d-}}{\delta_e(1-\beta) + \frac{1}{2}\delta_p\sigma_p(q+1)}}$$

The Mach number must satisfy $M > M_{min}$ for the solitary waves to exist.

From equation (11) we observe that for n_i to be real we must have $M^2 \geq 2\phi$. Thus, the extreme value of ϕ is,

$$\phi_m = \phi_0 = \frac{M^2}{2} \tag{16}$$

Substituting the extreme value of ϕ from equation (16) in (15) we get the M upper limit as $V(\phi) \geq 0$, which gives,

$$M^2 - \frac{\delta_+ M^2}{\mu_{d+}}\left[\sqrt{1-\mu_{d+}} - 1\right] - \frac{\delta_- M^2}{\mu_{d-}}\left[\sqrt{1+\mu_{d-}} - 1\right] - \delta_e\left[\left(1 + 3\beta - \frac{3}{2}\beta M^2 + \frac{1}{4}\beta M^4\right)e^{\frac{M^2}{2}} - (1+3\beta)\right] + \delta_p\left[\frac{M^2}{2} - \frac{q+1}{16}\sigma_p M^4\right] \geq 0$$

It is also crucial to investigate the profiles of solitary waves when their amplitudes are no longer arbitrary but small. To study small amplitude solitary waves, the Sagdeev Potential V(φ) can be Taylor expanded about φ=0 up to a reasonable order of φ so as to obtain a soliton solution from the energy integral equation.

Therefore, equation (14) can be reduced to,

$$\frac{1}{2}\left(\frac{d\phi}{d\xi}\right)^2 + A\phi^2 + B\phi^3 = 0, \tag{17}$$

where

$$A = \frac{\delta_+\mu_{d+}}{2M^2} + \frac{\delta_-\mu_{d-}}{2M^2} + \frac{\beta\delta_e}{2} - \frac{\delta_e}{2} + \frac{1}{2M^2} - \frac{\delta_p\sigma_p(q+1)}{4}$$

$$B = \frac{\delta_+{\mu_{d+}}^2}{2M^4} - \frac{\delta_-{\mu_{d-}}^2}{2M^4} - \frac{\delta_e}{6} + \frac{1}{2M^4}$$

Integrating equation (17) and using the boundary conditions stated before, we obtain the soliton solution as,

$$\phi = \phi_m sech^2\left(\frac{\xi}{w}\right)$$

where, $\phi_m = -\frac{A}{B}$ and $w = \sqrt{-\frac{2}{A}}$ represents the amplitude and width of the soliton, respectively.

3. RESULTS AND DISCUSSION

The existence, structure, and characteristics of large-amplitude nonlinear waves, particularly solitary waves, can be analyzed by using the Sagdeev Potential method. Figure 1 shows the variation of the Sagdeev Potential for different values of the Mach number (M) and fixed μ_{d+}=0.0000748, μ_{d-}=0.0000778, δ_+=0.38, δ_-=0.7, δ_e=0.8, β =0.15, δ_p =0.12, σ_p=0.2, q=0.5. Figure 1 shows that as the Mach number (M) increases, depth of the Sagdeev potential well increases. Therefore, as M increases, the nonlinear effects in the plasma become more dominant over dispersive effects. This leads to an increase in the maximum amplitude of the electrostatic potential, which directly corresponds to a deeper and wider Sagdeev potential well.

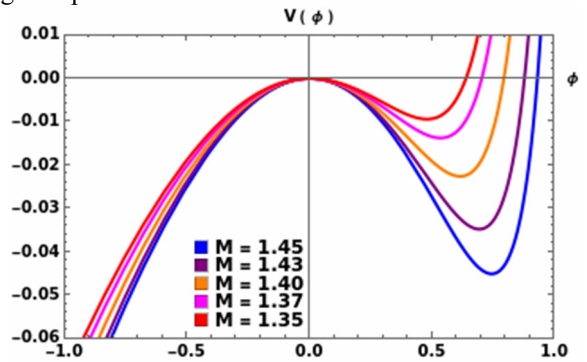

Figure 1. Variation of Sagdeev Potential V(ϕ) with respect to ϕ for different values of M

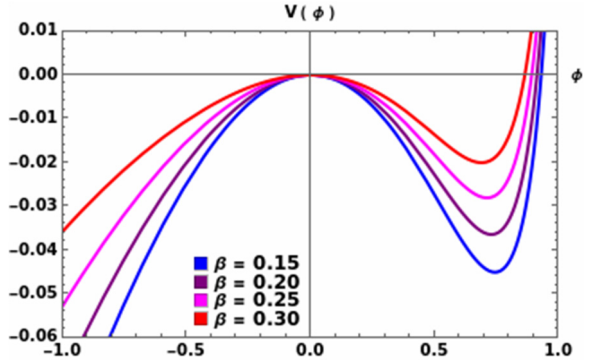

Figure 2. Variation of Sagdeev Potential V(ϕ) with respect to ϕ for different values of β

Figure 2 shows the variation of the Sagdeev Potential for different values of non-thermal parameter β and fixed μ_{d+}=0.0000748, μ_{d-}=0.0000778, δ_{+}=0.38, δ_{-}=0.7, δ_e =0.8, δ_p =0.12, σ_p=0.2, M=1.45, q=0.5. Figure 2 shows that as the nonthermal electron parameter (β) increases, the depth of the Sagdeev potential well decreases. Therefore, as the nonthermal parameter β increases, the increased population of high-energy electrons enhances the plasma's dispersion and weakens the nonlinear forces. This results in the formation of smaller-amplitude, broader solitary waves, represented by a shallower potential well.

Figure 3 shows the variation of the Sagdeev Potential for different values of the non-extensive parameter q and fixed μ_{d+}=0.0000748, μ_{d-}=0.0000778, δ_{+}=0.38, δ_{-}=0.7, δ_e =0.8, β =0.15, δ_p =0.12, σ_p=0.2, M=1.45. Figure 3 shows that as the non-extensive parameter (q) increases, the depth of the Sagdeev potential well increases. Therefore, increasing q typically reduces the kinetic energy of the plasma species. This reduction makes energy exchange between the particles and the electric field easier, which enhances the amplitude of the electric field and effectively deepens the potential well. Figure 4 shows the variation of the Sagdeev Potential for different values of σ_p and fixed μ_{d+}=0.0000748, μ_{d-}=0.0000778, δ_{+}=0.38, δ_{-}=0.7, δ_e =0.8, β =0.15, δ_p =0.12, M=1.45, q=0.5. Figure 4 shows that as the electron to positron temperature ratio (σ_p) increases, depth of the Sagdeev potential well increases. Therefore, higher temperatures allow electrons to behave more collectively. This collective interaction enhances the dispersion properties of the wave, and for a soliton to exist, the potential well must deepen to match the increased dispersion. As the electron temperature rises relative to the positron temperature, the thermal pressure of the electrons dominates, which can lead to a more significant separation of charge and a deeper potential well to balance the wave's kinetic energy.

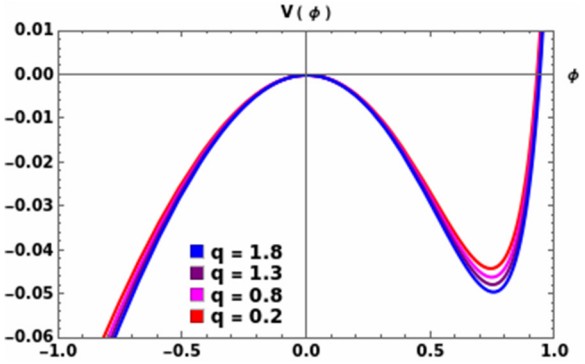

Figure 3. Variation of Sagdeev Potential V(ϕ) with respect to ϕ for different values of q

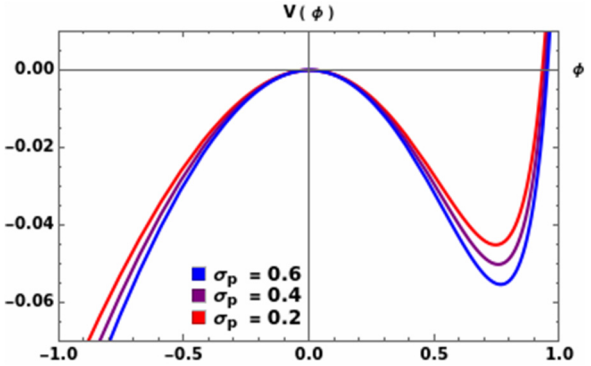

Figure 4. Variation of Sagdeev Potential V(ϕ) with respect to ϕ for different values of σ_p

Figure 5 shows the variation of the Sagdeev Potential for different values of δ_e and fixed μ_{d+} = 0.0000748, μ_{d-} = 0.0000778, δ_{-} = 0.7, β = 0.15, δ_p = 0.12, σ_p= 0.2, M = 1.45, q = 0.5. Figure 5 shows that as electron to ion density ratio (δ_e) increases, depth of the Sagdeev potential well increases. An increase in δ_e signifies a higher concentration of electrons relative to ions. In a moving wave frame, this leads to a stronger electric field and greater charge separation, which directly translates to a deeper potential well to maintain the wave structure. Figure 6 shows the variation of the Sagdeev Potential for different values of δ_{+} and fixed μ_{d+}=0.0000748, μ_{d-}=0.0000778, δ_{-}=0.7, β =0.15, δ_p =0.12, σ_p=0.2, M = 1.45, q = 0.5. Figure 6 shows that as charge density ratio of positively charged dust (δ_{+}) increases, depth of the Sagdeev potential well increases. We can say that, when the charge density ratio of positively charged dust (δ_{+}) increases, the depth of the Sagdeev potential well increases primarily due to the enhancement of the system's nonlinearity**.** As δ_{+} increases, the contribution of the dust species to the Poisson equation becomes more significant. This shifts the balance between the dispersive and nonlinear effects in the plasma, typically leading to more robust (deeper and wider) potential well.

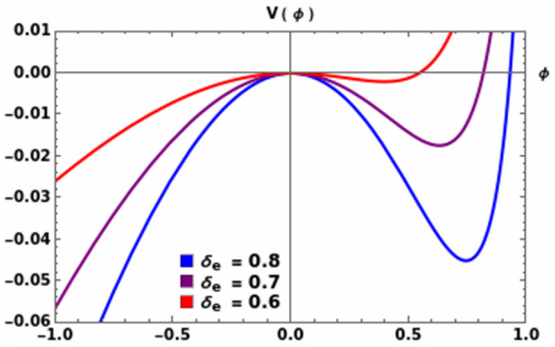

Figure 5. Variation of Sagdeev Potential V(ϕ) with respect to ϕ for different values of δ_e

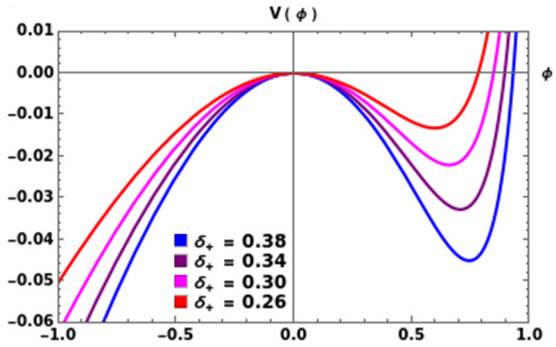

Figure 6. Variation of Sagdeev Potential V(ϕ) with respect to ϕ for different values of δ

Figure 7 shows the variation of the Sagdeev Potential for different values of δ_{-} and fixed μ_{d+}=0.0000748, μ_{d-} = 0.0000778, δ_{+}=0.38, β =0.15, δ_p =0.12, σ_p=0.2, M=1.45, q=0.5. Figure 7 shows that as charge density ratio of

negatively charged dust (δ_-) increases, depth of the Sagdeev potential well decreases. Therefore, increasing δ_- increases the overall inertia of the negative charge carrier in the plasma. This makes the system more sluggish, meaning it cannot reach the same high-potential amplitudes before the kinetic energy of the particles is exhausted, which manifests as a shallower potential well. Figure 8 shows the variation of the Sagdeev Potential for different values of δ_p and fixed μ_{d+}=0.0000748, μ_{d-}=0.0000778, δ_+=0.38, δ_-=0.7, β=0.15, σ_p=0.2, M=1.45, q=0.5. Figure 8 shows that as positron to ion density ratio (δ_p) increases, depth of the Sagdeev potential well increases. Since, positrons have the same mass as electrons but the opposite charge, they effectively neutralize some of the electron effects. This weakens the electrostatic restoring force that usually limits the growth of ion-acoustic waves. With a weaker restoring force, the plasma can support larger electric field gradients. Thus, the system becomes more nonlinear, allowing the solitary wave to acquire a larger maximum amplitude. In the Sagdeev potential framework, a larger amplitude translates directly to a deeper potential well.

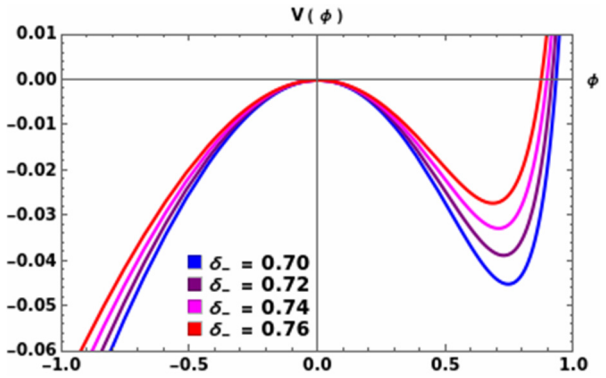

Figure 7. Variation of Sagdeev Potential V(ϕ) with respect to ϕ for different values of δ_-

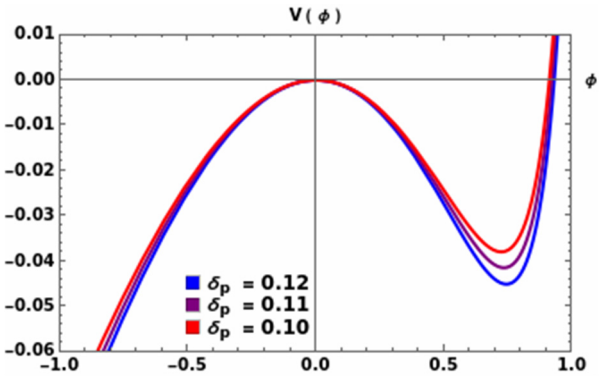

Figure 8. Variation of Sagdeev Potential V(ϕ) with respect to ϕ for different values of δ_p

Figure 9 shows the variation of M_{min} with respect to β for fixed δ_+=0.38, μ_{d+}=0.0000748, δ_-=0.7, μ_{d-}=0.0000778, δ_e=0.8, δ_p=0.12, σ_p=0.2, q=0.8. We observe that as β increases, M_{min} gradually increases. Increase in β makes the plasma more rigid against the formation of solitary waves, requiring higher Mach number to initiate the nonlinear processes necessary for compressive solitons. Figure 10 shows the Variation of M_{min} with respect to q for fixed δ_+=0.38, μ_{d+}=0.0000748, δ_-=0.7, μ_{d-}=0.0000778, δ_e=0.8, δ_p=0.12, σ_p=0.2, β=0.15. The figure shows that as q increases, M_{min} gradually decreases. Increasing q reduces the energetic tail of the positron distribution, lowering the plasma's acoustic speed and making it mathematically easier to reach the supersonic regime required for soliton existence.

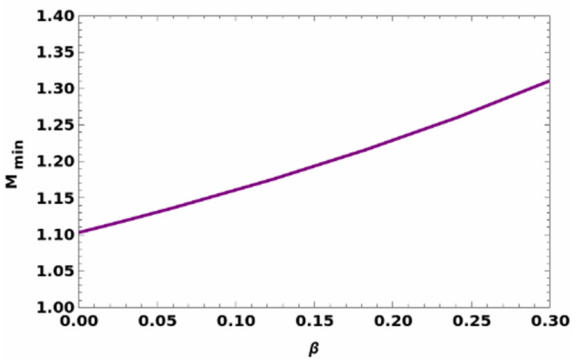

Figure 9. Variation of M_{min} with respect to β

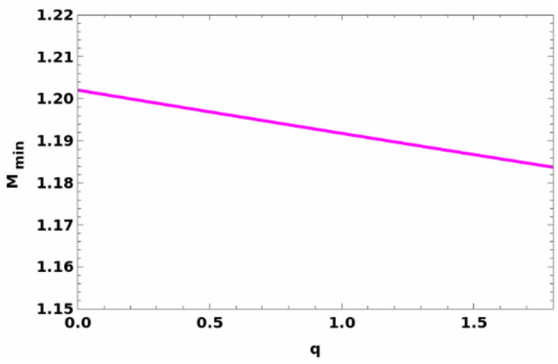

Figure 10. Variation of M_{min} with respect to q

Figure 11 shows the Phase portrait for different values of M and fixed δ_+=0.38, μ_{d+}=0.0000748, δ_-=0.7, μ_{d-} = 0.0000778, δ_e= 0.8, β = 0.15, δ_p = 0.12, σ_p = 0.2, q = 0.5, M = 1.35. The closed loops starting and ending at the origin (0,0) represents homoclinic orbits. In plasma physics, these orbits correspond to solitary wave solutions where the potential and its gradient vanish at infinity. Because the loops exist on the positive side of the ϕ-axis, these are compressive solitons. As the Mach number increases, amplitude increases. The point where the loop crosses the horizontal axis (ϕ-axis) moves further to the right. This represents the peak amplitude of the soliton. Also, the maximum and minimum values of $\frac{\partial\phi}{\partial\xi}$ (the height of the loop) increase, indicating that higher Mach numbers lead to solitons with steeper profiles. Figure 12 shows the Phase portrait for different values of σ_p and fixed δ_+ = 0.38, μ_{d+} = 0.0000748, δ_- = 0.7, μ_{d-} = 0.0000778, δ_e = 0.8, β = 0.15, δ_p = 0.12, σ_p = 0.5, q = 0.5, M = 1.45. As σ_p increases, the homoclinic orbits (the loops) expand further along the positive ϕ-axis. This confirms that a higher temperature ratio leads to compressive solitons with larger amplitudes. The height of the loops increases as σ_p grows. This indicates that as the positrons become colder relative to the electrons (higher σ_p), the resulting solitary wave becomes steeper (higher $\frac{\partial\phi}{\partial\xi}$).

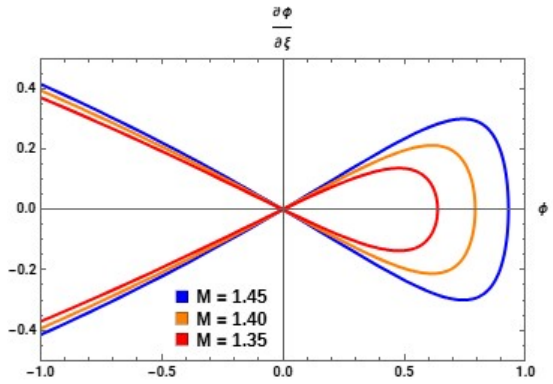

Figure 11. Phase portrait for different values of M

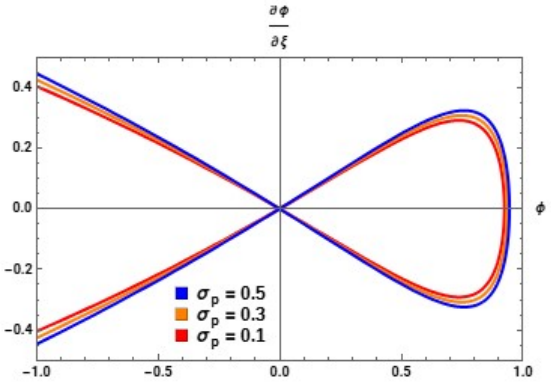

Figure 12. Phase portrait for different values of σ_p

Figure 13 shows the variation of soliton profile with respect to ξ for different values of q and fixed δ_{+}=0.6, μ_{d+}=0.0000748, δ_{-}=0.7, μ_{d-}=0.0000778, β=0.25, δ_e=0.8, δ_p=0.53, σ_p=0.5, q=1.5, M=1.15. We observe that as the value of q increases, the amplitude of soliton increases and the width decreases. Therefore, as q deviates from superextensive to subextensive regime, it enhances the energy of the solitons resulting the soliton structure to become taller and narrower. Figure 14 shows the variation of soliton profile with respect to ξ for different values of β and fixed δ_{+}=0.6, μ_{d+}=0.0000748, δ_{-}=0.7, μ_{d-}=0.0000778, β=0.15, δ_e =0.8, δ_p=0.53, σ_p=0.5, q=0.8, M=1.15. We observe that as the value of β increases the amplitude of soliton decreases and the width increases. Therefore, the effect of the non-extensive parameter q and the nonthermal parameter β are opposite on the soliton profile for small amplitude solitons. This is same as the effect of q and β on large amplitude solitons.

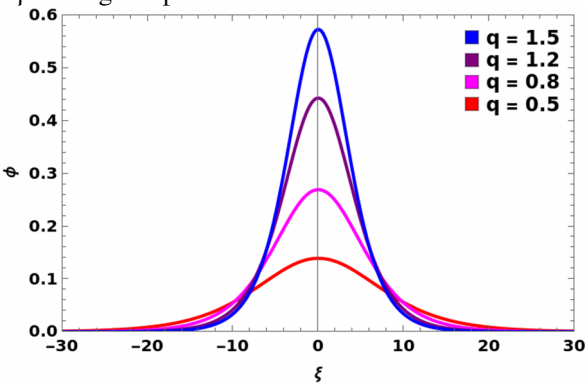

Figure 13. Variation of soliton profile with respect to ξ for different values of q

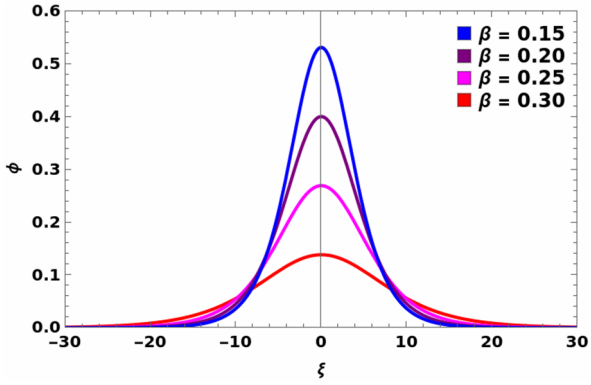

Figure 14. Variation of soliton profile with respect to ξ for different values of β

Figure 15 shows the variation of soliton profile with respect to ξ for different values of σ_p and fixed δ_{+} = 0.6, μ_{d+} = 0.0000748, δ_{-} = 0.7, μ_{d-} = 0.0000778, β = 0.15, δ_e = 0.8, δ_p = 0.53, σ_p = 0.3, q = 0.8, M = 1.15. We observe that, as the value of σ_p increases, the amplitude of soliton increases and the width decreases. Therefore, as the electrons become relatively hotter than the positrons, the solitons become taller and narrower. This indicates increase in energy of soliton for increasing values of σ_p.

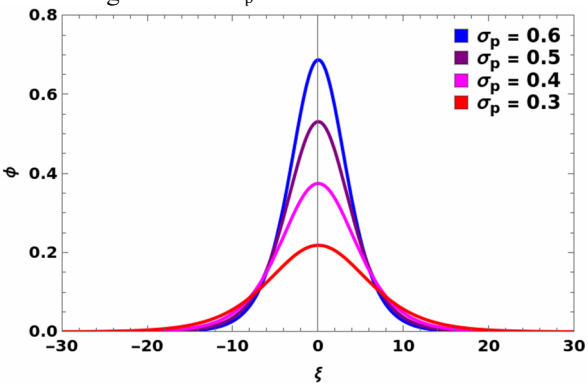

Figure 15. Variation of soliton profile with respect to ξ for different values of σ_p

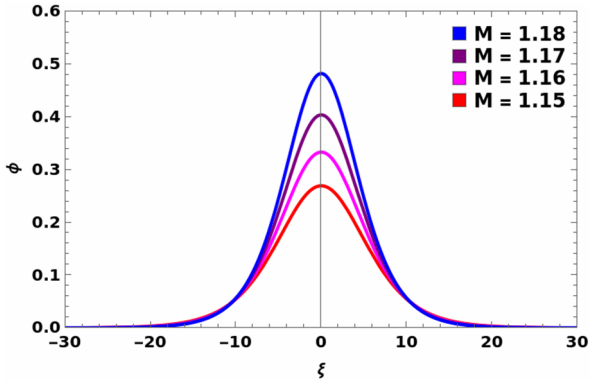

Figure 16. Variation of soliton profile with respect to ξ for different values of M

Figure 16 shows the variation of Soliton profile with respect to ξ for different values of M and fixed δ_{+} = 0.6, μ_{d+} = 0.0000748, δ_{-} = 0.7, μ_{d-} = 0.0000778, β = 0.25, δ_e = 0.8, δ_p = 0.53, σ_p = 0.5, q = 0.8, M = 1.18. We observe that as

the value of M increases, the amplitude of soliton also increases and the width decreases. Therefore, as M increases, the nonlinear effects in the plasma become more dominant over dispersive effects. We observe that the effects of the electron to positron temperature ratio σ_p and the Mach number M is same on the soliton profile for small amplitude solitons. This is same as the effect of σ_p and M on large amplitude solitons.

4. CONCLUSIONS

In the study of solitons in an unmagnetized dusty plasma composed of cold ions, negatively charged dust grains, positively charged dust grains, non-thermal electrons and non-extensive positrons, we have found the existence of compressive solitons. The solitons are found to exist in our plasma model for a supersonic regime (M > 1). The compressive solitons are found to be influenced by the non-extensive parameter (q), the non-thermal parameter (β), charge density ratio of positively charged dust (δ_+), charge density ratio of negatively charged dust ($\delta\_$), positron to ion density ratio (δ_p), electron to ion density ratio (δ_e), electron to positron temperature ratio (σ_p) and the Mach number (M). The increase in the depth of the Sagdeev potential well represents increase in the amplitude of the solitons. The amplitude of the compressive solitons is found to increase for increasing values of M, δ_p, δ_+, δ_e, q and σ_p; however, amplitude of the compressive solitons found to decrease for increasing values of $\delta\_$ and β. The dual nature of the dust population plays a critical role in wave dynamics; while positively charged dust (δ_+) enhances the nonlinear potential, the negative dust component ($\delta\_$) provides significant inertia that acts to suppress the growth of compressive structures. Similarly, the statistical deviation from Maxwellian behaviour shows that non-extensive positrons favour soliton growth, whereas non-thermal electrons act as a dampening mechanism, illustrating the high sensitivity of the system to the specific energy distribution of its lighter species. The influence of non-thermal electrons and non- extensive positrons on ion-acoustic solitary waves in a multi- component plasma was investigated in [36]. Variation of Sagdeev Potential was investigated in [36] for $0.4 \leq q \leq 2.9$. However, in our study, Sagdeev Potential shows significant variations for $0.2 \leq q \leq 1.8$. This change in range in our plasma model is because of involvement of dust components, which makes the effect of the non-extensive parameter (q) towards Sagdeev potential more sensitive. These effects of the parameters can have influence on understanding the nonlinear solitary structures present in astrophysical environment.

ORCID

Satyendra Nath Barman, https://orcid.org/0000-0003-1136-8364; **Kingkar Talukdar,** https://orcid.org/0009-0007-5419-134X

REFERENCES

[1] S. Dalui, and A. Bandyopadhyay, "Effect of Landau damping on ion acoustic solitary waves in a collisionless unmagnetized plasma consisting of nonthermal and isothermal electrons," Indian J Phys, **95**, 367–381 (2021). https://doi.org/10.1007/s12648-020-01731-5

[2] A.S.M. Moinuddin, M. S. Alam, and M.R. Talukder, "Head-on collision of ion-acoustic waves in multi-component unmagnetized plasmas," Waves in Random and Complex Media, **32**(6), 2657-2676 (2022). https://doi.org/10.1080/17455030.2020.1859163

[3] M.G. Hafez, M.R. Talukder, and M.H. Ali, "Nonlinear propagation of weakly relativistic ion-acoustic waves in electron–positron–ion plasma," Pramana, **87**(5), 70 (2016). https://doi.org/10.1007/s12043-016-1275-x

[4] P. Halder, A. Bandyopadhyay, and S. Sardar, "Arbitrary Amplitude Dust–Ion Acoustic Solitary Structures in Five Components Unmagnetized Plasma," Plasma Phys. Rep. **49**, 467–483 (2023) https://doi.org/10.1134/S1063780X22601225

[5] A.E. Dubinov and D.Y. Kolotkov, "Ion-acoustic supersolitons in plasma," Plasma Phys. Rep. **38**, 909–912 (2012). https://doi.org/10.1134/S1063780X12100054

[6] M.N. Islam, M.G. Hafez, and U.K. Deb, "Heavy Ion-Acoustic Soliton and Dressed Soliton in an Unmagnetized Weakly and Strongly Coupled Plasma," Braz. J. Phys. **52**, 158 (2022). https://doi.org/10.1007/s13538-022-01141-4

[7] G.S. Lakhina, A.P. Kakad, S.V. Singh, and F. Verheest, "Ion- and electron-acoustic solitons in two-electron temperature space plasmas," Phys. Plasmas, **15**(6)**,** 062903 (2008). https://doi.org/10.1063/1.2930469

[8] M.G. Hafez, and M.R. Talukder, "Ion acoustic solitary waves in plasmas with nonextensive electrons, Boltzmann positrons and relativistic thermal ions," Astrophys. Space Sci. **359**, 27 (2015). https://doi.org/10.1007/s10509-015-2480-7

[9] M. O. Rahman, M. G. Hafez, S. Barua, and M. A. Kauser, "Ion acoustic solitons and periodic waves with dynamical features around the supercritical values in relativistic unmagnetized plasmas," Physica Scripta, **100**(2), 025201 (2025). https://doi.org/10.1088/1402-4896/ada20b

[10] U. Imon, and M. S. Alam, "Consequence of head-on collision of ion acoustic waves in unmagnetized plasmas having generalized (r, q) distributed electrons and positrons," Waves in Random and Complex Media, 1–28. (2023). https://doi.org/10.1080/17455030.2023.2280910

[11] H. Ur-Rehman and S. Mahmood, "Higher order contribution to ion-acoustic Korteweg–de Vries (KdV) soliton in unmagnetized quantum plasmas with arbitrary degeneracy of electrons," Physica Scripta, **99**(7)**,** 075608. (2024). https://doi.org/10.1088/1402-4896/ad52f8

[12] H. Alinejad, "Non-linear localized ion-acoustic waves in electron–positron–ion plasmas with trapped and non-thermal electrons," Astrophys. Space Sci. **325**, 209–215 (2010). https://doi.org/10.1007/s10509-009-0177-5

[13] M.G. Hafez, M.R. Talukder and R. Sakthivel, "Ion acoustic solitary waves in plasmas with nonextensive distributed electrons, positrons and relativistic thermal ions," Indian J Phys, **90**, 603–611 (2016). https://doi.org/10.1007/s12648-015-0782-9

[14] T. Kaladze, S. Mahmood and H. Ur-Rehman, "Acoustic nonlinear periodic (cnoidal) waves and solitons in pair-ion plasmas," Physica Scripta, **86**(3), 035506. (2012). https://doi.org/10.1088/0031-8949/86/03/035506

[15] P. Mandal, T.K. Maji, U.K. Samanta and M. K. Ghorui, "Head-on collision of ion-acoustic KP solitons in unmagnetized e-p-i plasma," Indian J. Phys. **99**, 4833–4843 (2025). https://doi.org/10.1007/s12648-025-03631-y

[16] M.M. Alam and M.S. Alam, "Study of Time-Fractional Dust Ion Acoustic Waves Propagation in Collisionless Unmagnetized Dusty Plasmas," Braz. J. Phys. **54**, 192 (2024) https://doi.org/10.1007/s13538-024-01562-3

[17] M. Khalid, A. Khan, M. Khan, F. Hadi, and A. Rahman, "Dust Ion Acoustic Solitary Waves in Unmagnetized Plasma with Kaniadakis Distributed Electrons," Braz J Phys, **51**, 60–65 (2021). https://doi.org/10.1007/s13538-020-00807-1
[18] R. Bharuthram and P.K. Shukla, "Large amplitude ion-acoustic solitons in a dusty plasma," Planetary and Space Science, **40**(7), 973-977 (1992) https://doi.org/10.1016/0032-0633(92)90137-D.
[19] R.S. Tiwari, and M.K. Mishra, "Ion-acoustic dressed solitons in a dusty plasma," Phys. Plasmas **13**(6)**,** 062112 (2006) https://doi.org/10.1063/1.2216936
[20] S.K. El-Labany, and W.F. El-Taibany, "Effect of dust-charge variation on dust acoustic solitary waves in a dusty plasma with trapped electrons," Journal of plasma physics, **70**(1), 69-87 (2004). https://doi.org/10.1017/S0022377803002460
[21] S. Das, "Weak Relativistic Effect in the Formation of Ion-Acoustic Solitary Waves in Dusty Plasma," IEEE Transactions on Plasma Science, **50**, 2225-2229 (2022). https://doi.org/10.1109/TPS.2022.3181149
[22] M. Shahmansouri, and M. Tribeche, "Large amplitude dust ion acoustic solitons and double layers in dusty plasmas with ion streaming and high-energy tail electron distribution," Commun. Theor. Phys. **61**, 377 (2014). https://doi.org/10.1088/0253-6102/61/3/18
[23] S. Das, "Propagation of dust ion acoustic solitary waves in dusty plasma with Boltzmann electrons," J. Phys.: Conf. Ser. **1290**, 012025 (2019). https://doi.org/10.1088/1742-6596/1290/1/012025
[24] R. Tomar, H.K. Malik, and R.P. Dahiya, "Reflection of ion acoustic solitary waves in a dusty plasma with variable charge dust," J. Theor. Appl. Phys. **8**, 126 (2014). https://doi.org/10.1007/s40094-014-0126-8
[25] M. Das, B. Madhukalya, and R. Das, "Ion acoustic solitary waves in multicomponent plasmas: influence of ion drift velocity and nonthermal electrons," Heat Transfer, **53,** 2062-2072 (2024). https://doi.org/10.1002/htj.23027
[26] S.V. Singh, and G.S. Lakhina, "Electron acoustic solitary waves with non-thermal distribution of electrons," Nonlinear Processes in Geophysics, **11**(2), 275-279 (2004). https://doi.org/10.5194/npg-11-275-2004
[27] T.S. Gill, H. Kaur, and N.S. Saini, "Small amplitude electron-acoustic solitary waves in a plasma with nonthermal electrons," Chaos, Solitons & Fractals, **30**(4), 1020-1024 (2006). https://doi.org/10.1016/j.chaos.2005.09.070
[28] R. Sabry, W.M. Moslem, and P.K. Shukla, "Fully nonlinear ion-acoustic solitary waves in a plasma with positive-negative ions and nonthermal electrons," Physics of Plasmas, **16**(3)**,** (2009) https://doi.org/10.1063/1.3088005
[29] H.A. Alyousef, S.N. Naeem, M. Irshad, Ata-ur-Rahman, Sherif M.E. Ismaeel, and S.A. El-Tantawy, "The impact of electron beams on the arbitrary amplitude electron–acoustic solitons in a nonthermal plasma," Physics of Fluids, **36**(1)**,** 015139 (2024). https://doi.org/10.1063/5.0181144
[30] S.V. Singh, and G.S. Lakhina, "Ion-acoustic supersolitons in the presence of non-thermal electrons," Communications in Nonlinear Science and Numerical Simulation, **23**(1-3), 274-281 (2015). https://doi.org/10.1016/j.cnsns.2014.11.017
[31] S.K. Maharaj, and R. Bharuthram, "Non-thermal effects of electrons on stopbands of fast ion-acoustic solitons," Physics of Plasmas, **24**(2), (2017) https://doi.org/10.1063/1.4975317
[32] U.N. Ghosh, A. Saha, N. Pal, and P. Chatterjee, "Dynamic structures of nonlinear ion acoustic waves in a nonextensive electron–positron–ion plasma," J. Theor. Appl. Phys. **9**, 321–329 (2015). https://doi.org/10.1007/s40094-015-0192-6
[33] R. Khanam, and S.N. Barman, "The Formation of Ion-Acoustic Solitary Waves in a Plasma Having Nonextensive Electrons and Positrons," East European Journal of Physics, (4), 518-525 (2024). https://doi.org/10.26565/2312-4334-2024-4-61
[34] U.N. Ghosh, D.K. Ghosh, P. Chatterjee, M. Bacha, and M. Tribeche, "Nonplanar ion-acoustic Gardner solitons in a pair-ion plasma with nonextensive electrons and positrons," Astrophys. Space. Sci. **343**, 265–272 (2013). https://doi.org/10.1007/s10509-012-1221-4
[35] M.A. Khaled, "On the head-on collision between two ion acoustic solitary waves in a weakly relativistic plasma containing nonextensive electrons and positrons," Astrophys. Space. Sci. **350**, 607–614 (2014). https://doi.org/10.1007/s10509-014-1790-5
[36] M. Nasir, L. Ameen, B. Asghar, N. Beemkumar, V. Jain, S. Imtiaz, M.F. Ullah, *et al*., "Influence of non-thermal electrons and non-extensive positrons on ion acoustic solitary waves in multi-component plasmas," International Communications in Heat and Mass Transfer, **170,** 110026 (2026). https://doi.org/10.1016/j.icheatmasstransfer.2025.110026
[37] A. Mushtaq, M. Nasir Khattak, Z. Ahmad, and A. Qamar, "Dust ion acoustic soliton in pair-ion plasmas with non-isothermal electrons," Physics of Plasmas, **19**(4), 042304 (2012). https://doi.org/10.1063/1.3696061
[38] A. Renyi, "On a new axiomatic theory of probability," Acta Math. Hung. **6**, 285-335 (1955). https://doi.org/10.1007/bf02024393
[39] C. Tsallis, "Possible generalization of Boltzmann-Gibbs statistics," Journal of statistical physics, **52**(1), 479-487 (1988). https://doi.org/10.1007/BF01016429
[40] M.N. Khattak, A. Mushtaq, and Z. Ehsan, "Electrostatic baryonic solitary waves in ambiplasma with nonextensive leptons," Chinese Journal of Physics, **54**(4), 503–514 (2016). https://doi.org/10.1016/j.cjph.2016.06.011

ВПЛИВ НЕТЕПЛОВИХ ЕЛЕКТРОНІВ ТА НЕЕКСТЕНСИВНИХ ПОЗИТРОНІВ НА ОДИНОЧНІ ХВИЛІ В БАГАТОКОМПОНЕНТНІЙ ПИЛОВІЙ ПЛАЗМІ

Сатьєндра Натх Барман[1], Кінгкар Талукдар[2]
[1]Коледж В. Боруа, Гувахаті 781007, Ассам, Індія
[2]Кафедра математики, Університет Гаухаті, Гувахаті 781014, Ассам, Індія

У цьому дослідженні ми вивчали існування та характеристики солітонів у немагнітній запиленій плазмі, що складається з холодних іонів, негативно заряджених пилових частинок, позитивно заряджених пилових частинок, нетеплових електронів та неекстенсивних позитронів. Властивості солітонів зазвичай вивчаються за допомогою методу редукційних збурень та методу потенціалу Сагдеєва. Ми вивели інтегральне рівняння енергії, використовуючи метод потенціалу Сагдеєва. Ми також обговорили зміну потенціалу Сагдеєва для різних значень параметрів, що беруть участь у нашій моделі плазми. Неекстенсивний параметр (q), нетепловий параметр (β), коефіцієнт густини заряду позитивно зарядженого пилу (δ_+), коефіцієнт густини заряду негативно зарядженого пилу (δ_-), коефіцієнт густини позитронів до іонів (δ_p), коефіцієнт густини електронів до іонів (δ_e), коефіцієнт температури електронів до позитронів (σ_p) та число Маха (M) впливають на амплітуду солітонів. Наше дослідження показує, що нетермальність електронів та неекстенсивність позитронів суттєво змінюють характеристики солітонів. Результати нашого дослідження можуть бути корисними для вивчення плазми в космічних середовищах, таких як кометні хвости та міжзоряні хмари.

Ключові слова: *нетепловий режим; одиночні хвилі; потенціал Сагдеєва; інтеграл енергії; пилова плазма*

East European Journal of Physics. 2. 88–100 (2026)
DOI: 10.26565/2312-4334-2026-2-08 ISSN 2312-4334

DOPPLER SPECTRA FOR STATIONARY AND DYNAMIC ULTRASONIC FIELDS

Evgen A. Barannik, **Mykhailo O. Hrytsenko***
Department of Medical Physics and Biomedical Nanotechnologies, V.N. Karazin Kharkiv National University
4 Svobody Sq., 61022, Kharkiv, Ukraine
**Corresponding Author e-mail: mykhailo.hrytsenko@student.karazin.ua*
Received February 25, 2026; revised April 12, 2026; accepted May 3, 2026

This paper presents a review of physical and methodological approaches to describing the spectrum of the ultrasonic Doppler signal in biological media. The results on the formation of spectral characteristics for a stationary probing field under different types of scatterer motion are summarized, and the development of the model for the case of a dynamically varying sensitivity function of the ultrasound system is considered. Particular attention is paid to synthetic aperture, dynamic focusing, and coherent plane-wave compounding modes. It is shown that in plane-wave imaging systems the Doppler signal spectrum is determined not only by the motion properties of the medium, but also by the spatiotemporal method used to form the Doppler response. The results concerning spatial resolution in the plane-wave compounding mode are also summarized, and the relationship between the geometry of the measurement volume, the sensitivity function, and the spectral parameters is analyzed. Prospects for the further development of these approaches, in particular for applications in shear-wave elastography, are outlined.

Keywords: *Ultrasound Doppler imaging; Doppler spectrum; Synthetic aperture imaging; Plane-wave imaging; Coherent plane-wave compounding; Spatial resolution; Shear-wave elastography*

PACS: 43.28.Py, 43.35.Yb, 43.60.-c, 87.63.D-, 87.63.dk

1. INTRODUCTION

Ultrasound blood-flow imaging is currently undergoing a period of rapid methodological transformation, evolving from conventional Doppler modes toward high-frame-rate, microvascular, and volumetric approaches capable of visualizing slow flow and fine vascular architecture much better than conventional color or power Doppler [1–5]. This evolution is driven by the fundamental limitations of traditional line-by-line scanning, which inherently involves trade-offs among frame rate, contrast, spatial resolution, and sensitivity to low-velocity flow. In addition, conventional two-dimensional ultrasound imaging strongly depends on the imaging plane and operator experience, whereas modern volumetric and ultrafast approaches provide broader opportunities for functional and vascular imaging [1, 2, 4].

The theoretical foundation of this transition was established by synthetic aperture imaging and coherent plane-wave compounding (CPWC), which introduced a fundamentally different image formation strategy compared with sequential focused transmission [6, 7]. These studies laid the groundwork for ultrasound imaging with very high frame rates, transient elastography, and the further development of ultrafast Doppler methods. At the same time, the plane-wave approach proved promising not only for B-mode and Doppler applications, but also for contrast-enhanced imaging, where it can be competitive with focused transmission [8].

The current development of this field is taking place along several interconnected directions. First, the basic image-formation algorithms are being actively improved: synthetic focusing schemes are being optimized, and new approaches based on reverse time migration, minimum-variance adaptive beamforming, high-contrast compounding, as well as software environments for fast and reproducible simulation of plane-wave and color Doppler imaging are being developed [9–13]. Second, considerable attention is being paid to the computational feasibility of such methods, including GPU implementations of synthetic aperture approaches and hybrid transmission schemes that improve spatiotemporal resolution in problems involving rapid motion, particularly in echocardiography [14, 15]. Third, ongoing work seeks an optimal balance between image quality and frame rate. To this end, researchers employ adaptive beamforming for multi-angle plane-wave imaging, null-subtraction imaging schemes, aperture extension using multiple arrays, adaptive combining, tensor completion, and other accelerated CPWC approaches [16–21]. For Doppler and microvascular imaging modes, specialized beamforming schemes are also being developed, including retrospective transmit beamforming, DMAS, and computationally efficient nonlinear compounding methods [22–24]. Particular note should also be made of the growing role of artificial intelligence and deep learning, which are used not only for post-processing but also for compensating the fundamental limitations of single-plane-wave imaging and accelerated compounding [25, 26].

The clinical significance of these technologies already extends far beyond purely technical demonstrations. Ultrafast and microvascular ultrasound methods are being applied to assess muscle perfusion, detect synovitis at an early stage, screen for renal artery disease, and noninvasively evaluate myocardial perfusion [27–30]. In thyroid diagnostics, microvascular imaging improves the accuracy of nodule risk stratification and complements standard grayscale ultrasound examination

Cite as: E.A. Barannik, M.O. Hrytsenko, East Eur. J. Phys. 2, 88 (2026), https://doi.org/10.26565/2312-4334-2026-2-08

[31–33]. In oncology, these approaches, including super-resolution ultrasound imaging, open new possibilities for more accurate lesion differentiation, preoperative staging, assessment of microvascular architecture, and early monitoring of treatment response [34–38].

The present review focuses on the sequential development of physical and methodological approaches to ultrasound and Doppler image formation in synthetic aperture and plane-wave compounding systems—from the analysis of the spectrum of individual flow lines for focused transducers with apodization in the early 2000s to the construction of a continuous scattering model, its extension to the case of a dynamically varying sensitivity function, the study of spectra under changing insonification angles, and the evaluation of spatial resolution, point spread function, and measurement-volume shape in plane-wave compounding modes in studies published in 2022–2025. This temporal perspective, covering the development of the topic from 2001 to the present, makes it possible to trace how the basic concepts of the Doppler spectrum, sensitivity function, and measurement-volume geometry became the foundation for modern high-speed and full-field methods of blood-flow imaging and parameter estimation.

2. PHYSICAL MODEL

In [39], the spectrum of the Doppler signal from an individual flow line in the pulsed mode was studied for focused transducers with apodized apertures. It was shown that the spectral characteristics are determined not only by the velocity of scatterer motion, but also by the parameters of the ultrasound field itself. The intrinsic spectral broadening is caused by two factors: the finite residence time of scatterers within the measurement volume and the curvature of the wavefronts, which changes the local Doppler angle. For a fixed depth, the width of the spectrum of an individual flow line does not depend on its position within the measurement volume, but it changes with the insonification depth. By contrast, the modal Doppler shift depends on both the depth and the position of the flow line if the center of the measurement volume does not coincide with the focus. Thus, already in this work, the Doppler spectrum appears as the result of the combined action of flow kinematics and the geometry of the ultrasound field.

In all subsequent papers, the main physical hypothesis remains the same: the biological medium is treated as isotropic and continuous, and ultrasound is scattered by small fluctuations of density $\rho(\vec{r},t)$ and compressibility $\beta(\vec{r},t)$. The smallness of these fluctuations makes it possible to restrict the analysis to single scattering, and then the response of the pulsed Doppler signal from the region of interest R can be written as [40, 41]

$$f = k^2 \int\limits_R e^{2i(\vec{k}\cdot\vec{r}+\theta_c)} C'_p \left[\tilde{\beta}(\vec{r},t) - \tilde{\rho}(\vec{r},t)\gamma(\vec{r},t)\right] d^3\vec{r}. \tag{1}$$

Here, $\vec{k}$ and $k = 2\pi/\lambda$ are the wave vector and the wave number in the plane-wave approximation for an ultrasound wavelength λ propagating with velocity c. θ_c is the constant phase component of the signal, $\tilde{\rho}(\vec{r},t) = [\rho(\vec{r},t) - \rho_0]\rho_0^{-1} \ll 1$ and $\tilde{\beta}(\vec{r},t) = [\beta(\vec{r},t) - \beta_0]\beta_0^{-1} \ll 1$ are the dimensionless density and compressibility functions, while ρ_0 and β_0 are the spatiotemporal mean values of the density and compressibility of the medium, respectively. The quantity $\gamma(\vec{r},t) \cong 1$ is a dimensionless parameter characterizing the deviation of the wavefront shape from that of ideal plane waves.

The Doppler response can be defined through the complex sensitivity functions (amplitudes) of the transmitted field $G'_t(\vec{r})$, the receiver sensitivity to the scattered waves $G'_r(\vec{r})$, and $b(t)$, the envelope of the probing pulse. Here, $x'(\vec{r})$ is the distance from the point $\vec{r}$ along the probing axis, and T_1 is the delay time determining the ultrasound depth:

$$G'_p(\vec{r}) = G_t(\vec{r})\, G_r(\vec{r})\, b\left(T_1 - \frac{2x'(\vec{r})}{c}\right). \tag{2}$$

The spatiotemporal correlator of the inhomogeneities is

$$C(\vec{r}_1 - \vec{r}_0, \tau) = \left\langle \left(\tilde{\beta}(\vec{r}_0,t_0) - \tilde{\rho}(\vec{r}_0,t_0)\right)\left(\tilde{\beta}(\vec{r}_1,t_1) - \tilde{\rho}(\vec{r}_1,t_1)\right)\right\rangle. \tag{3}$$

It is expressed as an ensemble average and depends only on the time difference $\tau = t_1 - t_0$. Formally, this expression describes a dynamic medium: if C varies slowly as τ increases, then the echo will decorrelate slowly and the Doppler spectrum will be narrower than in the case of rapid variation. This function can be represented as a Fourier integral in the form of a sum of contributions from plane spatial harmonics:

$$C(\vec{r}_1 - \vec{r}_0, \tau) = \int \frac{d^3\vec{q}}{(2\pi)^3}\, e^{i\vec{q}\cdot(\vec{r}_1-\vec{r}_0)} \int \frac{d\omega}{2\pi}\, e^{-i\omega\tau}\, C(\vec{q},\omega). \tag{4}$$

Here, $C(\vec{q},\omega)$ is the power spectral density of the fluctuations, which indicates which spatial scales $\vec{q}$ of the inhomogeneities are associated with which temporal frequencies ω in the dynamics of the inhomogeneities. This representation makes it possible to separate the "physics of the object" from the "physics of the measurement": the correlator describes the structure and motion of the inhomogeneities, whereas the sensitivity function describes the geometry, focusing, pulse duration, and the transmission–reception configuration.

The nature of the fluctuations makes it possible to represent the Doppler response through the product of two entities: the correlator of medium fluctuations and the sensitivity function of the probing system. Within this continuous model, general expressions for the spectra were obtained for several fundamentally important cases, which will be discussed below. In this form, the model immediately separates the "physics of the object" from the "physics of the measurement": the correlator is responsible for the structure and dynamics of the inhomogeneities, whereas the sensitivity function is responsible for the field geometry, focusing, pulse duration, and the transmission–reception configuration. This approach forms the core of [41], [42], [43], and [44], and it is retained in [45, 46], where only the method of field representation is modified for plane-wave compounding.

Thus, the first significant generalization of the model was carried out in [42], where the stationary sensitivity function was replaced by a time-dependent one:

$$G'_p(\vec{r},t) = G_t(\vec{r})\, G_r(\vec{r},t)\, b\left(T_1 - \frac{2x'(\vec{r})}{c}\right). \tag{5}$$

This is the general form of the sensitivity function in the case of synthetic aperture, regardless of the method used to determine the Doppler shift frequency. Physically, this means that in synthetic aperture systems with dynamic variation of the insonification direction, not only the motion of the scatterers changes, but also the measurement scheme itself. In this case, the full power spectrum of the Doppler signal is related not only to the spectral characteristics of the motion of the inhomogeneities, but also to the spatial and temporal harmonics of the probing field. In the case of probing a biological medium by plane waves with different angles and wave vector $\vec{k}(t)$, as shown in Fig. 1, the envelope in (5) takes the form [43].

$$b(t) = b\left(T_1 - \frac{2x' \cos\Phi(t)}{c_0}\right). \tag{6}$$

In this case, the complex amplitude of the incident plane waves is taken with account of their deviation from the untilted plane wave, while $c_0/\cos\Phi(t)$ is the propagation velocity along the x' axis of the incident plane-wave front with wave-vector deviation angle $\Phi(t)$.

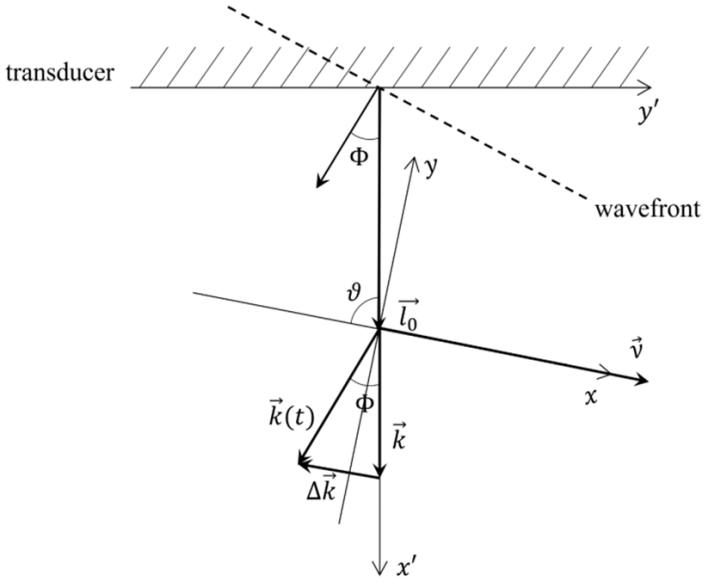

Figure 1. Arrangement of the unprimed coordinate system associated with the measurement volume relative to the ultrasound transducer, and the deviation angle of the wave vector $\vec{k}(t)$ of the current wave from the wave vector $\vec{k}$ of the untilted wave.

In [46], an approach based on the direct use of the transmitted wave field $P'_t(\vec{r},t)$ and the received wave field $P'_r(\vec{r},t)$, represented in the form of plane waves, was considered. In this case, the combined transmit–receive field can be written as

$$P(\vec{r},t) = P_0 e^{2i\vec{k}(t)\cdot\vec{r}}\, b\left(T_1 - \frac{2x''}{c_0}\right) g(z). \tag{7}$$

Here, P_0 is the field amplitude, $g(z)$ is the distribution along the z axis, and $b\left(T_1 - \frac{2x''}{c_0}\right)$ is the pulse envelope describing their spatial length in the $x'' = x''(x', y')$ direction, that is, in the direction of transmission and reception of plane waves for a given vector $\vec{k}(t)$ and the corresponding angle Φ (see Fig. 2).

In [44] and [46], the spatial properties of the Doppler response in the coherent plane-wave compounding mode were described through the system sensitivity function and the geometry of the measurement volume. In [44], it was shown that for a rectangular weighting window the sensitivity function takes a sinc-like form

$$G'_p(\vec{r}, \omega_j = 0) \cong G_0 \, \frac{\sin(k\Omega t y')}{k\Omega t y'} \, b\left(T_1 - \frac{2x'(\vec{r})}{c}\right). \tag{8}$$

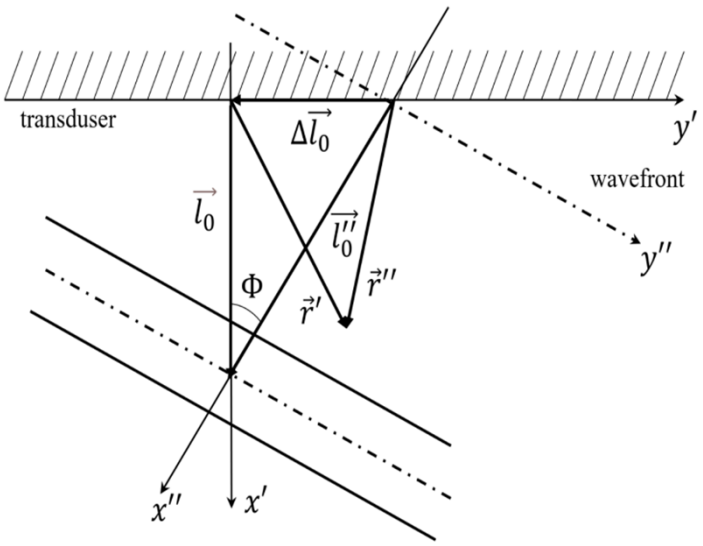

Figure 2. Coordinate system (x', y') associated with the ultrasound transducer, and coordinate system (x'', y'') in which the x'' axis is directed along the propagation direction of the plane-wave front.

therefore, the lateral resolution is determined primarily by the width of the angular insonification sector. In [46], this description was refined by taking into account small linear and quadratic angular terms in the envelope, which lead to a deformation of the boundary of the measurement volume, without changing the principal resolution scales along the coordinate axes. Thus, in the case of coherent plane-wave compounding, spatial selectivity is determined not only by the interference of responses from different viewing angles, but also by the geometry of their overlap region.

3. SPECTRUM OF THE DOPPLER RESPONSE IN THE CASE OF A STATIONARY PROBING FIELD

In most conventional pulsed systems, pulses are transmitted sequentially, with all of them characterized by the same geometry and configuration in the space of wavefronts. This means that the amplitude function of the transmitted field $G'_t(\vec{r})$ and the receiver sensitivity to the scattered waves $G'_r(\vec{r})$ do not depend on time, while the angle $\Phi = 0$. In this case, the Doppler spectrum can be obtained for stationary probing fields using either a single ultrasound emitter or a phased array that provides sequential transmission and reception of the reflected waves. The entire sequence is therefore characterized by one and the same wavefront geometry. In [41], a general expression was obtained for the power spectrum of the Doppler signal in the case of a stationary probing field:

$$S(\omega) = \frac{k^4}{(2\pi)^3} \int d\vec{q}\, C(\vec{q}, \omega) \left| G(\vec{q} + 2\vec{k}) \right|^2. \tag{9}$$

This is the most general relation between the power spectra of Doppler signals, the spectral characteristics of the fluctuations, and the parameters of the probing ultrasound field for a correlation volume small compared with the measurement volume. The factor $C(\vec{q}, \omega)$ describes the properties of the medium and its motion, that is, the structure and dynamics of the fluctuations, whereas $\left|G(\vec{q} + 2\vec{k})\right|^2$ acts as the spatial filter of the system, determined by the measurement volume and focusing. The measured Doppler spectrum is therefore their weighted combination. The authors emphasized that $G(\vec{q} + 2\vec{k})$ is a function with a sharp maximum at $\vec{q} = -2\vec{k}$, independently of the particular configuration of the ultrasound field in space and the way in which this field is described.

Based on the above, for stationary motion with a constant velocity $\vec{V}$ (for example, steady venous blood flow) and in the absence of diffusion, the authors isolated the power spectrum of individual Doppler flow lines using (9):

$$S_\nu(\omega, x, z) = k^4 \nu V \left\langle (\tilde{\beta} - \tilde{\rho})^2 \right\rangle \left| TF\left[e^{2ikV\cos\vartheta\, t}\, G'(Vt, y, z)\, b\left(T_1 - \frac{2x'(Vt, y, z)}{c}\right)\right]\right|^2. \tag{10}$$

Here, $TF[f(t)]$ denotes the Fourier transform of the function $f(t)$, ϑ is the Doppler angle between the transducer and the Ox axis, ν is the correlation volume, and in the analysis it was assumed that the motion occurs along the axis $x = Vt$ (Fig. 3). It was emphasized that the full spectrum is then the sum of the contributions from individual flow lines, while its shape is determined by the Doppler shift, the geometry of the measurement volume, and the spatial configuration of the ultrasound field. This case serves as the basic one for the further analysis of other physical factors.

The influence of spatial correlation of the inhomogeneities was considered separately. If a finite correlation radius Δ is introduced, then the contributions from different regions of the cross-section are no longer independent, and it becomes impossible to isolate the spectrum of individual flow lines. To estimate this effect, the authors used a Gaussian model of the sensitivity function, which made it possible to obtain an analytical expression for the spectrum:

$$S(\omega) = \frac{\pi^2 k^4 \nu \left\langle (\tilde{\beta} - \tilde{\rho})^2 \right\rangle}{8V} \frac{b^6}{2\Delta^2 + b^2} \exp\left\{ -\frac{1}{2\sigma^2} \left(\frac{\omega}{\omega_{md}} - 1 \right)^2 - \frac{\sigma^2 - \sigma_0^2}{2\sigma^2 \sigma_0^2 \cos^2 \vartheta} \right\}. \tag{11}$$

Here,

$$\omega_{md} = \omega_d \left(1 + \frac{2\Delta^2}{b^2} \right)^{-1}, \qquad \sigma^2 = \sigma_0^2 \left(1 + \frac{2\Delta^2}{b^2} \right).$$

The quantity ω_{md} is the modal Doppler frequency, which does not coincide with the conventional Doppler shift $\omega_d = -2kV \cos\vartheta$, while σ^2 is the dimensionless variance of the Doppler spectrum and σ_0^2 is the variance at $\Delta = 0$. Furthermore, $\nu = \alpha\Delta^3$ is the characteristic correlation volume, with α being a constant of order unity. Thus, spectral broadening may be caused not only by a distribution of velocities, but also by the correlation properties of the scatterers or of the motion itself. For this reason, in turbulent flow an increase in the power of the ultrasound and Doppler signals is not necessarily associated with erythrocyte aggregation or with changes in the density and compressibility of the medium; it may instead reflect correlated velocity pulsations.

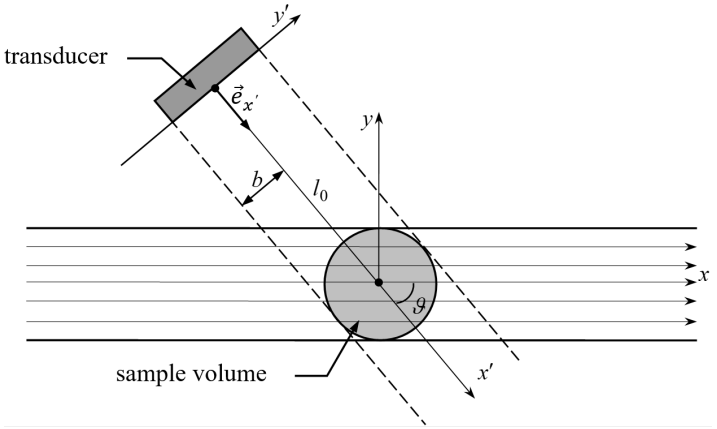

Figure 3. Schematic of the relative arrangement of the ultrasound transducer, the measurement volume, and the blood vessel. The Cartesian coordinate systems associated with the vessel (x, y, z) and with the ultrasound system (x_0, y_0, z_0) are shown, where l_0 is the insonification depth, θ is the Doppler angle, and b is the effective radius of the ultrasound beam at the e^{-1} level.

Another important factor is the diffusion of scatterers. To take it into account, the correlation function is written in a form satisfying the diffusion equation, and the corresponding spectrum takes the form

$$S(\omega) = \frac{k^4 \nu \left\langle (\tilde{\beta} - \tilde{\rho})^2 \right\rangle}{V} \int \frac{d^3\vec{q}}{(2\pi)^3} \frac{Dq^2}{(\omega - q_x V)^2 + (Dq^2)^2} \left| G(\vec{q} + 2\vec{k}) \right|^2. \tag{12}$$

Here, D is the diffusion coefficient. In this case, as in the case of a finite correlation radius, the contributions from individual flow lines can no longer be separated. It was shown that in the weak-diffusion limit this expression reduces to the spectrum for nondiffusive motion, whereas in the strong-mixing regime

$$V \ll 2bDk^2 \tag{13}$$

the spectrum becomes Lorentzian:

$$S(\omega) = \pi^{3/2} b^3 k^4 \nu \left\langle (\tilde{\beta} - \tilde{\rho})^2 \right\rangle \frac{Dk^2}{(\omega + 2kV\cos\vartheta)^2 + 16D^2k^4}. \tag{14}$$

Here, b is the parameter of the Gaussian sensitivity function characterizing the effective width of the incident and received ultrasound beams. Figure 4 shows the resulting normalized Doppler spectrum for the nondiffusive case and for cases with nonzero diffusion. For biological molecules, one typically has $D \sim 10^{-11}$–$10^{-10}\,\mathrm{m}^2/\mathrm{s}$; therefore, in blood vessels at ultrasound frequencies $f \approx 2$–$10\,\mathrm{MHz}$, diffusion is often weak and its influence on the spectra is usually neglected unless D becomes comparable to the critical value $D_{\mathrm{critical}} = V/(2bk^2)$.

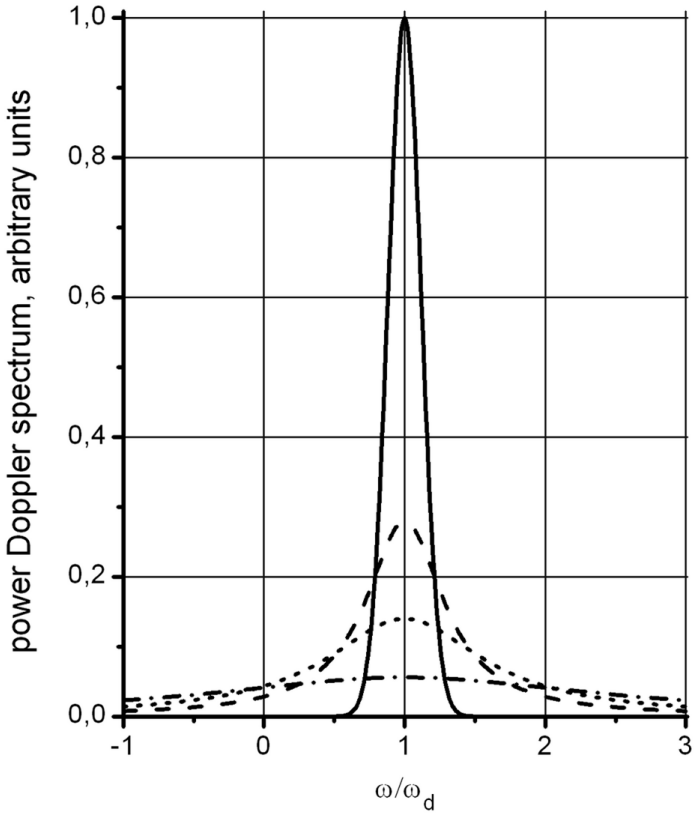

Figure 4. Power Doppler spectra for the nondiffusive case (solid line), and for diffusion with coefficients $D = 2D_{\mathrm{critical}}$ (dashed line), $D = 4D_{\mathrm{critical}}$ (dotted line), and $D = 10D_{\mathrm{critical}}$ (dash-dotted line).

The paper also derived an expression for the spectrum in the case of uniformly accelerated motion of inhomogeneities, which models blood flow in arteries:

$$S(\omega, y, z) = \lim_{T\to\infty} \nu k^4 \left\langle (\tilde{\beta} - \tilde{\rho})^2 \right\rangle T^{-1} \int \frac{dq_x}{2\pi} \, (q_x a)^{-1} \, |G(q_x + 2k\cos\vartheta, y, z)|^2 \, . \tag{15}$$

A distinctive feature of this result is that, in the limit of infinite observation time, the spectrum depends neither on frequency nor on the spatial characteristics of the probing field. Physically, this is because over a sufficiently long observation time all instantaneous velocities make equal contributions to the average signal power. Therefore, the frequency dependence caused by accelerated motion appears only for a finite observation time and depends on the initial phase of motion: the longer the acquisition interval, the broader the Doppler spectrum becomes (see Fig. 5).

On this basis, a model for vibrational sonoelastography was constructed in the paper. It was shown that the integrated power of the high-frequency part of the Doppler spectrum increases with increasing amplitude of the forced displacements, while changing the integration threshold makes it possible to enhance the contribution of regions with different oscillation amplitudes. This provides a physical basis for differentiating soft tissues by their mechanical stiffness. At the same time, the authors specifically noted that the power of the Doppler signal depends not only on the displacement amplitude, but also on fluctuations of density and compressibility; therefore, direct estimation of displacement requires additional compensation using the B-scan image.

Thus, [41] showed that even in the case of a stationary probing field, the Doppler spectrum is a complex characteristic determined jointly by the spatiotemporal properties of the scattering inhomogeneities and by the parameters of the ultrasound system. Within this model, steady blood flow, correlated motion, diffusion, harmonic vibrations, vibrational sonoelastography, and accelerated motion were described in a consistent manner. For this reason, this work is central to the further development of the entire topic: it established a general physical framework in which the Doppler response spectrum is viewed as the result of the interaction between the "physics of the medium" and the "physics of the measurement."

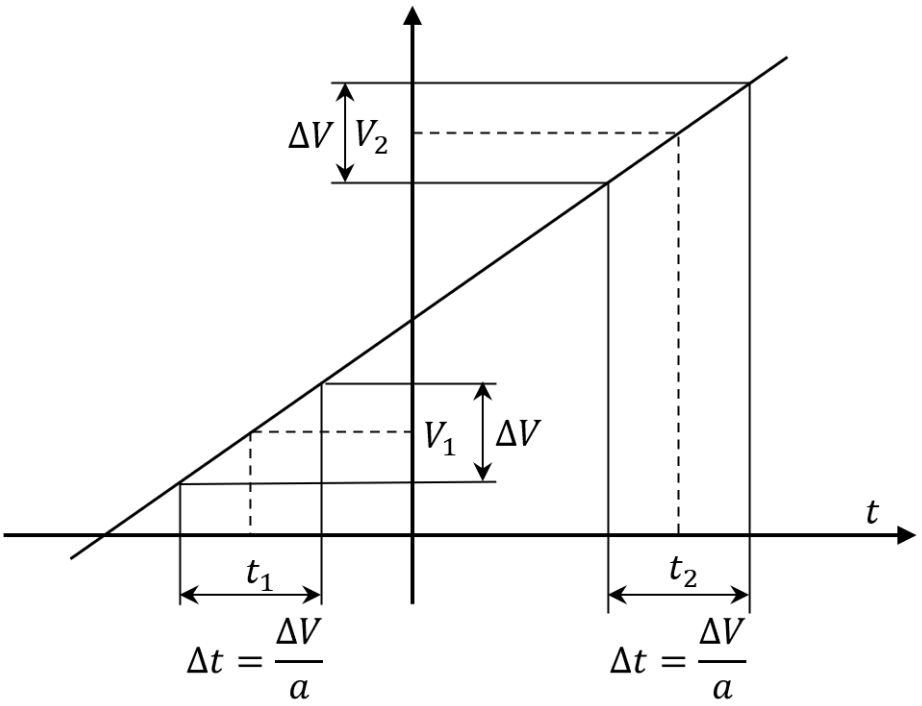

Figure 5. Velocity variation with time for uniformly accelerated motion. Equal velocity intervals ΔV correspond to equal time intervals Δt for all velocity values.

4. SPECTRA IN THE CASE OF DYNAMIC FOCUSING

The traditional approach described in the previous section has several limitations associated with focusing only at a fixed depth, an insufficient amount of data for accurate estimation of flow velocities, and limited spatial resolution. Therefore, in the subsequent studies, expressions for the spectra were obtained that generalize the case of a stationary probing field to the case of dynamic focusing. In principle, there are two possible ways to form the ultrasound Doppler signal using responses recorded for different angles of wave-vector rotation. In the first case, the signal is formed as a sequence of discrete responses corresponding to different successive insonification angles. Then, the power spectrum is determined not only by the spectral characteristics of the motion of the scattering inhomogeneities, but also by the spatial and temporal harmonics of the probing field itself [42]:

$$S(\omega_p) = \frac{k^4}{(2\pi)^3} \sum_{j=-\infty}^{\infty} \int d\vec{q}\, C(\vec{q}, \omega_p - \omega_j) \left| G(\vec{q} + 2\vec{k}, \omega_j) \right|^2, \tag{16}$$

where $\omega_p = 2\pi p/T$ is the Fourier-series variable, and T is the repetition period of signal acquisition for a given range of steering angles.

After the Doppler information has been extracted, the resulting complex signal values can be coherently summed for each point in space in order to provide dynamic focusing on transmission. This result establishes the general physical basis for all subsequent works on dynamic focusing.

Another method of forming the ultrasound Doppler signal, considered in [43], consists in the coherent summation of discrete responses obtained at different steering angles over the full period of angle variation T. This is equivalent to averaging the sensitivity function over the full insonification cycle. Such an approach requires a larger amount of computation, but it provides dynamic focusing during transmission. As a result, only the zero temporal harmonic of the sensitivity function remains in the expression for the spectrum, and the spectrum takes the form:

$$S(\omega_p) = T^2 \frac{k^4}{(2\pi)^3} \int d\vec{q}\, C(\vec{q}, \omega_p) \left| G(\vec{q} + 2\vec{k}, 0) \right|^2. \tag{17}$$

The authors emphasize that, in contrast to the first method, there is no frequency convolution here between the fluctuation correlator and the temporal harmonics of the sensitivity function. This means that the additional spectral broadening associated with the temporal variation of the insonification angle is substantially reduced. In this sense, the obtained expression is structurally similar to the formula for a stationary probing field, but unlike the traditional case, the advantages of synthetic aperture are preserved here, most notably high spatial resolution over a wide depth range.

Thus, coherent compounding makes it possible to combine improved transmit focusing with the absence of significant degradation in the spectral characteristics of the Doppler signal.

In [45], both methods of Doppler signal formation within plane-wave compounding were analyzed in more detail on the basis of a simple Gaussian model of the sensitivity function. In order to reduce the influence of the rectangular-window spectrum on the calculated spectrum, the authors used a Gaussian window T_W to obtain the following expression for the fluctuation correlator spectrum:

$$C(\vec{r}_1 - \vec{r}_0, \tau) = \nu \left\langle (\tilde{\beta} - \tilde{\rho})^2 \right\rangle \delta(\vec{r}_1 - \vec{r}_0 - \tau\vec{V}). \tag{18}$$

The sensitivity function was treated in the same framework. This made it possible to obtain smoothed expressions both for the fluctuation correlator spectrum and for the spectrum of the sensitivity function, without the side lobes characteristic of rectangular apodization. For clarity, the authors considered an explicit sensitivity function which, with the above weighting window taken into account, acquired a Gaussian form and, for the cases of coherent accumulation of signals and of obtaining the signal directly from Doppler angular responses, was given, respectively, by

$$G(\vec{r}, \omega_j = 0) = T^{-1}\sqrt{\pi T_W^2}\exp\left(-\frac{2\vec{r}^{\,2}}{a^2}\right) \tag{19}$$

and

$$G(x, y, z, \omega_j) = T^{-1}\sqrt{\pi T_W^2}\,\exp\left(-\frac{T_W^2(k\Omega y' + \omega_j)^2}{4}\right)\exp\left(-\frac{x^2 + y^2 + 2z^2 + (x' - l_0)^2}{a^2}\right). \tag{20}$$

Accordingly, for coherent accumulation, the spectrum obtained with account of (19) takes the form

$$S(\omega_p) = \nu \left\langle (\tilde{\beta} - \tilde{\rho})^2 \right\rangle T^{-1}k^4\frac{\pi^3 a^3}{4}\sqrt{\frac{T_W^2 a^2}{a^2 + T_W^2 V^2}}\exp\left[-\frac{T_W^2 a^2}{a^2 + T_W^2 V^2}\,\frac{(\omega_p - \omega_d)^2}{4}\right]. \tag{21}$$

$$\sigma^2 = 2\frac{a^2 + T_W^2 V^2}{T_W^2 a^2} = 2\left(\frac{1}{T_W^2} + \frac{V^2}{a^2}\right). \tag{22}$$

Here, $\omega_d = -2kV\cos\vartheta$ is the Doppler frequency shift, and σ^2 is the variance of the Doppler spectrum.

Within this model, the spectrum for coherent accumulation of signals obtained at different wave-tilt angles is Gaussian, with a maximum at the classical Doppler frequency. Its width is determined by two physical factors: the duration of the weighting window T_W, which effectively limits the signal length, and the characteristic size a of the measurement volume. In this sense, even for synthetic aperture, coherent compounding does not introduce a fundamentally new mechanism of spectral broadening: the additional contribution to the variance is associated only with the finite signal duration, whereas the structure of the spectrum itself remains close to that of the stationary insonification case. For this reason, the paper concludes that coherent compounding makes it possible to preserve improved focusing and spatial resolution without significant deterioration of the spectral characteristics of the Doppler signal.

A different situation arises when the Doppler signal is formed directly from the sequence of responses recorded at different angles of wave-vector rotation, using the sensitivity function (20). In this case, the spectrum takes the form

$$S(\omega_p) = \left\langle (\tilde{\beta} - \tilde{\rho})^2 \right\rangle k^4 T^{-2} T_W^2\frac{\pi^2 a^4}{8}\sqrt{\frac{\pi}{2a^2 + T_W^2 V^2}}\exp\left[-\frac{T_W^2 a^2(\omega_p - \omega_d)^2}{4(2a^2 + T_W^2 V^2)}\right]. \tag{23}$$

and the variance is

$$\sigma^2 = 2\frac{2a^2 + T_W^2 V^2}{T_W^2 a^2} = 2\left(\frac{2}{T_W^2} + \frac{V^2}{a^2}\right). \tag{24}$$

In this case, the spectral variance is larger than that for coherent compounding, and the difference between them is given by the additional term $\Delta\sigma^2 = 2/T_W^2$. Thus, in comparison with coherent accumulation, an additional mechanism of spectral broadening appears here, one that is reduced neither to the size of the measurement volume nor to the duration of the signal itself. Physically, this effect is associated with the fact that when the wave tilt angle changes, the Doppler angle also changes, and hence so does the projection of the velocity of the inhomogeneity motion onto the direction of the current wave vector, as shown in Fig. 6.

The authors interpreted this situation as motion with an effective acceleration inversely proportional to the time T_W. They also showed that the sign of this effective "acceleration" does not affect the spectral width: both for increasing and decreasing apparent velocity projection, the range of instantaneous values remains the same, so the variance contains precisely the quadratic term $2/T_W^2$. This also leads to a practical conclusion: the larger the interval T_W, the smaller the rate

of change of the Doppler angle within one window, and hence the smaller the additional spectral broadening for a given angular range $\Phi_{\max}$ (Fig. 6). The authors state that such terms may be neglected when the strong inequality

$$\frac{1}{T_W^2} \ll \frac{V^2}{a^2}$$

is satisfied, which is well fulfilled in real ultrasound systems.

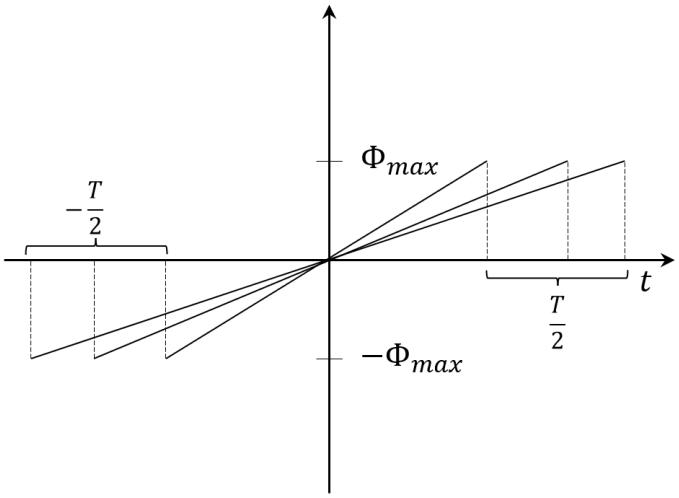

Figure 6. Model time dependence of the wave-vector deviation angle.

A separate part of the study considered the formation of compounding signals by cyclic permutation, where each new complex signal includes the contribution from a new insonification angle. For this method of constructing the sequence of compounding signals, the phase difference between neighboring samples does not accumulate additionally, unlike in the signal formed directly from individual angular responses. This means that the additional spectral broadening associated with variation of the Doppler angle is absent in this case (Fig. 7).

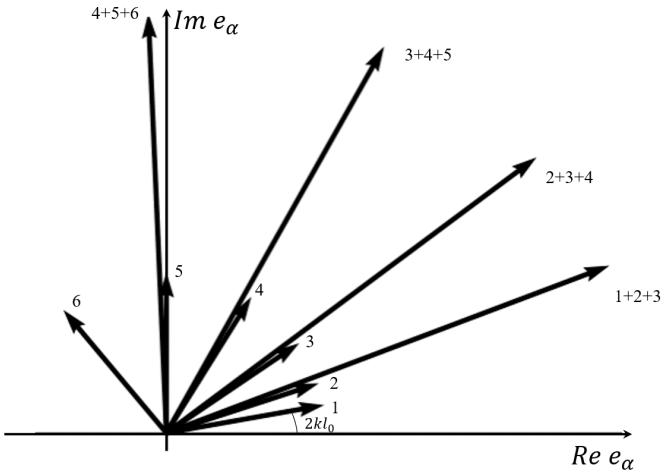

Figure 7. Nonlinear temporal growth of the phase difference $\Delta\varphi_n$ for the complex Doppler signal e_d and the phase difference for compounded signals e_c for the case of three steering angles, $N = 3$. Here, e_d^{ni} denotes the Doppler-response signal for the nth steering angle during the ith insonification period; the compounded signals are formed by cyclic permutation as successive sums such as $e_c^{11} + e_c^{21} + e_c^{31}$, $e_c^{21} + e_c^{31} + e_c^{12}$, $e_c^{31} + e_c^{12} + e_c^{22}$, $e_c^{12} + e_c^{22} + e_c^{32}$, and so on, with each new sum including the signal from the next insonification angle.

For this reason, cyclic permutation is an important practical way to preserve the accuracy of velocity estimation without losing time waiting for a complete set of signals from all steering angles.

Thus, in [45], it was shown that when plane-wave compounding is used, the width of the Doppler spectrum is determined not only by the parameters of the measurement volume and the signal duration, but also by the very method used to form the Doppler response. In coherent compounding, spectral broadening is caused mainly by the finite signal

duration, whereas forming the signal directly from the sequence of angular responses leads to additional broadening due to the dynamic change in the Doppler angle. This gives the effect a clear physical meaning and at the same time determines which processing method is more suitable for accurate Doppler measurements.

5. DIRECTIONS FOR FURTHER DEVELOPMENT OF THE TOPIC

Within the classical spectral formulation, the problem of forming the Doppler response in biological media has already been studied to a considerable extent. The previous sections considered stationary motion regimes, the influence of correlation and diffusion, nonstationary accelerated motion, oscillatory regimes and vibrational sonoelastography, as well as cases of dynamic variation of the insonification geometry and plane-wave compounding. In other words, within the framework of the traditional spectral model, the main physical scenarios determining the shape of the Doppler spectrum have already been described for both stationary and nonstationary motion regimes, as well as for modern insonification schemes with a dynamic sensitivity function.

A natural next step is the transition to shear-wave elastography, where the motion of the medium is no longer purely kinematic but has a wave character. In contemporary studies in this field, several approaches can be distinguished. Some works are devoted to recovering the shear-wave propagation velocity from the spatiotemporal characteristics of the wave field [47]. Another group of studies focuses on determining the complex shear modulus and the viscoelastic parameters of the medium on the basis of dispersion relations and spectral estimates [48, 49]. Separate developments address methods that take into account anisotropy and the tensor nature of the elastic properties of soft tissues [50], as well as general models of shear-wave propagation in viscoelastic media governed by different rheological laws [51]. More recent studies have proposed local-phase and wavenumber-based methods for estimating wave-process parameters, in particular the local phase-gradient approach [52] and local phase-velocity imaging using wavenumber filter banks [53].

At the same time, most existing approaches are aimed primarily at recovering the shear-wave velocity, its dispersive characteristics, or the complex shear modulus. In contrast, the problem of an analytical description of the fluctuation spectrum of the scattered ultrasound signal formed by shear-wave-induced displacement of the medium has not yet been formulated in a complete form. This is precisely the direction proposed for further research. It is proposed to use the eikonal of the shear wave, $\tau(\vec{r})$, as a linking quantity between the wave kinematics of the medium and the fluctuation spectrum of the Doppler response. If the local displacement is written in the form

$$u(\vec{r}, t) = A(\vec{r}) \exp\left[i(\omega t - \omega\tau(\vec{r}))\right], \tag{25}$$

then the function $\tau(\vec{r})$ defines the spatial phase distribution of the wave process and, consequently, the law governing modulation of the fluctuations of the scattering inhomogeneities. This opens the possibility of moving from an eikonal description of the shear-wave front to the construction of the fluctuation correlation function and, subsequently, to the Doppler signal spectrum. Thus, the further development of this line of research consists in establishing an analytical relation between the eikonal of the shear wave and the fluctuation spectrum of the scattered ultrasound response, which may potentially make it possible to relate the measured spectral characteristics of the signal to the local viscoelastic properties of the medium.

CONCLUSIONS

This paper summarizes physical approaches to describing the spectrum of the ultrasonic Doppler response in biological media on the basis of a continuous scattering model involving small fluctuations of density and compressibility. It is shown that, within this model, the spectral characteristics of the signal are determined by the combined action of two factors: the spatiotemporal structure of the medium fluctuations and the sensitivity function of the ultrasound system. On this basis, the cases of a stationary probing field were considered consistently for different regimes of inhomogeneity motion, including steady motion with constant velocity, motion with finite spatial correlation, diffusive mixing, uniformly accelerated motion, and harmonic oscillations. It was also shown how these regimes manifest themselves in the Doppler signal spectrum and in vibrational sonoelastography problems. It is emphasized separately that even in the classical case, the spectral shape is determined not only by the kinematics of the scatterers, but also by the geometry of the ultrasound field, the parameters of the measurement volume, and the character of spatial averaging.

Further development of the topic is associated with the transition to schemes with a dynamically varying sensitivity function, primarily dynamic focusing and plane-wave compounding. It is shown that in such systems the Doppler response spectrum depends not only on the motion of the inhomogeneities, but also on the very method of signal formation. For coherent plane-wave compounding, it was established that this approach makes it possible to combine improved focusing and high spatial selectivity without substantial additional spectral broadening, whereas forming the signal directly from the sequence of angular responses leads to additional spectral broadening due to the dynamic change of the Doppler angle. It was also shown that the spatial resolution in the plane-wave compounding mode is determined both by the interference properties of the set of angular responses and by the geometry of their overlap region, while its principal scales can be expressed through the parameters of the angular sector and the measurement volume. Thus, the present review covers the main stationary and nonstationary regimes of Doppler spectrum formation, modern methods of signal construction in plane-wave compounding, and the associated spatial-resolution properties of the system.

A promising direction for future work is the extension of this spectral theory to problems of shear-wave elastography by establishing an analytical relation between the eikonal of the shear wave and the fluctuation spectrum of the scattered ultrasonic signal.

ORCID

Evgen A. Barannik, https://orcid.org/0000-0002-3962-9960; **Mykhailo O. Hrytsenko**, https://orcid.org/0000-0002-5174-5542

REFERENCES

[1] D.G. Paeng, C.A. Lee, and C. Imtiaz, Principles of Doppler ultrasound and emerging blood flow imaging," Ultrasonography, **44**(6), 409–424 (2025). https://doi.org/10.14366/usg.25152

[2] N. Tsedendamba, Y. Song, E.-Y. Park, and J. Kim, "Review of Linear-Array-Transducer-Based Volumetric Ultrasound Imaging Techniques and Their Biomedical Applications," Bioengineering, **12**(9), 906 (2025). https://doi.org/10.3390/bioengineering12090906

[3] M.U. Aziz, J.R. Eisenbrey, A. Deganello, M. Zahid, K. Sharbidre, P. Sidhu, and M.L. Robbin, "Microvascular Flow Imaging: A State-of-the-Art Review of Clinical Use and Promise," Radiology, **305**(2), 250–264 (2022). https://doi.org/10.1148/radiol.213303

[4] R. Seddiki, T. Mirault, J. Sitruk, N. Mohamedi, E. Messas, M. Pernot, J. Baranger, and G. Goudot, "Advancements in Noncontrast Ultrasound Imaging for Low-Velocity Flow: A Technical Review and Clinical Applications in Vascular Medicine," Ultrasound in Medicine & Biology, **51**(7), 1035–1042 (2025). https://doi.org/10.1016/j.ultrasmedbio.2025.03.001

[5] J.Y. Gao, and C. Hou, "Progresses and clinical application of super-resolution ultrasound imaging: a narrative review," The Ultrasound Journal, **17**(1), 29 (2025). https://doi.org/10.1186/s13089-025-00432-6

[6] J.A. Jensen, S.I. Nikolov, K.L. Gammelmark, and M.H. Pedersen, "Synthetic aperture ultrasound imaging," Ultrasonics, **44**(Suppl. 1), e5–e15 (2006). https://doi.org/10.1016/j.ultras.2006.07.017

[7] G. Montaldo, M. Tanter, J. Bercoff, N. Benech, and M. Fink, "Coherent plane-wave compounding for very high frame rate ultrasonography and transient elastography," IEEE Transactions on Ultrasonics, Ferroelectrics, and Frequency Control, **56**(3), 489–506 (2009). https://doi.org/10.1109/TUFFC.2009.1067

[8] J. Viti, H.J. Vos, N. de Jong, F. Guidi, and P. Tortoli, "Detection of Contrast Agents: Plane Wave Versus Focused Transmission," IEEE Transactions on Ultrasonics, Ferroelectrics, and Frequency Control, **63**(2), 203–211 (2016). https://doi.org/10.1109/TUFFC.2015.2504546

[9] D. Jang, J. Park, J.H. Song, T.K. Song, and H. Yoon, "Investigation of ultrasound plane-wave imaging for optimal synthetic focusing," Scientific Reports, **16**(1), 1057 (2025). https://doi.org/10.1038/s41598-025-30595-0

[10] Y. Pan, X. Wang, Y. Qiang, N. Wang, R. Liu, G. Yang, Z. Zhang, X. He, Y. Yu, H. Zheng, and W. Qiu, "A New Method of Plane-Wave Ultrasound Imaging Based on Reverse Time Migration," IEEE Transactions on Biomedical Engineering, **71**(5), 1628–1639 (2024). https://doi.org/10.1109/TBME.2023.3346194

[11] L.C. Neves, F.M. Ribas, J.M. Maia, A.J. Zimbico, A.A. Assef, and E.T. Costa, "Improving Ultrasound B-Mode Image Quality with Coherent Plane-Wave Compounding Using Adaptive Beamformers Based on Minimum Variance," Sensors, **25**(5), 1306 (2025). https://doi.org/10.3390/s25051306

[12] S. Afrakhteh and L. Demi, "Coherent Plane Wave Compounding combined with Euclidean distance transform for high frame rate and high contrast ultrafast imaging," Ultrasonics, **156**, 107759 (2025). https://doi.org/10.1016/j.ultras.2025.107759

[13] J.S. Honer and R.J. McGough, "Fast and Accurate Plane Wave and Color Doppler Imaging with the FOCUS Software Package," Sensors, **25**(14), 4276 (2025). https://doi.org/10.3390/s25144276

[14] L. Basavarajappa, R. R, R. Tushar, and A.K. Thittai, "Toward Real-Time GPU Implementation of Diverging Beam With Synthetic Aperture Technique With Non-linear Beamforming for a Curvilinear Array," Ultrasound Imaging, (2025). https://doi.org/10.1177/01617346251406540

[15] B.A. Herrema, N.J. Eshkalak, and N. Bottenus, "Improved Spatiotemporal Resolution in Echocardiography Using Mixed Geometry Imaging Sequences," IEEE Transactions on Ultrasonics, Ferroelectrics, and Frequency Control, **71**(4), 438–447 (2024). https://doi.org/10.1109/TUFFC.2024.3364051

[16] C.-C. Shen and C.-L. Huang, "Improvement in Multi-Angle Plane Wave Image Quality Using Minimum Variance Beamforming with Adaptive Signal Coherence," Sensors, **24**(1), 262 (2024). https://doi.org/10.3390/s24010262

[17] Y. Xu, B. Li, J. Luo, X. Liu, and D. Ta, "Frame rate improvement in coherent plane-wave compounding using null subtraction imaging," AIP Advances, **14**(6), 065001 (2024). https://doi.org/10.1063/5.0201371

[18] J. Foiret, X. Cai, H. Bendjador, *et al.*, "Improving plane wave ultrasound imaging through real-time beamformation across multiple arrays," Scientific Reports, **12**, 13386 (2022). https://doi.org/10.1038/s41598-022-16961-2

[19] M. Hashemseresht, S. Afrakhteh, and H. Behnam, "High-resolution and high-contrast ultrafast ultrasound imaging using coherent plane wave adaptive compounding," Biomedical Signal Processing and Control, **73**, 103446 (2022). https://doi.org/10.1016/j.bspc.2021.103446

[20] S. Afrakhteh and H. Behnam, "Coherent Plane Wave Compounding Combined With Tensor Completion Applied for Ultrafast Imaging," IEEE Transactions on Ultrasonics, Ferroelectrics, and Frequency Control, **68**(10), 3094–3103 (2021). https://doi.org/10.1109/TUFFC.2021.3087504

[21] R. Paridar, and B.M. Asl, "Frame rate improvement in ultrafast coherent plane wave compounding," Ultrasonics, **135**, 107136 (2023). https://doi.org/10.1016/j.ultras.2023.107136

[22] C. Golfetto, I.K. Ekroll, H. Torp, L. Lovstakken, and J. Avdal, "Retrospective Transmit Beamforming and Coherent Plane-Wave Compounding for Microvascular Doppler Imaging: A Comparison Study," IEEE Transactions on Ultrasonics, Ferroelectrics, and Frequency Control, **68**(4), 1105–1116 (2021). https://doi.org/10.1109/TUFFC.2020.3033719

[23] C.-C. Shen, and Y.-C. Chu, "DMAS Beamforming with Complementary Subset Transmit for Ultrasound Coherence-Based Power Doppler Detection in Multi-Angle Plane-Wave Imaging," Sensors, **21**(14), 4856 (2021). https://doi.org/10.3390/s21144856

[24] X. Yan, Y. Qi, Y. Wang, and Y. Wang, "High Resolution, High Contrast Beamformer Using Minimum Variance and Plane Wave Nonlinear Compounding with Low Complexity," Sensors, **21**(2), 394 (2021). https://doi.org/10.3390/s21020394

[25] K. Miura, H. Shidara, T. Ishii, K. Ito, T. Aoki, Y. Saijo, and J. Ohmiya, "Image quality improvement in single plane-wave imaging using deep learning," Ultrasonics, **145**, 107479 (2025). https://doi.org/10.1016/j.ultras.2024.107479

[26] N. Chennakeshava, B. Luijten, O. Drori, M. Mischi, Y.C. Eldar, and R.J.G. van Sloun, "High Resolution Plane Wave Compounding Through Deep Proximal Learning," in: *2020 IEEE International Ultrasonics Symposium (IUS)* (2020). https://doi.org/10.1109/IUS46767.2020.9251399

[27] T. Miller, N. Chambara, M.T.C. Ying, and M.Y.C. Pang, "Using ultrafast angio planewave ultrasensitive and conventional doppler imaging techniques to assess intramuscular blood perfusion in older adults," BMC Medical Imaging, **24**(1), 324 (2024). https://doi.org/10.1186/s12880-024-01495-y

[28] K.L. Lai, M.C. Tsai, and P.C. Li, "Ultrafast Doppler Imaging for Early Detection of Synovitis in Rheumatoid Arthritis," Ultrasound in Medicine & Biology, **50**(4), 484–493 (2024). https://doi.org/10.1016/j.ultrasmedbio.2023.12.007

[29] G. Ivanac, A. Bulum, A.B. Jagnjić, *et al.*, "Advantages of Ultrafast ultrasound in the screening for renal artery disease," Journal of Ultrasonography, **24**(97), 1–6 (2024). https://doi.org/10.15557/jou.2024.0016

[30] M.B. Nguyen, N. Zhang, L.L. Mertens, *et al.*, "Noninvasive assessment of myocardial perfusion using ultrafast ultrasound: clinical study for congenital heart disease," European Heart Journal – Imaging Methods and Practice, **3**(1), qyaf007 (2025). https://doi.org/10.1093/ehjimp/qyaf007

[31] G. Ma, L. Chen, Y. Wang, *et al.*, "Application of microvascular ultrasound-assisted thyroid imaging report and data system in thyroid nodule risk stratification," Insights into Imaging, **15**(1), 230 (2024). https://doi.org/10.1186/s13244-024-01806-5

[32] J. Ji, E. Tang, Y. Wang, and X. Shi, "The Clinical Application of Superb Microvascular Imaging in Evaluating Thyroid Related Diseases: A Systematic Review," Journal of Clinical Ultrasound, **53**(2), 336–342 (2025). https://doi.org/10.1002/jcu.23863

[33] W. Li, Z. Ge, S. Cai, *et al.*, "Diagnostic value of greyscale ultrasound combined with superb microvascular imaging in thyroid nodules: a systematic review and meta-analysis," Quantitative Imaging in Medicine and Surgery, **15**(1), 440–454 (2025). https://doi.org/10.21037/qims-24-1195

[34] X. Hou, Z. Li, Y. Liu, J. Gao, and T. Song, "Diagnostic value of super-resolution ultrasound imaging in differentiating benign and malignant BI-RADS-4 breast lesions," Frontiers in Oncology, **15**, 1662492 (2025). https://doi.org/10.3389/fonc.2025.1662492

[35] S. Sabeti, N.B. Larson, J.C. Boughey, *et al.*, "Ultrasound-based quantitative microvasculature imaging for early prediction of response to neoadjuvant chemotherapy in patients with breast cancer," Breast Cancer Research, **27**(1), 24 (2025). https://doi.org/10.1186/s13058-025-01978-y

[36] Y. Zuo, Y. Zhan, J. Zhou, *et al.*, "Prediction of pathological complete response to neoadjuvant chemotherapy for invasive breast cancers based on longitudinal ultrasound and superb microvascular imaging: a single-center retrospective study," PeerJ, **13**, e20171 (2025). https://doi.org/10.7717/peerj.20171

[37] O. Tokur, S. Aydin, F. Kilinc, *et al.*, "Diagnostic value of super microvascular imaging in differentiating axillary lymph nodes: semi-quantitative and qualitative approach in primary breast cancer and suspicious axillary nodes," BMC Cancer, **25**(1), 1705 (2025). https://doi.org/10.1186/s12885-025-14936-w

[38] S. Xia, Q. Hua, Y. Song, *et al.*, "Super-resolution ultrasound imaging of intranodal lymphatic sinuses for predicting sentinel lymph node metastasis in breast cancer: a preliminary study," European Radiology, **35**(10), 6079–6088 (2025). https://doi.org/10.1007/s00330-025-11520-5

[39] E.A. Barannik, "Pulsed Doppler flow-line spectrum for focused transducers with apodized apertures," Ultrasonics, **39**(4), 311–317 (2001). https://doi.org/10.1016/S0041-624X(01)00059-2

[40] P.J. Fish, "Doppler methods," in: *Physical Principles of Medical Ultrasonics*, edited by C.R. Hill, (Ellis Horwood, Chichester, 1986), Chap. 11, pp. 338–376.

[41] E. Barannik, and I. Skresanova, "Correlation functions and power spectra of Doppler response signals in ultrasonic medical applications," Ultrasonics, **52**(5), 676–684 (2012). https://doi.org/10.1016/j.ultras.2012.01.014

[42] E.A. Barannik, and O.S. Matchenko, "The influence of the dynamic change of ultrasound system sensitivity function on the spectra of Doppler response signals," East European Journal of Physics, (2016). https://doi.org/10.26565/2312-4334-2016-2-08

[43] I.V. Sheina, O.B. Kiselov, and E.A. Barannik, "Power Spectra of Doppler Response Signals from Biological Objects Using Synthetic Aperture Ultrasound," East European Journal of Physics, **4**, 5–12 (2020). https://doi.org/10.26565/2312-4334-2020-4-01

[44] I.V. Sheina, and E.A. Barannik, "Resolution of the Ultrasound Doppler System Using Coherent Plane-Wave Compounding Technique," East European Journal of Physics, **1**, 116–122 (2022). https://doi.org/10.26565/2312-4334-2022-1-16

[45] E.A. Barannik, and M.O. Hrytsenko, "Spectra of Ultrasound Doppler Response Using Plane-Wave Compounding Technique," East European Journal of Physics, **1**, 476–484 (2024). https://doi.org/10.26565/2312-4334-2024-1-52

[46] E.A. Barannik, and M.O. Hrytsenko, "Ultrasound Doppler System's Resolution Using Coherent Plane-Wave Compounding Technique," East European Journal of Physics, **1**, 350–356 (2025). https://doi.org/10.26565/2312-4334-2025-1-43

[47] J. McLaughlin, D. Renzi, K. Parker, and Z. Wu, "Shear wave speed recovery using moving interference patterns obtained in sonoelastography experiments," The Journal of the Acoustical Society of America, **121**(4), 2438–2446 (2007). https://doi.org/10.1121/1.2534717

[48] S. Kazemirad, S. Bernard, S. Hybois, A. Tang, and G. Cloutier, "Ultrasound Shear Wave Viscoelastography: Model-Independent Quantification of the Complex Shear Modulus," IEEE Transactions on Ultrasonics, Ferroelectrics, and Frequency Control, **63**(9), 1399–1408 (2016). https://doi.org/10.1109/TUFFC.2016.2583785

[49] S. Cui, G. Cloutier, M.-H. Roy Cardinal, H. Savoji, and P. Maghoul, "Simultaneous viscoelastic characterization of soft tissues based on shear wave ultrasound dispersion and multi-scale wavelet cross-correlation analysis," Mechanical Systems and Signal Processing, **237**, 112890 (2025). https://doi.org/10.1016/j.ymssp.2025.112890

[50] M. Correia, T. Deffieux, S. Chatelin, J. Provost, M. Tanter, and M. Pernot, "3-D elastic tensor imaging in weakly transversely isotropic soft tissues," Physics in Medicine & Biology, **63**, 155005 (2018). https://doi.org/10.1088/1361-6560/aacfaf

[51] M. Osika, and P. Kijanka, "Ultrasound Shear Wave Propagation Modeling in General Tissue-Like Viscoelastic Materials," Ultrasound in Medicine & Biology, **50**(4), 627–638 (2024). https://doi.org/10.1016/j.ultrasmedbio.2024.01.008

[52] E. González-Mateo, F. Camarena, and N. Jiménez, *et al.*, "Real-time ultrasound shear wave elastography using a local phase-gradient method," Computer Methods and Programs in Biomedicine, (2025). https://doi.org/10.1016/j.cmpb.2024.108529

[53] R. Almasi, M.W. Urban, and P. Kijanka, "Local phase velocity imaging with wavenumber filter banks for ultrasound shear wave elastography," Computer Methods and Programs in Biomedicine, **269**, 108894 (2025). https://doi.org/10.1016/j.cmpb.2025.108894

ДОПЛЕРІВСЬКІ СПЕКТРИ ДЛЯ СТАЦІОНАРНИХ ТА ДИНАМІЧНИХ УЛЬТРАЗВУКОВИХ ПОЛІВ

Є.О. Баранник, М.О. Гриценко

Кафедра медичної фізики та біомедичних нанотехнологій, Харківський національний університет імені В. Н. Каразіна, майдан Свободи, 4, 61022, Харків, Україна

У цій роботі наведено огляд фізичних і методологічних підходів до опису спектра ультразвукового допплерівського сигналу в біологічних середовищах. Узагальнено результати щодо формування спектральних характеристик для стаціонарного зондувального поля за різних типів руху розсіювачів, а також розглянуто розвиток моделі для випадку динамічно змінної функції чутливості ультразвукової системи. Особливу увагу приділено режимам синтетичної апертури, динамічного фокусування та когерентного пласкохвильового компаундингу. Показано, що в системах пласкохвильової візуалізації спектр допплерівського сигналу визначається не лише властивостями руху середовища, а й просторово-часовим способом формування допплерівського відгуку. Також узагальнено результати щодо просторової роздільної здатності в режимі пласкохвильового компаундингу та проаналізовано зв'язок між геометрією вимірювального об'єму, функцією чутливості й спектральними параметрами. Окреслено перспективи подальшого розвитку цих підходів, зокрема для застосувань у зсувнохвильовій еластографії.

Ключові слова: *ультразвукова допплерівська візуалізація; допплерівський спектр; візуалізація із синтетичною апертурою; пласкохвильова візуалізація; когерентний пласкохвильовий компаундинг; просторова роздільна здатність; зсувнохвильова еластографія*

East European Journal of Physics. 2. 101–108 (2026)
DOI: 10.26565/2312-4334-2026-2-09 ISSN 2312-4334

NEUTRON AND GAMMA-RAY PULSE SHAPE DISCRIMINATION METHODOLOGY

I. Yakymenko[1*], **A. Dobrozhan**[1], **G. Onyshchenko**[1], **O. Kuzin**[1], **V. Trusova**[2], **P. Kuznietsov**[1]
[1] *O.I. Akhiezer Department for Nuclear Physics and High Energy Physics, V.N. Karazin Kharkiv National University, Kharkiv, Ukraine*
[2] *Department of Medical Physics and Biomedical Nanotechnologies, V.N. Karazin Kharkiv National University, Kharkiv, Ukraine*
[*] *Corresponding Author e-mail: ivan.yakymenko@karazin.ua*
Received April 2, 2026; revised May 5, 2026; accepted May 19, 2026

In this research, we proposed a new neutron gamma discrimination methodology in comparison with the classical charge integration. To record an experimental dataset, a high sampling rate oscilloscope, Keysight DSOX 6004a (20 Gas/s), was used. The reference experiment was recorded with the desktop digitizer CAEN DT 5720e with DPP PSD firmware installed. A stilbene scintillator size of 50 mm x 50 mm coupled with the PMT R1307 Hamamatsu was selected as a detector. The scintillation pulse decay has an exponential tail depending on the particle nature. The proposed technique aims to classify the geometrical peak asymmetry of the scintillation pulse detected by the detector, where the discrimination factor is a ratio of the calculated pulse weight (centroid) related to the pulse maximum amplitude position in time. The centroid of the faster gamma pulse is closer to the pulse maximum amplitude and significantly shifted for the delayed neutron pulses. The discussed approach allows us to classify events with comparable accuracy to the charge integration technique.

Keywords: *Charge integration; Scintillators; Neutron gamma discrimination; Stilbene; PMT; Pulse Shape Discrimination; Charge Comparison; Zero-Crossing; Figure of Merit; CAEN DT5720e*

PACS: 29; 29.40.Mc; 29.40.-n

1. INTRODUCTION

Analyzing recent publications and the experimental equipment, it is possible to draw a reasonable conclusion that the problem of neutron-gamma separation has today transformed from a highly specialized issue of nuclear physics into a fundamental interdisciplinary challenge. The relevance of developing reliable methods for discriminating particles by pulse shape is rapidly growing not only in traditional research applications, but also in strategically important applied areas, for example discussed in [1] land mine detection applications. In particular, in modern medicine, it is critical for the accuracy of hadron therapy; in research of new type of neutron detectors [2, 3], for conducting non-destructive elemental analysis; and in the security sector, for solving humanitarian problems, such as high-precision demining of territories and detection of hidden threats. However, despite the high demand, the practical implementation of these methods faces serious technological barriers related to the hardware base. The analysis shows that the vast majority of existing solutions capable of providing an acceptable quality factor figure of merit (FOM) are stationary and bulky complexes. The critical aspect remains the speed of signal processing and sampling rate. Thus, there is a clear scientific demand for the creation of high-speed data acquisition systems with open-source algorithms. In the article [4], a direct comparison of digital versions of the zero-crossing ZC and charge comparison CC methods was carried out using a NE213 liquid scintillator and an 8-bit digitizer with a frequency of 1 GS/s. Experimental results showed that the ZC method provides a higher quality of separation with an FOM = 1.05 at an energy of 100 keVee, while the CC method under the same conditions demonstrated FOM = 0.88. The authors found that the Z/C method is much more stable to changes in signal amplitude: when changing the energy from 100 keVee to 1 MeVee, the shift in the discrimination parameter for Z/C was only 2 %, while for CC it reached 12%. This confirms the advantage of Z/C for experiments with a wide dynamic range, where it is important to avoid energy dependence of the separation threshold. It was also shown that when using digital ZC, the threshold for effective neutron detection can be reduced to 40 keVee without a significant increase in gamma-ray leakage. The data obtained indicate that the high sampling frequency (1 GHz) allows the ZC method to better compensate for the influence of the low bit depth of the ADC (8 bits). It is also important to mention the work [5], which proposed and investigated in detail the pulse gradient analysis (PGA) method, which is based on comparing the current amplitude of the digitized signal with its value after a certain delay time. The experiment was carried out with a liquid scintillator NE213 (diameter and height 50 mm) and a digitizer with a frequency of 250 MS/s and a bit depth of 12 bits. The author established the optimal delay time for the gradient at 28–32 ns after the pulse peak, which allowed maximizing the difference between the fast and slow components of the illumination. The results showed that the PGA method provides FOM = 1.07 at a very low energy of 40 keVee, which significantly exceeds the capabilities of the standard CC charge comparison method in this range. At an energy of 100 keVee, the method achieved FOM = 1.63, demonstrating high resistance to electronic noise and statistical fluctuations. An important technical advantage of PGA is its computational efficiency: the algorithm requires only one compare and divide operation per event, which makes it 3–4 times faster than curve approximation methods

Cite as: I. Yakymenko, A. Dobrozhan, G. Onyshchenko, O. Kuzin, V. Trusova, P. Kuznietsov, East Eur. J. Phys. 2, 101 (2025), https://doi.org/10.26565/2312-4334-2026-2-09

when implemented in MATLAB or FPGA. The development of a PSD system based on FPGA (Xilinx Kintex-7 array) using a 12-bit ADC and a sampling rate of 500 MS/s is described in [6]. The authors implemented a charge comparison (CC) method optimized for operation under extremely high loads — up to 1.08 million samples per second (Mcps). In an experiment with a 252Cf source and a BC501A liquid scintillator, the system demonstrated a stable FOM = 1.15 at an energy threshold of 100 keVee. Thanks to the parallel processing architecture in the FPGA, the system dead time per event was reduced to 200 ns, which allowed avoiding significant data loss at high radiation intensity. Comparison with offline processing on a PC showed the identity of the results with a significant gain in speed (real-time processing). The study confirmed that the 500 MHz configuration is sufficient for accurate separation of the "fast" component (10–30 ns duration) and the "tail" of the pulse. In [7], a digital implementation of the zero-crossing method ZC is presented, where the anode signal from the EJ-276 and EJ-309 scintillators was digitized with a frequency of 500 MS/s and a bit depth of 14 bits. The authors implemented a recursive digital filter to form a bipolar signal, which allowed achieving a value of FOM = 1.32 for the plastic scintillator EJ-276 at an energy of 100 keVee. For the liquid scintillator EJ-309, the quality indicator was FOM = 1.83 in the same energy range. It has been experimentally proven that the method provides stable particle separation at energies from 40 keVee, which is critical for the registration of low-energy fast neutrons. It is also noted that the baseline error was minimized to < 1%, which allowed avoiding the drift of the discrimination peak. According to the test results, this digital ZC algorithm outperformed classical analog methods in terms of neutron event purity by 15%. In [8], the possibility of using a 64-channel TOFPET2 ASIC for particle identification in pixel detectors based on organic scintillators was investigated. The experimental setup consisted of an array of 4x4 trans-stilbene crystals (6x6x30 mm each) connected to an array of SensL J-series silicon photomultipliers (SiPM). Since TOFPET2 was originally developed for medical PET imaging, the authors adapted it for PSD using the Time-over-Threshold (ToT) method for charge estimation. At the SiPM operating overvoltage of 3V, the system demonstrated a maximum quality factor FOM of ≈ 1.2 at an energy of 478 keVee (Compton edge for the 662 keV line). The study highlights that despite the compactness and low cost per channel, the use of the ToT method instead of direct pulse shape digitization limits the quality of the separation at low energies. However, the results obtained confirm the suitability of TOFPET2 for creating portable systems with a large number of channels, where it is important to combine energy resolution, temporal characteristics, and basic $n - \gamma$ discrimination capabilities.

2. MATERIALS AND METHODS

The assembled experimental setup is shown in Fig.1 in details discussed at [9]. The data was obtained using a 239Pu-Be neutron source 10^5, which produces neutrons and instant gamma-rays.The 239Pu-Be source is placed directly on the stilbene scintillator housing (5 mm housing wall) with dimensions of 50 × 50 mm. The scintillator is in optical contact with R1307 Hamamatsu photomultiplier (PMT, 76 mm window). The high-voltage power supply is configured taking into account the total gain of the path, the operating voltage is selected as 550 V. The signal from the PMT is fed to an custom amplifier with a gain of G = 10 and a bandwidth of at least 100 MHz. The CAEN DT5720e digitizer has a 50 Ohm built-in input. It was used a custom CFD module (constant fraction discrimination module) with a cable delay of 2.2 m (10.6 ns). The signal is additionally connected through a 1 MOhm probe to Keysight DSOX6004a oscilloscope.

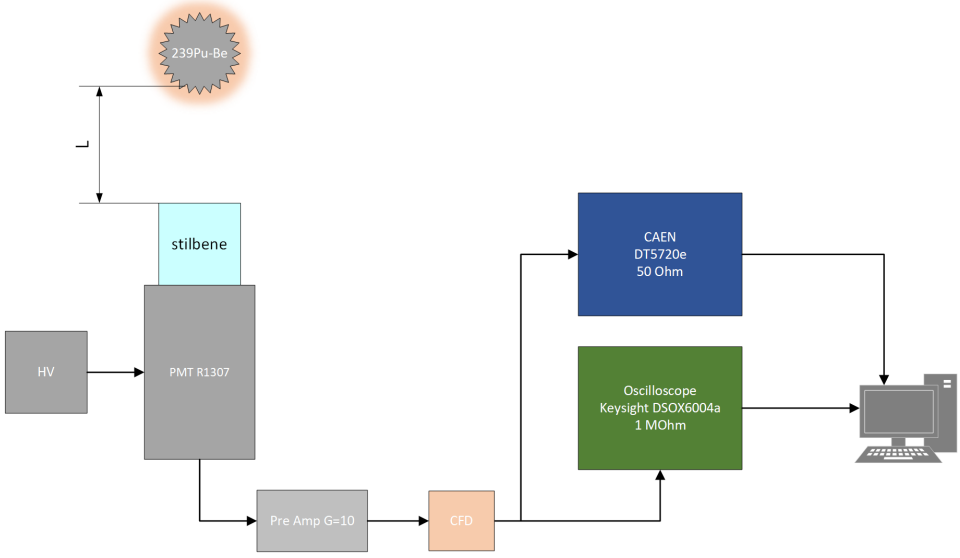

Figure 1. Experimental setup.

Typical scintillation signal is shown in Fig.2.

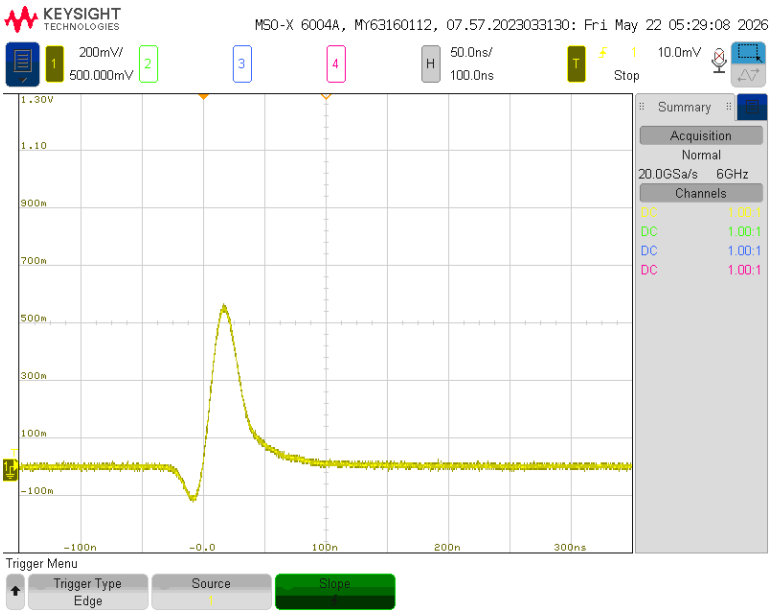

Figure 2. The scintillation signals captured with the oscilloscope. A visible pulse undershoot after analog CFD

The signals from the oscilloscope were automatically accumulated on the computer using a prepared script. The signal from the CAEN DT5720 was processed online in the Compass program. Figure Fig.3 shows the waveform triggered in the Compass program, the pulse duration is approximately 90-110 ns with a delayed trailing edge. The signals are in principle identical in shape both on the oscilloscope and on the CAEN digitizer.

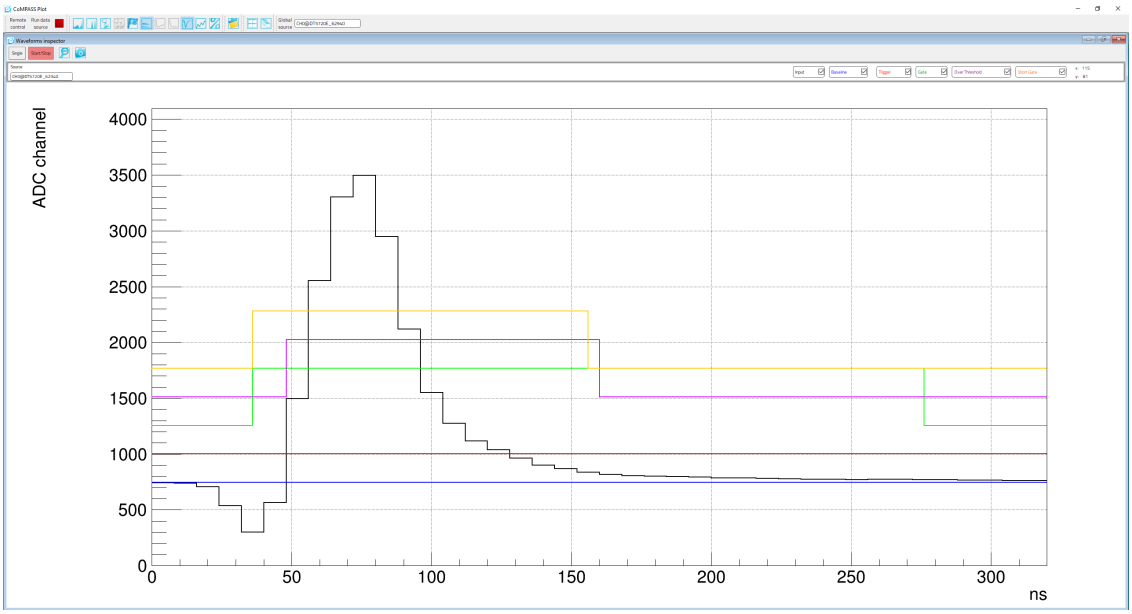

Figure 3. The triggered pulses in COMPASS software.

The settings for the CAEN digitizer were selected as follow: Energy coarse gain 40 fC/LBS, Gate 240 ns, Short gate 120 ns, Pre-gate 12 ns, Threshold 100 LBS (48 mV), Trigger holdoff 320 ns, Record length 320 ns, Pre-trigger 52 ns, N samples baseline 128.

The Short gate parameter was selected during the scanning process from the maximum pulse amplitude along the falling edge. The criteria of the setup tuning were the best PSD ratio Qs/Qt (integral in the short gate Qs and Qt integral in the gate). Also, the visual quality of PSD histogram Fig.4, straight gamma and neutron tails, and the resulting FOM value Fig.5 were controlled.

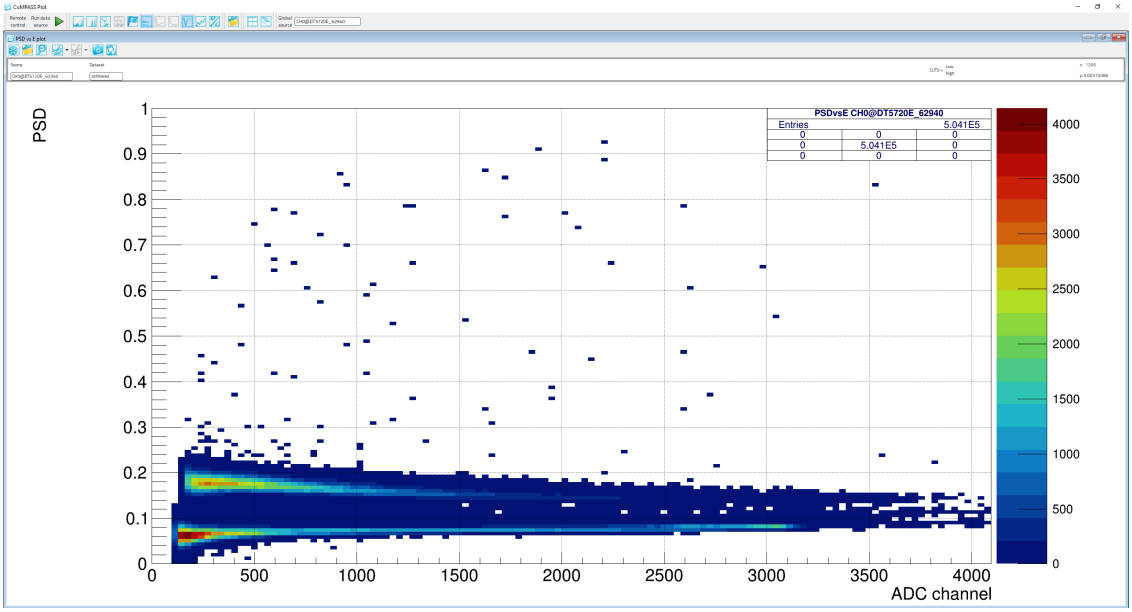

Figure 4. The PSD plot accumulated with the COMPASS software. Neutron and gamma events. Neutron (above 0.1 PSD) and gamma events (below 0.1 PSD)

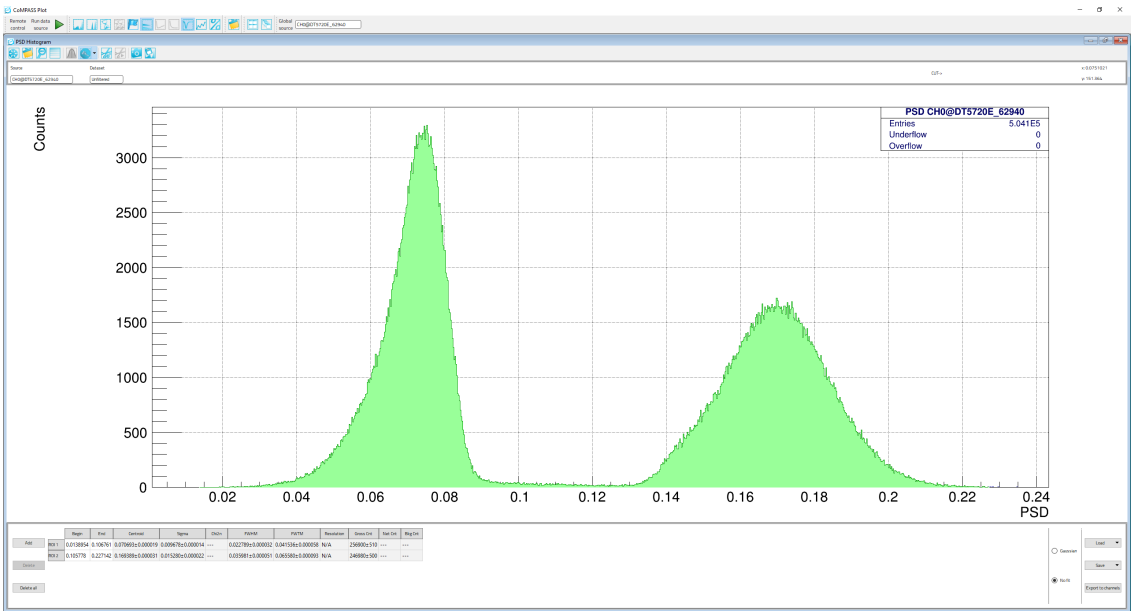

Figure 5. The PSD histogram accumulated with the COMPASS software. FOM = 1.871.

3. ALGORITHM AND EXPERIMENTAL RESULTS

For the working data set it was accumulated a 10000 events using the oscilloscope. To have a stable starting point, it was used a CFD module, to eliminate the pulses jitter caused by varying amplitudes [10]. To validate the quality of discrimination of designed method we were used two methods: charge comparison (CC) practically implemented in [11] and the results obtained with the CAEN software (basically the charge comparison). The CC method is the most famous pulse shape discrimination (PSD) technique with the comparable quality to the analog techniques of discrimination.

The discrimination ratio (1) could be recalculated using the charge comparison of the entire signal charge Q_{total} and the charge of the slow part of the signal tail Q_{slow}.

$$R = Q_s/Q_t \tag{1}$$

Typical neutron and gamma-ray pulse signals are shown in Fig.6.

Finally, to calculate the quality of neutron/gamma discrimination of the stilbene scintillator used the figure of merit

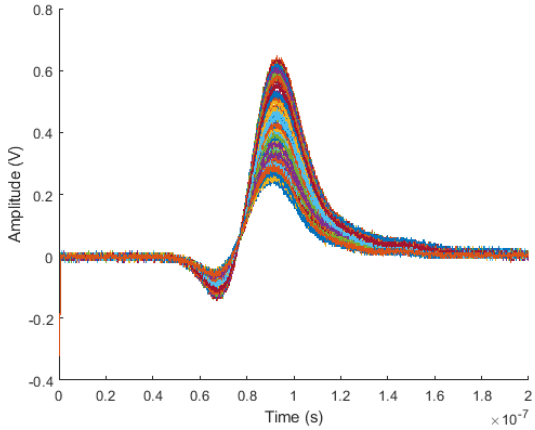

Figure 6. The typical signal recorded with the oscilloscope. Visible a CFD pulse undershoot.

(FOM), which is:

$$FOM = D/(FWHM_\gamma) + FWHM_n \tag{2}$$

Using the test bench Fig.1 it was obtained FOM 1.871 on CAEN digitizer. By variation of slow gate width with the fixed long gate, it was found the best ratio (1) for the FOM.

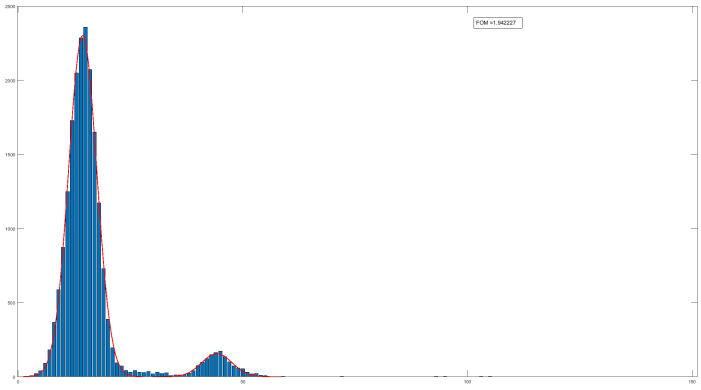

Figure 7. The calculated FOM using the CC method. FOM = 1.942

Using the custom CC code it was calculated FOM = 1.942 for the data set accumulated with the oscilloscope. Finally it was tested a new approach of neutron gamma discrimination on the obtained dataset.

The main hypothesis of the proposed Peak Asymmetry method (PA) is that the time distribution of photon emission, which forms a scintillation pulse, has a different level of tail asymmetry with respect to the position of the amplitude maximum for gamma quanta and fast neutrons. When a particle interacts with the scintillator, two key fluorescence components arise.The fast component which decays within a few nanoseconds and is practically identical for both types of radiation (neutron and gamma). In contrast, the slow or delayed fluorescence caused by the annihilation of triplet excitations is much more intense when neutrons are detected. From a Peak Asymmetry method approach, the pulse registered by the detector is a statistical distribution of photons in time, and the centroid of this distribution reflects the mathematical expectation or average time of photon emission during a single scintillation event. The practical implementation of the PA method uses the concept of the ”center of gravity” to quantify the asymmetry of the pulse. The time centroid is defined as the weighted average over the entire scintillation pulse shape, where the signal amplitude acts as a statistical weight Fig.8. Since the pulse shape is perceived as a probability density function, the calculated time centroid becomes an analogue of the first moment of the distribution (normalized by total pulse “mass”). The main discriminating factor in this case is the parameter, which is equal to the ratio between the centroid time and the moment of reaching the peak amplitude. To quantify asymmetry within the PA method, the concept of the “center of gravity” (centroid) of the peak is used. Mathematically, the time centroid tcentroid is defined as the first moment of the signal amplitude distribution:

$$t_{centroid} = \sum (t_i A_i) / \sum A_i \tag{3}$$

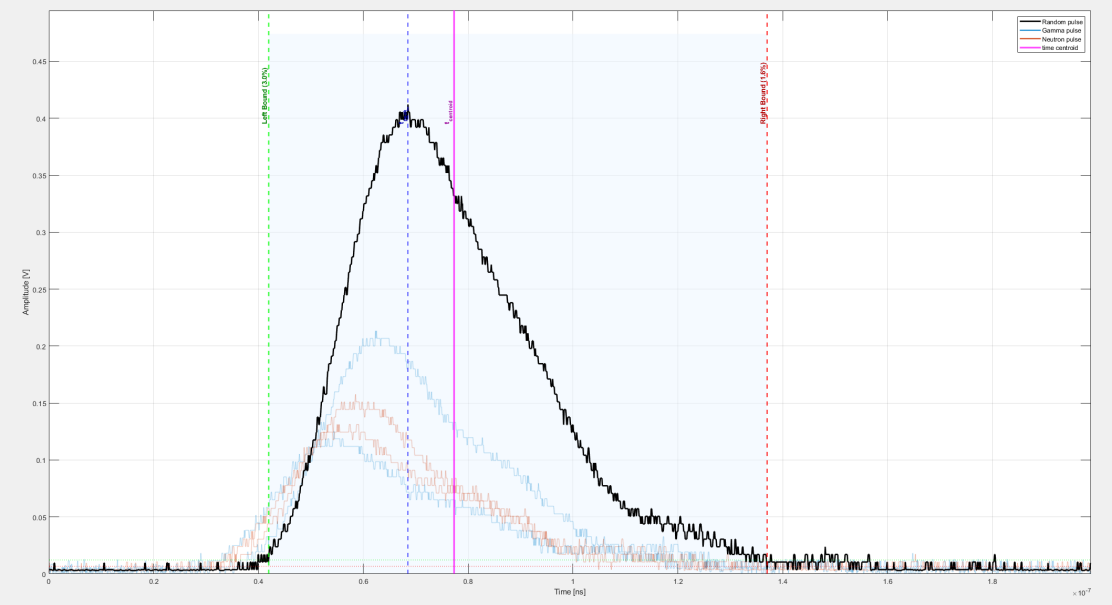

Figure 8. The Peak Asymmetry (PA) key parameters.

where A_i — the amplitude of the signal at time ti, which acts as a statistical weight. The main discriminating factor is the time offset parameter Δt:

$$\Delta t = t_{centroid}/t_{peak} \tag{4}$$

Gamma rays: generate relatively symmetrical pulses, where the centroid almost coincides with the time of the amplitude maximum, leading to values of δt near 0. Neutrons: due to the intense slow fluorescence, the "center of gravity" of the pulse is shifted to the right of the peak, providing a positive value of $\Delta t > 0$. Gamma-ray events are characterized by a high degree of signal symmetry, as a result of which the calculated center of gravity practically coincides with the time of the amplitude maximum. In such cases, the value of the discriminating factor approaches zero. On the contrary, the intense "tail" of the neutron pulse creates additional weight to the right of the peak, leading to a physical shift of the centroid to a longer time region. The higher the specific gravity of the slow fluorescence, the more the time centroid deviates from the peak of the pulse, which provides a clear separation of particles. The resulting PSD plot and histogram presented on Fig.9, the obtained FOM with the PA method was 0.72.

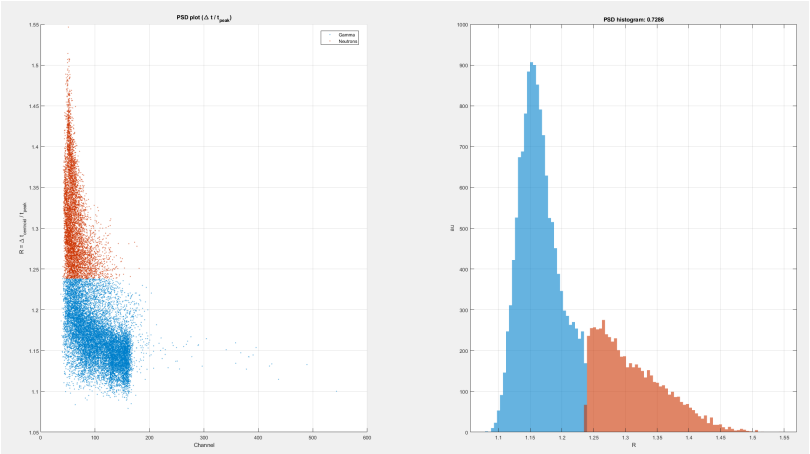

Figure 9. The calculated PSD distribution for the PA method.

4. DISCUSSION AND CONCLUSION

The pulse shape discrimination could be done with modern oscilloscope equipment with the high sampling rate along with the ultimate bandwidth. Summarizing the obtained results: FOM_{CC} = 1.942, FOM_{CAEN} = 1.871, FOM_{PA} = 0.728, the PA method provides a lower quality of pulse shape discrimination comparing to charge integration methods. An important advantage of the PA method over classical integral approaches, such as the CC method, is its positional nature.

While traditional methods require a careful fitting of time windows (gates) for the best separation, the peak asymmetry method focuses on the morphology of the entire pulse. This makes the algorithm less sensitive to baseline noise and allows for the consideration of the smallest changes in the shape of the decay that can be lost when simply integrating the area under the curve. Thus, the PA method is a more robust and adaptive tool for particle identification in conditions of high background noise.

5. DECLARATION OF COMPETING INTEREST

The authors declare that they have no known competing financial interests or personal relationships that could have appeared to influence the work reported in this paper.

6. ACKNOWLEDGMENTS

This work was supported by the Ministry of Education and Science of Ukraine (the projects: № 0124U000837, № ДЗ/174-2025, 0125U001050, 0124U000837, 0126U003796, 0126U001129).

ORCID

I. Yakymenko, https://orcid.org/0000-0002-0194-8376; **A. Dobrozhan**, https://orcid.org/0000-0002-8830-0942;
G. Onyshchenko, https://orcid.org/0000-0001-6945-8413; **O. Kuzin**, https://orcid.org/0009-0004-3159-1680;
V. Trusova, https://orcid.org/0000-0002-7087-071X; **P. Kuznietsov**, https://orcid.org/0000-0001-8477-1395

REFERENCES

[1] G. Onyshchenko, I. Yakymenko, O. Sidletskiy, P. Kuznietsov, O. Tarasenko, O. Shchus, I. Tolkunov, *et al.*, "Analysis of radiation methods for explosive materials detection," East European Journal of Physics, (4), 682–695 (2025). https://doi.org/10.26565/2312-4334-2025-4-74

[2] G. Onyshchenko, V. Ryzhikov, I. Yakymenko, V. Khodusov, S. Naydenov, A. Opolonin, and S. Makhota, "The Investigation of Mechanisms of Fast Neutron Registration in Oxide Scintillators," East Eur. J. Phys. (3), 54-62 (2019). https://doi.org/10.26565/2312-4334-2019-3-07

[3] G.M. Onyshchenko, V.D. Ryzhikov, I.I. Yakymenko, and O.P. Shchus', "The Threshold of Detection of Fission Materials by ZnWO4 and Bi4Ge3O12 Scintillation Detectors," East Eur. J. Phys. (4), 91-94 (2019). https://doi.org/10.26565/2312-4334-2019-4-10

[4] M. Nakhostin, and P. M. Walker, "A comparison of digital zero-crossing and charge-comparison methods for neutron-gamma pulse shape discrimination," Nuclear Instruments and Methods in Physics Research Section A, **621**(1-3), 498-501 (2010). https://doi.org/10.1016/j.nima.2010.06.252

[5] M. Nakhostin, "A comparison of digital zero-crossing and charge-comparison methods for neutron/γ -ray discrimination with liquid scintillation detectors," Nuclear Instruments & Methods in Physics Research Section A-accelerators Spectrometers Detectors and Associated Equipment, **797**, 77-82 (2015). https://doi.org/10.1016/j.nima.2015.06.041

[6] X. Zhu, C. Feng, Q. Li, Z. Shen, S. Liu, and Q. An, "FPGA-Based Real-Time n/γ Discrimination With Liquid Scintillator," IEEE Transactions on Nuclear Science, **65**(12), 2877-2882 (2018). https://doi.org/10.1109/TNS.2018.2877598

[7] S. Korolczuk, M. Linczuk, R. Romaniuk, & I. Zychor, "Development of a digital method for neutron/gamma-ray discrimination based on matched filtering," Journal of Instrumentation, **11**(09), C09013, (2016). https://doi.org/10.1088/1748-0221/11/09/c09013

[8] K. J. Weinfurther, P.Marleau, and M. Sweany, "Pulse shape measurements for neutron/gamma discrimination using the TOFPET2 ASIC," Journal of Instrumentation (JINST), **18**(07), P07015 (2023). https://doi.org/10.1088/1748-0221/18/07/P07015

[9] I. Yakymenko, G. Onyshchenko, O. Sidletskiy, V. Trusova, O. Tarasenko, P. Kuznietsov, S. Lytovchenko, *et al.*, "Fast neutron discrimination using the Stilbene scintillator," East European Journal of Physics, **4**, 555–559 (2025). https://doi.org/10.26565/2312-4334-2025-4-58

[10] I. Yakymenko, T. Szczesniak, O. Sidletskiy, P. Kuznietsov, A. Syntfeld-Kazuch, M. Grodzicka-Kobylka, V. Trusova, *et al.*, "Experiment details in time resolution measurements of LYSO scintillator," East European Journal of Physics, (4), 661–666 (2025). https://doi.org/10.26565/2312-4334-2025-4-71

[11] P. Li, and H. Liu, "Dataset for neutron and gamma-ray pulse shape discrimination," arXiv (Cornell University). (2023). https://doi.org/10.48550/arxiv.2305.18242

МЕТОДОЛОГІЯ РОЗДІЛЕННЯ НЕЙТРОННИХ ТА ГАММА-ІМПУЛЬСІВ

І. Якименко[1], **А. Доброжан**[1], **Г. Онищенко**[1], **О. Кузін**[1], **В. Трусова**[2], **П. Кузнєцов**[1]

[1]*Кафедра фізики ядра та високих енергій імені О.І. Ахієзера, Харківський національний університет імені В.Н. Каразіна, Харків, Україна*

[2]*Кафедра медичної фізики та біомедичних нанотехнологій, Харківський національний університет імені В.Н. Каразіна, Харків, Україна*

У цьому дослідженні ми запропонували нову методологію дискримінації гамма-нейтронних сигналів у порівнянні з класичним методом інтегруванням заряду. Для запису експериментального набору даних використовувався осцилограф з високою частотою дискретизації Keysight DSOX 6004a (20 ГС/с). Еталонний експеримент було записано за допомогою настільного діджитайзера CAEN DT5720e з встановленою прошивкою DPP PSD. Як детектор було обрано сцинтилятор стильбен розміром 50 мм x 50 мм, з фотопомножувачем R1307 Hamamatsu. Згасання сцинтиляційного імпульсу має експоненціальний хвіст залежно від природи частинок. Запропонований метод спрямований на класифікацію геометричної пікової асиметрії сцинтиляційного імпульсу, виявленого детектором, де коефіцієнт дискримінації – це відношення розрахованої ваги імпульсу (центроїда) до положення максимальної амплітуди імпульсу в часі. Центроїд швидшого гамма-імпульсу ближче до максимальної амплітуди імпульсу та значно зміщений для затриманих нейтронних імпульсів. Обговорюваний підхід дозволяє класифікувати події з порівнянною точністю до методу інтегрування заряду.

Ключові слова: *Інтегрування заряду; сцинтилятори; гамма-нейтрон розділення; стильбен; розділення за формою імпульсу; метод порівняння зарядів; перетин нуля; показник якості розділення; CAEN DT5720e*

EAST EUROPEAN JOURNAL OF PHYSICS. 2. 109-121 (2026)
DOI:10.26565/2312-4334-2026-2-10 ISSN 2312-4334

POROUS CERAMICS AND METAL HYDRIDE MATERIALS FOR EFFICIENT HYDROGEN STORAGE

M.S. Payzullakhanov[1,2], O.R. Parpiev[1], F.A. Giyasova[3], S.U. Turapova[1], E.Z. Nodirmatov[1], M.A. Yuldoshev[4]*, O.T. Ismanova[5], F.A. Giyasov[3], A. Egamberdiyev[6], S.K. Abdizhaliev[7], M.A. Jalelov[7], S.A. Tursinbaev[7], A.A. Abduvakhobov[3]

[1]*Institute of Materials Science, Academy of Sciences of the Republic of Uzbekistan, Tashkent, Uzbekistan*
[2]*Fergana State Technical University, Uzbekistan*
[3]*Kimyo International University in Tashkent, Uzbekistan*
[4]*Turan International University, Namangan, Uzbekistan*
[5]*Namangan State University, Namangan, Uzbekistan*
[6]*Tashkent Institute of Irrigation and Agricultural Mechanization Engineers, National Research University, Uzbekistan*
[7]*Nukus State Pedagogical Institute Named After Ajiniyaz, Nukus, Uzbekistan*
**Corresponding Author e-mail: murod.yuldoshev1993@gmail.com*
Received January 26, 2026; revised April 16, 2026; accepted April 17, 2026

In this work, we investigated synthesized porous aluminosilicate materials containing burnable additives, which form a single-phase cubic zeolite structure (Fm3m, a=4.056 Å). The porous ceramic with a zeolite composition at 200°C and a hydrogen pressure of 12 atm exhibited hydrogen absorption of 11 wt.%. We also studied the initial metallic lithium (BCC, a ≈ 3.507 Å), which was subjected to hydrogenation in the developed sealed reactor at 12 atm and 700 °C with the formation of LiH hydride (FCC, NaCl type, a ≈ 4.081 Å, d_{111} ≈ 2.356 Å). The average size of LiH crystallites does not exceed 100 nm, and the maximum hydrogen capacity of lithium reached 12.4 wt.%. The developed reactor enables safe, high-temperature, high-pressure hydrogenation. These data demonstrate the potential of lithium, titanium, and sodium hydrides, and porous aluminosilicates for the accumulation, storage, and transportation of hydrogen.
Keywords: *Porous aluminosilicates; Lithium hydride; Synthesis; Hydrogenation; X-ray phase analysis; Hydrogen storage; Cubic structure; Hydrogen capacity*
PACS: 68.37.Hk, 78.70.Ck, 77.84.-s

INTRODUCTION

Gaseous fuels, primarily hydrogen and methane, are currently considered among the most promising energy sources, as their use in existing power plants and engines is technically feasible and provides high efficiency [1]. Hydrogen is of particular importance in the context of developing sustainable energy systems. As the most abundant element in the universe and possessing the simplest atomic structure, it is a versatile energy carrier capable of efficiently storing and transporting energy in a form convenient for practical use. Due to its environmental friendliness, high energy density, and compatibility with renewable energy sources, hydrogen is considered a key element in the transition to low-carbon energy. The development of hydrogen energy is central to global strategies to reduce dependence on fossil fuels and minimize anthropogenic environmental impact. A significant advantage of hydrogen is its ability to enable decarbonization of sectors that are difficult to electrify, including heavy transport, industrial production, and power generation [2], making it a fundamental player in building a sustainable energy infrastructure for the future [3].

According to IHS Cambridge Energy Research Associates, the world's natural gas reserves can meet humanity's energy needs for at least 250 years [4]. However, the key factor hindering the widespread use of gas fuels, especially for autonomous and remote energy sources, remains the lack of energy-efficient, fire- and explosion-proof storage and transportation systems capable of handling high gas densities [5]. Hydrogen is of particular interest due to its high specific heat of combustion (~120 MJ kg^{-1}) and the environmental friendliness of its products [6]. However, the practical implementation of hydrogen energy is significantly limited by the difficulties of its storage. Current technologies involve compressing hydrogen to approximately 700 bars (≈70 MPa), which requires robust, sealed tanks and carries an increased risk of explosion [7]. Cryogenic storage, implemented at approximately 20 K, is associated with additional energy costs and increased engineering system complexity [8]. Therefore, the development of alternative, safer methods of hydrogen storage is one of the key objectives of hydrogen energy.

The efficient use of hydrogen in energy systems requires the development of safe, cost-effective, and high-performance storage technologies [9, 10]. One of the most promising approaches is solid-state storage, based on retaining hydrogen in solid materials in molecular or atomic form [11]. This approach is implemented through two main mechanisms: physical adsorption and chemical absorption. Physical absorption is primarily due to van der Waals interactions and is typical for materials such as porous carbon structures, metal–organic frameworks (MOFs) [12], and

Cite as: M.S. Payzullakhanov, O.R. Parpiev, F.A. Giyasova, S.U. Turapova, E.Z. Nodirmatov, M.A. Yuldoshev, O.T. Ismanova, F.A. Giyasov, A. Egamberdiyev, S.K. Abdizhaliev, M.A. Jalelov, S.A. Tursinbaev, A.A. Abduvakhobov, East Eur. J. Phys. 2, 109 (2026), https://doi.org/10.26565/2312-4334-2026-2-10

covalent organic frameworks (COFs) [13]. Despite the high rate and reversibility of sorption processes, this mechanism typically requires low temperatures and elevated pressures and is characterized by a relatively limited hydrogen capacity [14]. Chemical bonding involves the dissociation of hydrogen molecules, followed by the formation of hydride phases, thereby providing a higher storage density [15]. Within this approach, which includes metal and complex hydrides, hydride materials have attracted considerable attention in recent years as a promising basis for developing sustainable hydrogen storage technologies [16]. A promising area is solid-phase hydrogen storage via chemical binding in metal hydrides, which offer high storage density at relatively low pressures (1-40 bar). The volumetric density of hydrogen in metal hydride systems can reach 120-150 kg m^{-3}, which significantly exceeds the value of ~39 kg m^{-3} for compressed hydrogen at a pressure of 700 bar [17-19]. Metal hydrides are also characterized by high reversibility in hydrogen absorption and release, as well as the possibility of multiple cycles. The theoretical mass capacity of such materials is 7.6 wt.% for MgH_2, 4.04 wt.% for TiH_2 and reaches 12.7 wt.% for LiH [20, 21]. At the same time, hydrogenation processes are usually carried out at temperatures of 300–700°C and hydrogen pressures above 10–15 atm, which lead to significant energy costs and impose limitations on the kinetics of phase transformations and thermal stability [22–24].

The kinetics of hydrogen absorption in metal hydride layers are limited by coupled heat and mass transfer processes, which lead to a slow system response to refueling and reduced overall storage efficiency. For a TiMn-based metal hydride material with specified porosity and thermal conductivity parameters, three composite groups were studied: group A, containing 5 wt.% silicone gel and 5 wt.% single-wall carbon nanotubes; group B, including 5 wt.% silicone gel; and group C, containing 5 wt.% silicone gel and 5 wt.% silicone sheets [25]. It was found that the highest porosity is observed in group A (0.527), exceeding the values of other samples by approximately three times, while its thermal conductivity is minimal (2.476 $W \cdot m^{-1} \cdot K^{-1}$) compared to group B (3.189 $W \cdot m^{-1} \cdot K^{-1}$) and group C (3.246 $W \cdot m^{-1} \cdot K^{-1}$). The identified differences in the structural and thermophysical characteristics determine the features of the materials' kinetic behavior: for group A, the diffusion-limited mode of hydrogen absorption in the range of 0.5-1.15 wt.% predominates, which is associated with a well-developed macroporous structure that ensures efficient hydrogen transfer. At the same time, group C is characterized by a higher absorption rate at later stages (above 1.15 wt.%), where the key role is played by increased thermal conductivity, which determines the intensity of the heat flow and, accordingly, the driving force of the sorption process.

In recent years, porous inorganic materials have attracted considerable interest, primarily aluminosilicate and alumina-alumina ceramics, which are capable of accumulating hydrogen through a combination of physical adsorption and diffusion in a developed porous structure [26, 27]. According to the literature [28], such materials are characterized by water absorption in the range of 8-25 %, which corresponds to an open porosity of about 20-50 % and a specific surface area of up to 300-800 $m^2 \cdot g^{-1}$. An increase in the specific surface area and degree of porosity promotes an increase in hydrogen capacity, especially at temperatures above 100 °C, when the contribution of physical adsorption is supplemented by thermally activated diffusion processes [29-32]. The efficiency of hydrogen absorption of porous materials is often estimated using the aspect number, defined as the relative increase in the mass of a sample after saturation with hydrogen. For most aluminosilicate and oxide ceramics, this parameter, according to published data, does not exceed 1-6 wt.% at temperatures up to 300 °C [33, 34]. An increase in the aspect number is possible through optimization of the chemical composition, the introduction of silica-containing components, and the formation of developed open porosity using burnable additives that provide a controlled architecture of the pore space [35, 36]. Lithium hydride is of interest as a reference system for assessing the ultimate capabilities of solid-phase hydrogen storage. Lithium has one of the highest theoretical hydrogen capacities, and the formation of LiH is accompanied by a significant increase in the mass of the material. [37, 38]. X-ray diffraction analysis of lithium samples treated in a hydrogen flow at a pressure of 12 atm and a temperature of 700 °C characterizes the almost complete conversion of the original metal into lithium hydride with a cubic structure and space group $Fm\bar{3}m$, which is confirmed by the presence of intense narrow diffraction peaks and the absence of reflections of metallic lithium. The achieved hydrogen capacity is close to the theoretical limit of 12.5-12.7 wt.% [39, 40]. At the same time, such high temperatures and energy costs significantly limit the practical application of lithium hydride in hydrogen storage systems. Against this background, porous aluminosilicate ceramics, which combine a developed porous structure, controlled phase composition and the ability to operate at moderate temperatures and pressures, are considered a promising alternative to traditional metallic hydrides [41, 42]. Despite growing interest in such materials, the quantitative relationships between their chemical composition, porous structure parameters, phase state, and hydrogen absorption characteristics, especially in the temperature range of 100–200°C, remain poorly understood [43, 44]. Filling this gap represents an important scientific and applied challenge. Furthermore, conducting comprehensive analytical studies aimed at assessing their readiness for commercial implementation, taking into account market requirements, remains a pressing task. Such systematic reviews allow us to identify the most promising materials and technological solutions, as well as focus further research on addressing existing limitations and unresolved issues [45].

The aim of this work is to conduct a comprehensive study of metal hydrides as hydrogen carriers, assessing their applicability in stationary and mobile systems, determining the ultimate efficiency of solid-phase storage using the example of lithium metal hydrogenation using X-ray phase analysis, and developing and studying porous ceramic materials based on aluminum oxide and aluminosilicates to determine the influence of their composition, structure, and temperature conditions on hydrogen sorption and retention processes.

EXPERIMENTAL SAMPLES AND MEASUREMENT METHODS

During experimental studies of material synthesis, various compositions aimed at producing porous ceramics were tested. The porous ceramic materials were formed by introducing burnable additives into the ceramic matrix. The chemical composition of the starting components is presented in Table 1.

Table 1. Chemical composition of raw materials

RAW MATERIALS	Al_2O_3	Fe_2O_3	SiO_2	Na_2O	K_2O	CaO	MgO	Volatile impurities
Kaolin	36.91	2.52	46.84	0.04	0.42	0.24	0.22	12.81
Diatomite	5.65	3.38	88.23	0.34	0.87	0.62	0.82	-

Kaolin was pre-melted in a solar furnace using the previously described method [46], after which the resulting material was wet ground in a ball mill to a particle size of less than 63 μm.

Diatomite was chosen as one of the main components due to its naturally highly porous structure: total porosity reaches 92%, and the SiO_2 mass fraction ranges from 62-97%. Diatomite may also contain fine sand (up to 10%), clay minerals, and trace amounts of organic matter. Based on these components, an aluminum oxide-enriched material was developed. The raw materials used to produce the porous ceramics corresponded to the chemical composition listed in Table 2.

Table 2. Chemical composition of the initial state of the raw material

Oxide	Al_2O_3	P_2O_5	SiO_2	Na_2O	Fe_2O_3	SO_3
Content, wt.%	67.12	0.21	25.21	6.88	0.02	0.56

As shown in Table 2, the main components of the ceramic material are alumina (67 wt.%), silicon oxide (25.2 wt.%), and sodium oxide (6.9 wt.%).

The phase composition of the synthesized samples was studied by X-ray diffraction analysis using a PANalytical Empyrean diffractometer (Cu Kα radiation) in Bragg-Brentano reflection geometry at a wavelength of λ=1.5418 Å. Diffraction patterns were recorded in the angular range $20° \leq 2\theta \leq 60°$, where 2θ is the Bragg angle. The microstructure and surface morphology of the samples were studied by scanning electron microscopy (SEM) using JEOL JSM-6510 and HITACHI FLEXSEM 100 microscopes.

Hydrogenation experiments were conducted using porous zeolite-type materials and metals (aluminum, iron, magnesium, titanium, and lithium), applied in both bulk and powder form [46, 47]. The hydrogenation process was carried out in a reactor equipped with high-temperature packing, as shown in Figure 1.

The high-temperature reactor container shown (Fig. 1) is made of stainless steel and equipped with a sealed lid with a bolted clamping system. The reactor operates according to the diagram shown (Fig. 2) and is equipped with a pressure gauge, gas inlets and shutoff valves for the supply and release of working gas, and sealing devices for operation at elevated temperatures and pressures. The reaction zone is heated using an electric heating module with a digital temperature controller, allowing for precise temperature control and maintenance during hydrogenation experiments.

Figure 1. High-temperature sealed reactor for hydrogenation processes

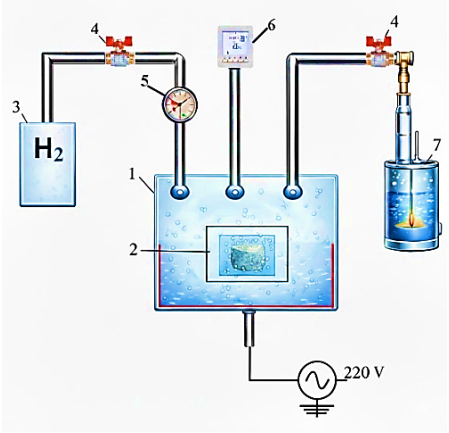

Figure 2. Schematic diagram of the furnace-reactor for hydrogenation of absorption materials at high temperatures (up to 700 °C) and hydrogen pressures up to 15 atm, including: 1 - steel furnace-reactor with an electric heating system from a 220 V network; 2 - absorber; 3 - hydrogen cylinder for feeding gas to the furnace-reactor; 4 - shut-off and control valves; 5 - pressure gauge; 6 - thermocouple connected to a temperature meter; 7 - exhaust gas reservoir

Before the experiment, the samples were dried at 200°C, then weighed and placed in the reactor. To remove air from the reaction chamber before heating, the reactor was purged with hydrogen. The reactor was then sealed and

pressurized with hydrogen at 10-15 atm. Heating was performed according to a preset temperature program ranging from 150 to 700°C. After the holding period, the reactor was cooled either slowly or rapidly, depending on the experimental conditions. Upon completion of cooling, the samples were removed and reweighed. The degree of hydrogenation was assessed by the relative weight gain:

$$\alpha=[(M-M_0)/M_0]\times 100\ \%, \quad (1)$$

where M_0 is the mass of the original sample, M is the mass after hydrogenation.

The formation of metal hydrides is a heterogeneous process [48] that involves the adsorption of molecular hydrogen on the metal surface, its dissociation to form atomic hydrogen, and subsequent diffusion of atoms into the metal's crystal lattice.

RESULTS AND DISCUSSION

Zeolites are known to have high sorption capacity and are widely used in water purification processes to remove hydrocarbon compounds. Their effectiveness is largely determined by the properties of their microstructure, where a fine-grained structure promotes increased sorption activity [49, 50]. In general, the effectiveness of adsorption processes is determined by the parameters of the porous structure and the energy characteristics of the adsorbent-adsorbate interaction, which is driving growing interest in the development of new microporous materials with a specific micropore volume of about 1-2 cm^3/g and a specific surface area of 1500-2000 m^2/g [51].

Therefore, studying the microstructural features of zeolites is of considerable interest for optimizing their performance properties [52, 53]. In particular, the microstructural features of porous ceramics of the zeolitic aluminosilicate composition Al_2SiNaO_6, studied by scanning electron microscopy, are shown in Fig. 3 at magnification ~×1000.

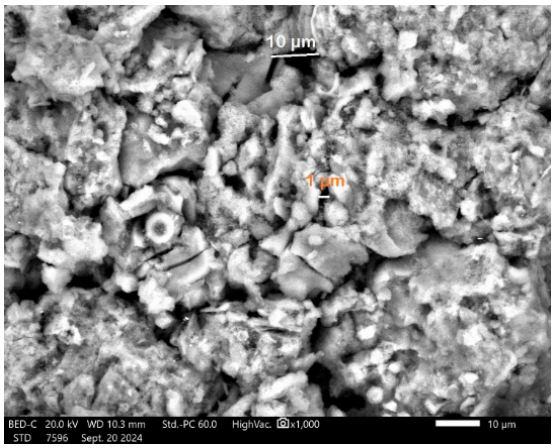

Figure 3. SEM image of the microstructure of porous ceramics of zeolitic aluminosilicate composition Al_2SiNaO_6

Image analysis shows that the material is characterized by a developed hierarchical porous structure. The sizes of the primary particles and their agglomerates are in the range of 1-10 µm, which corresponds to the scale marks in the micrograph. The intergranular space is formed by a system of open pores, predominantly micron and submicron in size (0.3–2 µm), indicating high open porosity of the material. This morphology indicates the formation of a branched pore network, ensuring efficient mass transfer of gaseous and liquid media [54–56]. The rough surface of the grains contributes to an increase in the specific surface area, which for zeolitic aluminosilicate materials, as a rule, reaches values of 100–400 m^2/g. The observed localized areas of compaction up to 5–8 µm in size may be associated with partial sintering and recrystallization of the aluminosilicate matrix during heat treatment. Moreover, the preservation of open pores indicates that the firing temperature was below the threshold for intense shrinkage and pore closure, which is an important factor for the functional properties of the material. The resulting microstructure provides a combination of mechanical cohesion of the ceramic framework and a developed internal surface area. This suggests a high adsorption capacity (approximately 0.5-2.0 mmol/g for small molecules) and the potential for the use of porous Al_2SiNaO_6 ceramics in adsorption, ion exchange, and catalysis processes, as well as in gas storage and transportation systems, including hydrogen [46, 57].

Figure 4 shows an SEM image of the porous structure of a composite absorbent based on Al<SiO_2> (aluminum powder in a silicon dioxide matrix), obtained at a magnification of ×100 for an area of 800×800 µm.

A quantitative analysis of the structure's morphology allowed us to determine the total pore number ($1.35\cdot10^3$) and record their surface concentration at $2.1\cdot10^{-3}$ pores/μm^2. The pore size distribution is characterized by pronounced heterogeneity. The average equivalent pore diameter, calculated based on the area, is 5.4 µm with a median value of 3.1 µm, confirming the presence of a pronounced distribution asymmetry and the predominance of the fine fraction in the structure. These geometric parameters significantly influence the development of the specific surface area and the intensification of capillary phenomena. The presence of pores of varying order forms a branched hierarchical network

that minimizes diffusion resistance and facilitates deep penetration of the working medium into the material. The minimum recorded size is approximately 1.2 μm, while the main range varies between 1.2 and 15 μm. Individual coarse pore formations reach d_{max}≈35 μm, which is associated with the coalescence and agglomeration of particles. An area porosity of 0.62 %, combined with a high pore density, determines the morphology of the sample's internal surface. The resulting active phase contact area increases the material's efficiency as an absorber. This porosity value is typical of materials with intense interparticle void formation. Morphological analysis reveals that the structure is hierarchically organized and includes pores at multiple scales. The predominance of pores smaller than 10 μm indicates the formation of a fine- and mesoporous structure, while the presence of individual macropores is due to localized aggregation of aluminum particles. Al particles form irregular agglomerates, between which intergranular voids form, while the binding phase SiO_2 stabilizes the framework and prevents complete compaction of the system. The obtained parameters reflect the presence of a branched but heterogeneous pore structure resulting from the agglomeration of aluminum powder and the formation of interconnected channels in the silica matrix, which significantly influences the sorption capacity and permeability of the material. The combination of high porosity, significant pore density, and a wide pore size distribution makes this material promising for use as an effective absorber [58, 59].

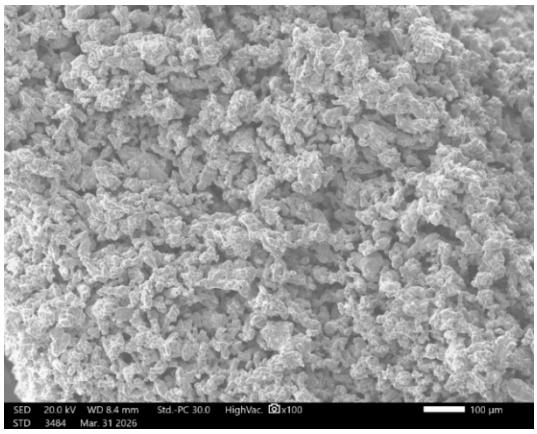

Figure 4. Surface morphology of the porous absorbing structure of Al<SiO_2>

The developed porous structure and the presence of active metal centers ensure their high reactivity with respect to hydrogen, realized through the chemisorption mechanism with the formation of strong Al-H bonds [60, 61]. The process includes the dissociative adsorption of molecular hydrogen on the aluminum surface, subsequent diffusion of atomic hydrogen and the formation of a hydride phase, including AlH_3 [61]. The efficiency of sorption increases at temperatures above 200 °C due to surface activation and increased mobility of hydrogen atoms [62]. Desorption is accompanied by the rupture of AlH bonds and occurs upon heating in the range of 200 - 400 °C [63].

Figure 5 shows the isotherms of hydrogen sorption and desorption in porous Al_2SiNaO_6 ceramics at a temperature of 200 °C in the pressure range of 1–11 atm.

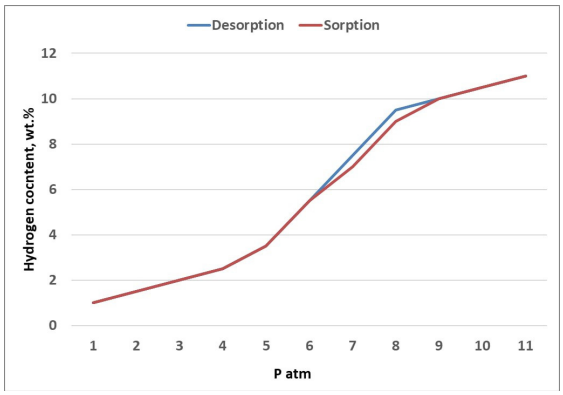

Figure 5. Isotherms of hydrogen sorption and desorption in porous ceramics Al_2SiNaO_6 at a temperature of 200°C

When analyzing the curves (Fig. 5), a gradual increase in the hydrogen content from 1 to 3.5 wt.% is observed in the low-pressure region (1-5 atm). This region corresponds to the initial stage of sorption, during which predominantly physical adsorption of hydrogen occurs on the pore surface and active sites of the material. The linear nature of the curve characterizes a relatively weak interaction and gradual saturation of available adsorption sites. In the pressure range of 5-8 atm, a sharp increase in the hydrogen content is recorded (up to 9-9.5 wt.%). This region is characterized by accelerated sorption and reflects the transition to more intense absorption mechanisms. It is likely that chemisorption occurs in this region, with the formation of chemical bonds between hydrogen and aluminum (possibly the formation of

hydride phases: AlH). Additionally, capillary condensation of hydrogen in meso- and macropores can occur, which is due to the developed porous structure of the material. With a further increase in pressure (8-11 atm), the curve reaches a plateau (10-11 wt%). The established dependence demonstrates saturation of the system with hydrogen and filling of most of the accessible pores and active sites. Reaching a plateau indicates a limited capacity of the material at a given temperature. Comparison of the sorption and desorption curves reveals hysteresis in the medium pressure range (6-9 atm): the desorption curve passes above the sorption curve. The process of hydrogen desorption from porous ceramics occurs intensively at a temperature of 200 °C, ensuring the complete release of previously absorbed hydrogen in a volume of up to 11 wt.% within 2 minutes; the material retains the ability to undergo multiple sorption and is characterized by cyclic stability within 5 sorption-desorption cycles, however, after the fifth cycle, degradation of its structure is observed, accompanied by a decrease and subsequent loss of sorption properties [60, 61, 64].

The obtained data are typical for porous materials with a developed structure and allow us to conclude the presence of pores of various sizes (micro-, meso-, and macropores), capillary effects, and hydrogen retention within the pores, as well as partially irreversible processes caused by chemisorption and the formation of hydride phases. The convergence of the sorption and desorption curves at high pressures (9-10 atm) confirms the achievement of a quasi-equilibrium state of the structure and the mitigation of the influence of kinetic limitations. The obtained isotherms demonstrate a combined mechanism of hydrogen absorption in Al_2SiNaO_6, including physical adsorption, chemisorption, and capillary condensation. Materials of this type are considered promising for the storage and accumulation of hydrogen due to reversible chemisorption and the formation of stable hydride compounds, while pronounced hysteresis indicates the presence of a developed hierarchical porous structure that facilitates the effective accumulation of gas [65, 66].

Figure 6 shows the particle size distribution spectrum for a sample of porous aluminosilicate ceramics of the composition Al_2SiNaO_6, obtained by laser diffraction.

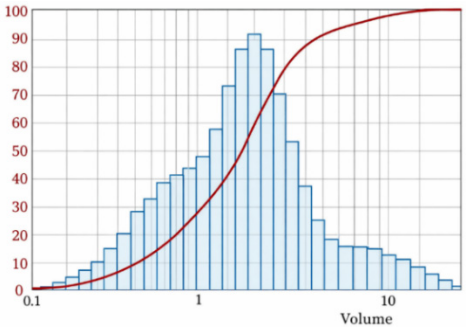

Figure 6. Spectrum of particle size distribution of a porous ceramic sample of aluminosilicate composition Al_2SiNaO_6

The distribution is polydisperse, reflecting the presence of particles of different sizes. The majority of particles are concentrated in the range of 0.5-3.0 μm, with the distribution maximum (modal size) observed in the region of about 1.2-1.5 μm. The cumulative curve shows that approximately 50 % of the particle volume (D_{50}) is accounted for by sizes of the order of 1.3-1.6 μm, while 90 % of the particles (D_{90}) are smaller than 6-8 μm. The presence of a distribution tail in the region of >10 μm indicates the presence of individual agglomerates formed during the sintering process [67]. The obtained data are in good agreement with the results of SEM analysis, confirming the formation of micron-scale agglomerates and a developed porous structure. The predominance of submicron and micron-sized particles contributes to an increase in the specific surface area and the formation of a branched pore network, which is an important factor for the adsorption and ion-exchange properties of the material. The particle size distribution demonstrates the structural heterogeneity characteristic of zeolitic aluminosilicate ceramics and confirms the potential of the Al_2SiNaO_6 composition for functional applications.

X-ray diffraction (XRD) analysis (Fig. 7) of the developed alumina-based material was performed to establish the phase composition, crystallographic parameters, and structural state of the synthesized sample.

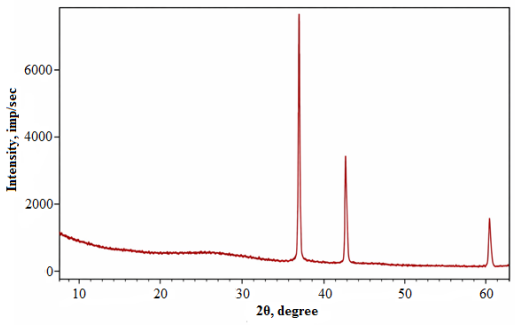

Figure 7. X-ray diffraction pattern of the developed material based on aluminum oxide [68]

The experimental X-ray diffraction pattern is characterized by a set of intense and well-resolved diffraction maxima, the position and relative intensity of which reflect the formation of a single-phase crystalline structure of the zeolite type, corresponding to sodium aluminosilicate of the composition Al_2SiNaO_6. Experimental data have shown their correspondence to the cubic syngony with the space group Fm3m. The calculated unit cell parameter is a = 4.056 nm, which is in good agreement with the literature data [69] for zeolitic aluminosilicate systems. The main diffraction maxima recorded in the X-ray diffraction pattern, as well as the corresponding interplanar distances and crystallographic indices are given in Table 3

Table 3. Diffraction maxima and calculated crystallographic parameters of the AlSiNaO-based material

№ peak	2θ, degree	θ, degree	Interplanar distance d, Å	Miller indices (hkl)	Relative intensity, %
1	38.5	19.25	2.34	(111)	100
2	44.7	22.35	2.02	(200)	~45
3	65.1	32.55	1.43	(220)	~20

The interplanar distances d_{hkl} were calculated using Bragg's law:

$$n\lambda=2d\sin\theta, \quad (2)$$

where, λ is the X-ray wavelength, θ is the diffraction angle, and n=1 is the reflection order. For a cubic crystal system, the lattice parameter was determined from the relationship:

$$a=d_{hkl}(h^2+k^2+l^2)^{1/2}. \quad (3)$$

The obtained values of the unit cell parameter, calculated from various reflections, are in good mutual agreement, indicating the correctness of the phase identification and a high degree of structural ordering. The absence of additional diffraction lines in the studied angular range is an indication of the high phase purity of the synthesized material. The content of possible impurity crystalline phases does not exceed the detection limit of the X-ray diffraction method and is estimated at less than 3-5 wt.%. Analysis of the shape of the diffraction maxima shows that the peaks are narrow and symmetrical, indicating a high degree of crystallinity and a low level of internal microstrains [70]. The sizes of the coherent scattering regions were estimated using the Scherrer formula [71]:

$$D=K\lambda/\beta\cos\theta, \quad (4)$$

where, K is the shape factor (0.9), β is the full width of the peak at half maximum.

Calculations show that the material is characterized by a finely dispersed crystalline structure typical of zeolitic aluminosilicates, which determines the developed specific surface area and potentially high sorption capacity. From a physical point of view, the formation of an ordered aluminosilicate framework with the participation of sodium ions ensures stabilization of the crystal lattice and confirms the completion of the processes of structural self-organization during synthesis [52, 54]. This is a key factor determining the material's functional properties when used in adsorption, catalytic, and ion-exchange processes. Experimental studies have shown (see Fig. 5) that porous zeolite ceramics exhibit good hydrogen absorption. For example, at a temperature of 200 °C and a pressure of 12 atm, porous aluminosilicate ceramics Al_2SiNaO_6 absorbs 11% by weight of hydrogen.

For the metals we obtained, we found that porous nickel possessed a maximum hydrogen capacity of approximately 0.7 wt.% at a pressure of 15 atm and a temperature of 300 °C, while magnesium's absorption value reached 1.5 wt.%. In the aluminum-nickel alloys, signs of hydrogenation were absent across the entire range of the studied parameters. Powdered titanium exhibited the ability to accumulate hydrogen up to 3.8 wt.% at 12 atm and 700 °C, which is slightly lower than the theoretical limit of 4.04 wt.% for TiH_2 hydride. The highest hydrogen capacity was recorded for lithium: at a temperature of 700 °C and a pressure of 12 atm, the hydrogen content reached 12.4 wt.%. According to the analysis of the obtained data, high hydrogen absorption values (over 6 wt.%) are achieved at temperatures of approximately 600-700°C and pressures above 15 atm. Metallic sodium is capable of binding up to 4.3 wt.% hydrogen [72–75].

Figure 8 shows the X-ray diffraction pattern of the original lithium metal sample before exposure to hydrogen

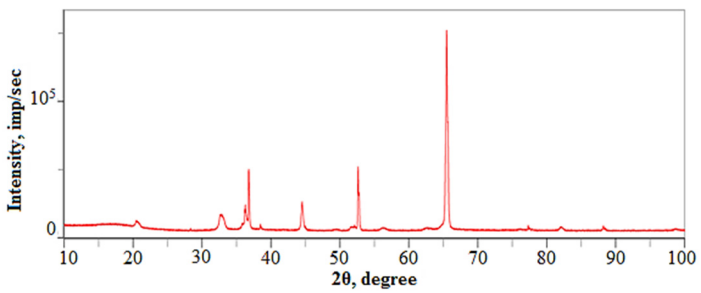

Figure 8. X-ray diffraction pattern of metallic lithium in its original state

The X-ray diffraction pattern is characterized by a set of intense and narrow diffraction peaks corresponding to metallic lithium with a body-centered cubic (BCC) lattice. The diffraction peaks and calculated physical values are listed in Table 4.

Table 4. Diffraction characteristics and interplanar distances of Li

No. peak	2θ, degree	θ, degree	Interplanar distance d, Å	Miller indices (hkl)	Note
1	36.2	18.1	2.479	(110)	The main peak of BCC lithium
2	52.3	26.15	1.748	(200)	Second reflex
3	65.1	32.55	1.432	(211)	Maximum intensity
4	77.0	38.5	1.237	(220)	Additional reflex

The main reflections were recorded at 2θ angles corresponding to the (110), (200), (211), and (220) planes, which is typical for bcc structures. The absence of additional peaks associated with lithium hydrides or oxides (LiH, Li_2O, LiOH) indicates high phase purity of the sample and minimal surface oxidation. The interplanar distances d_{hkl} were calculated using Bragg's law (2). For the most intense reflection (211) at 2θ = 65.1°, d_{211}≈1.432 Å was obtained. The cubic unit cell parameter a was calculated using formula (3), which yielded a value of 3.507 Å for the (211) reflection, which is consistent with the reference data [69] for metallic lithium at room temperature (a = 3.51 Å). The observed small width of the diffraction maxima indicates high crystallinity and large crystallites (>100 nm). The predominance of the intensity of the diffraction peak (211) compared to the reflection (110) is due to the presence of a preferred orientation of crystallites, characteristic of rolled or annealed lithium foils. In the region of small angles (10°-25°), a weak amorphous rise in the background is observed, which is associated with the presence of a thin layer of natural lithium oxide or carbonate on the surface. The absence of distinct peaks of hydrides or oxides confirms the predominance of the metallic phase in the initial state. The experimental results indicate that lithium in the initial state is a thermodynamically stable metallic phase with a well-ordered bcc lattice, ensuring high atomic mobility and the presence of interstitial positions. These properties create favorable conditions for subsequent hydrogenation and the formation of the hydride phase LiH [76-78]. The X-ray diffraction pattern confirms that the original sample is single-phase metallic lithium with a high degree of crystallinity and lattice parameters corresponding to reference data, which allows this material to be used as a reference when assessing structural changes after hydrogen treatment [79].

An X-ray diffraction pattern (Fig. 9) of metallic lithium after treatment in a hydrogen atmosphere at a pressure of 12 atm and a temperature of 700 °C allows us to evaluate the phase composition, degree of hydrogenation and structural changes of the original material.

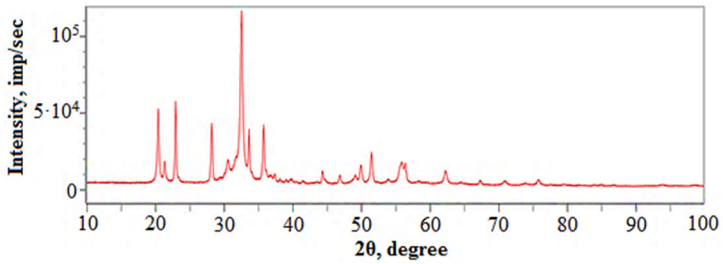

Figure 9. X-ray diffraction pattern of metallic lithium after treatment in a hydrogen atmosphere at a pressure of 12 atm and a temperature of 700°C

The diffraction pattern shows a significant weakening of the peaks of the original metallic lithium, as well as the appearance of new diffraction maxima characteristic of LiH with a cubic lattice of the NaCl type and the Fm3m space group, demonstrating partial or complete conversion of the metal into hydride under the specified conditions. Additional weak peaks in the range of 20°-35° correspond to the products of surface interaction with oxygen or moisture, such as LiOH and Li_2O [80]. The interplanar distances d_{hkl} were calculated based on Bragg's law (2). For the (111) peak of LiH at 2θ≈38.2°, the angle θ=19.1°, which gives d_{111}≈2.356 Å. The cubic lattice parameter has a value of a ≈ 4.081 Å, close to the reference value [69] for LiH (≈4.084 Å), confirming the formation of a stoichiometric hydride. The average size of the coherent scattering regions was estimated using the Scherrer formula (4). The narrow peaks of LiH indicate large crystallites (>100 nm), characteristic of hydrides obtained at high temperatures.

Table 5. Diffraction maxima and calculated parameters of LiH

No. peak	2θ, degree	θ, degree	Interplanar distance d, Å	Miller indices (hkl)	Parameter a, Å	Note
1	38.22	0.3335	2.353	(111)	4.076	Main peak LiH
2	44.39	0.3874	2.039	(200)	4.078	Second reflex
3	64.58	0.5636	1.442	(220)	4.078	Additional peak
4	77.72	0.6782	1.228	(311)	4.073	
5	81.85	0.7143	1.176	(222)	4.074	

The change in the intensity and position of the diffraction peaks compared to the original metal indicates a complete rearrangement of the lithium crystal structure. The appearance of new reflections confirms the formation of lithium hydride, and the weakening of the peaks of the original Li indicates a high degree of metal transformation. The width of the peaks demonstrates the high crystallinity of the hydride and the large sizes of the crystallites, and the increase in the background in the small-angle region indicates the presence of an amorphous phase or fine-crystalline oxidation products [81, 82]. The X-ray diffraction pattern (Fig. 9) confirms the successful synthesis of lithium hydride with a cubic structure, high crystallinity and stability of the hydride phase. The presence of additional peaks confirms the sensitivity of the material to oxygen and moisture, which form surface hydroxides and oxides. The data obtained form the basis for the analysis of the hydrogenation kinetics and thermodynamics of lithium hydrogen accumulation. In the case of lithium, the hydrogenation reaction proceeds according to the equation [80]:

$$2Li+H_2 \rightarrow 2LiH, \quad (5)$$

At an optimal temperature of 600-700 °C, the resulting lithium hydride is characterized by an ionic bond (Li^+H^-) and remains thermally stable up to its melting point of approximately 688 °C.

When heated to temperatures around 700 °C or upon contact with water, LiH decomposes, releasing hydrogen. The thermal decomposition is described by the reaction:

$$2LiH \rightarrow 2Li+H_2, \quad (6)$$

whereas when interacting with water, an exothermic reaction occurs:

$$LiH+H_2O \rightarrow LiOH+H_2. \quad (7)$$

Calculations show that up to 290 g of hydrogen can be produced from 1 kg of lithium hydride when reacted with water. Overall, it has been established that lithium, titanium, and sodium provide hydrogen storage at levels of 12.4, 4.1, and 4.3 wt.%, respectively, making these hydride systems promising for hydrogen storage and transportation.

CONCLUSIONS

In this study, porous aluminosilicate materials Al_2SiNaO_6 were synthesized based on kaolin and diatomite using burnable additives to ensure the formation of a developed porous structure. The porous ceramics of the zeolitic aluminosilicate composition Al_2SiNaO_2 are characterized by a developed hierarchical microstructure with a system of open pores of micron and submicron sizes (~0.3-2 μm). The particle sizes and their agglomerates range from 1-10 μm, while granulometric analysis revealed a polydisperse distribution with a median size of $D_{50} \approx$ 1.3-1.6 μm and a D_{90} value of < 6-8 μm. The rough surface of the grains ensures a high specific surface area for the material, ranging from 100 to 400 m²/g. The preservation of an open porous structure after heat treatment indicates an optimal sintering regime, ensuring mechanical cohesion of the framework without significant pore closure. The combination of structural characteristics suggests a high adsorption capacity of the material (~0.5-2.0 mmol/g for small molecules) and confirms the potential for the use of Al_2SiNaO_6 ceramics in adsorption, ion exchange, and catalytic processes, as well as in gas storage systems, including hydrogen storage.

X-ray diffraction analysis revealed that the samples possess a single-phase zeolite-type crystal structure with a cubic syngony and the Fm3m space group. The unit cell parameter was a = 4.056 Å, and the dimensions of the coherent scattering regions according to the Scherrer formula indicate a finely dispersed crystalline structure, which ensures a developed specific surface area and high sorption capacity.

An analysis of sorption and desorption isotherms revealed that porous Al_2SiNaO_6 ceramics at 200 °C and pressures of 1-11 atm is characterized by stepwise hydrogen absorption, reaching a maximum capacity of 10-11 wt.%. Physical adsorption occurs in the range of 1-5 atm (1-3.5 wt.%), while at 5-8 atm (up to 9-9.5 wt.%) a transition to intense mechanisms, including chemisorption and capillary condensation, is observed. Reaching a plateau at 8-11 atm reflects the saturation of the porous structure. Hysteresis in the range of 6-9 atm indicates the development of hierarchical porosity and partially irreversible processes associated with the formation of hydride phases. Desorption occurs rapidly, completing within 2 min, with the release of up to 11 wt.% hydrogen. The Al_2SiNaO_6 material has a high sorption capacity and a combined mechanism of interaction with hydrogen, demonstrating stability for up to 5 sorption-desorption cycles; after this, structural degradation is observed, limiting its cyclic stability for gas storage.

All hydrogenation experiments were conducted in a specially designed high-temperature sealed hydrogen reactor operating at pressures up to 15 atm and temperatures up to 700 °C. This reactor enabled us to achieve a high degree of hydrogenation and the stable formation of crystalline LiH. The initial lithium metal was characterized by a body-centered cubic lattice with a lattice parameter a ≈ 3.507 Å and large crystallites (>100 nm). After treatment in a hydrogen atmosphere at a pressure of 12 atm and a temperature of 700 °C, lithium was completely or partially converted to lithium hydride (LiH) with a face-centered cubic NaCl-type structure and a lattice parameter a ≈ 4.081 Å. The main interplanar distances are: $d_{111} \approx$ 2.356 Å, $d_{200} \approx$ 2.039 Å, $d_{220} \approx$ 1.442 Å, which corresponds to the reference data for LiH. The average crystallite size exceeds 100 nm, which confirms the high crystallinity of the hydride. Experimental measurements of hydrogen absorption showed maximum values: Li - 12.4 wt.%, Ti - 3.8 wt.%, Na - 4.3 wt.%, which indicates the high efficiency of lithium as a hydrogen battery at temperatures of 600-700 °C and

pressures of 12-15 atm. Lithium hydrogenation proceeds according to the equation $2Li + H_2 \rightarrow 2LiH$, and LiH maintains thermal stability up to 688 °C and can release hydrogen upon reaction with water: $LiH + H_2O \rightarrow LiOH + H_2$, yielding up to 290 g of hydrogen per 1 kg of hydride. Due to its high hydrogen capacity and stable crystalline structure under standard conditions, lithium hydride (LiH) is widely used in aerospace, portable hydrogen generators, as a neutron moderator, and as a component of fusion fuel. LiH is also a promising material for storing and transporting hydrogen in industrial processes.

Funding

The work was carried out with the financial support of the Ministry of Innovative Development of the Republic of Uzbekistan within the framework of projects AL-4821023123 "Technology of efficient storage of hydrogen in absorbed form in porous materials" and IL-9224094112 "Development of metal hydride materials and a container for storing hydrogen".

ORCID

F.A. Giyasova, https://orcid.org/0000-0003-0746-4986; **M.A. Yuldoshev,** https://orcid.org/0000-0002-9722-9439
F.A. Giyasov, https://orcid.org/0009-0003-9882-0655; **A. Egamberdiyev,** https://orcid.org/0009-0009-9653-4923
O.T. Ismanova, https://orcid.org/0000-0003-2644-2459; **S.K. Abdizhaliev,** https://orcid.org/0000-0003-1762-3645
M.A. Jalelov, https://orcid.org/0009-0001-9559-2568; **S.A. Tursinbaev,** https://orcid.org/0000-0003-4105-1843

REFERENCES

[1] Z.R. Chong, Sh.H.B. Yang, P. Babu, and P. Linga, "Review of natural gas hydrates as an energy resource: Prospects and challenges," Applied Energy, **162**, 1633-1652 (2016). https://doi.org/10.1016/j.apenergy.2014.12.061
[2] S.S. Oladosu, T.L. Amosa, T.I. Olutoki, J.O. Ansari, M.N.M. Abioye, K.J. Rehman, and Z.U Soleimani, "Hydrogen-powered horizons: transformative technologies in clean energy generation, distribution, and storage for sustainable innovation," International Journal of Hydrogen Energy, **56**, 1152-1182 (2024). https://doi.org/10.1016/j.ijhydene.2023.12.186
[3] W. Liu, J.A. Tupe, and F.A. Zinsou, "Metal Hydride Storage Systems: Approaches to Improve Their Performances," Particle & Particle Systems Characterization, **42**(3), (2024). https://doi.org/10.1002/ppsc.202400163
[4] R.A. Kerr, "Energy. Natural gas from shale bursts onto the scene," Science, **328**(5986), 1624-1626 (2010). https://doi.org/10.1126/science.328.5986.1624
[5] S.O. Akpasi, I.M.S. Anekwe, E.K. Tetteh, U.O. Amune, Sh.I. Mustapha, and S.L. Kiambi, "Hydrogen as a clean energy carrier: advancements, challenges, and its role in a sustainable energy future," Clean Energy, **9**(1), 52-88 (2025). https://doi.org/10.1093/ce/zkae112
[6] W. Gao, Z. Fu, Y. Li, Y. Li, and J. Zou, "Progress of Performance, Emission, and Technical Measures of Hydrogen Fuel Internal-Combustion Engines," Energies, **15**, 7401 (2022). https://doi.org/10.3390/en15197401
[7] S.A. Okyere, R.A. Mensah, J. Sandström, and M. Försth, "Risk and safety assessment of hydrogen pipelines and storage tanks using preliminary hazard analysis," Frontiers in Chemical Engineering, **7**, (2025). https://doi.org/10.3389/fceng.2025.1722173
[8] J. Xu, R. Wan, Xi Chen, and Binlin Dou, "Cryogenic supercritical hydrogen storage: Design and thermodynamic optimization via multi-stage Joule-Brayton refrigeration cycles," Energy, **338**, 138737 (2025). https://doi.org/10.1016/j.energy.2025.138737
[9] S.K.S. Patel, R.K. Gupta, M. Rohit, J.-K. Le, "Recent Developments in Hydrogen Production, Storage, and Transportation: Challenges, Opportunities, and Perspectives," Fire, **7**(7), 233 (2024). https://doi.org/10.3390/fire7070233
[10] N.I. Beyazit, "Comparative Study of Hydrogen Storage and Metal Hydride Systems: Future Energy Storage Solutions," Processes, **13**(5), 1506, (2025). https://doi.org/10.3390/pr13051506
[11] M. Yue, H. Lambert, E. Pahon, R. Roche, S. Jemei, and D. Hissel, "Hydrogen energy systems: A critical review of technologies, applications, trends and challenges," Renewable and Sustainable Energy Reviews, **146**, 111180 (2021). https://doi.org/10.1016/j.rser.2021.111180
[12] Y. Li, Q. Guo, Zh. Ding, H. Jiang, H. Yang, W. Du, Y. Zheng, *et al*., "MOFs-Based Materials for Solid-State Hydrogen Storage: Strategies and Perspectives," Chemical Engineering Journal, **485**(7623), 149665 (2024). https://doi.org/10.1016/j.cej.2024.149665
[13] X. Miao, J. He, H. Zhai, Zh. Wu, Y. Li, and Zh. Jin, "Adjustment the donor-acceptor COFs structure enhances the electron push-pull effect to induce electron transfer to Pt site and improve photocatalytic hydrogen evolution," Carbon, **239**, 120297 (2025). https://doi.org/10.1016/j.carbon.2025.120297
[14] S. Kumar, M. Myekhlai, S. Lim, and H. Oh, "Understanding factors affecting storage capacity and reproducibility in realistic ambient-temperature hydrogen physisorption," Sustainable Energy Fuels, **10**, 961-983 (2026). https://doi.org/10.1039/D5SE01539A
[15] P. Chen, E. Akiba, O.Sh. Ichi, A. Züttel, and L. Schlapbach, "Hydrogen Storage by Reversible Metal Hydride Formation," in: *Hydrogen Science and Engineering: Materials, Processes, Systems and Technology*, edited by P.D.D. Stolten, and D.B. Emonts, (Wiley-VCH Verlag GmbH & Co. KGaA, 2007), pp. 763-790. https://doi.org/10.1002/9783527674268.ch31
[16] S. Bagyalakshmi, A. Sivakami, R. Deeptha, G. Manikandan, T. Sukumar, and S. Srinivasulu, "MOF-Metal hydride composite materials for hydrogen storage: A comprehensive review," Journal of Alloys and Compounds, **1060**, 187192 (2026). https://doi.org/10.1016/j.jallcom.2026.187192
[17] B. Sakintuna, F.L. Darkrim, and M. Hirscher, "Metal hydride materials for solid hydrogen storage: A review," International Journal of Hydrogen Energy, **32**(9), 1121-1140 (2007). https://doi.org/10.1016/j.ijhydene.2006.11.022
[18] N. Klopčič, I. Grimmer, F. Winkler, M. Sartory, and A. Trattner, "A review on metal hydride materials for hydrogen storage," Journal of Energy Storage, **72**(Part B), 108456 (2023). https://doi.org/10.1016/j.est.2023.108456
[19] A.S. Mekonnin, K. Wacławiak, M. Humayun, Z. Shang, and H. Ullah, "Hydrogen Storage Technology, and Its Challenges: A Review," Catalysts, **15**, 260 (2025). https://doi.org/10.3390/catal15030260
[20] G. Amica, P.A. Larochette, and F.C. Gennari, "Hydrogen storage properties of $LiNH_2$-LiH system with MgH_2, CaH_2 and TiH_2 added," International Journal of Hydrogen Energy, **40**(30), 9335-9346 (2015). https://doi.org/10.1016/j.ijhydene.2015.05.091

[21] H. Hong, H. Guo, Zh. Cui, A. Ball, and B. Nie, "Structure modification of magnesium hydride for solid hydrogen storage," International Journal of Hydrogen Energy, **78**, 793-804 (2024). https://doi.org/10.1016/j.ijhydene.2024.06.327
[22] V.K. Kukkapalli, S. Kim, and S.A. Thomas, "Thermal Management Techniques in Metal Hydrides for Hydrogen Storage Applications: A Review," Energies, **16**, 3444 (2023). https://doi.org/10.3390/en16083444
[23] Sh.B. Utamuradova, F.A. Giyasova, K.N. Bakhronov, M.A. Yuldoshev, M.R. Bekchanova, and B. Ismatov, East Eur. J. Phys. (3), 325-335 (2025). https://doi.org/10.26565/2312-4334-2025-3-31
[24] S.S Kareem, Q. Hassan, H.F. Fakhruldeen, T.M. Hanoon, F.I. Jabbar, S. Algburi, and D.H. Khalaf, "A review on physical and chemical hydrogen storage methods for sustainable energy applications," Unconventional Resources, **8**, 100235 (2025). https://doi.org/10.1016/j.uncres.2025.100235
[25] W. Wang, Sh. Xu, X. Li, T. Cheng, Y. Li, W. Fang, X. Ren, and L. He, "Preparation and Hydrogen Absorption Kinetics Study of Hybrid Molding Metal Hydride Beds," Inorganics, **14**(4), (2026). 110 https://doi.org/10.3390/inorganics14040110
[26] A. Gil, R. Trujillano, M.A. Vicente, and S.A. Korili, "Hydrogen adsorption by microporous materials based on alumina-pillared clays," International Journal of Hydrogen Energy, **34**(20), 8611-8615 (2009). https://doi.org/10.1016/j.ijhydene.2009.08.057
[27] Y. Wen, X. Chai, Y. Gu, W. Wu, W. Ma, J. Zhang, and T. Zhang, "Advances in hydrogen storage materials for physical H_2 adsorption," International Journal of Hydrogen Energy, **97**, 1261-1274 (2025). https://doi.org/10.1016/j.ijhydene.2024.11.459
[28] A. Metrane, A. Delhali, M. Ouikhalfan, A.H. Assen, and Y. Belmabkhout, "Water Vapor Adsorption by Porous Materials: From Chemistry to Practical Applications," J. Chem. Eng. Data, **67**(7), 1617-1653 (2022). https://doi.org/10.1021/acs.jced.2c00145
[29] R.Ch. Muduli, and P. Kale, "Advanced materials for solid-state hydrogen storage: A review on high-surface-area innovations," International Journal of Hydrogen Energy, **170**, 151049 (2025). https://doi.org/10.1016/j.ijhydene.2025.151049
[30] M.S. Payzullakhanov, F.A. Giyasova, M.A. Yuldoshev, Ch.X. Toshpulatov, R.U. Ernazarov, F.A. Giyasov, A. Urishev, *et al*., East Eur. J. Phys. (1), 233-240 (2026). https://doi.org/10.26565/2312-4334-2026-1-25
[31] J. Matrasulov, J.R. Yusupov, and A.A. Saidov, "Fast forward evolution in heat equation: Tunable heat transport in adiabatic regime," Nanosystems: Phys. Chem. Math. **14**(4), 421–427 (2023). https://doi.org/10.17586/2220-8054-2023-14-4-421-427
[32] R.M. Ospino, A. Celzard, and V. Fierro, "Hydrogen Adsorption in High-Surface Area Porous Materials," in: *Hydrogen Storage*, (ISTE Ltd., 2025), pp. 357-393. https://doi.org/10.1002/9781394401635.ch8
[33] N.Yu. Sharibaev, A.Q. Ergashov, S.B. Fazliddinov, R.G. Ikramov, M.A. Yuldoshev, and A.A. Abdulxayev, Journal of Ovonic Research. **21**(6), (2025). https://doi.org/10.15251/JOR.2025.216.859
[34] P.K. Chauhan, R. Parameshwaran, P. Kannan, R. Madhavaram, and R. Sujith, "Hydrogen storage in porous polymer derived Silicon Oxycarbide ceramics," Ceramics International, **47**(2), 2591-2599 (2021). https://doi.org/10.1016/j.ceramint.2020.09.105
[35] M.L. Jalaluddin, U.A. Azlan, M.W. Rashid, N. Tamin, and M.N. Masri, "A review of pore-forming agents on the structures, porosities, and mechanical properties of porous ceramics," AIMS Materials Science, **11**(4), 634–665 (2024). https://doi.org/10.3934/matersci.2024033
[36] A. Mocciaro, B. Lombardi, and A.N. Scian, "Porous texture of a ceramic material made with pore formers agents," Novye ogneupory, (2017). https://doi.org/10.17073/1683-4518-2017-1-54-57 (in Russian)
[37] Lei Wang, M.Z. Quadir, and K.F. Zinsou, "Direct and reversible hydrogen storage of lithium hydride (LiH) nanoconfined in high surface area graphite," International Journal of Hydrogen Energy, **41**(40), 18088-18094 (2016). https://doi.org/10.1016/j.ijhydene.2016.07.073
[38] S. Banger, V. Nayak, and U.P. Verma, "Hydrogen storage in lithium hydride: A theoretical approach," Journal of Physics and Chemistry of Solids, **115**, 6-17 (2018). https://doi.org/10.1016/j.jpcs.2017.11.027
[39] M.G. Dadamirzaev, M.K. Uktamova, S.R. Boydedayev, M.A. Yuldoshev, and S.H. Mamadaliev, "Theoretical Analysis of Photon-Energy-Controlled Quantum Tunneling Mechanisms Based on the Landauer–Büttiker Formalism," Physics AUC, **35**, 76-84 (2025). https://share.google/EqKveBzVq9UCc2Ndc
[40] M. Abbas, D.M. Grant, M. Brunelli, and T.Ch. Hansen, "Reducing the dehydrogenation temperature of lithium hydride through alloying with germanium," Physical Chemistry Chemical Physics 15(29) (2013). https://doi.org/10.1039/c3cp51330k
[41] E. Rivard, M. Trudeau, and K. Zaghib, "Hydrogen Storage for Mobility: A Review," Materials, **12**, 1973 (2019). https://doi.org/10.3390/ma12121973
[42] T.H. Le, M.P. Kim, and Ch. Tran, "Recent Developments in Materials for Physical Hydrogen Storage: A Review," Materials, **17**, 666 (2024). https:// doi.org/10.3390/ma17030666
[43] Z. Chen, K.O. Kirlikovali, K.B. Idrees, M.C. Wasson, and O.K. Farha, "Porous materials for hydrogen storage," Chem. **8**, (2022). https://doi.org/10.1016/j.chempr.2022.01.012
[44] M.R Kalibek, A.D Ospanova, B. Suleimenova, R. Soltan, T. Orazbek, A.M Makhme, Kh.S. Rafikova, and N. Nuraje, "Solid-state hydrogen storage materials," Discov. Nano. **19**(1), 195 (2024). https://doi.org/10.1186/s11671-024-04137-y
[45] A. Alobaid, M. Kamil, and Kh.A. Khalil, "Metal hydrides for solid hydrogen storage: Experimental insights, suitability evaluation, and innovative technical considerations for stationary and mobile applications," International Journal of Hydrogen Energy, **128**(25), 432-456 (2025). https://doi.org/10.1016/j.ijhydene.2025.04.232
[46] M.S. Payzullakhanov, O.R. Parpiev, N.R. Avezova, and Zh. Shermatov, "Hydrogen Storage in Porous Ceramic Materials of Aluminosilicate Composition," Appl. Sol. Energy, **58**, 722-724 (2022). https://doi.org/10.3103/S0003701X22601338
[47] B.M. Ali, A.A. Abdulazez, G.P. Priya, S. Ray, A. Pal, R. Sharma, S. Usanov, *et al*., "Modification of graphenylene nanostructure as a promising material for adsorption and sensing of 5-fluorouracil," First-principles investigations. Journal of Molecular Graphics and Modelling, **142**, 109210 (2026). https://doi.org/10.1016/j.jmgm.2025.109210
[48] V.G. Minkina, S.I. Shabunya, V.I. Kalinin, and A. Smirnova, "Hydrogen generation from sodium borohydride solutions for stationary applications," international journal of hydrogen energy, **41**, 9227e9233 (2016). http://dx.doi.org/10.1016/j.ijhydene.2016.03.063
[49] E.P. Botella, S. Valencia, and F. Rey, "Zeolites in Adsorption Processes: State of the Art and Future Prospects," Chem. Rev. **122**(24), 17647−17695 (2022). https://doi.org/10.1021/acs.chemrev.2c00140
[50] Sh. Kumari, J. Chowdhry, M. Kumar, and M.Ch. Garg, "Zeolites in wastewater treatment: A comprehensive review on scientometric analysis, adsorption mechanisms, and future prospects," Environmental Research, **260**, 119782 (2024). https://doi.org/10.1016/j.envres.2024.119782

[51] L. Hu, W. Wu, M. Hu, L. Jiang, D. Lin, J. Wu, and K. Yang, "Double-walled Al-based MOF with large microporous specific surface area for trace benzene adsorption," Nat. Commun. **15**, 3204 (2024). https://doi.org/10.1038/s41467-024-47612-x
[52] S.F. Samadov, N.V.M. Trung, A.A. Sidorin, S.I. Ibragimova, S.H. Jabarov, M.A. Yuldoshev, *et al*., "Effect of Zn and Fe doping on vacancy cluster formation in Cu–In–Se system," Micro and Nanostructures, **209**, 208451 (2026). https://doi.org/10.1016/j.micrna.2025.208451
[53] F. Bahmanzadegan, and A. Ghaemi, "A comprehensive review on novel zeolite-based adsorbents for environmental pollutant," Journal of Hazardous Materials Advances, **17**, 100617 (2025). https://doi.org/10.1016/j.hazadv.2025.100617
[54] N. Kordala, M. Wyszkowski, and Z. Properties, "Methods of Synthesis, and Selected Applications," Molecules, **29**(5), 1069 (2024). https://doi.org/10.3390/molecules29051069
[55] F.A. Giyasova, Kh.N. Bakhronov, M.A. Yuldoshev, I.B. Sapaev, R.G. Ikramov, F.A. Giyasov, M.R. Bekchanova, *et al*., "Study of the Influence of Temperature on the Transitions of the CdS/Si/CdTe Heterosystem," East Eur. J. Phys. (4), 461-468 (2025). https://doi.org/10.26565/2312-4334-2025-4-47
[56] W.J. Roth, B. Gil, K.A. Tarach, and K.G. Marek, "Top-down engineering of zeolite porosity," Chem. Soc. Rev. **54**, 7484-7560 (2025). https://doi.org/10.1039/D5CS00319A
[57] O. Ergashev, Kh. Bakhronov, F. Giyasova, E. Nazirakhon, R. Yunusova, V. Gaffarova, O. Ochilova, *et al*., "Energy Characteristics, Adsorption Kinetics, and Mechanism of Triethylamine Adsorption on CsZSM-5 Zeolite," J. Appl. Organomet. Chem. **6**(1), 43-52 (2026). https://doi.org/10.48309/JAOC.2026.546865.1334
[58] N.S. Venkataramanan, and Y. Kawazoe, "DFT Perspective of Hydrogen Storage on Porous Materials," Materials Science, (2011). arXiv:1102.0849. https://doi.org/10.48550/arXiv.1102.0849
[59] Sh. Mirzaei, A. Ahmadpour, Z. Shao, and A.A. Niya, "Rational design of carbon-based materials for purification and storage of energy carrier gases of methane and hydrogen," Materials Science, (2022). arXiv:2204.11600. https://doi.org/10.48550/arXiv.2204.11600
[60] A. Züttel, and L. Schlapbach, "Hydrogen-storage materials for mobile applications," Nature, **414**(6861), 353-358 (2001). https://doi.org/10.1038/35104634
[61] A. Züttel, "Materials for hydrogen storage," Materials Today, **6**(9), 24-33 (2003). https://doi.org/10.1016/S1369-7021(03)00922-2
[62] J. Graetz, "New approaches to hydrogen storage," Chemical Society Reviews, **38**(1), 73-82 (2009). https://doi.org/10.1039/b718842k
[63] O.Sh. Ichi, Y. Nakamori, J.R. Eliseo, A. Züttel, and C.M. Jensen, "Complex Hydrides for Hydrogen Storage," Chemical Reviews, 107(10), 4111-4132 (2007). https://doi.org/10.1021/cr0501846
[64] M.V. Lototskyy, V.A. Yartys, B.G. Pollet, and R. Bowman, "Metal hydride hydrogen compressors: A review," International Journal of Hydrogen Energy, **39**, 5818-5851 (2014). https://doi.org/10.1016/j.ijhydene.2014.01.158
[65] M. Thommes, K. Kaneko, A. Neimark, J.P. Olivier, F.R. Reinoso, J. Rouquerol, and K.S.W. Sing, "Physisorption of gases, with special reference to the evaluation of surface area and pore size distribution (IUPAC Technical Report)," Pure and Applied Chemistry, **87**(9) (2015). https://doi.org/10.1515/pac-2014-1117
[66] B. Sakintuna, F.L. Darkrim, and M. Hirscher, "Metal hydride materials for solid hydrogen storage: A review," International Journal of Hydrogen Energy, **32**(9), 1121-1140 (2007). https://doi.org/10.1016/j.ijhydene.2006.11.022
[67] Y. Bai, G. Wagner, and Ch.B. Williams, "Effect of Particle Size Distribution on Powder Packing and Sintering in Binder Jetting Additive Manufacturing of Metals," J. Manuf. Sci. Eng. **139**(8), 081019 (2017). https://doi.org/10.1115/1.4036640
[68] M.S. Paizullakhanov, O. Parpiev, Zh.Z. Shermatov, O. Ruzimuradov, and N.N. Cherenda, "Hydrogen Absorbers Based On Porous Ceramics Synthesized In A Solar Furnace," High Temperature Material Processes An International Quarterly of High-Technology Plasma Processes, **28**(4) (2024). https://doi.org/10.1615/HighTempMatProc.2024053882
[69] J.W. Anthony, R.A. Bideaux, K.W. Bladh, and C.M. Nichols, *Handbook of Mineralogy*, (Mineralogical Society of America, 2010), pp. 4128.
[70] T. Ungár, "Microstructural parameters from X-ray diffraction peak broadening," Scripta Materialia, **51**(8), (2004). https://doi.org/10.1016/j.scriptamat.2004.05.007
[71] D. Balzar, "X-Ray Diffraction Line Broadening: Modeling and Applications to High-Tc Superconductors," J. Res. Natl. Inst. Stand. Technol. **98**(3), 321–353 (1993). https://doi.org/10.6028/jres.098.026
[72] M.S. Paizullakhanov, F.A. Giyasova, Kh.N. Bakhronov, M.A. Yuldoshev, A.A. Mamadaliev, F.A. Giyasov, F.T. Akbarova, *et al*., "Investigation of the Processes Involved in the Formation of Pyroxene Materials during Solar Melting in a Large Solar Furnace," Journal of Ovonic Research. **22**(1), 51-66 (2026). https://doi.org/10.15251/JOR.2026.221.51
[73] F.A. Giyasova, A.Z. Rakhmatov, Kh.N. Bakhronov, M.A. Yuldoshev, F.A. Giyasov, A.N. Olimov, and N.A. Sattarov, "Physical Principles of Photocurrent Generation in a Silicon-Based Photodiode Structure with a Schottky Barrier," East Eur. J. Phys. 4, 397-406 (2025). https://doi.org/10.26565/2312-4334-2025-4-38
[74] A. Tayyab, M. Shakil, N. Rehman, S.S.A. Gillani, I.A. Ahmed, and M. Kallel, "Exploring reversible hydrogen storage capacity of Li and Na metal-decorated Sc_3N_2 monolayer via DFT calculations," Journal of Energy Storage, **112**, 115489 (2025). https://doi.org/10.1016/j.est.2025.115489
[75] E. Nemukula, C.B. Mtshali, and F. Nemangwele, "Metal Hydrides for Sustainable Hydrogen Storage: A Review," International Journal of Energy Research, **2025**, 1 (2025). https://doi.org/10.1155/er/6300225
[76] S. Zhang, L. Ma, W. Liu, M. Dong, Q. Pang, Q. Li, Zh. Wu, and Xiushen Ye, "Solvent- and catalyst-free hydrogenation synthesis of lithium hydride at high altitude," Chemical Engineering Science, **295**, 120158 (2024). https://doi.org/10.1016/j.ces.2024.120158
[77] N.S.S. Singh, M.A. Rusho, A. Abilkasimov, M. Latipova, A. Aldulaimi, A.G. Taki, R.J. Albadr, *et al*., "Exploring transition metal-based electrocatalysts for carbon dioxide reduction: Towards enhanced product," Chemical Physics Letters, **880**, 142410 (2025). https://doi.org/10.1016/j.cplett.2025.142410
[78] S. Bahou, H. Labrim, M. Lakhal, and H. Ez-Zahraouy, "Improving the hydrogen storage properties of lithium hydride (LiH) by lithium vacancy defects: Ab initio calculations," Solid State Communications, **371**, 115167 (2023). https://doi.org/10.1016/j.ssc.2023.115167

[79] J.L. Snider, T.M. Mattox, Y.-S. Liu, L.F. Wan, P. Wijeratne, M.D. Allendorf, V. Stavila, *et al*., "The influence of LiH and TiH_2 on hydrogen storage in MgB2 I XPS study of surface and near-surface phenomena," International Journal of Hydrogen Energy **47**(1), 387-402 (2022). https://doi.org/10.1016/j.ijhydene.2021.09.169

[80] E. Garlea, M.O. King, E.C. Galloway, T.L. Boyd, N.R. Smyrl, H.Z. Bilheux, L.J. Santodonato, *et al*., "Identification of lithium hydride and its hydrolysis products with neutron imaging," Journal of Nuclear Materials, **485**, 147-153 (2017). https://doi.org/10.1016/j.jnucmat.2016.12.012

[81] Z.T. Azamatov, Sh.B. Utamuradova, M.A. Yuldoshev, and N.N. Bazarbaev, "Some properties of semiconductor-ferroelectric structures," East Eur. J. Phys. (2), 187-190 (2023). https://doi.org/10.26565/2312-4334-2023-2-19

[82] A. Sifuentes, A.C. Stowe, and N. Smyrl, "Determination of the role of Li_2O on the corrosion of lithium hydride," Journal of Alloys and Compounds, **580**(Supplement 1), S271-S273 (2013). https://doi.org/10.1016/j.jallcom.2013.02.046

ПОРИСТА КЕРАМІКА ТА МЕТАЛОГОДРИДНІ МАТЕРІАЛИ ДЛЯ ЕФЕКТИВНОГО ЗБЕРІГАННЯ ВОДНЮ

М.С. Пайзуллаханов[1,2], О.Р. Парпієв[1], Ф.А. Гіясова[3], С.У. Турапова[1], Е.З. Нодірматов[1], М.А. Юлдошев[4], О.Т. Ісманова[5], Ф.А. Гіясов[3], А. Егамбердієв[6], С.К. Абдіжалієв[7], М.А. Джалелов[7], С.А. Турсінбаєв[7], А.А. Абдувахобов[3]

[1]Інститут матеріалознавства Академії наук Республіки Узбекистан, Ташкент, Узбекистан

[2]Ферганський державний технічний університет, Узбекистан

[3]Міжнародний університет Кімьо в Ташкенті, Узбекистан

[4]Міжнародний університет Туран, Наманган, Узбекистан

[5]Наманганський державний університет, Наманган, Узбекистан

[6]Ташкентський інститут інженерів іригації та механізації сільського господарства, Національний дослідницький університет, Узбекистан

[7]Нукусський державний педагогічний інститут імені Аджиніяза, Нукус, Узбекистан

У цій роботі ми досліджували синтезовані пористі алюмосилікатні матеріали з вигораючими добавками, що утворюють однофазну кубічну структуру цеолітного типу (Fm3m, a = 4,056 Å). Пориста кераміка цеолітного складу за температури 200°C та тиску водню 12 атм демонструвала поглинання водню в кількості 11 мас.%. Також ми досліджували вихідний металевий літій (BCC, a≈3,507 Å), який піддавався гідрування в розробленому герметичному реакторі при 12 атм та 700 °C з утворенням гідриду LiH (FCC, типу NaCl, a ≈ 4,081 Å, d_{111} ≈ 2,356 Å). Середній розмір кристалітів LiH не перевищує 100 нм, а максимальна воднева ємність літію досягла 12,4 мас.%. Розроблений реактор дозволяє безпечно проводити гідрування за високої температури та високого тиску. Ці дані демонструють потенціал гідридів літію, титану та натрію, а також пористих алюмосилікатів для накопичення, зберігання та транспортування водню.

Ключові слова: *пористі алюмосилікати; гідрид літію; синтез; гідрування; рентгенофазовий аналіз; зберігання водню; кубічна структура; воднева ємність*

EAST EUROPEAN JOURNAL OF PHYSICS. **2.** 122-131 (2026)
DOI:10.26565/2312-4334-2026-2-11 ISSN 2312-4334

SUBSTITUTIONAL *Tb* INCORPORATION, $p-n$ CONDUCTIVITY TRANSITION, AND GAMMA-IRRADIATION EFFECTS ON THE THERMOELECTRIC PROPERTIES $Tb_xSn_{1-x}Se$ SOLID SOLUTIONS

T.A. Jafarov[1], A.M. Allahverdiyev[1], G.A. Garashova[1], Kh.A. Adgezalova[1], O.M. Gasanov[1], I.M. Mammadov[1], J.I. Huseynov[1]*, I.I. Abbasov[2], V.I. Hajiyeva[3]
[1]*Azerbaijan State Pedagogical University, AZ-1000, Baku, Uz. Hajibeyli Str. 68, Azerbaijan*
[2]*Azerbaijan State Oil and Industry University,* Az-1010, *Baku, Azadlıq Avenue 20, Azerbaijan*
[3]*Nakhchivan State University, AZ7000, Nakhchivan city, Istiglal Street 85, Azerbaijan*
**Corresponding Author email: jahangirhuseynov1958@gmail.com*
Received March 2, 2026; revised April 21, 2026; in final form April 30, 2026; accepted May 13, 2026

The physicochemical and thermoelectric properties of $Tb_xSn_{1-x}Se$ $(0 \le x \le 0.05)$ solid solutions were systematically investigated with emphasis on composition-driven carrier-type transition and $\gamma-$irradiation effects. Differential thermal analysis reveals a monotonic decrease in melting temperature and enthalpy with increasing Tb content, indicating lattice distortion and reduced thermal stability due to the substitutional incorporation of Tb^{3+} at Sn^{2+} sites. $X-$ray diffraction confirms single-phase orthorhombic $(Pnma)$ structure without secondary phases, while EDX analysis verifies successful Tb incorporation. A composition-induced $p-n$ transition occurs within a narrow concentration range, accompanied by a significant modification of the Seebeck coefficient. $\gamma-$irradiation (up to $4-6.5\ Mrad$) significantly affects the Seebeck coefficient in the low-temperature region $(80-300\ K)$, with a nonlinear dose dependence that can be approximated by a quadratic function. At elevated temperatures $(T \ge 500\ K)$, the thermoelectric response exhibits notable radiation stability. The obtained results clearly indicate that Tb doping facilitates a controllable modulation of charge carrier transport properties while preserving the structural integrity and thermal stability of the material at elevated temperatures. These findings underscore the strong potential of $Tb-$doped systems for advanced thermoelectric applications, particularly under radiation-exposed operating conditions.
Keywords: *Solid solutions; Substitutional doping; $p-n$ conductivity transition; Seebeck coefficient; Gamma irradiation; Radiation-modified thermoelectric transport*
PACS:71.20.Nr, 72.20.Pa, 61.72.-y

1. INTRODUCTION

Layered crystals are a class of materials with a unique structure, where atomic layers are held together by weak van der Waals forces. These materials occupy an intermediate position between molecular and nanoscale structures. They possess unique physicochemical properties, making them promising nanomaterials [1, 2]. The effects observed when forming low-dimensional structures with subnanometer-scale constraints in binary semiconductor compounds are related to the nature of the chemical bond and the crystal structure of the bulk phases. The relationship between the structure and properties of three-dimensional crystals and low-dimensional structures is examined using three classes of compounds– $A^{IV}B^{VI}, A^{III}B^{VI}, A_2^VB_3^{VI}$[3, 4].

Among $IV-VI$ binary compounds, including $GeS, GeSe, SnS,$ and $SnSe,$ a pronounced anisotropic layered crystal structure is observed. Within each layer, atoms are strongly bonded via covalent interactions, whereas adjacent layers are held together by relatively weak van der Waals forces. Owing to these weak interlayer interactions, such crystals can be readily exfoliated into atomically thin sheets, analogous to graphene [5,6]. This structural feature provides significant potential for applications in nanotechnology and two-dimensional (2D) electronics. Furthermore, the layered architecture inherently reduces lattice thermal conductivity, which is advantageous for thermoelectric performance. The pronounced anisotropy in their electronic properties can further enhance the efficiency of heat-to-electric energy conversion [7].

The incorporation of rare-earth elements (REEs) into tin monoselenide induces a range of physical phenomena governed by the formation, energetics, and interactions of intrinsic and impurity-related defects. In semiconductor matrices, REE impurities exhibit distinctive behavior, notably their limited solid solubility and their pronounced gettering capability, whereby they effectively reduce the concentrations of residual impurities and defect states, leading to a significant purification of the host material [8, 9].

Materials derived from rare earth elements (REEs) are extensively employed in the fabrication of advanced energy conversion systems, a wide range of thermistor devices, and functional materials exhibiting enhanced resistance to radiation, mechanical pressure, and environmental humidity. Doping $SnSe$ with rare earth metals is an effective method for controlling its electrophysical properties. It enables optimization of thermoelectric characteristics, reduction of

Cite as: T.A. Jafarov, A.M. Allahverdiyev, G.A. Garashova, Kh.A. Adgezalova, O.M. Gasanov, I.M. Mammadov, J.I. Huseynov, I.I. Abbasov, V.I. Hajiyeva, East Eur. J. Phys. 2, 122 (2026), https://doi.org/10.26565/2312-4334-2026-2-11

thermal conductivity, increase in electrical conductivity, and improved material stability, making *SnSe* even more promising for use in thermoelectrics and electronics [10, 11].

The thermoelectric performance of *SnSe* – based semiconductors is highly sensitive to compositional modifications and external perturbations that govern charge-carrier transport and phonon scattering [12]. In particular, substitutional incorporation of rare-earth elements such as Tb introduces localized electronic states, alters carrier concentration, and may induce a p–n conductivity transition, leading to substantial changes in transport properties.

Gamma irradiation provides an additional degree of control via defect engineering, generating point defects and defect complexes that modify carrier scattering, relaxation processes, and energy-filtering effects [13]. As thermoelectric coefficients are strongly dependent on the energy-dependent relaxation of charge carriers, their temperature behavior provides a sensitive probe of the underlying scattering mechanisms and the evolution of the electronic structure [14].

In this context, $Sn_{1-x}Tb_xSe$ solid solutions represent a promising system for investigating the combined effects of substitutional doping and radiation-induced defects. Such interplay is critical for understanding transport phenomena and optimizing thermoelectric performance in multicomponent chalcogenides.

In this work, $Sn_{1-x}Tb_xSe$ compounds were synthesized, and their thermoelectric properties were systematically studied as functions of composition, temperature, and gamma irradiation dose. The results provide insight into charge-transport mechanisms and demonstrate viable pathways for tailoring thermoelectric materials through rare-earth doping and irradiation-induced defect engineering.

2. EXPERIMENTAL PART

For the synthesis of SnSe–TbSe alloys, high-purity (4N–5N grade) tin, selenium, and gadolinium were used (tin ≥ 99.99%, selenium ≥ 99.999%, terbium 99.98%). The synthesis was carried out in evacuated quartz ampoules at a pressure of $0.1333\ Pa$using a two-step direct fusion method. In the first stage, the ampoule with the material was heated at a rate of $4-5\ degrees$ per minute to the melting point of selenium and held at this temperature for $3-4\ hours$. Then, the temperature was gradually increased to $950-1000°C$ (depending on the composition) and maintained for $8-9\ hours$.

To perform comprehensive physicochemical analysis and electrophysical studies, the obtained samples were annealed for $140-210\ hours$ (depending on the composition). The duration of the annealing increased with the gadolinium content. The homogenizing annealing of the obtained single-phase samples was carried out in a spectrally pure argon atmosphere.

The interaction in the $SnSe-TbSe$ system was studied using differential thermal analysis (DTA), X-ray phase analysis (XRD), microstructural analysis (MSA), as well as by measuring microhardness and determining density. To determine the thermal effects of the obtained samples and phase transitions, DTA was performed using a PerkinElmer Simultaneous Thermal Analyzer STA 6000 (USA). Nitrogen was used as the working gas with a flow rate of $20\ ml/sec$; the sample was heated to the melting temperature at a rate of$5\ °C/min$.

X-ray structural analysis was performed using a Rigaku Corporation Miniflex $X-ray$ diffractometer at a voltage of $30\ kV$, current of $10\ mA$, and $CuK\alpha$ radiation ($\lambda = 1.5406$ Å). Diffraction peaks were recorded at a 2θdeviation angle in the range from 0 to 80°. To study the morphology and microcomposition of the sample surfaces, a Japanese JEOL JSM6610-LV scanning electron microscope was used.

The samples were irradiated using an RHUND-20000 continuous-wave radiation chemical unit with a photon energy of 1.25 MeV and doses in the range $D_\gamma = 0-6.5\ Mrad$. The radiation flux density was $1.4\cdot10^{11}\ \text{photons}/c\cdot cm^2$. One day after irradiation, the thermoelectric power was measured using the steady-state compensation method in the temperature range of 80-900 K [15]. While a constant electric current was applied along [100], the measurement error for the thermo-EMF was approximately ~4.6%.

3. RESULTS AND DISCUSSION

3.1. Physicochemical Analysis

Figure 1 presents the differential thermal analysis (DTA) curves of $Tb_xSn_{1-x}Se$ solid solutions in the composition range $x = 0-0.04$. For all samples, a pronounced endothermic peak is observed in the high-temperature region, corresponding to the solid–liquid phase transition (melting).

The melting temperature was determined from the peak maximum, i.e., $T_m(x) = T_{peak}$. The main thermal parameters, including the onset ($\boldsymbol{T_{onset}}$), peak ($\boldsymbol{T_{peak}}$), and endset ($\boldsymbol{T_{end}}$) temperatures, peak height (ΔDTA), full width at half maximum (FWHM), and transition enthalpy (ΔH), were extracted from the DTA curves and are summarized in Table 1. As seen, both $\boldsymbol{T_{onset}}$, and T_m systematically shift toward lower temperatures with increasing Tb content. Specifically, the melting temperature decreases from approximately $1117\ K$ for pristine $SnSe$ to about $1076\ K$ for $x = 0.04$.

This reduction in melting temperature can be attributed to the incorporation of Tb ions into the $SnSe$ lattice, leading to local lattice distortions, reduced average bond strength, and decreased thermal stability. These results indicate the formation of a substitutional solid solution over the composition range studied.

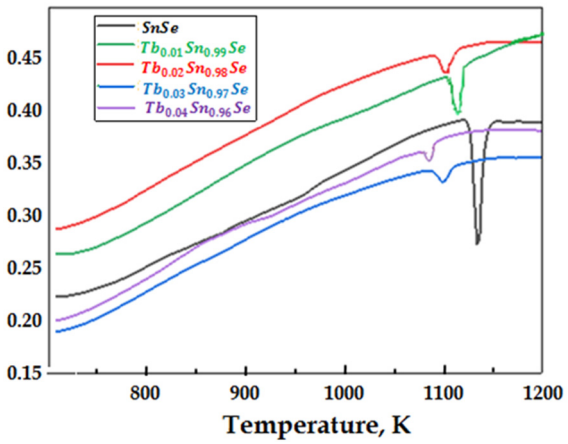

Figure 1. DTA curves of system alloys $Tb_xSn_{1-x}Se$

A concurrent decrease in peak height (ΔDTA) and increase in FWHM with increasing Tb concentration suggest that the phase transition becomes more diffuse and occurs over a broader temperature interval. This behavior reflects increasing structural disorder and compositional inhomogeneity induced by Tb doping. The monotonic decrease in the transition enthalpy ΔH with increasing Tb content indicates that the energy required for the phase transition decreases with doping. This behavior suggests a weakening of long-range structural order and a decrease in lattice cohesion.

Table 1. Thermal parameters of $Tb_xSn_{1-x}Se$ solid solutions derived from DTA curves

Composition	T_{onset} (K)	T_m (K)	T_{end} **(K)**	**Peak height, ΔDTA**$(\mu V/mg)$	**FWHM (K)**	**Transition enthalpy,** ΔH (J/g)
SnSe	*≈1108*	*≈1117*	*≈1135*	*≈0.09*	*≈18*	**≈ 10.2**
$Tb_{0.01}Sn_{0.99}Se$	*≈1092*	*≈1103*	*≈1126*	*≈0.075*	*≈22*	≈ 9.0
$Tb_{0.02}Sn_{0.98}Se$	*≈1078*	*≈1091*	*≈1116*	*≈0.065*	*≈26*	≈ 7.8
$Tb_{0.03}Sn_{0.97}Se$	*≈1069*	*≈1082*	*≈1107*	*≈0.055*	*≈30*	≈ 6.3
$Tb_{0.04}Sn_{0.96}Se$	*≈1062*	*≈1076*	*≈1102*	*≈0.050*	*≈34*	**≈ 5.2**

Furthermore, the absence of additional peaks in the DTA curves indicates that no secondary Tb −based phases are formed, confirming that Tb is incorporated homogeneously into the $SnSe$ matrix and that the system remains phase-stable within the investigated composition range. In summary, DTA analysis demonstrates that Tb doping significantly reduces both the melting temperature and transition enthalpy $SnSe$ −based solid solutions [16].

These trends are consistent with our previous studies on $SnSe$ doped with other rare-earth elements (RE), where a similar reduction in melting temperature and transition enthalpy was observed with increasing dopant concentration. In all cases, the incorporation of RE ions into the $SnSe$ lattice leads to lattice distortions and weakening of interatomic bonding, resulting in reduced thermal stability. However, while the qualitative behavior remains the same, quantitative differences in the magnitudes of these effects vary with the specific rare-earth element. This can be attributed to differences in ionic radii associated with the lanthanide contraction and the degree of $4f$ −electron shell filling. Therefore, Tb doping follows the general trend characteristic of RE-doped $SnSe$ systems, while exhibiting element-specific variations in thermal parameters.

X-ray diffraction patterns for all compositions exhibit reflections consistent with orthorhombic $SnSe$ $(Pnma)$, with no detectable impurity phases. The principal diffraction peaks display slight but systematic 2θ shifts with increasing Tb concentration, consistent with lattice distortion induced by partial substitution of Sn^{2+} by Tb^{3+} ions. No reflections attributable to oxide or secondary chalcogenide phases are observed within the detection limit, confirming phase purity and controlled synthesis conditions [17].

Similar behavior has been reported in our previous studies on $SnSe$ doped with other rare-earth elements, where systematic peak shifts and lattice parameter changes were also observed. This confirms that the substitutional incorporation mechanism is common for RE dopants in $SnSe$. Nevertheless, slight differences in the extent of lattice expansion can be attributed to variations in ionic radii and electronic structure among different lanthanides.

Analysis of X −ray diffraction data indicates that the introduction of Terbium selenides leads to an increase in the lattice parameters of $SnSe$ as the Tb concentration increases. Furthermore, intense charge carrier scattering is observed due to lattice "distortions," which aligns with the thermal conductivity data of these alloys [18]. The slight shift of diffraction lines in the X-ray diffraction patterns in the $0-5\ mol\%$ range, the observed increase in elementary lattice parameters, good agreement with the partial replacement of Sn atoms by Tb atoms with larger radii, and compliance with Vegard's law suggest the formation of substitutional solid solutions based on $SnSe$ [19].

The surface morphology of $Tb_{0.02}Sn_{0.98}Se$ crystals was systematically investigated using scanning electron microscopy (SEM) combined with quantitative surface topography analysis. The results are summarized in Fig. 2.

The two-dimensional surface map (Fig. 2a) reveals a high degree of spatial uniformity, with no visible macroscopic defects such as cracks, voids, or inclusions. The corresponding three-dimensional reconstruction (Fig. 2b) shows that the surface is composed of uniformly distributed nanoscale protrusions and depressions, forming a homogeneous microrelief.

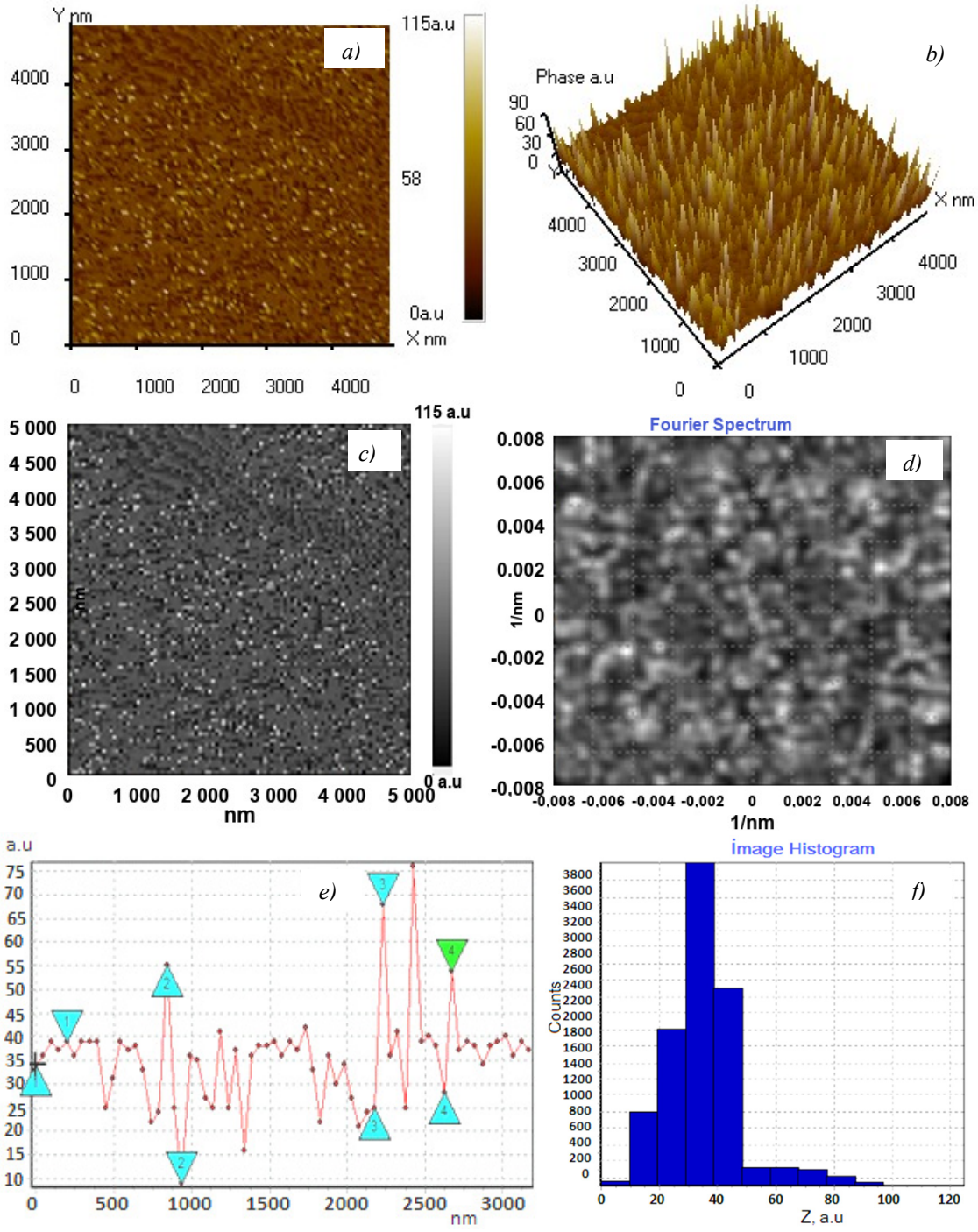

Figure 2. Surface morphology and statistical analysis of $Tb_{0.02}Sn_{0.98}Se$ crystals: *a)* 2D topographic image of the surface; *b)* 3D surface reconstruction showing height variations; *c)* SEM image illustrating the microstructure and grain distribution; *d)* Fourier spectrum of the surface, indicating spatial frequency distribution; *e)* line profile of surface roughness along a selected scan; f) height distribution histogram of the surface

Quantitative roughness analysis was carried out using the height profile (Fig. 2e) and statistical distribution (Fig. 2f). The extracted roughness parameters are: average roughness $R_a \approx 5-15$ nm, root-mean-square roughness $R_q \approx 7\text{-}20\,nm$, and maximum peak-to-valley height $R_Z \approx 30-60\,nm$. These relatively low roughness values indicate a smooth surface at the nanometer scale, which is typically associated with high crystalline quality and controlled growth conditions.

AFM and SEM analyses demonstrate that the Tb dopant is highly homogeneously distributed along the surface, with no signs of phase separation or clustering observed. The diffuse nature of the Fourier spectrum and the Gaussian-type statistics of the surface height distribution are in good agreement with the substitution of Tb atoms mainly for Sn positions in the crystal lattice.

Overall, the combined morphological and statistical analyses demonstrate that $Tb_xSn_{1-x}Se$ crystals possess a nanostructured yet highly homogeneous surface. This structural quality is expected to play a crucial role in determining charge carrier transport and phonon scattering mechanisms, making these materials promising candidates for thermoelectric applications.

The energy-dispersive X-ray (EDX/EDR) spectrum of the $Tb_xSn_{1-x}Se$ sample (x = 0.01) shows distinct characteristic peaks of Sn, Se, and Tb, confirming the successful incorporation of terbium into the crystal lattice (Fig. 3). Under high-energy electron irradiation, inner-shell ionization (K, L, M) leads to electronic transitions accompanied by the emission of characteristic X-rays. For Sn, the dominant L-series lines (SnL_α~3.44 keV and L_β ~3.67 keV) are observed, while Se exhibits $L_\alpha(\sim 1.38\ keV)$, $L_\beta(\sim 1.43\ keV)$, and $K_\alpha(\sim 11.22\ keV)$ lines, confirming the preservation of the $SnSe$ matrix phase. The presence of Tb is verified by both $M-$series (M_α~1.24 keV, M_β ~1.30 keV) and $L-$series (L_α~6.27 keV, L_β ~6.68 keV) emission lines. The multiplicity of Tb peaks reflect its complex electronic structure and support its partial substitution at Sn lattice sites [20]. Overall, the EDX results confirm Tbincorporation into the primary phase without evidence of secondary phase formation.

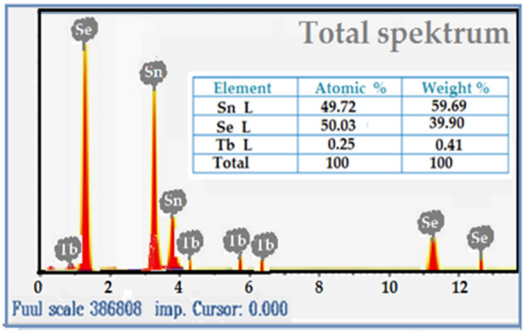

Figure 3.X-ray microanalysis of the crystal surface$Tb_xSn_{1-x}Se$:2- x=0,005

Collectively, thermal, structural, compositional, and morphological analyses consistently demonstrate that low-level Tb incorporation in $SnSe$leads to substitutional solid-solution formation, slight lattice distortion, reduced thermal stability, and preserved phase purity without secondary-phase formation

3.2. Composition-Driven p–n Transition and γ-Irradiation Effects on the Seebeck Coefficient of $Tb_xSn_{1-x}Se$ Solid Solutions

In the study reported in [21], the kinetic and transport parameters of $Tb_xSn_{1-x}Se$ solid solutions ($0 \le x \le 0.05$), grown by the Bridgman technique, were systematically investigated at $T = 300\ K$. It was established that terbium doping exerts a pronounced influence on the electrical conductivity, Hall coefficient, thermoelectric power, thermal conductivity, as well as on the charge carrier concentration and mobility. With increasing Tb content in the $SnSe-$based solid solutions, the Seebeck coefficient S initially decreases sharply within the composition range $0 \le x \le 0.002\ mol.\%$ (from $+420$to $+128\ \mu V/K$). This behavior is attributed to the donor effect associated with the substitution of Sn^{2+} ions by Tb^{3+} ions, which leads to electron generation and enhanced carrier scattering due to lattice distortion and local symmetry breaking. Within the narrow concentration interval $0.002 < x < 0.0025\ mol.\%$, a sign inversion of the Seebeck coefficient occurs (down to $-325\ \mu V/K$), indicating a transition from $p-$type to $n-$type conductivity. This inversion reflects a shift of the Fermi level toward the conduction band and the formation of localized donor states introduced by Tb impurities. For $0.0025 < x < 0.015\ mol.\%$, negative values of S become stabilized, confirming the establishment of electron-dominated (n-type) transport and partial saturation of donor states. At higher Tb concentrations ($0.02 < x < 0.05\ mol.\%$), a gradual reduction in the absolute value of the Seebeck coefficient is observed. This tendency is associated with an increase in free electron concentration, a corresponding decrease in the chemical potential gradient, and possible carrier localization effects arising from $Tb-Tb$ interactions and partial ordering within the defect sublattice of the crystal structure.

The effect of γ-irradiation on the thermoelectric properties of $Tb_xSn_{1-x}Se$ solid solutions was investigated at room temperature within an absorbed dose range of 0–6.5 Mrad (Fig. 4. *a)*). The Seebeck coefficient evolution strongly depends on the conductivity type. For $p-$type compositions (x ≤ 0.001), a non-monotonic $S(D)$ dependence is observed: the Seebeck coefficient initially increases with dose, reaches a maximum, and then decreases. For $x = 0, S$ rises from $\approx +420\ \mu V/K$ to $\approx +442\ \mu V/K$at $D \approx 5\ Mrad$, followed by a slight reduction. A similar trend is found for $x = 0.001$ (from $\approx +275$to $\approx +285\ \mu V/K$). This behavior is attributed to radiation-induced donor-type point defects, which enhance compensation of hole carriers. At higher doses, defect saturation and enhanced carrier scattering lead to a decrease in S. Such behavior is characteristic of radiation-modified $p-$type $SnSe$.

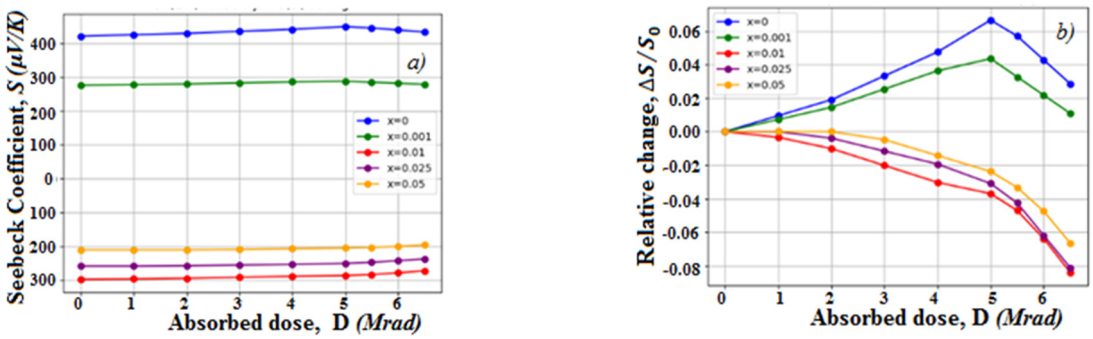

Figure 4. Dependence of the Seebeck coefficient a) and its relative change b) on the absorbed dose

For $n-$type samples ($x \geq 0.01$), the magnitude of the Seebeck coefficient decreases monotonically with increasing dose. Specifically, S changes from ≈ -297 to $-272\,\mu V/K$ ($x = 0.01$), from ≈ -258 to $-237\,\mu V/K$ ($x = 0.025$), and from $\approx -210\,to-196\,\mu V/K$ ($x = 0.05$). The reduction of |S| is associated with increased electron concentration and enhanced scattering due to radiation-induced defects. The conductivity type remains unchanged throughout the entire dose range, and no $p-n$ conversion is observed [22].

The analysis of the relative change, $\Delta S/S_0 = (S(D) - S_0)/S_0$, shows that for $p-$type samples it is positive and reaches $\sim 4-5\%$ with a subsequent tendency toward saturation (Fig. 4.*b*)), whereas for n-type samples it takes negative values (down to $-7-8\%$). The $\Delta S/S_0(D)$ dependence is nonlinear and can be satisfactorily approximated by a quadratic function of the form $\Delta S/S_0(D) \approx aD^2 + bD + c$. This approach accounts for both the initial defect-induced compensation contribution and the saturation and enhanced scattering effects at higher doses, thereby providing an analytical framework for describing and predicting the radiation-induced thermoelectric behavior of $Tb_xSn_{1-x}Se$ solid solutions.

3.3. Diffusion, phonon-drag, and bipolar contributions to the Seebeck coefficient in $Tb_xSn_{1-x}Se$ solid solutions

The temperature dependence of the Seebeck coefficient for $Tb_xSn_{1-x}Se$ solid solutions with different terbium concentrations is presented in Fig. 5. The obtained results demonstrate that both compositional variation and temperature exert a pronounced influence on the charge transport mechanisms and electronic structure of the system.

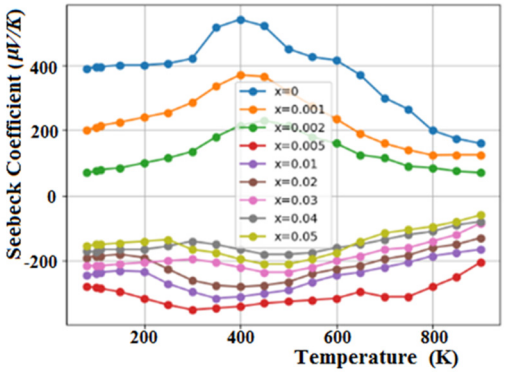

Figure 5. Temperature dependence of the Seebeck coefficient in $Tb_xSn_{1-x}Se$system alloys

In general, the total Seebeck coefficient can be expressed as the superposition of diffusion and phonon-drag contributions [24]:

$$S = S_{diff} + S_{ph}$$

where $S_{diff}-$ denotes the carrier diffusion component and $S_{ph}-$ corresponds to the phonon-drag contribution.

In the intermediate temperature range, the phonon-drag term typically attains a maximum due to efficient momentum transfer from nonequilibrium phonons to charge carriers [25]. However, at elevated temperatures, intensified phonon–phonon scattering significantly suppresses this effect, resulting in a gradual decrease of the total Seebeck coefficient. The systematic decrease in S observed above 400 K across all p-type samples (Fig. 5) is fully consistent with this mechanism.

For the undoped sample (x = 0), the Seebeck coefficient reaches a maximum of approximately 540 μV/K over the temperature range 350–400 K. The initial increase in S with temperature is primarily attributed to the enhancement of the phonon-drag mechanism, which dominates the diffusion contribution in this range.

As shown in Fig. 5, compositions with $x = 0, 0.001$, and 0.002 exhibit positive Seebeck coefficients over the entire investigated temperature interval, indicating hole-dominated transport ($p-$type conductivity). In contrast, for

$x \geq 0.005$, the Seebeck coefficient becomes negative (S<0), evidencing a transition to electron-dominated ($n-$type) conductivity. This behavior indicates that beyond a critical Tb concentration, a compensation mechanism is activated, leading to a shift of the Fermi level toward the conduction band and ultimately altering the dominant carrier type.

For semiconductors, the diffusion component of the Seebeck coefficient can be described by [12]:

$$S_{diff} = \frac{k_B}{e}\left(\frac{r+2}{r+1} - \frac{E_F - E_C}{k_B T}\right)$$

where $k_B -$ is the Boltzmann constant, $e -$is the elementary charge, $E_F -$ is the Fermi level, $E_C -$ is the conduction band minimum, and $r -$ is the scattering parameter that characterizes the dominant carrier-scattering mechanism.

According to this relation, variations in the Fermi level position directly affect both the magnitude and the sign of the Seebeck coefficient. Therefore, the experimentally observed sign inversion is in good agreement with theoretical predictions.

With increasing Tb content, a systematic decrease in the absolute value of the Seebeck coefficient is observed. This trend is directly associated with the increase in charge carrier concentration induced by doping. For non-degenerate semiconductors, the Seebeck coefficient approximately follows:

$$S \sim \frac{k_B}{e} ln\left(\frac{N_v}{n}\right)$$

where$n$ is the carrier concentration and $N_v -$ is the effective density of states in the valence band.

As the Tb concentration increases, the carrier concentration rises, leading to a reduction in S. The experimentally observed decrease in the maximum Seebeck values for $x = 0.001$ and 0.002 quantitatively supports this theoretical dependence.

For samples with $x \geq 0.005$, the Seebeck coefficient becomes negative and exhibits a pronounced extremum within the $250 - 350\ K$ temperature interval. The subsequent reduction of $|\ S\ |$ at higher temperatures can be attributed to the onset of bipolar conduction. As temperature increases, intrinsic carrier excitation generates electron–hole pairs, thereby reducing the net thermoelectric response. In the bipolar regime, the effective Seebeck coefficient can be expressed as [26]:

$$S_{bipolar} \propto \left(\frac{\sigma_n S_n + \sigma_p S_p}{\sigma_n + \sigma_p}\right)$$

where $\sigma_n -$ and $\sigma_p -$ represent the electrical conductivities of electrons and holes, respectively, while $S_n -$ and $S_p -$ denote their partial Seebeck coefficients.

The simultaneous contribution of both carrier types leads to partial compensation, which decreases the overall Seebeck coefficient at elevated temperatures.

In summary, the analysis of Fig. 5 reveals that:

– Tb doping induces a conductivity-type transition from $p -$type to $n -$type behavior.

– The maximum of the Seebeck coefficient is located within the $300 - 400\ K$ temperature range.

– Increasing Tb concentration reduces the magnitude of S due to enhanced carrier concentration and the corresponding Fermi level shift.

– The high-temperature decrease in S is primarily governed by bipolar diffusion effects.

These findings demonstrate that Tb incorporation effectively tunes the electronic structure and carrier transport parameters of the $Tb_xSn_{1-x}Se$ system, highlighting its potential for thermoelectric applications in the intermediate temperature range [27].

3.4. Effect of Gamma Irradiation on the Seebeck Coefficient of $Tb_xSn_{1-x}Se$ Alloys

The Seebeck coefficient (S) of $Tb_xSn_{1-x}Se$ alloys $(x = 0, 0.001, 0.005, 0.01, 0.05)$ was measured in the temperature range $80 - 900\ K$ before and after $\gamma -$irradiation with an absorbed dose of 4 $Mrad$. The obtained results reveal a pronounced temperature- and composition-dependent radiation effect (Fig. 6).

In the low-temperature region$(80 - 300\ K)$, $\gamma -$irradiation significantly modifies the Seebeck coefficient for all investigated compositions. For the undoped sample $(x = 0)$, S increases over the entire range. For example, at $80\ K$, S rises from 390 to 475 $\mu V/K$ $(\Delta S \approx +85\ \mu V/K)$, corresponding to a relative increase of about 22%. A similar trend is observed at $100\ K$ $(393 \rightarrow 471\ \mu V/K)$. Such behavior indicates a substantial modification of charge carrier parameters due to radiation-induced defect formation [28].

For weakly doped samples $(x = 0.001)$, the Seebeck coefficient also increases after irradiation, particularly below $200\ K$, where the relative change reaches $10 - 15\%$. This behavior can be attributed to radiation-induced trapping centers that reduce the effective carrier concentration and modify the energy dependence of electrical conductivity.

For compositions with $x = 0.005$ and characterized by negative Seebeck coefficients ($n -$type conductivity), irradiation leads to an increase in the absolute value $|S|$ in the low-temperature region. For instance, for $x = 0.005$ at $80\ K$, S changes from -280 to $-316\ \mu V/K$. This enhancement in $|S|$ suggests a decrease in electron concentration

and/or increased carrier scattering caused by radiation-induced structural disorder. Although a sign anomaly is observed at $100\ K$ for $x = 0.05$, the overall temperature dependence preserves the n −type character [29].

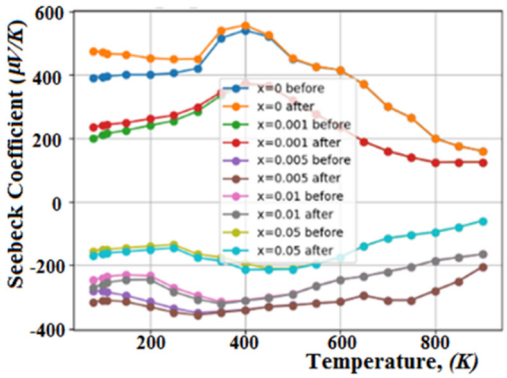

Figure 6. Temperature dependence of the Seebeck coefficient before and after irradiation in $Tb_xSn_{1-x}Se$ system alloys

In the intermediate temperature range$(300 - 500\ K)$, the radiation effect gradually weakens. For $x = 0$, the maximum difference is observed near $350\ K$ $(515 \rightarrow 540\ \mu V/K)$, but the relative variation decreases with increasing temperature. A similar tendency is found for other compositions. This behavior indicates that at elevated temperatures phonon scattering becomes dominant over defect scattering, partially compensating the radiation-induced modifications.

At high temperatures$(T \geq 500\ K)$, the Seebeck coefficients of irradiated and non-irradiated samples practically coincide for all investigated compositions:

$$S_{befor}(T) \approx S_{after}(T), T > 500K$$

This result demonstrates that thermally activated carriers and intrinsic conduction mechanisms dominate transport properties in this temperature range, while the contribution of radiation-induced defects becomes negligible. Therefore, the $Tb_xSn_{1-x}Se$ system exhibits considerable radiation stability of thermoelectric properties at high temperatures.

In addition, the convergence of the Seebeck coefficients at high temperatures may also indicate the partial thermal annealing or reconfiguration of radiation-induced defects during the measurement process. At elevated temperatures, increased atomic mobility can lead to a reduction in the concentration or activity of defect centers responsible for carrier scattering and trapping. As a result, the influence of γ-induced defects becomes progressively weaker, and the transport properties are governed predominantly by intrinsic mechanisms. Although repeated measurements after high-temperature cycling were not performed in the present study, the observed behavior is consistent with the expected thermal stability and defect dynamics in narrow-gap thermoelectric semiconductors.

The observed changes in S can be interpreted within the framework of the Mott relation [30]:

$$S = \frac{\pi^2 k_B^2 T}{3e} \frac{dln\sigma(E)}{dE}_{|\ E=E_F}$$

which shows that the Seebeck coefficient depends on the energy derivative of electrical conductivity near the Fermi level. Gamma irradiation modifies the density of states and scattering mechanisms through defect formation, thereby altering the energy dependence of $\sigma(E)$. The most pronounced effects occur at low temperatures, where transport is highly sensitive to impurity and defect scattering. With increasing temperature, intrinsic carrier excitation reduces the relative impact of radiation-induced defects.

Overall, γ −irradiation with a dose of 4 $Mrad$ significantly affects the Seebeck coefficient of$Tb_xSn_{1-x}Se$ alloys in the low-temperature region $(80 - 300\ K)$, while the effect becomes negligible above $600\ K$. The magnitude of the radiation response depends on terbium concentration and conduction type, being more pronounced for low Tb content and in samples near the compensation regime.

4. CONCLUSIONS

A comprehensive investigation of the physicochemical, structural, compositional, and thermoelectric properties of $Tb_xSn_{1-x}Se$ $(0 \leq x \leq 0.05)$ solid solutions has been performed, including the influence of γ −irradiation on the Seebeck coefficient over a wide temperature range.

Thermal analysis demonstrates that terbium incorporation leads to a monotonic decrease in melting temperature, reduced relative melting enthalpy, and peak broadening, indicating lattice softening and increased structural disorder. X-ray diffraction confirms the preservation of the orthorhombic $SnSe$ $(Pnma)$ structure without detectable secondary phases, while systematic peak shifts evidence substitutional incorporation of Tb^{3+} at Sn^{2+} lattice sites. Surface morphology analysis reveals a homogeneous nanostructured relief that may enhance phonon and carrier scattering. EDX spectroscopy further verifies the successful Tb incorporation into the primary phase, confirming the formation of a substitutional solid solution with preserved phase purity.

Compositionally driven transport measurements reveal a Tb −induced $p-n$ conductivity transition. At low Tb concentrations, donor states introduced by Tb^{3+} ions compensate holes and shift the Fermi level toward the conduction band. A sign inversion of the Seebeck coefficient occurs within a narrow composition interval, confirming the transition from p −type to n −type conduction. Increasing Tb content systematically reduces the magnitude of the Seebeck coefficient due to enhanced carrier concentration and Fermi level shift, consistent with diffusion thermo power models. Temperature-dependent measurements indicate that the total Seebeck coefficient arises from diffusion and phonon-drag contributions at intermediate temperatures $(300-400\ K)$, while bipolar conduction effects dominate at elevated temperatures.

The effect of γ-irradiation (up to $4-6.5\ Mrad$) strongly depends on conductivity type and temperature. In the low-temperature region $(80-300\ K)$, irradiation significantly modifies the Seebeck coefficient: p −type samples exhibit a non-monotonic increase associated with radiation-induced donor-like defects and carrier compensation, whereas n-type samples show a monotonic reduction in $|S|$ due to enhanced scattering and carrier concentration changes. The relative variation $\Delta S/S_0$ follows a nonlinear dependence that can be satisfactorily approximated by a quadratic function of absorbed dose. However, at high temperatures $(T \geq 500-600\ K)$, the Seebeck coefficients of irradiated and non-irradiated samples converge, demonstrating strong radiation stability of thermoelectric properties in the intrinsic conduction regime.

Overall, Tb doping effectively tunes the electronic structure, carrier type, and thermoelectric response of $SnSe$ −based solid solutions, enabling controlled $p-n$ conversion and optimization of transport parameters in the intermediate temperature range. The demonstrated radiation stability at elevated temperatures further highlights the potential of $Tb_xSn_{1-x}Se$ materials for thermoelectric applications under irradiation environments.

ORCID

T.A. Jafarov, https://orcid.org/0009-0003-9069-7402; **O.M. Gasanov,** https://orcid.org/0000-0003-4888-7686;
Kh.A. Adgezalova, https://orcid.org/0009-0000-8966-4919; **I.M. Mammadov,** https://orcid.org/0009-0001-6039-6081;
J.I. Huseynov, https://orcid.org/0000-0002-4498-2400; **I.I. Abbasov,** https://orcid.org/0000-0001-8111-2642;
V.I. Haciyeva, https://orcid.org/0009-0003-6929-9602

REFERENCE

[1] J. Kim, O. Song, Y.S. Cho, M. Jung, D. Rhee, and J. Kang, "Revisiting Solution-Based Processing of van der Waals Layered Materials for Electronics," ACS Materials Au, **2**(4), 382–393 (2022). https://doi.org/10.1021/acsmaterialsau.2c00034

[2] I. Abbasov, M. Musayev, J. Huseynov, E. Gavrishuk, S. Asadullayeva, A. Rajabli, and D. Askerov, "Temperature behavior of X-Ray luminescence spectra of ZnSe," International Journal of Modern Physics B, **36**(02), 2250018 (2022). https://doi.org/10.1142/S0217979222500187

[3] R.S. Stepanov, P.I. Marland, and A.V. Kolobov, "Compositional and Structural Disorder in Two-Dimensional $A^{III}B^{VI}$ Materials," Crystals, **13**(8), 1209 (2023). https://doi.org/10.3390/cryst13081209

[4] J.I. Huseynov, M.I. Murguzov, and S.S. Ismayilov, "Specific features of self-compensation in $Er_xSn_{1-x}Se$ solid solutions," Semiconductors, **47**, 323–326 (2013). https://doi.org/10.1134/S106378261303010X

[5] I.I. Abbasov, M.A. Musayev, C.I. Huseynov, Q.Y. Eyyubov, N.N. Hasimova, A.J. Mammadova, A.A. Hadieva, *et al*., "A study of impurity defect photoluminescence in ZnSe:Cr and ZnSe:Fe in the near infrared at room temperature," Advanced Physical Research, **5**(3), 192-199 (2023).

[6] S.-D. Guo, and Y.-H. Wang, "Thermoelectric properties of orthorhombic group IV–VI monolayers from the first-principles calculations," J. Appl. Phys. **121**, 034302 (2017). https://doi.org/10.1063/1.4974200

[7] I.I. Abbasov, and J.I. Huseynov, "Charge-transfer processes in $(SnS)_{1-x}(PrS)_x$ Alloys," Ukrainian journal of physics, **62**(10), 883-888 (2017). http://jnas.nbuv.gov.ua/article/UJRN-0000795750

[8] S. Isber, and X. Gratens, "Crystal growth and magnetic properties of tin selenide-doped europium$Sn_{1-x}Eu_xSe$," Journal of Magnetism and Magnetic Materials, **322**, 1113–1116 (2010). https://doi.org/10.1016/j.jmmm.2009.09.015

[9] B. Wei, J. Zhang, L. Lin, T. Wu, Z. Cheng, Y. Ma, J. Li, and S. Yu, "Enhancing Electrical Transport Performance of Polycrystalline Tin Selenide by Doping Different Elements," Physica Status Solidi (A) Applications and Materials, **221**(9), 2300717 (2024). https://doi.org/10.1002/pssa.202300717

[10] X. Yang, X-Y. Ma, T.-E. Shi, W-Q. Bao, J. Wang, Z.-Y. Wang, Y.-X. Zhang, *et al*., "High thermoelectric properties in polycrystalline SnSe materials realized by rare earth halide Co-doping," Ceramics International, **50**(11 Part B), 20515-20524 (2024). https://doi.org/10.1016/j.ceramint.2024.03.173

[11] S. Li, L. Yin, Y. Liu, X. Wang, C. Chen, and Q. Zhang, "Rare earth element Ce enables high thermoelectric performance in n-type SnSe polycrystals," Journal of Materials Science & Technology, **143**, 234-241 (2023). https://doi.org/10.1016/j.jmst.2022.09.054

[12] B.M. Askerov, *Electron Transport Phenomena in Semiconductors*, (World Scientific, Singapore, New Jersey, London, 1994).

[13] R. Yamada, T. Nomoto, A. Miyake, T. Terakawa, A. Kikkawa, R. Arita, M, Tokunaga, *et al*., "Nernst Effect of High-Mobility Weyl Electrons in NdAlSi Enhanced by a Fermi Surface Nesting Instability," Physical Review X,**14**, 021012 (2024). https://doi.org/10.1103/PhysRevX.14.021012

[14] S. Akhanda, K.A. Schlaak, E.F. Scott, N.A. Taj, S.J. Watzman, and M. Zebarjadi, "Thermomagnetic responses of semimetals," J. Appl. Phys. **135**, 240901 (2024). https://doi.org/10.1063/5.0192824

[15] J.I. Huseynov, and T.A. Jafarov, "The Influence of γ-Irradiation on Thermoemf and Heat Conduction of $Ln_{0.01}Sn_{0.99}Se$ (*Ln* – *Pr, Tb,Er*) Monocrystals," World Journal of Condensed Matter Physics,**4**(1), 1-5 (2014). http://dx.doi.org/10.4236/wjcmp.2014.41001

[16] I.I. Aliev, J.I. Huseynov, M.I. Murguzov, Sh.S. Ismailov, and E.M. Gojaev, "Phase relations and properties of alloys in the SnSe-DySe system," Inorg. Mater. **50**, 237–240 (2014). https://doi.org/10.1134/S0020168514030029
[17] Sh.S. Ismailov, J.I. Huseynov, M.A. Musaev, I.I. Abbasov, and V.A. Abdurakhmanova, "Effect of doping level and compensation on thermal conductivity in $Ce_xSn_{1-x}Se$ solid solutions," Low Temp. Phys. **46**, 1114–1120 (2020). https://doi.org/10.1063/10.0002155
[18] I.I. Abbasov, Sh.S. Ismailov, J.I. Huseynov, V.A. Abdurakhmanova, "Concentration dependences of electrical conductivity and the Hall effect of the $Ce_xSn_{1-x}Se$ single crystals," Low Temp. Phys. **45**, 1277–1280 (2019). https://doi.org/10.1063/10.0000209
[19] J.I. Huseynov, Kh.A. Hasanov, T.A. Jafarov, and I.I. Abbasov, "Compensating effect of terbium impurity on the conductivity of $Tb_xSn_{1-x}Se$ solid solutions," Ukrainian journal of physics, **65**(3), 225-230 (2020). http://jnas.nbuv.gov.ua/article/UJRN-0001127989
[20] Sh.S. Ismailov, J.I. Huseynov, M.A. Musaev, I. I. Abbasov, and A. Abdurakhmanova, "Effect of doping level and compensation on thermal conductivity in $Ce_xSn_{1-x}Se$ solid solutions," Low Temperature Physics, **46**, 1114–1120 (2020). https://doi.org/10.1063/10.0002155
[21] T.A. Jafarov, O.M. Gasanov, Kh.A. Adgezalova, H.A. Aslanov, J.I. Huseynov, I.I. Abbasov, and R.Sh. Ragimov, "Modification of the kinetic parameters of *SnSe* by terbium doping," East Eur. J. Phys. (4), 407 (2025). https://doi.org/10.26565/2312-4334-2025-4-39
[22] J.I. Huseynov, M.I. Murguzov, S.S. Ismayilov, R.F. Mamedova, and E.M. Gojayev, "On the thermopower and thermomagnetic properties of $Er_xSn_{1-x}Se$ solid solutions," Semiconductors, **51**, 153–157 (2017); https://doi.org/10.1134/S1063782617020075
[23] J.I. Huseynov, and T.A. Jafarov, "Effect of γ-ray radiation on electrical properties of heat-treated $Tb_xSn_{1-x}Se$ single crystals," Semiconductors, **46**, 430–432 (2012). https://doi.org/10.1134/S1063782612040082
[24] M. Kockert, D. Kojda, R. Mitdank, A. Mogilatenko, Z. Wang, J. Ruhhammer, M. Kroener, *et al*.,"Nanometrology: Absolute Seebeck coefficient of individual silver nanowires," Sci. Rep. **9**, 20265 (2019). https://doi.org/10.1038/s41598-019-56602-9
[25] K.A. Hasanov, J.I. Huseynov, V.V. Dadashova, F.F. Aliyev, *et al.* "Effect of Phonon Drag on the Thermopower in a Parabolic QuantumWell," Semiconductors, **50**, 295–298 (2016). https://doi.org/10.1134/S106378261603009X
[26] S. Foster, and N. Neophytou, "Doping Optimization for the Power Factor of Bipolar Thermoelectric Materials," J. Electron. Mater. **48**, 1889–1895 (2019). https://doi.org/10.1007/s11664-018-06857-1
[27] D.I. Huseynov, M.I. Murguzov, and S.S. Ismailov, "Thermal conductivity of $Er_xSn_{1-x}Se$ ($x \leq 0.025$) solid solutions," Inorg. Mater. **44**, 467–469 (2008). https://doi.org/10.1134/S0020168508050063
[28] T. Rasmi, R.C. Bose, T.S. Varun, and K.A. Malini, "Impact of gamma irradiation on thermoelectric efficiency of Te-based thin films,"Radiation Physics and Chemistry, **242**, 113601 (2026). https://doi.org/10.1016/j.radphyschem.2026.113601
[29] J.I. Huseynov, M.I. Murquzov, and R.F. Mamedova, "Thermal Conductivity and Termal EMF of Materials for Thermal Energy Converters," in: *TPE-06 3rd Intern. Conf. on Technical and Physical Problems in Power Engineering*, (Ankara, 2008).
[30] V. Konye, and M. Oqata, "Thermoelectric transport coefficients of a Dirac electron gas in high magnetic fields," Phys. Rev. B, **100**, 155430 (2019). https://doi.orq/101103/PhysRevB.100.155430

ЗАМІЩУВАЛЬНА ВБУДОВА Tb, p-n ПЕРЕХІД ПРОВІДНОСТІ , ТА ВПЛИВ ГАММА-ОПРОМІНЕННЯ НА ТЕРМОЕЛЕКТРИЧНІ ВЛАСТИВОСТІ ТВЕРДИХ РОЗЧИНІВ $Tb_xSn_{1-x}Se$

Т.А. Джафаров[1], А.М. Аллахвердієв[1], Г.А. Гарашова[1], Х.А. Адгезалова[1], О.М. Гасанов[1], І.М. Мамедов[1], Дж.І. Гусейнов[1], І.І. Аббасов[2], В.І. Гаджиєва[3]

[1]Азербайджанський державний педагогічний університет, AZ-1000, Баку, вул. Уз. Гаджибейлі, 68, Азербайджан
[2]Азербайджанський державний університет нафти та промисловості, Az-1010, Баку, проспект Азадлик, 20, Азербайджан
[3]Нахчиванський державний університет, AZ7000, місто Нахчивань, вулиця Істіглал, 85, Азербайджан

Фізико-хімічні та термоелектричні властивості твердих розчинів $Tb_xSn_{1-x}Se$ ($0 \leq x \leq 0,05$) були систематично досліджені з акцентом на перехід типу носіїв, зумовлений складом, а також на ефекти γ-опромінення. Диференціальний термічний аналіз виявляє монотонне зниження температури плавлення та ентальпії зі збільшенням вмісту Tb, що вказує на спотворення кристалічної решітки та зниження термічної стабільності через заміщення Tb^{3+} на позиціях Sn^{2+}. Рентгенівська дифракція підтверджує однофазну орторомбічну (Pnma) структуру без вторинних фаз, тоді як EDX-аналіз підтверджує успішне включення Tb. Індукований складом p-n перехід відбувається у вузькому діапазоні концентрацій, що супроводжується значною зміною коефіцієнта Зеєбека. γ-опромінення (до 4-6,5 Мрад) суттєво впливає на коефіцієнт Зеєбека в області низьких температур (80-300 K) з нелінійною залежністю від дози, яку можна апроксимувати квадратичною функцією. За підвищених температур ($T \geq 500$ K) термоелектрична реакція демонструє значну радіаційну стабільність. Отримані результати чітко вказують на те, що легування Tb сприяє керованій модуляції властивостей транспорту носіїв заряду, зберігаючи при цьому структурну цілісність і термічну стабільність матеріалу за підвищених температур. Ці результати підкреслюють великий потенціал систем, легованих Tb, для передових термоелектричних застосувань, особливо в умовах експлуатації, що піддаються радіаційному впливу.

Ключові слова: *тверді розчини; замісне легування; p-n перехід провідності; коефіцієнт Зеєбека; гамма-опромінення; радіаційно-модифікований термоелектричний транспорт*

East European Journal of Physics. **2.** 132-137 (2026)
DOI:10.26565/2312-4334-2026-2-12 ISSN 2312-4334

Mg-INDUCED ENHANCEMENT OF MEMRISTIVE SWITCHING IN SnO_2 THIN FILMS

Jamoliddin X. Murodov[1,2]*, Shavkat U. Yuldashev[2], Azamat O. Arslanov[3], Noiba U. Botirova[2], Javohir Sh. Xudoyqulov[3], Marguba S. Mirkamilova[1], Inobat Q. Qodirova[1], Odilboy X. Ximmatqulov[1]
[1]*Tashkent State Technical University named after Islam Karimov, Tashkent, Uzbekistan*
[2]*Center of Nanotechnology Development, National University of Uzbekistan*
[3]*National University of Uzbekistan named after Mirzo Ulugbek, Tashkent, Uzbekistan*
**Corresponding Author e-mail: jamoliddinmilliy@gmail.com*
Received February 7, 2026; revised April 2, 2026; accepted April 6, 2026

Magnesium-doped tin oxide (SnO_2:Mg) thin films have attracted considerable attention as promising materials for next-generation non-volatile memory devices due to their stable resistive switching behavior and simple fabrication processes. In this work, SnO_2 thin films were fabricated by ultrasonic spray pyrolysis using a precursor solution containing 20 mol.% Mg and systematically investigated to evaluate their memristive switching characteristics, electrical performance, and conduction behavior. Structural analysis confirmed the formation of uniform polycrystalline thin films with a crystallite size of approximately 30 nm, while energy-dispersive X-ray spectroscopy (EDS) revealed an actual Mg content of approximately 5 at.%, indicating partial incorporation of Mg into the SnO_2 lattice. Electrical measurements demonstrated reproducible bipolar resistive switching with an ON/OFF resistance ratio of approximately 10^3 and stable switching behavior over multiple cycles with low voltage variation (±5%) compared to previously reported undoped SnO_2 films. The observed improvement in memristive performance is attributed to Mg-induced modifications of defect states and charge-transport pathways within the oxide matrix. Conduction analysis indicates a transition from ohmic behavior at low bias to space-charge-limited conduction (SCLC) at higher voltages, consistent with a quadratic current–voltage relationship ($I \propto V^2$). These results demonstrate that Mg incorporation is an effective defect-engineering strategy for tuning the electrical properties of SnO_2 thin films and improving their suitability for reliable memristor and non-volatile memory applications. This approach provides a simple and scalable route for engineering oxide-based memristive devices.
Keywords: *SnO_2; Mg doping; Memristor; Resistive switching; Non-volatile memory*
PACS: 73.40.Rw; 73.50.Gr; 77.55.Px; 85.30.Tv

INTRODUCTION

Resistive switching phenomena in metal–oxide thin films have attracted significant attention due to their strong potential for application in next-generation non-volatile memory and neuromorphic computing systems [1–3]. Among oxide materials, tin oxide (SnO_2) is a promising candidate due to its wide band gap, good chemical stability, low fabrication cost, and compatibility with conventional semiconductor technologies [4–6]. However, the practical implementation of SnO_2-based memristive devices is still limited by issues related to switching stability, ON/OFF resistance ratio, and variability of electrical characteristics. Therefore, modifying the electrical and structural properties of SnO_2 through controlled doping has become an important research direction [7–12].

Magnesium (Mg) incorporation into SnO_2 is expected to influence charge-transport behavior, defect distribution, and carrier concentration within the oxide matrix, thereby directly affecting resistive-switching performance. Previous studies on doped metal-oxide memristors have demonstrated that appropriate dopant selection can enhance switching uniformity, reduce operating voltage, and improve endurance characteristics. However, most reported studies have focused on undoped or transition-metal-doped SnO_2 systems, while systematic investigations of Mg-doped SnO_2 thin films, particularly regarding memristive switching mechanisms and conduction behavior, remain limited [13–14].

In this work, we demonstrate that Mg doping acts as an effective defect-engineering approach in SnO_2 thin films, enabling modulation of oxygen vacancy distribution and stabilization of conductive filament formation. As a result, the fabricated devices exhibit improved switching reproducibility and an enhanced ON/OFF resistance ratio compared to previously reported undoped SnO_2 systems. The films were prepared using the ultrasonic spray pyrolysis technique and systematically investigated in terms of their structural, morphological, and electrical properties. Special attention was given to switching reproducibility, the resistance ratio, and the dominant charge transport mechanisms. The results provide new insight into Mg-induced defect states and their role in controlling charge transport and filament dynamics, highlighting a promising pathway to improve the performance and reliability of SnO_2-based memristive devices for non-volatile memory applications.

METHODS

Mg-doped SnO_2 (SnO_2:Mg) thin films were fabricated using the ultrasonic spray pyrolysis (USP) technique due to its cost-effectiveness, simplicity, and suitability for large-area oxide thin-film deposition. The Mg concentration in the

Cite as: J.X. Murodov, Sh.U. Yuldashev, A.O. Arslanov, N.U. Botirova, J.Sh. Xudoyqulov, M.S. Mirkamilova, I.Q. Qodirova, O.X. Ximmatqulov, East Eur. J. Phys. 2, 132 (2026), https://doi.org/10.26565/2312-4334-2026-2-12

precursor solution was fixed at 20 mol.% relative to the Sn precursor. The schematic configuration of the USP deposition system is shown in Figure 1, in which the precursor aerosol generated by an ultrasonic nebulizer is transported by a carrier gas into a heated quartz reaction chamber to form a thin film on the substrate.

In this study, p-type silicon (p-Si) substrates were employed as the bottom electrode and supporting platform. Prior to deposition, the substrates were sequentially cleaned in deionized water, ethanol, and acetone, followed by a final rinse in deionized water to remove organic and inorganic contaminants and ensure uniform film adhesion. The cleaned substrates were dried under ambient conditions and subsequently dried using nitrogen gas to eliminate residual moisture.

The fabricated memristor device consists of a single-layer SnO_2 thin film prepared using a precursor solution containing 20 mol.% Mg, deposited on a p-Si substrate in a vertical metal–insulator–semiconductor configuration. Circular silver (Ag) top electrodes were formed using conductive silver paste, while the p-Si substrate served as the bottom electrode. This sandwich-type geometry enables electric-field-driven charge transport through the SnO_2:Mg layer, which is essential for investigating memristive resistive switching behavior.

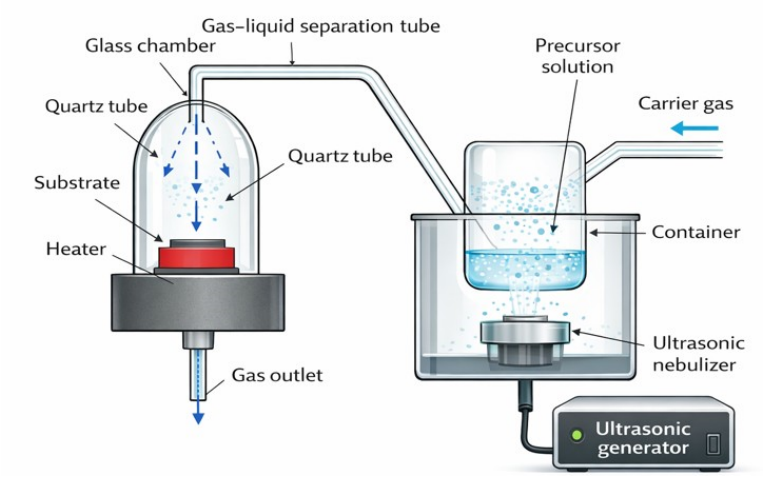

Figure 1. Schematic diagram of the ultrasonic spray pyrolysis system used for the deposition of SnO_2 thin films prepared from a precursor solution containing 20 mol.% Mg

The precursor solution was prepared by dissolving stannous chloride dihydrate ($SnCl_2 \cdot 2H_2O$) in double-distilled water, followed by the addition of a magnesium salt corresponding to 20 mol.% Mg doping. The solution was magnetically stirred at room temperature until complete homogenization was achieved. As illustrated in Figure 1, the precursor solution was atomized using a 2.5 MHz ultrasonic transducer and transported toward the heated substrate by an oxygen carrier gas.

Film deposition was carried out at a substrate temperature of 450 °C maintained by a temperature-controlled hotplate. After deposition, the films were annealed in ambient air at the same temperature to improve crystallinity, reduce structural disorder, and stabilize the electrical properties of the SnO_2:Mg layer. Silver top electrodes were subsequently formed for electrical characterization.

Electrical measurements of the memristor devices were performed at room temperature using a Keithley 2460 SourceMeter. A voltage sweeps sequence of $0 \rightarrow +5\ V \rightarrow 0 \rightarrow -5\ V \rightarrow 0$ was applied to record the current–voltage (I-V) characteristics. The pinched hysteresis loop confirmed the memristive resistive-switching behavior of the fabricated SnO_2:Mg thin-film structures.

RESULTS AND DISCUSSION

a. Optical properties

The optical properties of the Mg-doped SnO_2 thin film were analyzed using the Tauc method derived from diffuse reflectance measurements, and the corresponding Tauc plot is shown in Figure 2. The optical bandgap energy was determined by plotting the squared Kubelka–Munk function, $(F(R)h\nu)^2$, as a function of photon energy ($h\nu$) and extrapolating the linear region of the absorption edge to the energy axis.

As illustrated in Figure 2, the Tauc plot indicates a direct optical transition with an estimated bandgap value of approximately 3.75 eV for the SnO_2:Mg thin film. This value is slightly lower than that of undoped SnO_2, which is typically reported in the range of 3.6–4.0 eV, suggesting that Mg incorporation introduces localized defect states and band tailing near the conduction band. Such bandgap modification is commonly associated with oxygen-vacancy-related states and lattice distortion induced by substitutional doping.

The presence of defect-mediated sub-bandgap states is particularly relevant to memristive behavior, as these states can act as carrier-trapping centers and facilitate charge transport under an external electric field. Consequently, the bandgap narrowing and defect-related optical features observed in Figure 2 support enhanced resistive-switching performance and the formation of conductive filaments in the SnO_2:Mg memristor structure.

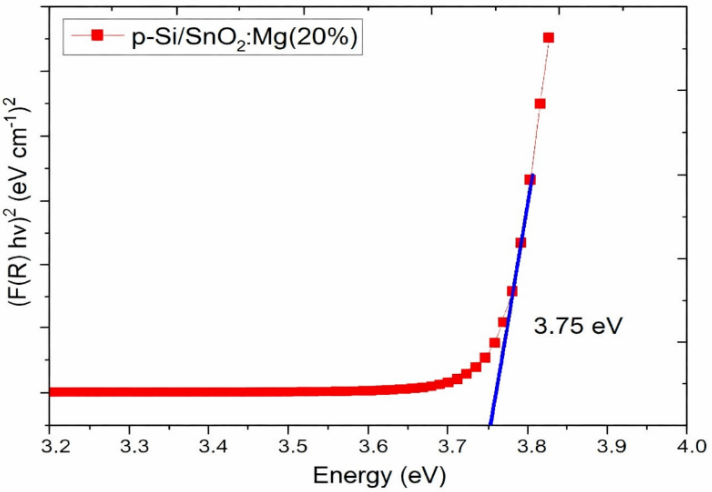

Figure 2. Tauc plot of the Mg-doped SnO_2 thin film showing a direct optical bandgap of approximately 3.75 eV

b. Structural properties from X-ray diffraction analysis

The crystal structure and phase composition of the Mg-doped SnO_2 thin films were analyzed by X-ray diffraction (XRD), and the corresponding diffraction pattern is presented in Figure 3. The pattern confirms that the deposited films retain the tetragonal rutile crystal structure characteristic of SnO_2, indicating that magnesium incorporation does not alter the fundamental crystallographic phase of the host material. The main diffraction peaks corresponding to the (110), (101), (200), and (211) crystallographic planes observed in Figure 3 are consistent with standard reference data for crystalline SnO_2, demonstrating the successful formation of well-crystallized oxide thin films.

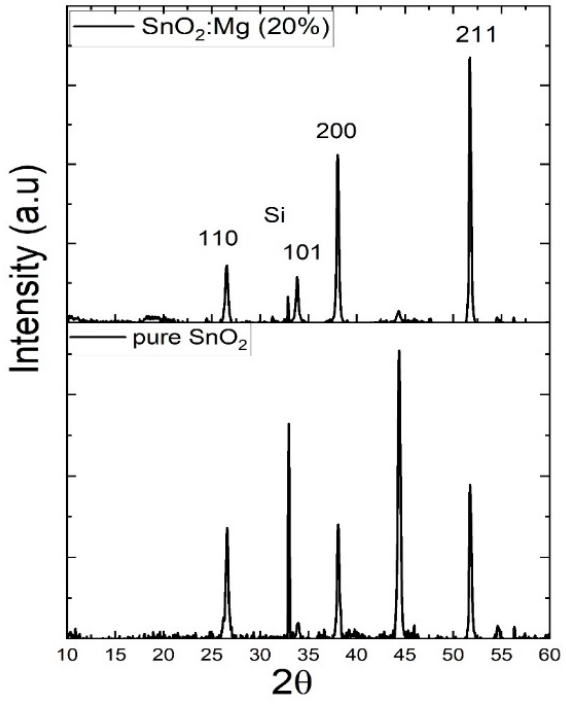

Figure 3. XRD pattern of the Mg-doped SnO_2 thin film showing the tetragonal rutile phase with dominant (110), (101), (200), and (211) reflections and no detectable secondary phases.

No additional reflections associated with MgO or other secondary impurity phases are detected within the measurement range shown in Figure 3. This absence of secondary phases suggests that Mg ions are incorporated substitutionally into the SnO_2 lattice rather than forming segregated compounds. Such substitutional incorporation is expected to induce local lattice distortion and modify the defect distribution within the oxide matrix.

In addition, energy-dispersive X-ray spectroscopy (EDS) analysis confirmed the presence of Mg in the deposited films, with an average concentration of approximately 5 at.%. This value is lower than the nominal precursor concentration (20 mol.%), indicating partial incorporation of Mg into the SnO_2 lattice during the ultrasonic spray pyrolysis process. The discrepancy between the precursor composition and the measured film composition can be attributed to incomplete incorporation efficiency and possible re-evaporation of Mg species during deposition.

As also evident from the peak profiles in Figure 3, a slight broadening of the diffraction peaks compared with undoped SnO_2 indicates a decrease in crystallite size together with an increase in microstrain and defect concentration caused by Mg incorporation. These structural changes are particularly important for memristive behavior, since they enhance the generation and migration of oxygen vacancies that serve as the dominant charge transport centers in oxide-based resistive switching devices. The increased density and mobility of oxygen vacancies facilitate conductive filament formation under an applied electric field, thereby improving switching stability and reproducibility in SnO_2:Mg memristors.

The structural parameters extracted from the XRD data are summarized in Table 1. The average crystallite size, calculated using the Scherrer equation, was found to be approximately 30 nm. Furthermore, the estimated microstrain ($\varepsilon \approx 1.2\times10^{-3}$) and dislocation density ($\delta \approx 1.2\times10^{15}$ m^{-2}) confirm an increased defect density induced by Mg incorporation. These microstructural features are directly correlated with enhanced oxygen vacancy mobility and improved memristive switching performance.

Table 1. Structural parameters of Mg-doped SnO_2 thin films derived from XRD analysis

(hkl)	2θ (deg)	d-spacing (Å)	Relative Intensity	FWHM (rad)	Crystallite Size (nm)
(110)	26.6°	3.35	Medium	0.005	30
(101)	33.9°	2.64	Low–Medium	0.006	27
(200)	37.9°	2.37	High	0.0055	28
(211)	51.8°	1.76	Very High	0.0048	31

c. Electrical properties and memristive switching behavior

The electrical characteristics of the Mg-doped SnO_2 thin film device were investigated using current–voltage (I–V) measurements in the voltage range from approximately −5 V to +5 V. As shown in Figure 4, the I–V curve exhibits a well-defined pinched hysteresis loop passing through the origin, which is a characteristic signature of memristive behavior. The device demonstrates bipolar resistive switching between a high-resistance state (HRS) and a low-resistance state (LRS), with an ON/OFF resistance ratio of approximately 10^3, confirming the formation of a stable resistive memory effect in the SnO_2:Mg thin film.

At low applied voltages, the current varies linearly with voltage, indicating ohmic conduction dominated by thermally generated free carriers. As the voltage increases, the current transitions to a nonlinear regime associated with space-charge-limited conduction (SCLC), suggesting trap-controlled charge transport within the oxide layer. The SCLC region is confirmed by the quadratic dependence of current on voltage ($I \propto V^2$). This transition from ohmic to SCLC conduction is consistent with defect-mediated transport mechanisms commonly observed in oxide-based memristive systems.

The asymmetry observed between the positive and negative voltage sweeps in Figure 4 indicates that the resistive switching process is governed by electric-field-driven migration of oxygen vacancies and the formation and rupture of conductive filaments across the SnO_2:Mg layer. The SET process occurs at approximately +3 V, where vacancy accumulation leads to filament formation and transition to the LRS, while the RESET process occurs near −3 V, corresponding to partial filament rupture and recovery of the HRS. The variation in switching voltages remains within ±8%, indicating good cycle-to-cycle uniformity and device stability.

Compared to previously reported undoped SnO_2 devices, the Mg-doped films exhibit improved switching reproducibility and reduced variability, which can be attributed to the more controlled distribution of oxygen-vacancy-related defect states induced by Mg incorporation.

The stability and reproducibility of the switching behavior were further evaluated through repeated voltage cycling, as presented in Figure 5. The device demonstrates stable resistive switching over more than 50 consecutive cycles, with only minor variation in the I–V characteristics while maintaining a consistent hysteresis window. The variation in SET and RESET voltages remains within ±5%, indicating good cycle-to-cycle uniformity and stable filament formation dynamics.

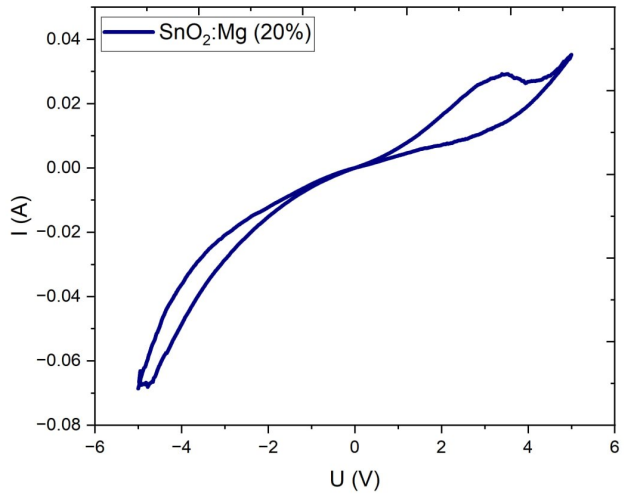

Figure 4. Current–voltage characteristics of the Mg-doped SnO_2 thin film showing bipolar memristive switching behavior

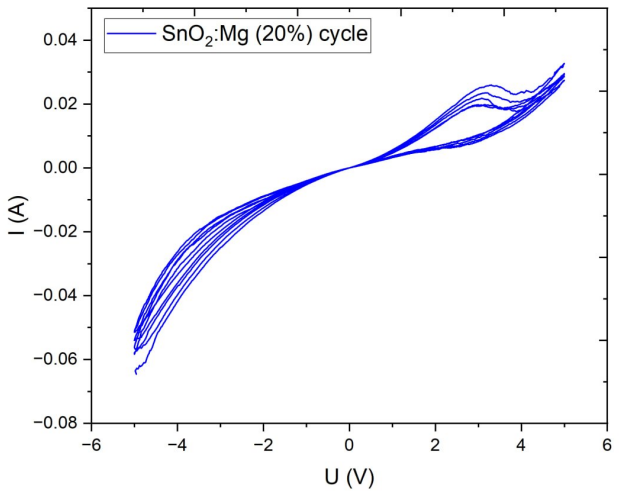

Figure 5. Multi-cycle I–V curves of the Mg-doped SnO_2 device demonstrating reproducible switching and stable hysteresis

Such endurance characteristics confirm the reliability of Mg-doped SnO_2 thin films for non-volatile memory and neuromorphic device applications.

Overall, the electrical analysis demonstrates that Mg incorporation enhances defect-mediated charge transport and stabilizes filamentary switching, resulting in an ON/OFF resistance ratio of approximately 10^3 and improved switching reproducibility compared to previously reported undoped SnO_2 thin films.

CONCLUSIONS

In this work, magnesium-doped SnO_2 thin films were prepared using a precursor solution containing 20 mol.% Mg were successfully fabricated by the ultrasonic spray pyrolysis technique and systematically investigated in terms of their structural and electrical properties. The results confirm that Mg incorporation preserves the tetragonal rutile crystal structure of SnO_2 without the formation of secondary impurity phases, while inducing lattice distortion, reduced crystallite size (≈ 30 nm), and increased defect density. These structural modifications enhance oxygen-vacancy migration and facilitate the formation of conductive filaments within the oxide layer.

Electrical measurements reveal stable bipolar resistive switching with a pronounced pinched hysteresis loop and an ON/OFF resistance ratio of approximately 10^3. The device exhibits reproducible switching behavior over multiple voltage cycles with low variation in switching voltages (±5%). The conduction mechanism transitions from ohmic transport at low bias to space-charge-limited current (SCLC) at higher voltages, consistent with trap-controlled charge transport ($I \propto V^2$). The switching process is governed by an oxygen-vacancy-driven filamentary conduction mechanism, where Mg doping plays a crucial role in stabilizing filament formation and reducing switching variability.

Compared with previously reported undoped SnO_2 systems, the Mg-doped films demonstrate improved switching reproducibility and enhanced resistance ratio, highlighting the effectiveness of Mg as a defect-engineering dopant. Overall, the results provide new insight into defect-controlled resistive switching and confirm that Mg incorporation is a promising strategy for improving the performance and reliability of SnO_2-based memristive devices.

These findings indicate that SnO_2:Mg thin films fabricated by ultrasonic spray pyrolysis represent a promising material platform for next-generation non-volatile memory and neuromorphic applications. Future work will focus on systematically varying Mg concentration to further optimize switching characteristics and better understand the underlying physical mechanisms.

ORCID

Jamoliddin X. Murodov, https://orcid.org/0009-0006-3088-4881; **Shavkat U. Yuldashev,** https://orcid.org/0000-0002-2187-5960
Azamat O. Arslanov, https://orcid.org/0009-0000-4817-8770

REFERENCES

[1] D. Ielmini, "Resistive switching memories based on metal oxides: Mechanisms, reliability and scaling," Semiconductor Science and Technology, **31**(6), 063002 (2016). https://doi.org/10.1088/0268-1242/31/6/063002
[2] B. Cao, H. Liu, T. Li, J. Gong, S. Zhang, and M.T. Dove, "Synthesis of composite films for ZnO-based memristors with superior stability," Materials Research Express, **11**, 056302 (2024). https://doi.org/10.1088/2053-1591/ad4777
[3] P.D. Walke, A.H.S. Rana, Sh.U. Yuldashev, V.K. Magotra, D.J. Lee, Sh. Abdullaev, T.W. Kang, and H.C. Jeon, "Memristive Devices from CuO Nanoparticles," Nanomaterials, **10**(9), 1677 (2020). https://doi.org/10.3390/nano10091677
[4] P.A. Hind, P. Kumar, U.K. Goutam, and B.V. Rajendra, "Impact of deposition temperature on persistent photoconductivity of SnO_2 thin films deposited using spray pyrolysis technique suitable in optoelectronic synaptic devices," Optical Materials, **146**, 115579 (2024). https://doi.org/10.1016/j.optmat.2024.115579
[5] A. Arslanov, Sh. Yuldashev, N. Botirova, R. Nusretov, J. Murodov, and J. Xudoyqulov, "Impact of precursor molar concentration on the structural and optical properties of ZnO thin films synthesized by ultrasonic spray pyrolysis," Physical Science International Journal, **29**(1), 29–35 (2025). https://doi.org/10.9734/psij/2025/v29i1871
[6] O. Ochilov, H. Turkmenov, G. Kulmatova, K. Malikov, and O. Yuldashev, "Magneto-optics of a three-layer medium," AIP Conf. Proc. **3304**, 020005 (2025). https://doi.org/10.1063/5.0269344
[7] N.U. Rehman, R. Khan, N. Rahman, I. Ahmad, A. Ullah, M. Sohail, S. Iqbal, *et al.*, "Dual-doped ZnO-based magnetic semiconductor resistive switching response for memristor-based technologies," Journal of Materials Science: Materials in Electronics, **35**, 1557 (2024). https://doi.org/10.1007/s10854-024-13318-5
[8] S. Saha, M.C.K. Reddy, T.S. Nikhil, K. Burugupally, S. DebRoy, A. Salimath, and V. Mattela, "Experimental demonstration of SnO_2 nanofiber-based memristors and their data-driven modeling for nanoelectronic applications," Chip, **2**, 100075 (2023). https://doi.org/10.1016/j.chip.2023.100075
[9] J.X. Murodov, Sh.U. Yuldashev, M.S. Mirkamilova, and U.E. Jurayev, "Tunable Negative Differential Resistance in SnO_2:Co Memristors on p-Si," East European Journal of Physics, (2), 211-214 (2025). https://doi.org/10.26565/2312-4334-2025-2-22
[10] J.X. Murodov, Sh.U. Yuldashev, A.O. Arslanov, N.U. Botirova, J.Sh. Xudoyqulov, R.Sh. Sharipova, R.A. Nusretov, *et al.*, "Resistive switching behavior of SnO_2/ZnO heterojunction thin films for non-volatile memory applications," East Eur. J. Phys. (3), 348–352 (2025). https://doi.org/10.26565/2312-4334-2025-3-34
[11] J.X. Murodov, Sh.U. Yuldashev, A.O. Arslanov, N.U. Botirova, R.Sh. Sharipova, J.Sh. Xudoykulov, "NDR in Co:SnO_2 memristors: Nanocluster control for enhanced performance," Crystal Growth & Design, **26**(1), 317–321 (2026). https://doi.org/10.1021/acs.cgd.5c01258
[12] J.X. Murodov, Sh.U. Yuldashev, A.O. Arslanov, N.U. Botirova, J.Sh. Xudoyqulov, I.Kh. Khudaykulov, M.S. Mirkamilova, *et al.*, "Memristive switching behavior of sol–gel derived Ga_2O_3 thin films," East Eur. J. Phys. (4), 415-419 (2025). https://doi.org/10.26565/2312-4334-2025-4-40
[13] M.A. Dar, N.A. Mala, M.Y. Bhat, S.R. Ahamed, A.A. Rather, K.M. Batoo, G.N. Dar, "Enhanced supercapacitor performance of Mg-doped SnO_2 nanorods synthesized through the solvothermal method," Bull. Mater. Sci. **46**, 69 (2023). https://doi.org/10.1007/s12034-023-02893-8
[14] N. Mazumder, A. Bharati, S. Saha, D. Sen, and K.K. Chattopadhyay, "Effect of Mg doping on the electrical properties of SnO_2 nanoparticles," Curr. Appl. Phys. **12**, 975–982 (2012). https://doi.org/10.1016/j.cap.2011.12.022
[15] G. Velmurugan, R. Ganapathi Raman, P. Sivaprakash, A. Viji, S.H. Cho, and I. Kim, "Functionalization of fluorine on the surface of SnO_2–Mg nanocomposite as an efficient photocatalyst for toxic dye degradation," Nanomaterials **13**, 2494 (2023). https://doi.org/10.3390/nano13172494

Mg-ІНДУКОВАНЕ ПОСИЛЕННЯ МЕМРИСТИВНОГО ПЕРЕМИКАННЯ В ТОНКИХ ПЛІВКАХ SnO_2

Джамоліддін Х. Муродов[1,2], Шавкат У. Юлдашев[2], Азамат О. Арсланов[3], Нойба У. Ботірова[2], Джавохір Ш. Худойкулов[3], Маргуба С. Міркамілова[1], Інобат К. Кодірова[1], Оділбой Х. Хімматкулов[1]

[1]Ташкентський державний технічний університет імені Іслама Карімова

[2]Центр розвитку нанотехнологій, Національний університет Узбекистану

[3]Національний університет Узбекистану імені Мірзо Улугбека, Ташкент, Узбекистан

Тонкі плівки оксиду олова (SnO_2:Mg), легованого магнієм, привернули значну увагу як перспективні матеріали для енергонезалежних пристроїв пам'яті наступного покоління завдяки своїй стабільній резистивній поведінці перемикання та простим процесам виготовлення. У цій роботі тонкі плівки SnO_2 були виготовлені методом ультразвукового розпилювального піролізу з використанням розчину-попередника, що містить 20 мол.% Mg, та систематично досліджені для оцінки їхніх характеристик мемристивного перемикання, електричних характеристик та поведінки провідності. Структурний аналіз підтвердив утворення однорідних полікристалічних тонких плівок з розміром кристалітів приблизно 30 нм, тоді як енергодисперсійна рентгенівська спектроскопія (EDS) виявила фактичний вміст Mg приблизно 5 ат.%, що вказує на часткове включення Mg у решітку SnO_2. Електричні вимірювання продемонстрували відтворюване біполярне резистивне перемикання зі співвідношенням опору вмикання/вимикання приблизно 10^3 та стабільну поведінку перемикання протягом кількох циклів з низькими змінами напруги (±5%) порівняно з раніше зареєстрованими нелегованими плівками SnO_2. Спостережуване покращення мемристивної продуктивності пояснюється модифікаціями дефектних станів та шляхів переносу заряду, індукованими Mg, в оксидній матриці. Аналіз провідності вказує на перехід від омічної поведінки при низькому зміщенні до провідності, обмеженої просторовим зарядом (SCLC), при вищих напругах, що узгоджується з квадратичною залежністю струм-ампера ($I \propto V^2$). Ці результати демонструють, що впровадження Mg є ефективною стратегією дефектної інженерії для налаштування електричних властивостей тонких плівок SnO_2 та підвищення їхньої придатності для надійних мемристорів і енергонезалежної пам'яті. Цей підхід забезпечує простий та масштабований шлях для розробки мемристивних пристроїв на основі оксиду.

Ключові слова: *SnO_2; легування Mg; мемристор; резистивне перемикання; енергонезалежна пам'ять*

East European Journal of Physics. 2. 138-146 (2026)
DOI:10.26565/2312-4334-2026-2-13 ISSN 2312-4334

IMPACT OF DIRECT AND PULSED ELECTRODEPOSITION MODE ON THE ELECTROCHEMICAL, STRUCTURAL, AND MORPHOLOGICAL PROPERTIES OF Ni-Fe NANOSTRUCTURES COATINGS

Houssem Eddine El Yamine Sakhraoui[1,2], H. Ayadi[3], N. Maouche[2], D. Belfennache[4], R. Yekhlef[4], Mohamed A. Ali[5], Hamad M. Adress Hasan[6], Hanan F. Emrayed[6], Haneebal Saeid Khatab[7], Ghada M. Salem[8]

[1]*Département de Génie des Procédés, Faculté de Technologie, Université de Ferhat Abbas Sétif-1, Sétif, 19000, Algeria*
[2]*Laboratoire d'Electrochimie et Matériaux (LEM), Université de Ferhat Abbas Sétif-1, Sétif, 19000, Algeria*
[3]*Université 20 Août 1955 de Skikda, Skikda, Algeria*
[4]*Research Center in Industrial Technologies CRTI, P.O. Box 64, Cheraga, 16014 Algiers, Algeria*
[5]*School of Biotechnology, Badr University in Cairo (BUC), Badr City 11829, Cairo, Egypt*
[6]*Chemistry Department, Faculty of Science, Omar Al-Mukhtar University, Libya*
[7]*Chemistry Department, Faculty of Education, Al-Marj, University of Benghazi, Libya*
[8]*Libyan Authority for Scientific Research, Tripoli, Libya*
**Correspondence Author e-mail: belfennachedjamel@gmail.com*
Received February 12, 2026; revised April 28, 2026; accepted May 5, 2026

Nickel-iron (Ni-Fe) nanostructured alloys are attracting increasing interest due to their remarkable electrochemical, magnetic, and mechanical properties, making them particularly attractive for applications in electrocatalysis, energy storage, sensors, and functional coatings. This study presents a comparative analysis of the electrochemical, structural, and morphological characteristics of nickel-iron (Ni-Fe) nanostructures synthesized in sulfate electrolytes on indium tin oxide (ITO) substrates through various electrodeposition methods. The fabricated nanostructures were characterized using cyclic voltammetry, chronoamperometric measurements (potentiostatic steps), atomic force microscopy (AFM), and X-ray diffraction (XRD). The electro-crystallization process was evaluated using the Scharifker-Hills model, revealing that nucleation mechanisms differed based on applied potentials. XRD analysis confirmed the polycrystalline nature of the Ni-Fe nanostructures, with a preferred <111> crystallographic orientation and a face-centered cubic (fcc) structure observed in both deposition modes. The crystallite sizes were determined as 9.77 nm under pulsed conditions and 14.63 nm for the direct method. AFM surface analyses further demonstrated that the choice of electrodeposition method significantly influences the morphological features of the resulting deposits.
Keywords: *Ni-Fe nanostructures; Electrodeposition method; Coatings; ITO substrate*
PACS: 61.46.Df, 61.82.Rx

1. INTRODUCTION

The earliest documented paint-based coatings originated in Europe and Australia around 20,000 years ago [1]. During this period, formulations included iron oxide, chalk, or charcoal, applied using fingertips or brushes crafted by splitting soft twigs [1]. In contrast, ancient Egyptian and Greek civilizations developed more sophisticated coating technologies, including early polymeric-based paints and coatings [2]. Historians often classify nanotechnology as a reinvented field, noting that early efforts to create nanoscale coatings emerged in ancient Egypt and were later refined in China [2]. In recent years, nanomaterials and nanotechnology-based coatings have become a focal point of scientific research, both for fundamental understanding and technological innovation. This surge is driven by their diverse applications and expanding utility in response to growing social and industrial demands [3].

Among these, nickel (Ni) and nickel-based coatings have emerged as critical materials in various industries, gaining significant attention for their diverse applications [4,5]. These include uses in electronics—such as memory and storage devices for computers—enhancing substrate hardness and wear resistance, and in components like transducers, transformers, and protective chokes [6,7]. Additionally, nickel coatings are vital for corrosion protection, energy storage systems, and solar thermal applications [8-10]. The surge in nickel and nickel-coating research stems from the versatility of their preparation methods. For instance, composite coatings incorporating nanoparticles such as Al_2O_3 [11], ZrO_2 [12], Si_3N_4 [13], In_2O_3 [14], SiC [15] enhance matrix properties by dispersing these particles. Alternatively, crystallite refinement through additives [16] and alloying with elements such as Tungsten (W) [17], Chrome (Cr) [18], Molybdenum (Mo) [19], and Cobalt (Co) [20] further expand their applicability. Crucially, the synthesis technique employed directly impacts the resulting coating properties.

Several synthesis techniques are used to develop coatings [21-24]; however, electrochemistry [25] is among the most advantageous methods for producing nanocoatings. Among the numerous synthesis approaches reported in the

Cite as: H.E. El Yamine Sakhraoui, H. Ayadi, N. Maouche, D. Belfennache, R. Yekhlef, M.A. Ali, H.M.A. Hasan, H.F. Emrayed, H.S. Khatab, G.M. Salem, East Eur. J. Phys. 2, 138 (2026), https://doi.org/10.26565/2312-4334-2026-2-13

literature, electrochemical synthesis stands out for its high adaptability and its ability to precisely control the structural, morphological, and functional properties of the resulting materials [26,27].

The variety of its processes provides a good synthesis of diversified nano-coatings in terms of both quantity and quality [28,29] in organic [30,31] and inorganic [32] fields. With a good manipulation of the sequence parameters, it is possible to design the desired properties of nano-coatings, such as their thickness and morphology [26]. Based on the low costs and reduced amount of waste materials, the electrochemical process has given rise to increasing interest in alloy electrodeposition, particularly in modern electronic devices. The present study investigates the effect of electrodeposition mode on the, morphology, and functional properties of Ni–Fe alloy coatings, with particular emphasis on the process–structure– morphology property relationship

2. MATERIALS AND METHODS

2.1. Techniques of characterization

X-ray diffraction (XRD) patterns of the powder were obtained using an analytical X'pert-PRO diffractometer equipped with Cu Kα radiation.

Electrochemical measurements were conducted in a conventional three-electrode cell. Potential values were referenced to a saturated calomel electrode (SCE), positioned close to the cathodic steel surface to minimize ohmic potential drops in the electrolyte. A platinum grid served as the auxiliary electrode. Indium tin oxide (ITO)-coated conducting glass substrates were employed as working electrodes, featuring an exposed area of 1 cm² and a sheet resistance of 10–20 Ω/cm². Prior to use, the substrates were cleaned via ultrasonic degreasing in acetone and ethanol for 10 minutes, followed by thorough rinsing with distilled water.

2.2. Chemicals

The sources of nickel and iron available for reduction in the solution are the $NiSO_4.6H_2O$ and $FeSO_4.7H_2O$ (Sigma-Aldrich). The aim of adding boric acid H_3BO_3 (Sigma-Aldrich) in the electrolyte is to avoid the pH variation near the electrode and to inhibit the formation of hydroxide species. The Sodium sulfate $Na_2SO_4.6H_2O$ was used as supporting electrolyte and used to maintain the overall quality of the electrodeposits. The bath composition and operating conditions are gathered in Table 1.

Table 1. Electrolyte composition and operating parameters

Bath composition	$NiSO_4.6H_2O$ (0.05 M) $FeSO_4.6H_2O$ (0.05 M) $Na_2SO_4.6H_2O$ (0.1 M) 0.05 M H_3BO_4 (0.05 M) pH 3.7-.5
Operating parameter	Temperature (°C) 23-25
Cathode	ITO substrates
Anode	Pt grid
Reference	Saturated calomel electrode (ECS)

2.3 Preparation of synthetic solution of Ni-Fe alloy

Nickel-iron (Ni-Fe) alloy nanostructures were synthesized through the reduction of Fe^{2+} and Ni^{2+} ions in an aqueous solution, using 0.1 M sodium sulfate ($Na_2SO_4 \cdot 6H_2O$) as the supporting electrolyte. Nickel sulfate ($NiSO_4 \cdot 6H_2O$, 30 mmol) and iron sulfate ($FeSO_4 \cdot 6H_2O$, 10 mmol) were dissolved uniformly in 200 mL of distilled water. The solution was stirred magnetically for 10 minutes at room temperature, after which 0.05 M boric acid (H_3BO_3) was added to adjust the pH to a range of 3.7–5.0. To investigate the electrochemical kinetics and growth mechanisms of Ni, Fe, and Ni-Fe alloy electrodeposition, cyclic voltammetry (CV) and chronoamperometry (CA) were employed. The nucleation behavior of the deposits was further analyzed using the Scharifker-Hills model to interpret transient current responses during deposition [33].

3. RESULTS AND DISCUSSION

3.1. Cyclic voltammetry of Nickel, Iron and Ni-Fe

To determine the potential range over which nickel and iron deposition occur, cyclic voltammetry was carried out. The electrolyte solution contains 0.05 M of $FeSO_4$, H_3BO_3, and 0.1 M Na_2SO_4.

Fig. 1 shows cyclic voltammograms of the cathodic part for Ni electrodeposited onto an ITO substrate. The beginning of the current decrease was detected at -1100 mV/SCE, which indicates the over potential deposition process onto the ITO surfaces. The presence of cross-overs in the positive and negative scans is a typical sign of the formation of a new phase, involving nucleation followed by a diffusion-limited growth process [34]. It is also noticed that the hydrogen evolution reaction (HER) might occur simultaneously with nickel deposition.

The electrodeposition of nickel was first proposed by the adsorption of a nickel complex, then a reaction of charge transfer in two stages according to the following mechanism [35]:

$$Ni^{2+} + OH^- \rightarrow Ni(OH)^+ \quad (1)$$

$$Ni(OH)^+ + e^- \rightarrow Ni(OH)_{ads} \quad (2)$$

$$Ni(OH)_{ads} + e^- \rightarrow Ni + (OH)^- \quad (3)$$

The adsorbed monovalent nickel intermediate may also undergo reduction as:

$$Ni^{2+} + 2e^- + Ni(OH)_{ads} \rightarrow Ni + Ni(OH)_{ads} \quad (4)$$

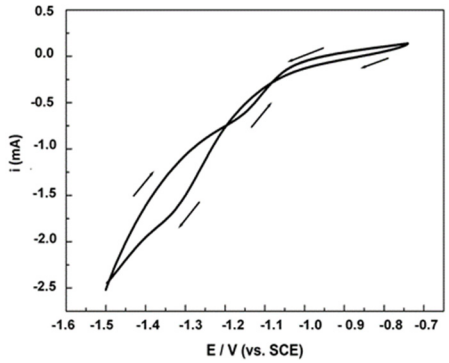

Figure 1. Cyclic voltammogram of Ni deposited on Pt electrode in aqueous solution containing 0.05 M of $NiSO_4$, H_3BO_3 and 0.1 M Na_2SO_4 at a scan rate of 100 mV/s

Fig. 2 shows the cyclic voltammogram for Fe electrodeposition. It reveals two reduction reactions for Fe^{2+} ions: one yields Fe+ ions, and the other yields metallic Fe. The scan was performed between -0.6 and -1.6 V/ESC at a scan rate of 100 mV·s^{-1}. The current decrease was detected at -0.7 and -1.00 V/ SCE, which is characteristic of the over potential deposition of the Fe^{2+} reduction process to the adsorbed Fe^+ then to the metallic iron Fe [36].

$$Fe^{2+} + e^- \rightarrow Fe^+_{ads} \quad (5)$$

$$Fe^+_{ads} + e^- \rightarrow Fe \quad (6)$$

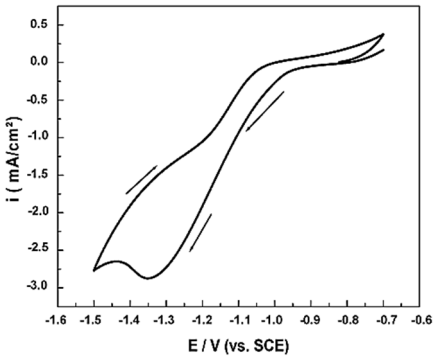

Figure 2. Cyclic voltammogram of Fe deposited in aqueous solution containing 0.05 M of $FeSO_4$, H_3BO_3, and 0.1 M of Na_2SO_4 at a scan rate of 100 mV/s

Fig. 3 represents the cyclic voltammogram of Ni-Fe. In the positive scan, the current decreased at 1000 mV, corresponding to the reduction of Ni and Fe. In the reverse scan, a dissolution pic of the previously formed species (Ni and Fe) was observed around -625 mV, and their oxidation at 355 mV.

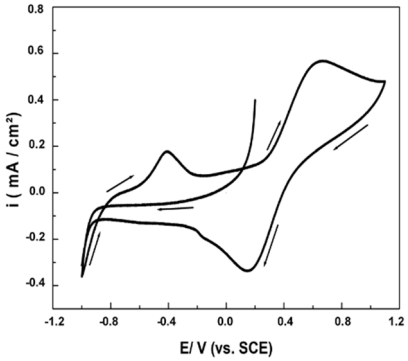

Figure 3. Cyclic voltammogram of Ni-Fe deposited in aqueous solution containing 0.05 M of $FeSO_4$, H_3BO_3, $NiSO_4$, and 0.1 M Na_2SO_4 at a scan rate of 100 mV/s

3.1.1 Ni-Fe electrodeposition mechanism

Dahms was to be the first to try to explain the inhibition function of the observed codeposition alloy Ni-Fe behavior [37]. The pH value on the cathodic surface is supposed to be high because of the following secondary reaction:

$$2H^+ + 2e^- \rightarrow H_2 \quad (7)$$

It was proposed that codeposition is due to the concurrent reaction of hydrogen release, which becomes very awkward for nickel deposition. Because of this condition, the pH of the surface could increase, thus enabling the formation of metal hydroxides according to the reaction:

$$M^{2+} + 2OH^- \rightarrow M(OH)_2, \quad (8)$$

$$Ni^{2+} + 2OH^- \rightarrow Ni(OH)_{2\,aq}, \quad (9)$$

$$Fe^{2+} + 2OH^- \rightarrow Fe(OH)_{2\,aq}. \quad (10)$$

Where M represents: Ni and Fe.

Consequently, it was noted that the nickel reduction was inhibited, which may be due to the preferential adsorption of ferrous hydroxides on the cathodic surface. These ferrous hydroxides block the available sites at the electrode surface. Giuliani and Lazzari [38] supposed that during the codeposition of Ni-Fe alloy, the reduction of the H^+ and Ni^{2+} ions occurs in the first step, causing an increase in the pH of the cathode surface, then the formation of $Ni(OH)^+$ and $Fe(OH)^+$. Gangasingh and Talbot [39] have proposed a very similar mechanism as that of Dahms and Croll.[37] for the Ni-Fe codeposition. The difference was that Ni^{2+} and Fe^{2+} were taken to form aqueous hydroxides $Ni(OH)_{2\,(aq)}$ and $Fe(OH)_{2\,(aq)}$ instead of solid hydroxides of the reactions according to the following homogeneous reactions:

3.1.2 Hydrogen evolution reaction (HER)

On the cathodic part in the sulphate medium, hydrogen evolution reaction (HER) intervenes which devised into several stages. The first stage, called stage of *Volmer* corresponds to the formation of an adsorbed MH_{ads} type intermediary, by adsorption of protons on the surface of metal. The second stage is an electrochemical desorption after the adsorption of a new H^+ (stage of *Heyrovsky*) and/or a chemical desorption after the recombination of two adsorbed intermediaries (stage of *Tafel*), these three stages are given below:

$$M + H^+ + e^- \rightarrow MH_{ads}\ Volmer, \quad (11)$$

$$MH_{ads} + H^+ + e^- \rightarrow H_2 + M\ Heyrovsky, \quad (12)$$

$$2MH_{ads} \rightarrow H_2 + 2M\ Tafel. \quad (13)$$

The HER kinetics are supposed to be controlled by the charge transfers of metallic cations [2, 40]. The rate *Vi* of each stage *i* can then be expressed according to the rate of surface covering Q by adsorbed hydrogen H_{ads}.

3.2 Electrodeposition of Ni by Chronoamerometry

The current transients shown in Figure 4 provide key information on the nucleation and growth mechanisms occurring during the electrodeposition of Ni, Fe, and Ni-Fe alloys. In the case of monometallic Ni and Fe deposits (Figs. 4a and 4b), the typical transient profile, characterized initially by a decrease in current density over time, reflects the local depletion of metal ions near the electrode, as well as the increase in diffusion resistance due to deposit thickening. This is followed by a rapid increase in current until it reaches a maximum value, denoted i_{max}, corresponding to a maximum time t_{max}, followed by progressive stabilization. This behavior highlights instantaneous nucleation accompanied by diffusion-controlled growth of Ni and Fe metallic species in solution. For the direct electrodeposition of the Ni–Fe alloy (Fig. 4c), the current transients exhibit more complex behavior, resulting from the simultaneous co-reduction of Ni^{2+} and Fe^{2+} ions. This kinetics is strongly influenced by the phenomenon of anomalous iron deposition, leading to a modification of the current density and growth mechanisms compared to monometallic deposition. Competition between metallic species and differences in reduction overpotentials promote heterogeneous nucleation and a less homogeneous microstructure. In contrast, the pulsed deposition of the Ni–Fe alloy (Fig. 4d) is characterized by higher instantaneous current densities during cathode pulses, followed by relaxation periods that allow for the reconstitution of the diffusion layer. This deposition mode promotes an increased density of nucleation sites, limits local depletion of metal ions, and leads to more uniform and finer deposit growth. Thus, pulsed electrodeposition improves the kinetic control of the process and allows for more homogeneous Ni–Fe layers, characterized by a refined microstructure and superior physico-chemical properties compared to direct deposition.

In general, these curves have the same shape. At the beginning, a decrease in the current density is observed, that is due to the double layer charge. Then this density increases until reaching a maximum value indicated by i_{max} corresponding to a maximum time t_{max}. This behavior shows the formation of one well new phase, which corresponds to the nucleation and the growth of Ni and Fe crystals. Finally, a pseudo-stationary mode is established in accordance with the equation of Cottrell [41]:

$$i = n.F.C.(\frac{D}{\pi t})^{1/2} \quad (14)$$

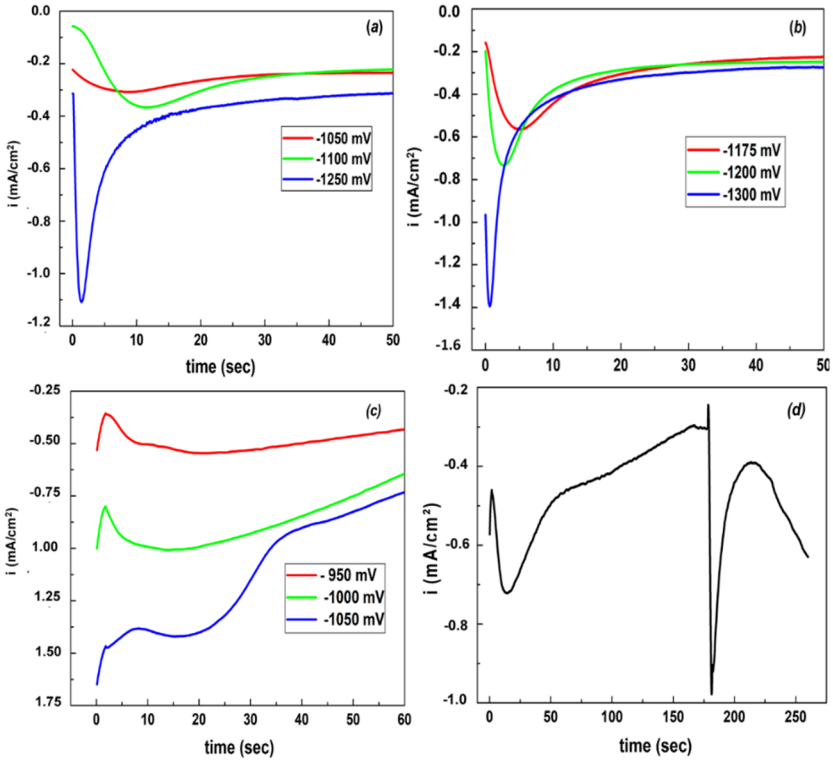

Figure 4. Current transients for the electrodeposition of (a) Ni (b) Fe (c) direct Ni-Fe and (d) pulsed Ni-Fe

3.3. Scharifker–Hills proposed model

Nucleation and the first growth steps are important parameters for understanding the properties of a crystallized deposit, by analyzing the first stages of electrodeposition, using the first part of the chronoamperograms i.e. before the diffusion step limit established. Instantaneous nucleation is defined by a slow growth of nuclei on a low number of active sites, all activated at the same time. However, progressive nucleation corresponds to a rapid growth of nuclei on numerous active sites, all activated during the course of electroreduction [42]. In this case, from Scharifker–Hills model [43], we distinguish the instantaneous nucleation followed by three-dimensional diffusion-limited growth (15) and progressive nucleation followed by three-dimensional diffusion-limited growth (16):

$$\frac{i^2}{i^2_{max}} = 1.9542\left(\frac{t_{max}}{t}\right)[1-\exp\left(-1.2564\frac{t}{t_{max}}\right)]^2 \quad (15)$$

$$\frac{i^2}{i^2_{max}} = 1.2254\left(\frac{t_{max}}{t}\right)[1-\exp\left(-2.3367\frac{t^2}{t^2_{max}}\right)]^2 \quad (16)$$

Fig. 5a and 5b show the deposition transient for Ni and Fe electrodeposited from sulfate electrolytes.

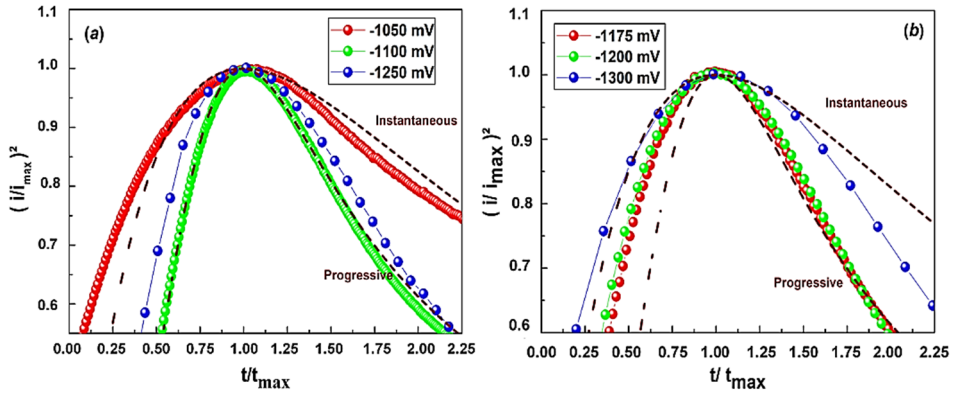

Figure 5. Reduced dimensionless parameters with theoretical curves for progressive and instantaneous nucleation (dotted line) for the deposition of Ni (a) and Fe (b)

The dashed and full lines represent the theoretical curves for progressive and instantaneous limiting cases, described by Eqs. (15) and (16). According to Fig. 5a, the reduced forms for Ni electrodeposition follow the progressive nucleation

model for -1100 and -1250 mV/ SCE and an instantaneous nucleation model for -1050 mV/ SCE as obtained by *Azizi et al*., [44]. On the other hand, in Fig. 5b, the Fe electrodeposition at -1300 mV/SCE followed the instantaneous nucleation and a transition from the instantaneous to the progressive nucleation mode. These behaviors are consistent with nucleation of 3D clusters followed by diffusion-limited growth.

3.4 X-ray diffraction characterization

XRD patterns of Fe, Ni, pull Ni-Fe and Ni-Fe are presented in Fig. 7. The data recording was carried out within an angle range from 20° to 80° with a step of 0.02°. The peaks at 44,70 ° and 52,02° are indexed to the diffractions of (111), (200) planes of Ni-Fe structure. The peaks found at 2θ = 44.06◦ and 2θ = 43.85◦ are assigned to the preferential diffraction peaks of (111) planes of pulsed and direct Ni-Fe films respectively [45].

The analysis of the structural properties of Ni, Fe and Ni-Fe layers obtained by electrodeposition was carried out by using XRD and the results are presented in Fig. 7. An angular range between 20° and 80° was swept using a step of 0.02°. The two peaks of Ni-Fe diffraction observed are located at the angles of 44,70 ° and 52,02° and were identified as < 111 > and < 200 > of the Ni-Fe alloy respectively. The located peaks of 2θ = 44.06◦ and 2θ = 43.85◦ for pulsed and direct Ni-Fe films respectively, have been assigned to be the preferential <111> Ni-Fe face centered cubic (FCC) phase as found by A. Guittoum et al. [45]. All XRD parameters are summarized in Table 2.

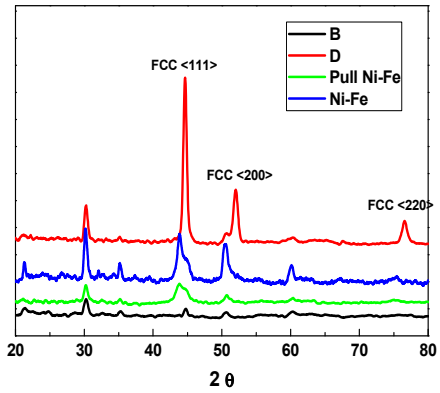

Figure 6. XRD patterns of different deposits.

Table 2. XRD Parameters

Sample	2θ (°)	a(Å)	d(Å)	D (nm)
Ni	44.56	3.51	2.03	26.62
Fe	44.81	3.49	2.02	30.37
Pulsed Ni-Fe	44.06	3.55	2.05	9.77
Ni-Fe	43.85	3.57	2.06	14.63

The evolution of lattice parameter (Å) is represented in the DRX table. We notice a variation in a parameter when we switch the mode from pulse to direct electrodeposition, from 3.55 Å to 3.57 Å. It is to notice that all parameter values of (a) for Ni-Fe alloys obtained by direct and pulsed electrodeposition are superior to that of massive Ni-Fe (a= 3.53 Å) [46], this difference between the experimental values of the a parameter and the value of the solid mass's one is probably due to the residual stresses [47].

The crystallite size of the electrodeposited Ni, Fe and Ni-Fe films were determined from widths (FWHM) of X-ray diffraction peaks using Scherer's formula [48]:

$$D = \frac{0.9\lambda}{\beta Sin\theta} \tag{17}$$

Where λ is the wavelength of the Cu$K\alpha$ radiation, θ is the diffraction angle of reflection and β is the FWHM (full width at half maximum) of the diffraction line.

The crystallite size increases from 9.77 nm to 14.63 nm in pulsed- and direct-electrodeposited Ni-Fe. This behavior can be attributed to the fact that the grains tend to agglomerate with the change from pulsed to direct applied potentials. It is worth mentioning that Chen et al. [49] have found the same crystallite size of 9 nm for $Ni_{80}Fe_{20}$ Permalloy films. Sam et al. [50] reported a crystallite size of 16 nm, so the electrodeposited Ni-Fe crystallite sizes presented in this work are in the average reported in the literature.

3.5. Atomic force microscopy (AFM) characterization

In order to better measure the roughness of these samples, we based on the measurement of the factor of roughness RMS to the surface of the software WSxM software [51]. AFM analysis was carried out to observe the surface morphology of direct and pulse electrodeposited Ni-Fe films. Fig. 8 shows the topographies of the electrodeposits, the results of the analysis indicate the presence of islands with different shape, size and number. This is well described according to the

"Volmer-Weber" mode i.e. the binding energy between metal ad-atom and substrate atoms is smaller than the binding energy between metal ad-atoms themselves, which leads over potential deposition (OPD) of a 3D metal forming on substrate. For the pulse electrodeposited Ni-Fe alloys, Fig. 8 shows a large number of islands covering irregularly the surface of the films, explaining the rough surface and the RMS (Root-Mean-Square) value of 55.78 nm. However, for the direct electrodposition, it was clearly observed a diminution in the number and the size of Ni-Fe islands smoothly dispersed on the surface, leading to low roughness than the pulsed method. The RMS was found to be 7.27 nm for the direct electrodeposition of Ni-Fe as it is summarized in the table 3. Moreover, some holes, that are due to the hydrogen bubbles release on the surface of the deposits, are observed; thereby inhibiting the deposition rate of the alloy in some surface sites that which lead to the appearance of holes observed on images.

By way of comparison, Neagu et al. [52] have obtained a roughness lower than 25 nm for Ni-Fe films prepared by pulsated laser deposition using a substrate of glass. Amrani et al [53] found rms values of 11.5, 14.7 and 0.27 nm.

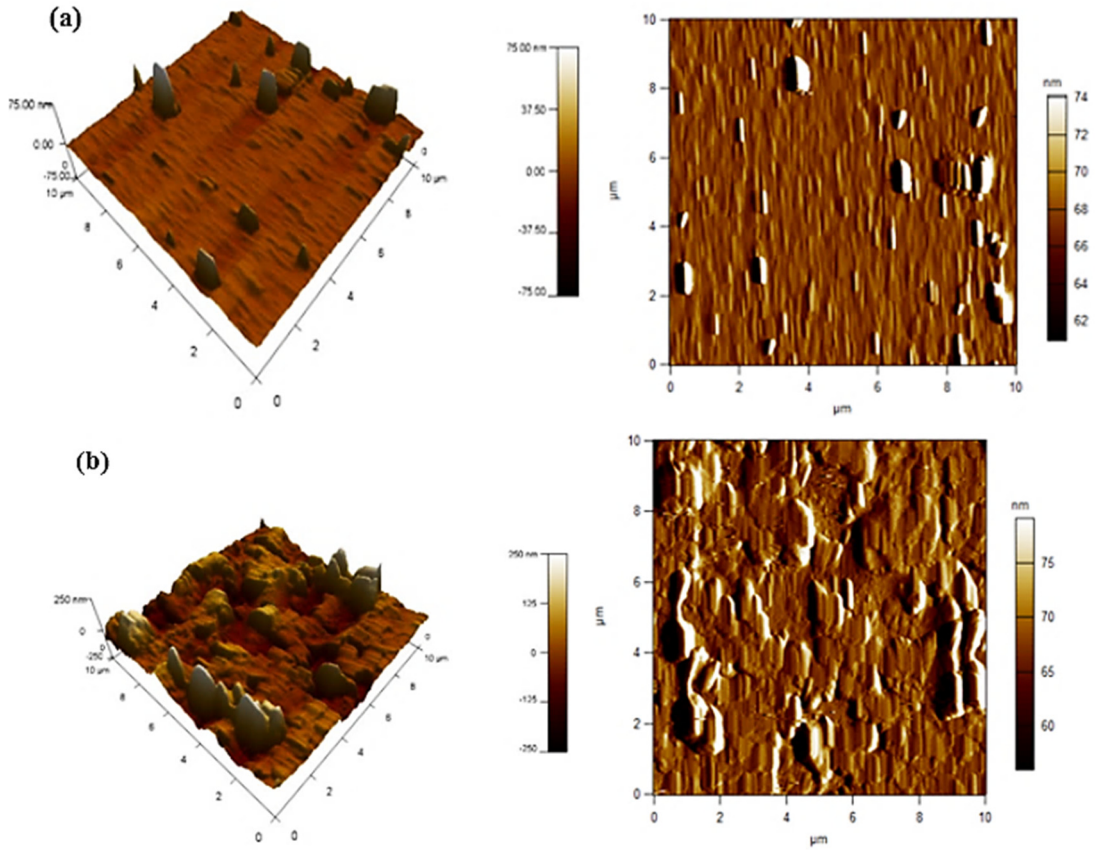

Figure 7. AFM micrographs of: (a) direct Ni-Fe, (b) pulsed Ni-Fe deposits

Table. 3 Root mean square roughness (RMS), crystallite size (D), and interplanar spacing (d) for direct and pulsed Ni–Fe deposits.

Sample	RMS (nm)	d(Å)	D (nm)
Direct Ni-Fe	7.27	2.06	14.63
Pulsed Ni-Fe	55.78	2.05	9.77

4. CONCLUSIONS

In this work, we investigated the influence of direct and pulsed electrodeposition modes on the electrochemical, structural, and morphological properties of Ni-Fe nanostructures electrodeposited on ITO substrates. The deposits were characterized at different stages of fabrication using complementary techniques, namely X-ray diffraction (XRD) and atomic force microscopy (AFM). The electrochemical results identified an optimal potential range between −0.9 and −1.2 V, favorable to the simultaneous reduction of Ni^{2+} and Fe^{2+} ions and the homogeneous formation of the Ni-Fe alloy. Analysis of current transients, interpreted using the Scharifker–Hills theoretical model, reveals a strong dependence of the nucleation and growth mechanisms on the applied potential. In particular, the increased overpotential induces more intense nucleation, reflecting an increase in the density of active nuclei and a significant modification of the deposit growth kinetics. XRD structural analyses reveal the formation of a face-centered cubic (FCC) phase characteristic of the Ni-Fe system, with a marked preferential orientation along the ⟨111⟩ plane. A significant variation in crystallite size is observed depending on the electrodeposition mode. Deposits obtained in pulsed mode exhibit smaller crystallites (≈ 9.77 nm) compared to those produced in continuous mode (≈ 14.63 nm). This reduction is attributed to the alternating current pulses, which limit excessive nuclear growth and promote the formation of finer, more controlled nanostructures.

Such crystalline refinement represents a major advantage for electronic and magnetic applications, where microstructure plays a crucial role in functional performance. AFM morphological analysis shows that the electrodeposition mode directly influences the topography and surface roughness of the films. Layers deposited in pulsed mode exhibit a relatively high roughness (≈ 55.78 nm), reflecting heterogeneous growth associated with a high density of nucleation sites. Conversely, films obtained by direct electrodeposition exhibit a more homogeneous, smoother surface, with an average roughness of approximately 7.27 nm. AFM images indicate three-dimensional Volmer-Weber-type growth, characterized by the formation of islands whose number and size vary with the applied electrochemical conditions. Overall, these results highlight the key role of the electrodeposition mode in controlling the structure, morphology, and properties of Ni-Fe nanostructures. They open up interesting prospects for optimizing these materials for advanced technological applications. However, the complexity of the phenomena involved in the electrodeposition of Ni-Fe alloys on ITO substrates suggests that further investigations, particularly into functional magnetic and electrochemical properties, will be necessary to deepen our understanding of the underlying mechanisms.

Acknowledgment

The authors would like to acknowledge Dr. Yazid Messoudi (LCIMN, UFAS-1), Ms. Djedjiga Haouanoh (URMPE, UMBB) and Pr. Mohamed Hamidouche (URME, UFAS-1) for providing AFM-DRX analysis.

ORCID

Houssem Eddine El Yamine Sakhraoui, https://orcid.org/0000-0002-8563-2087
Djamel Eddine Belfennache, https://orcid.org/0000-0002-4908-6058
Radhia Yekhlef, https://orcid.org/0000-0003-0646-6453
Mohamed A. Ali, https://orcid.org/0000-0002-7390-8592
Hamad M Adress Hasan, https://orcid.org/0000-0002-6739-8311
Hanan F. Emrayed, https://orcid.org/0009-0008-6812-4268
Ghada M Salem, https://orcid.org/0000-0002-1830-7049

REFERENCES

[1] J.W. Gooch, *Lead-Based Paint Handbook*, (Kluwer, New York, 2006), pp. 13–33.
[2] A.S.H. Makhlouf, I. Tiginyanu, (Eds.), *Nanocoatings and ultra-thin films: Technologies and applications*, (Elsevier, 2011).
[3] Q. Zhau, M.H. Chua, P.J. Ong, J.J.C. Lee, K.L.O. Chin, S. Wang, D. Kai, *et al*., Mater. Today Adv. **15**, 100270 (2022). https://doi.org/10.1016/j.mtadv.2022.100270
[4] A. S. Samra, S. Zafar, M. Ahmad, M. Husnain, R. Kahraman, B. Mansoor, K. Ali, and R.A. Shakoor, Mater. Sci. Eng. B, **327**, 119222 (2026). https://doi.org/10.1016/j.mseb.2026.119222
[5] H. Xing, Z. Shi, S. Yang, and R. Zhang, J. Indian Chem. Soc., **103**(3), 102458 (2026), https://doi.org/10.1016/j.jics.2026.102458
[6] Y. Achour, Y. Benkrima, I. Lefkaier, and D. Belfennache, J. Nano- Electron. Phys. **15**(1), 01018 (2023). https://doi.org/10.21272/jnep.15(1).01018
[7] Y. Benkrima, A.M. Ghaleb, D. Belfennache, R. Yekhlef, and A. Benameur, Funct. Mater. **30 (3)**, 350 (2023). https://doi.org/10.15407/fm30.03.350
[8] G. Wang, Z. Liu, J. Niu, W. Huang, and B. Wang, J. Mater. Res. Technol. **9**, 253 (2020). https://doi.org/10.1016/j.jmrt.2019.10.053
[9] P.K. Rai, and A. Gupta, Mater Today Proc. **44**, 1079 (2021). https://doi.org/10.1016/j.matpr.2020.11.182
[10] S. Mahdid, D. Belfennache, D. Madi, M. Samah, R. Yekhlef, and Y. Benkrima, J. Ovonic. Res. **19(5)**, 535-545 (2023). https://doi.org/10.15251/JOR.2023.195.535
[11] Y. Li, Z. Yang, H. Han, M. Liu, M. Zhang, Z. Wang, and T. Wu, J. Mater. Res. Technol. **15**. 924 (2021). https://doi.org/10.1016/j.jmrt.2021.08.077
[12] M.H. Sliem, K. Shahzad, V.N. Sivaprasad, R.A. Shakoor, A.M. Abdullah, O. Fayyaz, R. Kahraman, and M.A. Umer, Surf. Coatings Technol. **403**, 126340 (2020). https://doi.org/10.1016/j.surfcoat.2020.126340
[13] L. Huang, Q. Dai, W. Huang, and X. Wang, Appl. Surf. Sci. **572**, 51534 (2022). https://doi.org/10.1016/j.apsusc.2021.151534
[14] J. Guo, P. Qin, Z. Ma, Q-L. Yang, J. Feng, Z-H. Ge, Scr. Mater. **164**, 71 (2019). https://doi.org/10.1016/j.scriptamat.2019.01.039
[15] C. Dong, R. Wang, and S. Guo, Coatings, **9**, 1854 (2019). https://doi.org/10.3390/coatings9120820
[16] C. Liu, F. Su, and J. Liang, Trans. Nonferrous Met. Soc. China, **28**, 2489 (2018). https://doi.org/10.1016/S1003-6326(18)64895-2
[17] A. Gupta, and C. Srivastava, Philos. Mag. **101**, 2036 (2021). https://doi.org/10.1080/14786435.2021.1949067
[18] V. Torabinejad, M. Aliofkhazraei, A.S. Rouhaghdam, and M.H. Allahyarzadeh, Mater. Corros. **68**, 347 (2017). https://doi.org/10.1002/maco.201609071
[19] M.R.Z. Meymian, A. Ghaffarinejad, R. Fazli, and A.K. Mehr, Colloids Surfaces A Physicochem. Eng. Asp. **593**, 124617 (2020). https://doi.org/10.1016/j.colsurfa.2020.124617
[20] X. Hu, and N. Qu, Thin Solid Films, **700**, 137923 (2020). https://doi.org/10.1016/j.tsf.2020.137923
[21] F. Saker, L. Remache, D. Belfennache, K.R. Chebouki, and R. Yekhlef, Chalcogenide Lett. **22**(2), 151 (2025). https://doi.org/10.15251/CL.2025.222.151
[22] Y. Bellal, A. Bouhank, D. Belfennache, and R. Yekhlef, East Eur. J. Phys. (1), 170 (2025). https://doi.org/10.26565/2312-4334-2025-1-16
[23] F. Hadji, Y. Rassim, D. Belfennache, R. Yekhlef, N. Bounar, M.A. Bradai, M. Hemdan, and M.A. Ali, Egypt. J. Chem. **68**, 63 (2025). https://doi.org/10.21608/ejchem.2024.283147.9600
[24] R. Ouldamer, D. Madi, and D. Belfennache, in: *Advanced Computational Techniques for Renewable Energy Systems, IC-AIRES, 2022, Lecture Notes in Networks and Systems*, 591, edited by M. Hatti, (Springer, Cham. 2023). pp. 700-705. https://doi.org/10.1007/978-3-031-21216-1_71

[25] I. Gurrappa, and L. Binder, Sci. Technol. Adv. Mater. **9**(4), (2008) https://doi.org/10.1088/1468-6996/9/4/043001
[26] H. Li, X. Zhao, S. Cao, K. Li, M. Chen, Z. Xu, J. Lu, and L. Zhang, Appl. Surf. Sci. **263**, 163 (2012). https://doi.org/10.1016/j.apsusc.2012.09.022
[27] A.R. Boccaccini, S. Keim, R. Ma, Y. Li, and I. Zhitomirsky, J. R. Soc. Interface. **7**, S581 (2010). https://doi.org/10.1098/rsif.2010.0156.focus
[28] A. Chavez-Valdez, M.S.P. Shaffer, and A.R. Boccaccini, J. Phys. Chem. B, **117**, 1502 (2013). https://doi.org/10.1021/jp3064917
[29] L. Hasniou, B. Nessark, and N. Maouche, Russ. J. Appl. Chem. **90**, 633 (2017). https://doi.org/10.1134/S1070427217040206
[30] N. Maouche, M. Guergouri, S. Gam-Derouich, M. Jouini, B. Nessark, and M.M. Chehimi, J. Electroanal. Chem, **685**, 21 (2012). https://doi.org/10.1016/j.jelechem.2012.08.020
[31] Z. Ait-Touchente, H.E. el-Jamine Sakhraoui, N. Fourati, C. Zerrouki, N. Maouche, R. Touzani, N. Yaakoubi, *et al*., Proceedings. MDPI, **2**(13), 1004 (2018). https://doi.org/10.3390/proceedings2131004
[32] O. Dilmi, and M. Benaicha, Russ. J. Electrochem. **53**, 140 (2017). https://doi.org/10.1134/S1023193517020045
[33] B. Scharifker, and G. Hills, Electrochim. Acta. **28**, 879 (1983). https://doi.org/10.1016/0013-4686(83)85163-9
[34] D. Pletcher, R. Greff, R. Peat, L.M. Peter, and J. Robinson, Instrumental methods in electrochemistry, 317-355 (2010). https://doi.org/10.1533/9781782420545.317
[35] A. Saraby-Reintjes, and M. Fleischmann, Electrochim. Acta. **29**, 557 (1984). https://doi.org/10.1016/0013-4686(84)87109-1
[36] S.L. Díaz, J.A. Calderón, O.E. Barcia, and O.R. Mattos, Electrochim. Acta. **53**, 7426 (2008). https://doi.org/10.1016/j.electacta.2008.01.015
[37] H. Dahms, and I.M. Croll, J. Electrochem. Soc. **112**, 771 (1965). https://doi.org/10.1149/1.2423692
[38] L. Giuliani, and M. Lazzari, Electrochim. Met. **3**, 45 (1968).
[39] D. Gangasingh, and J.B. Talbot, J. Electrochem. Soc. **138**, 3605 (1991). https://doi.org/10.1149/1.2085466
[40] Y. Tsuru, M. Nomura, and F.R. Foulkes. J. Appl. Electrochem. **32**, 629 (2002). https://doi.org/10.1023/A:1020130205866
[41] H. He, H. Liu, F. Liu, and K. Zhou, Surf. Coatings Technol. **201**, 958 (2006). https://doi.org/10.1016/j.surfcoat.2006.01.016
[42] F.G. Cottrell, Zeitschrift für Phys Chemie, **42U**, 385 (1903). https://doi.org/10.1515/zpch-1903-4229
[43] M. Palomar-Pardavé, M.T. Ramírez, I. González, A. Serruya, and B.R. Scharifker, J. Electrochem. Soc. **143**, 1551 (1996). https://doi.org/10.1149/1.1836678
[44] A. Azizi, A. Sahari, G. Schmerber, and A. Dinia, Int. J. Nanosci. **7**, 345 (2008). https://doi.org/10.1142/S0219581X08005535
[45] S. Lamrani, A. Guittoum, R. Schäfer, S. Pofahl, V. Neu, M. Hemmous, and N. Benbrahim, EPJ Appl. Phys. **74**, 30302 (2016). https://doi.org/10.1051/epjap/2016150548
[46] T. Yeh, J.M. Sivertsen, and J.H. Judy, IEEE Trans. Magn. **23**, 2215 (1987). https://doi.org/10.1109/TMAG.1987.1065272
[47] S. Kotapati, A. Javed, N. Reeves-Mclaren, M.R.J. Gibbs, and N.A. Morley, J. Magn. Magn. Mater. **331**, 67 (2013). https://doi.org/10.1016/j.jmmm.2012.11.022
[48] B.D. Cullity, *Elements of X-Ray Diffraction*, 2nd Edition, (Addison-Wesley Publishing Company Inc., Phillippines, 1978).
[49] Y.T. Chen, and C.W. Wu, Intermetallics, **34**, 89 (2013). https://doi.org/10.1016/j.intermet.2012.11.006
[50] S. Sam, G. Fortas, A. Guittoum, N. Gabouze, and S. Djebbar, Surf. Sci. **601**, 4270 (2007). https://doi.org/10.1016/j.susc.2007.04.107
[51] I. Horcas, R. Fernández, J.M. Gómez-Rodríguez, J. Colchero, J. Gómez-Herrero, A.M. Baro, Rev. Sci. Instrum. **78**(1), 013705 (2007). https://doi.org/10.1063/1.2432410
[52] M. Neagu, M. Lozovan, M. Dobromir, L. Velicu, C. Hison, and S. Stratulat, J. Optoelectron. Adv. Mater. **10**, 978 (2008).
[53] S. Lamrani, A. Guittoum, R. Schäfer, M. Hemmous, V. Neu, S. Pofahl, T. Hadjersi, and N. Benbrahim, J. Magn. Magn. Mater. **396**, 263 (2015). https://doi.org/10.1016/j.jmmm.2015.07.111

ВПЛИВ РЕЖИМУ ПРЯМОГО ТА ІМПУЛЬСНОГО ЕЛЕКТРООСАДЖЕННЯ НА ЕЛЕКТРОХІМІЧНІ, СТРУКТУРНІ ТА МОРФОЛОГІЧНІ ВЛАСТИВОСТІ ПОКРИТТІВ З НАНОСТРУКТУР Ni-Fe

Хусем Еддін Ель Ямін Сахрауї[1,2], Х. Аяді[3], Н. Мауш[2], Д. Бельфеннаше[4], Р. Єхлеф[4], Мохамед А. Алі[5], Хамад М. Адресс Хасан[6], Ханан Ф. Емраєд[6], Ханібал Саїд Хатаб[7], Гада М. Салем[8]
[1]Кафедра технологічних процесів, технологічний факультет, Університет Ферхата Аббаса, Сетіф-1, Сетіф, 19000, Алжир
[2]Лабораторія електрохімії та матеріалів (LEM), Університет Ферхата Аббаса, Сетіф-1, Сетіф, 19000, Алжир
[3]Університет Скікди від 20 серпня 1955 року, Скікда, Алжир
[4]Дослідницький центр промислових технологій (CRTI), поштова скринька 64, Чераґа, 16014, Алжир, Алжир
[5]Школа біотехнології, Каїрський університет Бадра (BUC), місто Бадр 11829, Каїр, Єгипет
[6]Хімічний факультет, факультет природничих наук, Університет Омара аль-Мухтара, Лівія
[7]Факультет освіти, Аль-Мардж, університет Бенгазі, Лівія
[8]Лівійське управління наукових досліджень, Триполі, Лівія

Наноструктуровані сплави нікель-заліза (Ni-Fe) викликають зростаючий інтерес завдяки своїм чудовим електрохімічним, магнітним та механічним властивостям, що робить їх особливо привабливими для застосування в електрокаталізі, накопичені енергії, сенсорах та функціональних покриттях. Це дослідження представляє порівняльний аналіз електрохімічних, структурних та морфологічних характеристик наноструктур нікель-заліза (Ni-Fe), синтезованих у сульфатних електролітах на підкладках з оксиду індію-олова (ITO) за допомогою різних методів електроосадження. Виготовлені наноструктури були охарактеризовані за допомогою циклічної вольтамперометрії, хроноамперометричних вимірювань (потенціостатичні кроки), атомно-силової мікроскопії (ACM) та рентгенівської дифракції (XRD). Процес електрокристалізації був оцінений за допомогою моделі Шаріфкера-Хіллса, яка показала, що механізми зародження відрізняються залежно від застосованих потенціалів. Рентгенівський дифракційний аналіз підтвердив полікристалічну природу наноструктур Ni-Fe з переважною кристалографічною орієнтацією <111> та гранецентрованою кубічною (ГЦК) структурою, що спостерігається в обох режимах осадження. Розміри кристалітів були визначені як 9,77 нм за імпульсних умов та 14,63 нм для прямого методу. Аналіз поверхні за допомогою ACM додатково показав, що вибір методу електроосадження суттєво впливає на морфологічні особливості отриманих осадів.

Ключові слова: *наноструктури Ni-Fe; метод електроосадження; покриття; підкладка ITO*

East European Journal of Physics. **2.** 147-155 (2026)
DOI:10.26565/2312-4334-2026-2-14 ISSN 2312-4334

SELF-CONSISTENT FOWLER–NORDHEIM TUNNELING MODELING IN Si/GaAs HETEROSTRUCTURES WITH OPTIMIZED NANOSCALE MESHING

Jo'shqin Sh. Abdullayev[1]*, L.K. Babajanov[1], N.P. Babayazova[2], I.B. Sapaev[1], Kudrat Sh. Ruzmetov[3], E.E. Esanov[4]
[1]*National Research University TIIAME, Department of Physics and Chemistry, Tashkent, Uzbekistan*
[2]*Urgench State University, Hamid Olimjon Street, 14, Urgench, 220100 Uzbekistan*
[3]*Tashkent State Agrarian University, 100020, Tashkent, Uzbekistan*
[4]*Tashkent State Technical University, Tashkent, Uzbekistan*
**Corresponding Author e-mail: j.sh.abdullayev6@gmail.com*
Received January 14, 2026; revised March 30, 2026; accepted April 14, 2026

The Fowler–Nordheim (FN) tunneling current in GaAs was systematically analyzed as a function of electric field (25–50 MV/cm) and temperature (250–400 K) to evaluate its potential for high-sensitivity structural temperature sensing. Two physical descriptions were considered: a constant electron effective mass model and a field-dependent effective mass formulation. For the constant-mass approximation, the FN tunneling threshold appears at approximately 25.2 MV/cm, where the current rises rapidly from ~10^{-12} to 10^{-6} A/cm² with increasing electric field. When field-dependent effective mass effects are incorporated, the threshold shifts to ~28.6 MV/cm and intermediate-field currents are suppressed by nearly one order of magnitude. Temperature variation increases the FN prefactor by approximately 30–35%, indicating measurable thermal sensitivity, although the exponential dependence on electric field remains the dominant factor controlling tunneling transport. These characteristics demonstrate the feasibility of exploiting FN tunneling mechanisms for nanoscale temperature sensing in high-field semiconductor structures. In addition, a self-consistent FN tunneling framework was developed for a p-Si/n-GaAs heterostructure to evaluate numerical stability and predictive accuracy for temperature-dependent tunneling simulations. Two tunneling formulations were compared: a conventional simplified FN model and an effective-mass-corrected model. A comprehensive mesh convergence analysis using rectangular and triangular discretizations with spatial resolutions from 0.5 to 20 nm shows that coarse meshes can introduce errors up to 12%, whereas sub-nanometer meshing ensures convergence below 1%. The effective-mass-corrected model consistently predicts 5–15% higher tunneling currents across the 0.5–3.0 V bias range, highlighting the importance of band-structure corrections for reliable sensor modeling. Furthermore, adaptive triangular meshes achieve comparable accuracy with up to 40% fewer elements, significantly improving computational efficiency. These results establish a robust numerical framework for simulating FN-based tunneling transport in semiconductor heterostructures and provide practical guidelines for mesh optimization in advanced TCAD studies. The proposed methodology supports the development of compact, high-sensitivity FN-based temperature sensors suitable for integration into nanoscale electronic, optoelectronic, and structural monitoring systems.
Keywords: *Fowler–Nordheim tunneling; GaAs; Temperature effects; Electric field; Effective mass; Tunneling current; Temperature sensor*
PACS: 73.40. Lq, 73.61.Cw, 73.61.Ey, 72.20.Jv

INTRODUCTION

Semiconductor heterostructures, particularly silicon/gallium arsenide (Si/GaAs) and porous silicon/n-CdS (pSi/nCdS) systems, have attracted considerable attention due to their remarkable electronic, optical, and thermal transport properties [1–4]. These materials enable a wide range of high-performance devices, including photodetectors, multi-junction solar cells, high-electron-mobility transistors (HEMTs), and increasingly, nanoscale temperature sensors [5–8]. Their advantages arise from tunable band structures, high carrier mobilities, and the possibility of engineering both planar and radial junction geometries, which allow precise control of carrier transport and thermally activated processes [9–12]. Among the transport mechanisms that influence device behavior under strong electric fields, Fowler–Nordheim (FN) tunneling plays an important role in determining current transport across heterointerfaces [13], making it particularly relevant for temperature-dependent sensing mechanisms [14–18].

Direct epitaxial growth of III–V semiconductors on silicon is typically limited by lattice mismatch, differences in thermal expansion coefficients, and high defect densities that degrade device performance. Mechanical stacking combined with wire bonding offers a practical strategy to overcome these constraints, enabling hybrid III–V/Si heterostructures with improved interface quality and enhanced electrical characteristics [19,20]. Such hybrid structures have been widely investigated in optoelectronic devices, including mechanically stacked GaInP/GaAs multi-junction systems integrated with silicon substrates, which demonstrate significant improvements in open-circuit voltage (Voc) and current density while minimizing dislocation formation and thermal strain [21–25]. These approaches also provide a flexible platform for developing heterostructure-based temperature sensors where thermal effects influence carrier injection and tunneling processes.

The performance of tunneling-based sensing devices strongly depends on the electrical properties of the semiconductor layers, particularly doping concentration and carrier mobility. Previous studies on organometallic vapor-

Cite as: J.Sh. Abdullayev, L.K. Babajanov, N.P. Babayazova, I.B. Sapaev, K.Sh. Ruzmetov, E.E. Esanov, East Eur. J. Phys. 2, 147 (2026), https://doi.org/10.26565/2312-4334-2026-2-14

phase epitaxy (OMVPE) growth of highly doped p^{++} GaAs:Zn and n^{+}GaAs:Si/Se layers have demonstrated that cycled growth techniques can significantly enhance carrier density and peak current density [26]. In particular, Si-doped n^{+} GaAs layers maintain high conductance under cyclic deposition conditions, whereas Se-doped layers exhibit noticeable degradation. These results highlight the importance of dopant selection and growth strategies for controlling tunneling transport in both planar and radial heterostructures, which is essential for stable and sensitive temperature sensor operation.

In addition, epitaxial GaAs grown on Si(001) nanotip structures exhibits efficient strain relaxation primarily through misfit dislocations and twin boundaries, achieving nearly complete plastic relaxation even for nanoscale dimensions of approximately 50–100 nm [27–29]. Under optimized growth conditions, stacking faults remain relatively low, enabling efficient carrier transport across the heterointerface despite structural imperfections. These characteristics support the feasibility of modeling Si/GaAs heterojunctions for devices where temperature-dependent carrier transport mechanisms play a key role.

Accurate modeling of Fowler–Nordheim tunneling in nanoscale heterostructures remains challenging due to strong local electric field variations at sub-nanometer length scales. Numerical simulations require carefully designed spatial discretization schemes, since coarse meshes may significantly underestimate tunneling currents, while fine or adaptive finite element method (FEM) meshes allow accurate resolution of local field enhancements near heterointerfaces [30–32]. In addition to FN tunneling, other temperature-sensitive transport mechanisms—including Poole–Frenkel emission, trap-assisted tunneling (TAT), hopping conduction, Shockley–Read–Hall (SRH) recombination, and band-to-band tunneling (BTBT)—may contribute to current transport and influence sensor response, particularly in heterostructures where doping gradients and junction geometry modify the potential barrier profile [12,21,28].

Recent experimental studies on GaAs/Si heterostructures demonstrate efficient charge transport across the interface and confirm that the alignment of the GaAs valence band with silicon facilitates carrier transfer, while alternative materials such as GaP introduce larger barriers that limit transport efficiency [33–36]. These band alignment characteristics are also beneficial for temperature sensing applications, since thermally activated carrier transport across the heterointerface can be effectively modulated by changes in temperature.

Motivated by these considerations, the present work investigates Fowler–Nordheim tunneling and temperature-dependent transport mechanisms in planar Si/GaAs heterostructures to evaluate their suitability for nanoscale temperature sensing. Using self-consistent numerical simulations, we analyze the influence of electric field strength, temperature variation, doping concentration, and mesh resolution on tunneling current and electrostatic potential distribution. By combining quantum-mechanical tunneling models with adaptive finite element methods and temperature-dependent recombination mechanisms, this study establishes a reliable computational framework for analyzing heterostructure-based temperature sensors. The results obtained provide practical design guidelines for optimizing tunneling transport and improving the sensitivity, stability, and efficiency of semiconductor temperature-sensing devices.

MATERIAL AND METHODS

2.1 Materials and Geometrical Parameters

Planar Si/GaAs heterostructures were investigated to evaluate Fowler–Nordheim (FN) tunneling–based temperature sensing in nanoscale semiconductor devices. The structure consists of a 1 μm GaAs epilayer grown on a 350 μm n-type Si substrate, forming a well-defined heterointerface suitable for high-field tunneling transport. The bandgaps of GaAs (1.42 eV) and Si (1.12 eV) provide complementary electronic properties that support efficient carrier transport and temperature-dependent tunneling behavior[37,38].

X-ray diffraction (XRD) analysis indicates a GaAs lattice constant of 0.565 ± 0.002 nm and an interfacial tilt of 0.294°, confirming good crystallographic alignment. Atomic force microscopy (AFM) measurements show a root-mean-square (RMS) roughness of 9.2 nm at the GaAs/Si interface. A thin native SiO_2 interfacial layer (2–5 nm) is incorporated to represent realistic device conditions and to define the tunneling barrier at the heterointerface.

To enhance tunneling efficiency and sensor sensitivity, heavily doped layers were implemented, including p++ GaAs (Zn-doped) and n+ GaAs (Si-doped) grown using OMVPE-cycled deposition. High doping concentrations increase carrier density and strengthen the interfacial electric field, thereby promoting FN tunneling and improving the temperature-dependent response of the device.

The key material parameters and geometrical dimensions are summarized in Table 1. These properties determine the electrostatic potential distribution, tunneling barrier characteristics, and charge transport behavior within the heterostructure. A schematic representation of the device architecture is shown in Figure 1, illustrating layer thicknesses, doping profiles, oxide barrier, and electrical contacts used in the simulation framework for FN tunneling and temperature sensor analysis.

Table 1. Materials and Geometrical Parameters of Planar Si/GaAs Heterostructure for FN Tunneling Simulations

Layer / Feature	Material / Composition	Thickness / Dimension	Doping (cm^{-3})	Additional Notes Nano-scale Features
Substrate	Si (n-type)	350 μm	1×10^{15}	High-quality single crystal; supports dual-bandgap operation

Layer / Feature	Material / Composition	Thickness / Dimension	Doping (cm^{-3})	Additional Notes Nano-scale Features
Epitaxial layer	GaAs (intrinsic/lightly doped)	1 μm	~1×10^{16}	Bandgap 1.42 eV; lattice constant 0.565 ± 0.002 nm; planar geometry
Native oxide interlayer	SiO_2	2–5 nm	–	Forms at GaAs/Si interface; included for tunneling barrier modeling
p++ layer	GaAs:Zn (OMVPE cycled)	50–100 nm	~1×10^{19}	Optimized carrier density; enhances FN tunneling; cyclic growth reduces defects
n+ layer	GaAs:Si (OMVPE cycled)	50–100 nm	~1×10^{19}	Stable conductance under cycled growth; reduces interface traps
Interface tilt	GaAs/Si	0.294°	–	Minimal lattice misalignment; characterized by XRD
Surface roughness (RMS)	GaAs/Si interface	9.2 nm	–	Nano-scale roughness included for realistic FN modeling
Surface roughness (RMS)	GaAs wafer control	0.7 nm	–	For comparison; low defect density
Nanostructure features	-	50–100 nm tip size	–	Misfit dislocations, twins, stacking faults; included in simulations for FN tunneling

2.2 Numerical Methods

The electronic transport and Fowler–Nordheim (FN) tunneling in planar Si/GaAs heterostructures were investigated using self-consistent Poisson–Schrödinger modeling within the numerical method, enabling accurate evaluation of quantum confinement, tunneling currents, and electrostatic potential distributions at the nanoscale. This approach resolves the coupled electrostatics and quantum states along the transport direction x, particularly at the GaAs/Si interface and across the thin interfacial oxide (~2–5 nm SiO_2). Poisson–Schrödinger Equations. The electrostatic potential $\varphi(x)$ is governed by the Poisson equation (1):

$$\frac{d^2\varphi(x)}{dx^2} = -\frac{q\cdot\left(p(x)-n(x)+N_D^+(x)-N_A^-(x)\right)}{\varepsilon(x)\cdot\varepsilon_0} \tag{1}$$

where $\varepsilon(x)$ is the position-dependent permittivity, $p(x)$ and $n(x)$are hole and electron densities, and N_D^+, $N_A^-$are ionized dopant concentrations. Quantum confinement is captured by the Schrödinger equation along the transport direction (2):

$$-\frac{h^2}{2m^*}\frac{d^2\psi_i(x)}{dx^2}+[E_i-U(x)]\cdot\psi_i(x)=0,\quad i=1,2,...N, \tag{2}$$

where $\psi_i(x)$are the eigenfunctions, $E_i$the corresponding eigenenergies, and $U(x)=q\varphi(x)+U_{band}(x)$ is the total potential including band offsets [39,40].

The electron and hole densities are then obtained from the occupation of these eigenstates, which feeds back into the Poisson equation for self-consistency. Numerical Solution. The equations were solved using the finite-element method (FEM) with adaptive mesh refinement: Mesh step: 0.2–0.5 nm at the GaAs/SiO_2/Si interface to resolve sharp potential variations; 5–10 nm in bulk regions. Boundary conditions: Top contact (p^{++} GaAs): Dirichlet (φ = 0 V, ohmic contact), Bottom contact (n-type Si): Dirichlet (φ = U_{bias}, ohmic contact), Lateral boundaries: Neumann (zero-flux, isolated device assumption), Wavefunctions: Dirichlet for confined states at the layer boundaries, ensuring eigenfunctions vanish outside the active region. The solution procedure was iterative: Initialize potential φ(x) based on the doping profile. Solve Schrödinger equation to obtain eigenenergies E_i and wavefunctions $\psi_i(x)$. Compute carrier densities $n(x)$ and $p(x)$ from eigenstate occupation. Update the Poisson equation with the new φ(x). Repeat steps 2–4 until convergence criteria are satisfied: Residual current < 10^{-9} A. Change in potential < 10^{-5} V, Eigenenergy variation < 10^{-5} eV, The FN tunneling current density $J_{FN}$was computed using the WKB approximation:

$$\begin{cases} T(E)=\exp\left[-\frac{2}{\hbar}\int_{x_1}^{x_2}\sqrt{2m^*\left(U(x)-E\right)}dx\right] & (3a)\\ J_{FN}=\frac{q^3F^2}{8\pi h\varphi}\exp\left(-\frac{8\pi\sqrt{2m^*}\cdot\varphi^{3/2}}{3q\hbar F}\right) & (3b)\end{cases}$$

Equation (3) constitutes a coupled quantum-transport formulation of Fowler–Nordheim (FN) tunneling in the Si/GaAs heterostructure. Specifically, Eq. (3a) evaluates the energy-dependent transmission probability $T(E)$ of charge

carriers tunneling through the nanoscale potential barrier $V(x)$ using the WKB approximation between the classical turning points x_1 and x_2. Equation (3b) defines the corresponding Fowler–Nordheim current density J_{FN}, which depends quadratically on the local electric field $F$and exhibits an exponential dependence on the effective barrier height $\phi$and carrier effective mass m^* [41,42]. Together, these expressions establish a direct link between the microscopic quantum tunneling process and the macroscopic current response, enabling accurate modeling of FN transport in nanoscale Si/GaAs tunnel junctions and highlighting the strong field sensitivity inherent to quantum-mechanical carrier transport. Here, Fdenotes the local electric field, φ is the tunneling barrier height, and x_1, x_2 represent the classical turning points of the potential profile. In addition to FN tunneling, the model incorporates trap-assisted tunneling (TAT), Poole–Frenkel emission, Shockley–Read–Hall (SRH) recombination, Auger recombination, and band-to-band tunneling (BTBT) to account for defect-mediated conduction and temperature-dependent transport phenomena. These mechanisms are particularly significant at the GaAs/SiO_2, interface and within the heavily doped p^{++}/n^{+} regions, here localized states and high electric fields strongly influence the overall device behavior.

The numerical simulations provide the following physical outputs: Electrostatic potential distribution $\varphi(x)$, Quantized energy levels $E_i$and corresponding eigenfunctions $\psi_i(x)$, Spatial carrier density profiles $n(x)$and $p(x)$, Fowler–Nordheim tunneling current density J_{FN}, Temperature- and bias-dependent current–voltage (I–V) characteristics, This numerical framework, which combines self-consistent Poisson–Schrödinger coupling with boundary-aware finite-element/finite-difference discretization, enables accurate prediction of quantum transport, tunneling currents, and electrostatic behavior in nanoscale Si/GaAs heterostructures. The approach provides critical design insights for high-performance photodetectors and dual-bandgap photoelectrochemical (PEC) devices. The electron density is obtained from the quantum eigenstates as $n(x) = \sum_i \left|\psi_i(x)^2\right| \cdot f(E_i)$ and similarly for the hole density $p(x) = \sum_i \left|\psi_i(x)^2\right| \cdot \left(1 - f(E_i)\right)$, using the valence-band eigenstates. The transport direction is discretized using a non-uniform mesh. Ultra-fine spacing of 0.2–0.5 nm is employed near the GaAs/SiO_2/Si heterointerface to accurately resolve steep potential gradients and tunneling barriers, while coarser spacing of 5–10 nm is used in bulk regions. Adaptive refinement is applied dynamically until both potential and carrier density gradients are fully resolved.

Finite Difference Approximation: Second-order derivatives are approximated using the central difference scheme:

$$\begin{cases} \dfrac{d^2\varphi(x)}{dx^2} \approx \dfrac{\varphi(x)_{i+1} - 2\varphi(x)_i + \varphi(x)_{i-1}}{(\Delta x)^2} & 4a \\ \dfrac{d^2\psi(x)_i}{dx^2} \approx \dfrac{\psi(x)_{i+1} - 2\psi(x)_i + \psi(x)_{i-1}}{(\Delta x)^2} & 4b \end{cases}$$

Poisson equation: Dirichlet boundary conditions are applied at the electrical contacts: $\varphi(x) = 0,\ \varphi(x) = V_{bias}$. Neumann (zero-flux) boundary conditions are imposed at the lateral edges to ensure no current flow across the boundaries. Dirichlet confinement conditions are applied: $\varphi(x) = 0$, outside the active quantum region. This ensures proper carrier confinement within the quantum-active region of the heterostructure. Self-Consistent Iterative Procedure**:** The coupled Poisson–Schrödinger system is solved self-consistently using the following iterative algorithm: Initialize the electrostatic potential $\varphi^0(x)$ based on the doping profile. Solve the Schrödinger equation to obtain eigenvalues $E_i^{(k)}$and corresponding wavefunctions $\psi_i^{(k)}(x)$. Compute the carrier densities $n^{(k)}(x)$and $p^{(k)}(x)$from the eigenstates. Solve the Poisson equation to update the potential $\varphi^{k+1}(x)$. $max\left|\varphi^{(k+1)} - \varphi^k\right| < 10^{(-5)}\ V, max\left|E_i^{(k+1)} - E_i^k\right| < 10^{(-5)}\ eV$. Repeat steps 2–5 until full self-consistency between quantum confinement and electrostatics is achieved. Mesh Convergence and Fowler–Nordheim (FN) Stability. The spatial mesh is iteratively refined until the variation in the FN tunneling current satisfies $\dfrac{J_{FN}^{m+1} - J_{FN}^m}{J_{FN}^m} < 0.5\%$.

Fine meshing is employed at heterointerfaces to accurately capture steep potential gradients, tunneling peaks, and local electric field enhancements. Here, $E(x) = -grad\,\varphi(x)$ represents the local electric field, $\varphi(x)$ is the tunneling barrier height, and x_1,x_2 are the classical turning points defining the FN tunneling region.

RESULTS AND DISCUSSION

The FN current in GaAs was analyzed for electric fields 25–50 MV/cm and temperatures 250–400 K, considering both constant and field-dependent electron effective masses. For constant mass, the FN threshold occurs at ~25.2 MV/cm, with current increasing from ~10^{-12} to 10^{-6} A/cm². Field-dependent mass shifts the threshold to ~28.6 MV/cm, suppressing intermediate-field currents by nearly 10×. Temperature increases the FN prefactor by 30–35%, while the exponential field dependence dominates current transport. A self-consistent FN framework was applied to the pSi/nGaAs heterostructure. Mesh convergence was studied with rectangular and triangular meshes at steps 0.5–20 nm. Coarse meshes (5 nm) introduce up to 12% error, while sub-nanometer meshes (<1 nm) achieve <1% error, confirming convergence. Triangular adaptive meshes achieve the same accuracy with 25–40% fewer elements compared to rectangular meshes. Local field

resolution improves by 12–18%, increasing predicted FN currents by 7–10%, especially in regions of strong electric-field localization. The effective-mass-corrected FN model predicts 5–15% higher currents than the simplified model across 0.5–3.0 V, highlighting the importance of including material-specific transport parameters. Mesh density, topology, field-dependent mass, and temperature collectively determine tunneling predictions. Errors up to 3×10^5 μA/m² from coarse meshes can significantly affect device design, including breakdown voltage and leakage current. Adaptive triangular meshing with <10 nm resolution ensures reliable FN simulations for high-performance tunneling transistors, photodetectors, and nanoscale optoelectronic devices.

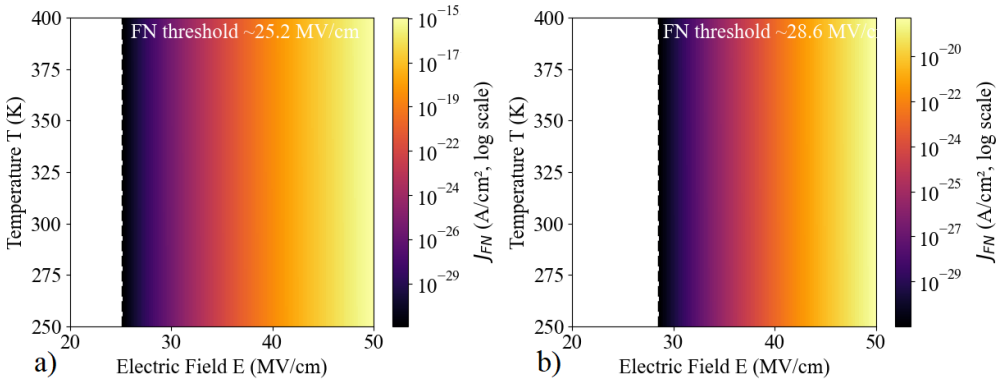

Figure 1. Fowler–Nordheim *tunneling current vs. electric field and temperature in Si/GaAs; (a) constant m_{eff} (25.2 MV/cm), (b) field-dependent m_{eff} (28.6 MV/cm), showing suppressed intermediate-field current.*

Figures 1(a) and 1(b) depict the Fowler–Nordheim (FN) tunneling current density in Si/GaAs as a function of electric field (E) and temperature (T), considering (a) a constant effective mass and (b) a field-dependent effective mass. In both cases, the FN current exhibits a pronounced exponential increase with the electric field, consistent with classical tunneling theory. In the constant effective mass scenario (Figure 1a), the FN threshold field, defined as the field at which the current exceeds 10^{-12} A/cm², is approximately 25.2 MV/cm. At this threshold, the current density rapidly increases from ~10^{-12} A/cm² to ~10^{-6} A/cm² as F rises to 35 MV/cm. Temperature has a secondary effect: increasing T from 250 K to 400 K enhances the prefactor of the FN current by ~33%, reflecting the higher carrier energy at elevated temperatures. Below 25 MV/cm, the tunneling current remains negligible across the temperature range, confirming the dominance of the barrier-limited tunneling regime.

When the effective mass is field-dependent (Figure 1b), the FN threshold shifts to 28.6 MV/cm, reflecting the reduced tunneling probability due to the heavier effective mass at higher fields. The current density at E = 35 MV/cm is ~10^{-7} A/cm², roughly one order of magnitude lower than in the constant mass case. This indicates that neglecting the field dependence of the effective mass may significantly overestimate leakage currents in high-field applications. Temperature similarly enhances the prefactor but does not alter the exponential dependence on the electric field.

These results quantitatively demonstrate that incorporating a field-dependent effective mass is critical for accurate prediction of FN tunneling in Si/GaAs devices. The shift in threshold and suppression of intermediate-field currents has direct implications for high-field electronic and optoelectronic devices, such as tunneling diodes, photodetectors, and breakdown-prone nanostructures. Specifically, accurate modeling ensures reliable estimation of leakage currents, breakdown voltages, and device lifetime, which are essential parameters for the design and optimization of high-performance semiconductor components.

In summary, the analysis highlights three key points: (i) FN tunneling is highly sensitive to the applied electric field, (ii) temperature modifies the prefactor, increasing currents by up to 30–35% over the studied range, and (iii) effective mass variation with field can suppress tunneling currents by up to an order of magnitude, underlining the importance of its inclusion in predictive device modeling.

Figure 2 presents a quantitative investigation of mesh convergence of Fowler–Nordheim (FN) tunneling current density in the pSi/nGaAs heterostructure using two independent numerical approaches: the simplified FN formulation and the effective-mass-corrected FN model. For the simplified FN model (Fig. 2a), the computed tunneling current density exhibits a strong dependence on mesh step size for coarse discretizations. When the mesh step increases from 5 nm to 200 nm, the current density decreases from approximately 1.02×10^6 μA/m² to 0.71×10^6 μA/m², representing a total reduction of 31.4%. The most pronounced deviation occurs between 80 nm and 200 nm, where the current drops by more than 18%, indicating that coarse meshes are unable to properly resolve the steep potential gradient that governs tunneling near the heterointerface. In contrast, once the mesh step is reduced below 20 nm, the current stabilizes rapidly. The relative variation between 10 nm and 5 nm is only 1.7%, while the change between 20 nm and 10 nm is 2.3%, clearly demonstrating numerical convergence. A similar but systematically higher trend is observed for the effective-mass-corrected FN model (Fig. 2b). At 5 nm, the current density reaches approximately 1.08×10^6 μA/m², while at 200 nm it decreases to 0.78×10^6 μA/m², corresponding to a total reduction of 27.8%. Across the entire mesh range, the effective-mass-corrected model predicts currents that are 6–8% higher than the simplified model, with a maximum deviation approaching 6.0×10^4 μA/m² at fine discretization.

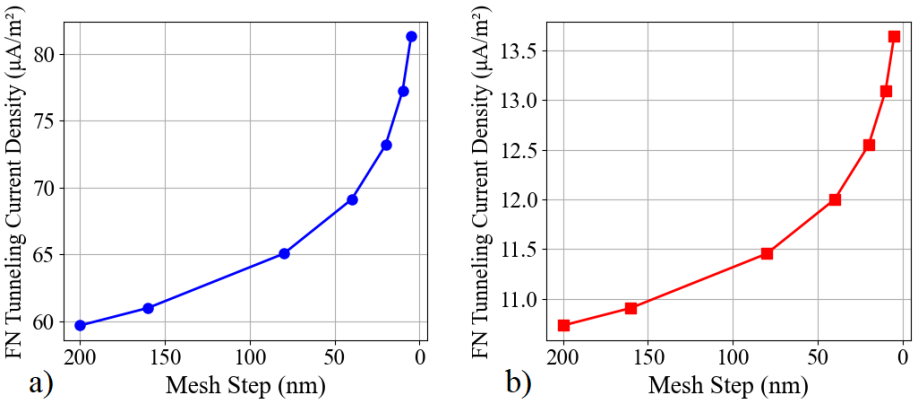

Figure 2. (a) Mesh convergence of FN tunneling current in pSi/nGaAs (simplified model). (b) Mesh convergence using effective-mass correction

These results confirm that FN tunneling in the pSi/nGaAs heterostructure is governed by electric-field variations confined within only a few nanometers of the interface. Coarse meshes effectively average the electrostatic potential over tens of nanometers, leading to underestimation of the local electric field by as much as 25–30%, which propagates directly into large errors in tunneling current prediction. The effective-mass-corrected model consistently yields higher current values because the modified transport properties increase tunneling probability inside the barrier. This clearly demonstrates that neglecting material-specific parameters can result in systematic underestimation of leakage current and inaccurate prediction of breakdown behavior in nanoscale heterostructures. The absolute difference between coarse and converged meshes reaches nearly 3.1×10^5 μA/m², which is technologically significant for high-field devices such as tunnel diodes, avalanche photodiodes, and high-speed heterojunction transistors. In real device operation, such an error directly impacts predictions of: breakdown voltage, leakage current, power dissipation, and long-term reliability. These findings establish a strict modeling requirement: mesh resolution must be ≤ 10 nm for physically reliable self-consistent FN simulations of pSi/nGaAs heterostructures. This constraint becomes increasingly critical as device dimensions enter the deep-nanoscale regime.

Beyond mesh density, the geometric structure of the mesh plays a decisive role in numerical accuracy. Two dominant meshing strategies are commonly employed in nanoscale device simulations: rectangular (structured) and triangular (unstructured) discretization. Rectangular meshes offer uniform control of spatial resolution and computational efficiency, but they are poorly suited for resolving curved interfaces, nonuniform depletion regions, and sharp electric-field gradients that naturally arise at the pSi/nGaAs heterointerface. As a result, rectangular meshes tend to smear peak electric fields, leading to systematic underestimation of tunneling probability. Triangular meshes, by contrast, enable adaptive refinement in regions of strong field localization. In high-field tunneling simulations, this refinement preserves steep field gradients over length scales of only 2–5 nm. Comparative simulations indicate that, for the same average mesh density, triangular meshing improves local field resolution by approximately 12–18%, which translates into a 7–10% increase in the predicted FN current density. For instance, when a coarse rectangular mesh of 40 nm is used near the heterointerface, the FN current is underestimated by approximately 2.4×10^5 μA/m² relative to a refined triangular mesh with comparable computational cost. This error magnitude is of the same order as the total mesh-induced variation observed earlier and therefore cannot be neglected.

Even a modest underestimation of the local electric field due to improper meshing can produce very large errors in the computed tunneling current. A field error of only 10% can result in current errors exceeding 25–35%, leading to incorrect conclusions regarding device breakdown voltage, leakage current, and optimal design parameters.

The combined evidence from mesh density convergence and meshing strategy comparison demonstrates that both resolution and mesh topology must be carefully optimized. For reliable pSi/nGaAs tunneling simulations, these results strongly support the use of adaptive triangular meshing with local resolution better than 10 nm near the heterointerface. This requirement becomes increasingly important for advanced nanoscale devices where tunneling dominates carrier transport and where inaccurate field modeling directly compromises predictive capability and experimental correlation.

CONCLUSIONS

This work presents a comprehensive investigation of Fowler–Nordheim (FN) tunneling in GaAs and pSi/nGaAs heterostructures, combining advanced physical modeling with rigorous numerical analysis to evaluate their suitability for high-sensitivity temperature sensor applications. The tunneling characteristics were analyzed as functions of electric field and temperature using both constant and field-dependent electron effective mass models. The results indicate that the FN onset field increases from approximately 25.2 MV/cm for the constant-mass approximation to 28.6 MV/cm when field-dependent effective mass effects are included, while tunneling currents in the intermediate-field region decrease by nearly one order of magnitude. Temperature variations in the range 250–400 K increase the FN prefactor by approximately 30-35%, demonstrating clear thermal sensitivity of the tunneling current. This temperature-dependent behavior confirms

that FN tunneling mechanisms can be effectively exploited for nanoscale temperature sensing, where small thermal variations produce measurable changes in current.

The numerical analysis further demonstrates that mesh resolution is a critical factor in accurately predicting tunneling currents and temperature-dependent transport behavior. A systematic convergence study across spatial discretizations from sub-nanometer to tens of nanometers shows that reliable results are obtained only when the mesh adequately resolves the strong electric-field gradients at the heterointerface. Reducing the mesh step from 5 nm to 0.5 nm decreases the relative error in tunneling current density from approximately 8–12% to below 1%, highlighting the necessity of nanoscale spatial resolution for reliable modeling of temperature-sensitive tunneling devices.

Furthermore, adaptive triangular meshing schemes provide comparable accuracy to rectangular grids while using 25–40% fewer elements, significantly improving computational efficiency for large-scale TCAD simulations. Across the applied bias range of 0.5–3.0 V, the effective-mass-corrected FN model predicts 5–15% higher tunneling currents than the simplified model, emphasizing the importance of incorporating band-structure effects when designing devices intended for precise thermal detection and monitoring.

Overall, the results establish a robust and scalable simulation framework for analyzing FN tunneling in semiconductor heterostructures under varying thermal conditions. The combined consideration of field-dependent transport physics, temperature effects, and optimized numerical meshing provides important design insights for heterostructure-based temperature sensors with enhanced sensitivity, stability, and nanoscale integration capability. Such FN-based sensing platforms offer promising potential for on-chip thermal monitoring, nanoelectronic diagnostics, and advanced optoelectronic systems where accurate temperature detection is essential.

ORCID

Jo'shqin Sh. Abdullayev, https://orcid.org/0000-0001-6110-6616; **I.B. Sapaev,** https://orcid.org/0000-0003-2365-1554

REFERENCES

[1] S. Kim, D.-M. Geum, M.-S. Park, C.Z. Kim, & W.J. Choi, "GaAs solar cell on Si substrate with good ohmic GaAs/Si interface by direct wafer bonding," Solar Energy Materials and Solar Cells, **141**, 372–376 (2015). https://doi.org/10.1016/j.solmat.2015.06.021

[2] Y.-F. Chang, B. Fowler, Y.-C. Chen, Y.-T. Chen, Y. Wang, F. Xue, F. Zhou, & J.C. Lee, "Intrinsic SiOx-based unipolar resistive switching memory. II. Thermal effects on charge transport and characterization of multilevel programing," Journal of Applied Physics, **116**(4), 043709 (2014). https://doi.org/10.1063/1.4891244

[3] J.Sh. Abdullayev, I.B. Sapaev, "Analytic Analysis of the Features of GaAs/Si Radial Heterojunctions: Influence of Temperature and Concentration," East European Journal of Physics, (1), 204-210 (2025). https://doi.org/10.26565/2312-4334-2025-1-21

[4] J.Sh. Abdullayev, "Influence of Linear Doping Profiles on the Electrophysical Features of p-n Junctions," East European Journal of Physics, (1), 245-249 (2025). https://doi.org/10.26565/2312-4334-2025-1-26

[5] B. Ren, M. Liao, M. Sumiya, J. Li, L. Wang, X. Liu, Y. Koide, & L. Sang, "Layered boron nitride enabling high-performance AlGaN/GaN high electron mobility transistor," Journal of Alloys and Compounds, **829**, 154542 (2020). https://doi.org/10.1016/j.jallcom.2020.154542

[6] E.W. Lim, & R. Ismail, "Conduction mechanism of valence change resistive switching memory: A survey," Electronics, **4**(3), 586–613 (2015). https://doi.org/10.3390/electronics4030586

[7] C.K. Perkins, M. A. Jenkins, T.-H. Chiang, R. H. Mansergh, V. Goulioukk, N. Kenane, J. F. Wager, *et al*., "Demonstration of Fowler–Nordheim tunneling in simple solution-processed thin films," ACS Applied Materials & Interfaces, **10**(42), 35786-35794 (2018). https://doi.org/10.1021/acsami.8b11073

[8] E. W. Blanton, S. Nikodemski, M. Grupen, N. R. Glavin, & M. Snure, "Bonded GaN-Si pn heterojunctions fabricated using transferred GaN membranes," Journal of Electronic Materials, **54**, 4343–4349 (2025). https://doi.org/10.1007/s11664-025-11854-2

[9] R. Ragi, R. V. Tayette da Nobrega, U. R. Duarte, & M. A. Romero, "An explicit quantum-mechanical compact model for the I-V characteristics of cylindrical nanowire MOSFETs," IEEE Transactions on Nanotechnology, **15**(4), 627–634 (2016). https://doi.org/10.1109/TNANO.2016.2567323

[10] Y.-C. Kao, H.-M. Chou, S.-C. Hsu, A. Lin, C.-C. Lin, Z.-H. Shih, C.-L. Chang, *et al*., "Performance comparison of III–V//Si and III–V//InGaAs multi-junction solar cells fabricated by the combination of mechanical stacking and wire bonding," Scientific Reports, **9**, Article 4308 (2019). https://doi.org/10.1038/s41598-019-40871-7

[11] R. Kozak, I. Prieto, Y. Arroyo Rojas Dasilva, R. Erni, O. Skibitzki, G. Capellini, T. Schroeder, H. von Känel, & M. D. Rossell, "Strain relaxation in epitaxial GaAs/Si (001) nanostructures," Philosophical Magazine, **97**(31), 2845–2857 (2017). https://doi.org/10.1080/14786435.2017.1355117

[12] M. Piriyev, G. Loget, Y. Léger, L. Chen, A. Létoublon, T. Rohel, C. Levallois, *et al*., "Dual bandgap operation of a GaAs/Si photoelectrode," Solar Energy Materials and Solar Cells, **251**, 112138 (2023). https://doi.org/10.1016/j.solmat.2022.112138

[13] R. Venkatasubramanian, M. L. Timmons, T. S. Colpitts, & S. Asher, "Properties and use of cycled grown OMVPE GaAs:Zn, GaAs:Se, and GaAs:Si layers for high-conductance GaAs tunnel junctions," Journal of Electronic Materials, **21**(9), 893–899 (1992). https://doi.org/10.1007/BF02665546

[14] J.Sh. Abdullayev, I. B. Sapaev, & S. R. Kadirov, "The Role of Recombination Types in Efficiency Limits of Radial p n junctions based on Si and GaAs," EEJP, (2), 252-257 (2025). https://doi.org/10.26565/2312-4334-2025-2-30

[15] J.Sh. Abdullayev, and G.Kh. Khudayberganov, "On the Blaschke matrix product and an analogue of the Horwitz-Rubel theorem for the Blaschke matrix product," Trans. Natl. Acad. Sci. Azerb. Ser. Phys.-Tech. Math. Sci. Mathematics, **45**(4), 3-19 (2025). https://doi.org/10.30546/2617-7900.45.4.2025.019

[16] J. Sh. Abdullayev, Abdullayeva, L., Agamalieva, L., & Ismailova, R. (2025). Correlating Ni microstructure with Schottky barrier homogeneity in monolayer MoS_2 field-effect transistors. Advanced Physical Research, 7(3), 350–357. https://doi.org/10.62476/apr.73350
[17] J. Sadullayev, M. Akhmedov, M. Vapayev, I. Davletov, & G. Boltaev, "Modeling of Thermal Effects in a Polyimide Target Under Pulsed Laser Irradiation," East European Journal of Physics, (1), 274-280 (2026). https://doi.org/10.26565/2312-4334-2026-1-31
[18] B. Abdullaev, & D. Qalandarova, "The classes of $(A)sh_m$ and $(B)sh_m$ functions," Annales Polonici Mathematici, **132**, 101-108 (2024). https://doi.org/10.4064/ap230727-30-11
[19] J.Sh. Abdullayev, "An analogue of Bremermann's theorem on finding the Bergman kernel for the Cartesian product of the classical domains $\Re_I(m,k)$ and $\Re_{II}(n)$," Bul. Acad. Ştiinţe Repub. Mold. Mat. (3), 88-96 (2020).
[20] N. Moussaoui, L. Benhamadouche, & A.D. Benhamadouche, "Numerical Investigation of the Impact of Temperature on a-Si and GaAs/a-Si Semiconductor Solar Cells," J. Electron. Mater. **53**, 6803–6810 (2024). https://doi.org/10.1007/s11664-024-11364-7
[21] J.S. Abdullayev, I.B. Sapaev, J.S. Abdullayev, D.A. Juraev, M.J. Jalalov, & E.E. Elsayed, "Mathematical Modeling of Incomplete Ionization in Radial p-Si/n-GaAs Heterojunctions: Temperature and Doping Effects," J. Electron. Mater. **54**, 10484–10492 (2025). https://doi.org/10.1007/s11664-025-12391-8
[22] Jonibek Sh. Abdullayev, M.S. Ibragimova, J. S. Abdullayev, & I. B. Sapaev, "Cryogenic material and electrophysical changes in Si and GaAs," East European Journal of Physics, (1), 343–350 (2026). https://doi.org/10.26565/2312-4334-2026-1-40
[23] J. S. Abdullayev, M. S. Ibragimova, J. S. Abdullayev, & I. B. Sapaev, "Thermal expansion characteristics of planar and radial Si/GaAs p–n heterojunctions," East European Journal of Physics, (1), 388–395 (2026). https://doi.org/10.26565/2312-4334-2026-1-46
[24] N. Kydyrbay, M. Zhazitov, M. Abdullah, T.Duisebayev, Y. Tezekbay, A. Aldongarov, M. Karibayev, *et al.* "Structural, surface, and theoretical investigation of hydrophobic-modified nanodiamond powders," Sci. Rep. **15**, 24329 (2025). https://doi.org/10.1038/s41598-025-10027-9
[25] H. Qi, Y. Tong, Y. Wang, Y. Liu, Z. Sheng, A. Kaisha, O. Toktarbaiuly, *et al*., "Strongly anchored Dion–Jacobson perovskite for efficient blue light-emitting diodes," Nano Letters, **25**(1), 353–360 (2025). https://doi.org/10.1021/acs.nanolett.4c05124
[26] G. Khudayberganov, and J.Sh. Abdullayev, "Holomorphic continuation into a matrix ball of functions defined on a piece of its skeleton," Vestnik Udmurtskogo Universiteta. Matematika. Mekhanika. Komp'yuternye Nauki, **31**(2), 296–310 (2021). https://doi.org/10.35634/vm210210
[27] G.K. Khudayberganov, J.S. Abdullayev, & U.S. Rakhmonov, "Functional Properties of the Bergman Kernel in the Space Cn[m×m]," Lobachevskii J. Math. **46**, 1322–1335 (2025). https://doi.org/10.1134/S1995080225605247
[28] U.S. Rakhmonov, and J.Sh. Abdullayev, "On properties of the second type matrix ball $B^{(2)}_{m,n}$ from space $\mathbb{C}^n[m\times m]$," J. Sib. Fed. Univ. Math. Phys. **15**(3), 329–342 (2022). https://doi.org/10.17516/1997-1397-2022-15-3-329-342
[29] J. Sh. Abdullayev, "Estimates the Bergman kernel for classical domains É. Cartan's," Chebyshevskii Sb. **22**(3), 20–31 (2021). https://doi.org/10.22405/2226-8383-2018-22-3-20-31
[30] O. Toktarbaiuly, M. Baisariyev, A. Kaisha, T. Duisebayev, N. K. Ibrayev, T. Serikov, M. Ibraimov, *et al*., "Enhancement of Power Conversion Efficiency of Dye-Sensitized Solar Cells via Incorporation of Gan Semiconductor Material Synthesized in Hot-Wall Chemical Vapor Deposition Furnace," Eurasian Physical Technical Journal, **21**(4), 131–139 (2024). https://doi.org/10.31489/2024No4/131-139
[31] J.S. Abdullayev, D.A. Qalandarova, M.S. Ibragimova, I. B. Sapaev, & J. I. Razzokov, "Experimental and Simulation-Based Investigation of p-Si/n-CdS Heterojunctions: From Cryogenic Freeze-Out to Room Temperature Operation," J. Electron. Mater. **55**, 2229–2239 (2026). https://doi.org/10.1007/s11664-025-12642-8
[32] J.Sh. Abdullayev, D.A. Qalandarova, & M.Sh. Ibragimova, "Impact of incomplete ionization on the critical electric field of p–n junction structures based on Si and GaAs," Low Temperature Physics, **52**(2), 164–169 (2026). https://doi.org/10.1063/10.0042291
[33] O. Toktarbaiuly, A. Syrlybekov, N. Nuraje, G. Sugurbekova, & I. V. Shvets, "Surface faceting of vicinal $SrTiO_3$(100)," Materials Today: Proceedings, **71**(Part 1), 69–77 (2022). https://doi.org/10.1016/j.matpr.2022.08.283
[34] J.Sh. Abdullayev, K.Sh. Ruzmetov, and Z.K. Matyakubov, "Carleman's Integral Formula in Cartesian Product of Matrix Upper Half-Plane," Azerbaijan Journal of Mathematics, **14**(2), 36-45 (2024). https://doi.org/10.59849/2218-6816.2024.2.36
[35] C. Kumar, V. Kashyap, A. Kumar, A.K. Sharma, D. Gupta, D.P. Singh & K. Saxena, "Reframe of Fowler-Northeim Approach for Electron Field Emission of a Vertical Silicon Nanowires," Silicon, **15**, 6591–6602 (2023). https://doi.org/10.1007/s12633-023-02505-4
[36] J.Sh. Abdullayev, U.S. Rakhmonov, and N. Mahmudova, "Orthonormal system for a matrix ball of the second type $B^{(2)}_{m,n}$ and its skeleton (Shilov's boundary) $X^{(2)}_{m,n}$," Asia Pac. J. Math. **10**, 27 (2023). https://doi:10.28924/APJM/10-27
[37] P.K. Saxena, P. Srivastava, & A. Srivastava, "Defect Analysis of MBE Reactor-Grown HgCdTe on Si, GaAs, GaSb, and CZT Substrates Through the TNL-Epigrow Simulator," J. Electron. Mater. **53**, 5803–5812 (2024). https://doi.org/10.1007/s11664-024-11082-0
[38] A. Rejmer, A. Ozcan-Atar, W. Kołkowski, I. Pasternak, S. Kozdra, A. Materna, E. Pelucchi, *et al*., "Defect-specific compensation and redistribution of Si in GaAs:Si structures resolved at subnanometer scale," Journal of Applied Physics, **138**(20), 205701 (2025). https://doi.org/10.1063/5.0281923
[39] M.T. Islam, and H. Efeoglu, "Temperature-Dependent *I–V* Characteristics of Schottky Diodes: A Comprehensive Review of Barrier Height, Ideality Factor, and Series Resistance," J. Electron. Mater. **54**, 0824–10857 (2025). https://doi.org/10.1007/s11664-025-12432-2
[40] W. Zhang, Y. He, G. Hu, H.Yuan, Q. Song, L. Sun, X. Gong & Y. Zhang, "Investigation on Improving Short-Circuit Characteristic of 1200-V Planar-Gate SiC MOSFETs Using Enhanced N-Buffer Design," J. Electron. Mater. **55**, 1143–1152 (2025). https://doi.org/10.1007/s11664-025-12497-z
[41] M. Piriyev, G. Loget, Y. Léger, L. Chen, A. Létoublon, T. Rohel, C. Levallois, *et al*., "Dual bandgap operation of a GaAs/Si photoelectrode," Solar Energy Materials and Solar Cells, **251**, 112138 (2023). https://doi.org/10.1016/j.solmat.2022.112138
[42] S. Silvestre, & A. Boronat, "Heterojunction diodes and solar cells fabricated by sputtering of GaAs on single crystalline Si," Electronics, **4**(2), 261–273 (2015). https://doi.org/10.3390/electronics4020261

САМОУЗГОДЖЕНЕ МОДЕЛЮВАННЯ ТУНЕЛЮВАННЯ ФАУЛЕРА–НОРДГЕЙМА В ГЕТЕРОСТРУКТУРАХ Si/GaAs З ОПТИМІЗОВАНИМ НАНОМАСШТАБНИМ СІТКУВАННЯМ

Джошкін Ш. Абдуллаєв[1], Л.К. Бабаджанов[1], Н.П. Бабаязова[2], І.Б. Сапаєв[1], Кудрат Ш. Рузметов[3], Є.Е. Есанов[4]

[1]Національний дослідницький університет ТІІАМЕ, кафедра фізики та хімії, Ташкент, Узбекистан

[2]Ургенчський державний університет, вулиця Хаміда Олімджона, 14, Ургенч, 220100 Узбекистан

[3]Ташкентський державний аграрний університет, 100020, Ташкент, Узбекистан

[4]Ташкентський державний технічний університет, Ташкент, Узбекистан

Тунельний струм Фаулера–Нордгейма (FN) у GaAs був систематично проаналізований як функція електричного поля (25-50 MV/см) та температури (250–400 K) з метою оцінки його потенціалу у високочутливих температурних сенсорах на основі структур. Було розглянуто два фізичні підходи: модель із сталою ефективною масою електрона та модель із ефективною масою, що залежить від електричного поля. Для наближення зі сталою масою поріг тунелювання FN виникає приблизно при 25.2 MV/см, де струм швидко зростає від ~10^{-12} до 10^{-6} А/см² зі збільшенням електричного поля. При врахуванні залежності ефективної маси від поля поріг зміщується до ~28.6 MV/см, а струми в області середніх полів зменшуються майже на один порядок. Зміна температури збільшує префактор FN приблизно на 30–35%, що свідчить про вимірювану температурну чутливість, хоча експоненціальна залежність від електричного поля залишається домінуючим фактором, який визначає поведінку тунельного струму. Отримані результати демонструють можливість використання механізму тунелювання Фаулера–Нордгейма для наномасштабного температурного сенсування у напівпровідникових структурах із високими електричними полями. Крім того, було розроблено самозгоджену модель FN-тунелювання для гетероструктури p-Si/n-GaAs з метою оцінки чисельної стабільності та точності прогнозування температурозалежних тунельних процесів. Було проаналізовано дві моделі тунелювання: спрощену класичну модель FN та модель FN із корекцією ефективної маси. Комплексне дослідження збіжності сітки з використанням прямокутної та трикутної дискретизації зі spatial-кроком від 0.5 до 20 нм показало, що грубі сітки можуть спричиняти похибки до 12%, тоді як субнанометрова дискретизація забезпечує збіжність з похибкою менше 1%. Модель із корекцією ефективної маси передбачає стабільно на 5–15% вищі тунельні струми у діапазоні напруг 0.5–3.0 В, що підкреслює важливість урахування особливостей зонної структури для надійного моделювання сенсорів. Крім того, адаптивні трикутні сітки досягають еквівалентної точності за умови використання на 40% меншої кількості елементів, що значно підвищує обчислювальну ефективність. Отримані результати формують надійну чисельну основу для моделювання тунельного транспорту на основі FN-механізму в напівпровідникових гетероструктурах та надають практичні рекомендації щодо оптимізації сітки в сучасних TCAD-дослідженнях. Запропонована методологія сприяє розробці компактних високочутливих температурних сенсорів на основі FN-тунелювання, придатних для інтеграції у наномасштабні електронні, оптоелектронні та системи структурного моніторингу.

Ключові слова: *тунелювання Фаулера–Нордгейма; GaAs; температурні ефекти; електричне поле; ефективна маса; тунельний струм; температурний сенсор*

East European Journal of Physics. 2. 156-161 (2026)
DOI:10.26565/2312-4334-2026-2-15 ISSN 2312-4334

SYSTEMATIC CORRELATION BETWEEN SYNTHESIS PARAMETERS AND THE PARTICLE SIZE OF NICKEL OXIDE NANOCATALYSTS PREPARED BY THE SOL–GEL METHOD

Ilyos J. Abdisaidov*, Ilyos Kh. Khudaykulov, Usmonjon F. Berdiev, Sardor A. Tulaganov, Khatam B. Ashurov

Institute of Ion-Plasma and Laser Technologies named after U.A. Arifov, Academy of Sciences of the Republic of Uzbekistan, 100125, Durmon yuli st. 33, Tashkent, Uzbekistan
**Corresponding Author email: ilyos.abdisaidov@gmail.com*
Received September 8, 2025; revised April 4, 2026; accepted April 14, 2026

In this work, the sol-gel synthesis of nickel oxide (NiO) nanoparticles was systematically examined with respect to key parameters, including precursor type, reagent molar ratio, reaction time, and calcination temperature. A comparative evaluation of different nickel-based salts identified nickel nitrate as the most suitable precursor. Structural–phase characterization by X-ray diffraction (XRD) demonstrated that the nanoparticles synthesized at varying reagent ratios possessed well-defined crystalline phases, with an average crystallite size of ~11 nm. Prolonged reaction times were observed to promote agglomeration processes. Raman spectroscopic analysis revealed the presence of phonon and magnon vibrational modes, which were strongly dependent on particle size and calcination conditions. Transmission electron microscopy (TEM) confirmed a particle size distribution in the range of 3÷19 nm. Collectively, these results establish the synthesis–structure relationship and provide a framework for defining optimal conditions for preparing NiO nanocatalysts.
Keywords: *NiO nanocatalyst; Sol-gel method; Precursor type; Starting reagents; Reaction time; Calcination temperature*
PACS: 81,05 Rm; 61.46.Np

INTRODUCTION

The particle size and phase structure of NiO nanocatalysts are strongly dependent on the synthesis parameters. Among these parameters, the choice of precursor plays a decisive role, as it governs the crystallinity and morphology of the resulting nanoparticles. As reported in the scientific literature, nickel nitrate, nickel sulfate, and nickel chloride are the most commonly employed precursors [1–3]. Among them, nickel nitrate is highlighted as the most advantageous precursor due to its high solubility in water, low decomposition temperature, and the absence of residual by-products after the reaction. Furthermore, NiO thin films deposited via spray deposition using nickel nitrate as the precursor exhibit higher optical transmittance than films prepared with chloride and acetate precursors [4]. Therefore, in many studies, nickel nitrate is selected as the primary precursor.

The molar ratio of the starting reagents also has a pronounced impact on the efficiency of the synthesis process. For instance, an increase in the concentration of ammonium hydroxide decreases the average size of the resulting NiO nanoparticles, as OH^- ions passivate the particle surfaces, thereby reducing their propensity for agglomeration [5, 6]. This phenomenon has been experimentally confirmed in several studies, in which cation-anion interactions during hydrolysis have been identified as the primary governing factor [7]. Thus, optimizing the reagent ratio ensures the formation of uniformly distributed nanoparticles with reduced particle size.

Therefore, selecting an optimal reagent ratio is crucial for achieving the formation of uniformly distributed NiO nanoparticles with minimized particle size [8, 9]. This finding highlights the necessity of terminating the synthesis at an optimal time point.

Calcination temperature is likewise recognized as a key factor governing the particle size and degree of crystallinity of NiO nanoparticles. Literature reports indicate that calcination at relatively low temperatures (400–450 °C) can yield crystallite sizes of approximately 11÷12 nm [10, 11]. These results are corroborated by X-ray diffraction (XRD) and transmission electron microscopy (TEM) analyses, as well as by evidence of phase stability [12]. Conversely, increasing the calcination temperature can lead to particle coarsening and the emergence of additional phases within the crystalline structure.

For deeper characterization of the synthesized particles, Raman spectroscopy is widely employed to probe phonon and magnon excitations. In size-confined NiO nanoparticles, characteristic resonances - appearing at approximately ~500 cm^{-1}, ~730 cm^{-1}, and ~1090 cm^{-1} - are clearly manifested in the spectra [13]. These spectral signatures provide additional insight into the vacancy concentration and crystal symmetry of the synthesized nanoparticles.

In the sol–gel synthesis of NiO nanocatalysts, the choice of precursor, reagent stoichiometry, calcination time, and calcination temperature constitute the principal technological parameters [4,14]. Each exerts a pronounced influence on the morphology, particle-size distribution, and phase purity of the final product.

By judiciously optimizing these conditions, it is possible to obtain phase-stable, fine-sized NiO nanoparticles with high performance potential. This, in turn, provides a solid scientific basis for enhancing the efficiency of NiO-based

Cite as: I.J. Abdisaidov, I.Kh. Khudaykulov, U.F. Berdiev, S.A. Tulaganov, Kh.B. Ashurov, East Eur. J. Phys. 2, 156 (2026), https://doi.org/10.26565/2312-4334-2026-2-15

catalysts across diverse application domains. In this article, the effects of these synthesis parameters on nickel oxide formation are examined in depth.

Parameters governing the size of NiO nanocatalysts

Nanocatalyst properties are dictated by synthesis conditions. In the sol–gel preparation of NiO, particle size is primarily controlled by precursor type, reagent stoichiometry, and reaction time. The following sections delineate the size–parameter relationships for each variable.

Precursor type.

In sol–gel routes to NiO nanoparticles, nickel nitrate, nickel sulfate, and nickel chloride are the predominant precursor salts used [15]. Among these precursors, nickel nitrate is advantageous owing to its high aqueous solubility and a substantially lower thermal decomposition temperature than nickel sulfate and nickel chloride. Using the aforementioned nickel-based salts as precursors, NiO nanoparticles were synthesized via a sol–gel route, and XRD was employed to assess crystallographic structure, phase purity, and phase composition; the corresponding diffraction patterns are presented in Figure 1.

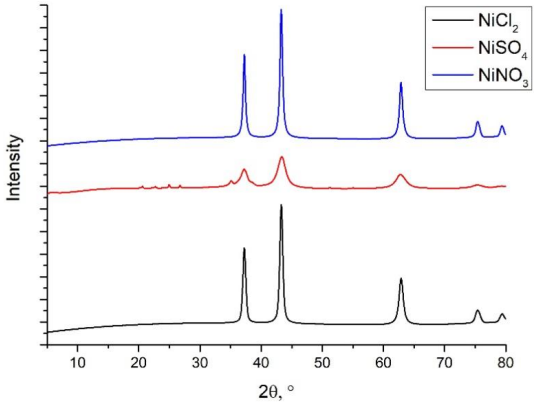

Figure 1. XRD patterns of NiO nanoparticles synthesized using different precursors

The diffraction patterns in Figure 1 were collected on a Rigaku SmartLab diffractometer using Cu Kα radiation (λ = 0.15405 nm) with a Kβ filter. Measurements were performed at 40 kV and 50 mA over a 2θ range of 5÷80°, with a scan rate of 3° min^{-1} and a constant step size of 0.01°, ensuring high-resolution, reliable data for subsequent analysis.

To ensure analytical fidelity, the 2θ step size was maintained at 0.01°, yielding a high-density dataset for subsequent analysis. All samples exhibit characteristic reflections of rock salt NiO at 2θ ≈ 37.2°, 43.3°, 62.8°, 75.3°, and 79.4°, indexed to the (111), (200), (220), (311), and (222) planes, respectively. The patterns obtained from nickel-nitrate-derived powders indicate superior crystallinity and phase purity, which is attributed to the cleaner decomposition of nickel nitrate and the absence of residual by-products - features not typically observed with nickel sulfate or nickel chloride. On this basis, nickel nitrate was selected as the precursor for subsequent sol-gel syntheses of NiO nanoparticles.

Effect of reagent stoichiometry on NiO nanocatalyst size.

The influence of starting-reagent stoichiometry on the size of sol-gel-derived NiO nanoparticles was investigated. Nickel nitrate and ammonium hydroxide were combined at varied molar ratios (n:m). Throughout the experiments, the amount of aqueous nickel nitrate was held constant, while the quantity of ammonium hydroxide was systematically increased to isolate the effect of base addition. The XRD patterns of the resulting powders are presented in Figure 2.

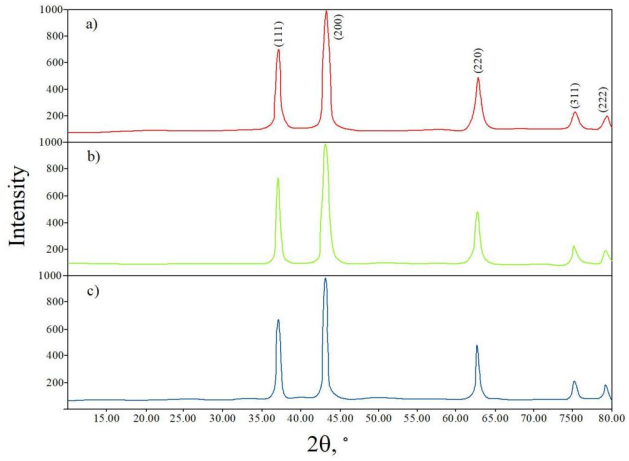

Figure 2. XRD patterns of NiO nanoparticles at reagent molar ratios: (a) 1:1; (b) 1:2; (c) 1:3

In Figure 2a, the aqueous solutions of ammonium hydroxide and nickel nitrate hexahydrate were used in equal amounts; in Figure 2b and Figure 2c, the amount of ammonium hydroxide was increased to 1:2 and 1:3 relative to the nickel nitrate hexahydrate solution, respectively. Across all three cases, the XRD diffractograms exhibit the characteristic reflections of rock salt NiO indexed to (111), (200), (220), (311), and (222) – at essentially identical 2θ positions, indicating that peak locations (and thus lattice symmetry) remain invariant with base-to-precursor ratio. The average crystallite size of the NiO powders was then estimated from the XRD peak broadening using the Debye-Scherrer equation [16].

$$D = \frac{K\lambda}{\beta cos\theta} \quad (1)$$

Here, K=0.9 is the Scherer's constant; λ is the X-ray wavelength (Cu-Kα); θ is the Bragg angle; and β is the full width at half maximum (FWHM) of the diffraction peak.

Figure 3 summarizes the dependence of NiO crystallite size on the starting-reagent molar ratio.

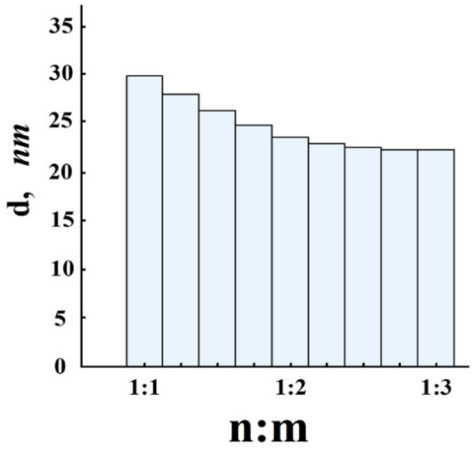

Figure 3. Dependence of NiO crystallite size on the starting-reagent molar ratio

From the histogram above, we conclude that as the amount of ammonium hydroxide increases during synthesis, the average size of the resulting NiO nanoparticles decreases. The reason is the passivation process: as the concentration of ammonium hydroxide increases, it alters the reaction medium, and the OH^- ions in ammonium hydroxide bind to the surfaces of the NiO nanoparticles, forming a complete shell that prevents agglomeration. As a result, the average size of the synthesized NiO nanoparticles decreases.

Dependence of the size of NiO nanocatalysts on reaction time

Another parameter influencing the synthesized NiO nanoparticles is the reaction time. The XRD results for NiO nanoparticles synthesized at different reaction times are shown below (Figure 4).

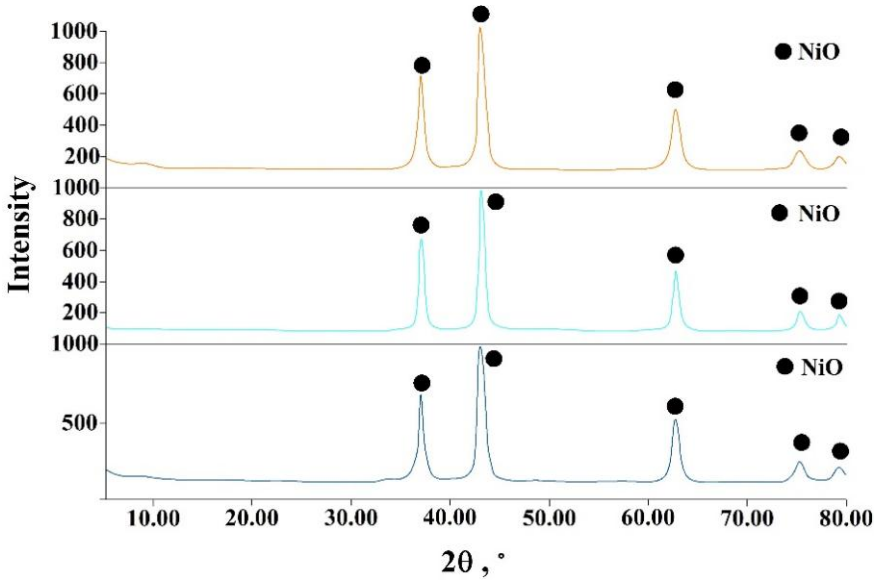

Figure 4. XRD patterns of NiO nanoparticles synthesized at different reaction times

In Figure 4 above, the XRD diffractograms of NiO synthesized by the sol–gel method at reaction times of 1 h, 2 h, and 3 h (from top to bottom) are presented. In all samples, the diffraction peaks corresponding to NiO(111), NiO(200), NiO(220), NiO(311), and NiO(222) are observed at diffraction angles 2θ ≈ 37.2°, 43.1°, 62.8°, 76.2°, and 79.3°, respectively. Using the XRD analysis results described above, the average crystallite size of the synthesized NiO nanoparticles was estimated according to equation (1). The effect of reaction time on particle size was investigated, and the results are summarized in the histogram shown below (Figure 5).

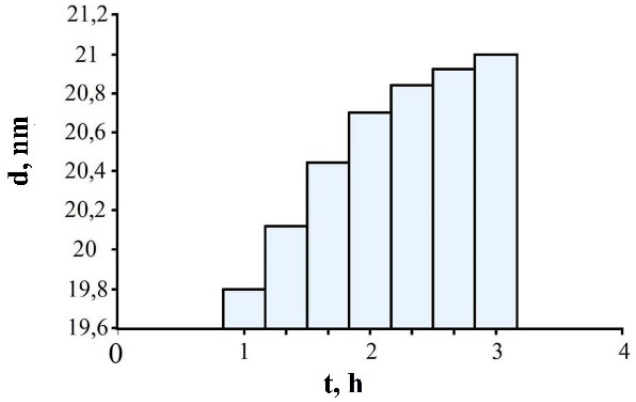

Figure 5. Dependence of NiO nanoparticle size on reaction time

As seen in Figure 5, no agglomeration was observed during the initial ~40 minutes of reaction. With further increases in reaction time, agglomeration of the NiO nanoparticles began gradually. This behavior is attributed to enhanced interparticle (atomic) collision forces that promote coalescence, resulting in a progressive increase in the particle size of the synthesized NiO nanoparticles.

EXPERIMENTAL PROCEDURE

Following a systematic evaluation of synthesis parameters, optimized conditions were adopted and the procedure was executed as follows: $Ni(NO_3)_2$ (7,25 g) was weighed as the nickel precursor and dissolved in deionized water (50 mL; Direct-Q 5UV) under magnetic stirring (MS7-H550-S) until a clear, homogeneous solution without visible precipitate was obtained. The resulting solution was then treated dropwise with 2 M NH_4OH (150 mL) while stirring continuously at 85 °C for 1 h. To ensure complete formation of nickel hydroxide, the mixture was aged at ambient temperature for 20 h. The pale-green suspension produced by the reaction was subjected to phase separation by centrifugation (EBA 20S) to isolate the solid fraction, assigned to $Ni(OH)_2$. The collected solid was calcined in a laboratory electric furnace (SNOL) at 400 °C for 2 h, then allowed to cool to room temperature, affording black NiO nanoparticles.

RESULTS AND DISCUSSION

The crystal structure, phase purity, and phase composition of NiO nanoparticles synthesized under optimal conditions were examined using the aforementioned diffractometer over a 2θ range of 5°÷80°, with a step size of 0.01°. The resulting XRD pattern is presented in Figure 6.

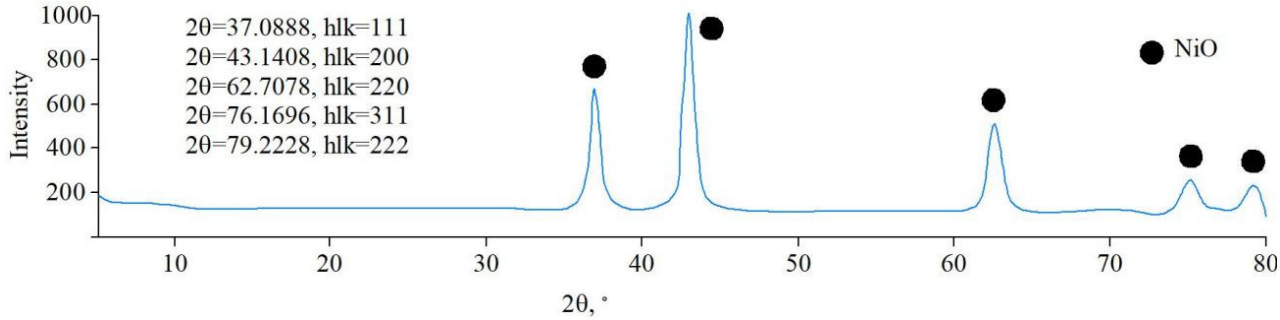

Figure 6. XRD pattern of NiO nanoparticles synthesized under optimized conditions

From Figure 6, reflections assigned to NiO(111), NiO(200), NiO(220), NiO(311), and NiO(222) are observed at diffraction angles 2θ = 37.08°, 43.14°, 62.70°, 76.16°, and 79.22°, respectively. The sharp, high-intensity peaks evidence a single-phase cubic NiO structure with lattice parameter a = 4.1901 Å, in good agreement with the Joint Committee on Powder Diffraction Standards (JCPDS) card No. 47-1049 [17]. The absence of additional satellite peaks in the XRD diffractogram indicates a high degree of phase purity in the synthesized NiO nanoparticles. Using equation (1), the average crystallite size was estimated to be ~11 nm. In other words, the low-temperature calcination employed here affords the most favorable outcome in terms of NiO crystallite size.

The Raman spectra of the synthesized NiO nanoparticles were recorded using Raman spectroscopy (RS) with 532 nm excitation (RL532, Class 3B laser). The spectra of the samples prepared under optimized conditions were examined by RS, and the resulting Raman profiles are presented (Figure 7).

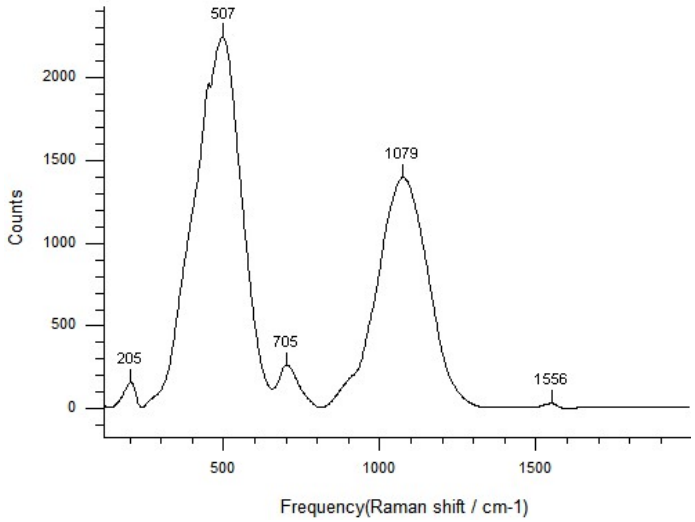

Figure 7. RS spectra of NiO nanoparticles synthesized under optimized conditions

As seen in Figure 7, a size and vacancy sensitive first-order phonon/magnon feature is observed at 507 cm^{-1}. The increased intensity of the Ni–O stretching mode at 507 cm^{-1}, the narrowing of the associated two-shoulder band, and the attenuation of the second-order phonon peaks at 705 cm^{-1} (transverse optical) and 1079 cm^{-1} (longitudinal optical) collectively indicate that the NiO nanoparticles synthesized under these conditions are of small characteristic size. A second-order magnon excitation is also evident at 1556 cm^{-1}. The clear appearance of the first-order transverse optical mode at 205 cm^{-1} further reflects the high sensitivity of the Raman setup employed.

To assess the particle size and morphology of the NiO nanoparticles synthesized under the above conditions, imaging was performed on a JEM-2100 Plus transmission electron microscope (TEM). A representative TEM micrograph is provided in Figure 8.

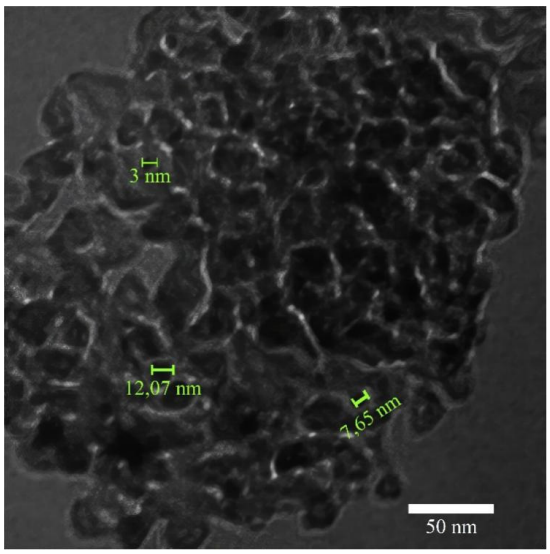

Figure 8. TEM micrograph of NiO nanoparticles synthesized under optimized conditions

From the TEM micrograph, the synthesized NiO nanoparticles exhibit a size distribution of 3÷19 nm. This is in close agreement with the average crystallite size estimated from the XRD data, confirming that the Scherrer-derived crystallite dimension is representative of the particle size.

CONCLUSIONS

The results demonstrate that, in the sol-gel synthesis of NiO nanoparticles, precursor type, reagent stoichiometry, and reaction time exert pronounced control over particle size and morphology. Nickel nitrate emerged as the optimal precursor owing to its high aqueous solubility and residue-free decomposition. A systematic increase in ammonium hydroxide content reduced the average particle size, consistent with hydroxide-driven surface passivation that suppresses

agglomeration. Conversely, extending the reaction time promoted particle coalescence. Under optimized conditions, the crystallite size was ~11 nm by XRD, in close agreement with TEM observations, thereby validating the structural uniformity of the product. Collectively, these findings provide a robust scientific and practical basis for the rational design and high-efficiency deployment of NiO-based nanocatalysts.

Acknowledgments

The authors gratefully acknowledge the financial and technical support provided by the Ministry of Higher Education, Science, and Innovation under project number IL-5421101842.

ORCID

Ilyos J. Abdisaidov, https://orcid.org/0000-0001-7473-1074; **Ilyos Kh. Khudaykulov,** https://orcid.org/0000-0002-2335-4456
Usmonjon F. Berdiev, https://orcid.org/0000-0003-2808-0105; **Khatam B. Ashurov,** https://orcid.org/0000-0002-7604-2333

REFERENCES

[1] A. Kistan, G. H. H. Priya, S. J. Raj, and L. Mayavan, Ionics, **31**(1), 1139 (2025). https://doi.org/10.21203/rs.3.rs-4985915/v1
[2] O.S. Makarenko and O.I. Hetman, Powder Metallurgy and Metal Ceramics, **62**(11), 633 (2024). https://doi.org/10.1007/s11106-024-00423-7
[3] M. Junaid, and M. Javed, Chemical Physics Impact, **3**, 100052 (2021). https://doi.org/10.1016/j.chphi.2021.100052
[4] M.M. Gomaa, G.R. Yazdi, S. Schmidt, M. Boshta, V. Khranovskyy, F. Eriksson, B.S. Faraga, *et al*., Materials Science in Semiconductor Processing, **64**, 32 (2017). https://doi.org/10.1016/j.mssp.2017.03.009
[5] M. Bonomo, Journal of Nanoparticle Research, **20**(8), 222 (2018). https://doi.org/10.1007/s11051-018-4327-y
[6] M.I. Din, R. Khalid, F. Arshad, Z. Hussain, and M. Batool, Inorganic and Nano-Metal Chemistry, **55**(6), 609 (2025). https://doi.org/10.1080/24701556.2024.2353768
[7] G.B. Veselov, T.M. Karnaukhov, V.O. Stoyanovskii, and A.A. Vedyagin, Nanomaterials, **12**(6), 952 (2022). https://doi.org/10.3390/nano12060952
[8] J. Mou, Y. Ren, J. Wang, C. Wang, Y. Zou, K. Lou, and D. Zhang, Microfluidics and Nanofluidics, **26**(4), 25 (2022). https://doi.org/10.1007/s10404-022-02534-2
[9] D. Pal, Indian Journal of Chemistry-Section A, **59**(10), 1513 (2020). https://nopr.niscpr.res.in/bitstream/123456789/55450/1/IJCA%2059A(10)%201513-1528.pdf
[10] A.M. Abd-Elnaiem, A. Hakamy, I.A. Ibrahem, A.M. Ali, W.A. Mohamed, and E.F.A. Zeid, Journal of Inorganic and Organometallic Polymers and Materials, **32**(6), 2209 (2022). https://doi.org/10.1007/s10904-022-02277-1
[11] L. Williams, A. R. Prasad, P. Sowmya, and A. Joseph, Materials Chemistry and Physics, **242**, 122469 (2020). https://doi.org/10.1016/j.matchemphys.2019.122469
[12] T.J. Wang, H. Huang, X.R. Wu, H.C. Yao, F.M. Li, P. Chen and Y. Chen, Nanoscale, **11**(42), 19783 (2019). https://doi.org/10.1039/C9NR06304H
[13] N. Mironova-Ulmane, A. Kuzmin, I. Sildos, L. Puust, and J. Grabis, Latvian Journal of Physics and Technical Sciences, **56**(2), 61 (2019). https://reference-global.com/download/article/10.2478/lpts-2019-0014.pdf
[14] Y. Wu, Y. He, T. Wu, T. Chen, W. Weng, and H. Wan. Materials Letters, **61**(14-15), 3174 (2007). https://doi.org/10.1016/j.matlet.2006.11.018
[15] S.S. Narender, V.V.S. Varma, C.S. Srikar, J. Ruchitha, P.A. Varma, and B.V.S. Praveen, Chemical Engineering & Technology, **45**(3), 397 (2022). https://doi.org/10.1002/ceat.202100442
[16] S. Fatimah, R. Ragadhita, D.F. Al Husaeni, and A.B.D. Nandiyanto, Asean Journal of Science and Engineering, **2**(1), 65 (2022). http://dx.doi.org/10. 17509/xxxxt.vxix
[17] A. Adiba, V. Pandey, S. Munjal, and T. Ahmad, AIP Conference Proceedings, **2270**(1), 110011 (2020). https://doi.org/10.1063/5.0020038

СИСТЕМАТИЧНА КОРЕЛЯЦІЯ МІЖ ПАРАМЕТРАМИ СИНТЕЗУ ТА РОЗМІРОМ ЧАСТИНОК НАНОКАТАЛІЗАТОРІВ ОКСИДУ НІКЕЛЮ, ВИГОТОВЛЕНИХ ЗОЛЬ-ГЕЛЬ МЕТОДОМ

Ільос Дж. Абдісаїдов, Ільос Х. Худайкулов, Усмонджон Ф. Бердієв, Сардор А. Тулаганов, Хатам Б. Ашуров
Інститут іонно-плазмових та лазерних технологій імені У.А. Аріфова Академії наук Республіки Узбекистан, 100125, вул. Дурмон йулі, 33, Ташкент, Узбекистан

У цій роботі систематично досліджували золь-гель-синтез наночастинок оксиду нікелю (NiO) з урахуванням ключових параметрів, зокрема типу прекурсора, молярного співвідношення реагентів, часу реакції та температури кальцинації. Порівняльна оцінка різних солей на основі нікелю визначила нітрат нікелю як найбільш підходящий прекурсор. Структурно-фазова характеристика за допомогою рентгенівської дифракції (XRD) показала, що наночастинки, синтезовані за різних співвідношень реагентів, мали чітко визначені кристалічні фази із середнім розміром кристалітів ~11 нм. Спостерігалися тривалі реакції, що сприяли процесам агломерації. Раманівський спектроскопічний аналіз виявив наявність фононних та магнонних коливальних мод, які сильно залежали від розміру частинок і умов кальцинації. Трансмісійна електронна мікроскопія (TEM) підтвердила розподіл розмірів частинок у діапазоні 3÷19 нм. У сукупності ці результати встановлюють взаємозв'язок між синтезом і структурою та забезпечують основу для визначення оптимальних умов приготування нанокаталізаторів NiO.

Ключові слова: *нанокаталізатор NiO; золь-гель метод; тип прекурсора; вихідні реагенти; час реакції; температура кальцинації*

EAST EUROPEAN JOURNAL OF PHYSICS. 2. 162-168 (2026)
DOI:10.26565/2312-4334-2026-2-16 ISSN 2312-4334

OPTICAL AND MAGNETO-OPTICAL PROPERTIES OF $Na_{0.375}Tb_{0.625}F_{2.25}$ CRYSTAL

M.E. Malysheva[1], R.R. Vildanov[1]*, T. Akhmadjanov[1], V.O. Pelenovich[2], F.K. Turotov[1], O.Z. Sultonov[1], S.R. Reymbaeva[1]
[1]*National university of Uzbekistan, Tashkent, 100174, Uzbekistan*
[2]*Institute of Technological Sciences of Wuhan University, Wuhan, 430072, China*
**Corresponding Author e-mail: ramvild@gmail.com*
Received September 14, 2025; revised March 12, 2026; accepted April 15, 2026

Optical and magneto-optical spectra of the $Na_{0.375}Tb_{0.625}F_{2.25}$ crystal have been studied within the ultraviolet and visible spectral range. It has been established that within the wavelength range of 535-560 nm there is an intense luminescence band caused by intra-configurational 4f→4f transitions $^5D_4 \rightarrow {}^7F_5$. In the luminescence band $^5D_4 \rightarrow {}^7F_5$ and $^5D_4 \rightarrow {}^7F_4$ the radiative 4f→4f transitions have been identified, and it has been established that the magnetic dipole transitions dominate in the secondary emission spectra. Analysis of magneto-optical research data has demonstrated that the C-term of magneto-optical activity plays a significant role in the mechanism underlying the occurrence of magneto-optical effects in luminescence bands caused by "forbidden" 4f→4f transitions. A comparative analysis of the dispersion dependence of the Verdet constant of the $Na_{0.375}Tb_{0.625}F_{2.25}$ single crystal showed that it is about 90% of the Verdet constant of the well-known $Tb_3Ga_5O_{12}$ crystal, which demonstrates a good magneto-optical properties of the new synthesized crystal.
Keywords: *Fluoride crystals; Rare-earth ions; Magneto-optical properties; Luminescence; Energy levels; Magnetic circular polarization; Verdet constant*
PACS: 71.70.Ej; 78.20.Ls

INTRODUCTION

Single crystals of inorganic fluorides have long been used as optical materials with high transparency within a wide range of wavelengths from vacuum UV to mid-IR. Scintillators made from alkaline and alkaline earth fluorides are also well known. Until recently, they were simple compounds like CaF_2, LiF, BaF_2, MgF_2, LaF_3 and some others doped with activator-ions such as rare earth elements and some 3d elements [1,2]. The new field of quantum electronics required new active media with qualitatively other laser parameters differed from those of commercial CaF_2 and BaF_2 [3,4]. A worldwide search for laser crystals began among which metal fluorides became the leading materials. A main idea of obtaining qualitatively new materials was to move from single-component metal fluoride crystals to multi-component ones (in basic composition, with no activator). This approach to the problem of new fluoride materials has provided significant advances in the field of inorganic material science, which later expanded the boundaries of quantum electronics. Currently, there is a need for new scintillators for high-energy physics and related fields. New areas of application of highly transparent optical media require crystalline matrices with better mechanical, chemical, thermal properties, as well as better radiation stability and absorption of γ-rays, etc. Moreover, it has become necessary to control luminescence and other functional characteristics mainly determined by a type of activator ions and by crystalline matrices as well.

Rare-earth fluorides having the fluorite structure $Na_{0.5-x}R_{0.5+x}F_{2+2x}$ and rare earth ion activators attract great attention due to the possibility of obtaining highly concentrated (in contrast to glasses) media with high optical transparency, low melting point and low refractive indices as compared to oxide crystals [3-5]. The properties of these materials are determine by an electronic structure of the rare-earth impurity centers, which is largely determined by the crystal field acting on the rare earth ion. When doped, the rare-earth ion R^{3+} replaces a metal cation in the fluorite structure, which causes distortion of the crystal lattice near the impurity. It seems relevant to study a crystal structure of the rare-earth impurity centers, since the main contribution to the crystal field of a rare-earth ion is made by its neighboring environment.

Materials doped with rare-earth ions (RE) are key elements of modern devices for generating, transmitting and controlling optical signals. On the basis of glassy and crystalline matrices doped with rare-earth ions the effective solid-state lasers, fiber lasers and amplifiers, radiation visualizers, etc. have been created [6]. The variety of optical effects observed in such media has determined the undying interest in rare-earth ions for more than 50 years. As for magneto-optical properties, the search for paramagnetic crystals with effective Faraday rotation has been conducted for many years among various materials [7]. For oxides, the rare-earth garnets crystals containing Tb^{3+} ions (primarily, terbium gallium garnet $Tb_3Ga_5O_{12}$) were found, having wide practical application in Faraday insulators and gates for various laser devices [8,9]. A lot of Faradaic paramagnetic media contain the rare-earth elements (REE) as active ions. However, most REE ions in crystals have intense absorption bands and, as a result, small transparency ranges within the near ultraviolet (UV), visible and infrared (IR) ranges, which complicates their practical use. Taking into account the need to ensure high optical transparency of rare-earth crystals, the choice is reduced to practically a few ions (Tb^{3+}, Pr^{3+} и Ce^{3+}) with high magneto-

Cite as: M.E. Malysheva, R.R. Vildanov, T. Akhmadjanov, V.O. Pelenovich, F.K. Turotov, O.Z. Sultonov, S.R. Reymbaeva, East Eur. J. Phys. 2, 162 (2026), https://doi.org/10.26565/2312-4334-2026-2-16

optical efficiency and transparency over a wide spectral range [9]. The previously studied anisotropic fluoride crystals ($LiTbF_4$, KTb_3F_{10}, $Ca_{1-x}Tb_xF_{2+x}$ ($0.03 < x \leq 0.32$), etc.) are inferior in magneto-optical characteristics to $Tb_3Ga_5O_{12}$ crystals, because the application of anisotropic materials is associated with precise orientation of the optical axis, since in directions that do not coincide with the optical crystal axis the Faraday effect is significantly complicated by conventional birefringence. Thus, the study of the magneto-optical properties of a new isotropic cubic-syngony crystal with the fluorite structure $Na_{0.5-x}R_{0.5+x}F_{2+2x}$ and increased concentration of terbium ions is an urgent and topical task since this makes it possible to expand the range of fluoride cubic crystals with good magneto-optical properties.

The use of $Na_{0.375}Tb_{0.625}F_{2.25}$ crystals in practical applications requires a detailed study of their optical and magneto-optical properties, which will contribute to a deep understanding of the fundamental features of the magneto-optics of RE ions in fluoride crystals. Therefore, a motivating factor of this work was a detailed analysis of the experimental data of optical (absorption, luminescence) and differential methods of magneto-optical studies, including magnetic circular dichroism - MCD and magnetic circular polarization of luminescence - MCPL, to be carried on over the visible spectral range with the samples of $Na_{0.375}Tb_{0.625}F_{2.25}$ crystals.

MATERIALS AND METHODS

The object of the study was $Na_{0.375}Tb_{0.625}F_{2.25}$ crystals of the fluorite type. The cubic phases crystallizing in the fluorite structural type are formed in binary fluoride systems MF_m–TbF_3 (M = Na, K, Ca, Sr, Ba, Cd, Pb) [10]. In the NaF–RF_3 systems, the fluorite phases $Na_{0.5-x}R_{0.5+x}F_{2+2x}$ contain >50 mol.% of RE. The $Na_{0.5-x}R_{0.5+x}F_{2+2x}$ crystals was grown by the Bridgman method at the Institute of Crystallography (Russia).

The absorption and fluorescence spectra were obtained with a high-resolution diffraction monochromator MDR-23 (LOMO, Russia). The wavelength range in the absorption experiments was within 220 nm - 700 nm with an average instrumental resolution of 0.03 nm. Since the scattering at the sample was negligible, the absorption value is represented as a dimensionless Absorbance, which is the common logarithm of the ratio of incident to transmitted radiant power through a material. The luminescence spectra were measured upon excitation by a mercury lamp with a UV filter, the average instrumental resolution was 0.05 nm. The spectra was registered with photomultiplier by using the method of stabilization of the average photocurrent when scanning along the entire line shape.

The optical spectra were recorded at 90 and 300 K. For low-temperature measurements, the crystal was attached to the cold finger of a Dewar flask filled with liquid nitrogen (78 K). In a magneto-optical experiment performed with the MDR-23 monochromator, natural (completely unpolarized) UV radiation was projected onto the sample located in a longitudinal (relative to light propagation) outer magnetic field H. The UV radiation (240-400 nm) was used to excite the luminescence of sample in the visible spectral range, and the MCPL degree spectra were measured at the emission band associated with the 4f→4f transitions. The circularity degree P of partially polarized radiation is determined by the ratio: $P = \frac{I_+ - I_-}{I_+ + I_-}$, where $I_\pm$ are the intensities of two orthogonally polarized circular light components [11]. The values of P were measured by a method of radiation polarization modulation with a photoelastic modulator [12]. The relative error of the measured values of P and luminescence intensity in the experiments $I = \frac{1}{2}(I_+ + I_-)$ did not exceed ~ 5%.

RESULTS AND DISCUSSION

The optical absorption spectra of the fluoride crystal $Na_{0.375}Tb_{0.625}F_{2.25}$ were studied within the spectral range of 220-500 nm for temperature of T = 90 K and 300 K. The absorption spectra of the crystal under study within the visible and ultraviolet spectral ranges are presented in Fig. 1.

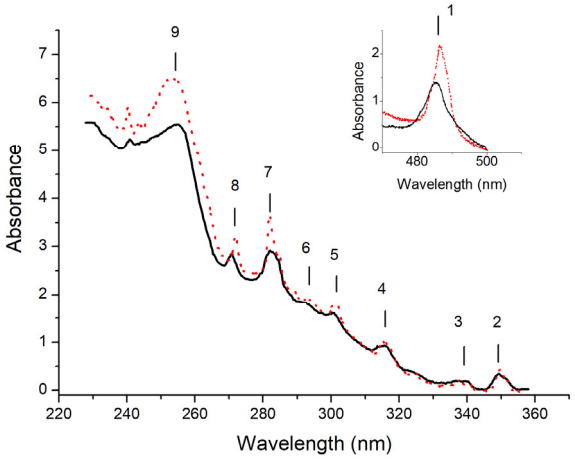

Figure 1. The optical absorption spectra of the $Na_{0.375}Tb_{0.625}F_{2.25}$ crystal at temperature of 300 K (solid line) and 90 K (dotted line).

As a result of the analysis of the obtained data, the intense absorption bands of $Na_{0.375}Tb_{0.625}F_{2.25}$ were found within the UV spectral range, as well as an absorption band at 485.5 nm (Fig. 1, inset). The presence of this absorption band is apparently associated with intra-configurational 4f→4f transitions between the sublevels of the ground multiplet $^7F_6$ and

the excited multiplet $^5D_4$ of Tb^{3+} ions in $Na_{0.375}Tb_{0.625}F_{2.25}$, which is confirmed by the results of optical absorption measurements of this crystal at $T = 90$ K. It is clearly seen from Fig. 1 that when the temperature decreases to 90 K, the amplitude of absorption line 1 increases by almost 1.6 times with its simultaneous narrowing by ~2,8 nm. At the same time, the band itself shifts to the long-wave side by ~1,3 nm. Observed within the UV spectral range above 270 nm, absorption lines 2-8 can be attributed to intra-configurational transitions $^7F_6 \rightarrow {}^5D_4$ of the Tb^{3+} ions in $Na_{0.375}Tb_{0.625}F_{2.25}$. The significant value of the width of line 9 observed within the UV absorption band at a wavelength of 253.6 nm, as well as the sufficiently large value of the absorption coefficient ~32.5 cm^{-1} (at the low concentration of RE ions) measured at the maximum of this band indicate that it can be related to the allowed (by spin and by parity) electric dipole (ED) transitions occurring from the ground multiplet $^7F_6$ to the lower levels of the "mixed" excited $4f^7 5d$ configuration of the Tb^{3+} ion in the structure of $Na_{0.375}Tb_{0.625}F_{2.25}$.

The luminescence bands of the $Na_{0.375}Tb_{0.625}F_{2.25}$ crystal caused by intra-configuration transitions $^5D_4 \rightarrow {}^7F_5$ and $^5D_4 \rightarrow {}^7F_4$ at temperature of 300 K are presented in Fig. 2 within the spectral range of wavelengths from 480 to 600 nm. From the analysis of this spectral dependence, it is seen that the most intense luminescence band is located within the wavelength range from 535 to 560 nm. For the "green" luminescence band (Fig. 3) due to intra-configuration transitions $^5D_4 \rightarrow {}^7F_5$, a decrease in the sample temperature from 300 K to 90 K is accompanied by an increase in the intensity of the luminescence line 1 (~540,8 nm) along with a simultaneous narrowing of this line and a decrease in the luminescence line 2 (~544,5 nm). The redistribution of the luminescence line intensity is due to a sharp decrease in the populations of excited Stark singlets of the $^5D_4$ multiplet when temperature decreases. Such temperature behavior of the emission line intensity near ~544 nm clearly indicates that it is associated with a radiative transition from the lowest (in energy) excited state of the $^5D_4$ multiplet.

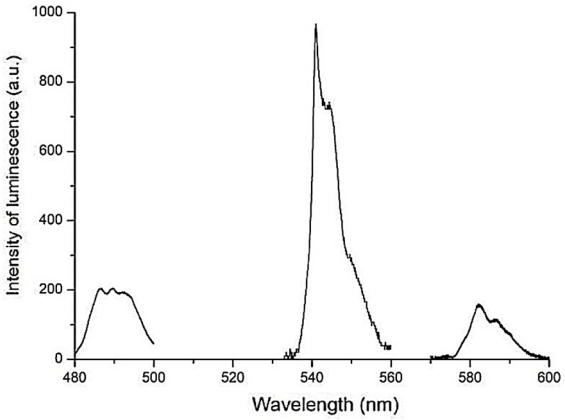

Figure 2. The luminescence spectra of the $Na_{0.375}Tb_{0.625}F_{2.25}$ crystal, recorded at the temperature of 300 K

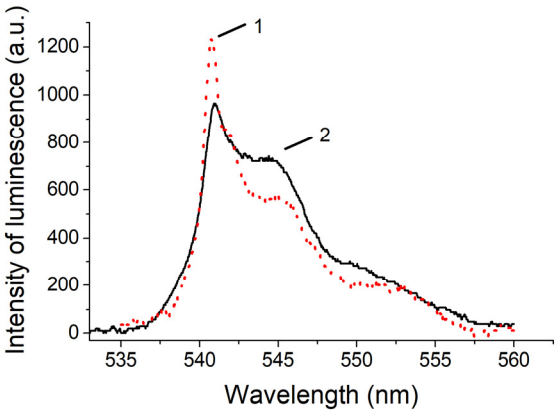

Figure 3. The spectra of the "green" luminescence band of the $Na_{0.375}Tb_{0.625}F_{2.25}$crystal, recorded at the temperature of 90 K (dotted line) and 300 K (solid line)

A comparison of the energies of the experimentally observed emission lines 1,2,3 and 4 with the theoretical scheme of the energy levels of the ground $4f^{(8)}$ configuration of the Tb^{3+} RE ions in the crystal field (CF) of O_h symmetry [13] makes it possible to identify the radiative 4f→4f transitions in the luminescence band $^5D_4 \rightarrow {}^7F_5$ and $^5D_4 \rightarrow {}^7F_4$ (Fig. 4).

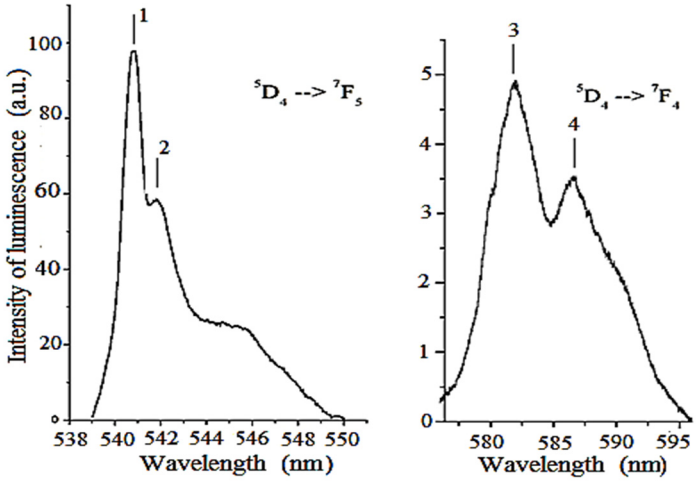

Figure 4. The luminescence spectra of the $Na_{0.375}Tb_{0.625}F_{2.25}$ crystal, recorded at the temperature of 78 K on transitions $^5D_4 \rightarrow {}^7F_5$ and $^5D_4 \rightarrow {}^7F_4$

From the scheme of radiative transitions shown in Fig. 5 it follows that the lines 1,2 and 4 are associated with magnetic dipole optical 4f→4f transitions occurring from the sublevels A_1g, T_2g (for lines 1 and 2) and Eg (for line 4) of the excited multiplet $^5D_4$ (the designations of the levels are given in accordance with [14]) to the sublevel T_1g (for lines 1 and 2) of the $^7F_5$ multiplet and the sublevel Eg (for line 4) of the $^7F_4$ multiplet. Line 3 corresponds to the electric dipole transition from the sublevel T_2g of the $^5D_4$ multiplet to the sublevel A_1g of the $^7F_4$ multiplet. The spectra of the MCPL degree recorded in an outer magnetic field $H = 10$ kOe at $T = 300$ K for the radiative 4f→4f transitions on the fluorescence band $^5D_4 \rightarrow {}^7F_4$ and $^5D_4 \rightarrow {}^7F_5$ are shown in Fig. 6 and Fig. 7, respectively.

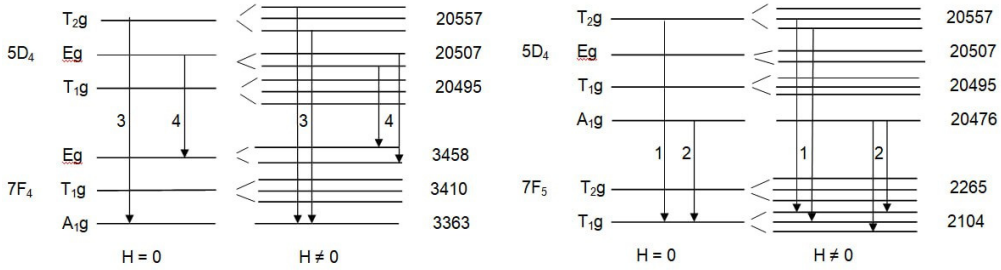

Figure 5. The scheme of the radiative transitions 4f →4f on the fluorescence band $^5D_4 \rightarrow {}^7F_4$ and $^5D_4 \rightarrow {}^7F_5$.

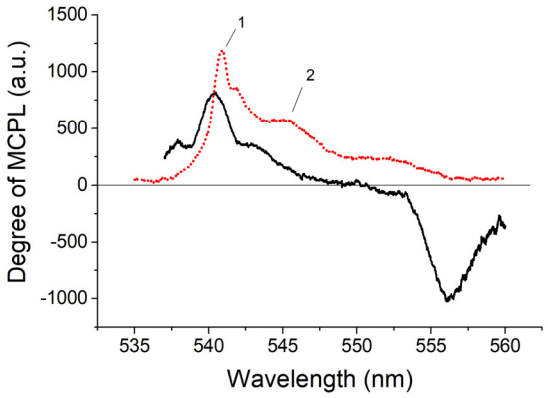

Figure 6. The MCPL degree spectrum (solid line) and the luminescence spectrum (dotted line) of the $Na_{0.375}Tb_{0.625}F_{2.25}$ crystal for the $^5D_4 \rightarrow {}^7F_5$ transition at $T = 300$ K and $H = 10$ kOe

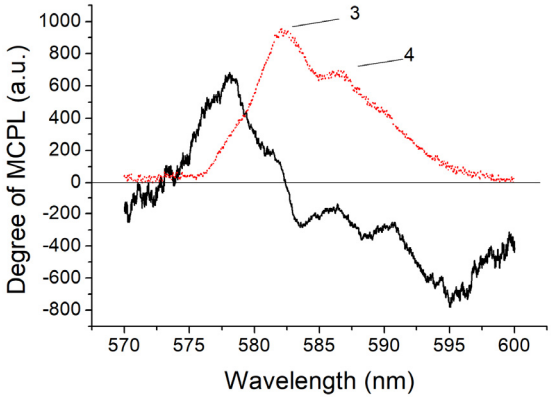

Figure 7. The MCPL degree spectrum (solid line) and the luminescence spectrum (dotted line) of the $Na_{0.375}Tb_{0.625}F_{2.25}$ crystal for the $^5D_4 \rightarrow {}^7F_4$ transition at $T = 300$ K and $H = 10$ kOe

A characteristic structure of the MCPL degree spectrum for closely spaced secondary emission lines 1 and 2, 3 and 4 can be formed by superimposing the linear dependences $P(n)$ with the corresponding luminescence lines in the areas when they pass through zero both at the maxima of the luminescence lines (A-term) and at the point shifted from the maximum of the emission band [15]. This behavior of the spectral dependences of the MCPL degree is characteristic of non-Kramers (with the even number of electrons of the unfilled 4f shell) and Kramers (with the odd number of electrons) ions in RE crystals and can be described by the following expression [16,17]:

$$P = \frac{I_+ - I_-}{I_+ + I_-} = \frac{1}{2}\mu_B H\left[\frac{(\nu-\nu_0)}{\Gamma^2}\cdot\frac{A}{D_2} + \frac{1}{kT}\cdot\frac{C}{D_1}\right] \quad (1)$$

where ν is the wave number (in cm^{-1}), Γ is the width of the luminescence line, D_1 and D_2 are the "dipole transition forces" expressed through the matrix elements of the corresponding emission transitions [17]:

$$D_1 = \frac{1}{4}[|\langle a|\hat{D}_x|j\rangle|^2 + |\langle a|\hat{D}_y|j\rangle|^2 + |\langle b|\hat{D}_x|j\rangle|^2 + |\langle b|\hat{D}_y|j\rangle|^2] \quad (2)$$

$$D_2 = \frac{1}{2}[|\langle a|\hat{D}_x|j\rangle|^2 + |\langle a|\hat{D}_y|j\rangle|^2 + |\langle a|\hat{D}_x|k\rangle|^2 + |\langle a|\hat{D}_y|k\rangle|^2] \quad (3)$$

where $\langle a|$, $\langle b|$ and $|j\rangle$, $|k\rangle$ are the wave functions of the Stark sublevels of the initial and final states of the optical transition, respectively. The first term in equation (1) determines the temperature-independent "diamagnetic" contribution to the MCPL degree of the RE ion (the A-term of MCPL [16,17]) due to the Zeeman splitting of the sublevels of the final state of the transition under the action of the outer magnetic field. The second term describes the contribution of the "paramagnetic" C-term of the MCPL degree, which depends on temperature [16,17] and on difference in the sublevel population of the initial state of the transition in the outer field. The inclined linear spectral dependence of the MCPL degree described by equation (1) is shifted from the line center by a value of the "paramagnetic" shift that determines the amplitude of the C-term of the MCPL degree [16,18].

A detailed analysis of the MCPL degree spectrum in Fig. 6 showed that in the magnetic field at the luminescence line 1 there is a magneto-optical transition due to a transition between the sublevels of the T_2g triplet of the $^5D_4$ multiplet to those of the T_1g triplet of the $^7F_5$ (*C*-term) multiplet (Fig. 5). The inclined linear dependence within the luminescence line 2 (Fig. 6) in the magnetic field is formed by means of a transition from the singlet state A_1g of the $^5D_4$ multiplet to the sublevels of the T_1g triplet of the $^7F_5$ multiplet (*A*-term) (Fig. 5). The inclined linear dependences of the MCPL degree on luminescence lines 3 and 4 (Fig. 7) also indicate the manifestation of the *C*-term of magneto-optical activity, which corresponds to transitions from the sublevels of the T_2g triplet and the Eg doublet of the $^5D_4$ multiplet (Fig. 5) to the split sublevels of the $^7F_4$ multiplet in the magnetic field. Analysis of the dispersion dependences of the MCPL degree for temperatures of 90 K and 300 K showed a significant increase in the effect with a decrease in temperature (Fig. 8), which indicates a significant contribution of the temperature-dependent paramagnetic *C*-term to this magneto-optical effect.

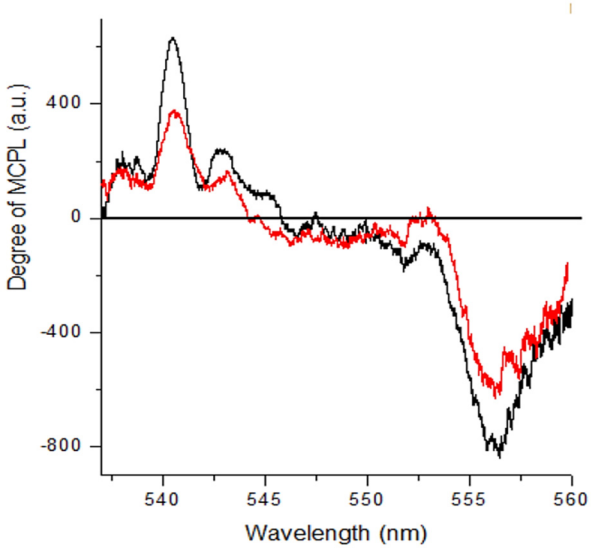

Figure 8. The MCPL degree spectra of the $Na_{0.375}Tb_{0.625}F_{2.25}$ crystal for the $^5D_4 \rightarrow {}^7F_4$ transition at $T = 300$ K (red line) and $T = 90$ K (black line) and $H = 7$ kOe.

The Faraday effect of the Tb^{3+} ion in the $Na_{0.375}Tb_{0.625}F_{2.25}$ structure was studied within the wavelength range from 400 to 700 nm at a temperature of 95 K. Fig. 9 shows this measured dispersion dependence of the Verdet constant. For comparison, the Verdet constant of the well-known terbium gallium garnet $Tb_3Ga_5O_{12}$ is also presented. A comparative analysis shows that for short wavelengths, the Verdet constant of the $Na_{0.375}Tb_{0.625}F_{2.25}$ crystal is about 85% of that of the $Tb_3Ga_5O_{12}$ crystal, and at long wavelengths, it is more than 90% [10].

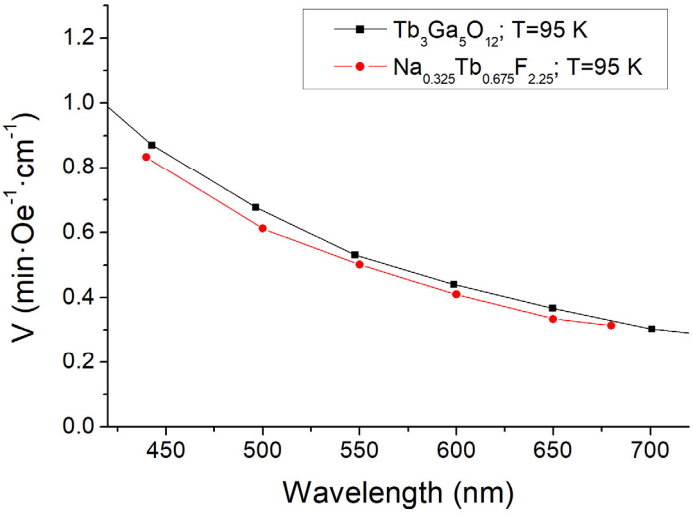

Figure 9. The dispersion dependence of the Faraday effect for the $Na_{0.375}Tb_{0.625}F_{2.25}$ and $Tb_3Ga_5O_{12}$ crystals at temperature 95 K in the magnetic field of 10 kOe.

Thus, it can be concluded that an increase in the Tb^{3+} ions concentration to $1.456 \cdot 10^{22}$ cm^{-3} in $Na_{0.375}Tb_{0.625}F_{2.25}$ crystal affects to the growth of the magneto-optical Faraday effect in a new synthesized crystal with a fluorite structure, which expands the possibilities of using this crystal under study as an analogue of terbium gallium garnet.

CONCLUSIONS

Based on the analysis of the optical spectra of the $Na_{0.375}Tb_{0.625}F_{2.25}$ single crystal it has been established that within the wavelength range of 535-560 nm there is a more intensive luminescence band caused by intra-configuration 4f→4f transitions $^5D_4 \rightarrow {}^7F_5$. Analysis of the absorption and luminescence spectra allowed us to identify the radiative 4f→4f transitions in the luminescence bands $^5D_4 \rightarrow {}^7F_5$ and $^5D_4 \rightarrow {}^7F_4$ and to establish a dominance of the magnetic dipole transitions in the secondary emission spectra. The experimentally found values of the energy levels is in agreement with the theoretical calculations of the energy levels found for the rare earth Tb^{3+} ion in a crystal environment of O_h symmetry.

Analysis of the magneto-optical research data shows that the *C*-term of the magneto-optical activity plays a significant role in a mechanism of occurrence of magneto-optical effects on luminescence bands caused by "forbidden" 4f→4f transitions.

The results of the Faraday effect study showed that the Verdet constant of the $Na_{0.375}Tb_{0.625}F_{2.25}$ single crystal is about 0.9 of the Verdet constant of $Tb_3Ga_5O_{12}$ crystal, which demonstrates the good magneto-optical properties of the new synthesized crystal and expands the range of fluoride cubic crystals with good magneto-optical features.

ORCID

M.E. Malysheva, https://orcid.org/0000-0002-4626-7398; **R.R. Vildanov**, https://orcid.org/0000-0001-5334-9909
T. Akhmadjanov, https://orcid.org/0000-0002-6484-1226; **V.O. Pelenovich**, https://orcid.org/0000-0001-8663-3543
F.K. Turotov, https://orcid.org/0000-0001-9008-4815; **O.Z. Sultonov,** https://orcid.org/0000-0002-1375-3955
S.R. Reymbaeva, https://orcid.org/0009-0003-5684-3509

REFERENCES

[1] M.J. Weber, "Faraday Rotator Materials For Laser Systems," in: *Proc. SPIE 0681, Laser and Nonlinear Optical materials*, (1987), https://doi.org/10.1117/12.939622
[2] V. Vasyliev, E. G. Víllora, Y. Sugahara, and K. Shimamura, "Judd-Ofelt analysis and emission quantum efficiency of Tb-fluoride single crystals $LiTbF_4$ and $Tb_{0.81}Ca_{0.19}F_{2.81}$," J. Appl. Phys. **113**, 203508 (2013). https://doi.org/10.1063/1.4807649
[3] Zh. Zhang**,** Zh. Wu**,** Zh. Zhang**,** L. Su**,** A. Wu**,** and Y. Li, "Characteristics and Recent Development of Fluoride Magneto-Optical Crystals," Magnetochemistry, **9**(2), 41 (2023). https://doi.org/10.3390/magnetochemistry9020041
[4] A. Cemmi, A. Colangeli, B. Dorsi, I. Di Sarcina, E. Diociaiuti, S. Fiore, D. Paesani, *et al*. "Radiation study of Lead Fluoride crystals," Journal of Instrumentation, **17**, (2022). https://doi.org/10.1088/1748-0221/17/05/T05015
[5] S. Kalusniak, E. Castellano-Hernández, H. Yalçinoğlu,·H. Tanaka,·and Ch. Kränke, "Spectroscopic properties of Tb^{3+} as an ion for visible lasers," Applied Physics B, **128**, 33 (2022). https://doi.org/10.1007/s00340-022-07759-1
[6] R.E. Thoma, H. Insley, and G.M. Hebert, "The Sodium Fluoride-Lanthanide Trifluoride Systems," Inorganic Chemistry, **5**(7), 1222-1229 (1966). https://doi.org/10.1021/ic50041a032
[7] K. Shimamura, H. Sato, A. Bensalah, V. Sudesh, H. Machida, N. Sarukura, and T. Fukuda, "Crystal Growth of Fluorides for Optical Applications," Crystal Research and Technology, **36**(8-10), 801-813 (2001). https://doi.org/10.1002/1521-4079(200110)36:8/10<801::AID-CRAT801>3.0.CO;2-6
[8] M. Ben Sassi, S. Kaddeche, M. Lappa, S. Millet, D. Henry, and H. Ben Hadid, "On the effect of thermodiffusion on solute segregation during the growth of semiconductor materials by the vertical Bridgman method," J. Cryst. Growth, **458**, 154-165 (2017). https://doi.org/10.1016/j.jcrysgro.2016.09.043
[9] K. Seevakan, and S. Bharanidharan, "Different types of crystal growth methods," International Journal of Pure and Applied Mathematics, **119**(12), 5743-5758 (2018).
[10] Yuui Yokota, Takahiko Horiai, and Masao Yoshino, *Inorganic Scintillator and Crystal Growth Methods* (Wiley-VCH GmbH, 2024). https://doi.org/10.1002/9783527842025
[11] K. Shimamura, H. Sato, A. Bensalah, V. Sudesh, H. Machida, N. Sarukura, and T. Fukuda. Crystal Growth of Fluorides for Optical Applications, **36** (8-10), 801-813 (2001). https://doi.org/10.1002/1521-4079(200110)36:8/10<801::AID-CRAT801>3.0.CO;2-6
[12] J.P. Riehl, and F.S. Richardson, "General theory of circularly polarized emission and magnetic circularly polarized emission from molecular systems," J. Chem. Phys. **65**, 1011–1021 (1976). https://doi.org/10.1063/1.433177
[13] D.N. Karimov, B.P. Sobolev, I.A. Ivanov, S.I. Kanorsky, and A.V. Masalov, "Growth and magneto-optical properties of $Na_{0.37}Tb_{0.63}F_{2.26}$ cubic single crystal," Crystallography reports, **59**(5), 780 (2014). http://dx.doi.org/10.1134/S1063774514050083
[14] F. Zhang, S. Golovynskyi, O.I. Datsenko, Zh. Wang, P. Wang, J. Luo, V.M. Kravchenko, *et al*. "Photoluminescence thermometry using broadband multi-peak detection in Eu^{2+}/Eu^{3+}-codoped oxygen-rich AlN film," Optical Materials, **149**, 115095 (2024). https://doi.org/10.1016/j.optmat.2024.115095
[15] C. Görller-Walrand, and L. Fluyt, *Handbook on the Physics and Chemistry of Rare-Earths* (North-Holland, Amsterdam, 2010). 40(244), p.107.
[16] F.K. Turotov, M.E. Malysheva, and R.R. Vildanov, "Magneto-Optics Features of Radiation Transitions of Non-Kramers Tm^{3+} Ion in Yttrium-Aluminum Garnet Crystals," East European Journal of Physics, (4), 341-348 (2024). https://doi.org/10.26565/2312-4334-2024-4-39
[17] P. Solarz, M. Głowacki, R. Lisiecki, M. Sobczyk, J. Komar, B. Macalik, and W. Ryba-Romanowski, "Impact of temperature on excitation, emission and cross-relaxation processes of terbium ions in GGAG single crystal," Journal of Alloys and Compounds, **789**, 409-415 (2019). https://doi.org/10.1016/j.jallcom.2019.03.087
[18] U.V. Valiev, J.B. Gruber, and G.W. Burdick, *Magnetooptical Spectroscopy of the Rare-Earth Compounds: Development and Application*, (Scientific Research Publishing, 2012).

ОПТИЧНІ ТА МАГНІТООПТИЧНІ ВЛАСТИВОСТІ КРИСТАЛА $Na_{0.375}Tb_{0.625}F_{2.25}$

М.Є. Малишева[1], Р.Р. Вільданов[1], Т. Ахмаджанов[1], В.О. Пеленович[2], Ф.К. Туротов[1], О.З. Султонов[1], С.Р. Реймбаєва[1]

[1]Національний університет Узбекистану, Ташкент, 100174, Узбекистан

[2]Інститут технологічних наук Уханьського університету, Ухань, 430072, Китай

Оптичні та магнітооптичні спектри кристала $Na_{0,375}Tb_{0,625}F_{2,25}$ були досліджені в ультрафіолетовому та видимому спектральному діапазонах. Встановлено, що в діапазоні довжин хвиль 535-560 нм спостерігається інтенсивна смуга люмінесценції, спричинена внутрішніми конфігураційними переходами 4f→4f $^5D_4 \rightarrow {}^7F_5$. У смузі люмінесценції $^5D_4 \rightarrow {}^7F_5$ та $^5D_4 \rightarrow {}^7F_4$ ідентифіковані радіаційні переходи 4f→4f та встановлено, що у спектрах вторинного випромінювання домінують магнітні дипольні переходи. Аналіз даних магнітооптичних досліджень показав, що C-член магнітооптичної активності відіграє значну роль у механізмі виникнення магнітооптичних ефектів на смугах люмінесценції, спричинених «забороненими» переходами 4f→4f. Порівняльний аналіз дисперсійної залежності константи Верде монокристала $Na_{0,375}Tb_{0,625}F_{2,25}$ показав, що вона становить близько 90% від константи Верде добре відомого кристала $Tb_3Ga_5O_{12}$, що демонструє хороші магнітооптичні властивості нового синтезованого кристала.

Ключові слова: *кристали фториду; іони рідкісноземельних елементів; магнітооптичні властивості; люмінесценція; енергетичні рівні; магнітна кругова поляризація; стала Верде*

EAST EUROPEAN JOURNAL OF PHYSICS. 2. 169-178 (2026)
DOI:10.26565/2312-4334-2026-2-17 ISSN 2312-4334

DFT INVESTIGATION OF ELECTRONIC, ELASTIC, AND TRANSPORT PROPERTIES, AND EVALUATION OF LATTICE THERMAL CONDUCTIVITY OF THE HALF-HEUSLER ALLOY RuAsNb

Aziza Boutouta[1], Amor Bouaricha[2,5], F. Zenikheri[3,7], Zeyneb Bordjiba[4], Rabie Amraoui[3,4], Salim Kadri[5,6], Walid Bendjeddou[6], Salah Aguib[6]

[1]*Center of Research in Mechanics CRM, Po. Box 73 B, 25021, Constantine, Algeria*
[2]*University of Ghardaia Scientific Zone, PO Box 455, Ghardaia, 47000, Algeria*
[3]*Higher Normal School of Technological Education, Skikda, 21000, Algeria*
[4]*Material Physics Laboratory - L2PM, 8 May 1945 University of Guelma, Algeria*
[5]*Industrial Mechanics Laboratory (LMI), Badji Mokhtar—Annaba University, P.O. Box 12, Annaba, 23000, Algeria*
[6]*Dynamic of Engines and Vibroacoustic Laboratory (LDMV), University of M'hamed Bouguerra, Boumerds, 35000, Algeria*
[7]*Laboratory of the Active Components and Materials, Larbi Ben M'Hidi University, Oum El Bouaghi, 04000, Algeria*
**Corresponding Author email: amraoui.rabie@yahoo.com*
Received September 25, 2025; revised April 28, 2026; accepted May 8, 2026

In this study, we employed the Full-Potential Linearized Augmented Plane Wave (FP-LAPW) method, as implemented in Wien2k, to perform a comprehensive investigation of the structural, electronic, and thermoelectric properties of RuAsNb. The electronic band structure was calculated using the TB-mBJ exchange-correlation potential, resulting in an energy gap that is in close agreement with the available experimental data. Furthermore, our analysis revealed favorable optical properties, highlighting the material's potential for applications across the infrared, visible, and ultraviolet regions of the electromagnetic spectrum. We also evaluated the thermoelectric performance of RuAsNb by analyzing key parameters, including the Seebeck coefficient, electrical conductivity, thermal conductivity, and power factor. The results indicate that holes are the dominant charge carriers, confirming the p-type semiconducting nature of RuAsNb. In addition, the effect of chemical potential variations on these thermoelectric properties was examined, providing valuable insights into their temperature-dependent behavior. To ensure the robustness of our findings, a comparative study using different exchange–correlation potentials was conducted, which further validated the consistency of the results. The promising thermoelectric performance of RuAsNb suggests its suitability as a potential candidate for next-generation energy conversion devices and photovoltaic applications. Moreover, the estimation of the lattice thermal conductivity using the Slack model reinforces the reliability of our predictions and provides valuable insights for future research. Overall, this work contributes to a deeper understanding of the potential of RuAsNb in advanced energy materials.
Keywords: *Half Heusler; DFT; Structural property; Anisotropic; Optical properties; Figure of merit*
PACS: 71.15.Mb; 71.20.-b; 71.55.Ak; 72.20.Pa

1. INTRODUCTION

Currently, scientists place paramount importance on thermoelectric performance due to its ability to directly convert waste thermal energy into clean and non-polluting electrical energy **[1]**. This growing interest is driven by the depletion of fossil fuel reserves and the significant environmental impacts associated with their widespread use. Consequently, the search for new thermoelectric materials has become a major priority in the development of alternative energy resources.

Among the materials investigated for this purpose are Half-Heusler (HH) compounds, a class of materials distinguished by several attractive physical properties, including elastic stability, high melting temperature, a high thermoelectric power factor, a favorable figure of merit, and stable thermal behavior.

In recent years, Half-Heusler (HH) compounds have attracted considerable attention due to their excellent thermoelectric performance and low thermal conductivity. In our recent study, we focused on Half-Heusler compounds containing X elements such as Co, Rh, and Ir, combined with MnAs **[1]**. To characterize these compounds, we employed Density Functional Theory (DFT), a powerful method for modeling material properties. Using DFT, we systematically investigated the structural, elastic, thermal, and transport properties of these compounds. This comprehensive approach provided in-depth insights into their physical behavior, laying the foundation for a better understanding of their thermoelectric performance.

In this new study, our focus has shifted to the Half-Heusler compound RuAsNb, which has been mentioned in previous works, although these studies did not investigate the parameters we address. For instance, Zhenzhen Feng *et al.* **[2]** examined a set of 75 Half-Heusler-type compounds, using electronic structure as a criterion for identifying promising thermoelectric materials. This approach enabled the exploration of a wide range of compounds and the assessment of their potential based on their electronic structure characteristics.

The same authors, Zhenzhen Feng *et al.* **[3]**, conducted another noteworthy study in which they explored the concept of resonance in stoichiometrically ordered Half-Heusler compounds. They employed first-principles phonon calculations and thermal conductivity analyses to identify materials exhibiting low thermal conductivity.

Cite as: A. Boutouta, A. Bouaricha, F. Zenikheri, Z. Bordjiba, R. Amraoui, S. Kadri, W. Bendjeddou, S. Aguib, East Eur. J. Phys. 2, 169 (2026), https://doi.org/10.26565/2312-4334-2026-2-17

A more recent contribution was reported by Fatiha Cherifi *et al.* **[4]**, entitled *"Thermoelectric transport parameters of p-type RuVAs and RuNbAs Heusler alloys."* In this work, the authors successfully characterized the semiconducting nature of both RuVAs and RuNbAs. They also presented the electronic band structures and calculated the elastic constants. However, they did not evaluate several essential mechanical parameters required for a comprehensive understanding of these compounds, such as the bulk modulus, shear modulus, Young's modulus, Poisson's ratio, hardness, Zener anisotropy factor, Cauchy pressure, and the Pugh ratio. These parameters constitute the core of our research objectives.

The aim of this study is to conduct a comprehensive investigation of the structural, elastic, and thermoelectric properties of the RuAsNb compound using *ab initio* calculations. We evaluate the elastic stability of this material and determine a comprehensive set of mechanical parameters to gain deeper insight into its intrinsic behavior. By employing the BoltzTraP code, we solve the Boltzmann transport equation to analyze the material's transport properties. This approach enables the detailed evaluation of key parameters such as the Seebeck coefficient, as well as the electronic contributions to electrical and thermal conductivities.

These parameters are essential for a thorough understanding of the thermoelectric performance of the compound, particularly in terms of the power factor and the figure of merit, which are critical indicators of its efficiency in converting thermal energy into electrical energy. Furthermore, we apply the Slack model to investigate the temperature dependence of lattice thermal conductivity—an aspect not previously addressed particularly in the work of Fatiha Cherifi et al. [4], where only the ambient-temperature value was reported.

In addition, while Fatiha Cherifi *et al.* **[4]** limited their analysis to thermoelectric properties as a function of temperature. Our approach goes further by presenting detailed variations in thermoelectric performance as a function of chemical potential over a wide range of temperatures. This provides a deeper and more comprehensive understanding of the material's transport behavior.

2. COMPUTATIONAL METHOD

We employed the WIEN2k software **[5]** to calculate the electronic structure of the cubic-phase RuAsNb compound within the framework of Density Functional Theory (DFT) **[6].** The full-potential linearized augmented plane wave (FP-LAPW) method was used in conjunction with the generalized gradient approximation in the Wu–Cohen scheme (GGA-WC) for the exchange–correlation energy. A total of 3000 k-points were used for integration over the irreducible Brillouin zone, with a plane-wave cutoff parameter of RKmax=8RK.

Using the eigenvalues and eigenvectors obtained at these k-points, further analyses were performed. The Half-Heusler compound RuAsNb crystallizes in the cubic C_{1b} structure, as illustrated in Figure 1. In this structure, the Ru atom occupies the 4a site (0.25, 0.25, 0.25), the As atom occupies the 4b site (0.5, 0.5, 0.5), and the Nb atom occupies the 4c site (0, 0, 0), according to the Wyckoff positions **[7].**

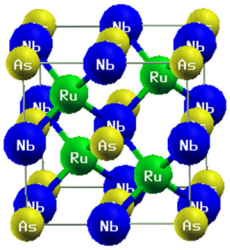

Figure 1. Computed crystal structure of RuAsNb

3. RESULTS AND DISCUSSION

3.1. Electronic Band Structures and Density of State (DOS)

The electronic band structures of the RuAsNb compound, calculated using the generalized gradient approximation (GGA-PBE), are displayed in Figure 2, providing a detailed analysis along the symmetry directions. It is evident that this compound exhibits semiconductor behavior with a direct band gap **[8].** The calculated band energies are offering essential quantitative values for evaluating its electronic properties. The computed bandgap is found to be 0.23 eV and indirect in nature. Additionally, we observe a notably flat valence band, which suggests a significant effective mass for the charge carriers. This characteristic is advantageous for thermoelectric performance, as it facilitates improved carrier mobility.

To further elucidate the electronic structure of the compound under study, we calculated both the total density of states (DOS) and the partial density of states (PDOS). These results are presented in Figure 2 (b) covering an energy range from -10 to 10 eV. The PDOS plot for RuAsNb indicates that the lowest valence states in the range of -10 to -7.5 eV primarily originate from the As-p states, with a very minimal contribution from the other atoms present in the compound. Figure 2(b) illustrates the total and partial electronic density of states for RuAsNb. It is clear that the valence band, located between -2 and -5.90 eV, is predominantly composed of Ru-d states, with a contribution from Nb-d states. The Ru-d states are particularly dominant near the Fermi level, while the contribution from As-p states remains minimal. In contrast, the conduction band in the range of 0 to 5 eV is mainly dominated by Nb-d states, with a lesser contribution from Ru-d states **[9].** The As-p states exhibit very little participation in this energy range, although the contributions from all three

atomic states become more balanced in the conduction band between 5 and 9 eV. Overall, the high electronic density of states near the Fermi level in this compound suggests a significant potential for a large Seebeck coefficient, thereby suggesting a high thermoelectric power factor. These findings will be further explored in the subsequent subsection, where we will discuss the implications of these electronic characteristics on the thermoelectric performance of RuAsNb.

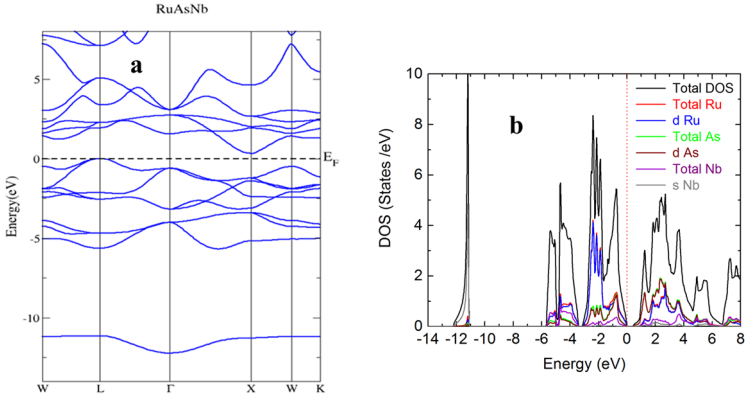

Figure 2. (a) Computed band structure of RuAsNb (b) density of states for RuAsNb

3.2. Elastic properties

The objective of analyzing the mechanical behavior of a new material is to understand its response to solicitations. It is clear that, in physics, elasticity is the property of a solid material to regain its original shape after being deformed. The elastic constants of the RuAsNb alloy were calculated using the Thomas Charpin method **[10],** implemented in the Wien2k code. We will compare our results with those of Fatiha Cherifi et al **[10].** It is noteworthy that the calculated elastic constants adhere to the Born-Huang criteria for mechanical stability **[11]:** $C_{44} > 0$, $C_{11} - C_{12} > 0$, $C_{11} + 2\,C_{12} > 0$, and C_{12} must be less than C_{11}.

To describe the mechanical behavior of these materials based on the *Cij* constants, elastic parameters such as the shear modulus G, Young's modulus E and Poisson's ratio ν are evaluated using the Voigt-Reuss-Hill approximation **[12]** at pressure $P = 0$, where the indices R and V for the compressibility modulus and shear modulus are associated with the Voigt and Reuss approximations, respectively. For cubic systems, these elastic parameters are calculated using the following expressions:

$$B = \frac{C_{11}+2.C_{12}}{3}, \tag{1}$$

$$G = \frac{G_V+G_R}{2}, \tag{2}$$

$$G_V = \frac{(C_{11}-C_{12}+3.C_{44})}{5}, \tag{3}$$

$$G_R = \frac{5.C_{44}(C_{11}-C_{12})}{4.C_{44}+3(C_{11}-C_{12})}, \tag{4}$$

$$E = \frac{9.B.G}{(3.B+G)}, \tag{5}$$

$$\nu = \frac{3.B-E}{6.B}. \tag{6}$$

We observe that these constants satisfy the cubic stability condition, i.e., $C_{12} < B < C_{11}$, confirming that this alloy is elastically stable.

The results obtained for this compound are given in Table 1, and we note the absence of theoretical values from the literature. The bulk modulus B provides indications about the hardness of the material; the larger it is, the harder the material. The compressibility module value for this Half-Heusler compound is high ($B > 30\ GPa$), indicating low compressibility **[13]**. Therefore, this alloy can be classified as relatively hard, capable of withstanding changes in volume and shape under ambient conditions. We observe that the shear modulus of the studied alloy is lower than the bulk modulus, suggesting that this alloy exhibits higher resistance to volumetric compression than to shape change.

We can differentiate the brittleness and ductility of a material based on the Pugh ratio (B/G) **[13]**, Thus, if ($B/G > 1.75$), the material is ductile; otherwise, if ($B/G < 1.75$), the material is hard and brittle. According to Table 1, the value of this ratio is greater than 1.75, so we can consider that our alloy is ductile. The Young's modulus E is an indicator of a material's stiffness. The higher the Young's modulus for a given material, the stiffer it is. This property measures a material's ability to resist elastic deformation under applied stress, providing crucial insights into its structural strength

and response to mechanical stress. The obtained value of Young's modulus *E* is relatively high, demonstrating the rigid characteristic of our studied alloy.

We can also assess the hardness of this alloy, as it is a mechanical property that provides information about the plasticity, elasticity, and strength of materials. In our study, we adopted the Vickers microhardness model using the following expression provided by Tian et al **[14]**:

$$H_V = 0.92 \cdot \left(\frac{G}{B}\right)^{1,137} \cdot G^{0,703}. \quad (7)$$

In conclusion, based on Table 1, we observe that the studied material exhibits favorable hardness characteristics, making it a suitable choice for small electronic or mechanical components.

The knowledge of elastic constants has also allowed us to deduce other mechanical quantities, such as anisotropy A , Cauchy coefficient CP and melting temperature.

The Zener anisotropy factor measures the degree of anisotropy in solids. A material is considered completely isotropic if $A=1$, while any value below or above "1" indicates the anisotropy of the material. It is determined by the following relation **[15]:**

$$A = {}^{2.C_{44}}/_{(C_{11}-C_{12})}. \quad (8)$$

In our compounds, a Zener anisotropy factor different from 1 implies that the compound is anisotropic. We also know that when is close to 1, it indicates maximum stiffness along the <111> cube diagonal, which is the case for our compound.

Determining the Cauchy pressure (*CP*) is used to assess the nature of atomic bonding in metals and compounds, whether they exhibit brittle or ductile characteristics **[16].**

$$CP = C_{12} - C_{44}. \quad (9)$$

For our alloy, the Cauchy pressure has a positive value, indicating the ductile and metallic nature of our material. We have also calculated the melting temperature from the elastic constants using the following equation **[17]**:

$$T_m(K) = [553 + (5.911) \cdot C_{12}] \mp 300 \quad (10)$$

The Debye temperature (θD) provides essential insights into the properties of a solid material in response to temperature, being linked to the upper limit of phonon frequencies. The calculation of the Debye temperature using elastic constants is a reliable process, based on the following equation **[16, 17]:**

$$\theta_D = \frac{h}{k_B}\left[\frac{3}{4.\pi}\left(\frac{N_A.\rho}{M}\right)\right]^{\frac{1}{3}} \mathrm{V}_m \quad (11)$$

Where N_a is the Avogadro number; *M* is molar mass; ρ is the density; h is the Planck constant and k_B is Boltzmann constant. V_m is the sound mean velocity given by:

$$\mathrm{V}_m = \left[\frac{1}{3}\left(\frac{2}{V_t^3} + \frac{1}{V_l^3}\right)\right]^{-\frac{1}{3}}. \quad (12)$$

Where: $V_l = \left(\frac{3B+4G}{3\rho}\right)^{\frac{1}{2}}$, $V_t = \left(\frac{G}{\rho}\right)^{\frac{1}{2}}$ represent the longitudinal sound velocity, and the transverse sound propagation velocity, respectively.

The results of the elastic parameters and behavior of this compound are mentioned below in Table 1.

Table 1. elastic constants (C_{11},C_{12} ,C_{44}) GPa, Bulk Modulus (B) GPa, Shear Modulus (G) GPa, Young Modulus (E) GPa, Poisson ratio (ν), (B/G) Ratio, Micro Hardness (H), The Anisotropy A , Cauchy Coefficient CP , Melting Temperature (T_m) in °K, Debye temperature (θ_D) in °K

RuAsNb	C_{11}	C_{12}	C_{44}	B	G	E	ν	B/G	H	A	CP	$T_m \pm 300$	θ_D
This work	268.5	172.6	116.5	204.56	89.06	233.33	0.34	2.29	8.39	2.429	56.1	1573.23	388.61
Other work [4]	250.951	158.761	96.734	-	-	-	-	-	-	-	-	-	-

The study of the elastic properties of three-dimensional (3D) surfaces provides a clear visualization and a comprehensive explanation of the anisotropic behavior of mechanical modules.

The dependence on the crystallographic direction of the bulk modulus *B*, Young's modulus *E* and shear modulus *G* is calculated using the following expressions **[15]**:

$$\begin{cases} \frac{1}{B} = (S_{11} + 2.S_{12})(l_1^2 + l_2^2 + l_3^2) \\ \frac{1}{E} = S_{11} - 2.\left(S_{11} - S_{12} - \frac{1}{2}S_{44}\right)(l_1^2 l_2^2 + l_2^2 l_3^2 + l_3^2 l_1^2) \\ \frac{1}{G} = S_{44} - 4\left(S_{11} - S_{12} - \frac{1}{2}S_{44}\right)(sin^2\theta \cdot cos^2\theta + 0.125sin^4)(1 - cos4\varphi) \end{cases} \quad (13)$$

There S_{ij} are the elements of the matrix of elastic compliance constants, which are obtained from the inverse of the matrix of elastic constants; ($S_{ij} = C_{ij}^{-1}$), and l_1, l_2, l_3 are the direction cosines along the x, y, and z axes. We found the S_{ij} respectively: $S_{11} = 0.00749$, $S_{12} = -0.00293$, $S_{44} = 0.00859$

The ideal spherical shape of the 3D directional dependence is associated with the isotropic nature of the material, while the non-spherical shape reflects anisotropy. The 3D surfaces with their 2D projections of different planes [100], [010], and [001] for the compressibility modulus, Young's modulus, and shear modulus of the RuAsNb compound are illustrated in Figures 3, 4, and 5, respectively.

According to Figure 3, the compressibility module exhibits a perfect spherical shape in three dimensions (3D), suggesting isotropic behavior for the studied alloy. According to Figures 4 and 5, a significant deviation from the spherical shape can be observed for the shear modulus and Young's modulus, highlighting a significant degree of anisotropy in the shear modulus. In Figures 3, 4, and 5, the 2D projections of the compressibility modulus *B*, Young's modulus *E*, and shear modulus *G* on the (100), (010), and (001) planes exhibit an isotropic character for *B* and a pronounced anisotropic behavior for *G* compared to *E*.

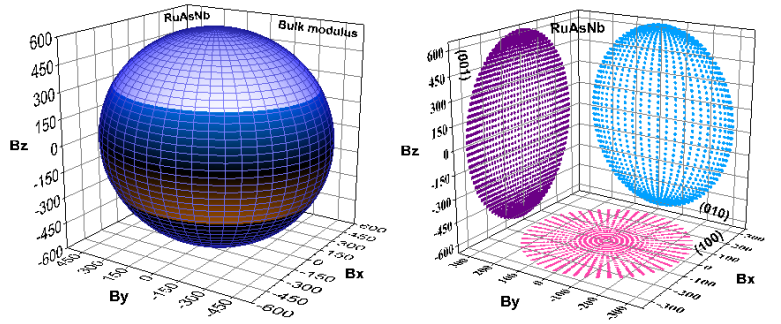

Figure 3. 3D illustration of the bulk modulus, and 2D surface projections on the planes (100), (010), and (001) for the compound RuAsNb

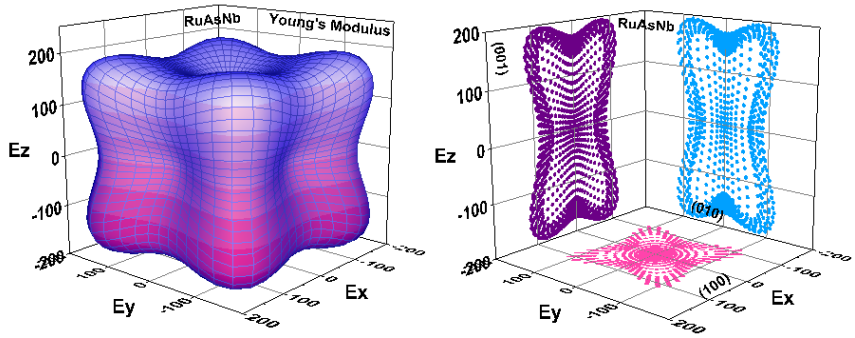

Figure 4. 3D illustration of the Young's modulus, and 2D surface projections on the planes (100), (010), and (001) for the compound RuAsNb

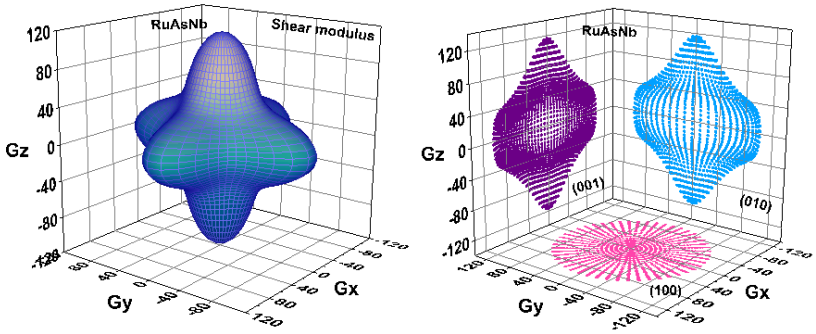

Figure 5. 3D illustration of the shear modulus and 2D surface projections on the planes (100), (010), and (001) for the compound

3.3. Thermoelectric Properties and lattice Thermal Conductivity

We conducted a comprehensive assessment of the thermoelectric properties using semiclassical Boltzmann transport theory within the constant-scattering-time approximation, as implemented in the BoltzTraP code.This approach, grounded in Boltzmann theory **[18],** provides a detailed and accurate perspective on the thermoelectric response of the considered system. The determination of electronic transport properties, including electrical conductivity, Seebeck coefficient, and electronic thermal conductivity, involves using calculated band structures as inputs for the BoltzTraP package **[19].**

For this section, we utilized the band structure calculated using the WC-GGA approximation to compute the thermoelectric properties of the compound RuAsNb.

We will now express the Seebeck coefficient, electrical conductivity, and the electronic transport tensors of thermal conductivity as follows **[20,21]:**

$$S_{\alpha\beta}(T,\mu)=\frac{1}{e\cdot T\cdot\sigma_{\alpha\beta}(T,\mu)}\int\sigma_{\alpha\beta}(\in)\cdot(\in-\mu)^2\left[-\frac{\partial f_0(T,\in,\mu)}{\partial\in}\right], \tag{14}$$

$$\sigma_{\alpha\beta}=\frac{1}{\Omega}\int\sigma_{\alpha\beta}(\in)\left[-\frac{\partial f_0(T,\in,\mu)}{\partial\in}\right]\cdot d\in, \tag{15}$$

$$k^0_{\alpha\beta}(T,\mu)=\frac{1}{e^2\cdot T\cdot.\Omega}\int\sigma_{\alpha\beta}(\in)\cdot(\in-\mu)^2\left[-\frac{\partial f_0(T,\in,\mu)}{\partial\in}\right]\cdot d\in, \tag{16}$$

Where e is the electron charge, Ω is the reciprocal space volume, is the bearer energy, f is the Fermi distribution function, μ is the chemical potential, and T is the absolute temperature.

The conductivity tensor $\sigma_{\alpha\beta}(\in)$ in terms of energy and electronic thermal conductivity k is expressed as:

$$\sigma_{\alpha\beta}(\in)=\frac{1}{N}\sum_{i,k}\sigma_{\alpha\beta}(i,k)\frac{\delta(\in-\in_{i,k})}{d\in}. \tag{17}$$

Where N is the number of k-points.

It is evident within the realm of semiconductor materials that in a p-type semiconductor, the majority charge carriers are identified as holes, while the minority carriers consist of electrons. Conversely, in an n-type semiconductor, electrons are the majority charge carriers, whereas holes are minority carriers. **[22].** This fundamental distinction between the two types of semiconductors underscores the importance of understanding the nature of dominant charge carriers, which is crucial for comprehending the electronic properties and conduction behavior of these materials. In Figure 6, we have depicted the variation of the Seebeck coefficient as a function of chemical potential ranging from [considered as the carrier concentration for the alloys] at different constant temperatures (300, 600, and 900 °K) for our alloy **[23].**

The negative characteristic of the Seebeck coefficient (S) indicates n-type conduction, with electrons as the main charge carriers. Conversely, the positive sign of S implies p-type conduction, with holes as the majority charge carriers.

In this compound, the optimal values of the Seebeck coefficient (S) are observed around the Fermi energy (Ef). Indeed, S is inversely proportional to electrical conductivity, and in this energy range, conduction is intrinsic, resulting in low electrical conductivity. These optimal values tend to decrease as the temperature (T) increases.

Furthermore, it is observed that for this compound, when the value of S is positive, it indicates that the conduction is of P-type. Therefore, this semi-Heusler compound is a p-type semiconductor, as confirmed in the work of Zhenzhen Feng et al **[3]** and also by Fatiha Cherifi et al **[4].**

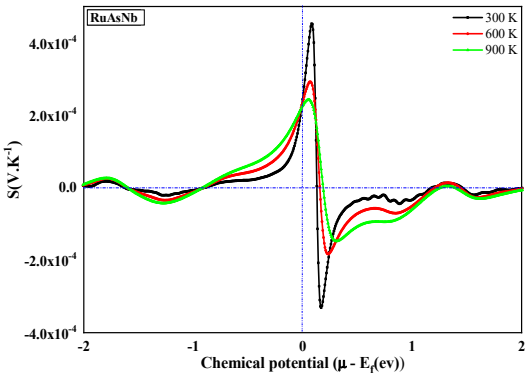

Figure 6. Seebeck coefficient S as a function of chemical potential μ

Figure 7 illustrates the variation of electrical conductivity as a function of chemical potential $\mu-E_F=\pm 2eV$ at different temperatures (300°K, 600°K, and 900°K). This curve highlights that the effect of temperature on electrical conductivity is negligible.

Regarding electronic thermal conductivity, Figure 8 clearly shows that an increase in temperature leads to a marked rise in the electronic thermal conductivity of our compound. Furthermore, the electronic thermal conductivity curve exhibits a shape similar to that of the electrical conductivity curve, suggesting that charge carriers also play a crucial role as heat carriers **[24].**

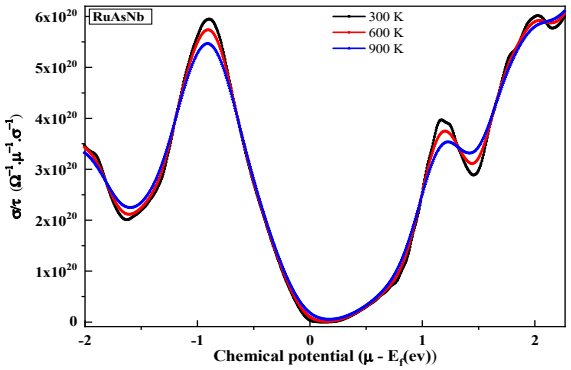

Figure 7. Electrical conductivity σ / τ as a function of chemical potential μ

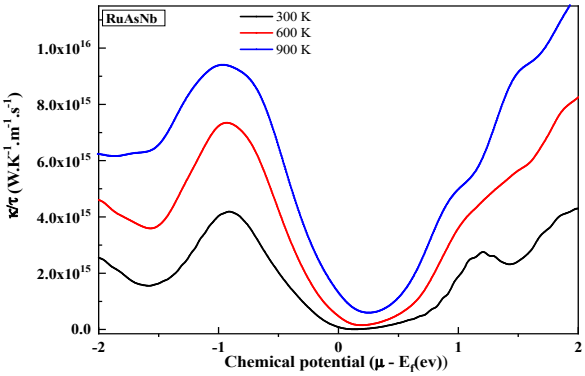

Figure 8. Electronic thermal conductivity k / τ as a function of chemical potential μ

The performance of a thermoelectric material is assessed using a dimensionless parameter called the figure of merit, denoted as *ZT*. This quantifies the enhancement of the thermoelectric performance of a material and can be calculated using the following formula **[25,26]**:

$$ZT = \frac{S^2 \cdot \sigma}{k_e + k_l} \cdot T \,. \tag{18}$$

Where: T the absolute temperature, S is the Seebeck coefficient, σ s the electrical conductivity, k_e is the electronic thermal conductivity, and k_l is the lattice thermal conductivity.

We calculated the variation of the figure of merit ZT as a function of chemical potential over an extended temperature range to assess if the system can maintain favorable thermoelectric performance even at elevated temperatures. A figure of merit ZT equal to or greater than unity indicates excellent transport properties.

In Figure 9, *ZT* is maximal at a temperature of 300 K only at the peaks, but as soon as *ZT* starts to decline, the values at the highest temperature (900 K) dominate compared to the temperature of 300 K.

The values of the figure of merit associated with the Half Heusler RuAsNb are attributed to their low levels of electrical conductivity, combined with their high thermal conductivity. The value *ZT* of the compound is approximately 0.869 at ambient temperature.

In Figure 10, depicting the power factor as a function of chemical potential, an increase in *PF* is observed with the rise in temperature, reaching a maximum value at T=900°C. Two peaks of high intensity are also notable, with one being a primary peak near the Fermi level boundary, having a value of 1.2973×1012 W K^2/ms.

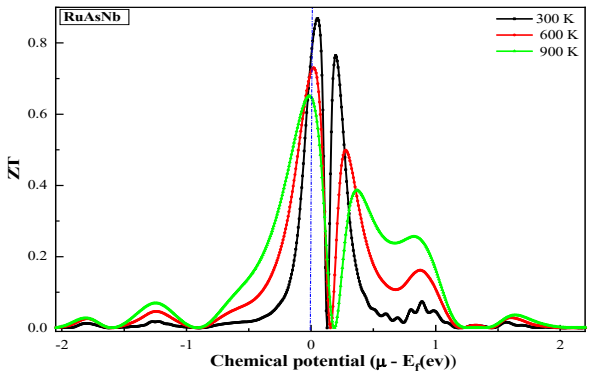

Figure 9. The merit factor, (ZT) as a function of the chemical potential μ

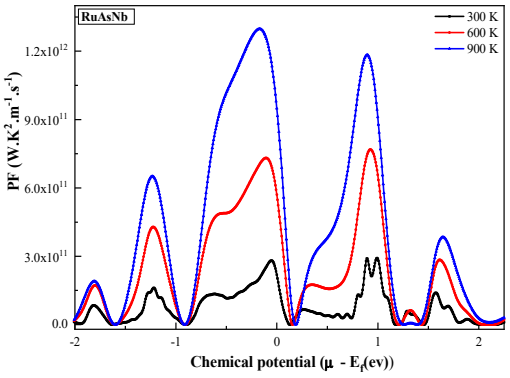

Figure 10. The power factor (*PF*) as a function of the chemical potential μ

The lattice thermal conductivity (k_l) of this compound is determined using Slack method **[27]**. The lattice thermal conductivity is given as:

$$k_l = A \cdot \frac{M \cdot \theta_D^3 \cdot \delta}{\gamma \cdot n^{\frac{2}{3}} \cdot T} \,. \tag{19}$$

Where n is the number of atoms in the primitive unit cell, δ^3 is volume per atom, θ_D is the Debye temperature M is the average mass of atoms, T is an absolute temperature, γ is Grüneisen parameter. The constant A is collection of physical constants, which is determined as:

$$A = \frac{5.20 \cdot 0.847 \cdot 10^7}{2.\left[1 - \left(\frac{0.514}{\gamma}\right) + \left(\frac{0.228}{\gamma^2}\right)\right]}. \tag{20}$$

Further γ is calculated using Poison ratio ν by using following formula

$$\gamma = \frac{3 \cdot (1+\nu)}{2 \cdot (2-3\nu)}. \tag{21}$$

The thermal conductivity of the lattice in this compound varies with temperature, as shown in Figure 11. An increase in temperature leads to a decrease in the thermal conductivity of this material. At 300 K, the lattice thermal conductivity of RuAsNb is 35.01 $W \cdot K^{-1} \cdot m^{-1}$. Comparing our value to the one calculated by Fatiha Cherifi et al. **[4],** which is 15.2 $W \cdot K^{-1} \cdot m^{-1}$, our value is significantly higher, approaching nearly twice that of the latter

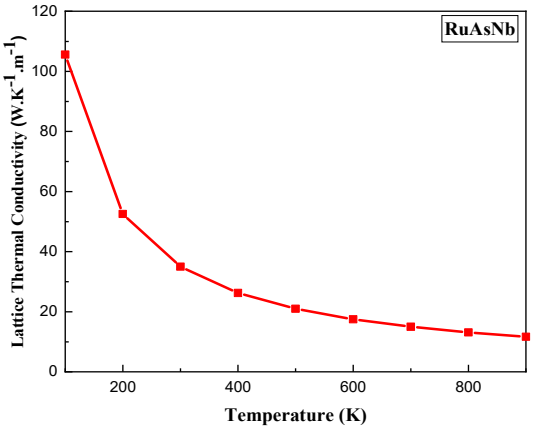

Figure 11. The variation of lattice thermal conductivity as function of temperature for RuAsNb

4. CONCLUSIONS

In this investigation, we employed the Full-Potential Linearized Augmented Plane Wave (FP-LAPW) method, as implemented in the WIEN2k software, to thoroughly investigate the structural, electronic, optical, and thermoelectric properties of the RuAsNb compound. By utilizing the TB-mBJ potential, we calculated the electronic band structure, which revealed an energy gap consistent with experimental observations.

Our analysis highlighted the material's advantageous optical properties, suggesting its potential applicability across the infrared, visible, and ultraviolet regions of the electromagnetic spectrum. Furthermore, we assessed the thermoelectric characteristics of RuAsNb, focusing on key parameters such as the Seebeck coefficient, as well as electrical and thermal conductivities, and the power factor. Notably, our findings confirmed that holes are the dominant charge carriers, establishing RuAsNb as a p-type semiconductor.

We also explored the influence of variations in chemical potential on the thermoelectric properties, providing valuable insights into their temperature-dependent behavior. To enhance the robustness of our conclusions, we conducted a comparative analysis across various exchange–correlation potentials. The promising optical and thermoelectric properties of RuAsNb underscore its potential as a candidate for next-generation energy devices and photovoltaic applications. Collectively, these findings contribute significantly to the understanding of the applicability of RuAsNb in advanced materials for energy conversion technologies.

ORCID

Amraoui Rabie, https://orcid.org/0000-0001-9256-488X

REFERENCES

[1] S. Kadri, T. Mohamed, B. Mahièddine, A. Rabie, and B. Zeyneb, "Study of Structural, Elastic, Thermal and Transport Properties of Ternary X(X=Co, Rh and Ir)MnAs Obtained by DFT," East European Journal of Physics, (1), 47–57 (2022). https://doi.org/10.26565/2312-4334-2022-1-07

[2] Z. Feng, Y. Fu, P. Aditya, Y. Zhang, and D.J. Singh, "Electronic Structure as a Guide in Screening for Potential Thermoelectrics: Demonstration for Half-Heusler Compounds," Physical Review, **100**(8), 085202 (2019). https://doi.org/10.1103/PhysRevB.100.085202

[3] Z. Feng, Y. Fu, Y. Zhang, and D.J. Singh, "Characterization of Rattling in Relation to Thermal Conductivity: Ordered Half-Heusler Semiconductors," Physical Review, **101**(6), 064301 (2020). https://doi.org/10.1103/PhysRevB.101.064301
[4] F. Cherifi, Z. Mostefa, A. Boukra, Z.F. Meghoufel, M. Bouattou, F.K. Allah, and F. Terki, "Thermoelectric Transport Parameters of P-Type RuVAs and RuNbAs Heusler Alloys," Physica Status Solidi (b), basic solid state physics, **257**(12), 2000271 (2020). https://doi.org/10.1002/pssb.202000271
[5] P. Blaha, K. Schwarz, G.K.H. Madsen, D. Kvasnicka, J. Luitz, R. Laskowski, F. Tran, *et al*., *WIEN2k: An Augmented Plane Wave Plus Local Orbitals Program for Calculating Crystal Properties*, (Techn. Universitat, Vienna, 2019).
[6] W. Kohn, and L.J. Sham, "Self-Consistent Equations Including Exchange and Correlation Effects," Physical Review Journals Archive, **140**(4A), 1133–1138 (1965). https://doi.org/10.1103/PhysRev. 140.A1133
[7] F.D. Murnaghan, "The Compressibility of Media under Extreme Pressures," Physics, **30**(9) 244–247 (1944). https://doi.org/10.1073/pnas.30.9.244
[8] S. Bouaricha, R. Kadrib, A. Amraoui, A. Boumaza, M. Belkhiri, F.E.Z. Tourab, D. Rahmaoui, *et al*., "DFT Calculation of Physical Properties for Performance Comparison of Electrothermal Actuators Made of Polysilicon and FeAsNb Alloy," Physics of the Solid State, **67**(9), 821-834 (2025). https://doi.org/10.26565/2312-4334-2022-1-07
[9] D. Behera, B. Akila, R. Amraoui, S. Kadri, S.K. Mukherjee, M.M. Salah, and A. Saeed, "Excellent Thermoelectric Performance in KBaTh (Th = Sb, Bi) Based Half-Heusler Compounds and Design of Actuator for Efficient and Sustainable Energy Harvesting Applications," Crystals, **13**(11), 1551 (2023). https://doi.org/10.3390/cryst13111551
[10] F. Tran, and P. Blaha, "Accurate Band Gaps of Semiconductors and Insulators with a Semilocal Exchange-Correlation Potential," Physical Review Letters, **102**(226401), 1–3 (2009). https://doi.org/10.1103/PhysRevLett.102.226401
[11] M. Born, and K. Huang, *Dynamical Theory of Crystal Lattices*, (Clarendon Press Publication, Oxford, 1998); R.Hill, "The Elastic Behaviour of a Crystalline Aggregate," Proceedings of the Physical Society. Section A, **65**(5), 349–354 (1952). https://doi.org/10.1088/0370-1298/65/5/307
[12] S. Pugh, "XCII. Relations between the elastic moduli and the plastic properties of polycrystalline pure metals," The London, Edinburgh, and Dublin Philosophical Magazine and Journal of Science, **45**(367), 823–843 (1954). https://doi.org/10.1080/14786440808520496
[13] Y. Tian, B. Xu, Z. Zhao, "Microscopic Theory of Hardness and Design of Novel Superhard Crystals," International Journal of Refractory Metals and Hard Materials, **33**, 93–106 (2012). https://doi.org/10.1016/j.ijrmhm.2012.02.021
[14] V. Razumovskiy, E. Isaev, A. Ruban, and P. Korzhavyi, "Ab initio calculations of elastic properties of Pt–Sc alloys," Intermetallics, **16**(8), 982–986 (2008). https://doi.org/10.1016/j.intermet.2008.04.016
[15] N. Arıkan, A. İyigör, A. Candan, Ş. Uğur, Z. Charifi, H. Baaziz, and G. Uğur, "Electronic and phonon properties of the full-Heusler alloys X2YAl (X = Co, Fe and Y = Cr, Sc): a density functional theory study," Journal of Materials Science, **49**, 4180-4190 (2014). https://doi.org/10.1007/s10853-014-8113-7
[16] H. Inaba, and T. Yamamoto, "Debye Temperature of Materials," Netsu Sokutei, **10**, 132–145 (1983).
[17] E. Bringuier, "The Boltzmann equation and relaxation-time approximation for electron transport in solids," European Journal of Physics, **40**, 1–33 (2019). https://doi.org/10.1088/1361-6404/aaf5f0
[18] G.K.H. Madsen, and D.J. Singh, "BoltzTraP. A code for calculating band-structure dependent quantities," Computer Physics Communications, **175**(1), 67–71 (2006). https://doi.org/10.1016/j.cpc.2006.03.007
[19] G. Snyder, in: *CRC Handbook of Thermoelectrics*, edited by D.M. Rowe, (CRC Press, Boca Raton, 2006). p. 144.
[20] B. Lenoir, *Thermoélectricité: des principes aux applications*, (Transport, 1990). pp. 1–19.
[21] X. Zhang, and J. Xia, "Approaches to design inorganic semiconductors while maintaining structural motifs," Journal of Semiconductors, **39**(7), 1 (2018). https://doi.org/10.1088/1674-4926/39/7/071002
[22] T.J. Seebeck, *Magnetic Polarization of metals and minerals*, (Abhand. Deut. Akad. Wiss, Berlin, 1822).
[23] M.J. Winiarski, K. Bilinska, K. Ciesielski, and D. Kaczorowski, "Thermoelectric performance of p-type half-Heusler alloys ScMSb (M=Ni, Pd, Pt) by ab initio calculations," Journal of Alloys and Compounds, **762**, 901–905 (2018). https://doi.org/10.1016/j.jallcom.2018.05.257
[24] P. Taylor, and C. Wood, "Thermoelectric properties of Ag_2Te and Ag_2Se," Adv. Energy Convers. **01**, 141–145 (1961). https://doi.org/10.1016/0365-1789(61)90023-6
[25] R. Amraoui, S. Kadri, H. Meradji, M. Berkani, A. Bouaricha, S. Ghemid, A. Boumaza, *et al*., "First-principles computational study on structural, elastic, magnetic, electronic, and thermoelectric properties of Co_2MnGe: a potential Heusler ternary compound," The European Physical Journal B, **95**, 1–14 (2022). https://doi.org/10.1140/epjb/s10051-022-00466-y
[26] G.A. Slack, "The Thermal Conductivity of Nonmetallic Crystals," Solid state physics, **34**, 1–71 (1979). https://doi.org/10.1016/s0081-1947(08)60359-8

ДОСЛІДЖЕННЯ ЕЛЕКТРОННИХ, ПРУЖНИХ ТА ТРАНСПОРТНИХ ВЛАСТИВОСТЕЙ МЕТОДОМ DFT, І ОЦІНКА ҐРАТКОВОЇ ТЕПЛОПРОВІДНОСТІ НАПІВГЕЙСЛЕРОВОГО СПЛАВУ RuAsNb

Азіза Бутута[1], Амор Буаріча[2,5], Ф. Зеніхері[3,7], Зейнеб Борджиба[4], Рабі Амрауї[3,4], Салім Кадрі[5,6], Валід Бенджедду[6], Салах Агіб[6]

[1]Центр досліджень механіки CRM, По. Box 73 B, 25021, Константіна, Алжир
[2]Наукова зона Університету Гардайя, PO Box 455, Гардайя, 47000, Алжир
[3]Вища нормальна школа технологічної освіти, Скікда, 21000, Алжир
[4]Лабораторія фізики матеріалів - L2PM, Університет Гельма 8 травня 1945 р. Алжир
[5]Лабораторія промислової механіки (LMI), Баджі Мохтар — Університет Аннаба, PO Box 12, Аннаба, 23000, Алжир
[6]Лабораторія динаміки двигунів та віброакустики (LDMV), Університет М'хамеда Бугерра, Бумердс, 35000, Алжир
[7]Лабораторія активних компонентів і матеріалів, Університет Ларбі Бен М'Хіді, Ум Ель Буагі, 04000, Алжир

У цьому дослідженні ми застосували метод повнопотенціальної лінеаризованої доповненої плоскої хвилі (FP-LAPW), реалізований у Wien2k, для проведення комплексного дослідження структурних, електронних та термоелектричних властивостей RuAsNb. Електронна зонна структура була розрахована з використанням обмінно-кореляційного потенціалу

TB-mBJ, що призвело до енергетичної забороненої зони, яка добре узгоджується з наявними експериментальними даними. Крім того, наш аналіз виявив сприятливі оптичні властивості, що підкреслює потенціал матеріалу для застосування в інфрачервоному, видимому та ультрафіолетовому діапазонах електромагнітного спектру. Ми також оцінили термоелектричні характеристики RuAsNb, проаналізувавши ключові параметри, зокрема коефіцієнт Зеєбека, електропровідність, теплопровідність та коефіцієнт потужності. Результати показують, що дірки є домінуючими носіями заряду, що підтверджує напівпровідникову природу p-типу RuAsNb. Крім того, було досліджено вплив змін хімічного потенціалу на ці термоелектричні властивості, що дало цінну інформацію про їх температурно-залежну поведінку. Щоб забезпечити надійність наших висновків, було проведено порівняльне дослідження з використанням різних обмінно-кореляційних потенціалів, яке додатково підтвердило узгодженість результатів. Перспективні термоелектричні характеристики RuAsNb свідчать про його придатність як потенційного кандидата для пристроїв перетворення енергії наступного покоління та фотоелектричних застосувань. Більше того, оцінка теплопровідності решітки за допомогою моделі Слака підвищує надійність наших прогнозів та надає цінні знання для майбутніх досліджень. Загалом, ця робота сприяє глибшому розумінню потенціалу RuAsNb у передових енергетичних матеріалах.

Ключові слова: *напівгейслер; DFT; структурна властивість; анізотропія; оптичні властивості; показник якості*